The Stability of Stratified Layers within Ventilated Enclosures

Konstantinos Pikos

A Thesis submitted in partial fulfilment of the
requirements of the University of Hertfordshire
for the degree of Doctor of Philosophy

The programme of research was carried out in the Faculty of Engineering and Information Sciences, Department of Aerospace, Automotive and Design Engineering, University of Hertfordshire

October 2006

THESIS
CONTAINS
CD/DVD

Acknowledgements

I would like to thank Professor A.E. Holdø from the University of Hertfordshire, leader of the Fluid Mechanics Research Group for his support while writing my thesis. I would also like to thank Dr M.R. Malin from CHAM (Concentration Heat & Momentum Ltd. London), Technical Support Group, for helping in the compilation PHOENICS and providing feedback in our telephone conversations and emails.

I want to extend my thanks to all the technicians involved in setting up the Environmental Chamber of the University of Hertfordshire.

Special thanks also go to Dr A. Georgiou and Dr R. Dorizzi from the University of Hertfordshire, Department of Physics, Astronomy and Mathematics regarding their feedback on certain theoretical issues. Many thanks to all those remotely involved who contributed in the validation of the content of this thesis.

This work was funded by a 3-year studentship from the University of Hertfordshire.

Abstract

The project consists of experimental and numerical investigation of buoyancy-dominated flow leading to thermal stratification in ventilated spaces for the range of Re from 4,000 to 50,000 and Ri_o below 40.

In the evolution of turbulence in stratified shear flows, solving for the primitive variables both in time and space is most important. Steady-state Reynolds-Averaged Navier Stokes (RANS) simulations have shown in the past to model adequately the flows that become eventually steady-state. Therefore, three-dimensional steady-state CFD models were used to simulate the flow.

The experimental set-up used an Environmental Test Chamber to investigate the stratification in buildings. Temperature differential was created by introducing cold air through a terminal at floor level and hot air through a diffuser pointing vertically downwards at the ceiling level. An extract point was located opposite to the inlets at the rear wall. Different combinations of inlet velocities/flow rates, temperatures as well as different arrangements of the exhaust height were studied to evaluate its effect on velocity and temperature distribution and the effect of jet flow interaction with the stratified layers. The experimental data obtained in this work were also used to validate the predictions from the numerical simulations so that CFD was used to perform more parametric simulations.

To model turbulence in the flow field, the appropriateness of several eddy-viscosity based turbulence models was evaluated. The turbulence models used were the standard $k-\varepsilon$ model, the $k-\varepsilon$ Chen-Kim modified model, a Low-Re modification and the RNG $k-\varepsilon$ model. All models are in close agreement with each other. The buoyancy extended standard $k-\varepsilon$ model gives a sharper prediction of mixing in the interface. The physics of the flow are well predicted. The hot jet from the ceiling is buoyed up when it reaches the height of the interface where buoyancy forces dominate gravitational forces marking its appearance on the temperature gradient.

From the simulations made at this stage, the characteristics of stratified layers are revealed. It is also shown that the interface height is proportional to the exhaust height for certain room temperatures and velocities. In a comparison between experimental results and numerical simulation, the differences are attributed on the non-adiabatic effects such as heat losses and radiation.

A correlation is found between inlet parameters and stratified flow in buildings obtained both experimentally and computationally.

Contents

The Stability of Stratified Layers within Ventilated Enclosures i

Acknowledgements i

Abstract ii

Contents iii

Nomenclature vi

Abbreviations xii

1. INTRODUCTION 1
   1.1 Aims of the Study 3

2. THEORETICAL BACKGROUND 4
   2.1 Governing Equations of Fluid Flow 4
   2.2 Stability of Stratification 6
      2.2.1 Richardson number and Froude number 8
      2.2.2 Grashof number and Raleigh number 12
      2.2.3 Archimedes number 14
   2.3 Ventilation Methods 16
      2.3.1 Natural ventilation 18
      2.3.2 Displacement ventilation 19
      2.3.3 Mixing ventilation 22
      2.3.4 Mixed Ventilation 24
   2.4 Ventilation with Stratification 24
   2.5 Turbulent Mixing in Stratified Fluids 32
      2.5.1 Development of length scales 33
      2.5.2 Entrainment in Stratified Fluids 37
      2.5.3 Vertical heat flux 38
      2.5.4 Counter-gradient heat flux and down-gradient heat flux 38
      2.5.5 CFD modelling of gradient fluxes and differences between air and water 40
   2.6 Radiation 44
   2.7 Summary 45
   2.8 Objectives of the Work 46

3. CFD MODELLING 47
   3.1 Numerical Methods to Solve the Governing Equations 47
      3.1.1 Finite Volume Method (FVM) 48
      3.1.2 Upwind-difference scheme 49
      3.1.3 The Hybrid discretization scheme 50
      3.1.4 Pressure correction technique 51
      3.1.5 Convergence 52
      3.1.6 Relaxation 57
   3.2 Iterative Methods 59
      3.2.1 Linear solver – Stone's-like extension of TDMA 61
      3.2.2 Implicit solver - Conjugate Gradient Solver (CGR) 62

3.3 Turbulence Modelling 62
3.3.1 The Standard $k-\varepsilon$ Model 64
3.3.2 The $k-\varepsilon$ Chen & Kim Model 66
3.3.3 Non-Linear RNG $k-\varepsilon$ Model 69
3.4 Near-Wall Modelling 73
3.5 Buoyancy Extension 75
3.6 Using CFD to Solve the Problem 82
3.6.1 Modelling inlet boundary conditions 86
3.6.2 The effect of the size of the building in flow modelling 89
3.6.3 A historical development on converged solutions 91
3.6.4 The CFD modelling of turbulence and the significance of the interface 96
3.7 Scope of the work 98

4. Experimental Development and Design of CFD Model 102
4.1 Introduction 102
4.1.1 Experimental apparatus 103
4.1.2 Practical considerations 106
4.1.3 Instrumentation 114
4.1.4 Location of the experimental measurements 120
4.1.5 Accuracy of the experimental model 121
4.1.6 Measured Profiles at the Air Supply Outlets 129
4.1.6.1 Hot Air Supply Velocity Measurements 129
4.1.6.2 Cold Air Supply Velocity Measurements 132
4.1.6.3 Inlet Turbulence Intensity from Current and Published Experiments 134
4.2 CFD Model 137
4.2.1 Boundary Conditions 138
4.2.1.4 Inlet profile 138
4.2.2 Initial Conditions 138
4.2.3 Convergence 139
4.2.4 Grid Resolution 140
4.2.5 Virtual CFD model 147
4.2.6 Radiation CFD model 148
4.2.7 Air-leakage CFD model 152
4.3 Test Series 153
4.3.1 Test Series I: Experiments 154
4.3.2 Test Series II: CFD simulations 154
4.4 Program developed for the Analysis of Results 154

5. RESULTS 156
5.1 Overview of CFD Results 156
5.1.1 CFD simulations: Physical Issues (Test Series II) 157
5.2 Numerical Issues 158
5.3 CFD Results and related Physical Issues 159
5.3.1 Effect of different $k-\varepsilon$ model 160
5.3.2 Effect of exhaust-outlet height 164
5.3.3 Effect of changing inlet momentum 166
5.3.4 Effect of differential momentum 167
5.3.5 Effect of differential momentum and mixing 169
5.3.6 Increasing inlet temperature difference 171
5.3.7 Effect of buoyancy extension 173
5.3.8 Effects of emissivity – surface radiation and flow rate 174

5.3.9 Effect of air leakages 177
5.3.10 Effect of stratification on the extract flow 178
5.3.11 Modelling the hot air supply momentum effect and direction for different cold air supply rates 180
5.3.12 The 3-dimensional ceiling air diffuser – Coanda effects and outlet profile 183
5.3.13 Jet throw using the 3-dimensional ceiling air diffuser and other investigations 184
5.3.14 Virtual CFD modelling of the cold air supply diffuser 186
5.3.15 Position of the hot air supply 188
5.4 Experimental Results (Test Series I) 191
5.4.1 Low *Re* cases 191
5.4.2 High *Re* cases 194

6. DISCUSSION 196
6.1 Physical Mechanisms 196
6.1.1 Experimental results 196
6.1.2 CFD results 201
6.1.3 Low *Re* cases – formation of thermal stratification 202
6.1.4 High *Re* cases – break-up of thermal stratification 204
6.1.5 Validation with other experimental work 205
6.2 Influence of Mesh Density and Convergence 210
6.3 Choosing the Correct Turbulence Model 212
6.3.1 Performance Evaluation of K – ε Models Applied To Stratified Ventilation 212
6.3.2 Effect of interface height using CFD 215
6.3.3 Comparison with experiments 216
6.3.4 Effect of changing momentum on the thickness of the interface 219
6.3.5 Effect of differential momentum on the height of the interface 221
6.3.6 Effect of differential momentum and mixing – mixing efficiency 222
6.3.7 Increasing inlet temperature difference – ratio of buoyancy force to momentum force 223
6.4 Buoyancy Extension 224
6.5 Influence of Modelling Radiation and Conduction 228
6.6 Influence of Leakage Modelling and other losses on the Temperature Gradient 234
6.7 Further issues attempted by using the Virtual CFD Model – a quantitative comparison with transient simulations 238
6.8 Quantitative comparison of mean room temperature 245
6.9 The Influence of Inlet Parameters on the Characteristics of Stratified Flow 247
6.10 Layers in Ventilation 248
6.10.1 Cool air zone 250
6.10.2 Hot air zone 252
6.10.3 Interface zone 252
6.10.4 Test cases 255

7. CONCLUSIONS 263

8. Recommendations for Further Work 265

References 266

Appendices on the CD-ROM disk

Appendix A: Equations In The Stratification Experiments 1-5
Appendix B: Stratification Experiments 1-62
Appendix C: Statistical Analysis Of The Errors In The Experiments 1-38
Appendix D: Matlab Program 1-3
Appendix E: Paper: A Numerical Study Of Stratified Layers In Vent. Enclosures 1-10
Appendix F: Paper: A Numerical Study Of Stratified Flow 1-1
Appendix G: Paper: Studying Stratification In Ventilated Enclosures 1-1

Nomenclature

Roman Symbol

a	height or length of the cross-section of the inlet openings, half the interface height, absorption coefficient and $\left(=\dfrac{k}{\rho c_p}\right)$ laminar diffusivity of heat	[m], [m], [m^{-1}], [m^2/s]
a_{nb}	discretization coefficient of diffusion (components of) at the neighbouring cell	[-]
a_P	$\left(=\dfrac{k_P}{(\delta x)_P}\right)$ (total) discretization coefficient of thermal diffusion at point P and $\left(=\dfrac{\rho u}{2}+\dfrac{\Gamma_P}{(\delta x)_P}\right)$ momentum diffusion at point P	[$W/m^2 \cdot s$], [$kg/m^2 \cdot s$]
A	inlet area	[m^2]
ACH	$\left(=\dfrac{Q_{in} \times 3600}{V_{\text{room}}}\right)$ air changes per hour	[h^{-1}]
Ar	$\left(=\dfrac{g\beta l \Delta T}{u^2}\right)$ Archimedes number	[-]
b	is the width of the cross-section of the inlet openings	[m]
$C_\mu, C_1, C_2, C_3,$ $C_{\varepsilon 1}, C_{\varepsilon 2}, C_{\varepsilon 3}, C_{\varepsilon 4}$	empirical constants in the $k-\varepsilon$ turbulence model	[-]
c_p	specific heat capacity	[J/kg·K]
D_{hyd}	hydraulic diameter	[m]
E	wall-roughness parameter and radiosity	[-],[W/m^2]
$f_{\mu,1,2}$	Lam-Bremhorst (1981) dumping function	[-]
f_i	body forces	[N/m^3]

F_S	supply buoyancy force	[N]
g_i	gravitational vector	[N/m^3]
g'	$(\equiv (\Delta\rho/\rho)g)$ modified buoyancy term	[m/s^2]
G_B	buoyancy destruction term	[m^2/s^3]
Gr	$\left(=\dfrac{gl^3\beta\Delta T}{\nu^2}\right)$ Grashof number	[-]
H	height of room	[m]
h	heat transfer coefficient and exhaust height	[W/m$^2\cdot$K], [m]
h_E	exhaust height	[m]
k	turbulence kinetic energy and thermal conductivity	m^2/s^2, [W/m$\cdot$K]
k_P	thermal conductivity at point P	[W/m$\cdot$K]
l	arbitrary length	[m]
L	integral length scale, characteristic length, layer height	
	scalar length-scale of wall distances and room length	[m], [m], [m], [m], [m]
L'	length scale of wave fluctuations	[m]
L_b	buoyancy length scale or Brunt-Väisälä frequency	[m]
L_H	Ellison (1957) length scale	[m]
L_K	Kolmogorov (1962) length scale	[m]
L_M	Morton (1959) length scale	[m]
L_R	Ozmidov (1965) or overturning length scale	[m]
L_T	Thorpe (1977) length scale	[m]
m	mass flow rate	[kg/s]
M_S	supply momentum force	[N]
p	static pressure	[N/m^2]
P_1, P_2	curvature points	[-]
P_{int}	inflection point	[-]
Pe	$\left(=\dfrac{UL}{a}\right)$ and equivalent to $(PrRe)$, Peclet number	
	(a measure of the *bulk heat transfer* over the	

	conductive heat transfer = *advection* to *diffusion* terms)	[-]
Pr	$\left(=\frac{\mu c_p}{k} \text{ or } \frac{\nu}{a}\right)$ and equivalent to (Re/Pe), Prandtl number (the relative measure of *thermal energy dissipation* with respect to *momentum dissipation*)	[-]
P_K	shear production rate (G_K used in some literature)	[m²/s³]
Q	volumetric flow rate	[m³/s]
q	heat generation from certain modes of heat transfer	[W]
Re	$\left(=\frac{ul}{\nu}\right)$ Reynolds number (ratio of the *inertia* to *viscous* forces = *advection* to *diffusion* terms)	[-]
Re_n	Reynolds number based on the normal distance from the wall	
Ri, Ri_g	Richardson (gradient) number	[-]
Ri_o	$\left(=g\frac{\Delta\rho}{\rho}\frac{L}{\Delta U^2}\right)$ Richardson number	[-]
Ri_f	Richardson flux number	[-]
S	$(=N^2)$ stratification parameter and stratification slope	[s⁻²], [-], [-]
S_ε	dissipation source term per unit volume	[m²/s³ · m³]
S_h	heat source term per unit volume	[W/m³]
S_ϕ	source term per unit volume (for momentum or heat generation)	[/m³]
s	scattering coefficient	[m⁻¹]
t	time	[s], [°C]
T	time period and instantaneous temperature	[1/Hz], [°C]
T_3	Solved-for variable for radiative temperature	[°C]
T_o	reference temperature	[°C]
T_{HS}	temperature of hot air supply	[°C]
T_{CS}	temperature of cold air supply	[°C]
T_{ext}	external temperature	[°C]
T_{nb}	discretized temperature (or variable) at the neighbouring cell	[°C]

T_P	discretized temperature (or variable) at centre point of discretization	[°C]
T_s	radiative temperature of surface	[°C]
T_{sur}	radiative temperature of surroundings	[°C]
T^*	normalised temperature and temperature (or variable) at the previous iteration	[°C]
T^0	temperature (or variable) at the previous time-step	[°C]
T_u	$\left(=\frac{\sigma}{\bar{u}}\cdot 100\%\right)$ turbulence intensity	[-]
u,v,w	Cartesian velocity components in x-, y- and z-directions	[m/s]
U_S	supply velocity	[m/s]
U_∞	free stream velocity	[m/s]
u_i	fluid velocity components or differentiable variable	[m/s]
u'	fluctuating velocity component	[m/s]
$\bar{u}$	mean velocity component in RANS	[m/s]
u_τ	friction velocity	[m/s]
u_r	absolute value of resultant velocity parallel to the wall	[m/s]
u^+	$\left(=\frac{1}{\kappa}\ln\left(Ey^+\right)\right)$ inner variable for velocity, the logarithmic law	[-]
$\mathbf{U}_i$	column vector for velocity	[m/s]
U-value	overall heat transfer coefficient (transmittance)	[W/m$^2\cdot$K]
V	room volume	[m]
w_e	entrainment rate	[-]
W	width of room	[m]
y^+	non-dimensional distance from the wall	[-]
x	downstream distance	[m]
x_i	differentiable distance	[m]
z	vertical height	[m]
z_0	interface height	[m]

Greek Symbol

α	entrainment constant, relaxation factor	[-]
β	volume expansion coefficient and	
	a constant in the RNG $k-\varepsilon$ model	[1/K], [-]
γ	radiative conductivity term	[m]
Γ_e	total exchange coefficient	[-]
δ	interface thickness	[m]
δ_w	withdrawal layer thickness	[m]
ΔT_S	supply temperature difference	[°C]
Δu	change in velocity component	[m/s]
Δx_i	mesh size in x-, y- and z- directions	[m]
Δy	change in y-direction	[m]
ε	dissipation rate of turbulent kinetic energy	[m^2/s^3]
ε_{tr}	$\left(= 24.5\nu N^2\right)$ energy dissipation at Richardson number transition	[m^2/s^3]
ε_P	residual error at point P	[-]
η	ratio of the turbulent to mean time scale (RNG model) and	
	small displacement distance from the position of equilibrium	[-], [m]
κ	(= 0.41) von Karman constant and wave number	[-], [m^{-1}]
Λ	spectral cut-off length scale	[m]
λ	Taylor (1935) length scale and radiative conductivity	[m], [W/m·K]
μ	laminar (dynamic) viscosity	[kg/m·s]
ν	laminar (kinematic) viscosity	[m^2/s]
ρ	density	[kg/m^3]
ρ_0	reference density	[kg/m^3]
σ	standard deviation and Stefan Boltzmann constant	[-], [$W/m^2 \cdot K^4$]
$\sigma_\varepsilon, \sigma_k$	empirical constants in the $k-\varepsilon$ turbulence model	[-]
σ_t	turbulent Prandtl number	[-]
τ_w	wall shear stress in $k-\varepsilon$ model	[N/m^2]

φ	interpolation or weighting column vector function	[-]
ϕ	differentiable variable	[-]
χ	dissipation rate of heat fluctuations	$[m^2/s^3]$

Suffixes

HS	hot air supply variable
CS	cold air supply variable
i, j, k	components of tensor notation
l	heat loss variable
L	characteristic layer height
o	reference variable, overall parameter and effective inlet variable
r	radiative heat variable
rms	root-mean square
s	generic supply and sink source variable and surface variable
sur	surroundings variable
t	viscous dissipation variable and turbulence variable

Abbreviations

BC	Boundary Conditions
b.l.	Boundary layer
CL	Centre Line
CGR	Conjugate Gradient method
CS	Cold air supply
CFD	Computational Fluid Dynamics
DNS	Direct Numerical Simulation
EMISS	Emissivity parameter in radiation model
FDM	Finite Difference Method
FVM	Finite Volume Method
HiRes	High grid Resolution
HS	Hot air supply
IC	Initial Conditions
IMMERSOL	Model for radiative heat transfer
LES	Large Eddy Simulation
NS	Navier-Stokes
PD	Percentage Dissatisfied
PDE	Partial Differential Equations
P,N,S,E,W,H,L n,s,e,w,h,l	Central Point and Pressure location, North, South, East, West, High and Low side, and equivalent face locations for discretization
RANS	Reynolds-Averaged Navier-Stokes
REFSUM	Reference sum of residual errors for a solved-for variable
RSM	Reynolds Stress Model
SGS	Subgrid-scale modelling
TEM1	Solved-for Temperature variable of the first phase
WDIS	Distance from the wall
WGAP	Distance between walls

1. INTRODUCTION

To design an effective building ventilation system, the sources that influence the behaviour of ventilation systems must be studied. The primary force used in the ventilation of buildings is the momentum force generated naturally or mechanically. In natural ventilation, the potential energy generated by the momentum difference caused by the temperature and pressure differentials between inside and outside air is utilised to displace air out of the building. Natural ventilation is a form of displacement ventilation. In mechanical ventilation, the momentum force is generated by a fan that is used to ventilate buildings by displacement or mixing methods. Sometimes also referred to as piston ventilation, displacement ventilation bases its principles on the pressure force developed between the supply and the ambient surroundings. The heat build-up by several objects occupying the building can result in temperature-stratification. In contrast to natural and displacement ventilation, mixing ventilation uses the momentum force of the supply to mix and dilute the pollutants in the building.

Ventilation related problems have received attention over the past 100 years. In 1887, multiphase motors made a significant appearance in the ventilation industry, with the discovery of alternating current (AC). Energy and environmental issues in 1970's brought in the need for low cost and energy saving air-conditioning installations. In the past 10 years, high engineering standards are used in the design of ventilation and air-conditioning systems to achieve maximum comfort with the minimum energy consumption. The quality of breathing air has become the issue of study by many scientists and engineers. The physical issues involved in the design of the ventilation system have been studied experimentally. Empirical correlations of the temperature distribution in the occupied space with supply parameters have proved very important in the design of the ventilation system. When studying ventilation, there are many physical parameters to consider and parametric equality can be difficult to achieve using scale models. Similarly, the disadvantage of the physical models, which are derived by theoretical investigations, is that due to the assumptions made to simplify the problem. These assumptions can often lead to the misinterpretation of the real problem or narrow

the range of the problem. Consequently, using Computational Fluid Dynamics (CFD) to model the complex physics of a full-scale problem can prove more advantageous than other investigation methods.

Over a period of many years, CFD has been the tool of investigating the physics involved in a wide range of engineering problems. CFD is now extensively used in Building Services Engineering. In most cases of ventilation of buildings, CFD is used to study flow patterns and dispersion of contaminants as well as, in certain cases, temperature distribution in order to find the best way to clean the occupied zone and improve the design of the ventilation system. The flow patterns are often affected by the geometry of the room and the location of the inlets and outlets. CFD problems are computed in both time and space, and more information can be extracted at the same time which is also cheaper than a full-scale experimental investigation. However, there are always differences between real and CFD results due to limitations in CFD modelling. To some extent, a numerical model is an idealised case of a real situation, where assumptions are made to simplify the physical dimensions and shapes of the real problem. This may include the representation of the geometry, i.e., supply air terminals, wall roughness, etc. and boundary conditions, i.e., shape of the inlet profile or an inlet variable. Issues concerning CFD simulations for ventilation problems, like boundary conditions and turbulence model, are still not investigated completely in literature. However, CFD can be used again to tackle the problem at the specific area or location and higher detail can be added at a little cost in contrast to experimental procedures involving further manufacturing and testing. In general ventilation problems, there are still fundamental questions as to what ventilation rates, how and where hot spots can be created and why one building ventilation method can be better than another. Therefore, a test model is required to investigate the behaviour of the various ventilation methods with respect to the sources that affect the ventilation system, for example, the sources that create and break up thermal stratification, and establish a mathematical relationship from test cases for better ventilation design.

1.1 Aims of the Study

The main aim of this study is to investigate issues relating to the CFD modelling of the flow field in ventilated enclosures with specific emphasis on stratified flow.

2. THEORETICAL BACKGROUND

Ventilation of buildings is a complex issue that is affected by a number of physical mechanisms. The purpose of this chapter is to set out the mechanisms involved in ventilation in general and in particular ventilation where stratification occurs.

2.1 Governing Equations of Fluid Flow

General ventilation problems are often associated with steady-state phenomena. The governing equations under steady-state conditions are the continuity equation, the Navier-Stokes equation and the energy equation,

$$\rho\frac{\partial u_i}{\partial x_i}+\rho\frac{\partial u_j}{\partial x_j}=0 \tag{2.1}$$

$$\rho u_j\frac{\partial u_i}{\partial x_j}=-\frac{\partial P}{\partial x_i}+\frac{\partial}{\partial x_j}\left[\mu\left(\frac{\partial u_i}{\partial x_j}+\frac{\partial u_j}{\partial x_i}\right)\right]-\rho_0 g\beta\left(T-T_0\right) \tag{2.2}$$

$$\rho u_j\frac{\partial T}{\partial x_j}=\frac{\partial}{\partial x_j}\left[\Gamma\left(\frac{\partial T}{\partial x_j}\right)\right]+S_h. \tag{2.3}$$

At room temperatures, air density is an approximately linear function of temperature. The density difference between a heat source and the reference density is also a function of temperature difference, with respect to the corresponding reference temperature. This particular case is termed the Boussinesq approximation,

$$\rho_0-\rho=\rho_0\beta\left(T-T_0\right) \tag{2.4}$$

which is the form used for the last term in equation (2.2).

The heat generation is represented by the heat component S_h and is given by the expression below,

$$S_h = q_s + q_t + q_r + q_l \tag{2.5}$$

where q_s is the heat generation due to the supply sources or sinks per unit volume,

q_t is the heat generation due to viscous dissipation,

q_r is the heat emitted between surfaces and

q_l is the heat loss to the outside.

The temperature difference between the inlet supply and the surrounding air can cause significant changes to the air flow in a room and it is therefore important when studying the ventilation of a building. These flow changes are mainly due to thermal stratification that is induced by the effect of gravity on the density variation, where heavier fluid settles at the lower levels and lighter fluid moves up over the heavier fluid by the counteracting the effect of the buoyancy force. The process of thermal stratification is a consequence of the relationship between density variation and temperature. The result is the appearance of horizontal isothermal layers of same density fluid. Stratification can be discrete, in which case there are layers of fluid at a fixed density, such as a non-linearly stratified two-layer fluid system, or continuous that is more gradual layering following smoother variations of density that closely resembles a large number of discrete layers stack across the height that makes it more difficult to define. Stratification can cause collapse of turbulence as entrainment ceases at high Ri_o and hence turbulence may be decreased by increasing stratification, Ellison and Turner (1959). The effect of thermal stratification is to reduce the degree of mixing between the layers.

The important issue to examine by solving the governing equations is whether the flow will become stratified or mixed. This will depend on the relative magnitude of the terms in the governing equations.

2.2 Stability of Stratification

The following model assumes heavier fluid discharge into a channel containing a stably-stratified two-layer system for defining the overall Richardson number, Ri_o. The dynamic effects of stratification become evident whenever fluid is displaced upwards, as the buoyancy force tries to bring the fluid to its neutral position of equilibrium. This can occur by a destabilising pressure force, P, acting on the lower plane at the floor level of a channel as shown in Figure 2.1,

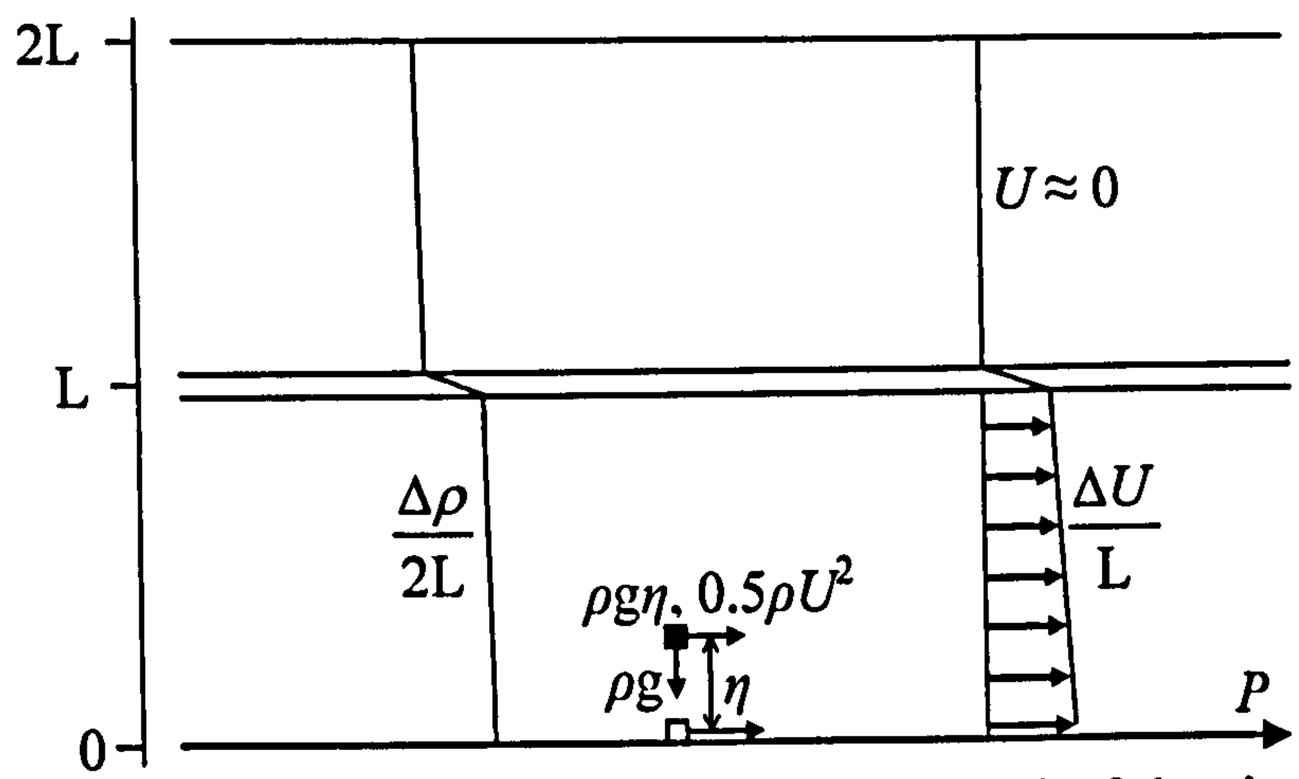

Figure 2.1: Fluid displacement in a stably-stratified channel of density gradient $\Delta\rho/2L$ and velocity gradient $\Delta U/L$.

A fluid parcel displaced by a small distance η from its equilibrium position, shown in Figure 2.1, experiences the density gradient across the entire channel, $\Delta\rho/2L$. By multiplying the gradient by the displacement distance η, the density difference can be obtained to use in the equation for the definition of potential energy of the fluid parcel. To obtain the potential energy of the fluid parcel with respect to the overall gradient, the density gradient needs to be multiplied by the product ($g.\eta$), i.e., $g \cdot (\Delta\rho / 2L \cdot \eta) \cdot \eta$. The potential energy per unit volume of the fluid parcel is,

$$PE = g\frac{\Delta\rho}{2L}\eta^2. \tag{2.6}$$

The velocity in one layer does not influence the velocity in the other layer and thus each layer must be considered separately. Therefore, the velocity gradient acts only over a distance L. The fluid parcel will move by means of the velocity gradient of the layer, $\Delta U/L$. By multiplying the velocity gradient by the displacement distance η, the velocity

difference can be used to define the kinetic energy of the fluid parcel. To obtain the change in the kinetic energy of the fluid parcel with respect to the overall gradient, the velocity gradient of the layer needs to be multiplied by the displacement distance the and the product {(1/2).ρ}, i.e., $1/2 \cdot \rho \cdot (\Delta U / \mathrm{L} \cdot \eta)^2$. The kinetic energy per unit volume of the fluid parcel is,

$$KE = \rho \frac{(\Delta U)^2}{2\mathrm{L}^2} \eta^2 . \tag{2.7}$$

A relative measure between the potential energy of the fluid parcel equation (2.6) and the kinetic energy of the fluid parcel equation (2.7) with respect to the overall gradients leads to the derivation of the overall Richardson number, Ri_o, for the stratified channel flow. The overall Richardson number is,

$$Ri_o = g \frac{\Delta\rho}{\rho} \frac{\mathrm{L}}{(\Delta U)^2} . \tag{2.8}$$

However, it is not an absolute condition that the fluid will always go to the same neutral position. This can occur due to turbulent mixing acting opposite to the buoyancy force changing the density of the fluid parcel. The potential energy of the fluid parcel can also increase further downstream in the channel which is important in estuarine mixing.

The Richardson number occurs at different scales. The Ri can be used to describe the overall stability of stratification in the channel denoted by Ri_o or similarly the stability of the interface denoted by Ri_L,

$$Ri_L = g \frac{\Delta\rho}{\rho} \frac{\mathrm{L}}{U^2} . \tag{2.9}$$

where in this case L is the depth of the interfacial layer and U is the interfacial velocity. In the case of layer Richardson number, the values by an order of magnitude higher than in the case of overall Richardson number.

2.2.1 Richardson number and Froude number

In stratified flows the density gradient creates the stabilising force that resists mixing by velocity shear. The Richardson number is a measure of the *buoyancy force* to *inertia force*. The local gradient Richardson number (sometimes also denoted as Ri_g), can be expressed as,

$$Ri = \frac{-g\left(\frac{\delta\rho}{\delta z}\right)}{\rho\left(\frac{\delta u}{\delta z}\right)^2} \tag{2.10}$$

where the minus sign accounts for the usual density decrease with increasing height. Negative Ri corresponds to destabilising density change where both shear and buoyancy give rise to instability and turbulence. If density increases with height, the buoyancy provides additional source of turbulence. The Richardson number is negative for non-stratified flows and increases with strength of stratification, while if $Ri = 0$ there is neutral stability between unstratified fluids that reside in two depths.

In gases, when density variations are caused by temperature variations and the ideal gas law is valid, Ri can be expressed in terms of the temperature gradient, equation (2.10) can be written as,

$$Ri = \frac{g\beta\left(\frac{\delta T}{\delta z}\right)}{\left(\frac{\delta u}{\delta z}\right)^2} \tag{2.11}$$

where β is the volumetric expansion coefficient.

Perturbation analysis has shown that a laminar layer of stratified fluid is stable with respect to small perturbations if the local Ri exceeds 1/4 everywhere in the flow Chandrasekhar (1961). If Ri becomes lower than 1/4 at any part, the shear across the interface becomes so large that the stable density gradient will no longer be of sufficient magnitude to stabilize the flow. However, this does not imply that in an existing

turbulent shear flow the turbulence would disappear if Ri exceeds 1/4. In fact it seems to be possible for turbulence to exist even when the overall Richardson number is well above 1/4, Hopfinger (1987), Gibson (1981). Based on the overall Richardson number, a turbulent shear layer between two fluid streams is expected to laminarise in the following transition range,

$$\frac{1}{4} < Ri_o = g\frac{\Delta\rho}{\rho}\frac{L}{(\Delta U)^2} \leq 1 \tag{2.12}$$

where L is the layer thickness between the fluids at shear and Δu is the difference in velocity between the fluids.

In general, stability is likely to occur if $Ri > 1$. If Ri is much less than unity, buoyancy is unimportant in the flow.

The Richardson number, Ri, may be written in a simplified form for a case of a fluid discharging into a reservoir,

$$Ri = g'L/U^2 \tag{2.13}$$

where $g'\left(\equiv (\Delta\rho/\rho)g\right)$ is the modified acceleration of gravity due to buoyancy.

The classical Froude number does not include the effect of density in the equation and it is a measure of the characteristic velocity versus the long waves on a free surface, given by the expression,

$$Fr = U/\sqrt{gL} \tag{2.14}$$

Primarily, this criterion is used for large-scale natural phenomena where a critical Fr is in the range of 0.7-1.4. For an unstable situation of two fluids at different density or surface flows to start picking up speed, $Fr \approx 1$ that also signifies the lower limit, in contrast to the Richardson number, for strongly stratified flows. The buoyancy velocity can be calculated from Fr number. Some examples are oceanic fronts, avalanches and other physical observations in nature that deal with the transportation of rock, mud and

lava. For an approximate Fr of 1, the velocity scale can be obtained by rearranging equation (2.14),

$$U \approx \sqrt{gL} \tag{2.15}$$

The square-root of the inverse of Ri is known as the densimetric Froude number in hydraulics engineering, i.e., $Ri^{-1/2}(= Fr)$, and it is often used instead of Ri. In some cases it is re-defined for practical purposes. This is because it contains a single velocity scale of the upstream flow that is often non-dimensionalised, but also it expresses the ratio of the flow velocity to the velocity of the propagation of a wave on a density interface,

$$Fr = \frac{U}{U_{\text{wave}}} = \frac{U}{\sqrt{g'L}}. \tag{2.16}$$

For the range of transitional stability, the Ri number gives values of the order of 0.1 to 0.01.

The Froude number, Fr, has been used instead of Ri in literature to relate the inlet flow rate to include a dimensionless inlet size and velocity scale, for example, in thermal storage tanks. The inlet velocity and temperature difference are the important variables considered in the scaling based on a modified Fr which determines whether the flow will stratify or mix for the specified geometry. The scaling method depends on the size of the enclosure as well as the size of the inlet that modifies the velocity in the flow rate. Thermal stratification is similar for both horizontal and vertical thermal storage tanks, Alizadeh (1999) and Nelson *et al.* (1999). Therefore, it is the inlet velocity that is more important in the description of the stability of stratification. The inlet size cubed in the denominator is used in a modified Fr formulation by Yoo *et al.* (1986), while the inlet flow rate is used in the numerator, in the place of U and L in equation (2.16). This is done to introduce the direct correlation between the inlet flow rate and Fr, in which formulation a value of 2 or less should be used in the selection of diffusers. Large storage tanks maintain more stratification than smaller tanks as found by Nelson *et al.* (1999) and Shin *et al.* (2004). The results are similar for an aspect ratio of up to 3 by Nelson *et al.* (1999) and similarities are expected to be found in buildings

for the same axial wall conduction rates because the flow is largely dependent on the ratio of Re/Ri irrespective of the scale. The overall Richardson number Ri_o is the parameter that characterises similarity in thermal storage tanks.

Although Fr_o is used to describe stratification in relation to non-dimensional length and inlet velocity (difference) or flow rate, the classical Ri_o is still used in many research papers due to the physical description of the buoyancy to inertia forces acting on the fluid. There are several Re/Ri correlations in the literature describing the flow exponent.

Hopfinger (1987) described the onset of turbulence collapse in relation to the frequency of buoyancy waves (given in s^{-1}) in stable stratified environment,

$$N = \left(\frac{g}{\rho} \frac{\delta \rho}{\delta z} \right)^{\frac{1}{2}} \tag{2.17}$$

the disturbance Froude number is,

$$F_r = \frac{u}{l \cdot N}$$

By making an isotropic turbulence assumption, an eddy of length l and tangential velocity u impinging on an interface, the turn over time scale of the eddy is $t_e = l/u$ (in seconds). The relaxation time scale of buoyancy field disturbed by an eddy of height l is related to the natural frequency of buoyancy waves, as given below,

$$t_b = \left(\frac{g}{l} \frac{\Delta \rho}{\rho} \right)^{-\frac{1}{2}} \tag{2.18}$$

The Ri will become less stable for larger enclosures. This will occur due to the reduction in temperature across a larger height compared to a smaller enclosure, mainly due to heat losses and air infiltration. On the other hand, the flow could become laminar because of the reduction in the horizontal velocity scale and in the absence of heat losses, there will be more undisturbed stratification. This will also affect the time scale

of the waves. The length scale is approximately the typical size for initiating a (Kelvin-Helmholtz) K-H wave. The local Ri number as a function of the eddy time-scales is,

$$Ri = g\frac{\Delta\rho}{\rho}\frac{l}{u^2} = \frac{t_e}{t_b} \tag{2.19}$$

Nearly after the release of a heat source in a uniform undisturbed environment, the flow is more stratified due to the shear force introduced by the gravity wave on the stagnant fluid. The effect of vertical turbulent diffusion is not yet established due to the relative horizontal interaction of the gravity wave with the stagnant fluid is more effective than the vertical one. After stabilisation conditions become closely established, there is a horizontal uniformity in the layers and the vertical turbulent diffusion mechanism becomes more effective resulting to a diffused interface at stabilised conditions. This effect is observed both in the CFD investigation by increasing iteration number and in the experimental work after waiting for over 2.5 hours to obtain stabilised conditions in obtaining repeatable measurements. After stabilised conditions are achieved, the correlations due to inlet parameters become valid.

On the other hand, a larger enclosure is more vulnerable to outside changes such as heat losses and stack effects. This is because the ratio of insulation thickness over the building height is smaller compared to a smaller building. For the same inlet parameters, after several hours of stabilised conditions, a larger enclosure will withhold stronger stratification if it is sealed from outside influences. It will take more time to fill up for the same volume flow rate to stabilise at the conditions of the current settings.

2.2.2 Grashof number and Raleigh number

In flows with no velocity due to momentum, a dimensionless group is needed to compare the *buoyancy force* to the *viscous force*. Assuming that buoyancy is the only source of movement, the velocity dimension can be obtained from $U \approx (gl\beta\Delta T)^{1/2}$. For this velocity scale the equivalent Reynolds number is $(gl\beta\Delta T)^{1/2} l/\nu$. The square of this is the so-called Grashof number,

$$Gr = \frac{gl^3 \beta \Delta T}{\nu^2}, \tag{2.20}$$

while an indication of turbulence at an opening that exerts a temperature difference on either side can be obtained by modifying Gr to include the inlet size of openings,

$$Gr = \frac{g(A_0)^{1.5} \beta \Delta T}{\nu^2}, \tag{2.21}$$

where A_0 is the effective area of any adventitious opening that may appear on the wall fabric and ΔT is the temperature difference between the inside and the outside.

Similar flow behaviour can be obtained between free and forced convention, $Gr \approx Re^2$. The Reynolds number obtained by Gr for a free convection boundary layer may be defined as Reynolds-Grashof number, Re_{Gr}, which determines in a similar way to Re whether the process is *laminar* or *turbulent*. Depending on a temperature gradient in most flows, transition occurs as suggested by CIBS (1976) in the range of $10^6 < Gr < 10^9$. If $Gr / Re^2 >> 1$, then buoyancy forces dominate the flow, while if $Gr / Re^2 << 1$, buoyancy forces may be ignored. Alternatively, transition in a thermal boundary layer is dependent both on viscosity and thermal diffusivity, i.e., the ratio of *buoyancy force* to the *thermal diffusion force*, which can be obtained by multiplying equation (2.21) with the Prandtl number. This product is called the Raleigh number, $Ra = PrGr$ and it is useful where the thermal diffusion due to the conductivity of the fluid is important. Transition to turbulence occurs at $Ra \approx 10^9$.

To reproduce a convective jet in a scale model it is necessary that $Ra \geq 2 \times 10^5$, Baturin (1972). In convective flow, molecular transfers are insignificant compared to the turbulent transfers. The l^3 is the characteristic scale of turbulence, which has a large effect on the magnitude of Gr number. Crawford and Leonard (1962) noted that reduced scale modelling is restricted using air, due to the temperature difference required in the small scale needs to be much higher than the full-scale. Other liquids such as water could be used instead of air, but the size of the model still needs to be large enough to maintain the Gr similarity with the full-scale model.

2.2.3 Archimedes number

Archimedes number, Ar, is conventionally used as the non-dimensional ratio to characterize non-isothermal flows in buildings instead of Re. Similar to the Ri, Ar is the ratio of the *buoyancy force* to *inertia force*, but it is rather used instead of Re to characterise the flow of non-isothermal supply outlets. In terms of temperature variation, Ar is commonly expressed as,

$$Ar = \frac{g\beta l \Delta T}{u^2} \tag{2.22}$$

where l in this case is the hydraulic diameter, D_{hyd}, of the supply given as,

$$D_{\text{hyd}} = \frac{2ab}{a+b} \tag{2.23}$$

where a is the length or height and b is the width of the cross-section of the opening. This is shown schematically in Figure 2.2,

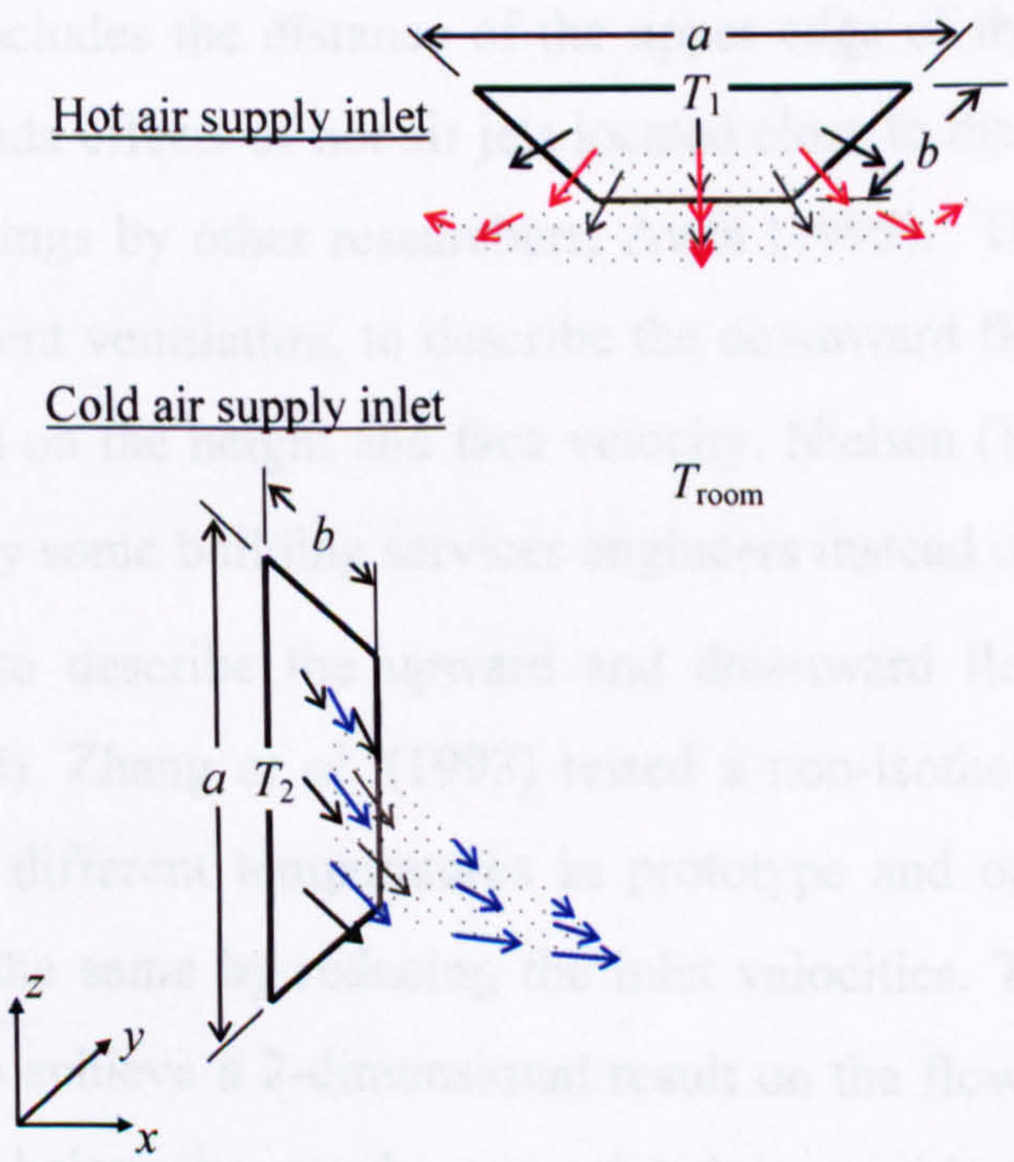

Figure 2.2: Nomenclature for the definition of Archimedes number. The mean temperature of the room is taken as the reference temperature, T_{room}.

The room temperature, T_{room}, is a function of the inlet temperatures and convective heat transfer, Δq_{in}, total convective coefficient, C, but also the outside reference temperature, T_{o}, and the ratio of total heat loss, q_{loss}, over the product of the U-value of the wall-fabric multiplied by the area of the openings A_{o}, i.e.,

$$T_{\text{room}} = (\Delta T_{in} - T_{\text{o}}) + (\Delta q_{in} / C - q_{\text{loss}} / UA_{\text{o}}). \tag{2.24}$$

In the case of natural motion of air, Ar can be transformed so that it no longer contains the velocity in the explicit form. Thus, Ar can be expressed as a function of Grashof number, Gr and Re,

$$Ar = \frac{Gr}{Re^2}. \tag{2.25}$$

Archimedes number is a critical non-dimensional ratio for determining the trajectory of the throws of non-isothermal ceiling air jets which is used by several researchers for industrial ventilation, Goodfellow and Tähti (2001). Modified Archimedes numbers, Ar', which includes the size of the opening and hydraulic diameter of the room, and Ar'', which further includes the distance of the upper edge of the opening, have been used to relate the coanda effects of hot air jets located close to the ceiling with high and low aspect ratio openings by other researchers, Awbi (1995). The Ar is also used in the case of displacement ventilation, to describe the downward flow of a wall-mounted terminal device based on the height and face velocity, Nielsen (1994). A modified Ar number is also used by some building services engineers instead of the Ri_{o} based on the height of the room to describe the upward and downward flow systems in lecture theatres, Linke (1962). Zhang *et al.* (1993) tested a non-isothermal similitude model using three cases of different temperatures in prototype and one-fourth-scale model, while Ar was kept the same by reducing the inlet velocities. They used a linear slot supply air opening to achieve a 2-dimensional result on the flow. The drop distance of the incoming air jet below the supply was related to a critical Archimedes number, Ar_{crit}, for which the air dropped immediately after entering the room, was found to decrease with room size. Although there was a good agreement of the mean velocity

profiles between the full-scale and the prototype in the downstream region, the mean velocity profiles in the upstream region did not agree very well. The turbulent kinetic energy was the parameter that was affected the greatest close to the supply and this was expected because by maintaining Ar similarity, the Re was distorted in the scale models. However, it has been mentioned by Baturin (1972) that this is still acceptable as long as $Re >> 2{,}320$ to ensure that the jet is in the turbulent region. The temperature distributions were greatly affected close to the ceiling and the floor, indicating that the thermal radiation and conduction effects were not very well accounted for by the scaling procedure. Baturin (1972) noted that heat balance similarity should be maintained in the domain eliminating the surface area of heat sources and sinks, i.e., heat losses. However, these effects can be considered to some extent in the model if the working medium is water rather than air. If the working medium is water, Pr similarity may not be satisfied.

Large differences of scale models in comparison with actual ventilation flows are less likely to occur when using Archimedes number are reported by Zhang *et al.* (1993). However, the mean velocity, turbulence kinetic energy and turbulence intensity were slightly different in a one-fourth scale model (11%, 15%, 14% and 26% respectively) that resulted in some disagreement with experimental results. This was accentuated at the wall boundaries (larger than 50%) and was attributed to air being used as a medium in the model.

2.3 Ventilation Methods

Primarily there are two ventilation methods used in buildings:

- Natural, and
- Mechanical ventilation

The latter can be subdivided into:

- Displacement ventilation, and
- Mixing ventilation

And a combination of the above:

- Mixed ventilation

In natural ventilation, stratified flows are dominant in the enclosure. In such cases, because of the relative importance of ratio of buoyancy induced momentum forces to viscous forces, the Gr number can adequately describe the flow, which is stated in equation (2.21).

In displacement ventilation, mixing is not as important as thermal stratification. In such cases, because of the ratio of the relative importance of the levelling force of buoyancy as opposed to the mixing force of momentum, the Ri number can adequately describe the flow, which is stated in equation (2.10). This has also been defined previously in section 2.1 can be used as a measure of the stability of stratification.

In mixing ventilation, the viscous terms are most important. In such cases, because of relative importance of the inertia to viscous forces and the associated influence of turbulence diffusion process on stratification, the Re number can adequately describe the flow.

In most buildings, a combination of the above ventilation methods may be realised, which has recently drawn attention, since it requires the understanding of the available ventilation systems in order to use certain correlations of the non-dimensional ratios to increase the efficiency of the building related to energy saving issues.

Based on a critical interface thickness of approximately 0.25 m of the experimental work, the maximum flow rate that has occurred is from the hot air supply is $Q_{HS} = 0.14$ m³/s for a constant cold air supply flow rate $Q_{CS} = 0.064$ m³/s, the ambient temperature about 20°C and the temperature of the hot air supply is 32°C and the inlet temperature difference is $\Delta T_{in} = 24°C$. The stability range of stratification is $0.2 < Ri_o < 3$ and the Reynolds number range is $11{,}000 < Re < 40{,}000$.

2.3.1 Natural ventilation

This is the simplest and most cost effective method to ventilate buildings and has been around for much longer than any other ventilation method. Clean air is provided by a pressure differential through openings or cracks in the building or by opening a window, while stale air, which is normally warmer than the surrounding air, moves to higher levels through openings to the outside. This happens by naturally occurring forces, such as by stack effect due to temperature difference or wind pressure that give rise to a pressure gradient between the inside and the outside of the building. As a result of this mechanism due to stack effect, the air at higher levels inside the building is more likely to be warmer, while the air at the lower levels is cooler and fresher. *In situ* experimental and analytical studies have been carried out in utilising wind pressure and draught, and monitoring weather conditions such as wind velocity and direction to ventilate offshore modules of rectangular shape, Dagestad and Holdø (1991). Shilkrot (1993) observed the air infiltration patterns in an industrial type building in combination with an indoor heat source that result to a separation level between hot and cold sources. The supply velocities were up to 2 m/s and infiltration rates increased the temperature range between hot and cold layers of air above and below the separation.

Natural ventilation is used as the main ventilation method in residential buildings to reduce indoor contaminant concentrations. BRE (1996) carried out a study of indoor air quality of several non-occupational British buildings. One of the studies was associated with airborne fungi and bacteria in the living room and bedroom. In these rooms, the parameters affecting air quality is humidity and temperature. The average relative humidity was around 60% and varied from 55.6% up to 70% in a smaller group of intensively monitored properties and depending on source location. The average temperature was 19.55°C and maxima exceeded 25°C, while the average in the smaller group of properties was 18.5-18.7°C. The mean indoor formaldehyde and volatile organic compound (TVOC) concentrations was respectively 12 and 10 times higher than outdoors. The TVOC concentrations were significantly higher in houses with occupants that smoked more than 50 cigarettes per week than in houses where no smoking was allowed. Fossil fuel burning and household size, which are associated with gas cooking and occupant density, influenced significantly the NO_2 concentrations. However, there was no consistent effect of ventilation factors such as extractor

ventilation and window opening, while non-ventilation mechanisms like green plants reduced concentrations.

Buildings today are designed with air-tightness and heat insulation considerations taken into account at design stage. Similarly, the naturally occurring mechanisms of ventilation need also be utilised in the design of the building. The facing-direction of the windows is very important in utilising the wind pressure force to ventilate the building. The ventilation effectiveness is not a primary consideration in the design process of the building with natural ventilation and thus 100% satisfaction is not ensured during the whole period of the year. Therefore, the ventilation of the building needs to be supplemented by mechanical means.

2.3.2 Displacement ventilation

This type of ventilation system was originally used in industrial buildings to effectively remove contaminants, but now it is also used in office buildings. An outlet velocity of less than 0.5 m/s for displacement ventilation is the highest found so far in literature and is suggested in ASHRAE (1993) Chapter 31: Section 31.5. When the primary air does not exceed certain lower limits for temperature, it can be supplied at a higher velocity. However, displacement ventilation can occur by both velocity and temperature. In this ventilation type, the primary air is supplied in the lower part of the room where it is heated by the heat sources and rises to a warmer upper part of the room. A temperature gradient is essential and needs to be increased when there are excessive heat loads by the temperature differential between the supply air and the occupied zone. The objective of this system is to achieve a temperature in the occupied zone close to the supply air temperature. Sandberg and Blomqvist (1989) suggested a maximum convective cooling load of 25 W/m^2 so that the temperature gradient in the occupied zone will not exceed 3°C that is equivalent to 5 l/s.m^2 at a maximum cooling differential of 4°C. Higher cooling loads were also suggested by Jackman (1991), up to 50 W/m^2. These heat loads are likely to occur within buildings with high ceilings, such as above 4.5-m high with heavy lighting. In latest standards, mechanical ventilation systems are used to introduce cooler air at a lower velocity typically less than 0.25 m/s and 2-4°C, CIBSE (2000a) AM13: Section 5.3.2, to a low part of the room below the room temperature and spreads out above the floor. Hot and stale/contaminated air rises to an uninhabitable upper hot

zone by buoyancy forces and stays there until it is extracted by the fan to the outside. It is a characteristic of this method that the ventilated space splits into two parts; the cool lower zone, which is known as the "occupied zone" and is continuously supplied with cool, fresh air straight from the outside or air-conditioned air, and the hotter upper polluted zone. Both zones are important because the cool zone keeps the occupied zone clean of pollutants and the hot zone needs to maintain its temperature in order to hold the contaminants until they are extracted. The displacement system saves energy because it ventilates the occupied zone only, while upper polluted zone is left intact. As a result, the contaminant distribution follows the temperature distribution to some extent. A good prediction of the non-dimensionalised smoke distribution is the non-dimensionalised temperature distribution, Dagestad (1991). Displacement ventilation has been mainly used in the flashing of contaminants of large enclosures such as shipyard huts, Säämanen *et al.* (1995). Some analytical studies have also been carried out for displacement ventilation assisted by wind, Hunt and Linden (1999). The displacement ventilation method is represented schematically in Figure 2.3,

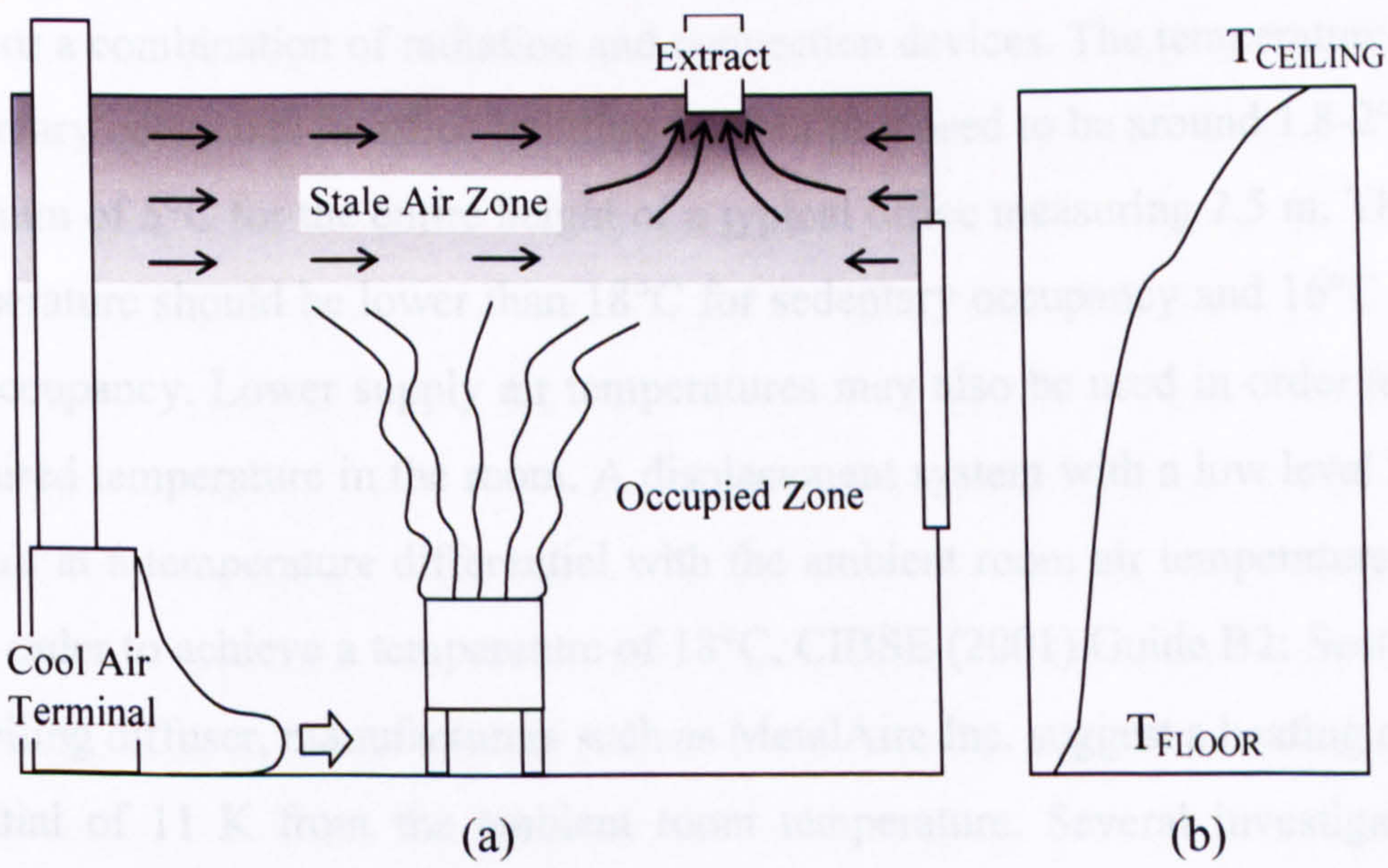

Figure 2.3: In (a), displacement ventilation is taking place by supplying cool air at low level in the building. In (b), temperature variation across the height of the building away from the heat source and window openings, adapted from Goodfellow and Tähti (2001).

The primary consideration in the design of the ventilation unit is not to mix the impurities in the occupied zone, but displace them into an uninhabited zone in the upper levels where the airflow is extracted. In the building design criteria, CIBSE (2001) Guide B2: Section 3.17, the range of room temperatures is 18-24°C, which is acceptable

for human comfort and commensurate with good energy efficient practice. Jaakkola *et al.* (1991) studied the Sick Building Syndrome (SBS)-score for indoor air quality requirements in office buildings. The recommended temperature was 21±2°C, though the range of temperatures may slightly vary with different working activities. The recommended minimum air flow rate with good mechanical ventilation was 10 l/s and there was already an increase in symptoms of SBS when the flow rate decreased below 15 l/s. In an alternative approach, Seppänen *et al.* (1999) reviewed the effect of CO_2 on the indoor air quality of commercial and institutional buildings and found that ventilation rates below 10 l/s per person were associated with significant prevalence of symptoms related to SBS symptoms, while above 20 l/s per person with significant decrease in SBS symptoms. The amount of the temperature differential between the ventilation unit and the occupied zone is the main design criterion for a fresher environment. The standards for displacement ventilation have been laid out by BS EN ISO 7730 (1995) and CIBSE (2001) Guide B2: Section 4 for ventilation and air conditioning. The maximum cooling load that can be delivered is 25 W/m^2. For a building with higher heating or cooling loads radiation type devices may prove more suitable or a combination of radiation and convection devices. The temperature gradient for sedentary occupants in office building is often proposed to be around 1.8-2°C/m and a maximum of 5°C for the entire height of a typical office measuring 2.5 m. The supply air temperature should be lower than 18°C for sedentary occupancy and 16°C for more active occupancy. Lower supply air temperatures may also be used in order to achieve the required temperature in the room. A displacement system with a low level input can supply air at a temperature differential with the ambient room air temperature of about 10 K in order to achieve a temperature of 18°C, CIBSE (2001) Guide B2: Section 4.2.3. For a ceiling diffuser, manufacturers such as MetalAire Inc. suggest a heating or cooling differential of 11 K from the ambient room temperature. Several investigators have studied displacement ventilation Fanger *et al.* (1988), Palonen *et al.* (1991), Li *et al.* (1993a), Li *et al.* (1993b), Nielsen (1994), Mundt (1995a), Mundt (1995b), whilst CIBSE (2001) Guide B2: Section 4.2.5 gives guidelines for design of displacement ventilation. It is found that buildings with high heat loads may be more efficient because the contaminants can be carried together with the heat loads, and that displacement ventilation may be especially effective when designing air-conditioning for spaces with high ceilings. However, a major disadvantage of displacement ventilation by

temperature gradient is that it cannot be used when contaminants have significantly higher density than air.

2.3.3 Mixing ventilation

In an alternative approach to natural and displacement ventilation, mixing ventilation bases its principles on mixing the air in the room, producing an even temperature throughout the space and diluting any pollutants. Typically, ventilation air is injected at sufficiently high speed at or near the ceiling. The momentum of the supply jet is counteracted by the buoyancy forces in the room creating an additional source of turbulence which dilutes the contaminants and drives them to an opening usually located close to the floor. If mixing is not sufficient, stagnant areas can occur in the occupied zone near the floor. In the design of energy-efficient ventilation systems, generally efforts are made to de-stratify the flow in order to achieve uniformly desired air temperature to reduce the heating load of the building. A typical study of applying the mixing ventilation method employing ceiling-mounted supply and exhaust has been carried out by Lee and Awbi (2004). They carried out experimental and isothermal studies using standard $k-\varepsilon$ turbulence model with a contaminant source to evaluate room air quality. The ventilation rates correspond to 13, 30, 50 and 70 ACH. The maximum resolution used by a CFD program called VORTEX for that model was 126,000 cells. Although the velocity profile along the vertical direction is underpredicted in the supply zone, a good comparison is achieved in the exhaust zone. Reposition of the contaminants occurs in the room by recirculation caused by the mixing jet and the presence of a vertical partition. Effective removal of the contaminant occurs by increasing the partition gap underneath because it increases the flow around the floor area. However, increasing of partition gap to just 10% causes adverse phenomena like reverse circulations above and underneath the partition that result to contaminant flow from the exhaust back into the supply zone. Mixing ventilation is also applied in the dilution of contaminants in clean rooms, Murakami *et al.* (1997) and Cheng *et al.* (1999). A schematic representation of mixing ventilation is shown in Figure 2.4,

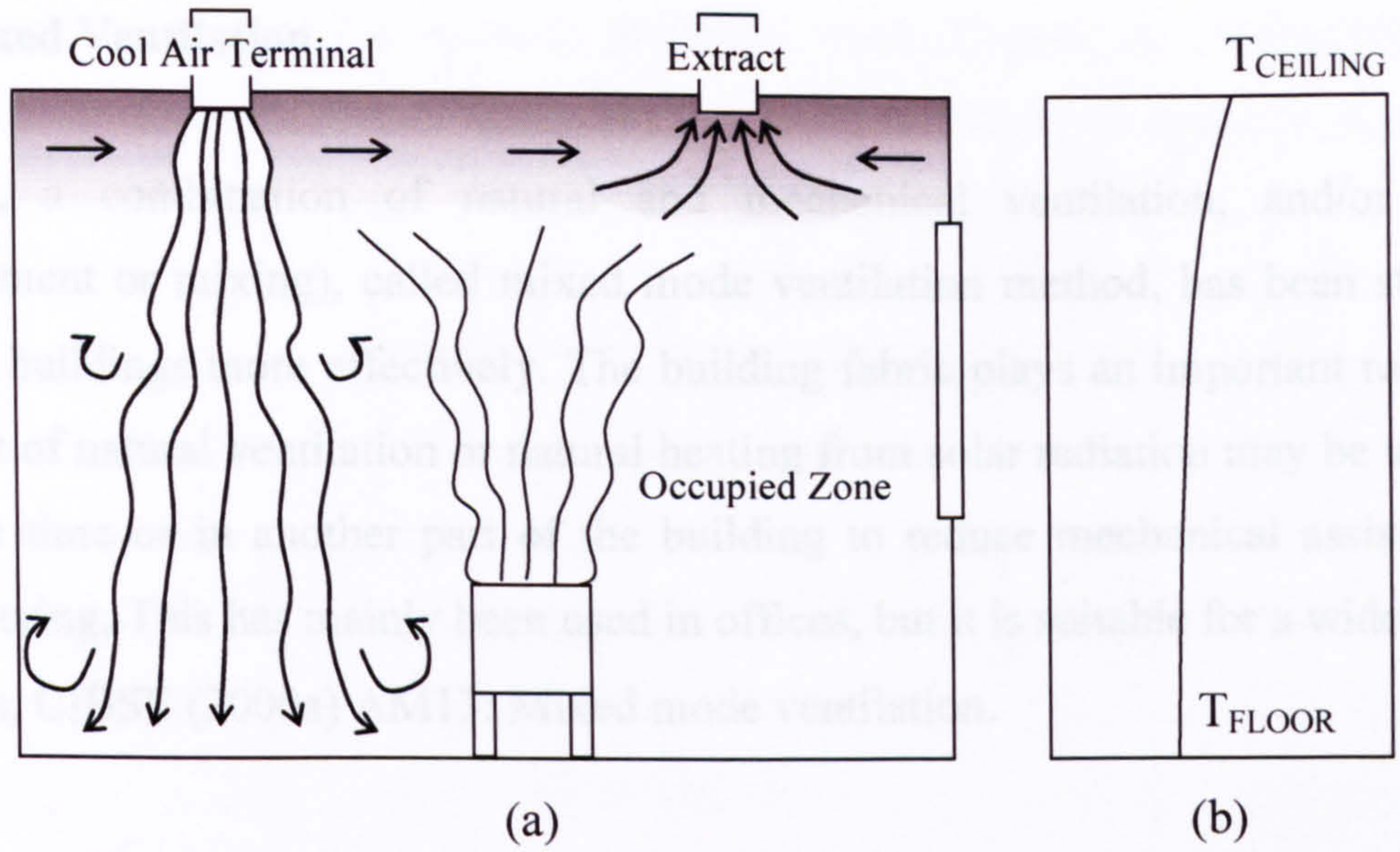

Figure 2.4: In (a), mixing ventilation occurring by supplying cool air at high velocity and at a high level in the building. In (b), temperature variation across the height of the building, away from the heat source and window openings.

In most mixing ventilation systems the cold air terminal is mounted on the ceiling, pointing downwards, towards the occupied zone. A suitable place for the terminal must be carefully selected in order to avoid direct contact of the supply air with the occupants. To design an effective mixing ventilation system, the size and velocity of the terminal must be calculated. The momentum of the jet should overcome the buoyancy force due to the temperature gradient in the building. This method is more efficient in smaller buildings. The supply air terminal in mixing ventilation is traditionally located at the ceiling level. The supply air temperature in mixing ventilation systems is more frequent for a cooling approach. The supply temperature commonly proposed by manufacturers is around 12-13°C for cooling with side wall diffuser. This can be as low as 6°C with ceiling air terminal devices, CIBSE (2000a) AM13: Section 5.3.2, depending on the heat load in the building. As a general rule for both ceiling and wall mounted air terminal devices, to avoid the risk of draught the suggested temperature is $T_S > 8$°C. There limitations with hot air supply jets at a downward angle located at ceiling level because of the associated stratified flow characteristics. This case is more common in industrial buildings with typical multicone diffusers. The effects have not been thoroughly investigated in literature.

2.3.4 Mixed Ventilation

Recently, a combination of natural and mechanical ventilation, and/or cooling (displacement or mixing), called mixed mode ventilation method, has been studied to ventilate buildings more effectively. The building fabric plays an important role, while the effect of natural ventilation or natural heating from solar radiation may be utilised at the same time or in another part of the building to reduce mechanical assistance for energy saving. This has mainly been used in offices, but it is suitable for a wide range of buildings, CIBSE (2000a) AM13: Mixed mode ventilation.

An integrated approach is a necessary requirement for every ventilation system. New technologies like Hybrid ventilation also utilise both mechanical and the natural ventilation/heating of the building in a two-mode system approach to minimise energy consumption. This depends both on the period of the year and on an individual day basis on the outdoor conditions. This is possible by an automatic controlled fan-extract system or supply air displacement system. The complex nature of the hybrid design has lead to some important features and problems being overlooked and in some cases this resulted to errors in selection parameters that had to be rectified in the commissioning phase, reported by Heiselberg (2002). The conclusions of 13 cases of cellular offices and schools were very diverse. This reflected the additional costs and the performance of the systems. A number of important parameters can be calculated at the same time by CFD that can lead to the consequent uptake of such ventilation types. The use of CFD as a prediction tool for best design performance is therefore very important.

2.4 Ventilation with Stratification

The flow patterns in ventilated enclosures are dominated by convection currents and temperature stratification, as shown previously in Figure 2.3 and Figure 2.4. The temperature variation across room height is measured instead of density. This is because of the linear relationship between temperature and density as well as the comparative ease of measuring temperatures. Stratification is evident in all methods of ventilation. Usually, there is a fine temperature differential between upper zone and lower zone. This is termed the stratified interface and it is very important in ventilation because it determines the height of a zone that can be used as the occupied zone. The thickness, δ,

of the interface between the zones is generally small. Depending on the temperature range between the hot and cold zones this can make it difficult to quantify. The zone is normally called the shift zone and is illustrated in Figure 2.5,

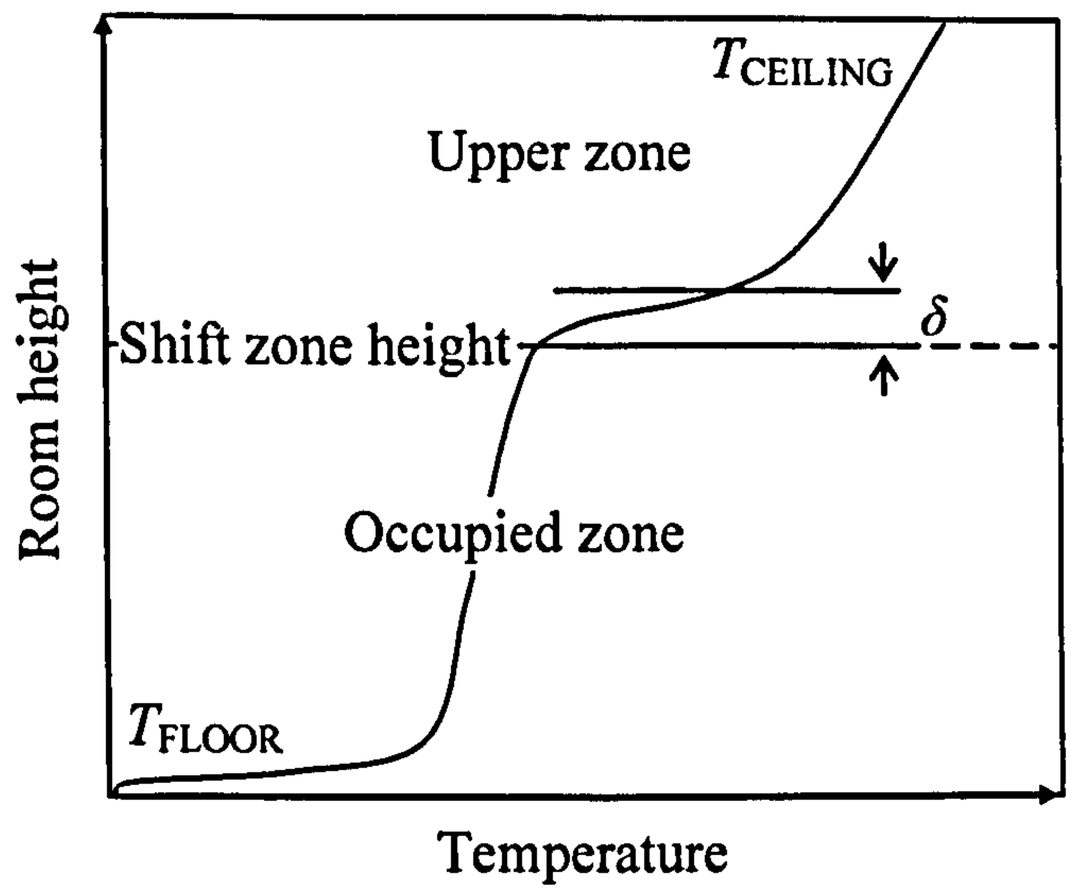

Figure 2.5: An expanded case of a temperature gradient of typical temperature stratification and the interface in buildings.

Turbulence effects are thought to be very weak in the interface. Thus, temperature is stably stratified and the vertical component of velocity is too small to mix the stratified layers in the interface. The horizontal component of velocity is much larger and fluid (such as a contaminant gas) can be carried on the layers without becoming mixed. Large-scale oscillations may be evident, which can cause periodic motion of the interface, due to stratified shear instabilities of Kelvin-Helmholtz (K-H) type. Turbulence fluctuations and the general shear instabilities on the interface become large depending on the Richardson number and these can take the form of K-H waves. At this stage, mixing becomes large and the interface has the form of a mixing layer above and below that mixes the two zones until the interface vanishes completely which leads to a constant density or temperature in the entire room.

In displacement ventilation systems, the convective flow and thermal stratification have a significant effect on the performance of the system, Mundt (1995a) and Nielsen (1994). In mixed ventilation, the momentum of the jet flow has to overcome the buoyancy force in the medium in order to sweep effectively the space clean of pollutants. Stratification can occur at different levels in enclosures and can affect the quality of breathing air. The thermal stratification in buildings and tunnels also

influenced the spread of smoke in fire scenarios, Hinkley (1988) and Xue *et al.* (1994). Therefore, the understanding of stratification in the ventilation of buildings is very important.

Previous studies of the mechanics relevant to natural ventilation in buildings were carried out by studying the flow properties such as the height of the interface in a "filling-box", Baines (1983), Linden *et al.* (1990), Cooper and Linden (1996). The studies were based on a box with high and low level openings. Fluid enters the box at different temperatures and densities that gives rise to differing ventilation patterns. The still air of the interior space is replaced and a horizontal sharply defined density/temperature interface builds between warmer and cooler fluids. Sources acting on the stratified interface are perpendicular to the interface. After the buoyancy source is applied for until the plume spreads sideways, the interface builds up and it depends on the pressure of the outside. The plume mixes with the surrounding environment inside the box that fills up the box with cloudy mixed striations of the source gas at certain level. The pressure differential of the interfacial layer at some height inside the box is the same with the value of the pressure differential at the same level outside the box. Thus, at $z = z_0$ the following equality is obtained,

$$\left(\frac{dp}{dz}\right)_{in} = \left(\frac{dp}{dz}\right)_{out} \tag{2.26}$$

providing that there is no vertical disturbance close to the interface to destabilise it nor any excessive increase or decrease in the dispersion rate to affect the contaminant content and hence under stable stratification, the velocity in the z-direction is zero, i.e., $\lim_{z \to z_0^+} \vec{w} = 0$ and $\lim_{z \to z_0^-} \vec{w} = 0$. The only velocity is the one generated by the entrainment of the plume which is pointing towards the plume. The interface defines a limit where the buoyant plume is only driven by its momentum where there is no buoyancy. The plume in the upper region mixes with the surrounding air filling up the space at the next neutral buoyancy level. The "filling-box" mechanism can be applied to natural and displacement ventilation. However, methods such as the “filling box” do not take into account the important mechanism of convection. This is one of the reasons for using CFD in this type of study. Additionally, the "filling-box" mechanism is based on the

observations of liquids. Liquids have very different diffusivity to gases and this in cases of ventilation can be of significant depth. The "filling-box" mechanism is shown in Figure 2.6 below,

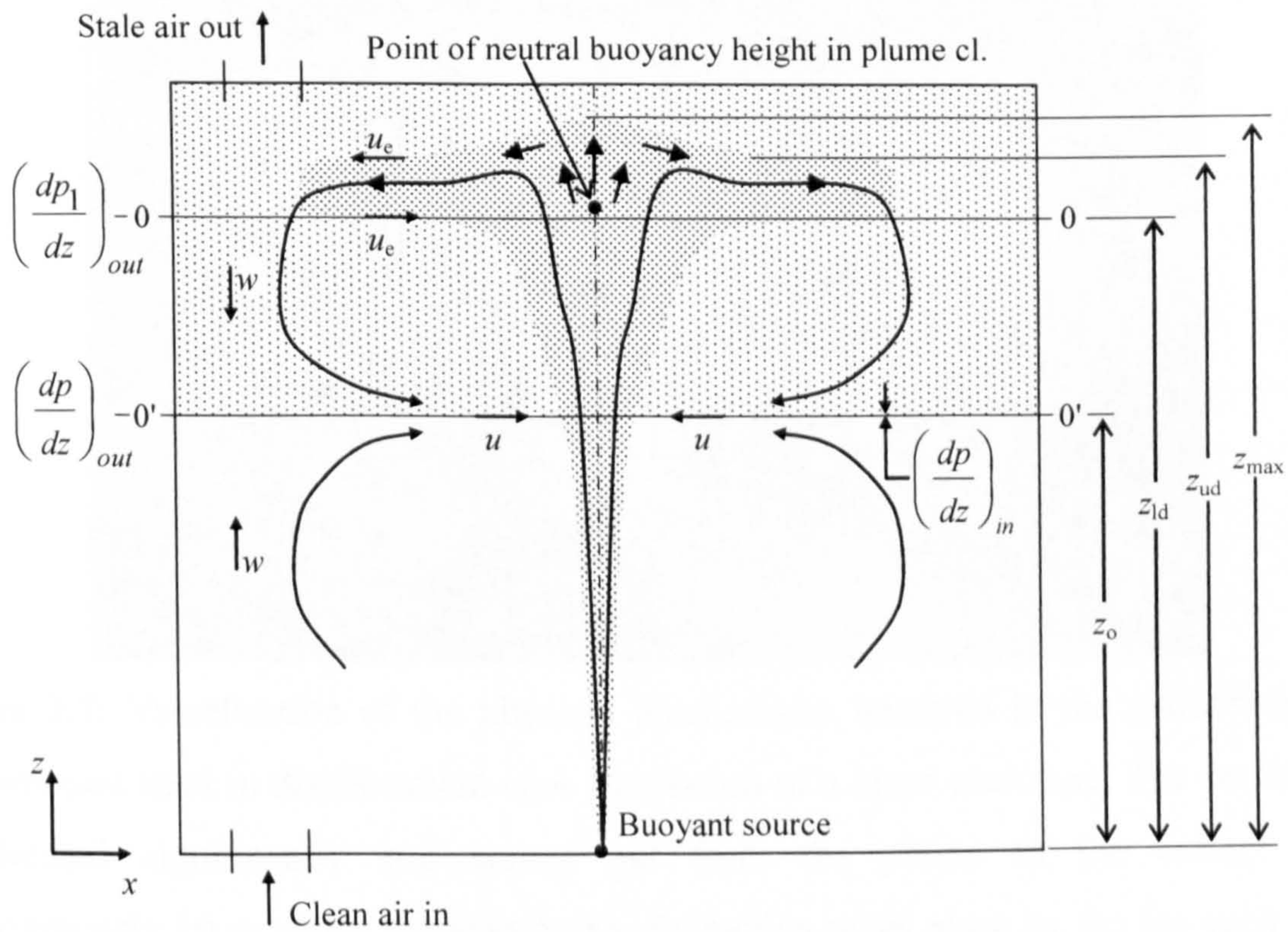

Figure 2.6: Schematical representation of contaminant dispersion in a box and pressure levels obtained from literature on buoyant plumes and filling boxes similar to Chen and Rodi (1980), Linden *et al.* (1990).

The best height for positioning the extract would be where the all contaminant plume in the building are likely to stop rising. This depends on the density of the contaminant and its mixing characteristics. Different contaminants will stratify at different levels. The temperature affects the density of gases that gives the contaminant an extra source of buoyancy. The utilisation of the extract height in a 40-m high shipyard hut is shown in Figure 2.7,

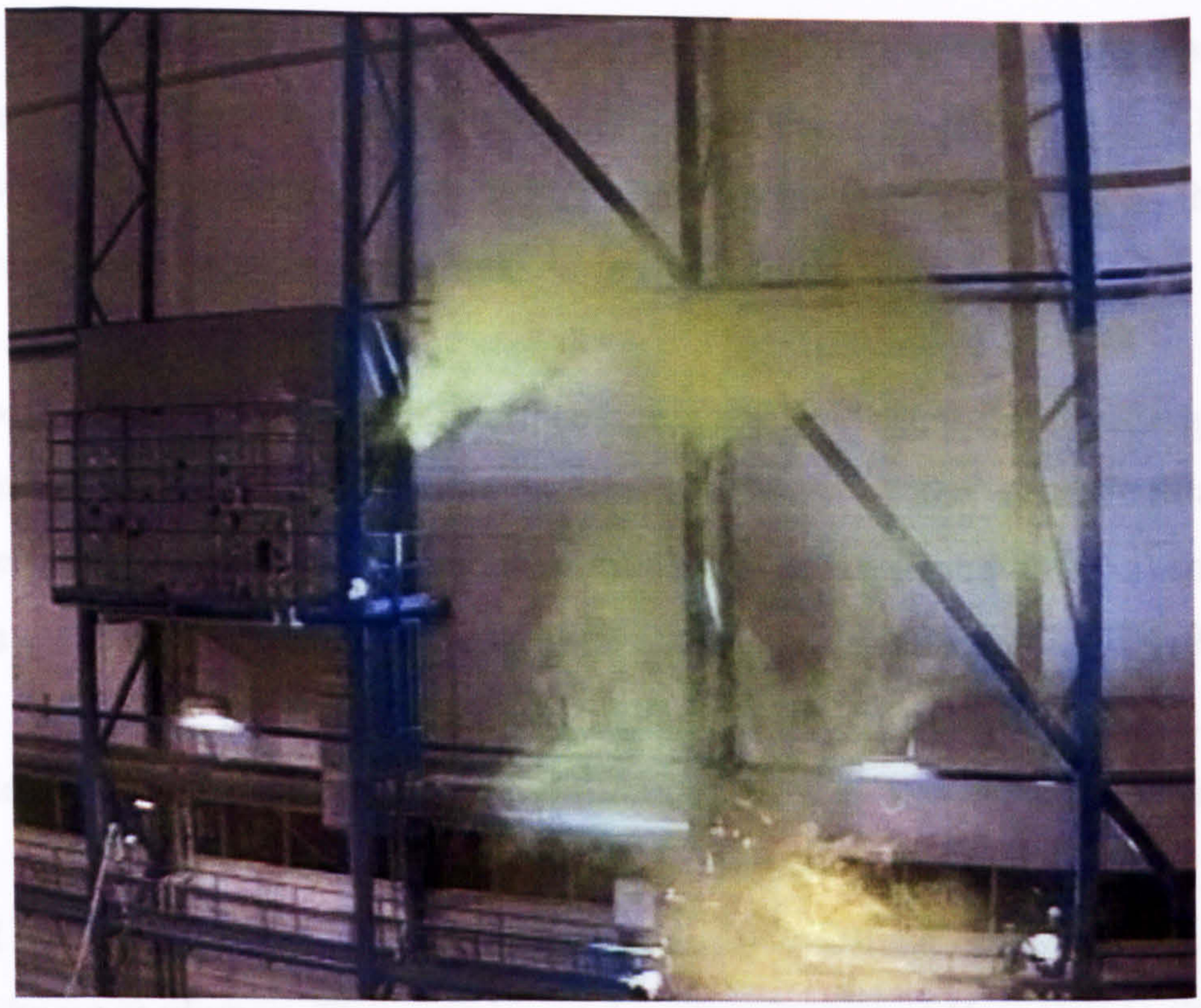

Figure 2.7: Visualisation of the physical mechanisms involved in the extraction of a contaminant used in displacement-type ventilation of a large enclosure. The smoke has decelerated significantly and spread out from the plume to the extract level approximately 10 m above the ship decks. Extraction takes place by the fan until all of the contaminant is withdrawn to the outside. The outside temperature is -30°C, Skistad (2000).

The contaminant release was observed inside the maintenance hut from the welding activity by smoke visualisation during the procedure of hull repair. The smoke and welding plumes were released from the deck level of the ships that were at approximately 8-9 m high, raised about 1.5 m above the ground. The extract point was at a fixed position at around mid-height inside the maintenance hut and the temperature interface occurs at the same height. There were occasions where the buoyancy force of the welding plumes was very high. This resulted from persistent welding causing the contaminant products to pass the extract level and head towards the ceiling where they disintegrated. However, in another occasion the welding plume at 2 m above the floor, occurring on the side of one ship, went over another ship's hull and was successfully flashed to the outside by the extraction unit. In a large shell-type building, when the repairing activity results in a highly buoyant plume, it may not be so desirable, because of large amounts of pollutant accumulating below the roof. This may also result in unstable stratification and downfall as the pollutants get cooled down by the external

cold temperature causing a downfall into the occupied zone resulting from penetrative convective cooling similar to the night cooling that occurs estuarine mixing. Fischer *et al.* (1979) described the diurnal cooling mechanism in water reservoirs as the surface penetrative convection effects dominate during nightfall.

The properties of the stratified interface are very important in the design of the ventilation system because it influences the efficiency of the system. Stratification effects are widely used in displacement ventilation systems, Mundt (1995a) and Nielsen (1994). In the design of the air-conditioning system stratification effects can be utilised to reduce the cooling load of the building, Allen (1979). Stratified cooling is also used to enhance the performance of the air-conditioning system, Bagheri and Gorton (1987).

Chen and Rodi (1980) mentioned that the non-linear stratification affects the deflection height of buoyant plumes. The experimental measurements of Hart (1961) showed that the deflection heights of a vertical buoyant jet under the presence of a thermocline in the non-linearly stratified environment were associated to an empirical correlation under three different flow situations. When the discharged fluid does not reach the surface and the deflection heights are at the level of the thermocline, the density difference between the hot layer and the thermocline is $0 < \Delta\rho / \rho_0 < 8$. The main flow characteristics of such plumes are shown in Figure 2.8,

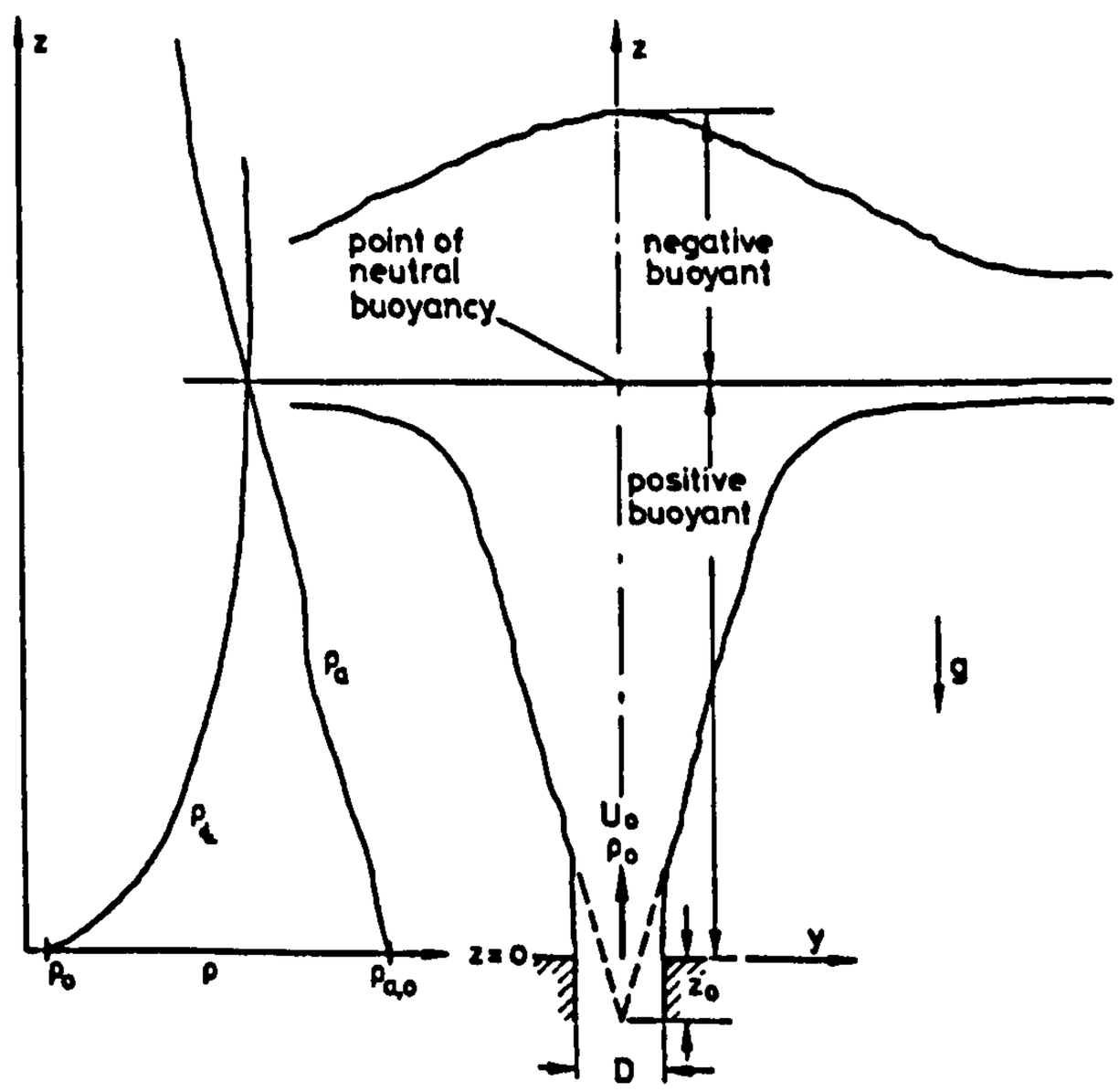

Figure 2.8: Buoyant fluid rising in linear stratified surroundings, adapted from Chen and Rodi (1980).

There is roughly an order of magnitude difference between the stratification that occurs in buildings and geophysical flows. In the current work, for the strong stratification case, this is 4.9. Therefore, for similar density ratios as those suggested in the literature, the contaminant is likely to stratify at the height of the interface.

In shipyard huts or aerospace hangars, where top open offices are likely to coexist with painting, manufacturing or assembly plant processes such as welding and painting, the quality of air can be affect across the entire working space. In order to ventilate such buildings separately, without the inclusion of any physical partitions that may obstruct the work or restrict the working space, it is usually a requirement of practicality to obtain higher controls over the physical phenomena involved in such ventilated spaces. The working principles of the ventilation system of a large building and the resulting temperature gradient as a result of the is shown in Figure 2.9,

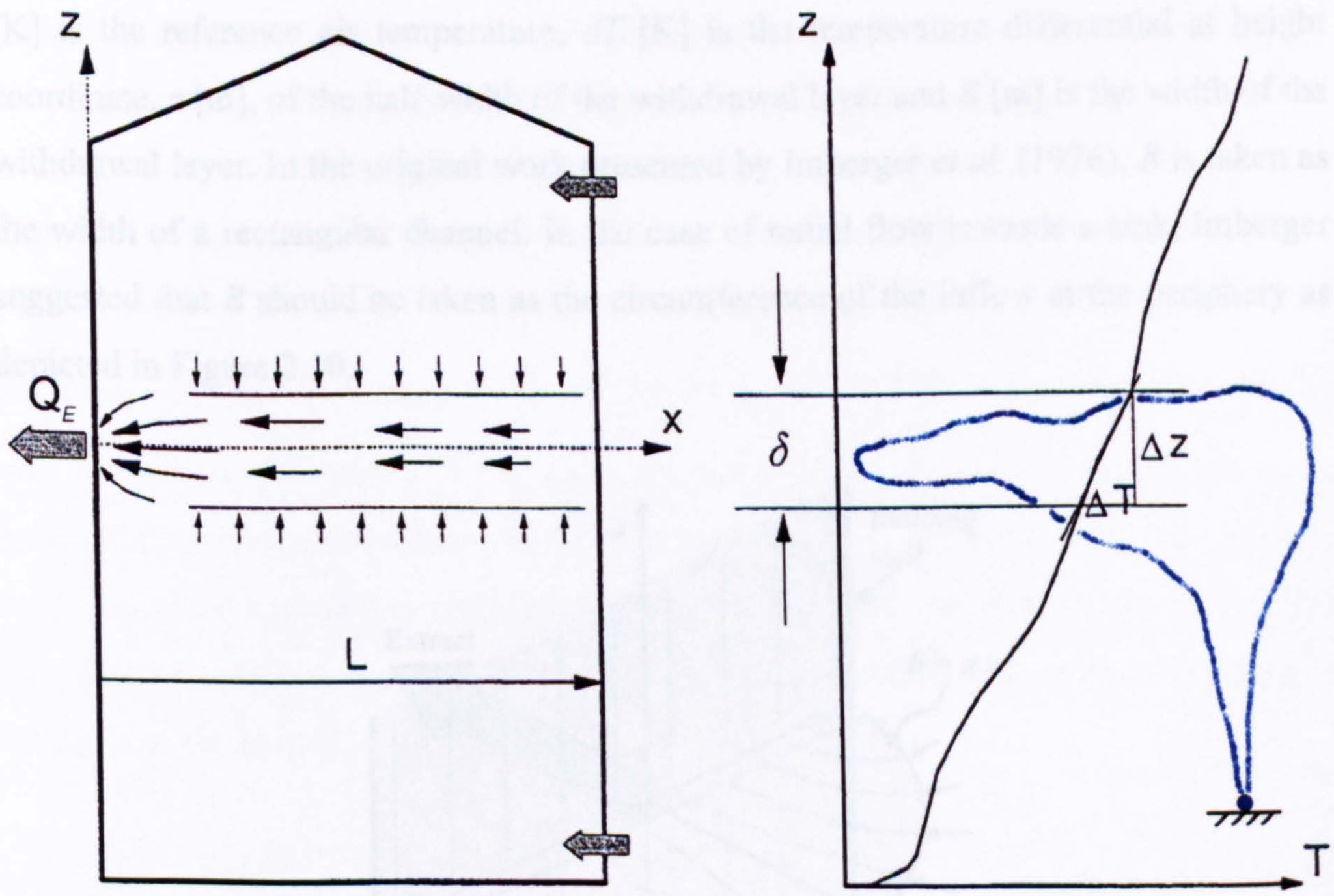

Figure 2.9: Withdrawal in a stably-stratified volume of air in a large building, adapted from Skistad (1998).

The thickness of the interface also affects the ventilation rates because it influences the thickness of the withdrawal layer, δ_w, which is proportional to the ventilation rate. In

zonal ventilation or zoning (ventilating a building in its local areas, i.e., kitchen, sitting room, etc. or manufacturing plant, offices, etc.), the calculation of extract rates is very important. In the technical paper by Skistad (1998) it is pointed out that the thickness of the interface, which is related to the volume of the withdrawal layer, is a very important parameter in the calculation of the extract rates for large enclosures in order to divide the space into vertical partitions. Skistad (1998) attempted using the idea of the withdrawal layer thickness, given for half the height, $(\delta_w)_{0.5}$,

$$(\delta_w)_{0.5} = k\left(\frac{Q_E}{B}\right)^{\frac{1}{2}}\left(\frac{g}{T}\frac{dT}{dz}\right)^{-\frac{1}{4}} \tag{2.27}$$

which has been presented by Imberger in Fischer *et al.* (1979), valid for stably-stratified layers in rivers and estuaries. In the equation (2.27) above, k is a constant which is equal to 2, Q_E [m^3/s] is the extract air flow rate, g [m/s^2] is the acceleration due to gravity, T [K] is the reference air temperature, dT [K] is the temperature differential at height coordinate, z [m], of the half-width of the withdrawal layer and B [m] is the width of the withdrawal layer. In the original work presented by Imberger *et al.* (1976), B is taken as the width of a rectangular channel. In the case of radial flow towards a sink, Imberger suggested that B should be taken as the circumference of the inflow at the periphery as depicted in Figure 2.10,

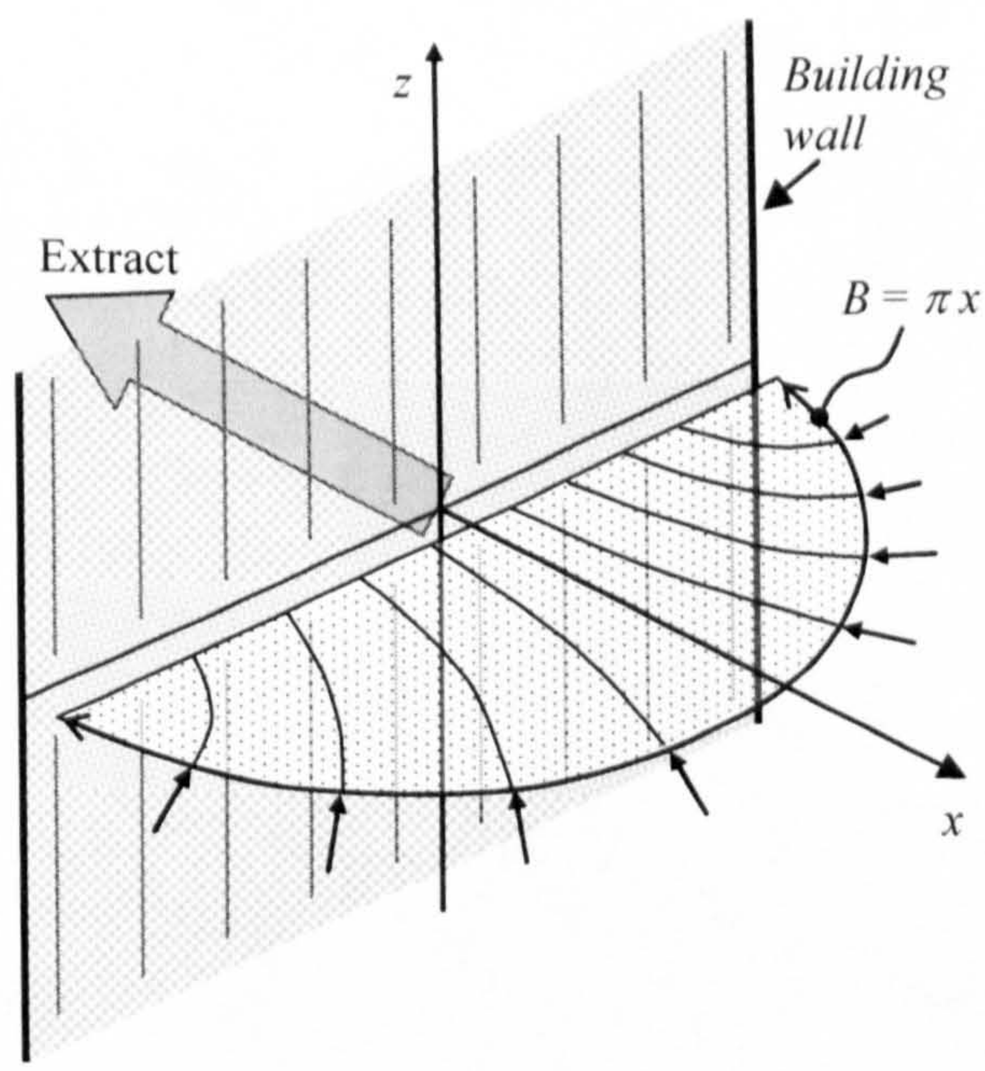

Figure 2.10: Withdrawal layer. The arrows show the direction of the flow, adapted from Skistad (1998).

Skistad (1998) demonstrated that selective withdrawal worked for temperature gradients as low as 0.125°C/m, but it was also mentioned that higher temperature gradients would be more resistant to disturbances and reduce the thickness of the withdrawal layer. The level of extract had an effect on stratification that created different stratified zones across the height of the building. The effects of stratification could then be utilised to ventilate the building in different zones. This could be done if the interface thickness was relatively small. However, if the thickness was too large for the given ventilation rates, higher extract force was required. This ventilation method was called selective ventilation because of the utilisation of the zonal system with room height to withdraw polluted air in a similar way to the selective withdrawal of reservoirs. The method was still at research level and no major work on the interface thickness has been reported so far. Finally, it was suggested that equation (2.27) could be used to determine the order of magnitude of the withdrawal layer thickness for buildings.

A theoretical estimation of the withdrawal layer thickness can be made by using the temperature of the hot air supply, T_{HS} = 32°C (since a higher temperature gradient exists in the interface), the average room temperature as a reference, T_{room} = 293 K, the length of the withdrawal layer at the periphery, x = L = 5.5 m and the two extract flow rates, 0.0138 and 0.0462 m³/s, we obtain $\delta_w = 0.18\,\text{m}$ and $\delta_w = 0.33\,\text{m}$. However, by including the inlet flow rates we obtain, $0.3 \le \delta_w \le 0.5$. Therefore, depending on the inlet conditions, the length of the room, the temperature distribution across the room height, the reference temperature and the extract flow rates, the extract will theoretically try to maintain interface at certain thickness. It may be worthwhile to notice that this theoretical prediction assumes that the height of the withdrawal layer from the floor is the same as the extract height from the floor.

2.5 Turbulent Mixing in Stratified Fluids

The mixing mechanism is very important in the break-up of stratification in certain building ventilation systems. Using mixing ventilation, the optimum turbulence levels need to be determined for the efficient design of the system. The turbulent mixing of stratified fluids has been studied in the literature of atmospheres and oceans by many

researchers, Linden (1979), Fernando (1991), Larson and Jönsson (1996), Redondo *et al.* (1996) using stirring grid apparatus or a jet. The effect of turbulence and wave propagation on the stratified layer thickness in the atmosphere and oceans have also been discussed in the literature, Moum and Smyth (2000), Staquet (2000), De Silva *et al.* (1999), Cardoso and Woods (1993), Fernando and Hunt (1996). Experiments also found in the literature have investigated the parameters that control the thickness of stratified layers of the thermocline in reservoirs containing saline water. Experiments in atmospheric flows have revealed a larger number of scales in stratified shear flow from co-flowing streams that are very similar to homogeneous turbulence, Turner (1973). Similarities have been observed between oceanic and atmospheric turbulence pertinent to engineering applications from several researchers, reviewed by Fernando (1991). Scale models using saline water as the working medium describe the effects of turbulent diffusion in the atmosphere and oceans, Folkard *et al.* (1997), and ventilation, Linden *et al.* (1990). Some disadvantages though may arise due to the scaling procedure, or from ideal laboratory conditions in reducing the range of scales associated with real conditions. Assumptions are often made to reduce the degrees of freedom in simplifying the analysis. From experiments on grid-generated turbulence in stratified flows by Hopfinger (1987), the smallest scales very close to the initiation location can be regarded as homogeneous turbulence. These length scales grow in size to form vortex pairings that decay to dissipative scales at a later stage as isotropic homogeneous turbulence. Eddies evolve in three dimensions and thus the 3-dimensionality of the problem is also important to describe correctly the real conditions. The interface is affected by turbulent shear and it propagates further downstream by the entrainment process. Hence, the mixing that occurs in un-sheared grid-generated turbulence experiments can provide control over the generation and dissipation scales in the understanding of turbulence.

2.5.1 Development of length scales

The flow is dominated by inertia, buoyancy and viscous forces. The inertial forces act on the turbulent scales and fluctuating motion, while the viscous forces act on the smallest of scales. Stratification acts as a damping mechanism to limit first the largest scales in the flow resulting to horizontal motion. The buoyancy scale, is characterised by the vertical velocity oscillations due to the turbulent vortices in the flow with respect

to the Brunt-Väisälä frequency, $L_b = w'/N$ where w' is the resulting rms vertical velocity fluctuation of turbulence, $\sqrt{\overline{w'^2}}$. The turbulence collapse starts when the scale of the oscillations is of the order of the dissipation range time-scale, $L_R = (\varepsilon / N^3)^{1/2}$ known as the Ozmidov (1965) scale, which is the largest scale of overturning in a stratified flow. The turbulence scales increase the potential energy in the flow causing redistribution. The consequent displacement of the fluid known as Thorpe (1977) scale, L_T, is not affected by the internal wave motion while the opposite is true. The largest scales are first affected by buoyancy. If the vertical oscillation from turbulence is larger than the Ozmidov scale, i.e., $L_b > L_R$, overturning does not occur as buoyancy dominates the exchange of kinetic energy between vertical length scales resulting to horizontal movements (internal seiching). However, if the scale of the vertical motion obtained from internal waves is small compared to the turbulent scale, the buoyancy scale can be used instead of the Ozmidov scale, i.e., $L_b \approx L_R$. The overturning scale in the flow is frequently denoted as l and is related to the density fluctuations used by Ellison (1957) to indicate the vertical distance travelled by the particles before either returning to their equilibrium level or mixing has as $L_H = \rho' / (\partial \overline{\rho} / \partial z)$ where ρ' is the resulting rms density fluctuation, $\sqrt{\overline{\rho'^2}}$. If the turbulence scale becomes too small, inertial forces are balanced at the viscous or Kolmogorov (1962) scale that is defined as $L_K = (\nu^3 / \varepsilon)^{1/4}$ where the kinetic energy of the eddies is converted into heat, i.e., at $L_R = L_K$. Various flow observations between turbulence and wave in typical stably-stratified turbulent shear flows are made more extensively in Stillinger *et al.* (1983) and Hopfinger (1987).

Gibson (1981) and Stillinger *et al.* (1983) found that the turbulence behaves the same way in stratified flows as in unstratified flows and follows the same statistical laws when classified as *'active turbulence'*, where the active turbulence range is,

$$1.4 L_R \geq L_b \geq 15.4 L_K \tag{2.28}$$

The eddy cascade making up the process of stratification can be seen in Figure 2.11,

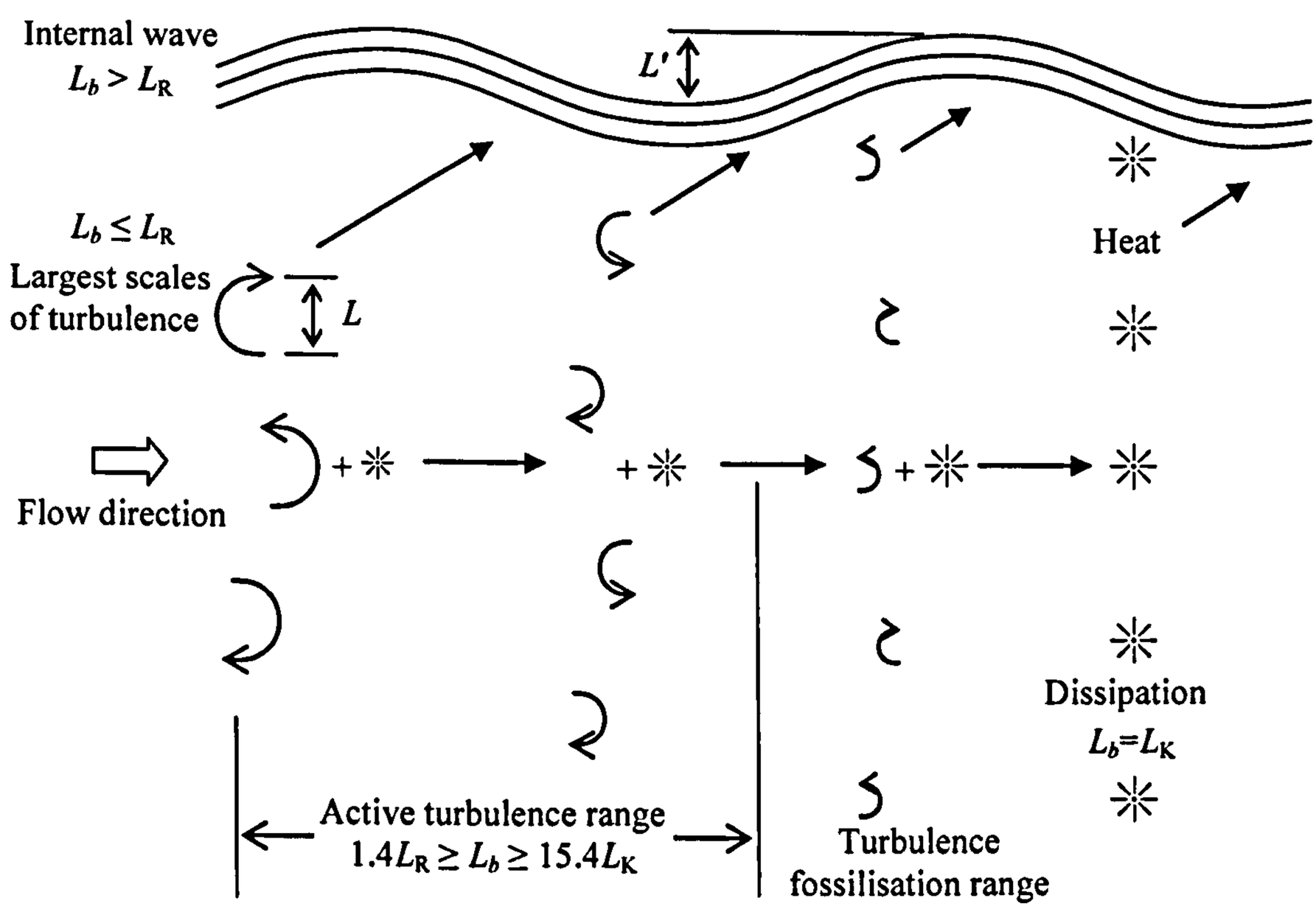

Figure 2.11: Horizontal development of length scales.

Fossil turbulence and intermittency are evident in most stratified flows where remnant fluctuations produced by turbulence are no longer active and are transported by the internal waves, Gibson (1987). Internal waves can also appear as remnant intermittent fluctuations that are produced by vorticity damped by buoyancy. This effect is also observed with temperature fluctuations in geophysical fluids. Although the effect of buoyancy and viscous forces is more evident at the highest and lowest of the scales, they act on the entire range of motions. The buoyancy force acts as another source of viscous damping to further dissipate energy from the turbulent motion that is 20% as efficient as viscosity, Stillinger *et al.* (1983). The kinetic energy of the turbulent eddies is dissipated faster in a stratified fluid as the friction forces are larger. Therefore, the critical dissipation rates in stratified flows are very important.

Stillinger *et al.* (1983) estimated the minimum dissipation rate at the transition to a wave field for the maintenance of turbulence is equal to $\varepsilon_{tr} = 24.5\nu N^2$ that was also supported by Gibson (1987), though his earlier work arrived at a slightly higher coefficient. For this to occur, $N^2/(d\bar{u}/dz)^2 = 1/4$, which is the equivalence criterion for stratified shear flows, is equal to ε_{tr}. The buoyancy frequency in the experiments is $N = 4.345\times10^{-1}\,\mathrm{s}^{-1}$, based on the temperature difference of the hot air supply outlet

and mean reference temperature. Hence, the dissipation is $\varepsilon_{tr} = 6.9578\times10^{-5}\ \mathrm{m^2/s^3}$ (at $T = 20\,°\mathrm{C}$, $\rho = 1.205\,\mathrm{kg/m^3}$ and $\mu = 1.813\,\mathrm{kg/s\cdot m}$). The critical dissipation scale is $L_\mathrm{R} = (\varepsilon_{tr}/N^3)^{1/2} \approx 0.0291\,\mathrm{m}$ which is $L_\mathrm{R} = 2.91\,\mathrm{cm}$. The Kolmogorov scale is $L_\mathrm{K} = (\nu^3/\varepsilon_{tr})^{1/4} = 0.00264\,\mathrm{m}$ which is $L_\mathrm{K} = 0.264\,\mathrm{cm}$. Thorpe (1973) observed in water experiments that the central linear region is 2.7 cm and the critical length is 0.24 cm. Eddies below this size were regarded as isotropic in stratified flow. These values are comparable with the size of length scales evaluated by Gerz *et al.* (1989) who additionally evaluated the integral scale as $L = 4.95\,\mathrm{cm}$. A mesh resolution of approximately twice the critical scale or of the size of the integral scale, which is of a comparable size to the higher scale in the inertial subrange, may be sufficient for steady-state simulations considering that the transport of turbulence scales is calculated by differential transport equations.

The kinetic energy becomes higher after the transition at $Ri = 0.25$. When the transition is reached at $1.4L_\mathrm{R}$, L_H has the largest size and this is given by a relationship derived by Taylor (1935) that is $k \approx (\varepsilon l)^{2/3}$. When $L_\mathrm{R} \approx 11L_\mathrm{K}$ all turbulent eddies have been damped either by buoyancy or viscosity. A typical example of transition of turbulence to waves from hydrodynamic experiments can be seen Figure 2.12,

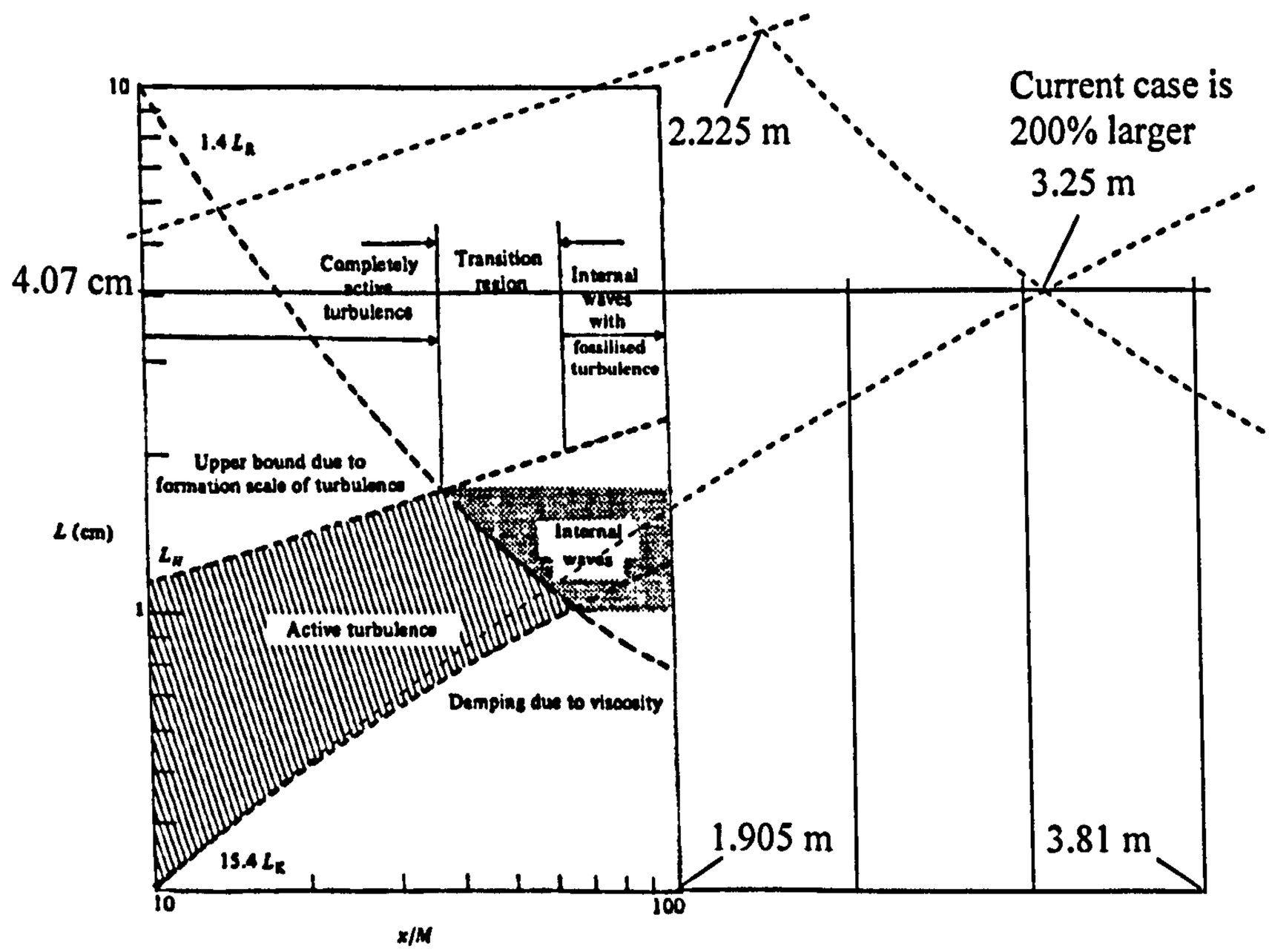

Figure 2.12: Evolution map for homogeneous stratified grid turbulence with normalised downstream distance, where initially $L_\mathrm{H} << L_\mathrm{R}$, adapted from Stillinger *et al.* (1983).

The sizes of the important scales are at the limits of the active turbulence range. These are at $1.4L_R = 4.08\,\text{cm}$. The smallest length scale in the CFD studies should therefore be able to account for the transition where the turbulence is still active, $15.4L_K = 4.07\,\text{cm}$. On the original picture, this point is reached at around 0.57 m, but it seems here that the scale needs to be extended to account for the occurrence of this transition. This is because the interface is slightly thicker in the experiments of this work. However, it can be concluded that since this is close to the test chamber boundaries, the occurrence of complete fossilisation of turbulence may be relatively small.

2.5.2 Entrainment in Stratified Fluids

The entrainment mechanism that occurs at the boundaries of the stratified interface can influence the thickness of the interface due to internal and external mixing, Turner (1973), Linden (1980). In buildings, this can influence the thickness of the withdrawal layer and as a result the stratification can become more linear. Similar observations can be made on the thermal stratification for large buildings due to rising plumes and extract ventilation that is studied by Skistad (1998). The interface can be mostly characterised by large wave instabilities. It is usually not mixed and the flow is pointing towards the exhaust. However, the flow in the hot and cold layers is more likely to be mixed by turbulence resulting in a weak temperature or density gradient. If the turbulent mixing in both the upper zone and the lower zone is high enough, the interface weakens until the point at which there is no interface but an almost even or closer to a linear temperature gradient across the height of the space. It can be argued that the most fundamental experimental case for testing stability of stratification could be set up by a jet flow impinging onto a stratified interface. Linden (1973) modelled experimentally the impingement of a vortex ring onto a thin stratified layer. The vortex ring momentarily forms an impingement dome at the interface and then rebounds away from it while entrainment occurs during the rebound process. Linden (1973) derived a model for turbulent entrainment mechanism. The entrainment rate w_e, normalized by the characteristic velocity of turbulence, w_1, or the characteristic velocity of the large eddies impinging on the interface, was found to follow a power law relationship with

the Richardson number, $w_e/w_1 = cRi^{\alpha}$, where α is the entrainment exponent. Many experimentalists followed this relationship and their analyses showed that the entrainment rate declines with increasing stratification. Several experimentalists obtained slightly different relationships. Linden (1973) derived an entrainment exponent of -3/2, consistent with Turner's (1968) results obtained by stirring grid experiments. When the density difference was produced by a temperature difference, Turner (1968) obtained an exponent equal to -1, while the value of -3/2 was obtained when salt was added in the water. Cotel *et al.* (1997) also carried out his experiments in a water tank, where in the case of moderate Ri the entrainment rate of the vertical jet was proportional to the Ri with an exponent of -1/2, while in the case of a rotated jet the value of the exponent was decreased to -3/2. Fernando (1991) pointed out that the value of α varies over a wide range, typically from -1/2 to -3/2 or -2. Consequently, the value of the exponent decreases with decreasing stratification as internal mixing becomes higher and this is associated with the curvature of the Ri_0 relationship. Stratification is weaker in buildings due to heat and mass losses to the outside which restrict the range of Ri number. For large buildings, stratification is also closer to a linear type that makes the value of the exponent weigh towards the lowest value suggested in the literature, i.e., around -1/2.

2.5.3 Vertical heat flux

There are certain important fluxes in a stratified flow associated with the buoyancy forces where $\overline{w'w'}$ couples with $\overline{w'T'}$ and $\overline{u'w'}$ couples with $\overline{u'T'}$. These four pairs of oscillating modes with two complex complex-conjugate eigenvalues introduce a certain degree of time dependency in the flow depending on the Ri number.

2.5.4 Counter-gradient heat flux and down-gradient heat flux

In the event of a heat source at the bottom of the lower layer, vertical vorticity associated with turbulent diffusion from the rising of a plume becomes the transport mechanism of vertical heat flux, $\overline{w'T'}$, or counter-gradient heat flux (CGHF) that acts along the direction of a positive temperature gradient to the upper layer. At certain circumstances, there will be opposite effects to the vertical heat flux. External mixing in

the interface caused by an oscillating grid in the upper layer increases the slope of the density distribution in the lower layer that is associated with the negative counter-gradient heat flux, $-\overline{w'T'}$, or down-gradient heat flux (DGHF), demonstrated schematically in Figure 2.13,

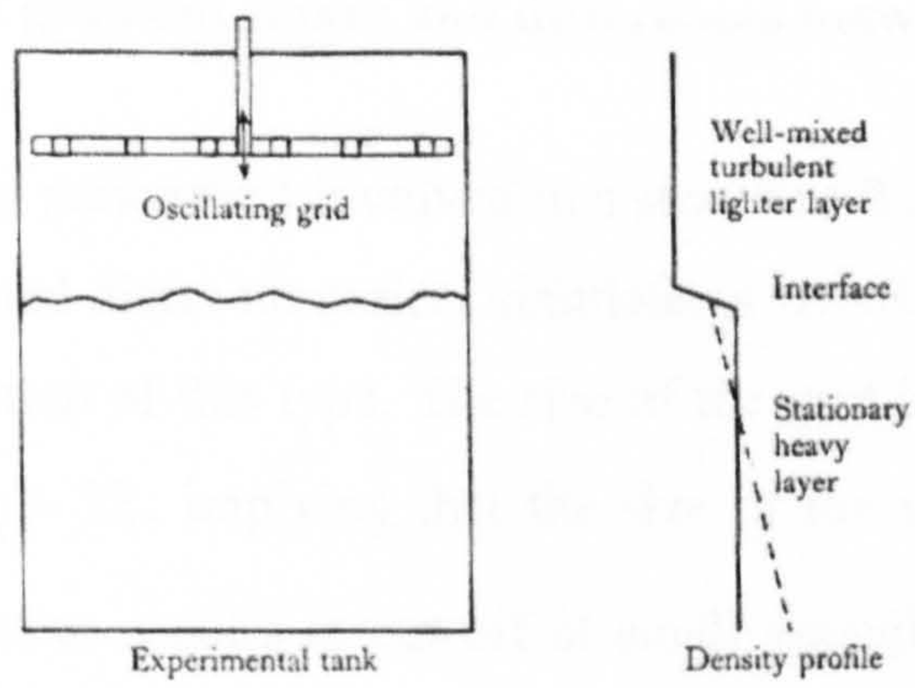

Figure 2.13: Schematic representation of an experimental configuration for testing the effect of penetrative mixing from the upper layer in an experimental tank and resulting temperature distribution for a two-layer system, adopted from Turner (1973).

External mixing in an initially stratified fluid produces a well-mixed layer bounded by a sharper interface that moves away from the stirrer as the fluid is entrained across it from the mixed layer. This also increases the slope of the bottom layer, as the turbulent eddies produced by the grid pass through the interface.

A typical example of this mechanism is penetrative cooling in lakes. The external mixing in the epilimnion caused by penetrative convection smears the thermocline and changes the temperature distribution of hypolimnion. This is shown in Figure 2.14,

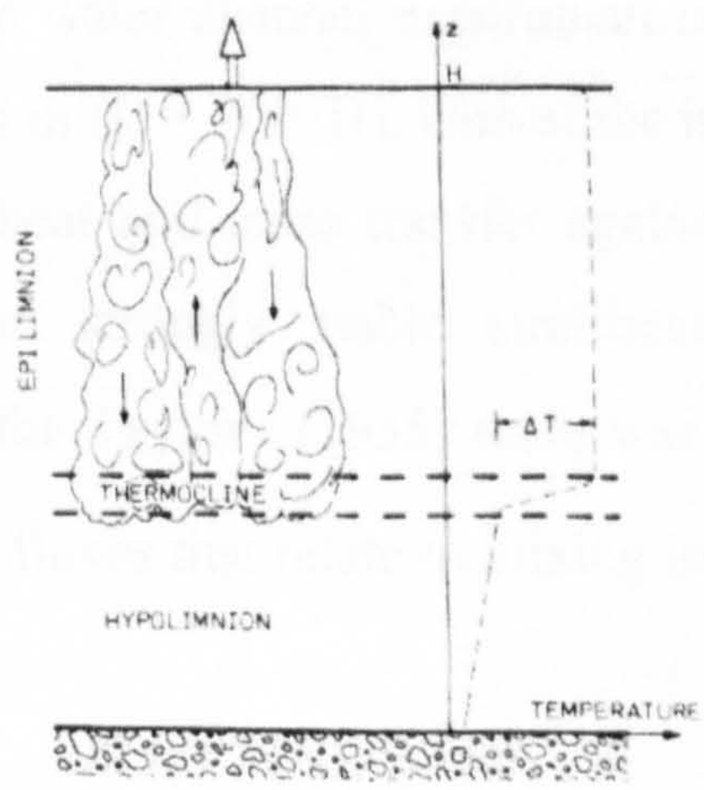

Figure 2.14: Schematic representation of penetrative convective cooling in lakes. Rising and falling plumes in the epilimnion corrode the thermocline while increasing the density distribution in the hypolimnion, adopted from Fischer *et al.* (1979).

Therefore, when using CFD modelling it is absolutely important to model certain gradient fluxes.

2.5.5 CFD modelling of gradient fluxes and differences between air and water

Several important mixing parameters involved in a stratified flow are studied by Gerz *et al.* (1989). They performed direct numerical simulations (DNS) of steam flow on water that was the first simulation of this type. The size of the grid is 64^3 (= 262×10^3). The wave number was $\kappa_{max} = 32$, implying that the size of the minimum length scale is $L_{min} = 3.125\,\text{cm}$, so that to spectra is cut-off at small enough scale size for accurate simulations. One of the finding was that the buoyancy forces suppress vertical motions so that the cells degrade to 2-dimensional fossil turbulence. The counter-gradient heat flux (CGHF) acts to enforce quasi-static equilibrium between potential and kinetic energy. The aim of their investigation was to compare results from Webster (1964) who carried out experiments in a wind tunnel to test the effect of Pr number. The CGHF was not evident in his study and Gerz *et al.* (1989) served the purpose to explain the difference. Another aim of Gerz *et al.* (1989) was to tune second-order closure models by Lauder (1975) and (1976). Shih *et al.* (2000) studied the scaling and parameterisation of a homogeneous stably-stratified turbulence flow subject to constant shear by DNS simulation similar to Gerz *et al.* (1989). The results obtained from the simulation of 256^3 (= 16.777×10^3) grid points confirmed that the simulation of 128^3 (= 2.097×10^6) was adequate for the purposes of their study. In all these cases, the model parameters were selected to simulate the water channel experiment by Komori *et al.* (1983) with dimensions of 6.1 × 0.3 × 0.6 m (L × W × H). One of the important findings was that in stable conditions, turbulent heat and mass transfer against the mean temperature and velocity gradients occurs in strongly stable stratification. The initial turbulence Reynolds number based on the Taylor's (1935) scale was $Re_\lambda \approx 25$ and $\lambda = 2.59\,\text{cm}$. The most important gradient fluxes that relate to mixing in stratified flows of water and air are shown in Figure 2.15,

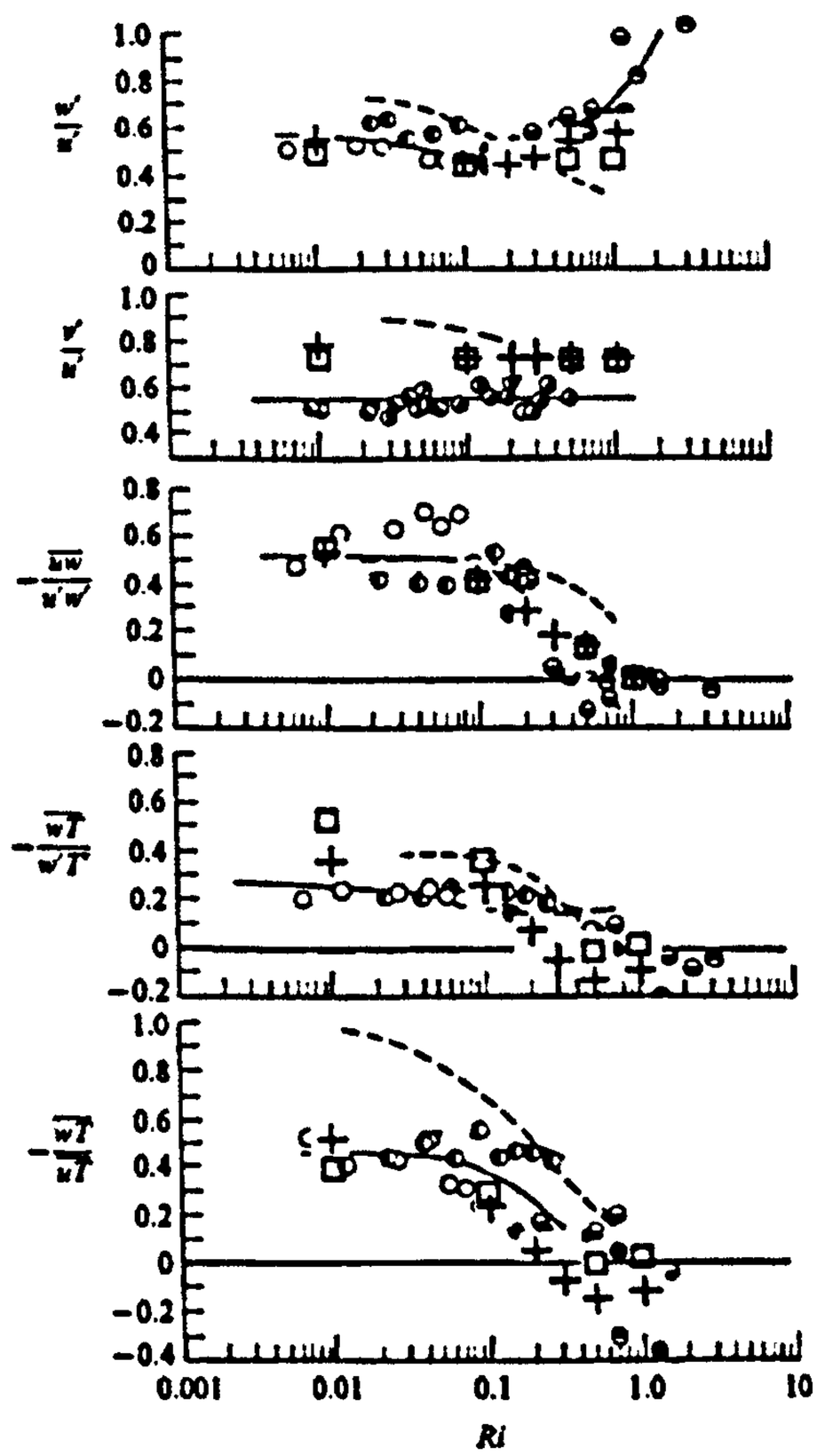

Figure 2.15: Variation of several turbulence quantities with Richardson number. The water experiments are represented by circles, Komori *et al.* (1983). The dashed curve represents measurements in air from the experimental data of Webster (1964). The crosses are for a simulation of $Pr = 5$ (water) and the squares are for $Pr = 0.7$ (air) at $t = 4.5$, adopted from Gerz *et al.* (1989).

It is suggested from Figure 2.15 that non-linearities reduce at $Ri \geq 0.5$. This occurs as the Batchelor's (1953) skewness factor decreases due to the reduced shear, below which it became difficult to obtain conclusive results from either simulations or experiments. A "quasi-steady" or "asymptotic" state could be reached exactly at $Ri \geq 0.5$, where all fluctuations became nearly constant causing the length scale to become constant. For low values of Richardson number, $Ri < 0.25$, counter-gradient heat fluxes and momentum fluctuations were in accordance with the gradient transport assumption. These change sign or become negative at higher Richardson number. Specifically, in the cases where air is used, this is $0.5 < Ri < 0.8$. However, it can be argued that in general $Ri > 1$ for stratification to become strong. Under stable stratification, these correlations indicated that the intermittent upward eddies with positive temperature fluctuations caused upward heat transfer against the gradient.

The turbulent eddies that are non-isotropic are mainly generated from fossilisation of turbulence in a stratified flow, Gibson (1987). The pressure correlations change sign, mainly due to the non-isotropic eddies that appear as inactive hot and hold spots in the flow at fossilisation. The dissipation of heat in some publications is indicated by χ and is related to the rate at which the thermal inhomogenities are removed by diffusion. This can change the dissipation levels and it is not accounted by second order closures. The turbulent-turbulent interactions, however, act to reduce the anisotropy in the flow but to some smaller extent. Thus the thermal dissipation rates are too small to produce the same rate of decay as the viscous dissipation does for kinetic energy. However, this has rarely occurred in the current work as suggested by Figure 2.12 and associated calculations for the current experiments.

The correlation between heat flux and counter-gradient heat flux with turbulent diffusion and wave is shown in Figure 2.16,

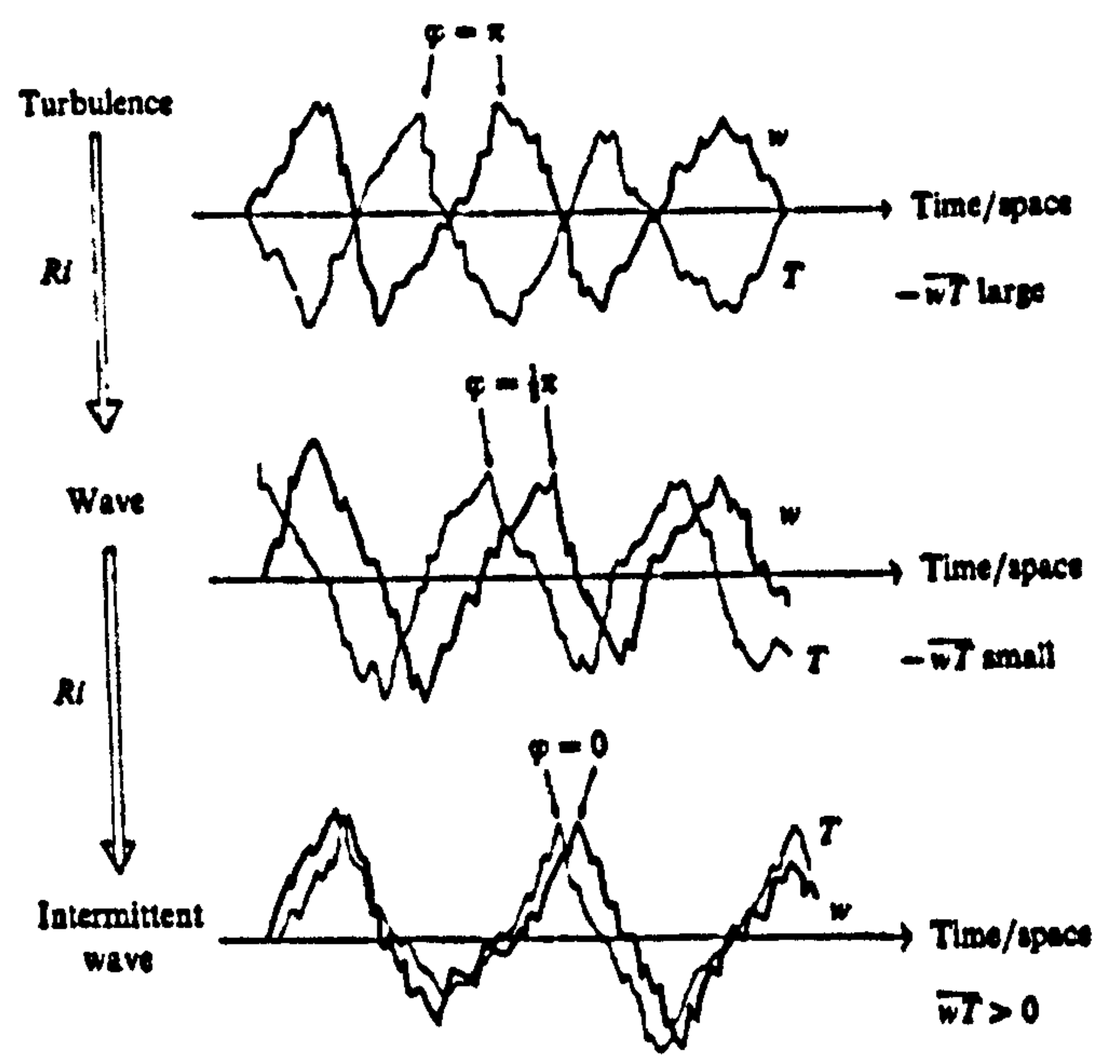

Figure 2.16: Turbulence and wave characteristics for stable stratification. The sketches of signals of w (thick curves) and T (thin curves) illustrate typical phase angles φ according to Richardson number which increases from top to bottom, adopted from Komori *et al.* (1983).

Figure 2.16 can be discussed bearing in mind Figure 2.15 that describes the relationship between DGHF and Ri regarding the motion of the fluid. For a small Ri, downward temperature fluctuations along the positive gradient are not affected by the

corresponding momentum fluctuations in the mean flow resulting to a phase angle equal to $\pm\pi$ between downward temperature transport and momentum transport. For a higher Richardson number, the temperature fluctuations are becoming smaller that is where the phase angle decreases to $\pm 1/2\pi$, wave motion appears and DGHF vanishes. At some higher Richardson number, momentum and temperature fluctuations are overlapping, i.e., the phase angle is equal to zero and the DGHF becomes positive. This state of motion was described as "intermittent waves" by Komori *et al.* (1983). A high DGHF is typical in weak stratified flows, while a very small vertical heat flux may indicate gravity-wave like motion.

Turbulence is associated with a number of scales that vary both in time and space. These vary from eddies that are of the size of the characteristic scale to the viscous dissipation, Kolmogorov scales. One way to describe the turbulent energy spectrum is by the power versus frequency the decay rate of -5/3, Hinze (1975) and Gerz *et al.* (1989). This is shown in Figure 2.17,

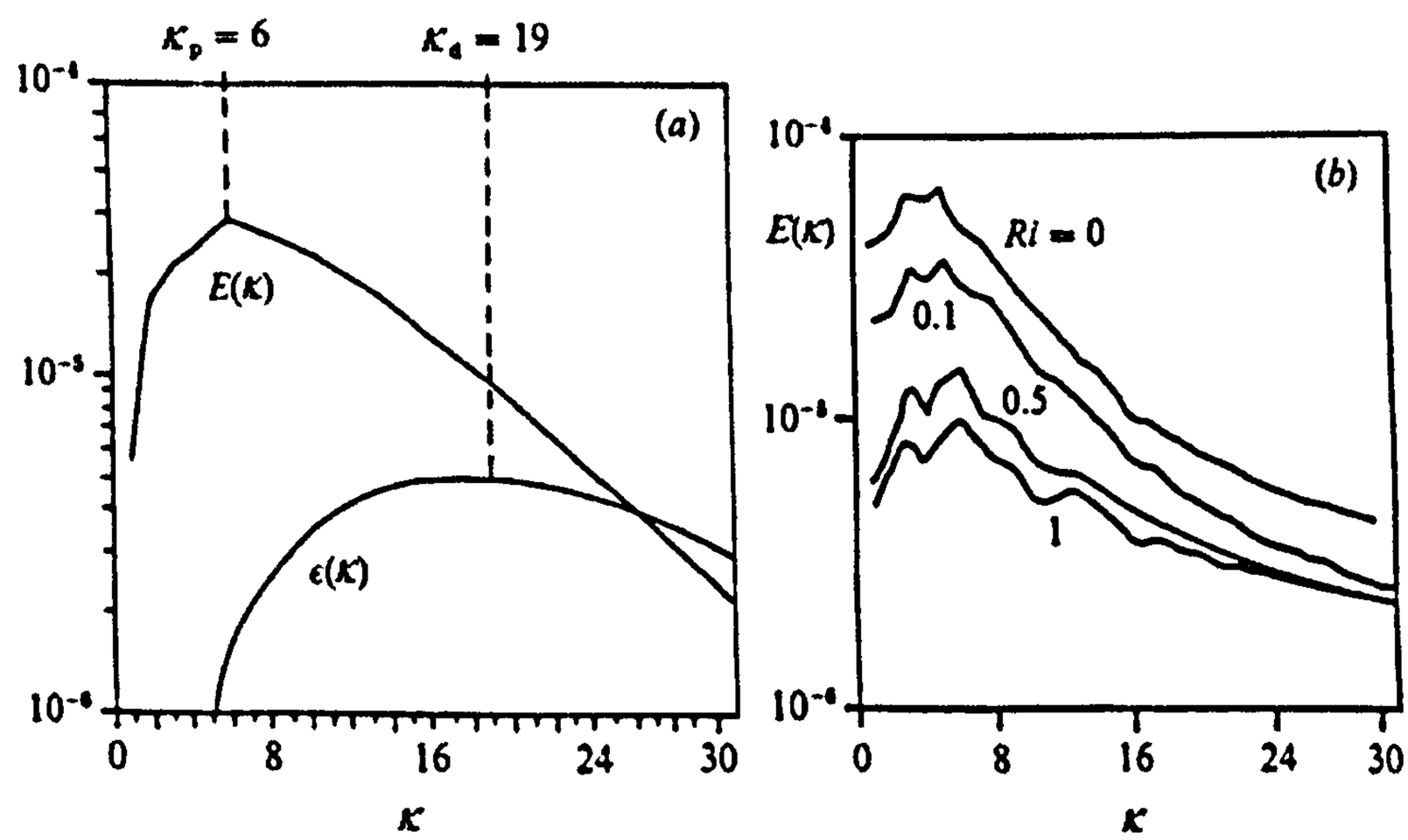

Figure 2.17: Energy spectra for kinetic energy and dissipation. In (a) Spectra of kinetic energy and dissipation at $t = 0$. In (b), kinetic energy spectra at $t = 6$ for $Ri = 0, 0.1, 0.5$ and 1, adopted from Gerz *et al.* (1989).

Higher flow rates and turbulence give rise to instabilities in the thermocline. These instabilities can appear as flapping motion in combination with increased mixing. When mixing is stopped, the wave instabilities decay into turbulence and turbulence dissipation occurs due to the internal friction in the fluid at some higher wave numbers. These wave motions interact with the local buoyancy in the fluid at certain length-scale

range. This action can suppress mixing by redistributing different density fluid to its neutral buoyancy level, providing that full mixing has not occurred. Alternatively, this extracts work from the fluid motion that is transformed into potential energy due to mixing to build internal wave motion further downstream that is dissipated again internally to a certain extent by viscosity.

2.6 Radiation

Unlike conduction and convection, radiation can occur without the presence of matter and a temperature gradient. The equation for radiative heat transfer between a surface and its surroundings is given by Stephan-Boltzmann's law,

$$q_{rad} = \varepsilon \times \sigma \times A \times \left(T_s^4 - T_{sur}^4\right). \tag{2.29}$$

Radiation is very important in ventilation where the rate of emissivity between the walls is significant. Li *et al.* (1993b) studied experimentally the effects of radiation of airflow with displacement ventilation. They mentioned that the difference between thermal and contaminant stratification is that thermal stratification is more gradual and thus the radiant heat transfer between room surfaces is very important. Contaminant stratification is more distinct in the way that there is a sharp division between the clean lower zone and the polluted upper zone. In their computational study, Li *et al.* (1993a) stress that convection and radiation are equally important. Thermal stratification did not show large gradients as for contaminant stratification due to the fact that heat was also transported by radiation between room surfaces. The radiative heat transfer affects primarily the air temperature and velocity at floor level and the vertical temperature profiles, which are important to assess the level of comfort and reduce the energy consumption of the building.

Radiation occurs mainly between the surfaces of the ceiling and the floor that is shown to reduce thermal stratification. The most apparent reason for not achieving 100% match with their experimental temperature gradient is that the radiation exchange calculations were decoupled from the energy equation. Although they concluded that thermal radiation effects are important in rooms with displacement ventilation, the

decoupled approach could have lead to thermal radiation effects considered to a higher degree. Their numerical results were overestimated by a maximum 1°C below the lower half of the temperature profile and underpredicted above the other half. A similar result of weakening thermal stratification is the radiation between the layers that was not considered in either of the studies mentioned above. They considered air as a transparent medium to radiation surfaces, but no humidity or any other gas, which can give rise to this effect, was reported in their studies. However, this occurs to a lesser extent and under normal conditions it can be considered to have a negligible effect on stratification.

2.7 Summary

It is evident from the preceding sections that thermal stratification is a very dominant flow feature in many types of ventilation. The forces involved here are due to buoyancy, inertia, viscous, conduction and radiation. In mixing ventilation efforts are made to break up the thermal stratification in order to achieve comfortable temperature in the occupied zone. Mixing also helps diluting the pollutants to a design level. The performance of displacement ventilation is also influenced by the interaction of plume rise from heat sources with stratified media. In zonal ventilation the effects of stratification could be utilised to remove pollutants without adding any physical partitions. In stratified cooling, thermal stratification plays an important role in the efficiency of the ventilation system, where the stratified layers near the ceiling are used as an insulating buffer reducing the cooling load for air-conditioning. The understanding of stratification is not only important in ventilation system design but it is also useful in the smoke management of fire scenarios. The physical mechanisms, like jet flows and buoyant plumes due to pressure and temperature differences, are responsible for the development and break-up of stratification. Temperature gradients can occur due to hot or cold sources as well as thermal radiation that can affect the efficiency of ventilation. It is, therefore, important to study the influence of physical mechanisms that lead to stratified flow. The non-dimensional numbers involved can give an estimation of the parameters involved in ventilation flows and help with the design of ventilation system requirements. Therefore, CFD investigation can be very useful in studying the effective range of non-dimensional number for stratified ventilation flow.

Forced plumes are a combination of buoyancy forces and inlet momentum where Froude number becomes important as opposed to pure plumes. Linear or otherwise known as continuous stratification follows closely a straight line relationship as opposed to a non-linear stratification, where a thermocline separates the two layers at different temperatures. Laminar plumes may occur from radiation heaters, Crawford and Leonard (1962). However, the practical importance is often concentrated to turbulent plumes.

There are a large number of studies and most are related to the pollution of the atmosphere and oceans as well as indoor air pollution. These analytical equations are dependent on assumptions for uniform or linearly stratified environment outside the plume and hence they may not be generalised. Empirical correlations as we have seen earlier, might not work for every application. There has not yet been found an exact equation that can describe the non-linear effect of the surrounding environment on the plume. Numerical integration using CFD can, therefore, prove a useful tool in solving for particular problems associated with such flows. In the future, the results from numerous studies of such test models from many researchers may shed more light to the undiscovered effects of non-linear stratification.

2.8 Objectives of the Work

The objectives of this work are the following:

- Use the University of Hertfordshire (UH) environmental chamber to study the fundamentals of ventilation flow containing stratification.
- Design a CFD model resembling the conditions tested in the UH environmental chamber to study ventilation flow with regard to stratification.
- Evaluate the performance of the standard industry turbulence model as applied to the modelling of stratified ventilation.
- Establish effects due to boundary conditions.
- Recommendations for best practice of CFD applied to stratified ventilation flows.

3. CFD MODELLING

3.1 Numerical Methods to Solve the Governing Equations

The Navier-Stokes equations involve non-linear partial differential expressions (PDE's) that cannot be solved by analytical means. The objective of the numerical methods is to reduce the continuum problem to a discrete problem. The discretization of the governing equations begins with subdividing a continuum into a number of small regions of a numerical mesh.

Taylor series is a usual method of obtaining the partial derivatives in the governing equations. These are typically truncated after the 3rd term for 2nd order accurate expressions. Considering three consecutive points in a flow domain and Taylor series expansion around points, Anderson (1995), the central difference formulation of the velocity gradients is as follows,

$$\left(\frac{\partial u}{\partial y}\right)_{ij} = \frac{u_{i+1,j} - u_{i-1,j}}{2\Delta y} \tag{3.1}$$

$$\left(\frac{\partial^2 u}{\partial y^2}\right)_{ij} = \frac{u_{i-1,j} - 2u_{i,j} + u_{i+1,j}}{(\Delta y)^2}. \tag{3.2}$$

Substituting expressions (3.1) and (3.2) into the dimensionless form of equations (2.1) to (2.2) in the previous chapter, leads to the finite difference equation. In the Finite Difference Method (FDM), the finite difference expressions of the governing equations are solved for each flow variable at each node of the numerical grid.

Finite Volume Method (FVM) and Finite Element Method (FEM) discretize the governing equations in their integral form within each volume or element respectively. Additionally, the flow variables are interpolated between different regions,

$$u_i = \varphi \mathbf{U}_i(t) \tag{3.3}$$

where φ is the weighting or interpolation function, which is unity for FVM and polynomial for FEM.

The major difference between the two methods is that FVM accounts for energy balance inside each control volume, while FEM accounts for energy balance in the entire domain. It is, however, more important in certain ventilation problems where boundary layers and jet flows are involved to achieve a good solution in these areas of the domain rather than one that abides exactly to energy balance in the entire domain but loosens the criteria in the inside the elements for the same computing effort. FEM may be more accurate than FVM but it requires higher computational resources and for the relatively coarse grid size FEM may suffer from convergence difficulties. FEM and FDM are acceptable for all types of fluid flow problems (hyperbolic, parabolic, elliptic and mixed). FDM can only work with structured meshes due to the nature of its formulation. However, FVM is computationally less intensive than FEM, it is a development of the FDM approach and has been used in the past by many researchers to model successfully many types of flow problems for both simple and complicated geometries with less computing effort.

3.1.1 Finite Volume Method (FVM)

The numerical simulations of this report discretize the governing equations over the flow domain by using the Finite Volume Method (FVM). This numerical method calculates for the velocity components u, v, w at the centres of the different faces of the volumes as shown in Figure 3.1,

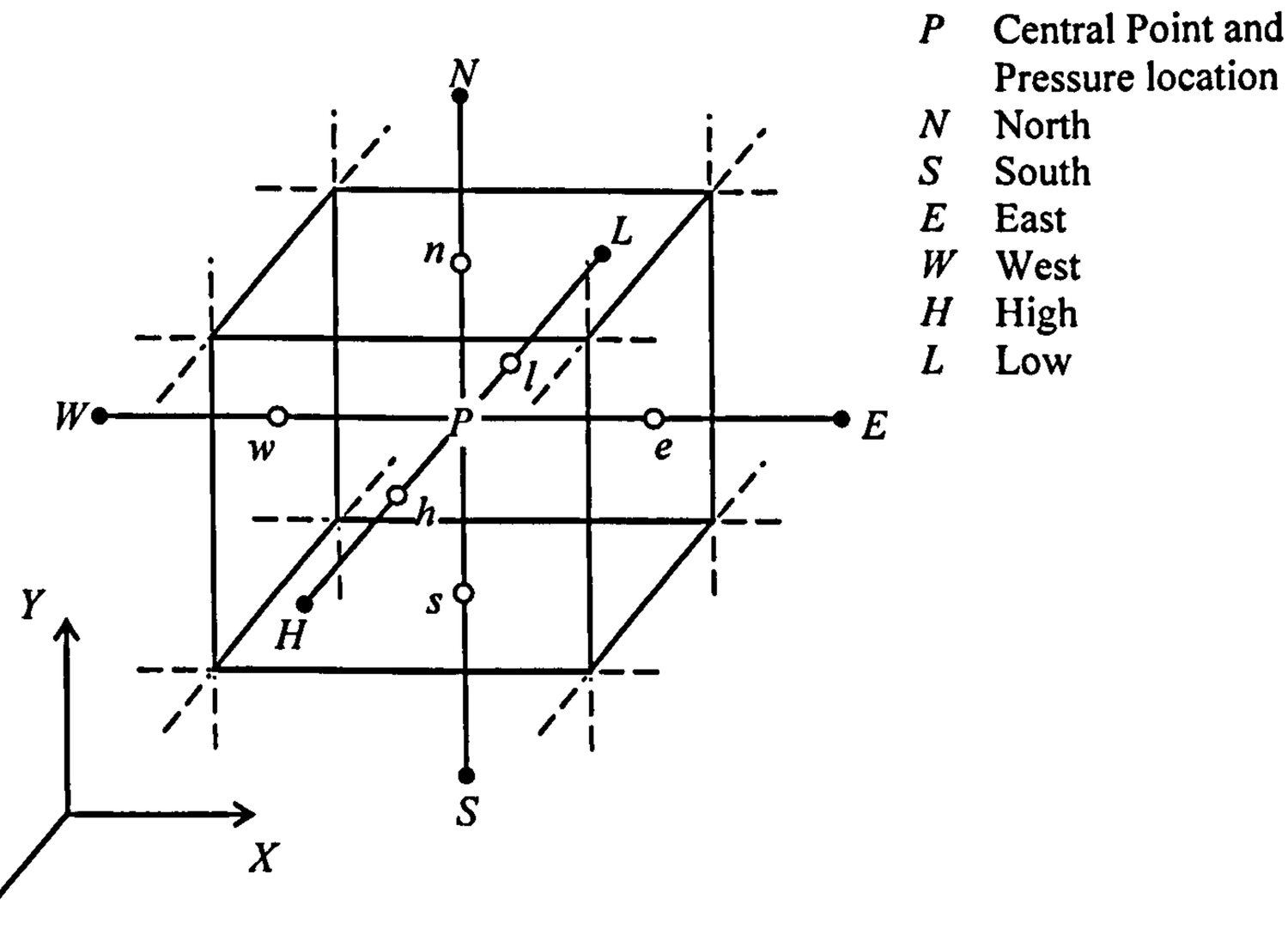

Figure 3.1: The discretization of computational domain is formed by small control volumes that make up a finite numerical grid. Note the co-ordinate system as used in PHOENICS.

The CFD package PHOENICS is used here to perform 3-dimensional simulations of densimetric stratified flow. The velocity component u in the x-direction is stored at the centre of the east face that is denoted by e, the component v in the y-direction is stored at the centre of the north face that is denoted by n and the component w in the z-direction is stored at the centre of the high face that is denoted by h. The letters E, W, N and S are points of the numerical grid, while small letters denote a control volume. The central discretization procedure will take the average velocity components at the face centre by taking the average of the component of the variable u say in the x-direction in the current cell and that in the west neighbouring cell. This convention is called the 'staggered-grid' arrangement. However, one of the problems of such a convention is that close to blockages or edges of the domain, this strategy may need to be modified where straightforward averaging is not possible due to the absence of the neighbouring cell.

3.1.2 Upwind-difference scheme

While central differencing can be applied successfully to low Re flows, there are issues involved relating to the discretization scheme of high Reynolds number flows, Patankar (1980). Turbulence fluctuations are also present adding more difficulty to the area where high refinement is required. The effect is that the numerical code may not sum up

correctly the values of the variables calculated from the adjacent points, because of the relative direction of the convection terms on the calculation point affecting the sign in the algebraic difference equation. Buoyancy forces give rise to turbulence that even at low Re, the choice of the discretization scheme still remains. In order to account for the flow direction and thus avoid any unwanted numerical oscillations or numerical diffusion due to the diagonality of the flow, the differencing procedure should be modified to account for such effects.

Higher order schemes are a compromise between oscillations and accuracy in contrast to the diffusive nature of low-order schemes and are used in the modelling of certain physical processes such as discontinuities in modelling shock waves. Limiters can be used as a stabilisation method to reduce oscillations such as flux limiters and gradient limiters applied to the discretization procedure. There is a range of higher order non-linear schemes that give slightly better accuracy and can be tuned to switch the accuracy depending on the region of the flow process that we need to model. However, convergence of higher order schemes requires tighter relaxation settings and sometimes it may be necessary to use results from a lower order scheme as initial conditions.

One of the further developments include a quadratic upstream scheme (non-linear) called QUICK, which although more difficult to converge, does produce good accuracy, Leonard (1979).

3.1.3 The Hybrid discretization scheme

For incompressible flow the hybrid discretization scheme is generally recommended for higher efficiency of the numerical algorithm and to apply linear higher order schemes to the momentum equations to provide satisfactory convergence.

The hybrid scheme combines both upwind and central difference (second order) method and can be applied more generally to solve equations which contain both convection and diffusion terms which is the one used in this work. Depending on the relative size of these terms across the cell face, it is identical to the central difference when the control volume cell Reynolds or Peclet number, i.e. value of convection over the diffusion terms over the cell, is $-2 \le Re, Pe \le 2$ and to the upwind scheme when $|Re|, |Pe| > 2$.

The face value of a variable ϕ on a stencil of adjacent cells can then be described by the following,

$$\phi_f = 0.5 \times (\phi_c + \phi_d) \quad \text{for } Pe < 2, \text{ and} \tag{3.4}$$

$$\phi_f = \phi_c \quad \text{for } Pe > 2 \tag{3.5}$$

where the subscript f denotes the face value between adjacent cells c and d.

It should be noted that the expressions of those discretization schemes with the convention used in PHOENICS have been derived for a scalar variable where in the case of finite volume a grid node is the centre of the control volume.

3.1.4 Pressure correction technique

The differential form of the momentum equation inherently satisfies continuity. However, the continuity equation is still used to achieve numerical stability in the results, due to the numerical errors arising from the discretization procedure that disrupt continuity. Additional numerical instabilities mainly arise in FVM, because velocity and pressure are not solved in the same locations on the numerical grid. Hence, the continuity equation is used along with the equation for pressure, which is solved on the cell faces instead of the centre of the cell volume, and that alone introduces further discretization errors. Therefore in PHOENICS, the continuity equation is written into an equation of pressure correction, also reported by Li *et al.* (1993a), which increases further the numerical stability of the code. PHOENICS utilises one of the most widely used methods to link pressure to velocity in order to satisfy continuity. This is done by a semi-implicit method for pressure-linked equations (SIMPLE) developed by Patankar and Spalding (1972). In this method, the velocity profiles are corrected using the pressure values at the neighbouring cells such that continuity is obtained. In PHOENICS, pressure is discretized in the middle of each volume, while on the contrary the velocity components are displaced from the grid nodes (pressure positions) so that the pressure forces act at the surfaces of the velocity control volumes. In this way the pressure field influences the velocity field and visa versa. SIMPLER is a revised algorithm of SIMPLE and it calculates the pressure field from the given velocity field at the first sweep-iteration in contrast to SIMPLE that uses a guessed pressure field. Since

the pressure is a direct consequence of velocity, SIMPLER gives faster convergence. However, it requires more time per iteration, hence it involves more computational effort per iteration, but this is compensated by the overall reduction in computational effort. A comparison of the algorithms, similarities and differences are discussed in Patankar (1980). The method used here is SIMPLEST (SIMPLE ShorTened), which is a derivative of SIMPLE discussed by Spalding (1980). SIMPLEST differs from SIMPLE and SIMPLER in the way the FV equations are formulated. Convection and diffusion influences differ radically. In SIMPLEST method, the corrections for the pressure are done by dividing the corrective coefficients into convection and diffusion terms to replace them with the "source terms" of the momentum balance, where they are treated as known constants. The SIMPLEST algorithm produces convergence much more smoothly than SIMPLE, and with less under-relaxation (slowing down convergence).

Other velocity-pressure algorithms are the SIMPLEC and PISO used in different CFD packages on collocated grids. In such cases, the velocity and pressure are both obtained at the centre of the control volume. The SIMPLEC (SIMPLE-Consistent) method will improve convergence only if it is being limited by the pressure-velocity coupling. PISO (Pressure-Implicit with Splitting of Operators) with neighbour correction has been highly recommended for transient flow calculations.

3.1.5 Convergence

Iterative methods are used to solve the system of equations on the grid points numerically. For a numerical solution to be accurate, or as close as possible to the exact solution, convergence needs to be obtained and appropriate criteria must be set to terminate the iteration. At the end of each iteration, the solution obtained should be checked to see whether it has converged within pre-set tolerances or whether the iteration is diverging. If the convergence tolerance is too loose, inaccurate results are obtained and if the tolerance is too tight, much computational effort is spent to obtain needless accuracy. For specific flows involving a combination of heat transfer and fluid flow, 10^{-5} reduction in the sum of the residual errors can assure convergence of the dependent variables as close as 99 %. However, this may require extensive CPU time and higher convergence criteria will be a better compromise between lead time and accuracy. In convergence criteria reported in the open literature showing realistic

results, values vary typically between 10^{-2} and 10^{-3}. For the convergence to be meaningful all associated variables would have to converge. In addition to the flow variables to be solved, mass and energy must be balanced. Depending on the problem solved, mass and energy into and out of the domain must be satisfied according to the convergence criteria set by the user. Further, also depending on the problem solved, using the appropriate iteration solver can speed up convergence.

The aim of reducing the residual errors for the iterative procedure is to obtain a solution as close to the exact solution as possible. Since CFD is based on iterative methods, it follows that reducing the difference between successive iterations should ensure that we are getting closer to the "real solution". The actual procedure is shown below where the relationship between the variables may be expressed by the single matrix equation for the entire flow field,

$$\mathbf{AX} = \mathbf{B}. \tag{3.6}$$

Here **A** is the global or coefficient matrix, **X** is the column vector of the unknown variables and **B** is column vector known as the solution matrix. However, the error matrix needs to be added on the left-hand side in order to satisfy the relationship in the beginning of the simulation. Assuming a convergence descent curve, the error in the first iteration has the highest value for certain initial guesses included in matrix **B**. To include the error **R**, the expression (3.6) may be modified to,

$$\mathbf{AX} - \mathbf{R} = \mathbf{B} \tag{3.7}$$

and by rearranging equation (3.7) above, we have,

$$\mathbf{R} = \mathbf{AX} - \mathbf{B}. \tag{3.8}$$

Equation (3.8) states that the error equals the current solution minus the initial solution. The error should follow normally a logarithmic decay and reduce to within specified tolerances (convergence criteria) in the subsequent iterations in order to ensure adequate convergence. Therefore, the expression above can be written as,

$$\mathbf{R}_n = \mathbf{AX}_n - \mathbf{B}_{n-1} \tag{3.9}$$

or

$$\mathbf{R}_n = \mathbf{B}_n - \mathbf{B}_{n-1} \tag{3.10}$$

where in the left-hand side, $\mathbf{R}_n$ is the matrix of residual errors for all the volumes and cell faces and in the right-hand side, $\mathbf{B}_{n-1}$ represents the values obtained by the solution procedure in the previous iteration and $\mathbf{AX}_n$ or $\mathbf{B}_n$ the result obtained at the nth iteration.

The numerical solution procedure employs iteration by sweeping through the solution domain, and using successively updated values of the dependent variables at each sweep so as to procure the final solution. The convergence criteria employed in all of the numerical simulations are,

1. For each set of finite volume equations, the sum of the absolute residual errors over the whole solution domain is less than 1% of reference quantities based on the total inflow of the variable in question.
2. The values of monitored dependent variables at a selected location do not change by more than 0.1% between successive iteration sweeps.
3. Checks are made on the overall conservation of mass and energy for the entire solution domain.

The residual values should go down by at least a factor of 100 from an arbitrary value obtained after the initial few sweeps. The criterion frequently adopted to check for convergence of each variable when applied to a computer is that the sum of the absolute errors contained in matrix $\mathbf{R}_n$ normalised by the reference inlet sum of the variable for the entire domain is,

$$\frac{\sum|\varepsilon_P|}{\mathrm{REFSUM}(\phi)} = \\ = \frac{\sum\left|\phi_{i,j}^{k+1} - \phi_{i,j}^{k}\right|}{\mathrm{REFSUM}(\phi)} \leq 10^{-2} \tag{3.11}$$

The monitoring point should be specified in the flow field such that the solution is most vulnerable to changes in the flow to ensure that convergence is obtained after several

sweeps. If first criterion is satisfied the solution is terminated automatically. For each grid node in FVM the residual error R_ϕ in (1) above is calculated from,

$$R_\phi = a_p \phi_p - \sum a_i \phi_i - S_\phi \tag{3.12}$$

Obviously, when the finite-volume equation for ϕ is satisfied, R_ϕ will be zero.

For each flow simulation of interest, the computational details such as the number of iteration sweeps required for a converged solution are provided in Chapter 4 of this thesis. Convergence windows are shown below,

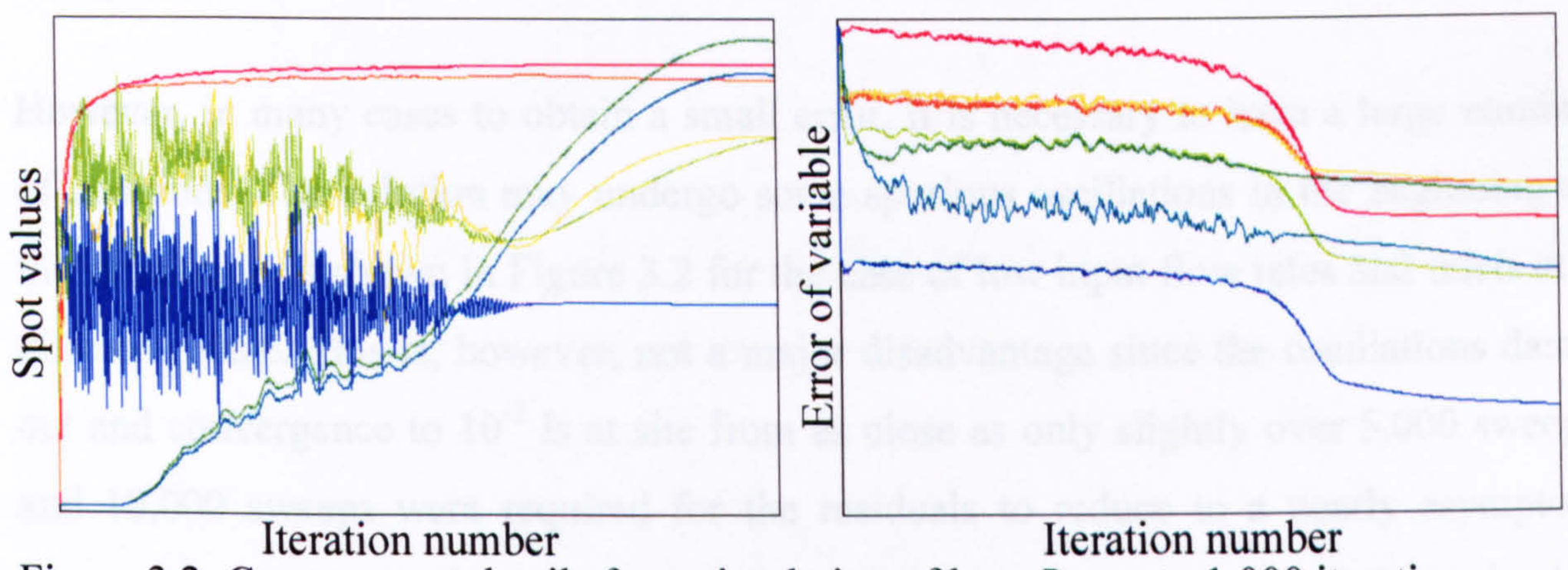

Figure 3.2: Convergence details from simulation of low Re up to 1,000 iterations.

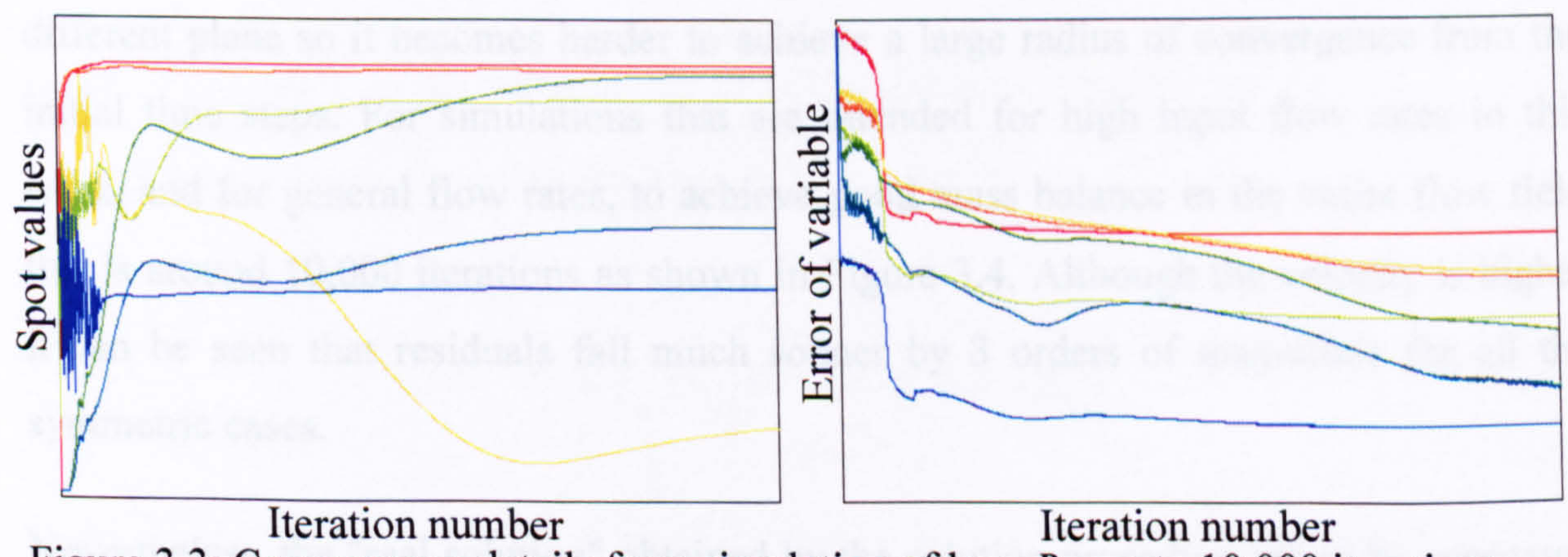

Figure 3.3: Convergence details from simulation of low Re up to 10,000 iterations.

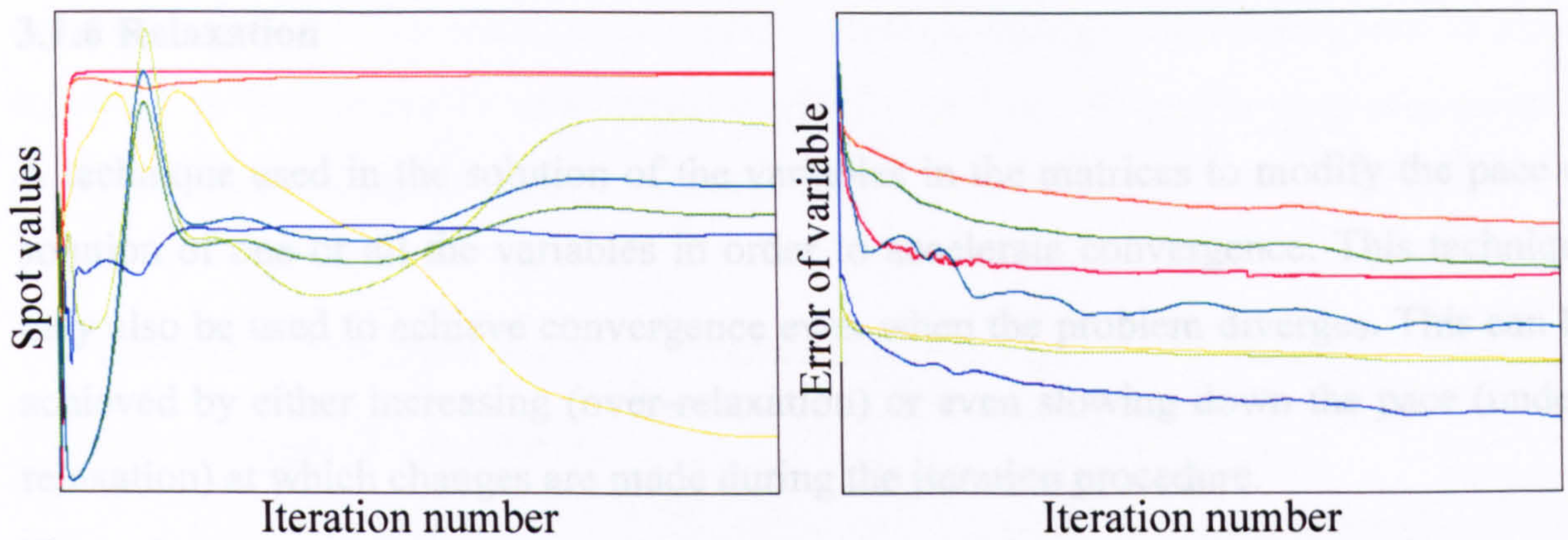

Figure 3.4: Convergence details from simulation of high *Re* for 10,000 iterations.

The window on the LHS in Figure 3.2, Figure 3.3 and Figure 3.4 show the spot values at the monitoring location and the window on the RHS show the sum of the absolute residuals for each variable, which are both on logarithmic scales.

However, in many cases to obtain a small error, it is necessary to have a large number of iterations. The solution may undergo some spurious oscillations in the beginning of the simulation as shown in Figure 3.2 for the case of low input flow rates and inlets at a different plane. This is, however, not a major disadvantage since the oscillations damp out and convergence to 10^{-2} is at site from as close as only slightly over 5,000 sweeps and 10,000 sweeps were required for the residuals to reduce to a nearly asymptote convergence curve as shown in Figure 3.3. At this stage a good mass balance is also achieved in the entire flow field. This case is from a simulation with the inlets at a different plane so it becomes harder to achieve a large radius of convergence from the initial time steps. For simulations that are intended for high input flow rates in this work, and for general flow rates, to achieve good mass balance in the entire flow field this is around 10,000 iterations as shown in Figure 3.4. Although the velocity is higher it can be seen that residuals fall much sooner by 3 orders of magnitude for all the symmetric cases.

Nevertheless, the "real solution" obtained by the solution procedure has to be compared to the actual solution obtained theoretically. Alternatively, if this does not apply, such as in test cases with complicated geometry and physics, the solution has to be compared with experimental results.

3.1.6 Relaxation

A technique used in the solution of the variables in the matrices to modify the pace of solution of one or all the variables in order to accelerate convergence. This technique may also be used to achieve convergence even when the problem diverges. This can be achieved by either increasing (over-relaxation) or even slowing down the pace (under-relaxation) at which changes are made during the iteration procedure.

This can be illustrated by considering the heat conduction equation in the finite-volume form by Patankar and Spalding (1972) and substituting for the temperature, T_P, at the centre of a finite grid, in place of the variable, ϕ , which gives,

$$a_P T_P = \sum a_{nb} T_{nb} + b, \tag{3.13}$$

where T_{nb} stands for every neighbouring temperature value at the cell faces N, S, E, W, H and L. Equation (3.13) can be rearranged to solve for T_P,

$$T_P = \frac{\sum a_{nb} T_{nb} + b}{a_P}, \tag{3.14}$$

and if T_P^* is taken as the value of T_P from the previous iteration and we add T_P^* to the right-hand side and subtract it, we have,

$$T_P = T_P^* + \alpha\left(\frac{\sum a_{nb} T_{nb} + b}{a_P} - T_P^*\right). \tag{3.15}$$

The contents in the parenthesis of equation (3.15) represent the change in T_P produced by the current iteration. This change can be modified by the introduction of a relaxation factor α. Convergence can be slowed down or speeded up by changing the value of α. If α is small, i.e., $0 < \alpha < 1$, the changes in T_P become very slow since T_P is very close to T_P^*, this is called under-relaxation and is usually applied to non-linear system of

equations or linear for which Gauss-Seidel method diverges or convergence is slow, resulting to Successive Over-Relaxation (SOR) method. If $\alpha > 1$, over-relaxation is produced accelerating the pace of convergence.

The solution is converged when T_P becomes equal to T_P^*, i.e., the converged values for T satisfy equation (3.13) such as,

$$\frac{a_P}{\alpha} T_P = \sum a_{nb} T_{nb} + b(1-\alpha)\frac{a_P}{\alpha} T_P^*. \tag{3.16}$$

Sometimes, the solution of a steady-state problem is obtained through the use of discretization equations for the corresponding unsteady situation. The time steps become the same as iterations, and the value of T_P at the old time step, T_P^0, represents the value of the previous iteration, T_P^*.

The relaxation criteria are problem dependent. Unfortunately, there are no universal guidelines for selecting the appropriate relaxation settings, because they depend not only on the physical processes being approximated, but also on the details of the numerical formulation. The velocity field is the dominant variable in the computation and under-relaxation should be applied to ensure slow development of velocity field. Quantities which both influence and are influenced by the velocity (or other dominant-variable) field should be updated frequently throughout the computation. The velocity field is influenced by the temperature field and visa versa. Therefore temperature needs to be updated more frequently by over-relaxation. There are several simulations cases of certain inlet velocities carried out in this work. The low Re simulations consist of the inlet velocity cases of 0.2 and 0.4 m/s and the high Re simulations consist of the velocity cases of 0.8 and 1.6 m/s. The initial conditions and relaxation settings for each variable are summarised in Table 3.1,

	U_o	P1	U1	V1	W1	KE	EP	*PRPS*	*SMOK*	*EPKE*	TEM1
Initial Conditions	low	1E-5	0.01	0.01	-0.01	1E-5	1E-5	*1E-5*	*0.01*	*1*	20
	high	1E-10	1E-7	1E-10	1E-10	1E-10	1E-10	*-1*	*1E-10*	*1E-10*	20
Relaxation Settings	low	-1	0.1	0.1	0.1	-0.5	-0.5	*-1*	*-1*	*-1*	1
	high	-0.1	0.01	0.01	0.01	-0.3	-0.3	*-0.1*	*-0.1*	*-1*	1

Table 3.1: Settings for achieving convergence in the simulations where the inlet velocity for hot and cold supply air is the same.

Convergence can also be achieved by using other types of relaxation methods such as through inertia and false-time step which are not used in this work.

3.2 Iterative Methods

Finite methods reduce the problem to a linear system of equations, $Ax = b$, where A is a sparse matrix. Direct methods, such as, the LU defactorisation Method or the Gaussian Elimination Method can be used only for linear problems of a system of equations, $Ax = b$. When using such methods, the computation is of the order of n^3, where n is the size of the problem, i.e., the size of matrix A, which is $n \times n$. When the problem becomes more complicated, the size of the matrix A becomes quite large, which could contain a significant number of zero elements. In the special problem cases considered here, the matrices are sparse, i.e., matrix A has relatively few nonvanishing elements. Iterative methods are better than direct methods because the computation becomes of the order of kn^2, where k is the number of iterations.

If the system of equations can be solved by non-iterative methods (Gauss-Seidel elimination method, LU defactorisation method) we refer to it as direct method, Lam (1994). The tridiagonal matrix algorithm (TDMA) (is the direct method used in PHOENICS that may not require iteration if the influence of viscosity on the velocity variable can be ignored.

The usual elimination methods cannot normally be applied here, since without special precautions, they tend to lead to the formation of intermediate matrices that require additional storage and CPU power to be solved. For this reason, researchers have moved

to iterative methods for solving non-linear systems of equations. Most numerical methods used by CFD to solve the governing equations, often employ the following iteration procedures, depending on the problem, in order to achieve convergence.

In PHOENICS there are two types of iterations that can be employed in the same run. LSWEEP refers to the total number of sweeps through the solution domain, i.e., one sweep is one iteration of the overall solution cycle. LITER refers to the number of iterations of the linear solver for solution of the given dependent variable, and in this sense it may be interpreted as an internal iteration within one given sweep (iteration) of the overall solution cycle. Both the CGR and default Stone's solvers are iterative solvers, and LITER is used to set the maximum number of iterations for a given variable. LITER can be set to whatever integer number one wishes, but there is little advantage in setting it above 20 for the momentum and turbulence equations because of the segregated nature of the SIMPLE-type solution algorithm.

In general, whether the flow is compressible or not, the pressure-correction equation is solved whole-field and the flow is largely pressure driven, and so it is advisable to have at least 50 iterations on LITER(P1). However, it can also be recommended for buoyant flow to set LITER(TEM1) to say 50 or 100, because the flow is driven by temperature differences and more iterations will produce a more rapid evolution of the temperature field. The internal iteration control settings for the low *Re* simulations, LITER(P1) = 100 and LITER(TEM1) = 20. In the high *Re* simulation cases LITER(P1) = 200 and LITER(TEM1) = 20. The rest of the variables have been given a value of 10 or 20. The values of the relaxation factors in combination with the LITER values gave a reasonable convergence in this work.

There are several solvers in PHOENICS that can be selected depending on the nature of the problem. For parabolic flows: unidirectional and 2-dimensional flows, where it is permitted to set NX or NY = 1, the effect of the a_H coefficient can be neglected and the solution can be obtain by a single sweep-iteration (i.e., no iteration is needed). This can be done by using either point-by-point (Jacobi) or slabwise calculation in 3-dimensional simulations. However, to account for non-linearities and interconnectedness of the values in the adjacent cells sufficient iteration is needed in order for the errors in the equations for the momentum balance to reduce sufficiently. The default method in

PHOENICS is the whole-field calculation which is also recommended for the pressure correction. The Direct solver in PHOENICS for the point-by-point (PBP) and slabwise calculation is the TDMA. In the whole-field type all links are correctly included which can be applied when non-linearities are slight, i.e., potential flow and heat transfer. When non-linearities play an important role in the flow, matrix solvers are available. For both slabwise and whole-field solution a matrix solver is required. The TDMA is modified to Stone's solver as the iterative version. Another matrix solver is a conjugate gradient solver (CGR) that takes longer per iteration while less overall iteration to convergence and will be discussed in the following sections.

3.2.1 Linear solver – Stone's-like extension of TDMA

Most common CFD programs use a simple solver as a default, which is very easy to implement and gives very good accuracy for simple problems without much computational effort. However, complex flows involving recirculation, turbulence and additional variables to be solved, contribute to the complexity of the problem. Consequently, the solution to the governing equations can become very slow.

The simplest one is the Jacobi Method, which needs to have a diagonally dominant system matrix. Problems can arise, however, using this method depending on the properties of the matrix. If the elements in the diagonal are not large enough or larger than off diagonal, the convergence becomes very slow or the solution diverges. An improvement to this method is the Gauss-Seidel method. Any values obtained for the unknowns are used as soon as they are obtained, ignoring the rest of the initial guesses. This method is more expensive per iteration than the previous method. However, this is frequently weighed by the fact that this method uses less iteration. Using better initial guesses can take even less iterations to convergence.

A large number of iterations using Gauss-Seidel or SOR method may be necessary if the coefficient matrix is not or marginally diagonally dominant. The Alternative Direction Implicit (ADI) Method splits the coefficient matrix into a linear system of tridiagonal coefficient matrices which can be solved by non-iterative methods.

3.2.2 Implicit solver - Conjugate Gradient Solver (CGR)

The conjugate gradient (CGR) solver has recently been introduced, Biggs (2000), which recalculates a new descent direction to improve convergence. The CGR solver often gives satisfactory accuracy after only a very few number of iterations. It is ideal for heat flow problems due to the slow convergence nature of the problem.

The CGR Method uses a search procedure to calculate the new search direction $d^{(k+1)}$ after the kth iteration. The search directions are orthogonal to the directions of the residual vector $r^{(k)}$ (= $Ax^{(k)}$ - b) in x, y, z. If the search direction is uphill, then it takes the negative value of the orthogonal distance to the convergence direction, or better, if it is going up it tries to change the search direction in order to minimise the residual. This is the reason why the method is more reliable than direct methods. When the new step is calculated, then the CGR solver checks for the non-linear part. This contains the step-length $s^{(k)}$. When all steps come down to be orthogonal the solution is stopped at the error cut-off, which is typically 10%. The following computation is performed in order to calculate the search direction and it is called the inner iteration,

$$s^{(k)} = -r^{(k)T} d^{(k)} / d^{(k)T} A d^{(k)} \tag{3.17}$$

$$\beta^{(k)} = r^{(k+1)T} r^{(k+1)} / r^{(k)T} r^{(k)} \tag{3.18}$$

$$d^{(k+1)} = -r^{(k+1)} + \beta^{(k)} d^{(k)} \tag{3.19}$$

All the simulations in this work are solved by using the CGR Method.

3.3 Turbulence Modelling

To account for turbulence, the instantaneous variables u and T in the governing equations (2.1), (2.2) and (2.3), are substituted by the time-mean and fluctuating components, i.e., $u = \bar{u} + u'$ and $T = \bar{T} + T'$. Modelling turbulence phenomena in a flow field involves taking into account the additional terms, $-\rho\overline{u'_i u'_j}$ and $-\rho c_p \overline{u'_j T'}$

called Reynolds stresses. They have a significant effect on the mean flow field. The additional terms, account for the turbulent fluctuations of momentum and energy. Due to the motion of the small eddies in the mean flow field, the transport of momentum and energy is greatly enhanced.

The turbulent viscosity μ_t, has the form,

$$\mu_t \frac{\partial \bar{u}}{\partial y} = -\rho \overline{u_i' u_j'} \tag{3.20}$$

and usually, this term is modelled by a turbulence model, which solves a set of extra equations in order to achieve closure. In general, closure is achieved when the momentum equation is balanced by adding the additional term,

$$-\rho \overline{u_i' u_j'} = \mu_t \frac{\partial}{\partial x_j}\left(\frac{\partial \bar{u}_i}{\partial x_j} + \frac{\partial \bar{u}_j}{\partial x_i}\right). \tag{3.21}$$

Similarly, the eddy or turbulent conductivity of heat may be defined by the following relationship,

$$k_t \frac{\partial \bar{T}}{\partial y} = -\rho c_p \overline{u_i' T'}. \tag{3.22}$$

Hence, the continuity equation (2.1), momentum equation (2.2) and energy equation (2.3) become,

$$\rho \frac{\partial \bar{u}_i}{\partial x_i} + \rho \frac{\partial \bar{u}_j}{\partial x_j} = 0 \tag{3.23}$$

$$\rho \bar{u}_j \frac{\partial \bar{u}_i}{\partial x_j} = -\frac{\partial P}{\partial x_i} + \frac{\partial}{\partial x_j}\left[\mu_e\left(\frac{\partial \bar{u}_i}{\partial x_j} + \frac{\partial \bar{u}_j}{\partial x_i}\right) - \rho \overline{u_i' u_j'}\right] - \rho g \beta (\bar{T} - T_o) \tag{3.24}$$

$$\rho u_j \frac{\partial \overline{T}}{\partial x_j} = \frac{\partial}{\partial x_j}\left[\Gamma_e\left(\frac{\partial \overline{T}}{\partial x_j}\right) - \rho c_p \overline{u'_j T'}\right]. \tag{3.25}$$

3.3.1 The Standard $k-\varepsilon$ Model

The standard high-Reynolds-number $k-\varepsilon$ model is used as presented by Launder and Spalding (1974) with inclusion of buoyancy effects. Turbulent viscosity is defined by the Kolmogorov-Prandtl expression given as,

$$\nu_t = C_\mu \frac{k^2}{\varepsilon} \tag{3.26}$$

where C_μ is an empirical constant.

There are two extra equations for turbulent kinetic energy and dissipation that can be presented without the inclusion of buoyancy,

$$\underbrace{\rho \frac{\partial}{\partial x_i}(u_i k)}_{\text{Convection}} = \underbrace{\rho \frac{\partial}{\partial x_i}\left(\frac{\nu_t}{\sigma_k}\frac{\partial k}{\partial x_i}\right)}_{\text{Diffusion}} + \underbrace{\rho\left(P_K - \varepsilon\right)}_{\text{Production - Destruction}} \tag{3.27}$$

$$\underbrace{\rho \frac{\partial}{\partial x_i}(u_i \varepsilon)}_{\text{Convection}} = \underbrace{\rho \frac{\partial}{\partial x_i}\left(\frac{\nu_t}{\sigma_\varepsilon}\frac{\partial \varepsilon}{\partial x_i}\right)}_{\text{Diffusion}} + \underbrace{\left(\rho \frac{\varepsilon}{k}\right)\left(C_{\varepsilon 1} P_K - C_{\varepsilon 2}\varepsilon\right)}_{\text{Generation - Destruction}} \tag{3.28}$$

where P_K (sometimes referred to in literature as G_K) is the shear production, i.e., the volumetric production rate of turbulent kinetic energy by shear forces. This is defined by,

$$P_K = \nu_t \frac{\partial u_i}{\partial x_j}\left(\frac{\partial u_i}{\partial x_j} + \frac{\partial u_j}{\partial x_i}\right). \tag{3.29}$$

The following constants are commonly used for the standard $k-\varepsilon$ model, $\sigma_k = 1.0$, $\sigma_\varepsilon = 1.314$, $C_\mu = 0.09$, $C_{\varepsilon 1} = 1.44$, $C_{\varepsilon 2} = 1.92$, Launder and Spalding (1974).

These five constants are derived from simple well-understood test cases where the equations of motion are simplified, Launder and Spalding (1974).

The rate of energy transfer from the large to the small scales can be interpreted dimensionally as the rate of decay of energy dissipation, i.e., $\chi \propto \varepsilon / \tau$, and expressed as the dissipation rate timescale k/ε that results to the following expression,

$$\chi = C_{\varepsilon 2} \frac{\varepsilon^2}{k}. \tag{3.30}$$

The coefficient $C_{\varepsilon 2}$ is considered to be a constant for isotropic flows. Measurements of homogeneous turbulence of a grid downstream of Comte-Bellot and Corrsin (1966) found that the best power law fit to the inverse turbulent energy during the early part of the decay is near $(x - x_1)^{1.25}$ give a value of $C_{\varepsilon 2} \approx 2.06$. The grid experiments reported by Gibson (2005) are fitted by the power law $k = k_0 x^{-\alpha}$ with $\alpha \approx 1.25$, which give $C_{\varepsilon 2} = (\alpha + 1)/\alpha \approx 1.8$. However, Launder and Spalding (1974) assigned a value of $C_{\varepsilon 2} = 1.92$ that has been acceptable for many flow predictions.

By using local equilibrium in a shear layer flow, such as fully developed flow, i.e., $\partial u / \partial x = 0$ and constant gradient, $\partial u / \partial y = C$, then k and ε are constant and the transport equations for kinetic energy and dissipation are reduced to,

$$C_\mu \frac{k^2}{\varepsilon} C = \varepsilon \text{ and } C_{\varepsilon 1} k C^2 = C_{\varepsilon 2} \frac{\varepsilon^2}{k}. \tag{3.31}$$

Thus $C_1 = C_\mu C_2$. Measurements on k, ε and the coefficient C give $C_\mu = 0.09$. Therefore, $C_1 = C_\mu C_2 = 0.17$, Mohammadi and Pironneau (1994). Additionally, measurements in the log-linear part of boundary layer flows give the same value C_μ.

Turbulent diffusion is represented by,

$$\frac{1}{2}\overline{u_i u_i u_j} = -\frac{\nu_t}{\sigma_k}\frac{\partial k}{\partial x_j} \tag{3.32}$$

and viscous dissipation is exact with $\sigma_k = 1.0$.

The spreading rates of constant-stress shear layers predicted Launder and Spalding (1974) where k and ε are in local equilibrium conditions and $dk/dy \approx 0$, were found in the ε-equation to be highly sensitive to $(C_{\varepsilon 2} - C_{\varepsilon 1})$, and the best values were obtained for $C_{\varepsilon 1} = 1.44$, $C_{\varepsilon 2} = 1.92$ and $\sigma_\varepsilon = 1.3$.

Despite of the slightly different formulation in the documentation of different publications, the values of the constants in the standard $k - \varepsilon$ model are the same up to two decimal places of accuracy for the majority of the constants.

3.3.2 The $k - \varepsilon$ Chen & Kim Model

There are several variations of the standard $k - \varepsilon$ model aiming to improve the capabilities of the standard model. The inconsistency of the standard $k - \varepsilon$ model is very often attributed to the dissipation rate equation which is highly empirical in nature. Turbulence comprises of fluctuating motions with a spectrum of time scales that a single-scale approach is unlikely to be adequate because different turbulence interactions are associated with different parts of the spectrum. To treat this deficiency in the standard model, Chen and Kim introduced an extra time scale to enable the energy transfer mechanism to respond to the mean strain more effectively. For the dissipation rate equation to respond to the mean strain, the two time scales are included: the production range time-scale, k/P_K and the dissipation rate time-scale, k/ε. The expression of a transport equation for the dissipation rate is given as,

$$\rho\frac{\partial}{\partial x_i}(u_i\varepsilon) = \rho\frac{\partial}{\partial x_i}\left(\frac{\nu_t}{\sigma_\varepsilon}\frac{\partial\varepsilon}{\partial x_i}\right)+\left(\rho\frac{\varepsilon}{k}\right)\left(C_{\varepsilon 1}P_K - C_{\varepsilon 2}\varepsilon + C_{\varepsilon 4}\frac{P_K^2}{\varepsilon}\right). \tag{3.33}$$

The Chen and Kim turbulence model (hereafter denoted as the Chen-Kim model) is derived by Chen and Kim (1987) which is a modified version of the $k-\varepsilon$ model. The Chen-Kim modification involves dividing the dissipation production term into two parts, the first of which is the same as for the standard model but with a smaller multiplying coefficient, $C_{\varepsilon 1}$. The second part allows the "turbulence distortion ratio" (P_K/ε) to exert an influence on the production rate of ε.

For flows in which turbulence is in local equilibrium, the two time scales are identical ($P_K = \varepsilon$). For off-equilibrium flows, the net effect is to increase ε, and thereby decrease k, when the mean strain is strong ($P_K/\varepsilon > 1$, associated with inequality $k/P_K < k/\varepsilon$ when multiplying out the left-hand side of equation (3.33)), and to decrease ε when the mean strain is weak ($P_K/\varepsilon < 1$). This feature may be expected to offer advantages in separated flows as well as in other flows, where the turbulence is removed from local equilibrium. To account for such effects, the extra time-scale k/P_K is included in the ε-equation via the following additional source term per unit volume,

$$S_\varepsilon = \frac{-\rho f_1 C_{\varepsilon 4} P_K{}^2}{k} \tag{3.34}$$

where $C_{\varepsilon 4} = 0.25$ and f_1 is the Lam-Bremhorst (1981) dumping function in the Low-Re modification of the model. This is given as,

$$f_1 = 1 + (0.05/f_\mu)^3 \tag{3.35}$$

with

$$f_\mu = \left[1 - e^{-0.0165 Re_n}\right]^{2(1+20.5/Re_t)} \tag{3.36}$$

where $Re_n = \sqrt{k}\frac{y}{\nu}$ is the Reynolds number at the wall, y is the normal distance to the nearest wall and $Re_t = \frac{k^2}{\varepsilon\nu}$ is the turbulent Reynolds number at the wall. Additionally, the empirical coefficients C_μ, $C_{\varepsilon 1}$ and $C_{\varepsilon 2}$ are multiplied respectively by the functions f_μ, f_1 and f_2, which is given by,

$$f_2 = 1 - e^{-Re_t^2}. \tag{3.37}$$

For high-turbulence Reynolds numbers, Re_n or Re_t, the functions f_μ, f_1 and f_2 multiplying the three constants, tend to unity changing the model back to the original Chen-Kim modification. The dumping function mimics the effect of the laminar flow closer to the wall where the value of the mixing coefficient C_μ can vary as a function of P_K/ε as reported by Rodi (1980) correlated in previous work.

The Low-Re extension does not employ wall functions and the flow field needs to be meshed into the laminar sublayer. The minimum distance to the nearest wall is determined for each cell once only, by the solution of an extra differential equation for a scalar length-scale variable, which is of the form, $\nabla\cdot(\nabla L) = -1$. The boundary conditions $k = 0$ and $d(\varepsilon)/dy = 0$ are applied at the wall. The authors claim that the extra source term represents the energy transfer rate from large-scale to small-scale turbulence controlled by the production-range time-scale and the dissipation-range time-scale. This means that the Chen-Kim model gives similar results compared to the standard model for simple flows and makes better predictions for complex flows involving re-circulation, streamline curvature and swirl, such as in jet flows.

A feasible range of model constants is determined from experimental data of the decay of homogeneous turbulent flows with and without mean strains and a simplified wall analysis. The final model constants are determined by numerical optimisation matching the predictions to the measured data for several turbulent flows and realizability conditions as described by Schumann (1977). The following model constants are used

instead of the standard ones in the $k-\varepsilon$ model, $\sigma_k = 0.75$, $\sigma_\varepsilon = 1.15$, $C_{\varepsilon 1} = 1.15$, $C_{\varepsilon 2} = 1.9$, Chen and Kim (1987).

3.3.3 Non-Linear RNG $k-\varepsilon$ Model

Renormalization Group (RNG) methods have been used extensively in Physics. The model has been derived by series of mathematical procedures, which make up the RNG method. In this approach, an RNG technique was used to develop a theory for larger eddies in which the effects of the small scales were represented by modified transport coefficients. This effect is based on the universality of isotropic scales less than the mesh size which follow the Kolmogorov power law.

The dissipation equation in the RNG case is,

$$\rho \frac{\partial}{\partial x_i}(u_i \varepsilon) = \rho \frac{\partial}{\partial x_i}\left(\frac{\nu_t}{\sigma_\varepsilon}\frac{\partial \varepsilon}{\partial x_i}\right) + \left(\rho \frac{\varepsilon}{k}\right)\left(C_{\varepsilon 1} P_K - C_{\varepsilon 2}\varepsilon + \alpha \varepsilon\right). \tag{3.38}$$

Similar to the standard $k-\varepsilon$ model, the effects of turbulence are accounted through the eddy viscosity in the momentum equation, which is modified to yield the RNG $k-\varepsilon$ model (hereafter denoted as the RNG model). The $C_{\varepsilon 2}$ coefficient multiplying the dissipation source term in the linear ε-equation is replaced by $C_{\varepsilon 2}$ and α. The eddy viscosity is modified in a way that the high-wave-number modes (i.e. small scales) affect the retained larger scales. This is accounted for in the model by calculating a non-dimensional number η, which is the ratio of the turbulent to the mean time-scale. This term appears in an additional production term in the ε-equation,

$$S_\varepsilon = -\rho \alpha \frac{\varepsilon^2}{k} \tag{3.39}$$

where $\alpha = C_\mu \eta^3 \left(\frac{1-\eta}{\eta_0}\right) \Big/ \left(1+\beta\eta^3\right)$, $\eta = S\frac{k}{\varepsilon}$, $S^2 = 2S_{ij}S_{ij}$ and $S_{ij} = \frac{1}{2}\left(\frac{du_i}{dx_j} + \frac{du_j}{dx_i}\right)$, and the model constants $\eta_0 = 4.38$ and $\beta = 0.012$.

The additional production term in the ε-equation, S_ε, becomes significant in rapidly distorted flows and flows removed from equilibrium, i.e., for flows with large strain rates, when $\eta >> \eta_0$. In the limit of weak strain where S and η tend to zero, the additional source term tends to zero and the original form of the $k - \varepsilon$ model is recovered.

In the limit of strong strain where S and η tend to infinity, the additional source term becomes,

$$S_\varepsilon = -\rho C_\mu \frac{\eta}{\beta\eta_0}\frac{\varepsilon^2}{k} \tag{3.40}$$

η_0 is the fixed point for homogeneously-strained turbulent flows and β is a constant evaluated to yield a von Karman constant of about 0.41 see Yakhot *et al.* (1992), Yakhot and Orszag (1986) and Yakhot and Smith (1992).

The different model constants in this model which are produced by the RNG procedure are the following, $\sigma_k = 0.7194$, $\sigma_\varepsilon = 0.7194$, $C_\mu = 0.0845$, $C_{\varepsilon 1} = 1.42$, $C_{\varepsilon 2} = 1.68$, Yakhot and Smith (1992).

The resulting high *Re* number form of the RNG $k - \varepsilon$ model proved successful for separated flows. However, it has been observed that the model results in substantial deterioration in the prediction of plane and round free jets in stagnant surroundings.

One of the characteristics of turbulence is that the small scale eddies, which are much less than the integral scale, L, can be considered as universal, following a graded relationship. The universality of the inertial subrange of the Kolmogorov power spectrum has been tested by Monin and Yaglom (1975) and found to hold up for a wide

variety of turbulent flows such as boundary layers or buoyancy-induced flows in liquids and air. The Kolmogorov power spectrum is shown graphically in Figure 3.5,

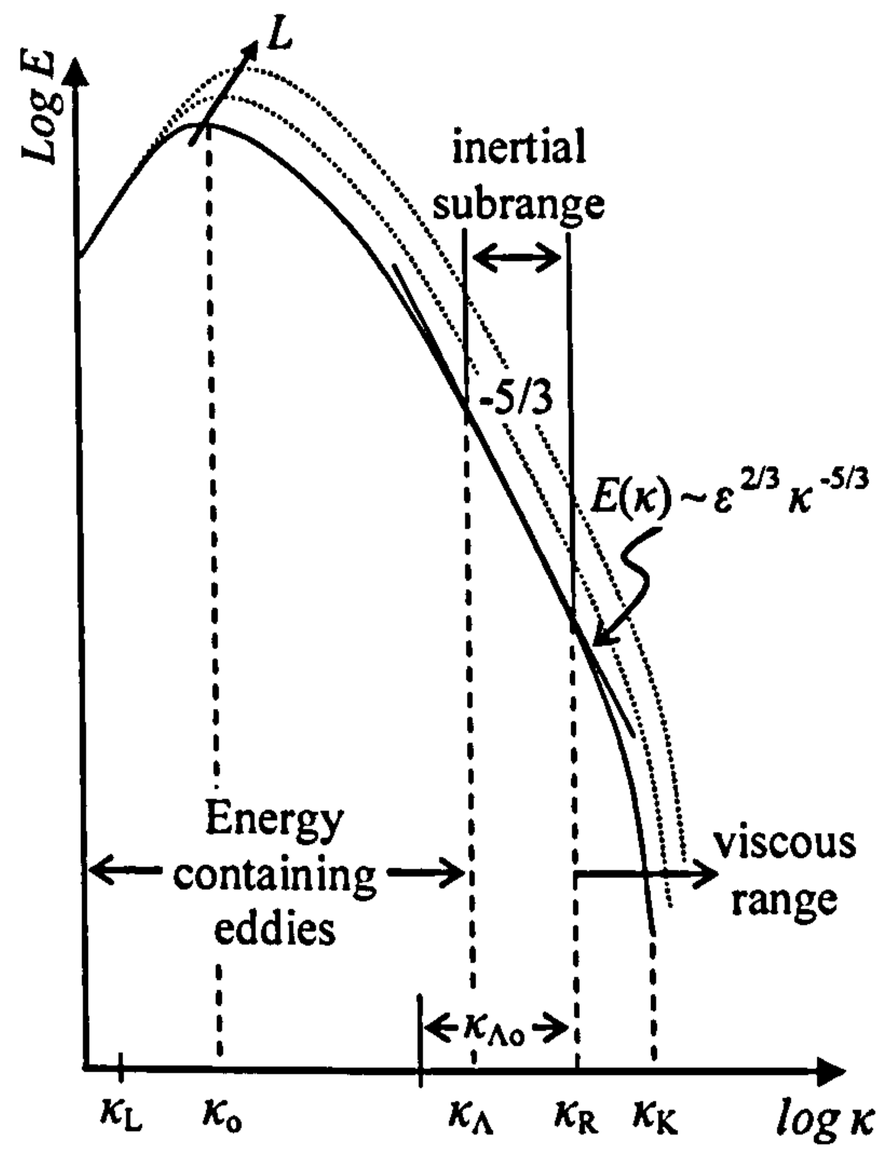

Figure 3.5: Kolmogorov power spectrum.

The wave number of turbulent eddies of Taylor size λ is slightly higher than the Kolmogorov size and is given as $\kappa = 2\pi / \lambda$ and the angular frequency is $\omega = 2\pi f$. For the integral scale L, the wave number taken as $\kappa = 1/L$. The Kolmogorov range is,

$$E(\kappa) = C_\kappa \varepsilon^{2/3} \kappa^{-5/3} \tag{3.41}$$

where $C_\kappa = 1.3 - 2.3$ is the Kolmogorov constant, ε is the rate of energy dissipation per unit volume and κ is the wave number for the range of length scales.

Energy propagates from the small scales to the internal wave motion due to the increase of the potential energy to result in the fluctuating motion of the internal waves. This is accentuated by the heat generation at the dissipation range, while heat is also scattered by the thermal radiation and lost to the outside. This results in a backscatter of energy mechanism, which is not a very regular phenomenon, and that is very difficult to consider accurately in a CFD simulation.

The standard $k-\varepsilon$ model considers isotropic turbulence that is of order of the mesh size. However, the RNG turbulence model is more advanced by taking into account the effect of turbulence scales of size smaller than the cut-off size Λ_0 that is of the order of the mesh size. This is carried out by applying RNG methods in order to construct a power law of the smaller scales. This takes into consideration the size of the integral scale and the size of the cut-off scale in extending the effect of the range down to the scales of the order of Kolmogorov scale. As long as the coarsening of the scale grading applied by the mesh size is close to the inertial range, the RNG model should perform well. One limitation is at very large Re where the properties of turbulent fluids are independent of the inertial subrange. Non-linearities produced by the RNG procedure are small. However, they do not tend to zero when the iteration tends to infinity. Turbulence acts in a different way to the mean flow depending on the size and scale. Higher order non-linear contributions are asymptotically unimportant and lead to small corrections in the results based on a second-order closures, Yakhot and Orszag (1986). The turbulent kinetic energy is much higher closer to the wall due to surface roughness resulting from anisotropic turbulence streaks which have a higher energy peak than in the mean flow. Not all eddies interact with the mean flow and consequently not all eddies contribute to the turbulent viscosity in the same way. Therefore, the non-linear effects that may arise from small anisotropy in flows that do not influence the mean velocity gradient can be neglected in the flow. The success of the RNG model can be attributed to the weak decoupling of the strongly anisotropic scales from the mean motion and the apparent success of the RNG methods to eliminate isotropic turbulence.

The exchange of energy from the larger to the smaller scales increases with the breaking up of the integral scale as shown in Figure 3.6,

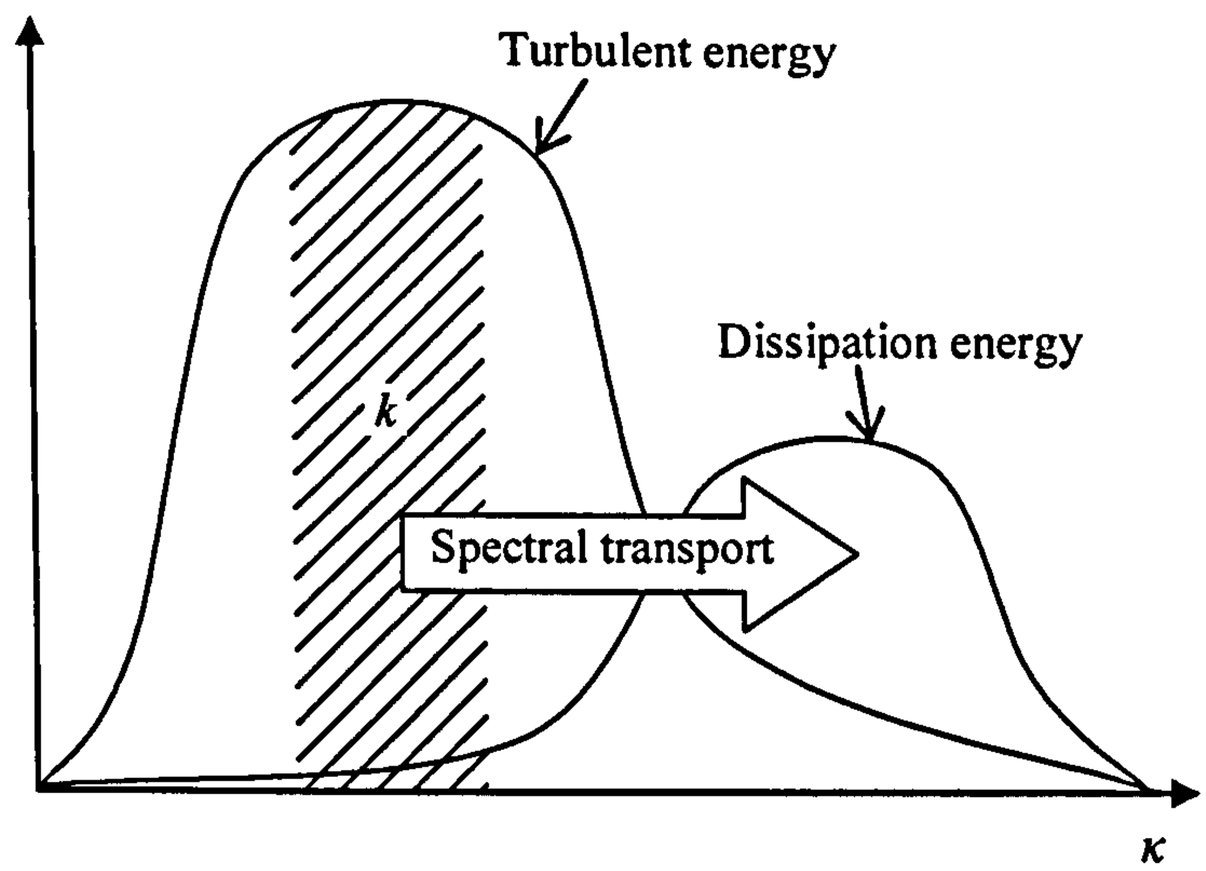

Figure 3.6: Turbulent energy transport.

The effect of energy backscatter can be assumed to be smaller than the effect of turbulence mixing, while the dissipation is larger due to the effect of both buoyancy and viscous forces that act on turbulence. The gradient fluxes are accounted for in 2-equation models by the solution of extra equation for the turbulent kinetic energy and dissipation that are linked to the momentum equation through the turbulent viscosity. The mean velocity gradient is influenced by the differential transport equation for the kinetic energy, k, which extracts kinetic energy from the mean flow by viscous dissipation into heat, while in stratified flows this is also influenced by the interaction of k with potential energy through the buoyancy action. There should be a mesh size that will adequately describe the flow based on the assumption of quasi-2-dimensional and close to isotropic nature of turbulence due to stratification.

3.4 Near-Wall Modelling

Since the geometric model of the current investigation is bounded by solid walls, modelling the laminar sublayer adjacent to the wall can be important. There is a number of near wall models involving wall functions, such as Reichard's law of the wall and Spalding's law of the wall. However, looking further into the effects of different wall models is beyond the scope of the current work. Therefore, the widely used logarithmic law of the wall was also used here.

The wall functions employed here are appropriate to an inner wall layer in local equilibrium. The inner variable for velocity u^+ is,

$$u^+ = \frac{u_r}{u_\tau} = \frac{1}{\kappa}\ln\left(Ey^+\right) \tag{3.42}$$

where u_r is the absolute value of the resultant velocity parallel to the wall at the first grid node. Hence k, ε and the resultant friction velocity or shear stress at the wall, u_τ, are,

$$k = \frac{u_\tau^{\,2}}{\sqrt{C_\mu}} \tag{3.43}$$

$$\varepsilon = \frac{C_\mu^{\frac{3}{4}} k^{\frac{3}{2}}}{\kappa y} \tag{3.44}$$

$$u_\tau = \sqrt{\nu\left(\frac{\partial u}{\partial y}\right)_w} = \sqrt{\nu\frac{|u|}{y}} \tag{3.45}$$

y is the normal distance of the first grid point from the wall, y^+ is the dimensionless wall distance $u_\tau y/\nu$ or cell Reynolds number at the wall when multiplied by u^+, C_μ (= 0.09) is the standard constant in the $k-\varepsilon$ model, κ (= 0.41) is the von Karman constant and E is a wall-roughness parameter.

Equation (3.42) is the well-known logarithmic law of the wall, and strictly this law should be applied to a point whose y^+-value is in the range $30 < y^+ < 130$.

The boundary condition for k assumes that the turbulence is in local equilibrium and consequently, this set of wall functions is not really suitable under separated conditions. As turbulent energy diffusion towards the wall becomes significant, this leads to appreciable departures from local equilibrium.

3.5 Buoyancy Extension

In the $k-\varepsilon$ model, stratification effects are introduced in the flow from both k- and ε-equations by the G_B term. However, the generation term G in the generation - destruction terms of the ε-equation is exchanged by G_ε, to include the buoyancy destruction term, G_B, and a coefficient $C_{\varepsilon 3}$. For stable stratification, this term acts as a destruction of turbulence production. For unstable stratification, the opposite effects occur. Some variations for buoyancy extension have been used in the past mainly applied to geophysical fluids.

Rodi (1979) investigated the effect of $C_{\varepsilon 3}$ coefficient on the production term G_ε when using a horizontal or a vertical jet. In this way more control was provided over the stratified layers in 2-dimensional shear flow by changing the value of the coefficient $C_{\varepsilon 3}$. The left part of the $k-\varepsilon$ equation then reads $G_\varepsilon = (P_K + G_B)(1 + C_{\varepsilon 3} Ri_f)$, where $Ri_f = -\frac{1}{2} G_{B\overline{v'^2}} \Big/ (P_K + G_B)$ is the ratio of buoyancy production to the total production of turbulent kinetic energy and $G_{B\overline{v'^2}}/2 (\approx G_B)$ is the production/destruction of the lateral fluctuations $\overline{v'^2}$ of the turbulent kinetic energy in the direction of gravity associated with the 2-dimensional effect of buoyancy for the 2-dimensional jet. He included the production of lateral fluctuations in the numerator in a similar way to Bradshaw (1969), though Bradshaw used only two components in the denominator. In vertical shear layers, the velocity component is perpendicular to the direction of gravity and receives no buoyancy contribution, thus $G_B = 0$ giving $Ri_f = 0$. However in a case of horizontal buoyant jet, all buoyancy production goes into the v-component so that $G_{B\overline{v'^2}} = 2G_B$ and $Ri_f = -G_B/(P_K + G_B) = -(-\beta g \overline{v'\phi'}) \Big/ \left(-\overline{u'v'}\frac{\partial U}{\partial y} - \beta g \overline{v'\phi'}\right)$. The value of $C_{\varepsilon 3}$ in this model should be chosen close to zero for vertical buoyant shear layers and close to one for horizontal shear layers. Rodi (1979) carried out simulations of buoyant vertical, horizontal and swirling jets, using an isotropic model in stably-stratified flow and obtained $C_{\varepsilon 3} = 0.6 - 0.8$, while cited work of Fornoff (1978) using the non-isotropic model obtained $C_{\varepsilon 3} = 0.9$. Rodi (1980) suggested that the alternative

definition for Ri_f enables $C_{\varepsilon 3} \approx 0.8$ to be used in both vertical and horizontal layers as well as swirling jets, and the same value had also been suggested by Hossain (1980).

Another extended model, developed by Goussebaile and Viollet (1982), accounts for confined turbulence flows under strong buoyancy by introducing a formula for the C_μ coefficient as well as varying $C_{\varepsilon 3}$ coefficient in the ε-equation. Goussebaile and Viollet (1982) extended the work done by Rodi (1980) on the left-hand side of the ε-equation to simplify the buoyancy extension, by removing the expression of Ri_f in which the coefficient $C_{\varepsilon 3}$ modifies the buoyancy production directly $G_\varepsilon = P_K + (1 - C_{\varepsilon 3})G_B$. For stable stratification, $C_{\varepsilon 3}$ was recommended to be set equal to one, i.e., no G_B term in the ε-equation. For unstable stratification, $C_{\varepsilon 3} = 0$ has given good results, also in the work by Viollet (1986). Dagestad (1991) suggested that the value of $C_{\varepsilon 3}$ should be kept equal to 1.0 for neutral, stable and unstable stratification of channel flow and for smoke stratification in a corridor not using the extension lead to divergence. Markatos *et al.* (1982) carried out a parametric study of $C_{\varepsilon 3}$ buoyancy induced smoke buildings. They obtained no significant difference of the results with $C_{\varepsilon 3}$ in the range of 0.3 to 1.0. However, when $C_{\varepsilon 3} = 1$ and $G_B = 0$ in the k-equation, the stratified layers disappeared and a more homogeneous flow occurred. Hence, neglecting the buoyant dumping in the production of turbulent kinetic energy resulted in too high production rates and thus, too well mixing. Markatos *et al.* (1982) concluded that it was far more important to keep the buoyancy term in the k-equation than to enter the precise value of $C_{\varepsilon 3}$ in the ε-equation. Additionally, these flow simulations due to fire smoke refer to laminar type systems due to high buoyancy characteristics created by high temperature differences obtained from the fire that develop a sharp interface and may not directly apply to typical ventilation flow. Although the temperature and the velocity gradients were in general good agreement, passing through the mean of the experimental points, there were differences close to the ceiling and the floor of the order of 100 K and there was a difference of 1 m/s for velocity at a mid-height, i.e., locally the disagreement was larger that 30%. The mismatch was attributed to the excessive air leakages in the full-scale experiment not being accounted for by the CFD model, the standard $k - \varepsilon$ model being used for the prediction of turbulence, the differences between the experimental and the CFD model,

and that the predominant 2-dimensional flow problem modelled by 2-dimensional equations that could be solved more effectively by extending the CFD code as a 3-dimensional flow problem. Computations with other buoyancy extended versions of the $k-\varepsilon$ model have also been described by Chow and Leung (1989) have been used to fire and smoke simulation. Hence, the value of $C_{\varepsilon 3}$ has been found to depend on the flow situation and most of the cases studied in the literature show that neglecting the buoyancy term G_B in the ε-equation results in less mixing.

PHOENICS uses the approach to Goussebaile and Viollet (1982) to modify the buoyancy production G_B but in a simplified formulation. The production term in the left-hand side of the ε-equation is $G_\varepsilon = C_{\varepsilon 1}P_K + C_{\varepsilon 3}G_B$. However, due to the different formulation of G_ε, the value of $C_{\varepsilon 3}$ is inverse in PHOENICS. To obtain the same effect as in the other studies, $C_{\varepsilon 3}$ should be close to zero for stably-stratified flow and close to 1.0, i.e., G_B is present in the ε-equation, for unstably-stratified flows. The term G_B is the destruction by buoyancy, i.e., the volumetric production rate of turbulent kinetic energy by gravitational forces interacting with density gradients and it is denoted by,

$$G_B = -\frac{\nu_t}{\sigma_t}\frac{g_i}{\rho}\frac{\partial \rho}{\partial x_i}. \tag{3.46}$$

The buoyancy extended $k-\varepsilon$ model containing the G_B term reads as follows,

$$\rho\frac{\partial}{\partial x_i}(u_i k) = \rho\frac{\partial}{\partial x_i}\left(\frac{\nu_t}{\sigma_k}\frac{\partial k}{\partial x_i}\right) + \rho\left(P_K + G_B - \varepsilon\right) \tag{3.47}$$

$$\rho\frac{\partial}{\partial x_i}(u_i \varepsilon) = \rho\frac{\partial}{\partial x_i}\left(\frac{\nu_t}{\sigma_\varepsilon}\frac{\partial \varepsilon}{\partial x_i}\right) + \left(\rho\frac{\varepsilon}{k}\right)\left(C_{\varepsilon 1}P_K + C_{\varepsilon 3}G_B - C_{\varepsilon 2}\varepsilon\right) \tag{3.48}$$

where g_i is the gravitational vector.

The buoyancy term is negative for stably-stratified flows, e.g., Rodi (1980), since it represents the destruction of k by buoyancy, i.e., $G_B \leq 0$, so that dense layers of fluid can flow below light layers without significant mixing, and thus kinetic energy is reduced and turbulence is damped as potential energy increases. Whereas buoyancy term is positive for unstably-stratified flows, i.e., $G_B > 0$, where dense layers of fluid flow above light layers of fluid, so that kinetic energy is increased at the expense of potential energy of the gravitational force. The Boussinesq approximation is employed, in which the variations in density are expressed by way of variations in temperature. For a stably-stratified condition, the equation of buoyancy destruction (3.46) reduces to,

$$G_B = \frac{\nu_t}{\sigma_t} \beta g_i \frac{\partial T}{\partial x_i}. \tag{3.49}$$

The additional constant, $C_{\varepsilon 3} = 1.0$, is used when buoyancy extension is activated.

Goussebaile and Viollet (1982) carried out 2-dimensional steady-state simulations of stable and unstable stratification using the standard $k - \varepsilon$ model without the C_μ modification and an algebraic stress/flux model with the C_μ modification to study a case of strong buoyancy. In the case of the standard model without C_μ modification, a stable set-up, reduced Froude number, $Fr << 1$ and $C_{\varepsilon 3} = 1.0$ (no G_B term in the ε-equation), the results are closer to the experimental values for a relatively large downstream distance. The algebraic model with the C_μ modification shows slightly less mixing characteristics that is further away from the experimental values. For an unstable set-up, at $Fr = 0.9$, the model with the C_μ modification and $C_{\varepsilon 3} = 0$ shows better mixing as it is closer to the experimental results with downstream distance than the case without C_μ modification but with $C_{\varepsilon 3} = 1.0$. However, when Fr increased to $Fr = 1.6$, the results resembled the case previously encountered with no C_μ modification, i.e., showed less mixing. Viollet (1985) carried out 2-dimensional steady-state simulations of stable and unstable stratification using the standard $k - \varepsilon$ model and an algebraic stress/flux model with modifications on the σ_t and C_μ to model a stratified shear layer development from a splitter plate. For very strong stratification,

both models performed equally well. However, when the stratification became weaker both models were in good agreement with the experimental results, while in the case of unstable stratification, the stress/flux model gave slightly better prediction. There is little difference between the two models when $C_{\varepsilon 3}$ coefficient is the same. This demonstrates that the mixing may have not depended mainly on the setting of the $C_{\varepsilon 3}$ coefficient or the modification by C_{μ} coefficient, but also on other parameters such as the mesh size and the 3-dimensionality of turbulence that is rather not well represented on a 2-dimensional grid. Older simulations test the value of $C_{\mu} = 0.09$ which is derived for flows that the production of turbulent kinetic energy P_K is the same as the dissipation of the rate of kinetic energy ε, but for far field jets and wakes P_K was found to take different values, Rodi (1975). Rodi (1972) correlated the experimental data and proposed a function for C_{μ} valid for thin shear layers which significantly improved the capabilities of $k-\varepsilon$ model for weak shear layers, $C_{\mu} = f(\overline{P_K/\varepsilon})$.

Wind induced entrainment of cold water from below due to the surface shear stress results in deepening the mixed layer above. Svensson (1978) carried out 1-dimensional simulations with $C_{\varepsilon 3} = 0.5$ using the standard $k-\varepsilon$ model, while Mellor and Strub (1980) simulated this with 2 1/2 algebraic stress/flux model. The decay is not predicted very well by either of the calculations for $Ri_0 > 100$. When taking side wall friction in Svensson (1978) calculation there was an initial agreement with $Ri_0^{-1/2}$ but then there was a strange change in the decay law.

Celik *et al.* (1999) carried out a set of tests to investigate mixing of miscible fluids in stratified shear flow apparatus using a splitter plate and by CFD. The CFD studies consisted of 2-dimansional simulations using grid sizes of 450 × 50 (= 22,500) and 600 × 80 (= 48,000). The size of the channel used in their experiments was relatively small, 5 × 0.1 × 0.2 m (L × W × H). The interface thickness is normalised by the total depth of the upper and lower layers. There was a difference regarding the coefficient of the relationship of the normalised interface thickness with Ri_0, most likely due to 2-dimensional assumption. In their experiments, the coefficient was n = -2.6, while in the

2-dimensional simulations the coefficient was n = -2.1. The dimensionless entrainment velocity is a function of Ri_o with an exponent n = -1.1.

Some discrepancies were reported in Rodi (1987) for water stratification where the thermocline was predicted slightly more diffused than the actual experiment. The velocity distribution and salinity distribution included thereby can be compared with the results of Celik *et al.* (1999). The problems are poor mesh resolution and the effect of the 3-dimenional mixing not represented correctly on a 2-dimensional grid. In Celik *et al.* (1999) the effect of K-H mixing on the thermocline is picked up, but this is still rather more diffusive than the corresponding experimental case. The interface sharpens with $Ri_o > 1$, also observed experimentally, while at $Ri_o = 0.5$ there are two interfaces above and below, due to wave instability. A droplet formation model was used to simulate the effect of the higher droplet size that increased this effect which is highlighted on their graphs. The mesh size was also very fine, the lowest resolution was 450 × 50 (= 22,500), while in Svensson (1978), the mesh resolution was 15 × 20 (= 300) grid points. Therefore, 2-dimensional cases need higher resolution in order to represent more closely wave instabilities and mixing that are actually 3-dimensional phenomena. It may be well realised by now that 3-dimensional simulations are better than 2-dimensional simulations in any aspect involving turbulence.

However, the correlation for Ri_f is because the stratification is mainly obtained as a 2-dimensional calculation. The 2-dimensional simulations lead to diffusive results due to turbulence being overpredicted in the 2-dimensional plane known as numerical diffusion that is also concluded by Rodi (1987). In the 2-dimensional plane, turbulence experiences less dumping due to the reduced strain rate. This is especially problematic with a coarse grid resolution that overestimates the length-scale of turbulence. The interface thickness was not predicted as sharp in the 2-dimesnional simulations by Svensson (1978) and the salinity and velocity profiles underpredicted the instability on the interface, although the results matched fairly well with the experiment curves. However, as the 3-dimensionality of the problem increases that is also associated with time-dependencies, so does the numerical diffusion in 2-dimensional simulations. This can trigger too much mixing or too strong recirculating motion. Turbulence can become accentuated further by increasing mesh resolution, as observed in the 2-dimensional studies by Celik *et al.* (1999), although a fairly good match was obtained with the

experiments. In some steady-state cases, secondary and tertiary vortices can appear when the resolution becomes too high. De With (2001) also observed the increase in turbulence on the grid with 2-dimensional LES simulations when compared to a 3-dimensional LES case. Older 2-dimensional simulations based on C_μ and σ_t modifications also deal with the improvement of the mixing characteristics mainly in 2-dimensional simulations. From the physical point of view, the inverse energy cascade is typical of 2-dimensional turbulence, Davidson (2004). The energy is transferred from the small scales to the large scales violating Richardson notion of vortex stretching that can result to increased turbulence in 2-dimensional simulations leading to overdiffusive results.

These problems were raised as 3-dimensional calculations were not practical at that time. Twenty years ago, 2-dimensional simulations employed a mesh size equal to the observed eddy size, while roughly 10 years ago, 2-dimensional simulations became more numerically intensive. Researchers in the past seem to focus more on the modelling of the resulting mean gradients, mainly the mean density gradient in the flow, but not the physical aspect of the problem that is 3-dimensional mixing. Turbulence instabilities are 3-dimensional phenomena. In this work unstable stratification may be created at very high Ri_0 where the velocity of the hot air from the top is much higher than the cold air flow at the floor level creating unstable gradients. In the process of achieving a better match with experimental results, researchers previously changed the value of the mixing coefficient C_μ for 1-dimensional and 2-dimensional simulations of stratified flows, and recently 2-dimensional simulations with a small mesh size achieve a slightly better evaluation of mixing. Therefore, the fine tuning C_μ or σ_t is of little practical use, because only a set of prescribed coefficients are acceptable. These coefficients are derived based on general theoretical and experimental observations that can be regarded as universal for most type of flows and the performance of any numerical calculation should be optimised based on similar conditions to reveal its actual capabilities. This would rather lead to non-universal solutions for any other optimised numerical calculation that uses coefficients defined for coarse simulations.

3.6 Using CFD to Solve the Problem

The historical evolution in computing power and the development of the CFD software have influenced the capabilities of the eddy-viscosity models. The previous incapacity of these models to predict heat transfer and air movement inside rooms well enough mainly relates to the mesh size and where 2-dimenisonal simulations are performed.

Jones and Whittle (1992) reviewed the status of the capabilities of CFD simulations since the birth of the CFD code for predicting air flow in building. The stream-function and vorticity formulation by Nielsen (1974) lead to the development of CFD code based on a computer code developments that had taken place at Imperial College. These simulations were restricted on a 2-dimensional plane as stream function does not apply in a 3-dimensional co-ordinate system. The more recent formulation of the conservation equations that we know today was used by the later work of Nielsen *et al.* (1978) to predict 3-dimensional flows. Lately, Nielsen (1992) developed the "inlet box" method where the computational domain was limited to exclude the initial developing region of the jet in the near field to reduce the computing time. A very good match was achieved by using the standard $k-\varepsilon$ model in comparison to experimental data that was obtained by a laser-doppler anemometer. However, it may be difficult to obtain a good match in the absence of experimental inlet conditions and this method became less popular.

It is reported in literature that the irregularities near boundaries with coarse Cartesian grids introduce turbulence in the flow. In the simulation of the diffuser vanes, which are at an angle to the horizontal, Cartesian grids have given good results. Recently, PHOENICS has implemented a method for partial solids treatment. A good solution was also obtained. However, this introduced some difficulties in convergence and current updates on this method are obtained by the latest version of PHOENICS. A block structured approach improves convergence difficulties due to the diagonality of the flow that is related to non-linearities. However, for simple geometries, Cartesian grids are still simpler to use and require less computing time. Methods for efficiently increasing mesh density in areas where higher resolution is required, like embedded grid objects, can provide local mesh refinement with FVM that have been used in the past with lower mesh resolutions and 2-dimensional simulations. The interfaces between the two grids are one of the difficulties to the code developer. However, previous

simulations of this work using grid embedded refinement in PHOENICS resulted in much longer computing times. This feature has recently been optimised for 3-dimensional simulations by PHOENICS, but has yet not been widely tested. Recent simulations of air movement and heat flow in buildings are steady-state and use the FVM with Cartesian grids obtained good convergence and mesh independent results with less storage requirements than FEM or curvilinear grids. Past simulations in the literature have used coarse grid resolutions due to the limited computing resources. It is suggested that these cases should be treated with careful exercise of engineering judgement. Fine grids exhibit better convergence because they describe better the physical problem, but they are resource demanding. Certain numerical issues like how the mesh density and convergence affect the solution are still the subject in every numerical investigation.

The physical issues involved in CFD simulations are associated with the interpretation of the real problem and turbulence. The thermal radiation component between surfaces plays an important role in the heat transfer mechanism in buildings and it should be modelled. Heat and mass transfer through the building walls influence the temperature and pressure inside the building and this yet again presents additional modelling components that raises further issues, how to model conduction and air infiltration in order to investigate the stratification behaviour.

A further solution for turbulent flows is the Reynolds Stress Model (RSM). Malin and Younis (1990) noted that the isotropic turbulence assumption and constant Prandtl number are unsupported assumptions by experiment. The eddy-viscosity models consider a constant dissipation time-scale ratio in the main ε-equation where the effects of thermal dissipation are also considered to occur in the same formulation, while a variable time-scale ratio can be determined via a transport equation for the thermal dissipation rate in Reynolds-stress models (RSMs). The RSMs and algebraic stress models, otherwise known as second-order closures, are a step further to eddy-viscosity based models in modelling turbulent flows and flows that are also affected by buoyancy. These models represent a step closer to the fundamental equations than the 2-equation $k-\varepsilon$ model in the way that the solutions are obtained for the Reynolds stress tensor. The RSM model in the case of Chen and Chao (1997) predicts the flow anisotropy of a buoyant jet, $\overline{u'u'}$, $\overline{u'w'}$ and $\overline{w'w'}$, which is shown to be very close to the

experimental results, while the $k-\varepsilon$ models averaged this effect and hence suppressed the anisotropy in the flow. There is an average difference of 20% in the maxima of the normalised velocity correlations, while similarity is satisfied by the mean values in most of the cases. The disagreement of the $k-\varepsilon$ models can be attributed on the first instance to $C_{\varepsilon 3} = C_{\varepsilon 1}$. The value of the $C_{\varepsilon 3}$ coefficient had already been corrected by Malin and Younis (1990) for the RSM case and given a value of $C_{\varepsilon 3} = 0.98$, because the dissipation rates were found to be 20% lower for a plane jet. RSMs are improvements to eddy-viscosity models, so for the anisotropic effects in the plume by using the same coefficient of $C_{\varepsilon 3}$ should improve the results for the corresponding eddy-viscosity cases.

Malin and Younis (1990) noted that the isotropic turbulence assumption and constant Prandtl number are both unsupported assumptions by experiment. One popular way to consider the anisotropic effects due to buoyancy has been to use algebraic stress/flux models where Reynolds stress is replaced by an algebraic relation. However, such models are found to be unsuccessful for situations removed too far from equilibrium as in strongly-stratified flows. The further improvement is obtained in RSMs by solving for the Reynolds stresses directly by additional differential transport equations. A drawback of the RSMs is that a further five equations need to be solved in addition to the k- and ε-equations. Similar to the $k-\varepsilon$ model, the formulation of the stresses contain only the most important correlations and are multiplied by coefficients in order to retain the effect of the transport of stresses originally accounted for by the model. Different coefficients are proposed by several researchers, for example, by Daly and Harlow (1970) for the diffusion term and by Launder *et al.* (1975) and Rodi (1980) for the pressure-strain terms. However, the coefficients given more recently by Gibson and Younis (1986) have proved more popular since the calculations are closer to experimental results for buoyant jet flow. The Reynolds stress and heat flux model proposed by Malin and Younis (1990) obtained good agreement for 2-dimensional simulations of turbulent plane jet and axisymmetric jet in comparison to experimental data from literature. The differences in the agreement partly owed to the fact that the experimental data were obtained for a slightly different case and due to experimental errors. For an axisymmetric jet, the experimental measurements of heat fluxes are too low to be accounted for with high confidence as a self similar profile and the computed measurements cut through the mean of the experimental values. The agreement was not

very good though for the plume cases. In the case of axisymmetric plume particularly, the model does not predict successfully the growth rate. One of the reasons could be the time-scale ratio of thermal dissipation. A constant time-scale ratio in the case of the jet flow and plane plume predicted better the magnitude of the temperature fluctuations than the variable time-scale ratio, while the opposite occurred in the case of the axisymmetric plume. Finally, the RSM was capable of reproducing with reasonable accuracy the main features of forced turbulent plumes and where the flow undergoes a gradual transition from jet-like to plume-like behaviour. Similarity with the computed result is determined through the mean of the measurements for several cases. Chen and Chao (1997) used the formulation presented by Malin and Younis (1990) and obtained a good agreement between with the RSM model and their experimental data for the axisymmetric jet case.

The 2-dimensional simulations could also have only affected the results of the eddy-viscosity models because they do not take into account the pressure-strain correlations as the RSM model. This model uses a linear return-to-isotropy approximation and the isotropization-of-production (IP) for pressure that determines the anisotropy in the flow. In general, the results RSM models indicate that the flow anisotropy could be relatively small. The flow in the area of the buoyant jet is also relatively smaller than the area of the entire room and hence the flow anisotropy in the rest of the room in the first place may be disregarded.

A number of researchers found that there are discrepancies among different experimental data of turbulent buoyant jets and plumes. Instrumentation errors were experienced in the analysis of plane and round buoyant jets by a number of researchers in the range of 10-15% reported by Chen and Rodi (1980). The unresolved directional ambiguity of the hot wire can have a reducing effect on the magnitude of the fluctuations. However, in using a laser-Doppler system the refractive index fluctuations play an important role in introducing fictitious turbulent fluctuations when the instrument is used in inhomogeneous density flows. This is exacerbated in plumes that exhibit high turbulence characteristics. From jet theory the measurements of the relative magnitude of velocity and temperature fluctuations should be of the same order. These parameters should be similar in the main flow region of the jets. It was reported by Chen and Chao (1997) that Dai *et al.* (1995) and Shabbir and George (1994) have also

found that there are discrepancies in experimental data. In the paper of Chen and Chao (1997) a velocity as high as 1 m/s was used in the simulation of flow anisotropy in the forced plume, the accuracy is in the range of 0.2 m/s which is already in the range of 20%. Typical displacement velocities are 0.5 m/s or less that should have an error 20%.

LES models require very fine grid spacing because the cut-off scale needs to be well inside the inertial energy subrange of the Kolmogorov power spectrum. Scales that are smaller than the smallest eddy size are modelled by a Subgrid-scale model, Ciofalo (1994). Isothermal flows have been successfully modelled using this method for simple flows, but it is still very expensive or even impossible to use this method for engineering applications that involve additional equations to solve and flow irregularities due to complex geometry. DNS requires to resolve on the grid turbulent eddies of size as small as the Kolmogorov scales. This method involves the use of supercomputers that only national research institutions can afford like the Von Karman Institute of Fluid Dynamics and NASA Ames Research Center.

3.6.1 Modelling inlet boundary conditions

There are several methods to apply the inlet boundary condition in CFD,

1. Direct description: the boundary conditions (BCs) are applied on a plane surface for the effective area of the specified velocity or the flow rate and same area.
2. Box method: the BCs are supplied from experimental measurements inside a volume box at some distance from the outlet.
3. Prescribed velocity method: the BCs are described analytically from existing jet theory inside a volume box at some distance from the outlet.
4. Computer generated: the BCs contain spectral information that is generated at the inlet using sinusoidal functions that are superimposed on the mean profile such as in the LES case studied by Simpson and Holdø (1998).

Models 1-3 are old type models. However, the direct description method, Model 1, is still quite popular due to the simple way in building a CFD model. The box methods, Models 2 and 3 have been used by Nielsen (1992) and good results were obtained compared to experimental results, however they are more difficult to apply especially in

the absence of experimental values. The development of these models was initiated due to the large number of grid points needed to carry out appropriate numerical simulations. However, simple to use models are still popular because they reduce the overheads associated with the available time and budgets.

Fontaine *et al.* (1994) used an academic CFD code EOL-3D to carry out numerical simulations of room air flow. They attributed the differences between the box and the basic model to the inability of the basic model to simulate the flow properly, however it is likely that this is not the case. Although they claimed 10^{-5} convergence in all their results, the discretization scheme used in that case may have still resulted in opposite flow direction which is evident in fig.11(b). This is observed from the comparatively large vectors close to the inlet that result in the upstream direction opposite to the flow. This could have occurred because they replaced the effective area of the diffuser with the total area of the openings which is very small compared to the average cell size previously used in the box model. The box model presumably performed well with the same discretization method for the same case, because of the imposed boundary conditions around a box that needs to be included in this method after the inlet. The flow from the basic model has been predicted reliably by many researchers in the literature. The experimental $1/6^{th}$ hydraulic model, however, gave relatively better results. The results showed that there was 15% difference. Similarity between liquid and air models has been obtained in the literature for a scale difference of around 1/10.

The results presented in the literature from simplified models are related to several sources of inaccuracies due to the sensitivity of the inlet boundary conditions. These boundary conditions were mostly applied to 2-dimensional simulations. Although most of the 2-dimensional models inherently luck physical plausibility, they have almost always been related to a number of errors that may be restricted due to the reduced degrees of freedom from the 2-dimensional assumption.

Djunaedy and Cheong (2002) carried out CFD simulations of several inlet modelling methods for a four way ceiling air diffuser to study the centreline decay. The RNG turbulence model outperformed the standard $k - \varepsilon$ model, although there was a very small difference. However, the 3-dimensional diffuser did not seem to achieve the same centreline decay and this may have been caused because of the micro-level modelling

required to capture as much of the detail of the inlet geometry as possible without unnecessarily meshing other parts of the domain. In view of the mesh size being smaller in the upstream direction, the mesh size in other locations further downstream can become larger that could have caused numerical diffusion in the results. Hence, the larger decay and disagreement compared to experimental results with further downstream distance.

Cehlin and Moshfegh (2002) carried out an experiential and CFD investigation of the flow patterns of a low velocity floor air diffuser. A perforated panel of 3600 holes was simulated using 200 holes in the total face area of the diffuser because it was impractical to model the size of the openings and reported that several researchers from literature encountered problems using several different methods. The negative buoyancy of the cold air discharge from the diffuser was in fair agreement with instantaneous thermography image. There was a slight displacement of the circulation bubble above the discharged flow by all 2-equation models; standard $k-\varepsilon$, RNG and Chen-Kim. The difference was attributed to some extent to the surrounding radiation observed as the measuring screen was at a higher temperature. The difference was an overestimation of the temperature at the floor by 1.1°C when using CFD in comparison to the experimental data. Convergence was achieved at 6000 iterations at 0.3% error of overall heat balance.

There are four zones inside jets that are presented for isothermal flow in several sources of literature, so these will be briefly discussed here. The first zone is where the velocity is the unchanged across the potential core, which is a conical shape of flow pattern, following $U_x / U_o = 1$ and is about four inlet diameters or up to the vena contracta. The second zone is the transition between the laminar flow in zone 1 and the fully turbulent flow in zone 3, where the velocity follows a square-root relationship with distance, $U_x / U_o = \left(K_{II}\sqrt{A_o} / x\right)^{1/2}$, where x is the distance from the virtual origin of the flow expansion and extends to eight diameters for round openings, or rectangular openings of small aspect ratio. The third zone is the profile similarity region where the velocity follows a linear relationship with distance, $U_x / U_o = K_{III}\sqrt{A_o} / x$ or $U_x / U_o = K_{III} Q_o / \left(x\sqrt{A_o}\right)$ and is of major engineering importance because the flow is governed by fully established turbulence motion that extends from 25 to 100 diameters

depending on the inlet shape. The fourth zone is the zone of jet degradation where the flow becomes less than 0.25 m/s (50 fpm), which is very difficult to measure very accurately, and the temperature is about 0.5°C (1°F) to 1°C (2°F) above or below room temperature depending whether the jet is heating or cooling. The decay coefficient K in each zone has attracted a lot of interest by many researchers, Koestel *et al.* (1950), Malmström *et al.* (1997), Zou (2000) and it is also given in standards and textbooks, ASHRAE (1993), Nevins (1976). The velocity decay coefficient, K, for a throw velocity less than 0.76 m/s (150 fpm) is around 6 for open outlets, 5 for square outlets, 4.8 for grilles (larger than 40% free area), 4 for perforated outlets and 1 for round ceiling diffusers. The angle of divergence measures at an average around 22°. The effect of temperature on the jet trajectory is studied by Abramovich (1963) and the decay coefficient for certain types of outlets is also studied more recently by Grimitlyn (1993). The C_d coefficient is a more acceptable way of defining the effective area of the diffuser. This is given by the expression $A_o = A_c \times C_d \times R_{fa}$, where R_{fa} is the ratio of the gross (core) area, however, for open outlets A_{in} is very close to A_o. The C_d coefficient is between 0.65 and 0.9, whilst R_{fa} is between 0.9 and 1. In this work the velocity obtained experimentally by the anemometer at the measuring point perpendicular to the vanes outside the diffuser is the same as the velocity at the neck of the diffuser that can be obtained from manufacturers. The throw obtained from manufacturers is multiplied by a coefficient that depends on the temperature difference between outlet and surrounding temperature.

3.6.2 The effect of the size of the building in flow modelling

In certain stratified conditions there is a clear cut between zones and the question could be raised as to whether a stratified model (heat modelled) is better than an isothermal model. This resulted in the development of flow element models that initially applied with good success for office rooms, Heiselberg *et al.* (1998). The large scale flow tends to be different within the stratified zones and for that reason these zones can be considered separately. In this case another type of flow element modelling, the engineering models applied more effectively due to the predictions in the more favourable direction of the flow. However, the turbulence in one zone seems to affect the other zone and the interaction of the flow elements became more important. The

modelling of two or more zones at the same time is carried out by many researchers experimentally, analytically and by CFD. A combination of cold and hot sources has been presented in many research papers. For example, experimental investigations are carried out for multiple buoyant sources inside containers affecting stratification by Linden and Cooper (1996), the effect of the displacement flow on heat sources inside rooms is carried out using general stratified flow theory and measurements by Nielsen (1994), the temperature and pressure differences due to stack ventilation strategy due to single-sided open windows to a certain angle where the flow can stratify at the room floor is studied experimentally by Heiselberg *et al.* (2001), the effect of the indoor thermals stratification is studied using CFD and scale model using thermography by Seifert *et al.* (2000). An abundance of CFD investigations for air movement and heat flow with stratification can be found in Annex 20 by Lemaire (1993) and a combination of experimental and CFD studies in Annex 26 by Heiselberg *et al.* (1998).

There are other models that are similar to element and engineering models and deal with the ventilation efficiency and energy characteristics of the building, are not that accurate but are favoured to other models mainly because they reduce complexity such as in large enclosures. Ventilation efficiency models deal with the stationary or transient effect of the efficiency of the system to either dilute a contaminant or achieve the optimum thermal performance according to Indoor Air Quality (IAQ) requirements. This is used as a measure of the effectiveness of the system, while wasting little energy in taking into consideration the efficiency of the system. Similarly, energy models deal with the analytical estimation of energy balance mainly of larger enclosures. These models consider only the sources that are most relevant in the analysis, such as machinery, number of employs, energy gains and losses, etc. are steady state and are integrated over a certain time period using pollutant or thermal constraints to assess the conditions according to standards. Since they are built on solid theoretical grounds, they can be used as validation tool for other models.

Flow element and engineering models are defined as *'macroscopic'* in relation to the size of the building and they suppress the details of the flows to a certain extent without increasing the need for higher accuracy. Energy models belong to the same classification. In smaller buildings, CFD and scale models are more applicable and are defined as *'microscopic'* because turbulence and the interaction between flow sources is

more important due to the higher ratio of the scale of the enclosure. However, the results from the smaller rooms can be used in the initial stages of the design process of the larger buildings. These models demand extra computational effort in the resolution of turbulence and close to the flow sources present in the entire flow field. More accurate boundary conditions and the time-dependency on the flow sources may need more complex CFD models that can deal with different flow regimes associated with larger buildings. These are not as expensive as scale models. However a significant amount of time is often required to build the grid system and the computer resources need to be large enough to sustain the computing time and effort.

3.6.3 A historical development on converged solutions

Early simulations with FVM define convergence by the reduction of the sum of the absolute residual errors with respect to the sum of the maximum errors at the start of the simulation. At convergence, if the residuals fall by one order of magnitude, which is associated with 10% error and one significant digit, i.e., 10^{-1}. This is often a too crude criterion and better convergence settings may often be applied by a reduction of two orders of magnitude, which is associated with 1% error and 2 significant digits, i.e., 10^{-2}. The magnitude of the variables solved is also very important, since 10% accuracy for a mean temperature of 20°C would mean approximately 2°C and 1% would mean 0.2°C. For velocity, this will be even smaller since the maximum velocity as a boundary condition can be around one or two orders of magnitude smaller than the mean temperature. However, the changes in the mean flow may be much smaller and appropriate levelling of the actual magnitudes at a monitoring point can assure convergence at certain iteration. Thus for ventilation flows, a general convergence criterion has been applied by 3 orders of magnitude that is 0.1% error in the residual sum, i.e., 10^{-3}.

Papakonstantinou *et al.* (2000) studied a single sided natural ventilation flow. The dimensions of the physical model are 5 × 2.76 × 2.75 m (L × W × H), i.e., 1/2 the size of the model used in the current work. A domain size of 69 × 25 × 49 was used in one of the models that took into account the geometry of the sun-shades with a maximum number of 84,525 cells for which it was claimed that a grid independent solution was achieved. Another model of less complicated geometry, which did not contain the

geometry of the sun-shades, had only 1/2 number of cells that was also grid independent. The CFD package PHOENICS was used to run steady-state simulations, the SIMPLEST algorithm to link velocity and pressure in a line-by-line procedure of the TDMA solver by Spalding (1981) with the standard $k - \varepsilon$ turbulence model. Convergence was achieved for all dependent variables to less than 10^{-3} using 'false transient' type relaxation, but no account was made on the number of iterations. The solutions provided physically satisfactory results of natural ventilation and were in good agreement with previous experimental measurements.

Chen and Chao (1997) used a similar model size of 5.6 × 3 × 3.2 m (for the second displacement case), but it appears from their velocity vector plot that they had only 1/2 the resolution of the smaller resolution model of Papakonstantinou *et al.* (2000) and used the same CFD package PHOENICS. In an initial set of simulations, they used three eddy-viscosity turbulence models: the standard $k - \varepsilon$ model, a modified $k - \varepsilon$ model and the RNG model, and a Reynolds stress model as well as a comparison was obtained with experimental data for an axisymmetric buoyant jet. The same comparison was carried out for the displacement ventilation case, but without the RSM model, because a heat source could be implemented at the time by the code. The heat source was modelled as a box instead of the actual radiative heat through the window blinds that affected the surface of the adjacent table. The SIMPLEST algorithm was used to link velocity and pressure. The residual errors were set to less than 10^{-3} of the mass inflow. The mesh size suggested was 0.114 m, which they calculated using an empirical equation of a buoyancy to momentum ratio reported by Shabbir and George (1994) that was originally obtained from Morton (1959). There was no reference to the number of iterations and the performance of the eddy-viscosity models was not very good as a result of the coarse grid and box modelled instead of the actual heat source. While the RSM model performed well due to additional equations solved for turbulence. The RNG model performed slightly better than the other eddy-viscosity models. However, mean velocity and temperature gradients were well predicted by all models.

Gan and Awbi (1994) studied comfort indices in an office room of 4.9 × 3.7 × 2.75 m also similar geometry to Papakonstantinou *et al.* (2000) with a mesh resolution of 30 × 36 × 26 (= 28,080). The simulations were also steady-sate using the CFD code VORTEX and the standard $k - \varepsilon$ model. The momentum equations were integrated

using QUICK scheme and the scalar transport equations were integrated by the HYBRID scheme. The SIMPLE algorithm was used for pressure. To achieve convergence and enhance the stability of solution, under-relaxation factors were used and claimed that 800 iterations were taken to achieve convergence. The data produced by the CFD program were suitable to assess the general performance of the ventilation system where thermal radiation and CO_2 concentrations are important in the thermal effectiveness and air quality in the room.

Gan (1995) studied winter heating and summer cooling conditions using the same model as Gan and Awbi (1994) also by steady-sate simulations and the standard $k-\varepsilon$ model as well as using VORTEX CFD code. Convergence was also considered when the sum of the normalised residuals for each flow equation was less than 10^{-3} that was claimed to have been observed at 800 iterations. The flow equations were integrated using the QUICK discretization scheme and SIMPLE algorithm was used for pressure. The results described the effectiveness of ventilation satisfactorily, but no comparison with experimental results, although mentioned, was presented in neither of the simulations.

Cook and Lomas (1998) studied the displacement flow using a 2-dimensional CFD model of 2.5 × 5.1 m with high and low level openings, modelled in one half by a symmetry line and engulfed inside a 5.1 × 7.65 m domain using CFX-F3D CFD package and compared with experimental results. They used the standard $k-\varepsilon$ and the RNG turbulence models. An approximation for the average number of cells could be obtained from the velocity vector plots that measured 50 × 50 (= 2,500) cells. The solution criteria was still not met by using default relaxation, while by tuning under-relaxation factors was still not satisfactory. As an alternative approach, false time-step relaxation was implicitly specified over the equation which reflects more closely to the time-scale over which the particular variable changes. The SIMPLEC algorithm, Van Doormal and Raithby (1984), with Rhie-Chow (1983) interpolation technique to prevent decoupling due to the collocated grid approach for velocity and pressure. Convergence was obtained by initially running the simulation for 2,000 iterations using "looser" under-relaxation that slowed down convergence and then restarting by another 2,000 iterations (i.e., a total of 4,000 iterations) using false time-step relaxation. This method produced convergence of the absolute values of the variables to 0.1% at the monitoring

point over 20 interactions and 1% for enthalpy of the total heat entering the domain. The study highlighted the difficulties in predicting such flows.

Xue and Shu (1999) studied the mixing characteristics of non-isothermal downward directed air-conditioning system at ceiling level using 2-dimensional CFD simulations of a domain size 3.5 × 2.5 m. The simulations were performed on 42 × 27 (= 1,134) cells and using the standard $k - \varepsilon$ turbulence model. The line-by-line TDMA solution procedure was used to solve the algebraic equations of the flow and the SIMPLE algorithm for pressure described by Patankar (1980). Steady-state solutions were obtained by under-relaxation techniques using a ratio of residual mass source to the maximum mass flux across a control surface to be less than 0.1%. A general convergence was satisfied after 6,000 iterations. Satisfactory results where achieved for mixed convection heat transfer for a simple geometry of a linear diffuser.

Cheng *et al.* (1999) carried out steady-state simulations to study the design parameters of the porosity of high raised floor, width and inlet profile for improving airflow uniformity of air flow distribution in cleanrooms. They used STAR-CD CFD package to run 2-dimensional steady-state simulations using a symmetry boundary of L/2 = 2, 3, 4, 5 m and H = 3 m surrounded by a porous floor and walls of 1 m width. The reduction in the geometry had to be invoked in order to take into account the small openings in the porous floor. A grid size of 33,400 cells (roughly 260 × 130) used in the simulations, a linear under-relaxation approach was applied and a convergence criterion for the residual errors was set to 0.1%. For each case, this required 1,000 iterations to reach a converged solution, which took 1 hour of CPU time. The standard $k - \varepsilon$ turbulence model was used and the SIMPLE algorithm to link velocity and pressure of Patankar and Spalding (1972). The simulation gave adequate information to describe the uniformity of the flow with the parameters studied.

Convergence is significantly different between 2- and 3-dimensonal simulations for a similar geometry in the literature. The reason for that is more likely the non-linearities associated with 2-dimensional simulations. It appears that the higher the mesh resolution, the smaller the number of iterations. Before the 90s, the computing power was still very limited and 2-dimensional simulations with modified mixing coefficients, either C_μ or σ_t, adequately described the problem. However, 3-dimensional

simulations with only 800 iterations are now superseded and the effect of iteration number is an important parameter for the validity of the simulation. In the case of Chen and Chao (1997), the RSM performs well with a poor resolution due to the additional equations solved to describe the turbulent characteristics of the flow. This does not represent all sizes of turbulence scales associated with the flow. The eddy-viscosity models, however, still need mesh independence tests to obtain a good solution. A length-scale calculation was suggested. This is based on the Morton's (1959) length scale L_M that is the distance from the source of a forced plume where the buoyancy forces dominate the momentum forces. This is still rather large for a turbulent flow. Heiselberg *et al.* (1998) also mentioned that a 10-cm cell is not able to model turbulence accurately. Therefore, according to spectral studies in the literature (Chapter 2), a size of two times smaller could have been acceptable that has a dramatic effect on the additional number of cells added in the mesh system. For a coarse, 2-dimensional simulation, a mass balance may be easier to obtain but with a higher cost in accuracy.

It can be seen from the convergence windows of the current work that the residual errors for the symmetric model fall by three orders of magnitude in the initial 500-1,000 iterations. This is equivalent to a reduction of 3 orders of magnitude in the residual errors that is the apparent reason why so many researchers consider the simulations as converged below 1,000 iterations. The simulations can still satisfactorily describe the general physics of the flow, although not in great accuracy. However, for valid simulations to represent the physics of the interface properly, convergence needs to be achieved for mass balance in the entire domain with respect to the inflow quantities.

In the current work, the velocity component in the main direction was most difficult to converge. Although it was observed that the residuals were reduced by several orders, the absolute residual sum for each variable normalised by the inlet fluxes indicated loser convergence. Values closer to 10^{-3} were achieved for the simulations of the lowest Re used in the current work. A value of approximately 10^{-2} was achieved for the medium Re and an error value in the region of 10^{-1} to 10^{-2} for the cases of high Re, for which the increased mixing associated with time-dependencies introduce a small degree of instability in the solution that make it difficult to obtain accurate qualitative convergence for high Re cases and $Ri < 0.5$, Gerz *et al.* (1989). The error values of the other variables were very small, mainly because they are related to the velocity

variables which are the primary mechanism that drives the flow. Typical values achieved for k and ε were 10^{-4} and temperature 10^{-9}. A converged solution was achieved when the mass balance was achieved in the entire domain that converges in a FVM code.

3.6.4 The CFD modelling of turbulence and the significance of the interface

The $k-\varepsilon$ turbulence model has been used extensively for CFD modelling of turbulence with buoyant flows in buildings and geophysical fluids. A number of numerical studies of air flow in buildings using the $k-\varepsilon$ model have been reported recently in the literature, Murakami and Kato (1989) and Ohira *et al.* (2000). Lemaire (1993) Annex 20 reported that application of CFD on ventilation flows was initiated in Switzerland in 1987 to reduce the costs of experiment in the modelling of complex flows. Large Gr or Ra number may dominate in several parts of the flow field. The $k-\varepsilon$ model is the industry standard turbulence model for engineering calculations in modelling complex flows involving heat and contaminant transport, and sufficient validation already exists in the literature for certain flows. The eddy-viscosity concept using the $k-\varepsilon$ model and its variables provides a reliable and economical prediction for room airflows. In CFD simulations of room airflow involving temperature, the previous computational time and effort lead in too expensive to achieve completely converged solutions for all variables. The coupled solution approach as opposed to the SIMPLE solver has corrected convergence problems with steady-state simulations, Liddament (1996b). It was believed that this occurs due to physical low frequency oscillations exhibited in the flow that are instigated with increasing flow rate found in the current study. The practical use of CFD has been possible with coarse mesh systems, Gan and Awbi (1994). This is in contrast with the Low-Re $k-\varepsilon$ model, without any wall functions that requires a very fine grid close to the wall to improve results, Liddament (1998). Previous research on room air flows by Xue and Shu (1999) use the standard $k-\varepsilon$ model to successfully simulate room air mixing under turbulence flow and mixed convection currents. This is based on a comparative study made by Chen (1995) to compute indoor airflow using different $k-\varepsilon$ models and previous work on Reynolds-stress models (RSM). Although Reynolds-stress models are designed to predict re-circulation and turbulence intensities more efficiently than the standard $k-\varepsilon$ model, much computational time and effort is required to obtain very small accuracy. The difference between standard $k-\varepsilon$ model

and the RSM models is not too large in a comparison to the magnitude of turbulence quantities, Chen (1996). Previous work has not been reported so far on the thermal stratification of buildings using the $k-\varepsilon$ model. Existing CFD simulations of thermal stratification are mainly concentrated in the research of thermal storage tanks. Shin *et al.* (2004) carried out both numerical and experiential studies with the standard $k-\varepsilon$ model and the RNG $k-\varepsilon$ model for a full-scale liquid thermal storage tank and found that the standard model gave good results with a slightly more diffused interface while the RNG predicted a slightly sharper interface. Cook and Lomas (1998) also used the same two eddy-viscosity models to simulate displacement ventilation flows. Both models gave good qualitative predictions. The RNG $k-\varepsilon$ model was preferred to the standard model because it predicted a narrower interface and better entrainment coefficient into the plume, although the interface was displaced slightly further away. The modified gravity predictions and the height of the interface are slightly closer for the theoretical and experimental results obtained from literature. The discrepancies due to the deviations of the model are attributed to the 2-dimensional symmetrical slice model of the simulations and to the analytical calculations where the discharge coefficient of the upper opening was not considered. The interface height was slightly over-predicted by the RNG model because it predicted a narrower plume due to the smaller entrainment coefficient.

The results of Chen and Chao (1997) using a relatively coarse grid highlight the importance of modelling turbulence accurately. However, it can be argued that the velocity circulation obtained by Chen and Chao (1997) using eddy-viscosity models with a higher $C_{\varepsilon 3}$ coefficient is predicted larger because of the poor grid resolution and the application of the boundary conditions. Although the amount of the experimental data points was not large enough to make a detail comparison with the CFD curves, the mean gradient could still be observed. The average quantities are in a good agreement. The RNG turbulence model performed better than the standard and a modified model. The deviation of the eddy-viscosity models was attributed to the poor experimental results and the flow anisotropy. However, by looking at the graphs in the same paper and taking into account the CFD work by Malin and Younis (1990), Chen (1995) and Chen (1996) as well as the cited experimental work, it can be concluded that flow anisotropy inside the plume is not that strong and it can be even less in the rest of the room. The flow anisotropy is instigated at high momentum to buoyancy ratios in the

near field of the source that was previously suggested in the literature that these flows will follow very closely the -5/3 Kolmogorov law which is derived for isotropic turbulence. Alternatively, a similar effect is observed when a contaminant is released in a temperature-stratified flow resulting to anisotropic eddies being detached from the mean flow. Therefore, the flow in the room away from the source is not likely to exhibit effects due to anisotropy.

The advantage of CFD is that it enables architects and civil engineers the ability to develop an understanding of the ventilation systems they are designing without the need to build expensive experimental models to carry out tests, while minor experimental work can benefit the calibration and validation of the CFD studies. The scale reduction may also reflect on the physics that are described by a scaling method and hence affect the accuracy of the results. More information can be extracted from a CFD investigation that is also cheaper. Additionally, CFD predictions can help in designing the experiments of the full-scale model to further decrease costs, hence experimental equipment of a relatively good accuracy could be used and log a selective number cases to cover only a discrete range of study. One of the weaknesses of CFD is that often validation needs to be made with existing or *in situ* experimental data. Additionally, the latest improvements in computing power have made CFD a more valid tool. This has been given the required consideration here by comparing the current CFD results with the current experimental work carried out in the Environmental Test Chamber.

3.7 Scope of the work

It is suggested in the literature that convergence may not be obtained without buoyancy extension, Dagestad (1991). This implies that all the simulations should be carried out with the G_B term that is included in both k- and ε-equations which are coupled with the momentum and energy equations. However, it has been suggested that the interface thickness is predicted much thicker than expected with $k-\varepsilon$ models that include the buoyancy extension. In the review of Rodi (1987), it seems that the buoyancy extension makes stratification sharper for 2-dimensional simulations of geophysical flows and it is used in order to achieve an improved agreement with experimental measurements. The RNG model has obtained better predictions compared to the standard model for 2-

dimensional liquid cases, Cook and Lomas (1998) and Shin *et al.* (2004). Although the standard $k-\varepsilon$ model may predict the interface slightly larger, it is only with negligible difference to the other models and the experiments, and it seems to be due to the inlet conditions affecting stratification. For example when the action of one of the inlet sources is larger than the other, as in the case of strong penetrative convection by Fischer *et al.* (1979).

It was concluded by Dagestad (1991) that for a stably stratified shear layer the simulations should be run with buoyancy extended Low-Re $k-\varepsilon$ model. But for unstably-stratified flows, the standard $k-\varepsilon$ was suggested. However, it is not clear whether it is due to the overdiffusive nature of the $k-\varepsilon$ model that the vertical thickness of the interface is predicted much larger than expected, or because the boundary conditions are often not well applied.

Nielsen (1992) obtained a good agreement with experimental measurements by applying the boundary conditions at a box around the inlet. The scale of the inlets are very small with respect to the overall dimensions of the room and the effective area is rather smaller than the gross (core) area of the diffuser. Therefore, the flow rate should be applied in CFD for the area obtained at the measurement distance of the inlet conditions in the experiment. The velocity should closely match the actual experimental model to predict accurately what is happening in reality. The interface is predicted much larger when the boundary conditions such as heat losses are not specified. The infiltration flow seems to be the cause of a separation level in an industrial building by Shilkrot (1993). Air leakage rates are very likely to exist in every building such as pressure differentials across window openings or cracks in the building fabric studies by Jensen (1986), which result to natural ventilation and should also be modelled. Jones and Whittle (1992) suggested that conduction heat loss and air infiltration are important in the CFD modelling because of the influence of the outside air temperature to the atmosphere inside the building. It has been proposed that radiation is an important mechanism of heat transfer that occurs between the surfaces of the building and should be modelled. This mainly occurs due to the influence of outside air temperature on the inner surfaces of the building walls that affect the U-value as it has been mentioned by Jones and Whittle (1992), modelled numerically by Li *et al.* (1993a), studied

experimentally by Li *et al.* (1993b), and observed using thermography by Heiselberg *et al.* (1998). This is the subject of the next chapters.

Awbi (1998) solves for the convective heat transfer coefficients close to room surfaces and had revealed a very small grid size that is still not entirely detainable for 3-dimensional simulations to maintain the proposed accuracy. This is when using the Low-*Re* modification to obtain a quantitative as well as qualitative prediction instead of the less intensive quantitative equivalent that is using wall functions. These problems still pose a challenge in ventilation modelling and influence the interior stratification as well as mesh size.

The physics observed in the experiments could be well reproduced in 3-dimensional simulations by all eddy-viscosity models such as the interface, and the mean temperature and velocity fields. The velocity vectors from the jets do not point directly towards the exhaust, and Int-Hout and Kloostra (1999) pointed out that unidirectional velocity does not occur in real world. This validates the current CFD observations that are also in accordance with experimental results and jet theory. The extract flow field interacts with the mean flow and it is usually measured at a distance of a standard velocity of 0.25 m/s or higher. However the shape of the extract flow field studied by Skistad (1994) is affected by stratification and visa versa. CFD can capture these flow details with relatively good accuracy and for smaller magnitudes. By observation the current CFD results are well adopted with jet theory, such as the entrainment mechanism and buoyant flow, and there is evidence of circulation regions. The flow patterns affect by stratification and they are in accordance with the turbulence effects on stratification introduced by Linden (1980) and (1990).

In the current work, full-scale ventilation experiments are carried out to establish a basis of comparison for the corresponding CFD case in a real room, where heat transfer characteristics affect the indoor solution. To maintain some theoretical basis while reduce the complexity of the flow, these are put into the right context below,

(1) Ventilation flow is affected by stratification that is developed from the supply sources by building up an inlet temperature difference.

(2) Ventilation flow is affected by stratification that is broken up from the supply sources by the inlet momentum.

This is based on a hydraulics model and 3-dimensional eddy-viscosity turbulence models that do not consider strong anisotropy in the flow. Turbulence in stratified fluids consists of linear quasi-2-dimensional structures, Hopfinger (1987). The modelling of the extent of flow anisotropy in the near field of plane and round plumes by Malin and Younis (1990) showed that such effects are relatively small. In order to use those cases above, CFD was used to run sets of tests.

The scope of the present work is:

(i) To investigate the relative importance of the mechanisms identified for stratified ventilation.

(ii) To compare experimental and CFD results and to point out the critical modelling parameters when using CFD for ventilation studies including stratification.

4. Experimental Development and Design of CFD Model

4.1 Introduction

There are several parameters affecting ventilated rooms that sustain stratification. The most important parameters are:

- Momentum force
- Buoyancy force
- Viscous force

To control these parameters it is necessary to control mass flow rate of the hot and cold air as well as temperatures into the room.

CFD studies are generally less expensive to carry out and not limited by any experimental apparatus. However, CFD studies still need to be validated against experimental results and this is done when comparing against measurements obtained experimentally. An experimental model needs to be developed to reflect the real problem and tested in order to apply and adjust the boundary conditions of the CFD model. As a consequence, a virtual CFD model is built, which reflects the physics that are observed in the experimental model. This is done by closely matching the geometric characteristics and boundary conditions, and by comparing the results. In order to speed up the yield time of the simulations and reduce grid refinement close to the complicated geometries like inlet diffusers, it was then required to further reduce the complicated geometry of the virtual CFD model. An idealised geometry is easier to model in CFD and hence a simplified model is finally used to reflect approximately the same conditions and carry out further parametric tests. The approach of testing and developing the CFD model are summarised in the steps below,

- Carry out key experimental tests of the real problem by measurements.
- Run selected corresponding experimental cases with the virtual CFD model based on theoretical justification to establish a link with CFD and use the results to prove that CFD and measurements validate each other.
- Run a series of parametric tests with the idealised CFD model to cover the range of the problem.

The first series of tests comprise of simulations that present the numerical aspect of the problem. In all numerical investigations, convergence and mesh density form a necessary part of the requirements for carrying out the numerical validation. The variations in these series of simulations were performed using mainly the idealised geometry and it is summarised below,

1. Convergence
2. Mesh density
3. Turbulence model

4.1.1 Experimental apparatus

The experiments in this work were carried out by using the Environmental Test Chamber of the University of Hertfordshire. The experimental testing facility is currently one of the largest of its kind in the HVACR sector in the UK next to the Building Research Establishment (BRE) in Watford. Bearing a negligible heat transfer coefficient, U-value $= 0.2\ \mathrm{W/m^2 \cdot K}$, but $0.44\ \mathrm{W/m^2 \cdot K}$ when including the openings to the laboratory room outside the test room under investigation, the fabrication of the entire Test Chamber is generally similar to the construction of a Cold Room. The walls are 12.5-cm thick with white polyester outer finish and the interior is made of polyurethane foam. The Test Chamber has nominal dimensions of 7.5 × 5.6 × 3 m (L × W × H), a floor area of 42 m² and a room volume of 126 m³. The Test Chamber resides inside a laboratory room of dimensions of 10 × 6.5 × 7 m (L × W × H) with a polyurethane insulated pitched roof at an angle of $\theta \approx 22°$, a floor area of 65 m² (when not including the chamber area, this is approximately 20 m²) and the room volume is 390 m³. The roof of the Test Chamber is of the same material as the walls. There are six access panels of 0.6 × 0.6 m on the top wall of the chamber provide the necessary

openings for the inflow and outflow ducts that are fitted in for supplying and extracting air. When not used, these are properly sealed by leads of the same materials as the walls of the chamber. The floor is laid with 10-cm thick concrete and has a light grey colour finish. The concrete is insulated underneath by another 10-cm thick layer of Styrofoam (polystyrene) insulation panels. Two quadruple glazed windows properly sealed in the front wall provide the necessary openings for visual inspection in the chamber.

For the purpose of this work, the Test Chamber had to be reduced to a chamber of dimensions of a standard office room comparable to the size of office rooms tested by Palonen *et al.* (1991) 4.80 × 4.20 × 2.68 m and Fanger *et al.* (1988) 6 × 6 × 3 m. This was achieved by positioning a partitioning wall facade approximately 0.75L downstream from the front wall that introduced a small amount of leakage in the room. The supply air ducts need to be covered inside the chamber so that the flow is not obstructed and there is direct contribution between the ducts and the main region of the flow. A supported ceiling with standard tiles, which occupied a space of 0.6 × 0.6 m each on an aluminium support framework, were laid out at 0.5 m below the top wall of the chamber. There are 8 tiles in the longitudinal direction and 9 tiles in the lateral direction with two additional, less than half tiles, adjacent to the walls. The supported ceiling provides additional shielding from the inflow and outflow duct connections in the access panels. This created a larger area of undisturbed space, while it closely matched the actual characteristics of a real room. The supported ceiling reduced the interior height of the chamber down to approximately 2.5 m. To increase the efficiency of heating, while at the same time save energy and acquire better control on the heating characteristics of the room, the additional wall facade was made out of 5-cm thick Styrofoam panels reinforced by aluminium back-sheets bonded together on the external side of the partitioning wall. The Styrofoam panels have a thermal conductivity of $0.025\ \mathrm{W/m \cdot K}$. The additional wall facade reduced the interior length of the chamber down to 5 m. Thus the new Test Chamber was a room of dimensions of 5 × 5.6 × 2.5 m (L × W × H), a floor area of 28 m^2 and a room volume of 70 m^3.

The hot and cold air is provided by the two air-handling units. An air-handling unit (AHU), called AHU-1, outside the laboratory equipped with a split-system water chiller which can reach temperatures as low as 6°C. The AHU-1 is a 39FD 230 type outdoor unit is located outside the laboratory room. An auxiliary air-handling unit AHU-2 inside

the laboratory room equipped with an electric heater can reach the temperature of 40°C as a safety precaution for the blue foam insulation that has a maximum intermittent use of 75°C in accordance with the fire classification: BS 3837 Pt2 (1990). AHU-2 is located on the top of the Test Chamber, shown schematically in Figure 4.1 top left and right. By using cold air from the cooling system of the AHU-1 and hot air from the AHU-2, stable temperatures were achieved at the outlets of the diffusers from approximately 10 to 30°C at floor and ceiling respectively. The AHU-1 was used to provide only cold air to the chamber which is passed through an 8 row × 20 cooling coil located in the AHU-1 duct behind a CP-9/9 (240/240) centrifugal forward-curved double-inlet type fan that can deliver a maximum static pressure of approximately 550 Pa. The cooling coil is connected to the water chiller 38AQS012 split-heat pump system. The flow rate by using the manufacturer's fan-pressure curve is 0.41 m^3/s. However, after the pressure losses in the air supply ductwork system, the measured velocity at the end of the duct is equal to 9.1 m/s (12.5 m/s before calibration) which yields a flow rate is 0.16 m^3/s. The AHU-2 has a T-HLZ radial backward curved double inlet type fan enclosed in a box cabinet. The outlet of the AHU-2 is equipped with an electric heater at the end of a 1.5-m total length of 30-cm diffuser and supply-duct plenum that can deliver a maximum static pressure of approximately 500 Pa. By using the manufacturer's fan-pressure curve, the flow rate is 0.36 m^3/s. However, after the pressure losses in the supply air ductwork system, the measured velocity at the end of the duct is equal to 10.55 m/s (14.55 m/s before calibration) and the equivalent flow rate is 0.186 m^3/s. Thus the maximum flow rate in the chamber is 0.35 m^3/s. The heating element in the AHU-2 is attached to a control circuit connected to a revolving switch that is used to increase the hot air volume into the chamber by varying the air speed. Controlled temperatures were maintained to within ±0.3°C for cold air and ±0.2°C for hot air. The air is conveyed to the chamber by extension leads made of PVC flexible duct approximately 5 and 6-m length, for hot and cold air, and 0.15-m diameter. The extract duct is 0.11-m diameter and insulated with 2.5-cm thick fibre-glass wool to minimise conduction losses and a 90° PVC bent as an outlet opening. Taking into consideration the insulation of the supply duct connections at the access panels, additional 5-cm thick Styrofoam panels were cut to fit the shape of the inflow and extract ducts and the interior square shape of the access panels. Styrofoam was also used for the flanges and the inlet ring resined together to form the inlet shape of the ceiling air-diffuser that was then connected to the supply duct by duct tape. All other

connections are also duct taped. The hot air was supplied from a standard 4-way louvred-face ceiling air diffuser, shown in Figure 4.2 top right. The cold air supply terminal was a flat-faced low velocity floor unit (AFQ) manufacturer by Gilberts (1999), which is a common wedge-type diffuser with a medium face perforation manufactured by Halton (1998), shown in Figure 4.2 lower left. A minimum speed could be achieved of around $U_S \approx 0.1$ m/s by using the diffusers.

4.1.2 Practical considerations

In an attempt to obtain a fundamental smooth pattern of stratification throughout the test room of the Test Chamber as found in displacement and natural ventilation, the space in the middle had to be clear of any additional source differentials to allow enough space for the flow to become stably stratified and thus reduce the complexity of the measurements. The immediate area to the air supplies is also affected by the flow pattern of the emerging jets. For that reason, it was more practical to position the supply sources away from the middle of the medium to allow for the momentum of the jets to diffuse in the available space of the room. Looking into this matter from the application side, the supplies are often positioned away from the middle of the room where normally occupants are present, because this can lead to discomfort. Also for convenience, but for the temperature measurements too, that should not be affected directly by the jet flow of the air-supplies if these are to be carried out in the middle of the room. The location of inlet and outlet ducts and equipment is also reported in ASHRAE (1996) Section 9.2 for obtaining the required temperature distribution in the room.

In this work both hot and cold air had to be provided at the same time as the relative sources producing thermal stratification across the height of the room so that the consequent effects on the ventilation system can be studied. Hot air in the room is usually provided from the top through a ceiling air diffuser. For air-conditioning large rooms, cold air is provided through a floor terminal usually located in one of the corners and this is also applied lately in office rooms. The hot air diffuser could not be located right at the wall for practical reasons, i.e., because of restrictions due to the diffuser casing and the smaller adjacent tiles to the walls, but it also had to be closely aligned with the cold air diffuser in front of the moving rails. Secondly, concerning the physical

characteristics studied, if it was possible to locate the diffuser right at the front wall, then the adjacent wall could have a larger influence on the flow field of the downward jet. Additionally, the hot air supply had to be located a certain distance away from the extract point to avoid short-circuiting, causing all the inflow to be discharged directly through the extract duct. The testing facility where the experiments were carried out including the experimental configuration and the existing apparatus in the room is shown in Figure 4.1,

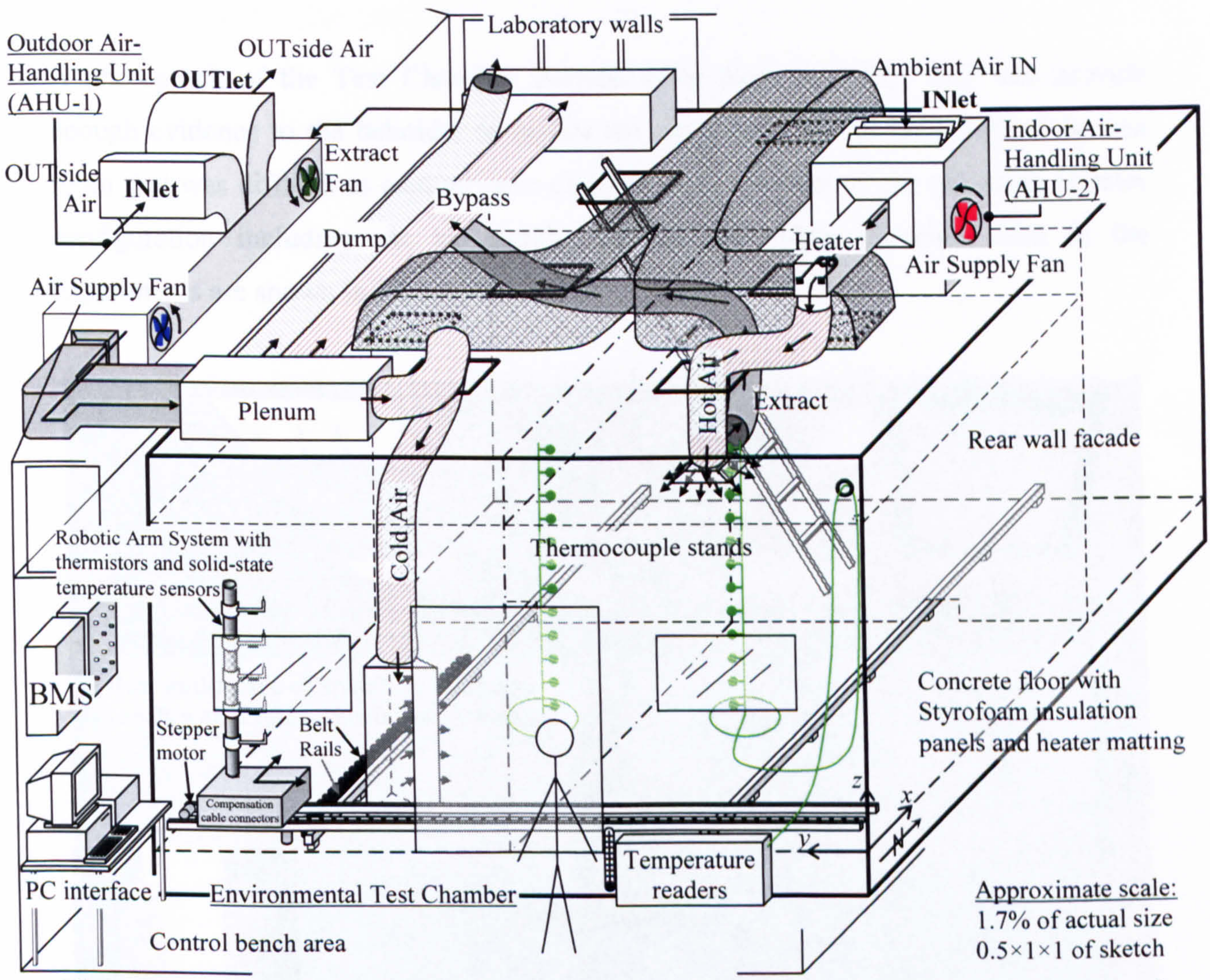

Figure 4.1: Schematical drawing of the complete testing facility including a condensed schematical representation of the experimental configuration of the reduced chamber and the air-supply system used in the experimental work. The ladder at the back of the rear wall facade is used for inspection of the external side of the wall and the external thermocouple, and another project running at the other side of the test room outside the operating hours of this project.

The horizontal shape in-between the rear access panels in Figure 4.1 in the back, behind the rear wall facade, is an extract outlet of a build-in supply-and-extract ductwork

system on the top of the chamber appropriately connected to the extract plenum of the AHU-1. This is not part of this work and it was shut during operation by an opposite blade valve operated above the top wall. There are also two inlets at the almost equivalent left and right locations between the pair of the front left and the pair of the front right access panels, but were also shut during operation with appropriate leads of the same materials as the walls of the chamber. The vertical rectangular shape in the middle is a structural end-plate with bolted steel cables extending up to the laboratory roof for reinforcing the top wall of the chamber when walked on for inspection.

A photograph of the Test Chamber interior taken from the front door can provide enough evidence to the beholder to realize the geometry and configuration of the test room that was difficult to capture on a single picture. Pictures of the test room interior configuration including the air supply devices and other materials used in the experiments are shown in Figure 4.2,

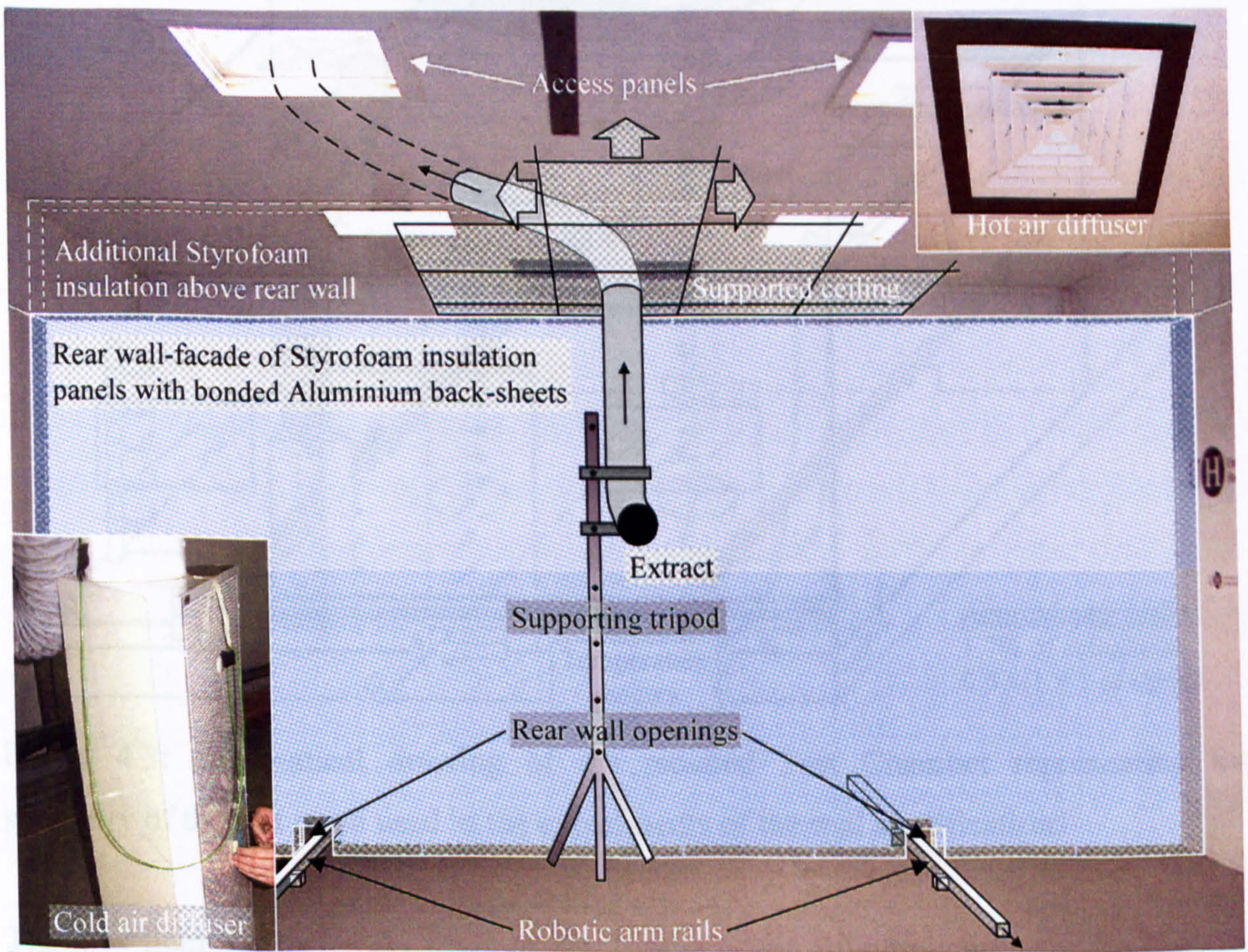

Figure 4.2: Pictures of the interior of the test room showing air supply diffusers, extract duct configuration, blue foam insulated panels of rear wall facade and wall openings.

Both diffusers were positioned closely to the middle plane of the chamber along the longitude. The stratification would not be affected if the near field of the discharge flow by the air supply devices extend at certain distance that is not obstructed by the existing experimental apparatus of the Test Chamber. One of the sides of the floor air diffuser was aligned at some small distance away of the side rail and the robotic arm so that there is minimal heat exchange between air supply device and the apparatus of the chamber. Although there is a gap between the stationary rails and the floor it was small and at certain boundary layer thicknesses, this would have obstructed the flow. Taking into consideration the aim of the experimental work and certain potentials and constraints, this led to the geometry of the test room that was later used as a basis for the idealised CFD model. The geometry of the test room is shown in Figure 4.3,

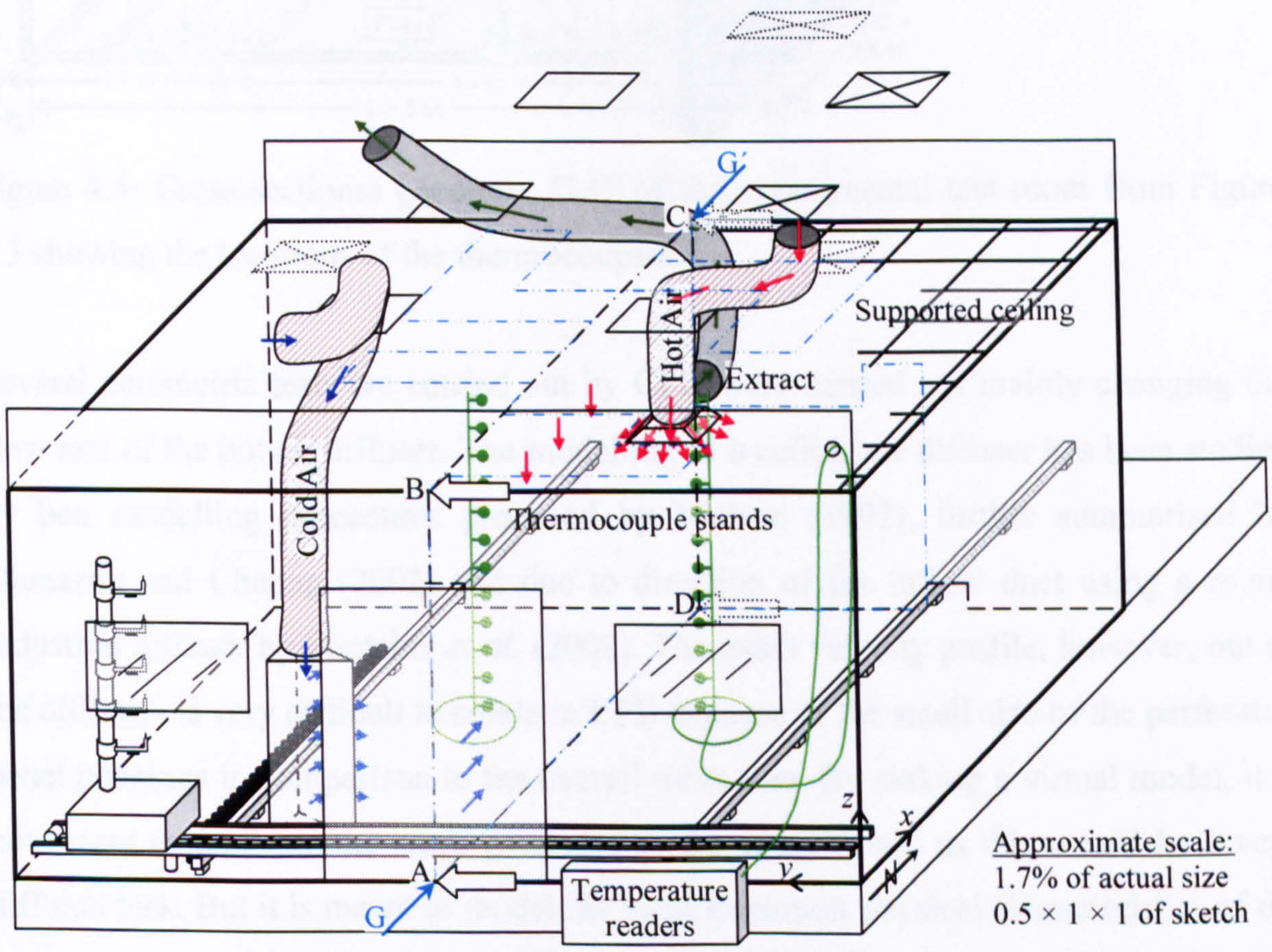

Figure 4.3: Schematical drawing of the reduced Test Chamber representing the geometry of the test room used in the experiments of thermal stratification.

The flow field is affected at certain distance away of the air-supply outlet of the floor air diffuser and therefore the measurement locations should be displaced when comparing the experimental results with the CFD results of the idealised model. The axial distance of the displacement jet flow can be obtained from tables given by the manufacturer of the floor terminal. However, this information is not available for the ceiling air diffuser

and therefore several thermocouples were located in the middle area below the ceiling to obtain an idea of the initial temperature field of the hot air jet. The measurement locations in the experimental model are shown in Figure 4.4,

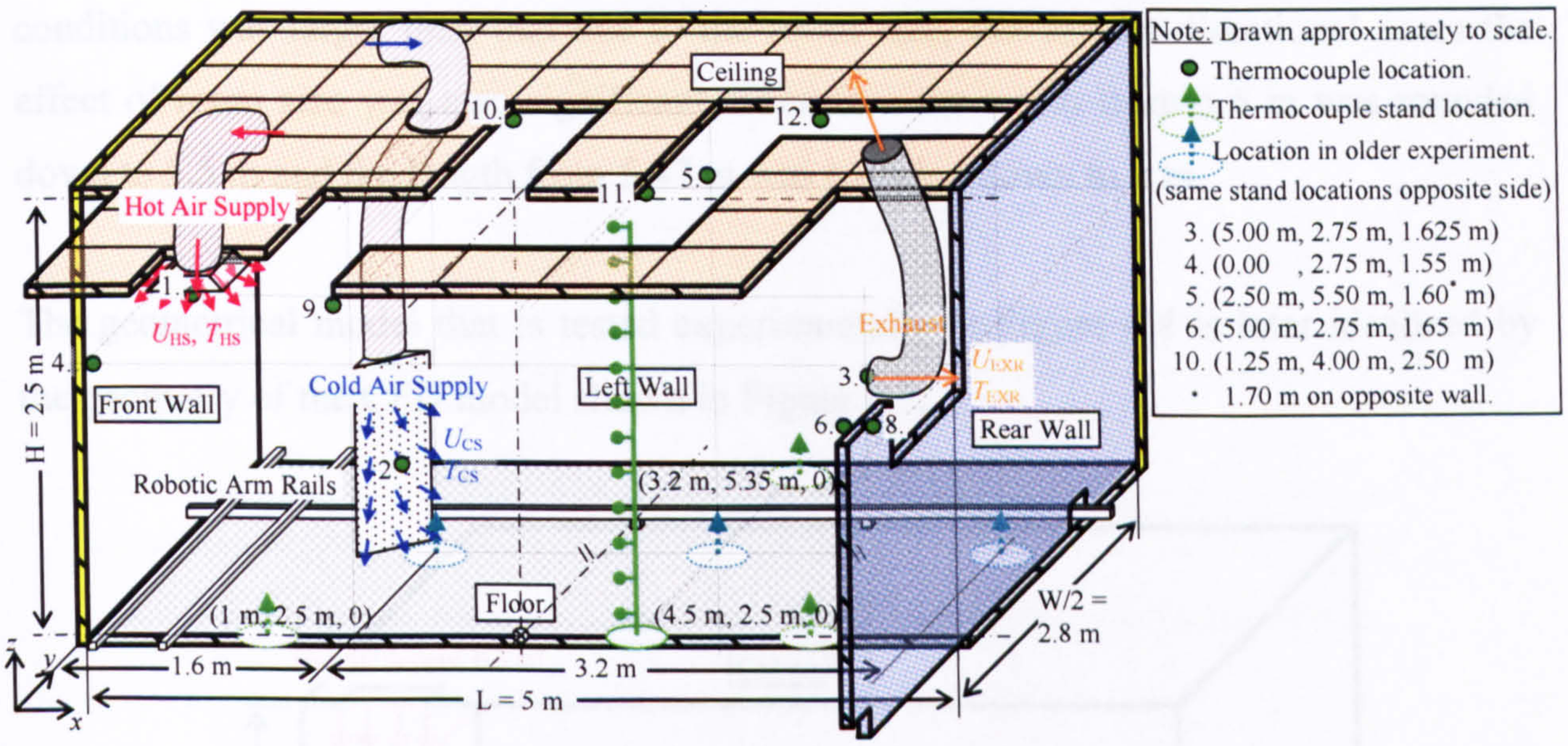

Figure 4.4: Cross-sectional geometry G-G' of the experimental test room from Figure 4.3 showing the locations of the thermocouples.

Several parametric tests are carried out by CFD were carried out mainly changing the flow rate of the hot air diffuser. The modelling of a ceiling air diffuser has been studied by box modelling procedures proposed by Nielsen (1992), further summarised by Djunaedy and Cheong (2002) and due to direction of the inflow duct using a round industrial diffuser by Fontaine *et al.* (2001). The exact velocity profile, however, out of the diffusers is very difficult to create in CFD because of the small size of the perforated panel openings in comparison to the overall room size. By making a virtual model, it is not meant to replicate the same geometry to the exact detail, as this would be a very difficult task. But it is meant to model the most important physical characteristics of the flow geometries that are likely to affect the interior stratification as in the real case. For simulating a perforated panel floor air diffuser the reader is referred to Cehlin and Moshfegh (2002). The intention here is also to reduce the total number of cells and consequently trim down simulation time due to the complexity of the parametric tests pertaining to the development of the model studied. As a complementary task to obtain good validation with the CFD investigation, it was suggested by the supervisory team to marginally reduce the dimensions of the CFD model because of the equipment space. Further simulations where then run to show how much the reduction in length could

have affected the results. Tests were carried out by CFD for two room sizes, by dividing in each case first the width and then the length of the room by a factor of two. Additionally this was also tested by either using the directional ceiling air diffuser or the downward jet for constant cold air supply flow rate. The difference due to the boundary conditions was larger than that due to the room size, but for the directional cases the effect of room size was also significant. Therefore the width from 5.6 m was rounded down to 5.5 m and the length from 5.47 m was rounded down to 5 m.

The geometrical model that is tested experimentally in Figure 4.4 is later idealised by the geometry of the CFD model shown in Figure 4.5,

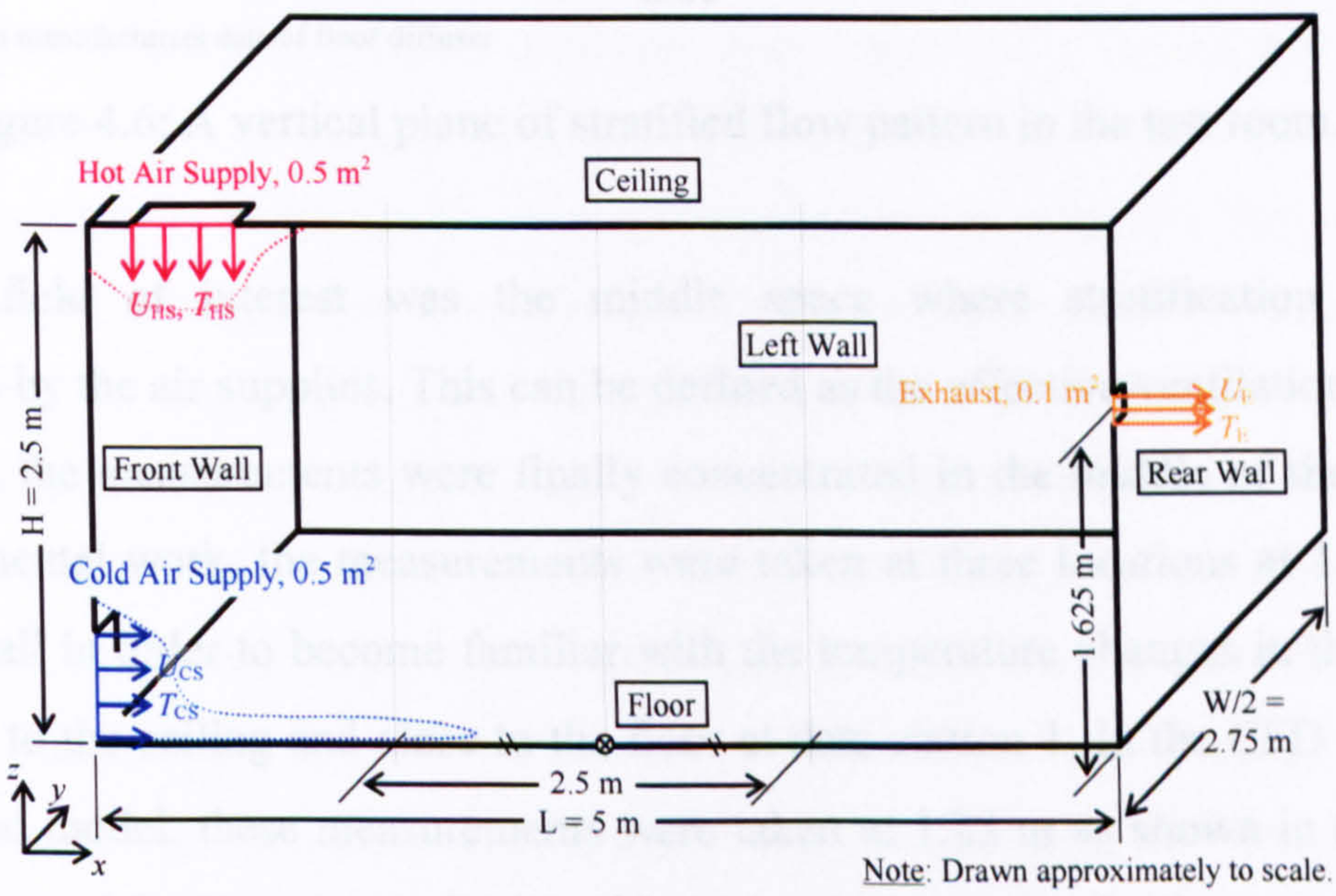

Figure 4.5: Idealised cross-sectional geometry ABCD of the test room from Figure 4.3 and equivalent measurement locations, including initial inlet area and inlet conditions used in CFD.

By using this geometric layout, it was possible to observe the separation of the cold and hot air volumes by a temperature-interface, which occurred in the entire room. The layer system studied in the current work can be presented diagrammatically in a cross-sectional plane as shown in Figure 4.6,

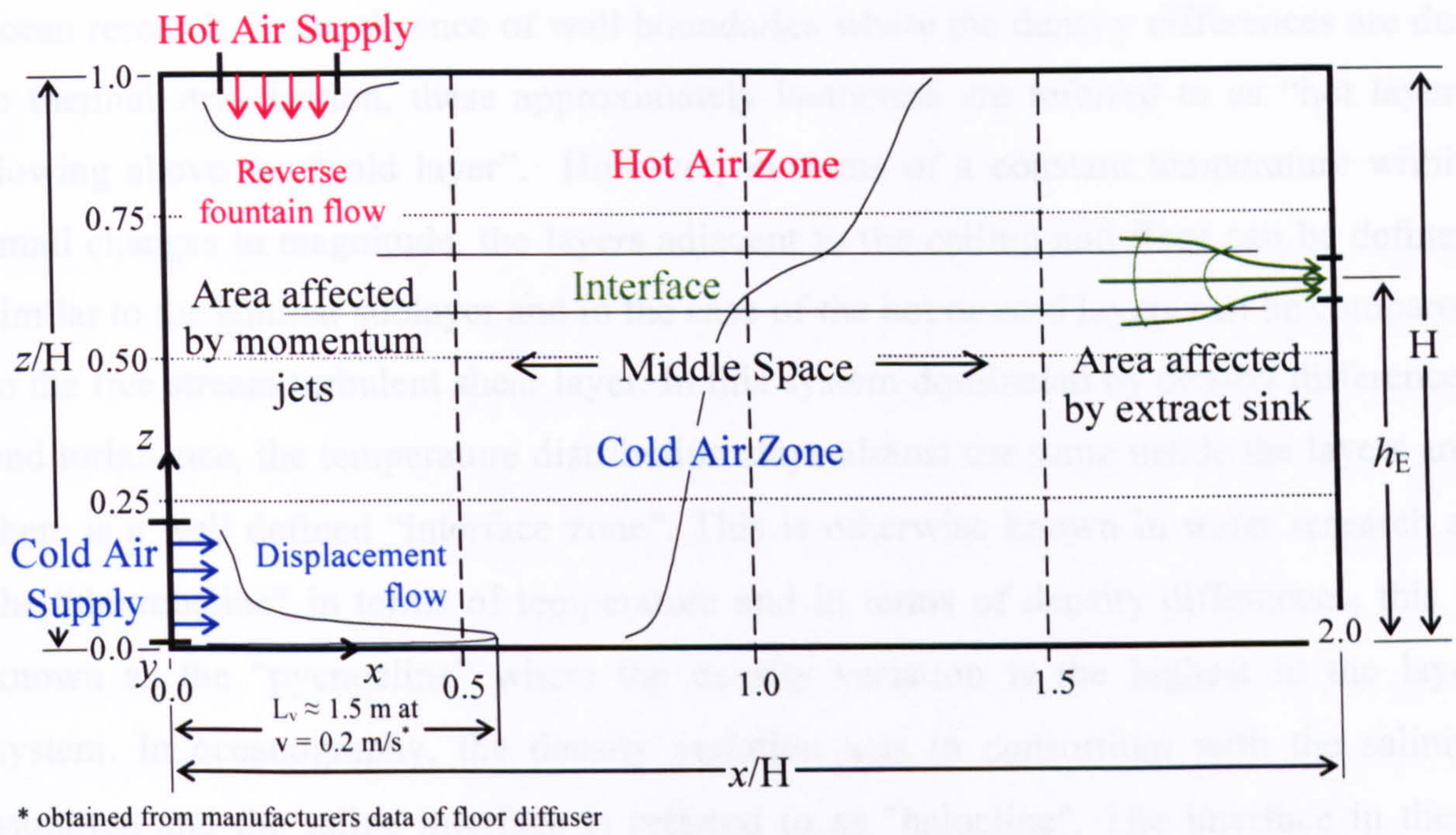

Figure 4.6: A vertical plane of stratified flow pattern in the test room.

The flow field of interest was the middle space where stratification prevailed undisturbed by the air supplies. This can be defined as the effective ventilation area. For that reason, the measurements were finally concentrated in the middle of the room. In the experimental work, the measurements were taken at three locations at 1.6 m from the front wall in order to become familiar with the temperature changes in the affected areas close to the ceiling and close to the floor at data-station 1. In the CFD work with the idealised model, these measurements were taken at 1.25 m as shown in the middle plane in Figure 4.6 where the similarity with the temperature distribution was observed.

There has not been a clear definition in the literature of the ventilation of buildings for the "zones" or "layers" occurring with thermal stratification. The term "zone" is preferred in buildings. The "hot air zone" may be defined as the volume of air that extends from the ceiling down to the point where the changes in the temperature distribution become much larger than the changes inside the zone and it consists of a stuck of horizontal isothermal layers of infinitesimally smaller thickness of mainly hot (and stale) air. Similarly, the "cold air zone" is the volume of air extending for the floor up to the point where changes in the temperature distribution become larger than inside this zone and is usually supplied with the ambient air from the outside. This is otherwise known as the "cool air zone" of surrounding air that is pleasant to breathe and at the required room temperature. The hereafter hot and cold air zones can be compared to the boundary layer away from a wall, the wall shear layer. In hydraulic engineering and

ocean research, in the absence of wall boundaries where the density differences are due to thermal stratification, these approximately isotherms are referred to as "hot layer" flowing above the "cold layer". However, in terms of a constant temperature within small changes in magnitude, the layers adjacent to the ceiling and floor can be defined similar to the laminar sublayer and in the case of the hot or cold layers can be compared to the free stream turbulent shear layer. In this system dominated by density differences and turbulence, the temperature distribution stays almost the same inside the layers and there is a well defined "interface zone". This is otherwise known in water research as the "thermocline" in terms of temperature and in terms of density differences, this is known as the "pycnocline" where the density variation is the highest in the layer system. In oceanography, the density variation acts in consortium with the salinity variation and the saline interface is referred to as "halocline". The interface in these liquids is usually very sharp and the flow is different above and below the separation. This is important in buildings because of the similarities with stratified ventilation systems. Layers of negligible thickness have the constant horizontal temperature in common with the larger layers. The interface zone is packed with layers of infinitely small thicknesses with an "interfacial layer" in the middle for monotonic stratification. This is different to an immiscible fluid at rest which undergoes almost no diffusion between the liquids and results to step-like stratification. The interface zone will be referred to here as the "interface". The interface is similar to the mixing layer in a free shear layer with the resulting shear profiles combined above and below with an interfacial layer in-between, where the diffusion taken place is mainly due to turbulent activity between the two main layers. The layer system is easier to understand by looking at the summary Table 4.1,

Hot Air Zone	Radiation/conduction layer Laminar sublayer Hot Air Layer
Interface Zone (Interface)	Interface Layer Interfacial layer (isothermal)
Cold Air Zone	Cold Air Layer Laminar sublayer Radiation/conduction layer

Table 4.1: Stratified layer system of air zones and infinitesimal isothermal layers. NB. The laminar sublayer includes a conduction-radiation layer, and hot and cold air layers may either be isothermal or include infinitesimal isothermal layers on a small temperature gradient.

4.1.3 Instrumentation

Temperature measurements inside the Test Chamber were made by 36 thermocouples type K. All thermocouples were numbered appropriately. The measurements were taken by two sets of 12 thermocouples[1] placed initially on a pair of supporting stands. The two sets of thermocouples were attached to a pair of Digitron 2751-K bench-type units. To monitor the temperatures at the walls, diffuser outlets and exhaust, another set of 12 thermocouples was used, attached to a Digitron 3750-K box-type unit. The cross section G-G' of the test room from Figure 4.3 is drawn separately in Figure 4.4 to show the location of the thermocouples. The nominal accuracy (tolerances) of the entire measuring circuit is much lower compared to that suggested by calibration standards, ASMT (1993) and recent literature of sensor manufacturers Labfacility Ltd. (1996), TC Ltd. (1999). This includes wiring errors (thermocouple wire, compensation cable with connectors), unit boxes and connectors, and circuit which adds up to ±5°C. The calibration tests of this work suggested an error value of approximately ±0.2°C against a Platinum Resistance Thermometer (PRT) probe with specifications of 3 mm diameter, 100 mm length and 25 mm sensing length with 15 mm minimum immersion length. Wire-wound mineral insulated stainless steel sheath Pt100 Class B sensor has a tolerance of ±0.4°C at room temperatures to IEC 751 and the accuracy of this sensor is ±0.06°C at 0°C. This has a temperature range between -50 to 250°C and manufactured to BS 1904, Class B 1984 (DIN43760). It was found that the response time of the PRT probe occasionally contributed an aliasing error of ±0.1°C at stabilising conditions. However, typical response times found on the Internet for this probe are from 50 s to a little over than 1 min for the probe to achieve the accuracy of up to 63% of the process temperature. The main disadvantage of the PRT sensors against thermocouples is response time and cost, yet the classical Pt100 probe has a smaller tolerance than thermocouples and therefore this type of sensor possesses higher reliability. The accuracy was tested by comparison between temperature values obtained from different calibration tests, values compared against different thermocouples at the same heights with stratification from the two sets of thermocouple sensors, wall thermocouples and different instruments, and repeated tests and measurements. The accuracy of the thermocouples obtained in this work is ±0.1°C, which is a typical accuracy for room

[1] This is the maximum number of thermocouples that each of the thermocouple readers can handle.

temperature measurements. The experimental accuracy varied between the cases of the low volumetric flow rates in the range of ±0.2°C and the high volumetric flow rates in the range of approximately ±0.5°C. This is shown in Figure 4.7 and Figure 4.8 below,

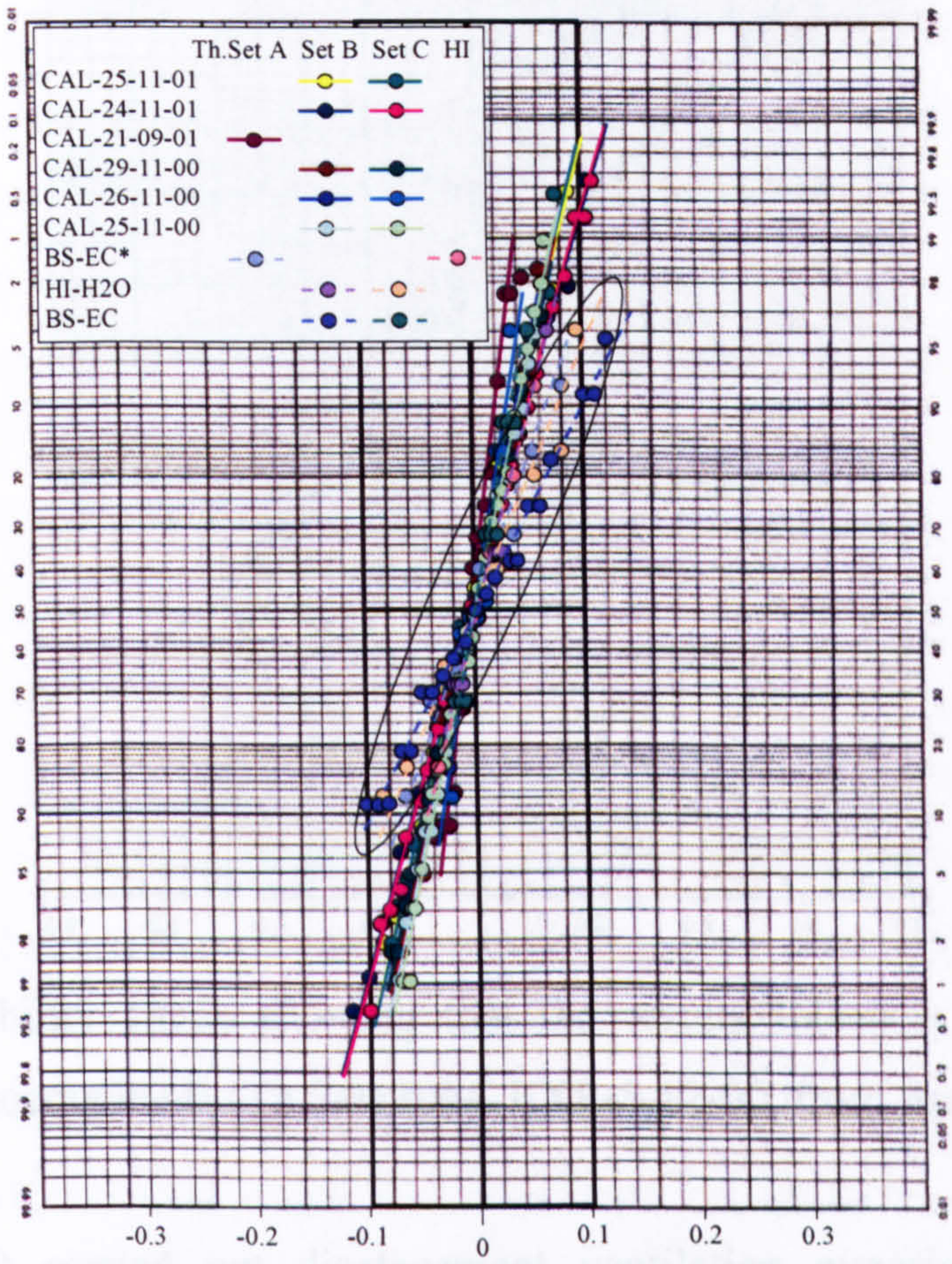

Figure 4.7: Probability check showing that the results follow a normal probability distribution; thermocouple set (Th.Set) A, B, C and HI temperature reader. *One calibration test for Th.Set A is shown here which corresponds to the worse case scenario and results from four individual tests are included for the HI instrument.

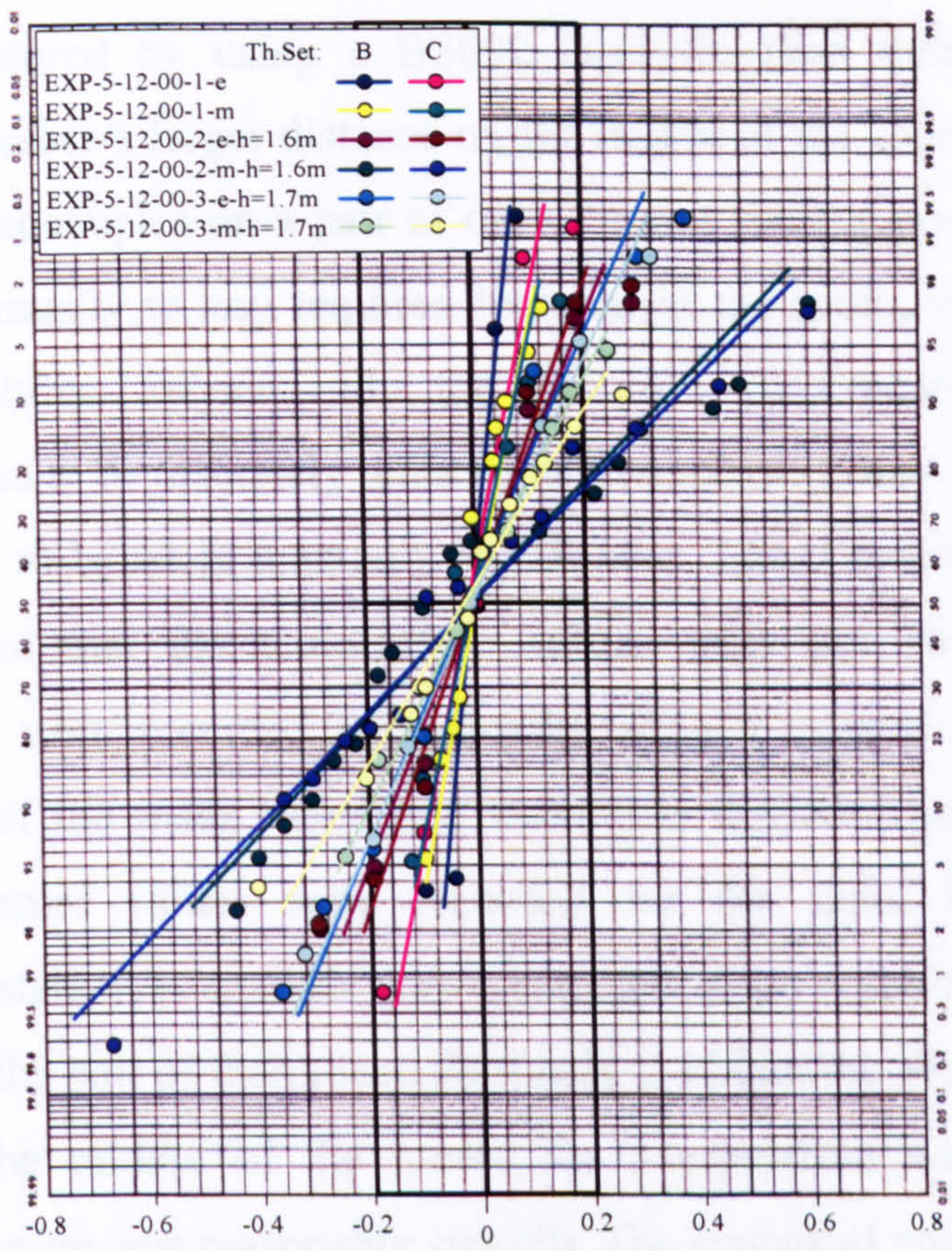

Figure 4.8: Probability check showing that the results follow a normal probability distribution; thermocouple set (Th.Set) B&C EXP-5-12-00, from Appendix B.

Li *et al.* (1993b) carried out displacement ventilation experiments with thermal radiation effects. They mentioned temperature fluctuations of less than 1°C in both their studies using thermocouples type T calibrated to ±0.1°C. A time period of 12 hours was endured for the thermal radiation cases to ensure stable conditions intended for accurate measurements. They included velocity measurements below 0.1 m/s for comparison, although these velocities could not be measured very accurately. The accuracy of both hot wire anemometer and Laser Doppler Anemometer (LDA) are 0.1-0.2% under controlled experimental conditions suggested in Bruun (1995). However, a general accuracy of 0.1 m/s is more realistic that has been suggested by many manufacturers for the normal conditions and temperatures of operation, given as 1% of accuracy. Chen and Chao (1997) also included velocity measurements less than 0.1 m/s, although measurements below this accuracy may be regarded as unreliable and the equipment specifications may suggest a lower value. The same value was obtained for the maximum temperature difference in the cases of the high volumetric flow rates between the stands, approximately 1°C, consistent also with the water experiments carried out by Nelson *et al.* (1999). The reference temperature in the laboratory room outside the Test

Chamber was monitored by using a BS692 liquid-in-glass thermometer. A larger number of sensors across a larger distance on the height of the room could be achieved by positioning thermocouples on a pair of only 20-mm thick supporting stands, which could be moved manually to any required location in the room, while every time the flow was left to stabilise. Subsequently, the amount of data recorded during hours of experiential work had to be discretely reduced in advance by observation because all the measurements were to be taken manually for all tests. Initial measurements of thermal stratification showed that the temperature values were periodical. Therefore, any temperature values were recorded strategically using a manual tactic to obtain the average deviation of the mean value and maximum deviation at specified intervals. Additional temperature values were recorded for the same location only when necessary. Further statistical analysis was conducted when combined the values at the same heights from the pair of thermocouple stands to obtain the average temperature for these heights in the middle of the room. No interpolation was needed since the temperature distribution was reasonably smooth. The statistical analysis was carried out using BS 2846-2:1981 and obtained a confidence level of experimental accuracy per experimental case approximately in the range of 90-95% depending on the inlet flow rate and stratified conditions. This was considered to be adequate for this type of measurements. A datalogger was used only when necessary. An HP 34970A data acquisition unit with a single effective channel of ±0.06°C reading accuracy when attached to a resistance thermometer was used with PRT probe, at 0.55 m from the floor to check and validate the measurements obtained from the thermocouples at the same heights, while carrying out some of the experiments. The temperature values obtained from the PRT of the datalogger or the thermocouples of the temperature readers using the tactic described above, were found to be the same within the range of experimental accuracy as shown in Figure 4.9,

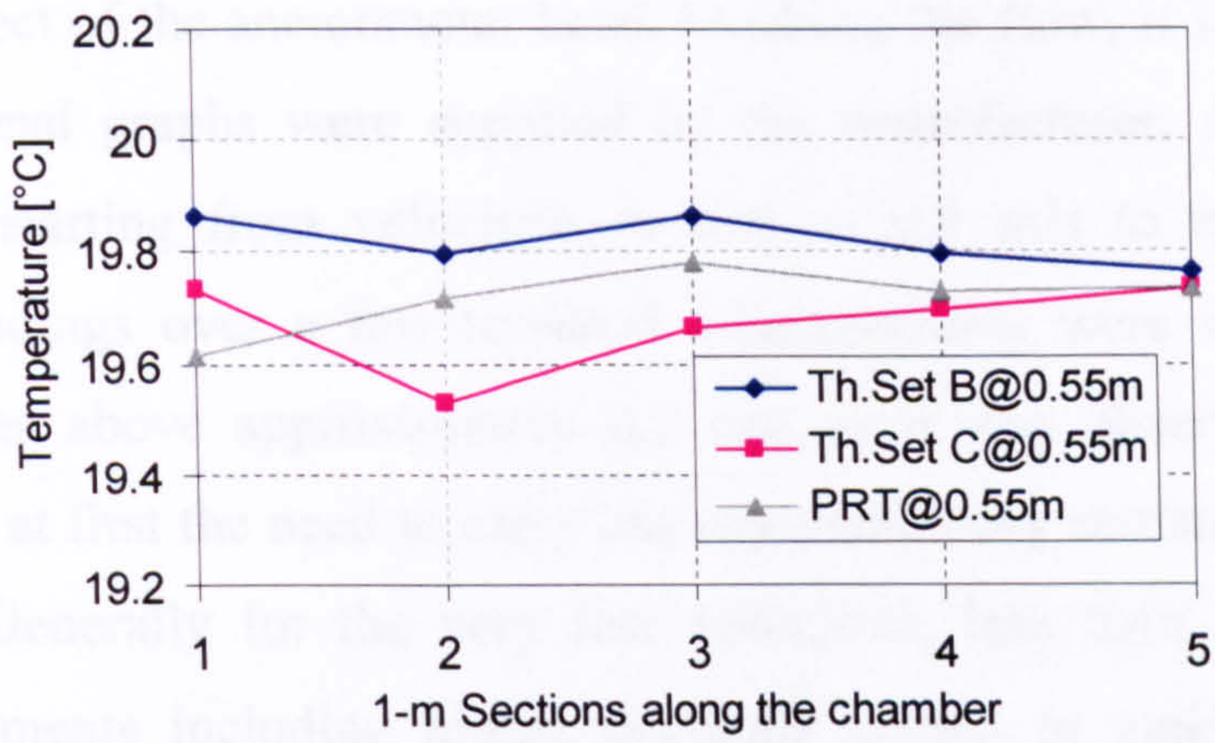

Figure 4.9: Values of thermocouple sets (Th.Sets) B and C compared to values obtained from a PRT at the same height, obtained from an experimental case without diffusers.

In the experimental case shown in Figure 4.9 there are no diffusers, the cold air supply is positioned on the floor closer to the hot air supply and the sections are taken on the diagonal starting from the location of the air supplies to the location of the extract. The thermocouple stands in this case were located at 0.8 m off the diagonal and thermal stratification was observed by making a contour plot from the temperature values (Appendix B). The large difference when closer to the air supplies, i.e., in the initial two or three sections, is because of the downward jet flow from the hot air supply (section-1) and cold air supply (section-2) had slightly affected the temperature magnitude obtained from the thermocouples located on the same heights on the two stands, and the different position of the PRT probe, which is approximately 1.5 m from the front and the right wall of the room.

The same datalogger and PRT robe were also used during the calibration procedure of the thermocouples to obtain high accuracy as suggested by ASMT (1993) and other literature.

Velocity measurements were taken at the duct outlets and at the face of the diffusers by a 100-mm head LCA 6000 hand-held rotary-vane anemometer of manufactured by Airflow, approved to BS EN ISO 9001. Experimental accuracy is attained by a statistical program incorporated in the anemometer that is activated when pressing and holding the press-down button in the handle, which takes the average value over a period of 3 seconds. The anemometer has an error of better than ±2% of reading for velocities above 5 m/s (up to 30 m/s) as prescribed in the user manual. However below this value, in the range of 0.25 m/s to 4.99 m/s, the percentage error increase due to

head blockage effect of the anemometer head, blocking the flow, is relatively high, i.e., ±0.1 m/s. Additional graphs were supplied by the manufacturer, Airflow (2001), to deduct the error starting from velocities as low as 0.1 m/s to maintain the given accuracy. The readings over a few repeated measurements were very consistent for indicated velocities above approximately 0.2 m/s as it was observed on the digital display ruling out at first the need to carry out any mandatory statistical analysis on the measurements. Generally for the very low velocities, less than 2 m/s, a series of repeated measurements including higher decimals helped in making more accurate calculations to deduct a proportionally larger percentage error increase.

Static pressure measurements were recorded by a low pressure electric manometer FCO10. The accuracy of the manometer is 1% of reading. During the experimental case without the diffusers at duct velocities of 2.8 m/s (Q = 0.05 m³/s), pressure differences in the range of 1-2 Pa between inside the Test Chamber and the laboratory room were recorded, consistent with CFD simulations. However, this was not in good agreement when the solar radiation was very strong that increased the difference between the inside of the test room and the laboratory room to 5 Pa. Pressurisation tests were also carried out to determine the leakage of the test room at low pressures. Although standards may suggest higher pressures for pressurisation tests, low pressure tests can determine different flow characteristics. The maximum attainable velocities on the Ø 0.15-m duct outlets were 10.55 m/s and 9.06 m/s respectively. The equivalent flow rates were 0.186 m³/s and 0.16 m³/s that give a total flow rate of 0.347 m³/s. Tests up to 8 Pa showed that there is a relatively loose air-tightness similar to that obtained in many industrial buildings by Brundrett (1997). However, the testing conditions are still good for the purpose of testing stratification as in real conditions. For this to be valid, air leakages are determined by CFD in Chapter 5. The air leakage tests of the test room are shown in Figure 4.10,

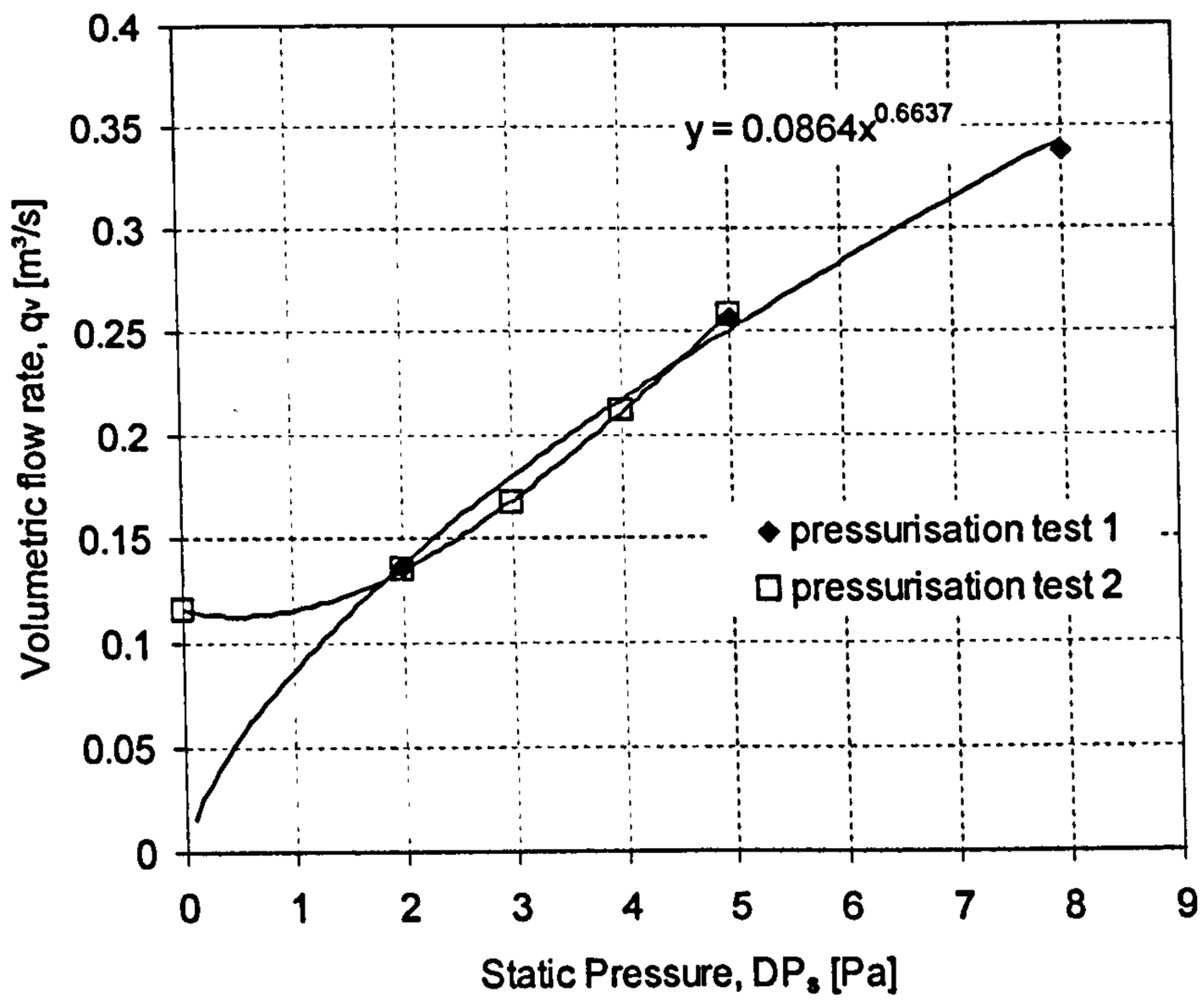

Figure 4.10: Experimental pressure-flow relationship.

4.1.4 Location of the experimental measurements

The thermocouples were concentrated in the initial set-up at 1.6 m. This is the usual height of the exhaust from the floor, i.e., the height of the average breathing zone. The purpose of the thermocouple stands was to check if the same temperature magnitude was obtained at the same height. At this experimental stage the measurements were taken at three midway locations that are denoted as vertical data-stations across the length of the middle space of the reduced chamber medium. However, the values between the two stands at the same heights and data-stations in the *y*-direction were too close to each other bearing a small difference in the range of the experimental error, i.e., ±0.5°C or less for the range of the experimental cases considered. Consequently, the average from the two stands was taken at the same data-stations and heights. Additionally, there was a very little difference in the temperature distributions obtained from the stands between data-stations along the length of the middle space in the *x*-direction. Therefore, it was realised that the same temperature-stratification was occurring across the height within a small fluctuating range ±0.5°C or less for the range of the experimental cases considered. After observing that similar temperature distributions were obtained across the test room, the temperature measurements were then concentrated at the centre of the test room to speed up the experimental procedure. The temperature gradients collected from other experimental cases showed similarity

with the ones obtained at other locations in the test room. The physics occurring across the height of the room could be better captured by including more thermocouples along the height of a single stand. Therefore, all 24 thermocouples from the pair of stands were placed on a single stand and the measurements were taken in the middle of the test room. Four other locations on the chamber walls at different heights: 1.55, 1.6, 1.65 and 1.7 m (front-, rear-, left- and right-wall) were also used in this case to check for similarity were the interface was mostly occurring, as shown in Figure 4.11 (and Appendix B). The rest of the thermocouples were located on the diffuser outlets, one on the extract inlet, one behind the rear wall, one in the middle below the supported ceiling and the final three thermocouples spread around the middle area of the supported ceiling to check the uniformity of the temperature distribution below the ceiling and the extent of convection. The location of the thermocouple stands in the test room during the experiments and the distances between the thermocouples, which were adopted in the final experimental cases, are shown in Figure 4.4. The middle space of the room was the area of interest where the temperature differences at the same heights were rather small.

Therefore, some of the measurements and CFD analysis were focused in the centre plane of the middle space of the room, as shown in Figure 4.5 and Figure 4.6. The temperature distribution in that plane showed all the important flow features that have been observed in the ventilation of buildings with reference to stratification. The temperature distributions obtained from the experimental cases were further combined together to demonstrate the influence of the inlet flow rates on the average temperature gradient and the equivalent heating characteristics of the room when compared with the thermocouples that were located at on the walls. Thus no additional experimental cases were required. These were also visualised from the CFD investigation that was carried out to analyse with a larger range of inlet parameters. First the different experimental cases were compared individually for each set of results and later combined together according to the inlet parameters to compare the experimental measurements in the middle of the room with the results obtained by CFD.

4.1.5 Accuracy of the experimental model

The presence of the walls can influence the temperature distribution in every building. Old dwellings, before the oil crisis in 1970, are built on a single block wall and have a

very poor *U*-value of around 2.3 W/m²·K. Awbi (1995) suggested that pre-1975 construction is likely to correspond to a *U*-value for the walls of about 1.6 W/m²·K and for the roof of about 2.6 W/m²·K. Cavity wall insulation has been carried out in homes built before 1976 that improved wall insulation by almost 40%. The 1976 change in the Building Regulations required a reduction in the *U*-value of walls from 1.7 W/m²·K to 1.0 W/m²·K to increase the energy efficiency of the property. New regulations show a very small increase in *U*-values since 1990 construction. The 1991 building regulations Part L: Conservation of Fuel and Power, HMSO (2000), require a minimum *U*-value for the wall construction of 0.6 W/m²·K. Cavity wall insulation was set as a standard requirement in 1997 regulations, to achieve a *U*-value of walls of 0.45 W/m²·K. In 2000, newer regulations set a limiting *U*-value of 0.35 W/m²·K as a standard practice for energy efficient buildings given by the latest Part L and 0.3 W/m²·K for the walls or less in some countries in the UK. For the roof and floor this is 0.25 W/m²·K, and for windows 2.2 W/m²·K that gives an area weighted average for a semi-detached house of 0.44-0.49 W/m²·K. Lecompte (1990) studied the heat transfer characteristics of the wall with 10 mm-void behind the insulation and 10-mm gaps above and below the insulation in a hot box to investigate the thermal resistance of the wall which is related to moisture damage. Natural convection occurs inside the cavity due to the temperature differential between the two gaps on the outer leaf occurred from voids in the insulation. The theoretical *U*-value of the test was 0.34 W/m²·K. The natural convection in the cavity resulted in a significant reduction of temperatures of the inner wall. The resulting *U*-value, after the gaps were applied, changed to 0.65 W/m²·K and that was estimated as 193% increase in heat transfer.

Shaw and Brown (1982) carried out a comparison of air infiltration on identical detached houses to evaluate the effect of the flow rates with and without chimney. In the house without chimney, the infiltration rate was 0.021 m³/s and in the house with chimney 0.032 m³/s. The pressure was induced by temperature from an electric heater and a furnace in each case respectively at $\Delta T = 28°C$, and achieved a maximum value of 5 and 6 Pa, ASHRAE (1993). Measurements in office buildings carried out by Brundrett (1997) also presented in CIBSE (2000b) TM 23 (fig. 11) show that 50% of the office buildings have a maximum air leakage index of 14 m³/h·m² at Q_{50}/A, while 50% of industrial buildings have a twice as high air leakage index. The surface area of the room is estimated as 107.5 m² and the leakage rate for this area using the 1/20 rule according

to CIBSE (2000b) TM 23 is 0.0209 m³/s due to infiltration. For a tight building classification at 50 Pa the air leakage index is 7 m³/h·m², using the 1/20 rule gives approximately 0.01 m³/s for the surface area in the current case. For a leaky building the leakage index is 35 m³/h·m² the leakage in this case is 0.052 m³/s. The air leakage can also be estimated for the case of residential buildings in the UK, using the data by Brundrett (1997) which is 4.5 m³/h·m² at 25 Pa and by dividing by 10 to achieve a pressure normally experienced by the building, this is 0.013 m³/s that is close to the value obtained for best practice given by standards. The airtightness specifications for certain building components are given in Liddament (1996a) by British and world wide standards from leakage flow rate measurements most commonly at 1 Pa and an exponent of 0.66. Air leakage through the building envelope and infiltration rate has been studied for room pressures at 4 Pa, assuming C_d = 1.0 for a range of building components, for example, ASHRAE (2001) and Liddament (1996a).

By using the current estimation code and direct measurements, the following calculations were obtained as shown in Table 4.2,

Std. crack thickness [m]	0.00025	0.0005	0.001	0.002	0.003		
Lower openings [m²]		**Square side [m]**		**Upper openings [m²]**			**Sq.s. [m]**
rear wall	0.0053	0.0728			rear wall	0.0055	0.074162
cs-area of rails	0.0024	0.04899		upper back panels		0.0065	0.080623
rail holes	0.02	0.14142		duct panels		0.00164	0.040525
vertical cracks	0.0125	0.1118		3 cables holes		0.00925	0.096167
chamber door	0.0033	0.05745		other ducts		0.00628	0.079267
chamber windows	0.001829	0.04277		4 access panels		0.015	0.122474
chamber floor	0.003675	0.06062		subtotal [m²]		**0.04417**	**0.210175**
subtotal [m²]	**0.044204**	**0.21025**					
			Total [m²]		**0.08838**	884 cm²	
			Square side [m]		**0.29728**	29.7 cm	

Table 4.2: Estimation of leakage area by measurement and standards.

The estimation in Table 4.2 has given approximately the same area of upper and lower openings. The calculation has been carried out independent to the pressurisation test. The area was found to be the same as the effective leakage area by the pressurisation test. This gives a discharge coefficient C_d = 0.95 that is also according to theory and the ASHRAE literature.

The temperature taken at a single measurement point on each wall, shown also in Figure 4.5, was also found to be the same as the temperature in the rest of the chamber at the same height. Additional evidence was already provided by taking measurements at four locations close to the walls and an additional location in the middle of the chamber which was also the same as the temperature on the walls, shown in Figure 4.11,

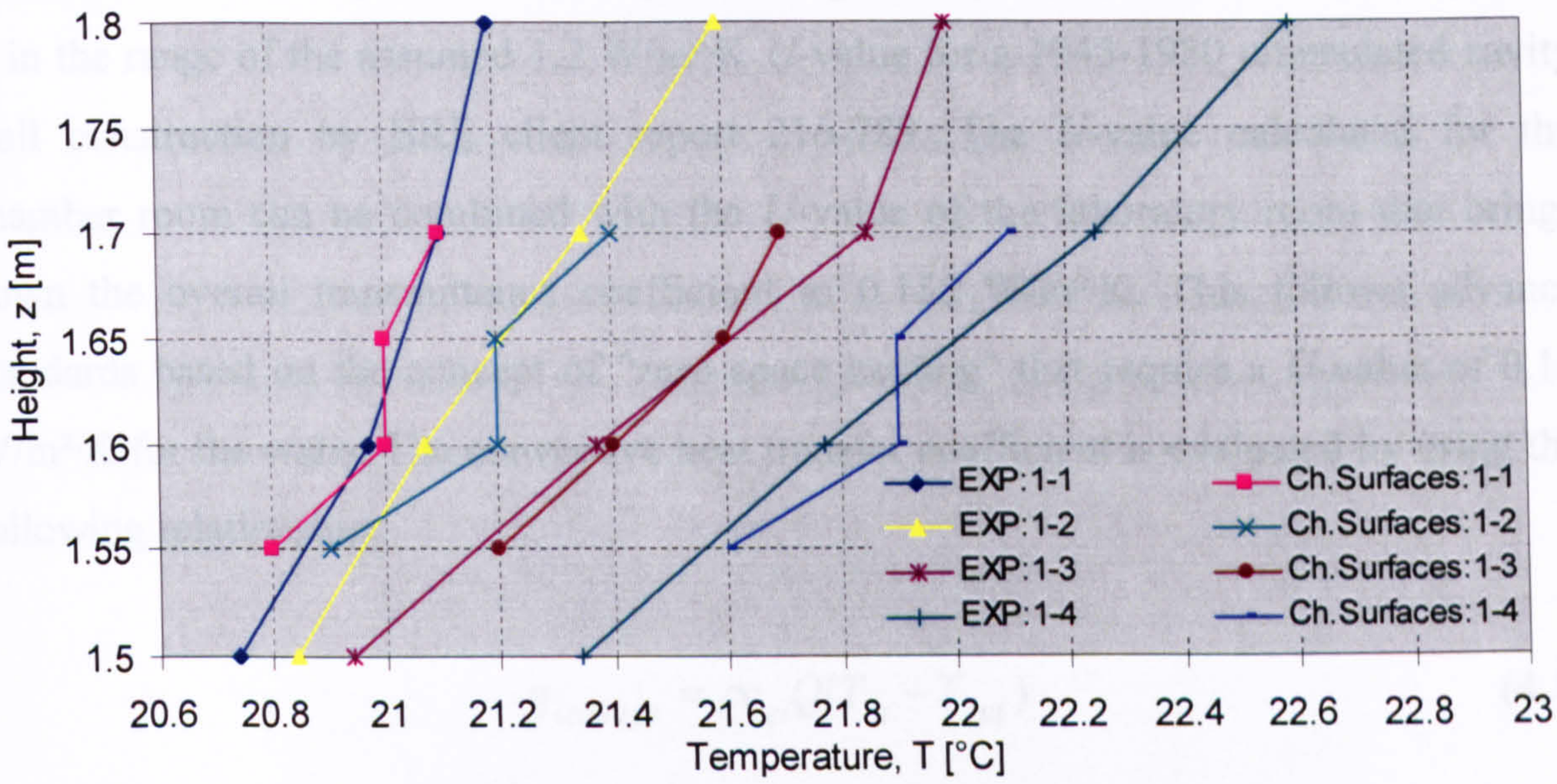

Figure 4.11: Temperatures at specific heights on the walls and the chamber medium by increasing inlet flow rate every 30 minutes; the wall thermocouple at 1.55 m is on front wall, at 1.6 m is on the rear wall (inside), at 1.65 m is on the left wall and at 1.7 m is on the right wall.

There is very little difference between the wall temperatures and the temperatures in the middle of the room medium. These are owing to the fact that the wall temperatures are slightly influenced, no matter how negligibly, by the temperatures of the laboratory room outside the chamber. The magnitude of the temperature on the right is also slightly influenced by the internal convection current from the hot air supply. In general, the temperatures of the wall during tests were about 0.1°C less than in the room space. The outside surface temperature was calculated about 0.4°C higher than the laboratory room space and there was approximately a temperature difference of 3°C across the polyurethane wall. The heat transfer across the wall by conduction is,

$$q_x = hA(T_{in} - T_{out}) \tag{4.12}$$

The coefficient per degree Kelvin is approximately 23 W/K and the heat transfer by conduction is 69 W. The transmittance coefficient for the test room can be evaluated from by using the combined *U*-value method that is for 1-directional heat transfer using CIBSE (1988) Guide A. The theoretical *U*-value of the test room is 0.213 W/m³·K. The *U*-value of the chamber wall alone is 0.186 W/m²·K. The *U*-value of the laboratory room is 1.14 W/m²·K, is calculated by including the adjacent wall and airspaces, which is in the range of the assumed 1.2 W/m²·K *U*-value for a 1945-1980 uninsulated cavity wall construction by BRE client report 216-789. The *U*-value calculated for the chamber room can be combined with the *U*-value of the laboratory room that brings down the overall transmittance coefficient to 0.155 W/m²·K. This follows advance standards based on the concept of "zero space heating" that require a *U*-value of 0.15 W/m²·K for the walls. The convective heat transfer coefficient is evaluated by using the following relationship,

$$q_{leakage} = \rho c_p Q(T_{in} - T_{out}) \tag{4.1}$$

where the convective heat transfer coefficient is $C = \rho c_p Q$ in W/K that is evaluated as $C = 24$ W/K and the heat transfer by convection is 72 W. This is shown in Table 4.3,

Floor	27.5	m²	×	0.16	W/m²·K	=	4.42	W/K		
Ceiling	27.5	m²	×	0.16	W/m²·K	=	4.53	W/K		
Front wall	13.75	m²	×	0.22	W/m²·K	=	2.96	W/K		
Right wall	12.5	m²	×	0.21	W/m²·K	=	2.59	W/K		
Left wall	12.5	m²	×	0.21	W/m²·K	=	2.59	W/K		
Rear wall	13.75	m²	×	0.42	W/m²·K	=	5.77	W/K		
Σ(*A*) =	107.5	m²				Σ(*AU*) =	22.85	W/K		
								Σ(*AU*) / Σ(*A*) =	**0.21**	W/m²·K
ACH		*V*		*ΔT*		Ventilation factor at 20°C	Ventilation heat loss			
1.05	×	68.75	×	-2.25	×	0.33	-54	W		
						Ventilation allowance =	-0.79	W/m³		
	ρ		c_p		m³/s		*ΔT*			
$q_{leakage}$ =	1.2	×	1006	×	0.02	×	-2.25	=	-54.32	W
									-0.79	W/m³
								Convective heat transfer coefficient, *C* =	**24.14**	W/K
Rest of walls	93.75	m²					17.09	W/K		

Rear wall	13.66	m^2	×	0.42	$W/m^2 \cdot K$	=	5.73	W/K		
Leakage openings	0.09	m^2	×	268.27	$W/m^2 \cdot K$	=	24.14	W/K		
$\Sigma(A)$ =	107.5	m^2		($h_{leakage}$)		$\Sigma(AU)$ =	46.96	W/K		
								$\Sigma(AU) / \Sigma(A)$ =	**0.44**	$W/m^2 \cdot K$
							Increase in heat transfer		**2.05**	

Table 4.3: Heat transfer calculations by degree method, using CIBSE (1988) Guide A Heating Example.

The temperature distribution at the front wall followed the same trend as the temperature distribution close to the other walls and the middle, except that there was an increase or decrease of the temperatures at ceiling and floor when getting closer to the hot or cold air diffuser respectively. Slightly higher temperatures were observed close to the extract point away from the middle space and close to diffusers as a result of location, shown in Figure 4.13,

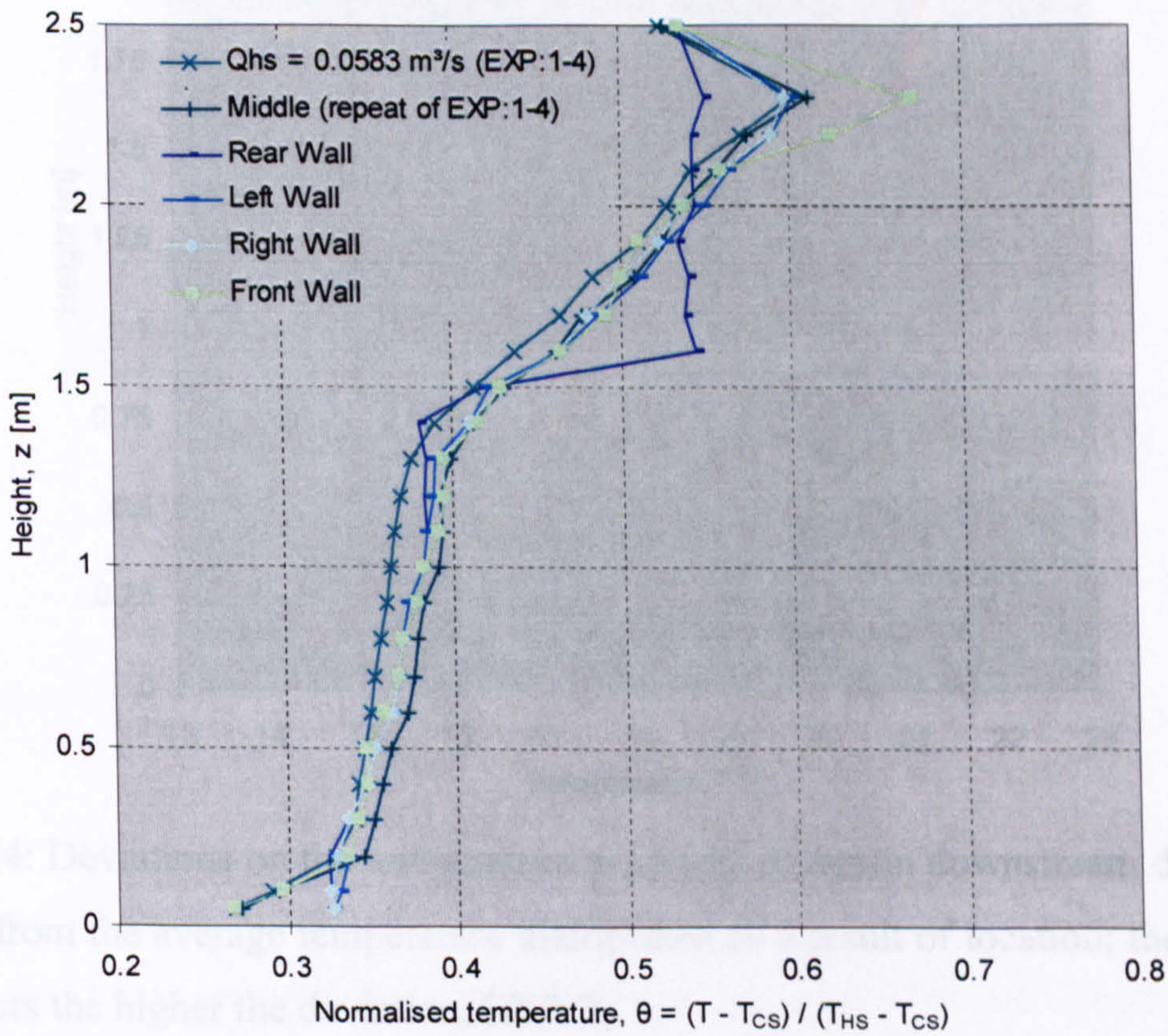

Figure 4.13: Deviations from the average temperature distribution as a result of location at the walls close to the diffusers and the extract point for relatively low air supply rates.

The temperature at some distance below about 0.25 m from the ceiling, the temperature distribution is affected by the convection current of the hot air supply. The low stratification makes the data points deviate from the values obtained at other locations in

the room at same height. Similarly, at some distance of about 0.25 m from the floor, the temperature distribution is affected by the convection current of the cold air supply. The temperature distribution close to the front wall, (NB. thermocouple stand locations are shown in Figure 4.4) is still affected by the cold air flow. Close to the extract, selective withdrawal of thinner hot air makes occasional changes to the distribution, due to the extract flow of hot air. At the other locations, i.e., at the left and right walls, the similarity is evident between all the data points on the distribution.

Similar flow characteristics are observed with higher flow rates and higher stratification as shown in Figure 4.14,

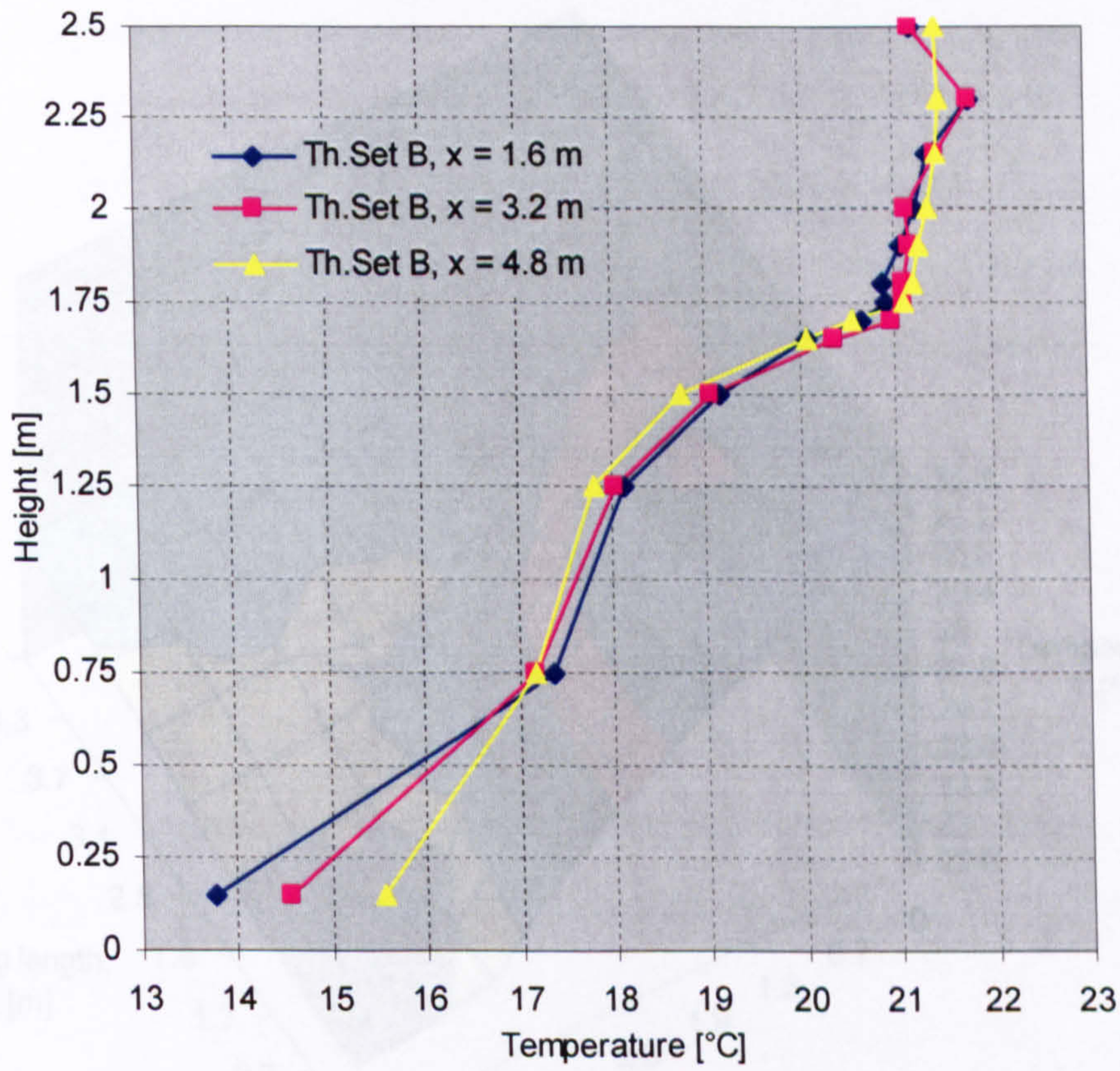

Figure 4.14: Deviations on the temperature gradients at certain downstream distances in the room from the average temperature distribution as a result of location; the closest to the diffusers the higher the deviation, EXP:2.

In any event, the thermal stratification in the room was represented by the middle space except very close to the supplies, extract and corners. The cold air supply did not seem to be strong enough to affect the temperature values at the floor away from the discharge area of the floor terminal. The length of the gravity front of the cold air supply was calculated from manufacturers data and it was found to measure to a length

of L_v = 1.5 m at v = 0.2 m/s. Looking at the temperature distributions at the station-2 where the effect is still evident and station-3 where the effect has decreased significantly, there is an apparent similarity with the current experiments which works out approximately 2.4 m.

The forced convection current of the hot air supply affected the temperature distribution to a certain radius away of the hot air supply diffuser. The extent of this effect occurs due to the higher convective velocities a certain distance below the ceiling as described above. These velocities are perpendicular to the centre axis of the hot air jet and result due to buoyancy. This effect occurs while stable thermal stratification established. The result obtained from a 2-square-slot diffuser is shown in Figure 4.15,

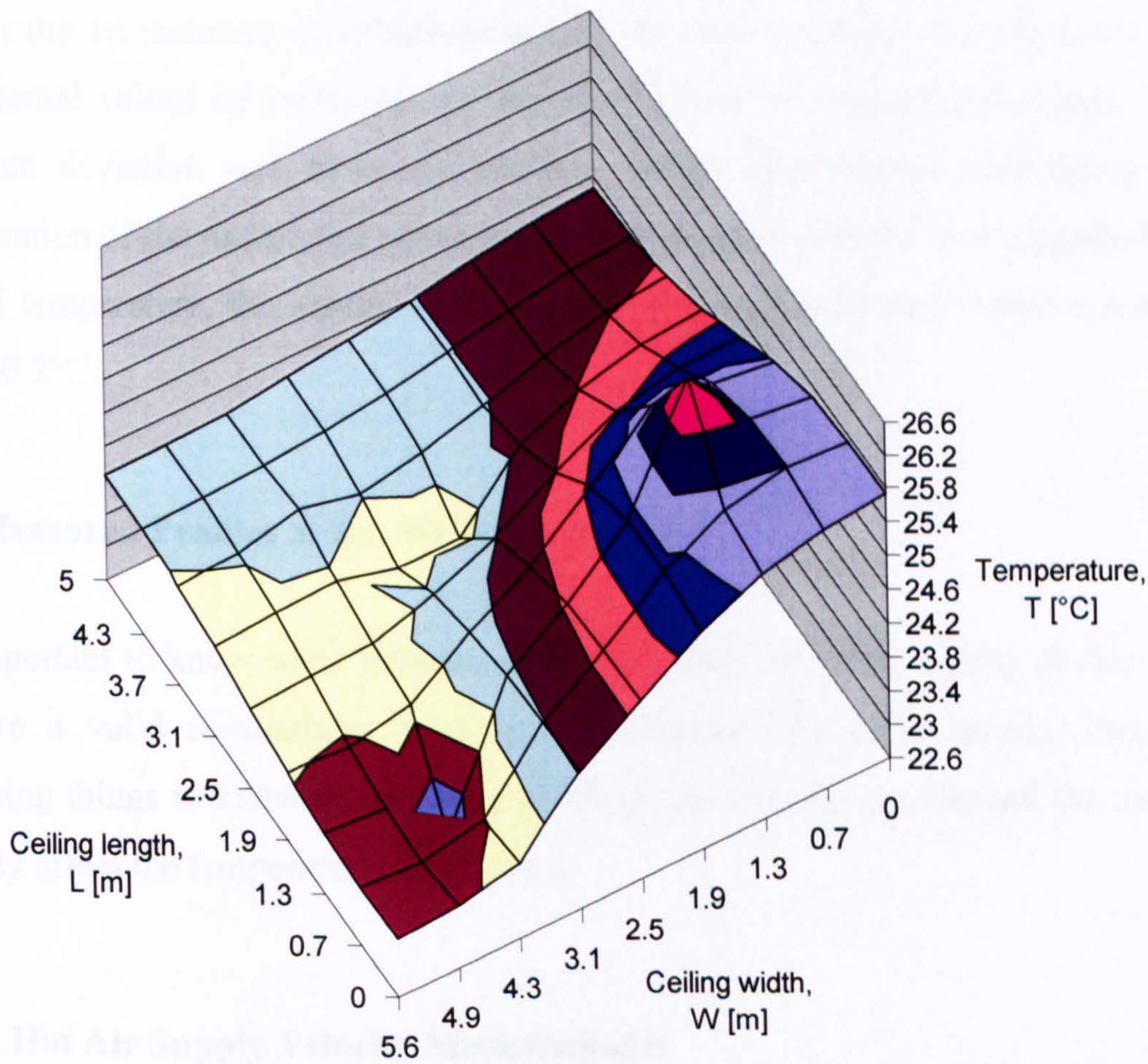

Figure 4.15: Isosurface contour plot showing an estimation of the variation of temperatures from measured values below the ceiling, EXP:1.

Linear interpolation was performed between values obtained from the thermocouples on a grid of size equal to the size of the tiles. The adjacent tiles to the walls were considered of equal length, i.e., 0.1 m and the measured values were weighed at the beginning of each surface line to reflect the thermocouple locations. The contour plot shown in Figure 4.15 is obtained from experimental cases of the low flow rates. There is

not much variation in the radius of the isotherms from the hot air diffuser in the other experimental cases and for higher flow rates and slightly higher range of temperatures. This indicates that the flow under the ceiling is affected at certain distance that is approximately equal to the jet throw. This length extends at some shorter distance compared to the displacement diffuser of the cold air supply. It is estimated to extend to a radius of approximately 1.8 m from the corner with the front-right walls and this is around 0.75 smaller than the jet throw of the displacement diffuser that is affected by the cold air diffuser on the floor.

However, comparing the measurements at different locations with previous measurements taken in the middle of the room, there is a high degree of similarity also between the temperature distributions across the entire height. The deviation of the experimental values by repeating the experiment was in a reasonable range, i.e., 3% maximum deviation was observed between similar experiments. Depending on the configuration of the model and equipment accuracies, the stability and magnitude of the external temperature, the results of this work could be reproduced within a reasonable range ±0.2°C.

4.1.6 Measured Profiles at the Air Supply Outlets

It is important to know some information at the outlet of the air supply device in order to make a valid comparison between experimental and CFD results. One of the interesting things to know is the extent at which the velocity profile and the turbulence intensity affect the temperature distribution.

4.1.6.1 Hot Air Supply Velocity Measurements

The velocity profile at the hot air supply outlet is not entirely symmetrical between axes. The orientation of the inflow duct and the bend at approximately 0.5 m from the diffuser affects the outlet profile. Although this is likely to introduce some directional effects on the temperature distribution, depending on the current orientation of the duct, it is not a strong contributor to thermal stratification (Chapter 5). However, this is rather more likely to occur in the transverse direction, as it can be deduced from Figure 4.16,

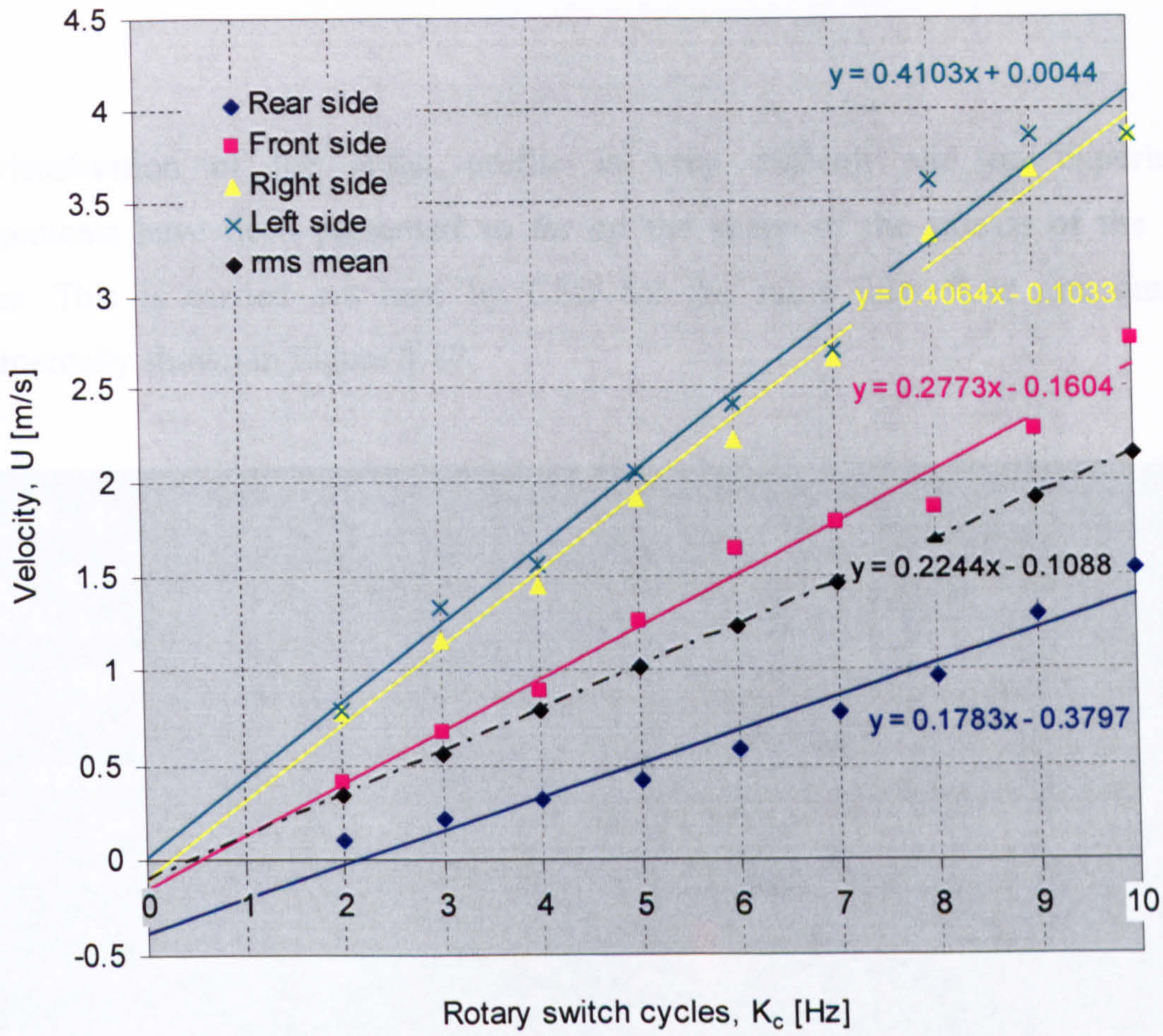

Figure 4.16: Profile asymmetry due to the orientation of the air supply duct before the inlet measured rms velocities on the middle of the side faces of the 4-square slot diffuser in the experimental work. The effect of C_d coefficient is not applied yet here.

By looking at the trend lines of the maximum velocities for each side in Figure 4.16, it can be deduced that the direction of the outlet flow is more favourable to the front wall. This implies that in this particular case the temperature distribution in the middle of the room is not affected directly by this effect. However at some high enough velocities, the directional effects will be affecting the temperature distribution and to show this effect, further simulations are performed in Chapter 5.

Initial measurements carried out in this work not including the diffusers showed that the temperature at the inlet is not the same in the immediate area of the jet. There was a change of at least 3°C in the region of 0.05 - 0.1 m. The potential core region of the jet is affected by the room temperature differential resulting in diffused flow right after it leaves the supply aperture. The temperature stabilises at some small distance after the inlet and it is equal to the constant temperature in the nearest layer of the stratification zone.

The visualisation of the outlet profile is very difficult and no experimental measurements have been presented so far on the shape of the profile of the 4-way diffuser. This is carried out here by CFD for the same inlet flow rate measured experimentally shown in Figure 4.17,

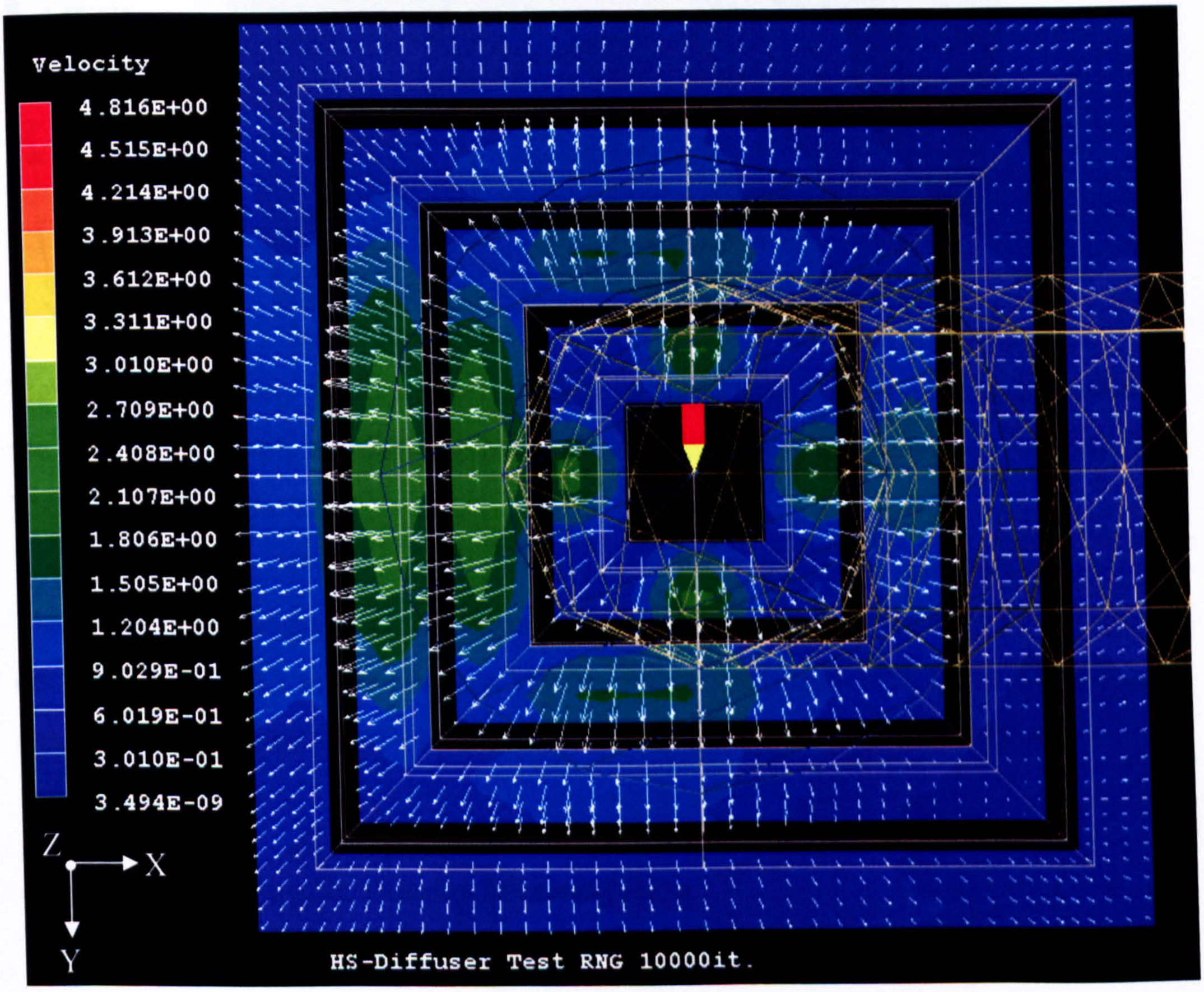

Figure 4.17: Velocity vectors superimposed on a velocity contour plot at the outlet of the 4-cone hot supply air diffuser.

There is a tendency in the outlet flow in Figure 4.17 to stick on the south side of the diffuser, while there is a proportional decrease in the flow of the north side of the diffuser. This occurs because of the orientation of the inlet duct is restricted by the height of the chamber. The flow at the other two sides is equal, while in the experiment there is only a very small difference in the magnitude due to the slight deviations from the longitudinal orientation.

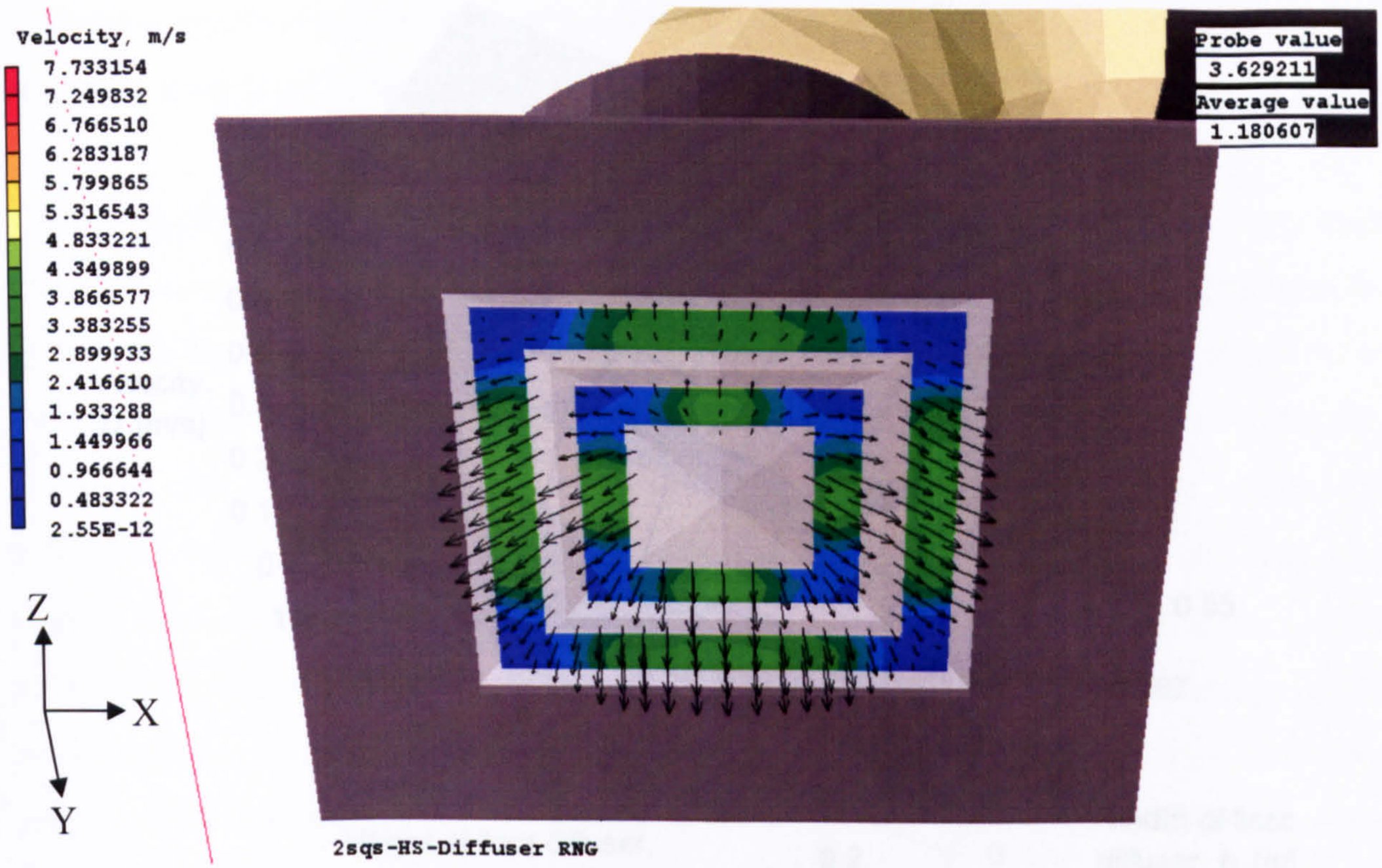

Figure 4.18: Velocity vectors superimposed on a velocity contour plot at the outlet of the 2-cone hot supply air diffuser. Note: the red line is the top corner of the front wall PHOENICS boundary.

The effect of the angle of an impinging free jet is reported by Heiselberg *et al.* (1998) on the work carried out by Beltaos (1976), in the industrial ventilation handbook by Goodfellow and Tähti (2001) on the work carried out by Grimitlyn (1993), etc.

4.1.6.2 Cold Air Supply Velocity Measurements

The velocity profile measured at the face of the diffuser is shown in Figure 4.19,

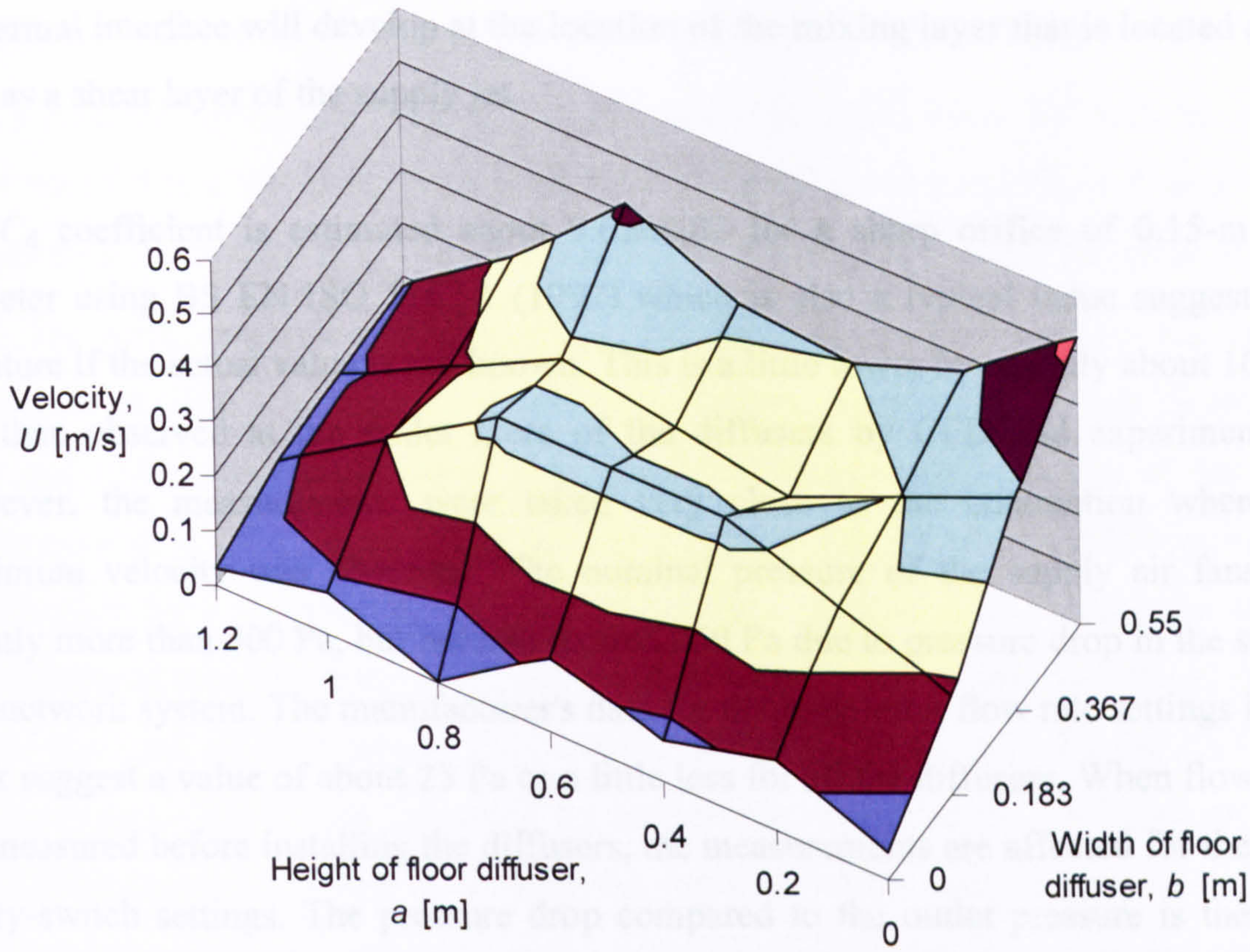

Figure 4.19: Velocity contour plot of floor diffuser.

The outlet velocity profile defined by the iso-surface contour plot in Figure 4.19 shows that the cold air supply has a tendency of occupying the lower three quarters of the floor diffuser. This is prevented to some extent by a horizontal perforated panel at the same location and a deflector at certain angle in the lower compartment in order to achieve a satisfactory outlet profile. The profile experiences off-centre velocity picks of saddle-backed shape. This also reveals the slight deviation in the downward flow direction of the air supply duct similar to the hot air supply diffuser. It is very difficult to achieve a perfectly vertical orientation of the inlet duct, one reason being the limited vertical space of the chamber.

Wall mounted terminal devices discharging horizontally at the floor level in combination with heat sources in the room can achieve thermal stratification, Nielsen (1994). Similar studies evaluate the flow paths discharging very close to the floor showing that there is very little effect on the flow field away from the jet, Skistad (1994). The flow consists of a primary zone near the terminal with reducing vertical height with radius. This follows a secondary zone where the flow attaches close to the floor due to shear forces that is otherwise known as Coanda effect. The flow field is expected to develop as a combination of flow features contained in the test room. An

isothermal interface will develop at the location of the mixing layer that is located at the edge as a shear layer of the supply jet.

The C_d coefficient is estimated about 0.62±0.02 for a sharp orifice of 0.15-m duct diameter using BS EN ISO 5167-1 (1997) which is also a typical value suggested in literature if the actual value is not known. This is a little lower by roughly about 10% or less than observed at the outlet faces of the diffusers by CFD and experimentally. However, the measurements were taken very close to the contraction where the maximum velocity was observed. The nominal pressure of the supply air fans was slightly more than 500 Pa, but became around 250 Pa due to pressure drop in the supply air ductwork system. The manufacturer's data for the maximum flow rate settings in this work suggest a value of about 25 Pa or a little less for all the diffusers. When flow rates are measured before installing the diffusers, the measurements are affected for the same rotary-switch settings. The pressure drop compared to the outlet pressure is therefore small and also about 10% or less when at the maximum setting which follows a square-root reduction. Since using a coefficient of 0.62 gave a slightly lower value, it overwhelmed the reduction in the flow due to pressure drop when adding the diffusers.

4.1.6.3 Inlet Turbulence Intensity from Current and Published Experiments

The investigation of turbulence forms part of every investigation of fluid flow. This is often carried out to account for the turbulent deviation of the velocity measurements, although it is not the aim of this work. Turbulence may originate or arrive at the inlet which is important in the mixing characteristics of room air flows. There is enough information in the open literature to estimate the average turbulence intensity for the specified ventilation system and ambient temperature. The magnitudes obtained from the literature are given at 0.05 m away from the inlets where the temperature measurements are stable.

The important issue to investigate is the values that the magnitude of T_u can take. Palonen *et al.* (1991) carried out an experimental investigation and tabulated a range of turbulence intensities for displacement and mixing ventilation at 0.75 m from the diffusing devices at 0.07 m above the floor and 0.05 at certain locations in the middle of the room where the highest velocities were measured. For mixing ventilation, the velocity is in the range of 0.05-0.19 m/s, the mean turbulence intensity is rather large

and approximately in the range of T_u = 30-40% and 25-35%. For the velocity range of 0.2-0.5 m/s, the turbulence intensity is approximately 25%, while for velocity values larger than 0.5 m/s this is likely to be 20%. For displacement ventilation, a large range of velocities correspond to an approximately magnitude of turbulence intensity of T_u = 20%. The turbulence intensity values are slightly lower at 0.75 m from the device. Palonen *et al.* (1991) obtained a relationship between vote of percentage dissatisfied (PD) and turbulence that is close to a linear relationship with velocity at the room temperature of 21°C. The equation for PD given by Fanger *et al.* (1989) includes a modification for a variation of temperatures in the occupied zone a round the subject and turbulence measurements some distance between the supply duct outlet and 0.15 m behind the neck of the subject. They carried out experiments only for the traditional mixing system. The model suggested by Fanger for predicting the performance of air distribution systems in terms of draught risk can be used for comparing systems with a fixed temperature in the occupied zone. A comparison of results to support and compare the expected range of turbulence intensities suggested in the literature is presented here in Figure 4.20,

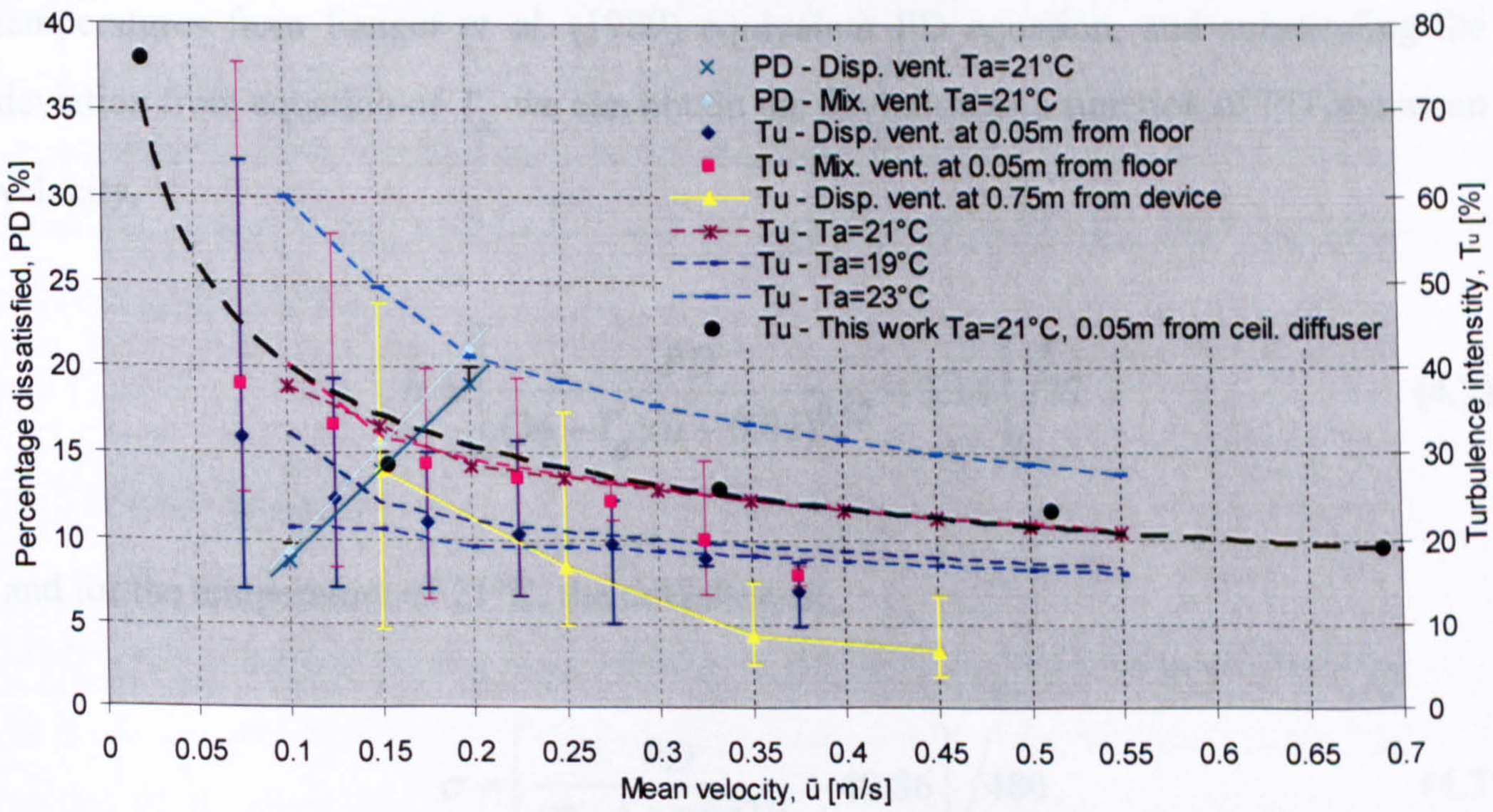

Figure 4.20: Percentage dissatisfied (PD) for specified diffuser outlet velocities and resulting turbulence intensities (T_u) for displacement and mixing ventilation obtained from tabulated experimental data of Palonen *et al.* (1991) (fist five curves). The data is fitted by an equation for PD from Fanger *et al.* (1989) (next three curves) and validated for the same temperature of 21°C and with current work (power law fit).

The dashed curves are obtained from the equation of PD. The turbulence intensity is difficult to measure for velocities lower than 0.2 m/s as it can be deduced from the error bars in. This is probably because the inaccuracy of the sensor and large deviations at these velocities in proportion to the measured values. Additional data regarding the accuracy of the anemometer supplied for individual use by the manufacturer dictates that the indicated velocity is likely to be progressively overestimated below 2 m/s. In this work, turbulence intensity was obtained from velocity measurements at a vertical distance to the flow of 0.05 m below the ceiling air-diffuser for the ambient temperature of 21°C. Any small deviations are difficult for the averaging period of the anemometer to handle a perfectly good statistical estimation. Detailed measurements of inlet turbulence are not in the scope of this work, nor the comfort characteristics. A comparison with other researchers shows that a good comfort is maintained (Five visitors voted 100%×4 slightly away from the cold air supply diffuser and 50%×1 when closer to the cold air supply diffuser.

The error deviation can be retrieved from Palonen *et al.* (1991) at the specified ambient temperature of 21°C by rearranging the equation for PD and at different ambient temperatures from Fanger *et al.* (1989) equivalent PD equation, and substituting the deviation from equation of T_u we can obtain the deviation as a function of PD and mean velocity,

$$\sigma = \left[\frac{PD}{(34 - T_a)(\bar{u} - 0.05)^{0.62}} - 3.14 \right] \Big/ 37 \tag{4.2}$$

and for the temperature of 21°C, the deviation is,

$$\sigma = \left[\frac{PD}{(\bar{u} - 0.05)^{0.6223}} - 40.86 \right] \Big/ 480 . \tag{4.3}$$

A comparison at 21°C can be made with this work. The error deviations for different temperatures, different researchers and this work are shown in Figure 4.21,

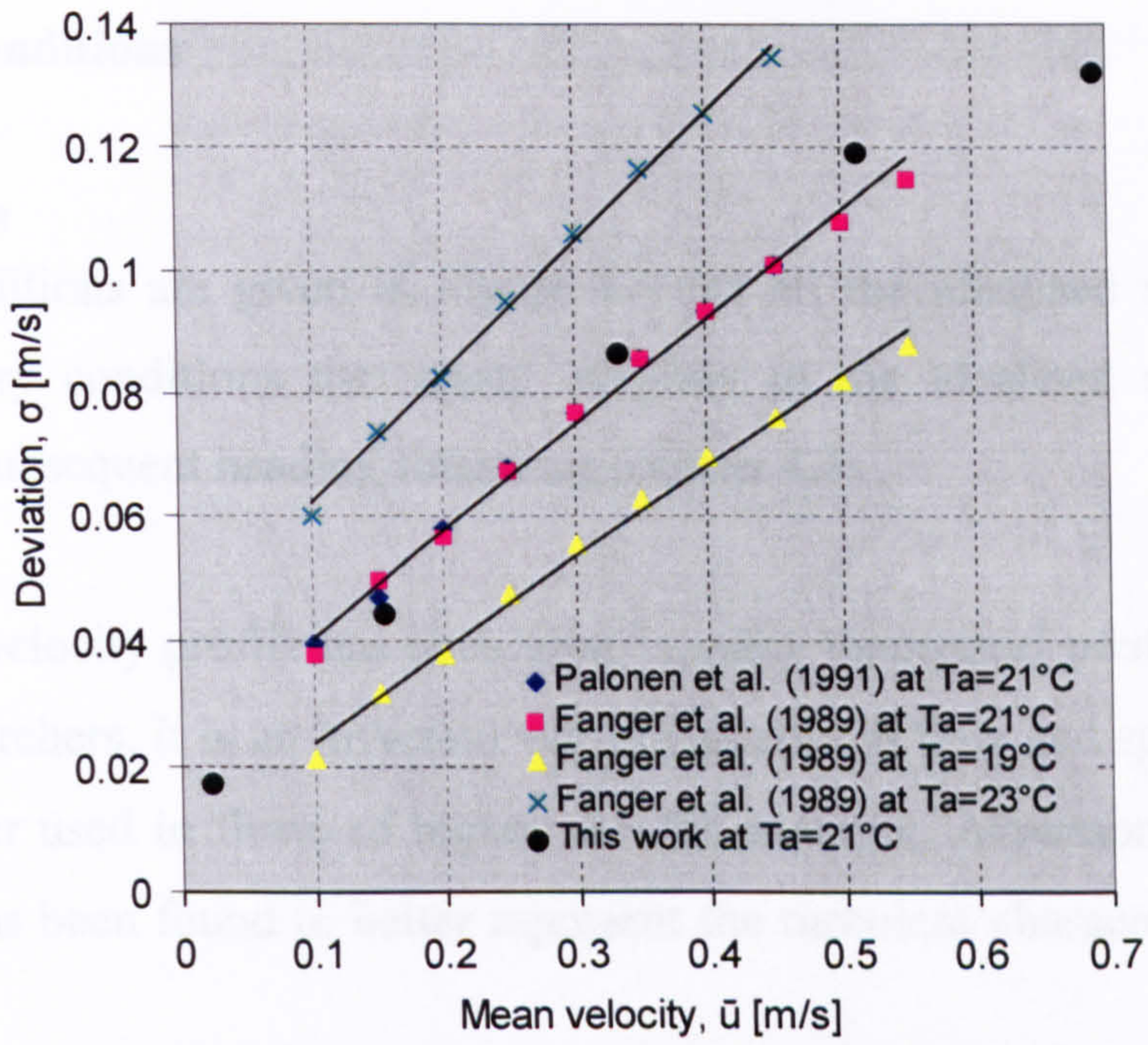

Figure 4.21: Deviation from the mean velocity using equations of Percentage dissatisfied (PD) from Palonen *et al.* (1991) and Fanger *et al.* (1989), and measured in this work.

The turbulence intensity for the displacement terminal on the floor is expected to be slightly less than 20%, while slightly over for the mixing diffuser on the ceiling. It can be concluded, however, that the average turbulence intensity of the inflow is approximately 20% throughout a large range of inlet conditions for ventilation. The turbulent deviation will eventually become higher with increasing inlet velocities and will affect stratification.

4.2 CFD Model

High level of control over a large number of parameters can be attained by using CFD to solve the problem. In this way, a CFD model needs to be designed accordingly by setting up the boundary conditions affecting the medium in the modelled room. These are mainly inlet velocities and temperatures. The thermal radiation as a result of the indoor flow over certain surfaces also affects the medium inside the room as well as heat conduction and mass losses.

4.2.1 Boundary Conditions

4.2.1.4 Inlet profile

The boundary conditions are given in Figure 4.5 for all the idealised models in this work. The boundary conditions that apply uniquely in the idealised model will be pointed out in the subsequent heading following section 4.3.

The uniform inlet velocity profile has been used in many theoretical predictions and by a variation of researchers. It is an invariant velocity profile in time and space. Although this profile is rather used in flows of higher Re for example, Albertson *et al.* (1948), Werle (1968), it has been found to better represent the turbulent characteristics of inlet ducts.

In the idealised model, both jets are issued from square openings located at right angles on the same plane that are of an initial side a = 500 mm. A uniform velocity profile was applied on the inlets of the modelled room by setting the velocity in the downward z-direction for the hot air jet and positive x-direction for the cold air jet to be equal to 0.2 m/s. For uniformly distributed inlet boundary conditions, the velocity in the transverse direction is equal to zero.

4.2.2 Initial Conditions

These need to be in the range of the expected temperatures in order to reduce the computational time. The fluid property inside the room domain is air at 20°C and 1 At which is one of the standard fluid properties in PHOENICS. Standard fluid properties are considered at normal conditions. The value of the initial velocity components in the main and downward flow direction for the hot and cold air jets, helps convergence when close to the inlet values, for an instance, 0.01 and -0.02 m/s. The initial velocity of the transverse velocity component v is several orders of magnitude lower than the magnitude of the inlet velocity because the flow inside the domain is of low velocity and can change direction. However, non-zero values can usually prevent divergence problems, while values that as close as to the actual solution speed up convergence and reduce the flow differentials during the solution can lead to divergence. The initial pressure is 0.01 Pa which is around one or two orders of magnitude of that measured experimentally depending on the case. The magnitudes of turbulence kinetic energy and

dissipation away from the turbulence region of the jets are low and therefore a preferred value is as low as 10^{-5}.

4.2.3 Convergence

Numerical algorithms that speed up convergence and relaxation factors are very important in minimising yield time while increasing the accuracy of the simulation.

The effect of increasing iteration number for the low *Re* case, can be observed by looking at the temperature gradients shown in Figure 4.22,

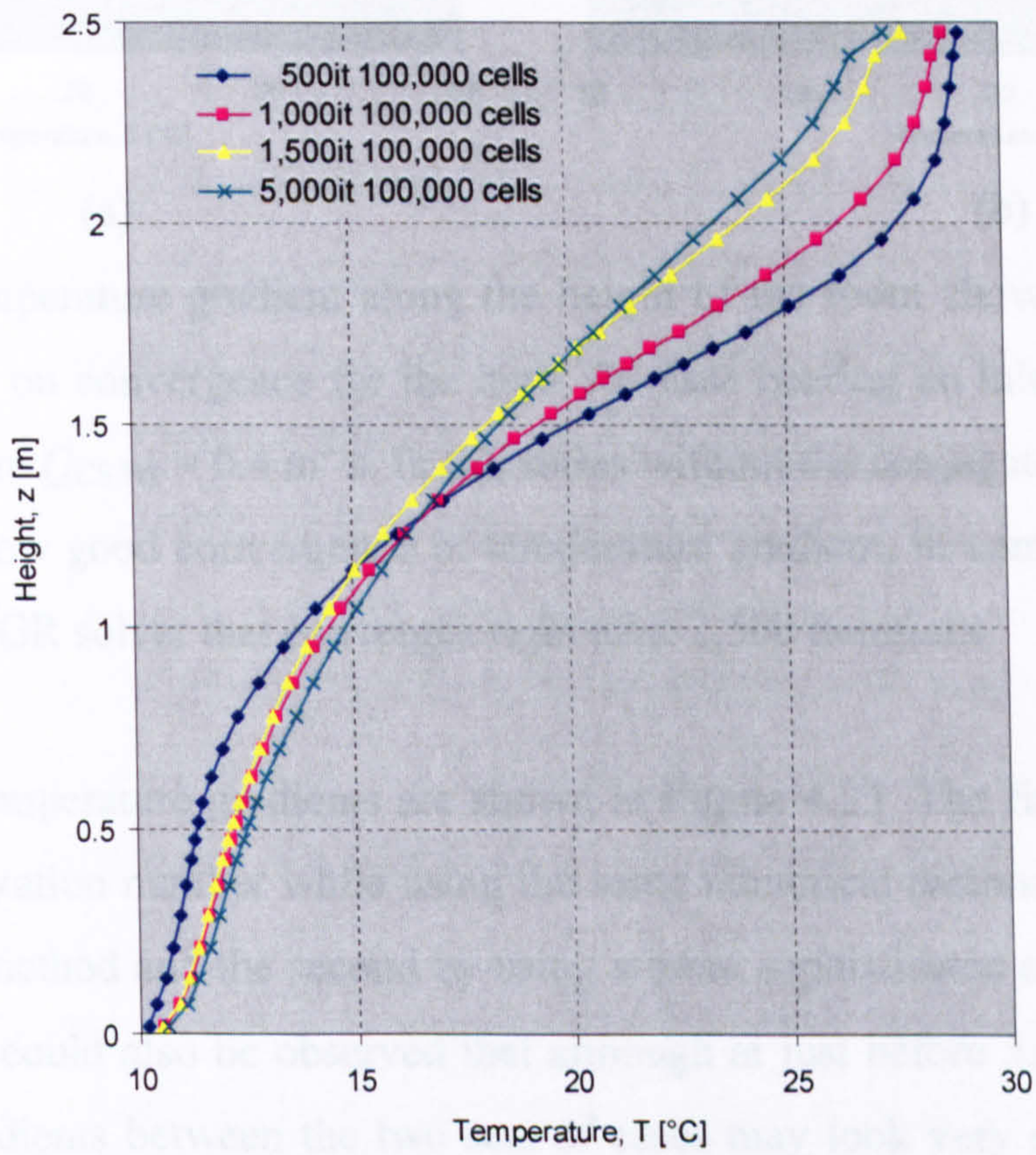

Figure 4.22: Temperature gradient along the height of the room showing the effect of iteration number on convergence for the low *Re* case bearing an inlet velocity of 0.2 m/s, flow rates are $Q_{in} = 0.05$ m^3/s.

The first three temperature gradients were taken at intervals of 500 iterations, up to 1,500 iterations. Similar effects could be observed for the medium *Re* case. The effect of increasing iteration number for the high *Re* case can be observed by looking at the temperature gradients shown in Figure 4.23.

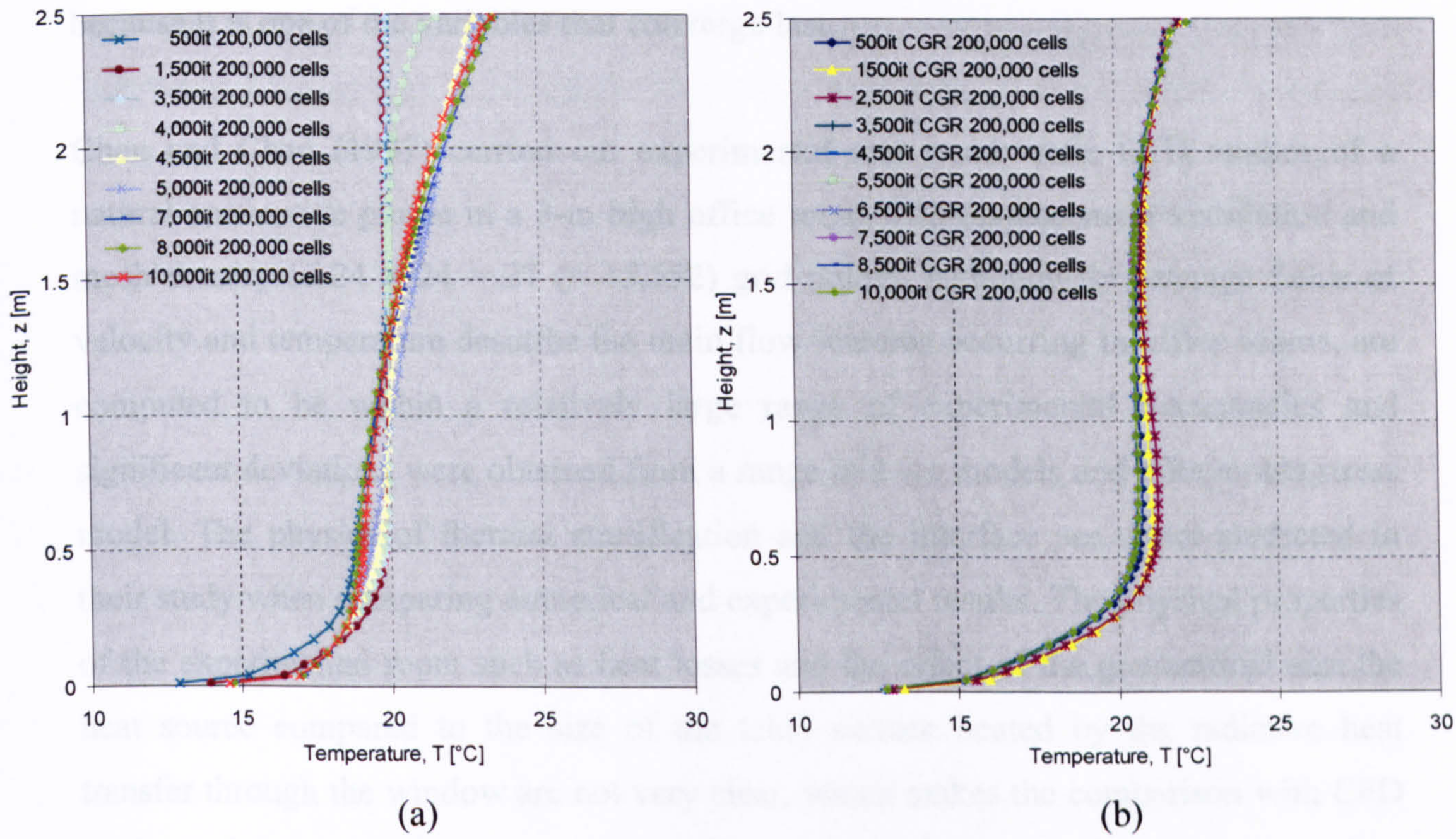

Figure 4.23: Temperature gradient along the height of the room showing the effect of iteration number on convergence for the high *Re* case bearing an inlet velocity of 1.6 m/s, flow rates are $Q_{CS,HS}$ = 0.4 m^3/s. In (a), series without the conjugate gradient (CGR) solver do not show good convergence of temperature gradient, in contrast to the series in (b) with the CGR solver that converges right after 2,500 iterations.

Two series of temperature gradients are shown in Figure 4.23. The first is obtained by altering the relaxation number while using the same numerical method as before which is a stone-type method and the second by using a more sophisticated conjugate gradient type method. It could also be observed that although at just before 5,000 iterations the temperature gradients between the two sets of cases may look very similar. However, the differences could then be observed at full convergence.

4.2.4 Grid Resolution

Mesh independence studies must be undertaken in order to make sure that the results are not biased by increasing the density of the grid. The higher the number of cells in the simulation, the longer it takes to converge. Mesh sensitivity studies are a necessity in optimising the computational resources available. The temperature gradient in the

middle of the room is again the criterion for checking on resolution of the mesh used, because it is one of the variables that converge last.

Chen and Chao (1997) carried out experimental and steady-state CFD studies of a natural convective plume in a 3-m high office room with displacement ventilation and mesh density of 24 × 24 × 27 (= 15,552) grid points. Although the average fields of velocity and temperature describe the main flow features occurring in office rooms, are computed to be within a relatively large range of experimental inaccuracies and significant deviations were obtained from a range of $k-\varepsilon$ models and a Reynolds stress model. The physics of thermal stratification and the interface are under-predicted in their study when comparing numerical and experimental results. The physical properties of the experimental room such as heat losses and the effect of the geometrical size the heat source compared to the size of the table surface heated by the radiative heat transfer through the window are not very clear, which makes the comparison with CFD difficult. Experimental and numerical studies are carried out by Komori *et al.* (1983), Gerz *et al.* (1989) and Shih *et al.* (2000) on the physics of penetrative convection of steam in a stratification water model by using DNS where the grid resolution in each direction was 64^3 (= 262,144). They give a theoretical mesh size compared to the scales present in the stratified flow which is reported in Chapter 2. Higher grid resolutions are currently challenging for any single PC to handle and the main reason to adopt a finer grid spacing is the fulfilment of the Kolmogorov assumption with -5/3 turbulence spectrum. The initial domain size comprises of approximately 50,000 cells and average mesh size in the vertical direction is 10 cm. A medium grading of approximately 100,000 cells was applied where the number of cells changes by a factor of 2 to see how this affects the flow field and the temperature distribution compared to the final case. In this case, the average mesh size in the vertical direction is 6.94 cm. The gradient in each of the three directions also needs to be modified by one digit for the higher resolution models to maintain the same grading each direction as the previous models. The final simulations are carried out by another factor of 2 in order to eliminate any suspicious error due grid resolution which is here slightly over than 200,000 cells. In this case there are 51 grid points in the vertical direction which give an average mesh size of 4.9 cm, which is consistent with the calculations in Chapter 2. However, the grid spacing needs to be really fine if the flow close to the walls is to be modelled with great accuracy. Awbi (1998) carried out a 2-dimensional CFD investigation of the optimum

grid size close to the wall by varying the first grid point from 5-30 mm to evaluate the optimum convective heat transfer coefficients compared to measured values. Grid independent results were reported for 38 × 24 (= 912) cells. The grid size near the wall using wall functions was obtained for a distance slightly larger than 5 mm. Although the wall functions did not produce qualitative results, the quantitative values of the heat transfer coefficient compared well with the experimental values for larger distances than using the Low-*Re* model. This distance is considered in the current work only when applied the air-leakage openings at the ceiling and floor levels. The amount of grid points was relatively large to consider this distance in all simulations although heat transfer was not considered. The distance of the fist grid point from these boundaries for the case of air-leakage was 8 mm. The correlation of the heat transfer coefficient is much cruder for up to a distance of close to 10 mm. A distance of 30 mm was considered for the ceiling where the wall function was shown to become sensitive to the distance. These distances were considered in the rest of the simulations by applying mesh grading in a 3-dimensional co-ordinate system.

The details of the mesh structures used are shown in Figure 4.24, Figure 4.25 and Figure 4.26,

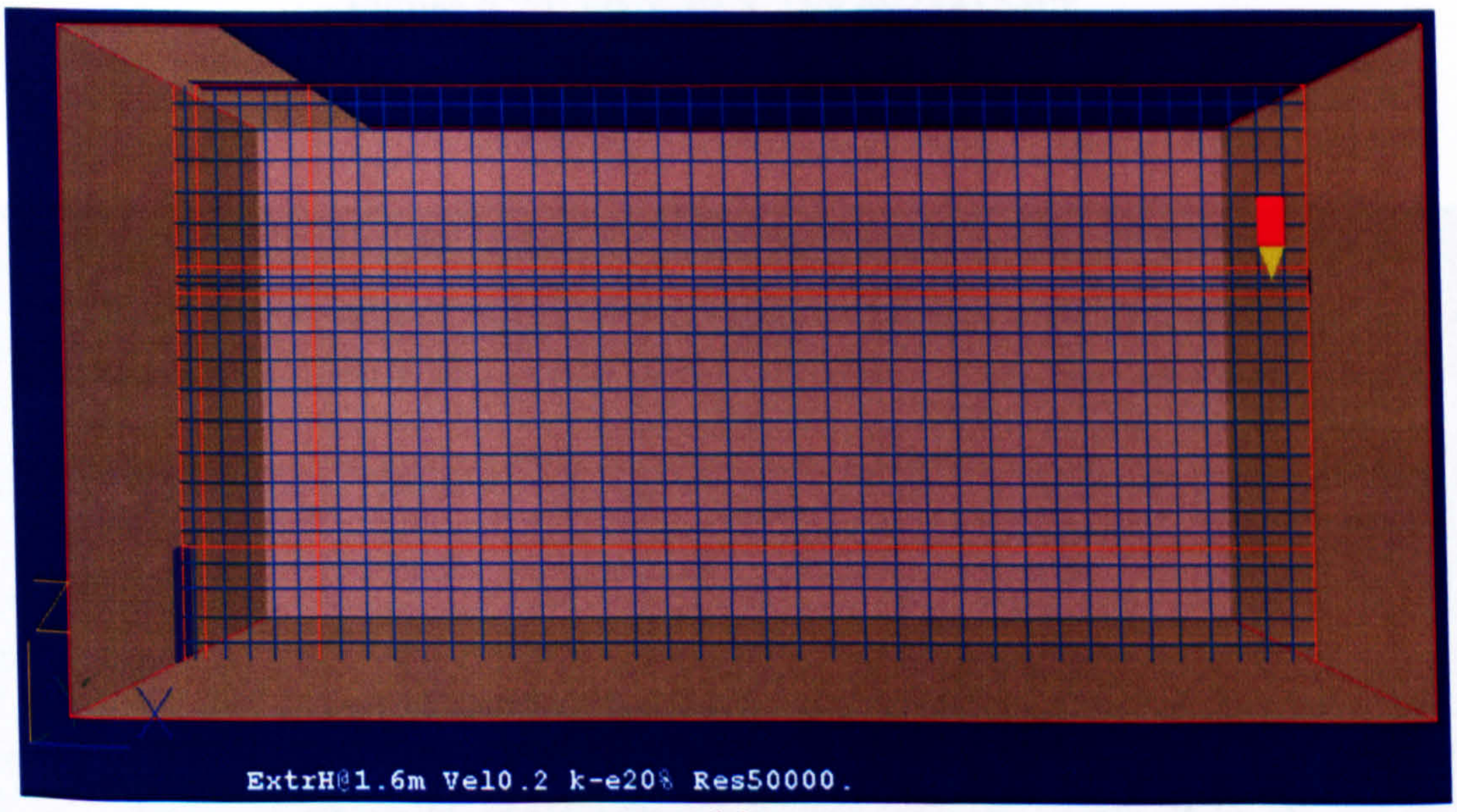

(a)

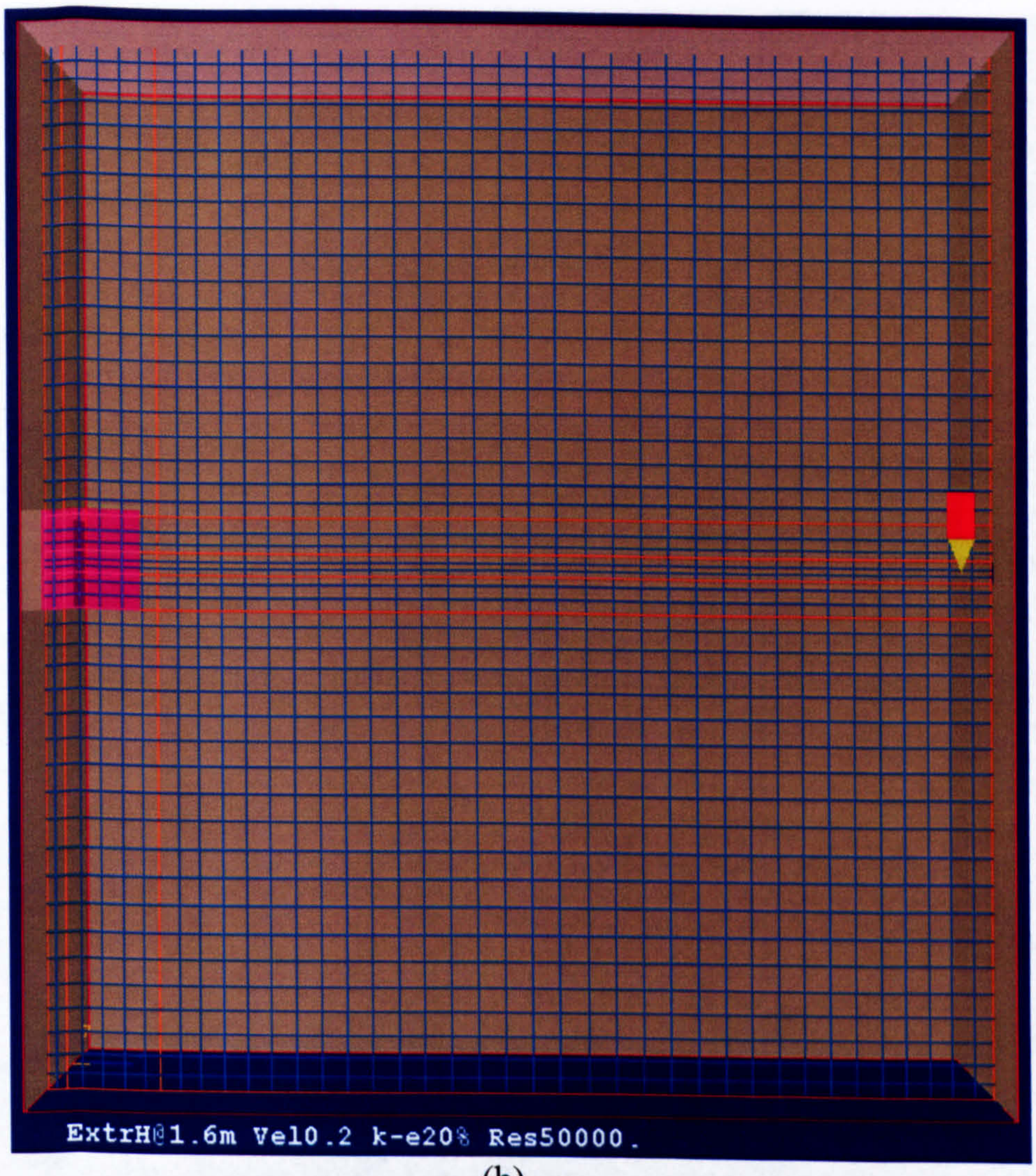

(b)

Figure 4.24: 40 × 49 × 25= 49,000 cells.

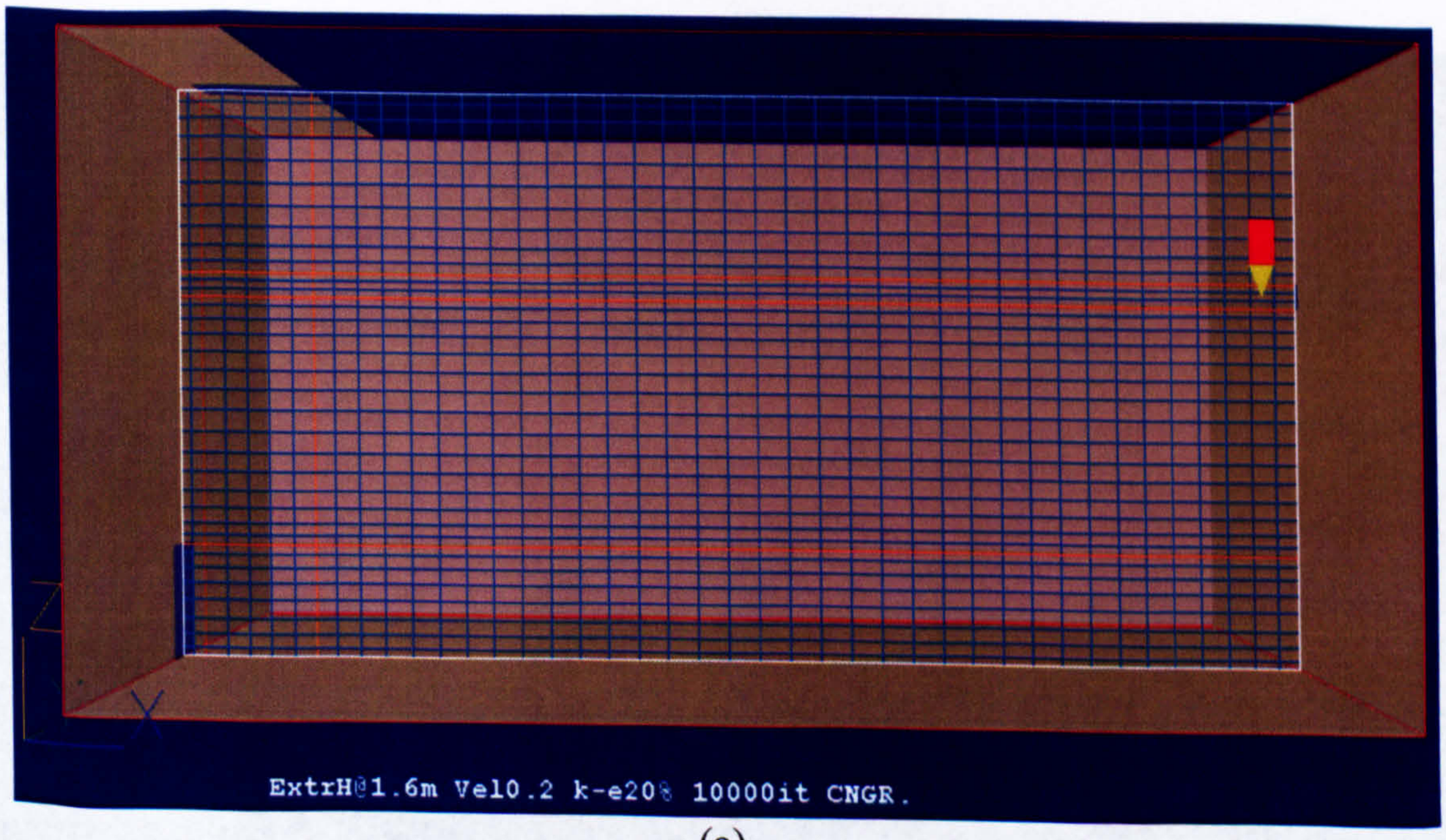

(a)

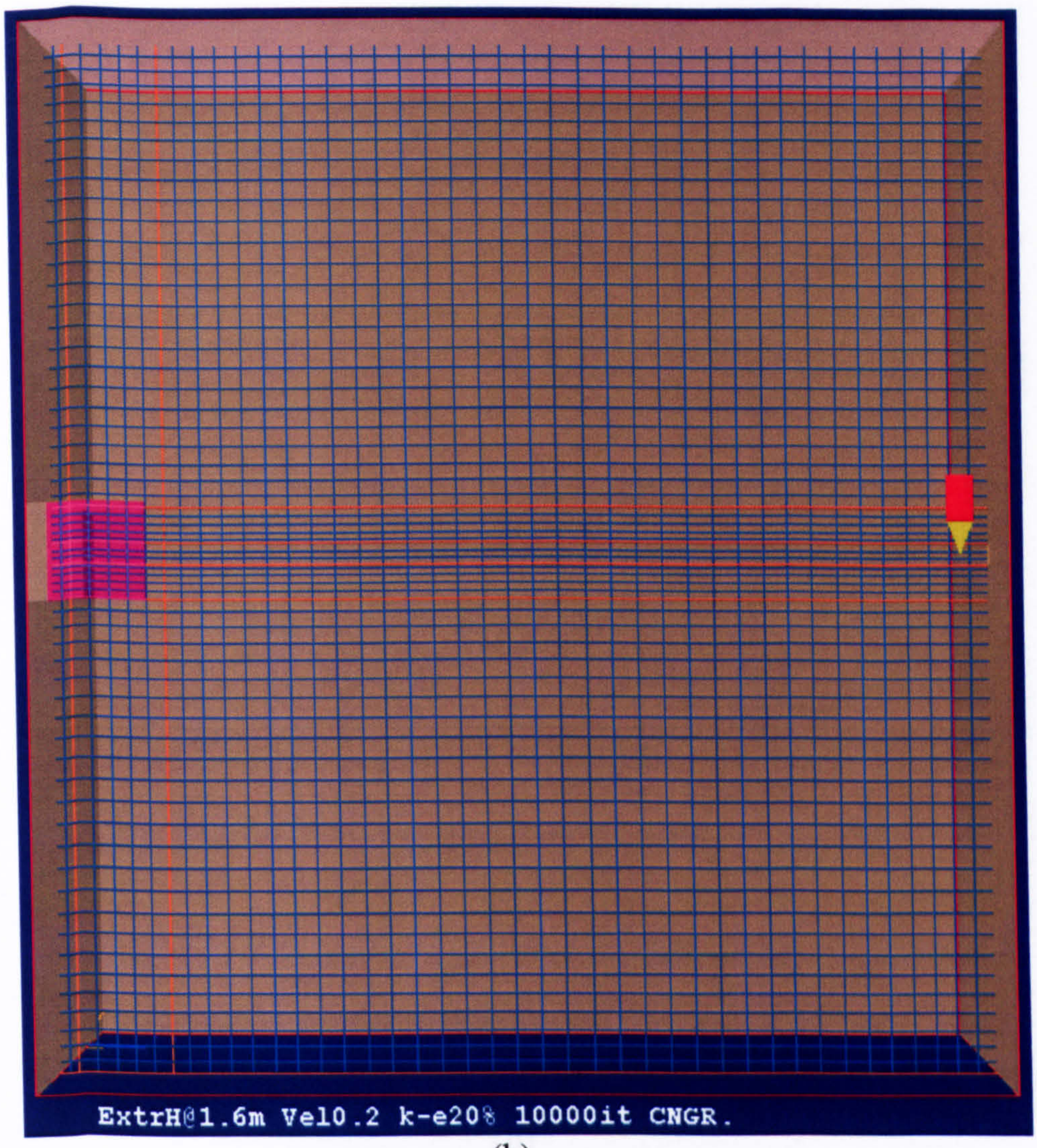

(b)

Figure 4.25: 42 × 63 × 36 = 95,256 cells.

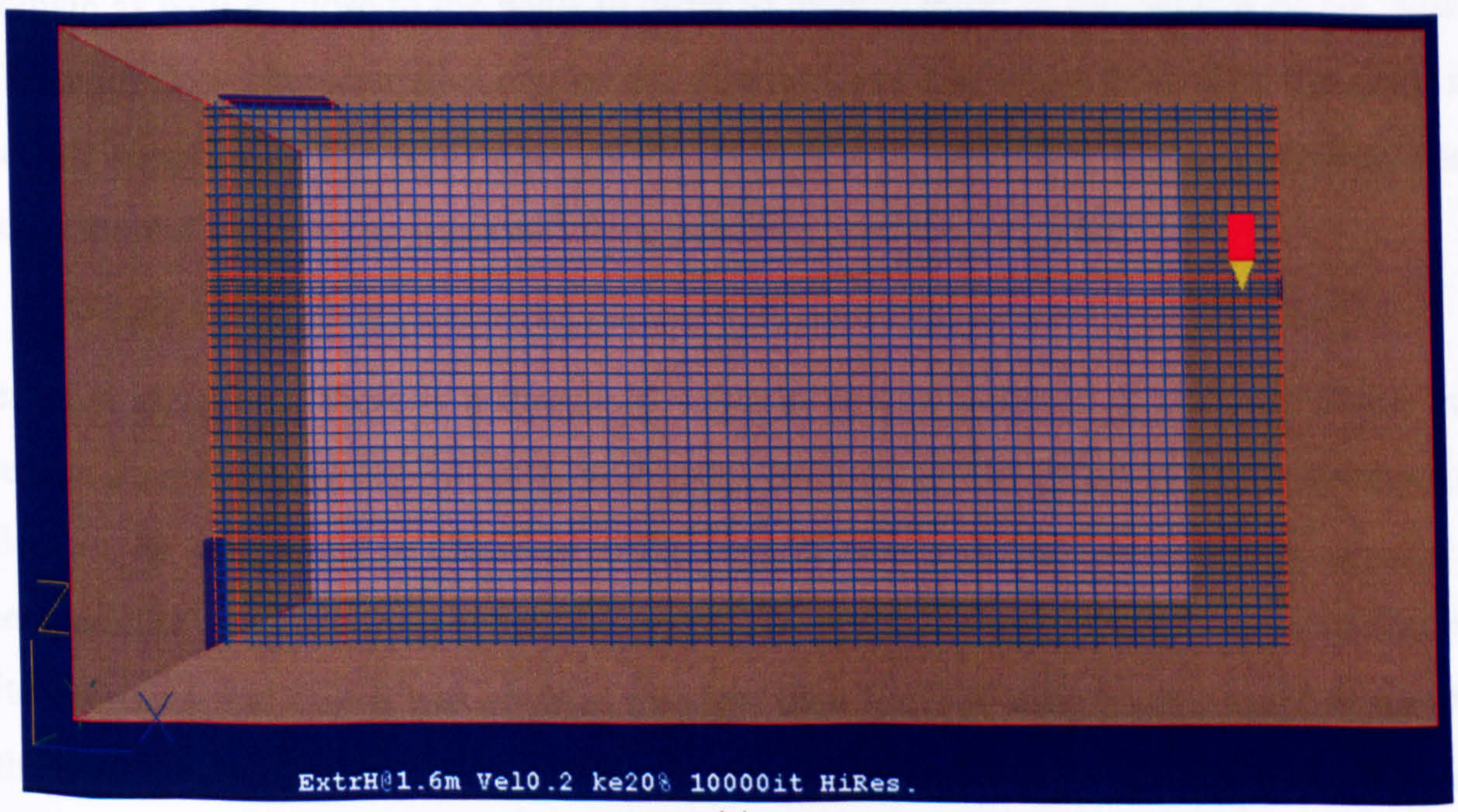

(a)

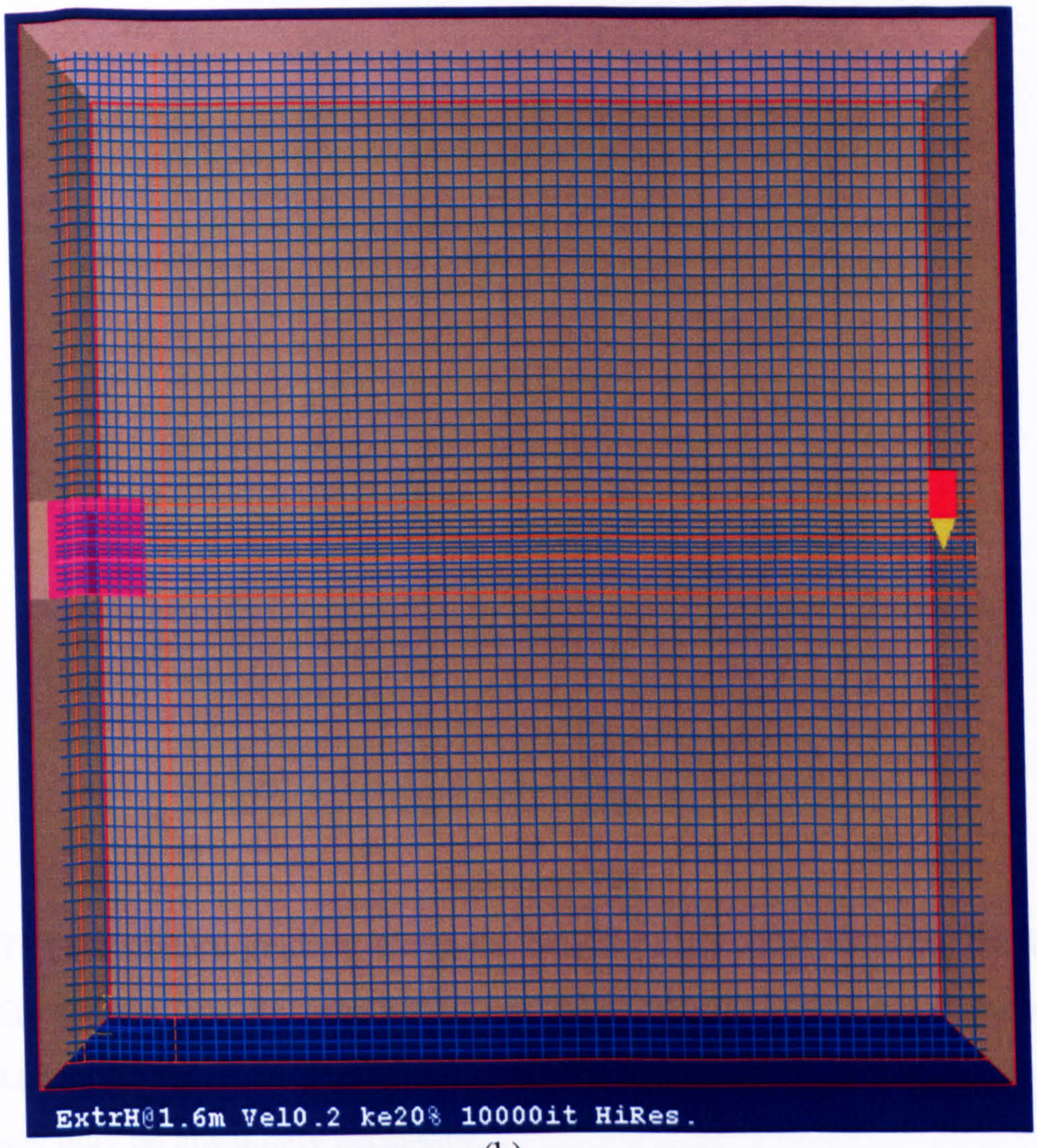

(b)

Figure 4.26: 60 × 74 × 51= 226,440 cells.

Higher grid refinement is used closer to the inlets and outlet of the computational domain as well as close to the walls in order to resolve more of the physics of the flow. The main flow characteristics can be the mixing layer due to jet flow after the cold or hot air supplies or the equivalent of the extract sink, boundary layer separation and reattachment close to the walls and the mixing layer of the interface.

In most situations, there is a threshold value at certain number of cells, at which the results do not change significantly with extra resolution. The effect of mesh density for the low Re case could be observed in Figure 4.27 which shows a comparison between a temperature gradient from a simulation of 100,000 cells and 200,000 cells at 10,000 iterations. In that case it was obvious that less than 100,000 cells were needed to signify the optimum number of cells for the low Re case of this work. The effect of optimum mesh density for medium Re case may be observed at about 130,000 cells.

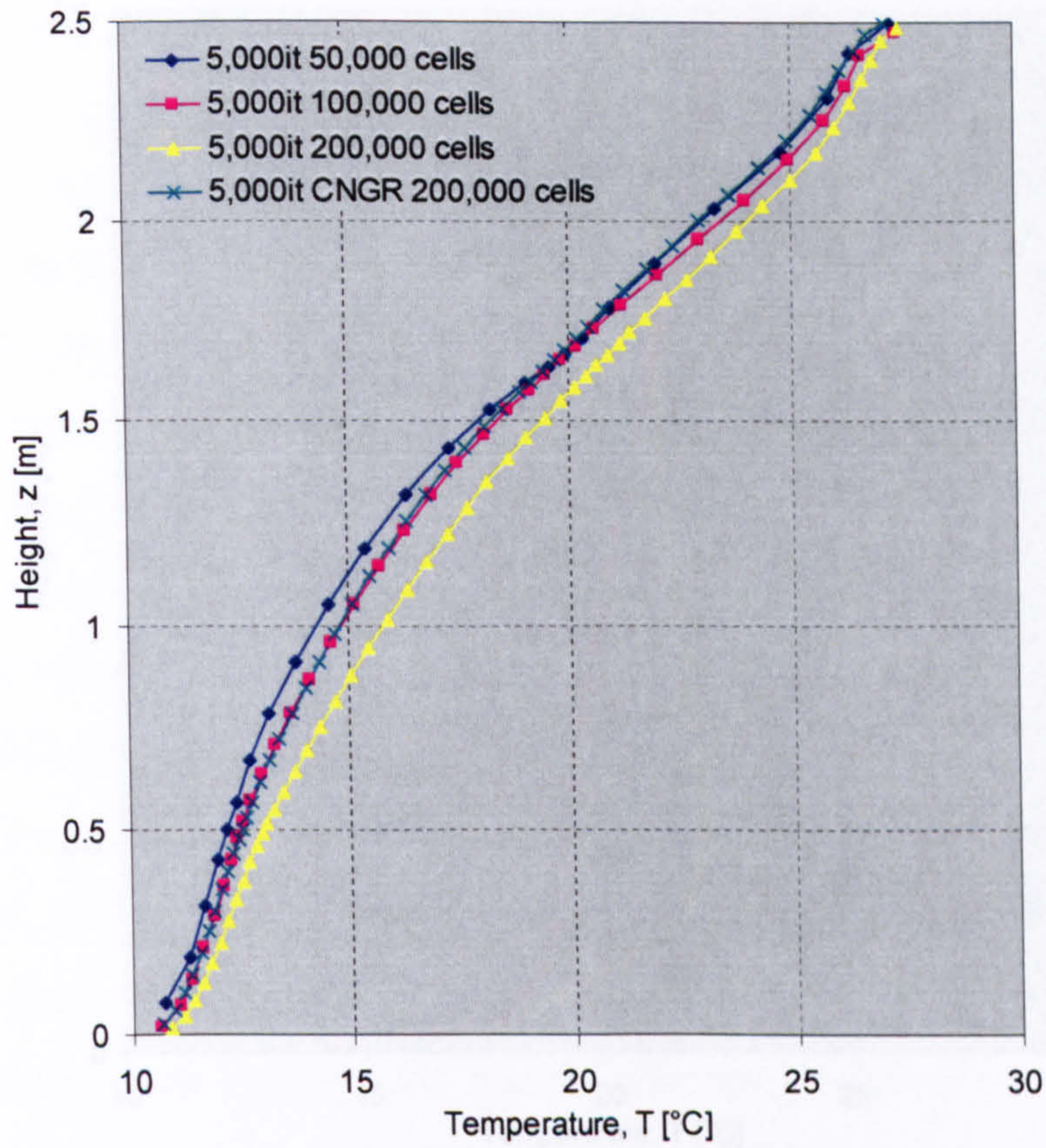

Figure 4.27: Temperature gradient along the height of the room showing the effect of mesh density for the low *Re* case bearing an inlet velocity of 0.2 m/s, flow rates are $Q_{CS,HS}$ = 0.05 m^3/s. As mesh density increases the inclusion of the conjugate gradient (CGR) solver may be absolutely necessary.

However in the high *Re* case, improved results were obtained by increasing the number of cells up to 200,000 cells as it can be seen in Figure 4.28.

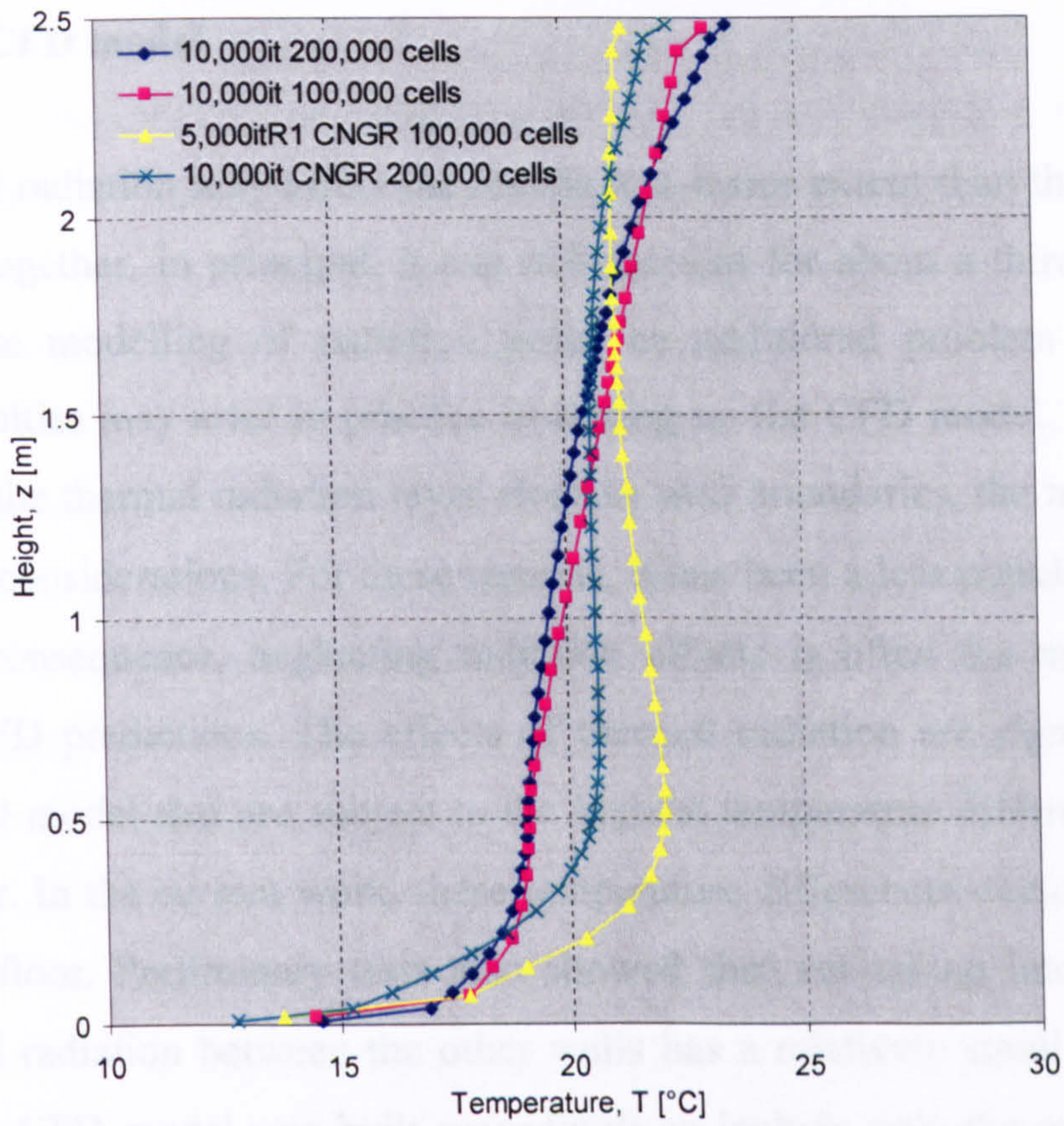

Figure 4.28: Temperature gradient along the height of the room showing the effect of mesh density for the high *Re* case bearing an inlet velocity of 1.6 m/s, flow rates are $Q_{CS,HS}$ = 0.4 m^3/s. The first two curves are of different mesh densities and they do not fully converge even at 10,000 iterations unlike the other two that use the CGR solver.

It can be observed in Figure 4.28 that the higher mesh resolution of 200,000 may be required for the high *Re* case.

4.2.5 Virtual CFD model

Experimental work often runs in parallel with a range parametric tests using CFD that although may embrace the entire range of parameters, on the other hand, direct comparison may be difficult due to the approximations in the geometry and boundary conditions of the CFD model and the tolerances obtained by the manufacturer or experimental inaccuracies. The conditions need to be set as accurate as possible in the CFD model, in order to obtain a direct comparison with the experiments. The virtual CFD model has adopted more appropriately the boundary conditions.

4.2.6 Radiation CFD model

Although thermal radiation may affect the results to a lesser extent than the convection and conduction together, in principal, it can still account for about a third of the total heat transfer. The modelling of radiation poses an additional problem to solve. A number of difficulties may arise in practice in setting up the CFD model, for example, how to consider the thermal radiation layer close to wall boundaries, the mesh size and other theoretical considerations. For these reasons, it has been a less popular subject for research. As a consequence, neglecting radiation effects is often the main cause of inaccuracy in CFD predictions. The effects of thermal radiation are significant at the walls of the CFD model that are subject to the highest temperature differences and are facing each other. In the current work, these temperature differences occur between the ceiling and the floor. Preliminary tests also showed that not taking into account the effect of thermal radiation between the other walls has a relatively small effect on the results. Thus the CFD model was built accordingly to include only the most important surfaces that are affected by thermal radiation, as shown in Figure 4.29,

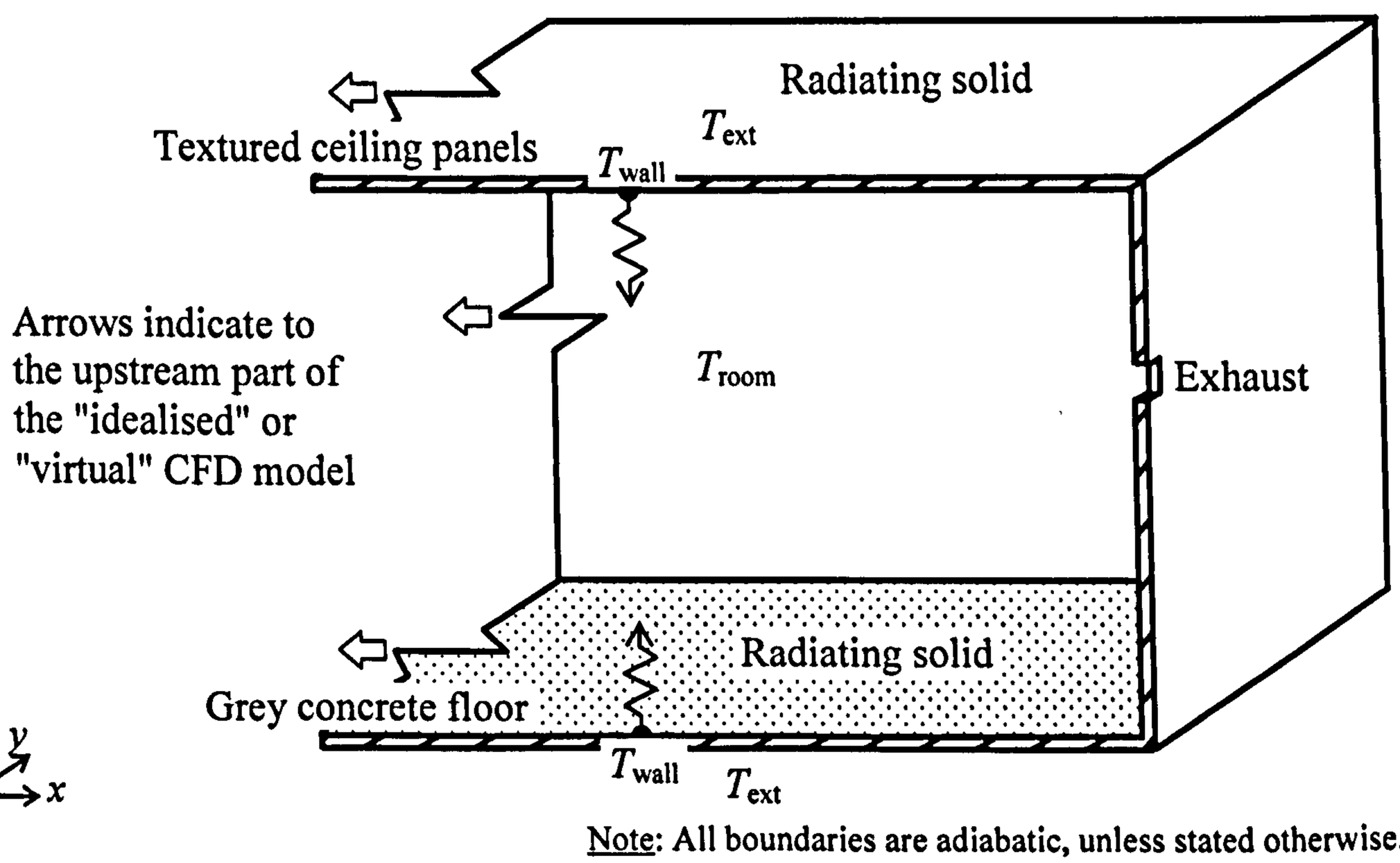

Figure 4.29: A cross-sectional geometry applied to the thermal radiation CFD models.

The two plates top and bottom influence each other in simple terms by a conduction equation. The three modes of heat transfer are in general about a third each and they all should be included for the calculation of the total temperature of the solid, T_3. This

becomes an even more complex task when taking into account that radiation needs to be based on rigorous theoretical considerations and that should require relatively small computer resources. The value of the emission and absorption coefficients of the solids is difficult to be known with high precision and there may be small wavelength dependencies that are difficult to consider very accurately.

The IMMERSOL radiation model in PHOENICS was introduced by Spalding (1996), it is a step closer to the complex physics occurring in a real problem and its predictions so far have been of the right order of magnitude. It is superior to other methods more empirical in essence, such as buoyancy modifications that are made to prescribe the level of buoyancy in the solution to achieve a good comparison with the experimental observation and still need further testing and validation. IMMERSOL model is an extension of previous radiation models in PHOENICS to account more accurately for additional modes of heat transfer besides radiation. Hence, IMMERSOL considers a more appropriate balanced system. In addition to radiation between solid and fluid phases, conduction in the solid phases and convection in the fluid phases affect each other at the interfaces between solids and fluids. This problem is known as "conjugate heat transfer" as it can handle heat conduction within large immersed solids in fluids and two-phase flow with additional suspended solid particle phases within the flowing medium. In convection and conduction, the mean free path is of the size of the molecules that is easy to apply in CFD as it is of the order of the mesh size. On the contrary, thermal radiation can travel much larger distances and thus the mean free path is inversely proportional to the amount of radiation-absorbing material per unit of path length. However, because the processes of thermal radiation occur between particles or surfaces, radiation can be regarded as similar to conduction with an increased thermal conductivity that can occur either between particles or surfaces. The magnitude of the radiative conductivity can be calculated by differentiating the radiosity equation that turns out to be of the order of $\sigma \times T^3/(a+s)$, where a is the absorptivity of the fluid and s is the scattering coefficient of the fluid in dimensions of m^{-1}. For practical reasons, air is regarded as a transparent medium and does not participate in the radiation process in the current work, as there are no solid particles considered in the air medium. EMISS is used for non-transparent solid such as surfaces, which is the same as the absorption coefficient in the solid and is dimensionless. The contribution of the radiative temperature, T_3, is solved by rearranging the radiosity equation for T_3 that can be solved

numerically instead of E_3. Hence, further away from the solid boundary, T_3 does not affect the fluid space, but the opposite surface by a conduction equation that accounts for the local radiosity term,

$$T_3 = \left(\frac{E_3}{\sigma}\right)^{1/4} \tag{4.4}$$

within the space of the solid phases a differential equation is solved for E_3,

$$\frac{\partial}{\partial x_j}\left[\gamma\left(u\frac{\partial E_3}{\partial x_i} + v\frac{\partial E_3}{\partial x_j}\right)\right] = (\alpha_1 + s_1)\times(E_1 - \sigma T_3^4) + (\alpha_2 + s_2)\times(E_2 - \sigma T_3^4) \tag{4.5}$$

where the conductivity term is:

$$\gamma = \frac{4}{3}\frac{1}{\left(a + s + \frac{1}{\mathrm{WGAP}}\right)}, \tag{4.6}$$

E_1 and E_2 stand for the face-surface average radiosity of $\sigma \times T_1^4$, $\sigma \times T_2^4$ that are not present in the current work (where T_1 is TEM1 in the current work and T_2 is not specified) and,

$$c\frac{dT_3}{dt} - \frac{\partial}{\partial x_j}\left[\lambda\left(\frac{\partial T_3}{\partial x_i} + \frac{\partial T_3}{\partial x_j}\right)\right] = q_{solid} \tag{4.7}$$

where c is the specific heat capacity of the solid, λ is the thermal conductivity and q_{solid} is the heat source per unit volume.

Between-solids spaces, a differential equation is solved for the radiative temperature (solid-phase temperature), T_3,

$$\frac{\partial}{\partial x_j}\left[\lambda\left(u\frac{\partial T_3}{\partial x_i} + v\frac{\partial T_3}{\partial x_j}\right)\right] = (\alpha_1 + s_1)\times(E_1 - \sigma T_3^4) + (\alpha_2 + s_2)\times(E_2 - \sigma T_3^4) \tag{4.8}$$

where the radiative conductivity is:

$$\lambda = \frac{16}{3}\frac{\sigma T_3^3}{\left(\alpha + s + \frac{1}{\mathrm{WGAP}}\right)}. \tag{4.9}$$

For practical purposes, every grid point needs to be assigned the wall distances that are used to add up the contributions from nearer and more remote locations. The distance between a grid point and the nearest wall, WDIS, and the gaps between the nearest bounding walls, WGAP, are based on the length-scale (LTLS) equation, Agonafer *et al.* (1996). These are obtained by a search procedure to calculate the wall distances for each grid point from the nearest wall using a differential equation prior to the simulation. The introduction of WGAP term into the radiation-conductivity term ($a + s + 1$ / WGAP) connects the radiation between intervening fluid spaces and the conduction between the immersed solids. The reciprocal of WGAP is much larger than a and s but also ensures that the conductivity will never become infinite as the sum will never be zero. In this work, the absorption and scattering coefficients of the fluid a and s are zero since the fluid medium does not participate in the radiation process and the parameter EMISS influences only the radiating solids. It is also supported that WGAP gives the correct prediction for general cases such as flow between wide parallel plates.

Adiabatic settings on the external part of the upper and lower walls will actually result in zero fluxes to the wall for each of T_3 and TEM1 individually, which is stronger than one might want. The energy balance at the wall needs to account for parameters that have a significant contribution in the heat flux across the wall. When the wall is bounded on the one end by the fluid and the other end by the edge of the domain, the temperature in the solid phase is considered by a heat balance for a shell type of wall subject to external heat flux, q_{wall}, by defining the wall as a "radiating solid". This is specified by the following formula,

$$q_{\mathrm{wall}} = a + b\left(T_{\mathrm{ext}} + T_{\mathrm{wall}}\right)^c + d\left(T_{\mathrm{ext}}^4 - T_{\mathrm{wall}}^4\right) \tag{4.10}$$

where by default, $a = b = c = 0$, i.e., the solid surface is adiabatic, $d = 1$ and $T_{\mathrm{ext}} = 300$ K. The coefficients can be specified in the appropriate way that will most realistically link the external temperature, T_{ext}, to the wall temperature, T_{wall}, that PHOENICS will

calculate from an energy balance. The current settings are specified for T_{ext} = 0 K to allow for the calculation of the connective heat transfer on either side of the wall. However, the specification of a small heat flux, a = 1.0E-6 produces a negligible contribution to the heat balance from the external convection. The plate temperature is linked to the in-cell values TEM1 and T_3 in the appropriate way. Hence the influence of the convective heat transfer on the inner part of the solid and radiative heat exchange with the opposite solid are solved adjacent to each of the walls. Thus the heat source will be split between convection, diffusion and radiation or conduction if the plate is adjacent to other solid cells. There are two main conditions consider here,

1) the external influence affects the mean room temperature, so that $T_{ext} = T_{room}$, and
2) the two solids influence each other.

The wall temperature is solved at the first cell adjacent to the wall. In reality, T_{room} actually tends to T_{ext} because they influence each other due to heat and mass losses, but not yet here. This CFD model solves for radiation exchange between the plates and for heat loss across the plates by considering each time the resulting mean temperature in the room. The external temperature is linked later in the air-leakage CFD model as the additional openings are assigned the average value of the temperatures inside the laboratory room to establish the correct effect from the outside temperature. This is approximately equal to an average of 18°C by considering most of the experimental cases here. The additional openings were also evident in the real room in the experimental work and were located in the rear-wall.

4.2.7 Air-leakage CFD model

Air leakage through cracks and openings is present in every building and the calculation of the flow rates has attracted a lot of attention. The flow rate through the cracks is very difficult to be determined because of the non-linear shape and velocity of the cracks and openings. Air from the inside of the building can leak to the outside or the opposite, depending on the pressure and temperature differential between inside and outside. The leakage characteristics of the room under investigation were simulated by adding a pair of linear openings as outlets to the adjusted model as shown in Figure 4.30,

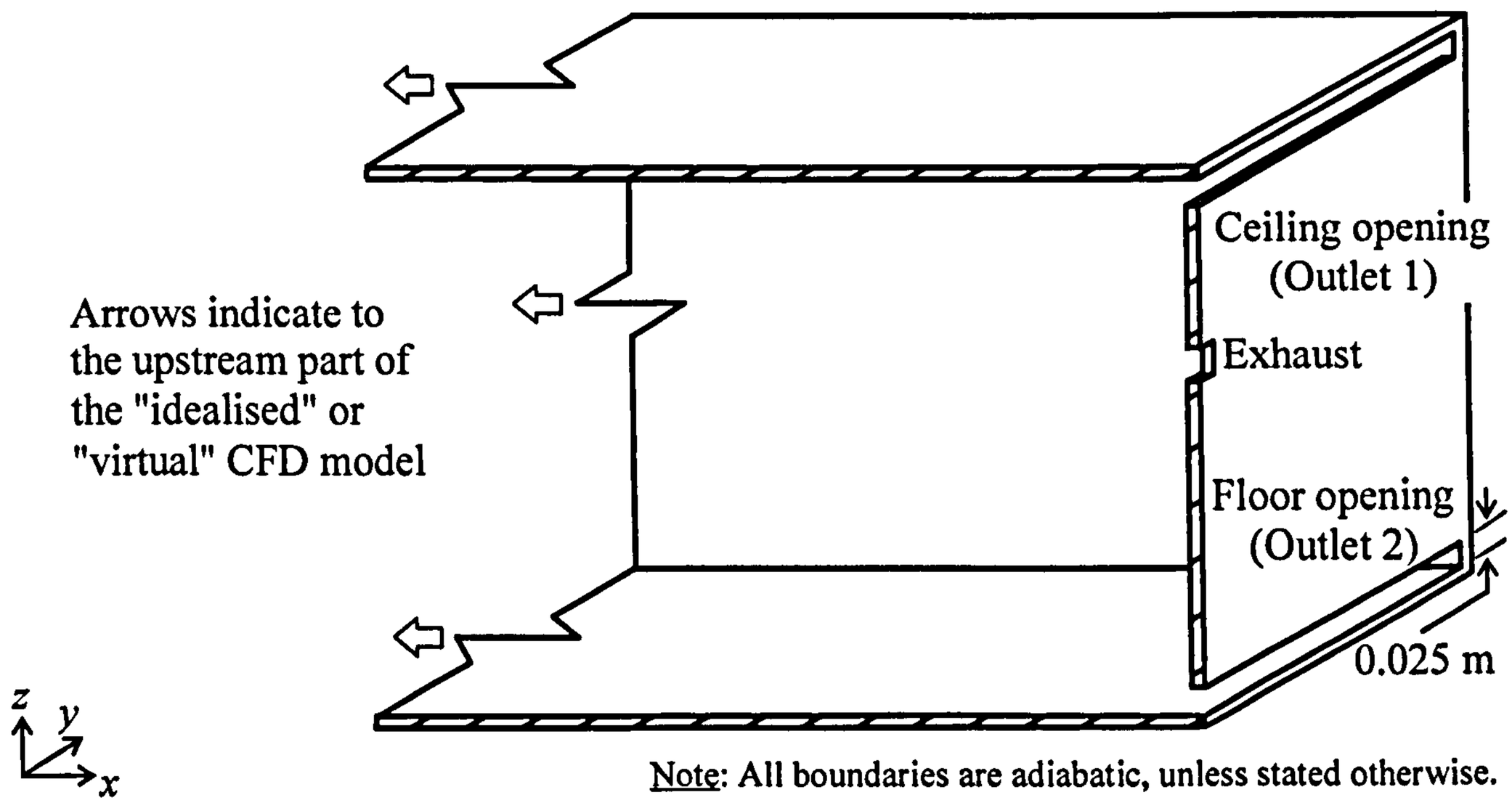

Figure 4.30: A cross-sectional geometry applied to the air-leakage CFD models with outlets to the outside for simulating the effect of air infiltration in the room.

Both openings represent the area of the gaps between the Styrofoam panels and robotic arm rails on the floor and the gaps between Styrofoam panels and duct connections in the access panels and above the rear wall. Other models have included square and rectangular openings of approximately the same area in the middle of the ones shown in Figure 4.30. The results were similar and small differences occurred due to the actual shape of the ceiling openings could not be exactly determined. The flow characteristics of openings follow a power law. This model, however, was used successfully as the CFD model to make a very close estimation of the effect of leakage on the temperature distribution obtained in the experiments as opposed to results obtained with a 100% air-tight room. The air on the other side of the rear wall was taken to be equal to the laboratory temperature that was measured by the thermometer outside the Test Chamber in all of the experimental cases. The default values were used for pressure as provided by default in PHOENICS, p = 1 At, on the other side of the openings.

4.3 Test Series

The low and high *Re* cases in this work are obtained by changing the speed of the hot air supply, which mainly aimed to establish a link between stratification strength and

input momentum. This was tested by making incremental changes to the hot air supply, while the cold air supply was maintained constant.

4.3.1 Test Series I: Experiments

There are three experimental sets of results. Two of the experiments are approximately the same range of temperatures and low flow rates and one with slightly higher incremental changes of hot air supply and final flow rate to full mixing. The hot air supply flow rates are in the range of 0.03 - 0.17 m^3/s and the cold air supply is 0.03 and 0.06 m^3/s depending on either low or high *Re* cases.

4.3.2 Test Series II: CFD simulations

The CFD investigation is carried out for two main types of CFD models. The virtual model is used to make a better comparison with the experimental measurements as the boundary conditions are more accurate, mainly for a hot air supply flow rate of slightly over than 0.06 m^3/s and a cold air supply flow rate of 0.03 m^3/s. The effect of radiation, air leakage and the influence of inlet diffuser have been tested by using this configuration. The idealised model is used to carry out more parametric tests for hot air supply flow rates 0.02 - 0.2 m^3/s to show full mixing. The effect of radiation has also been tested using this model. The effect of extract height was also tested using this model.

4.4 Program developed for the Analysis of Results

The CFD results are analysed by a software program developed by the author to handle a number of values from different files for comparison with other simulations. The data analysis program is written in Matlab language and it is included in the Appendix D.

The first part of the program reads in the PHOENICS results, i.e., files with "*.phi" extension, and stores it in a 3-dimensional array. In the second part, the coordinates of the line plots need to be specified and the results are finally arranged in text format in a data-file with "*.xls" extension. A batch file runs this program that reads through a

number of specified "*.phi" files processes the data in the files to return the required values at the specified locations of the three data-stations in the middle space of the room for each of the variables. These values are then linked to a programmed *Excel* file, where predefined line-plots are created in different *Excel*-sheets for velocity, temperature, pressure, kinetic energy and dissipation to compare with other simulations at the same locations.

5. RESULTS

Introduction

Numerical and experimental results are presented in this chapter. The main aim of this chapter is to show how well the results demonstrate the physical mechanisms of different flow regimes present in ventilation flows that lead to the understanding of thermal stratification and to identify appropriate influencing parameters to run further tests. The experimental model and the numerical model are very similar in most respects. The first part of this chapter deals with CFD results, whilst the second part deals with the experimental results.

5.1 Overview of CFD Results

A large number of simulations were carried out. These were performed for obtaining comparison with experiments in studying the effects of inlet velocity and temperature, and investigating certain issues involved when performing a numerical simulation.

The main purpose of the CFD studies is to investigate the effect that the inlet variables such as:

- Temperature
- Velocity/flow rate
- Inlet size
- Radiation
- Leakage

have on the stratification within the test model. However, to ensure that the results from the CFD studies are reliable, numerical and turbulence issues were also necessary to consider. The results from that part of the investigation are shown in Chapter 4 section 4.2.

5.1.1 CFD simulations: Physical Issues (Test Series II)

The second series of tests comprises of the main simulations that take into consideration the effects of inlet parameters and physical phenomena involved in the test cases and comparing the CFD results with the experimental results. As part of modelling the physics correctly on the numerical grid, different turbulence models were employed in modelling turbulence in ventilation flows for a range of Reynolds numbers. The effect of increasing inlet momentum, while the temperature gradient increased proportionally was also studied. Increasing the inlet momentum of both supplies equivalently identified the limits where the formation and break-up of stratification occurred. Starting from very low values, the convective heat transfer effects prevail compared to the radiative heat transfer to a value where mixing would occur in the entire room. The effect of increasing the inlet momentum by unequal amounts was investigated, in order to study the result that this parameter has on the thickness of the layers and the height interface. The effect of varying the inlet temperature difference and the effect of modelling radiation on the temperature gradient were also studied. The effect of boundary conditions that affect the physics of flows can be misrepresented by idealising the model; such effects may include leakages, directional effects from the diffusers as well as the geometry of the diffusers. These variations are summarised below,

Main Tests:

1. Exhaust height
2. Momentum
3. Inlet temperature difference
4. Radiation effects

Tests for realistic boundary conditions:

5. Leakages
6. Directional effects from hot air diffuser
7. Effect of detail geometry of hot air diffuser
8. Effect of detail geometry of cold air diffuser
9. Wall effects close to hot air diffuser
10. Draught versus position of the hot air supply

5.2 Numerical Issues

To evaluate the accuracy of the CFD simulations, the results obtained by the computational calculations should be monitored at the locations of interest inside the test model and compared for convergence and optimum number of cells. Three locations were chosen in the domain as shown in Figure 5.1. However, only the temperature gradients obtained in the middle of the room were shown, because similar changes were obtained for the other two locations, for the same number of iterations. Comparing for mesh density also looked at the changes in the temperature gradient in the middle of the test model. Turbulence and unsteadiness in the flow may differ with flow situations. This was studied in the test models of equal momentum change where the inlet flow rate was equally increased for both cold and hot air supply, and for the inlet side length of $a_{CS,HS}$ = 0.5 m. A corresponding laminar case by not using any turbulence model in the lowest Re case of 6,000 was also expected to be less computationally intensive compared to the highest Re case of 50,000 where there is more turbulence generation. Thus for the range of test cases in the current work, comparisons of temperature gradients for convergence and mesh density were carried out appropriately in Chapter 4 section 4.2 in terms of a range of inlet Re. Appropriate Re values were used to denote the low, medium and high Re cases in this work. Further tests were then carried out by changing only the hot air supply flow rate for an inlet side length of a_{HS} = 0.25 m, starting with a lowest Re of 4,000 up to a highest Re of 40,000. The effects due to modelling turbulence are discussed in concert with physical issues in the following sections.

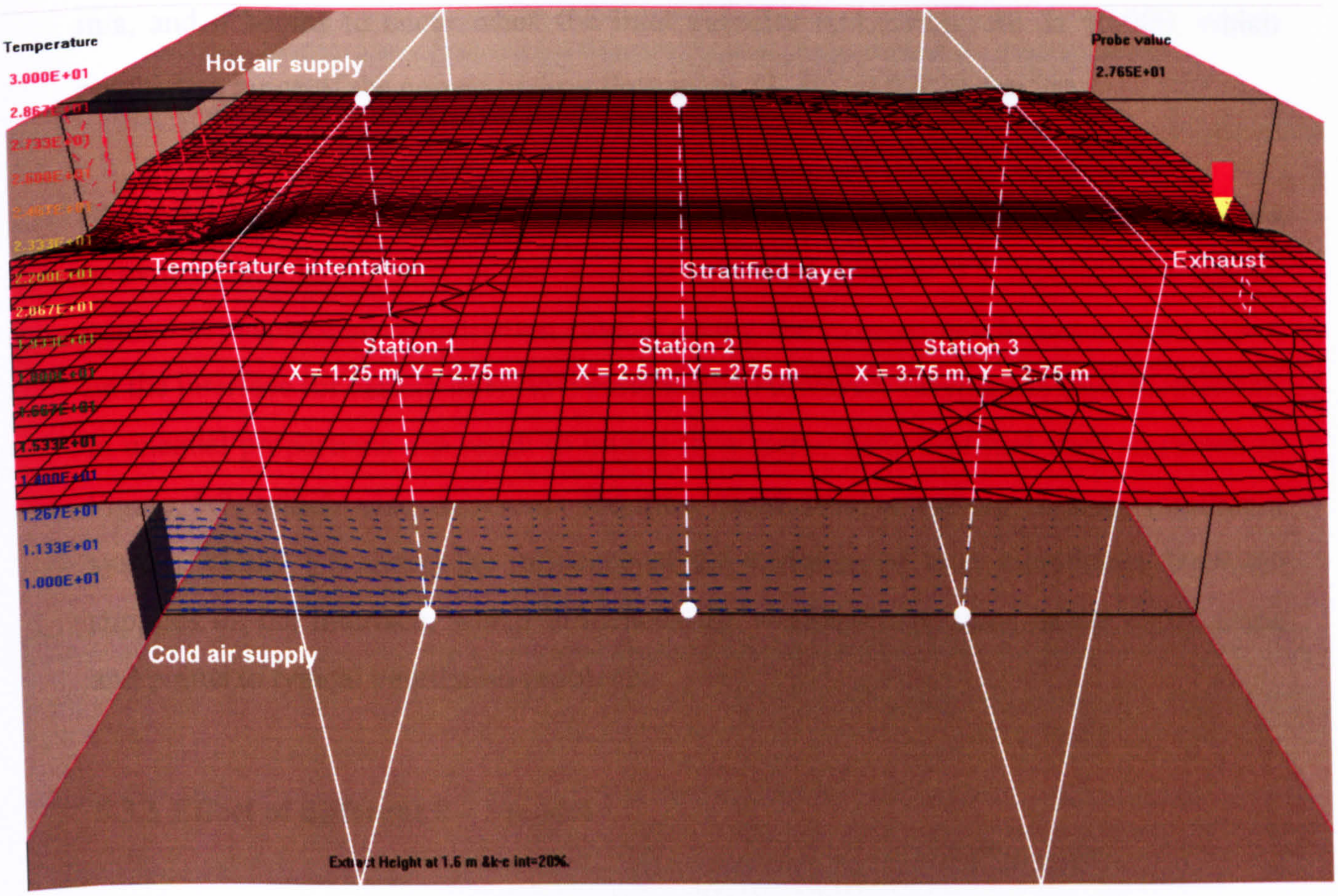

Figure 5.1: The temperature isosurface plot shows a single temperature layer and several flow patterns occurring in the simulation where the inlet velocities used are U_{in} = 0.2 m/s and ΔT_{in} = 20°C. Three data-stations are also shown which were set for obtaining and analysing results. The results were obtained by CFD using PHOENICS.

5.3 CFD Results and related Physical Issues

All features of the flow can be qualitatively observed in Figure 5.1, Figure 5.5, Figure 5.7 and Figure 5.8. The flow at the supply can be characterized as turbulent while the flow in the middle of the room is fairly laminar where only low frequency velocity fluctuations can occur. Additionally in the current work, vortices formed in the corners opposite to the supplies can also be observed. Turbulence is inherent even at very low inlet supply velocities as low as 0.2 m/s, $Q_{CS,HS} = 0.05\,\mathrm{m^3/s}$. However, large circulations that occur inside the zones only have a local effect on mixing and thus stratified flow is not entirely affected. Full mixing becomes entirely evident in the high Re case of 50,000 and Ri_o below 1, where the inlet velocity of the hot air supply is 1.6

m/s, and it begins to occur when the inlet velocity is 1.2 m/s, Re is 40,000, which results to a range of the corresponding flow rates $Q_{CS,HS} = 0.3 - 0.4\,m^3/s$.

Figure 5.1 shows a typical case of ventilation where the development of stratified layers is evident, similar to most of the cases of this work. Figure 5.5 represents a typical natural or displacement ventilation case. Varying the exhaust height has a direct effect on the interface for certain inlet flow parameters. However, varying the inlet momentum in unequal proportions can result to mixed flow rather than stratified flow as shown in Figure 5.7, which case represents the flow field from a typical mixing ventilation system. Figure 5.8 shows the influence of the variation of inlet momentum from the supplies on the interface, which influences the ventilation patterns in the entire room and points to typical ventilation problems.

5.3.1 Effect of different $k-\varepsilon$ model

The standard $k-\varepsilon$ model has been used extensively in the modelling of buoyancy driven displacement ventilation flows by several researchers, for example, Gan and Awbi (1994), Cook and Lomas (1998), Papakonstantinou *et al.* (2000). It will be shown here that the results obtained by using the standard $k-\varepsilon$ model are very close to its improved modifications. Four different turbulence models were tested, the standard $k-\varepsilon$ model, the RNG model and the Chen-Kim model as well as a Low-Re modification of the Chen-Kim model. Additionally, a laminar case was also used to test the effect of not using a turbulence model, i.e., not solving for μ_t. The temperature gradients in Figure 5.2 (a), (b) and (c), the vertical disturbances in Figure 5.3 (a), (b) and (c), and turbulent kinetic energies in Figure 5.4 were obtained using the geometry of the idealised test model. These show the effect of mixing in thermally stratified flow. The supply momentum for cold and hot air was the same, bearing a velocity of 0.2, 0.8 and 1.6 m/s in each case, the corresponding flow rates are $Q_{CS,HS}$ = 0.05, 0.2 and 0.4 m³/s, while the inlet temperature was ΔT_{in} = 20°C and the radiation model or any heat losses were not included.

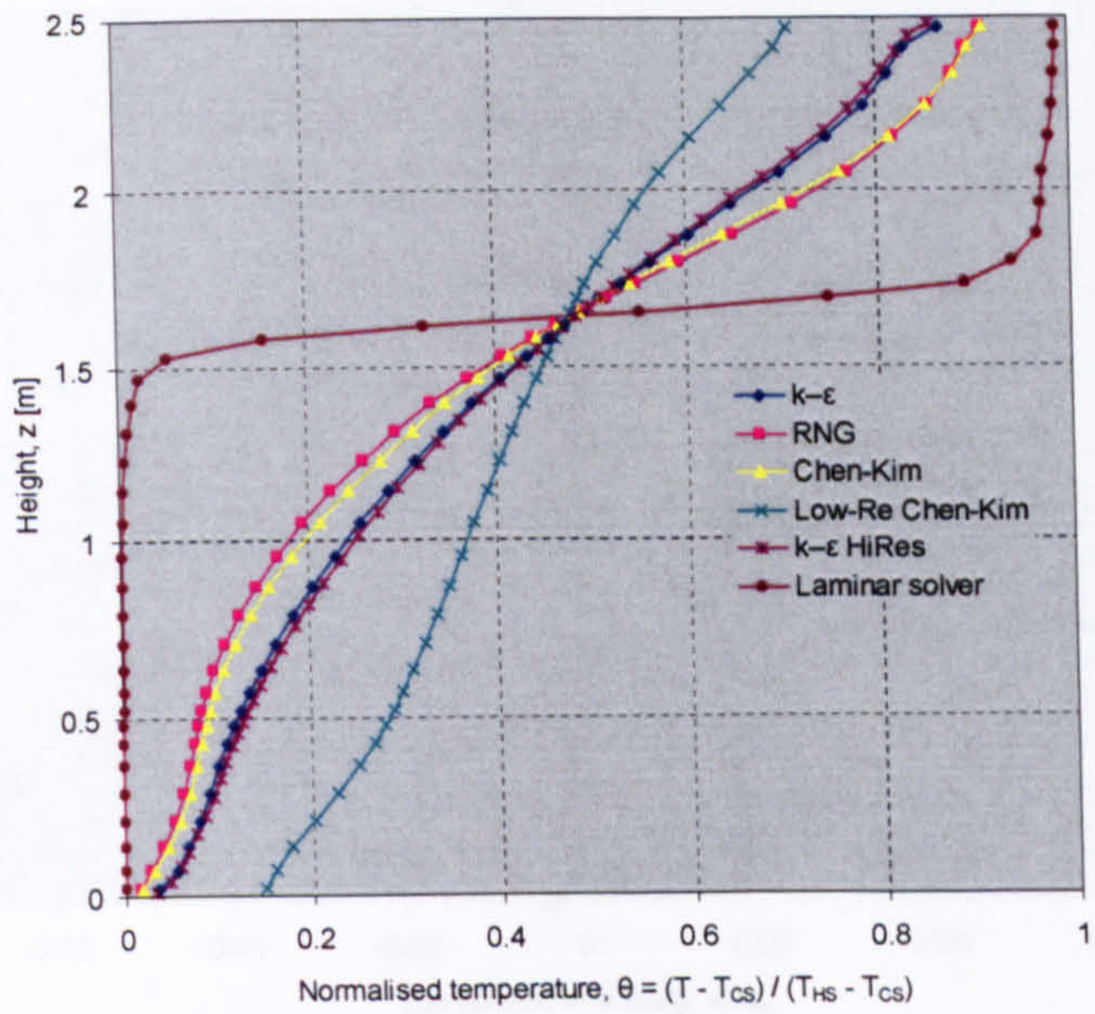

(a) U_{in} **= 0.2 m/s,** $Q_{CS,HS}$ **= 0.05 m³/s;** T_{CS} = 10°C, T_{HS} = 30°C; h_E = 1.6 m.

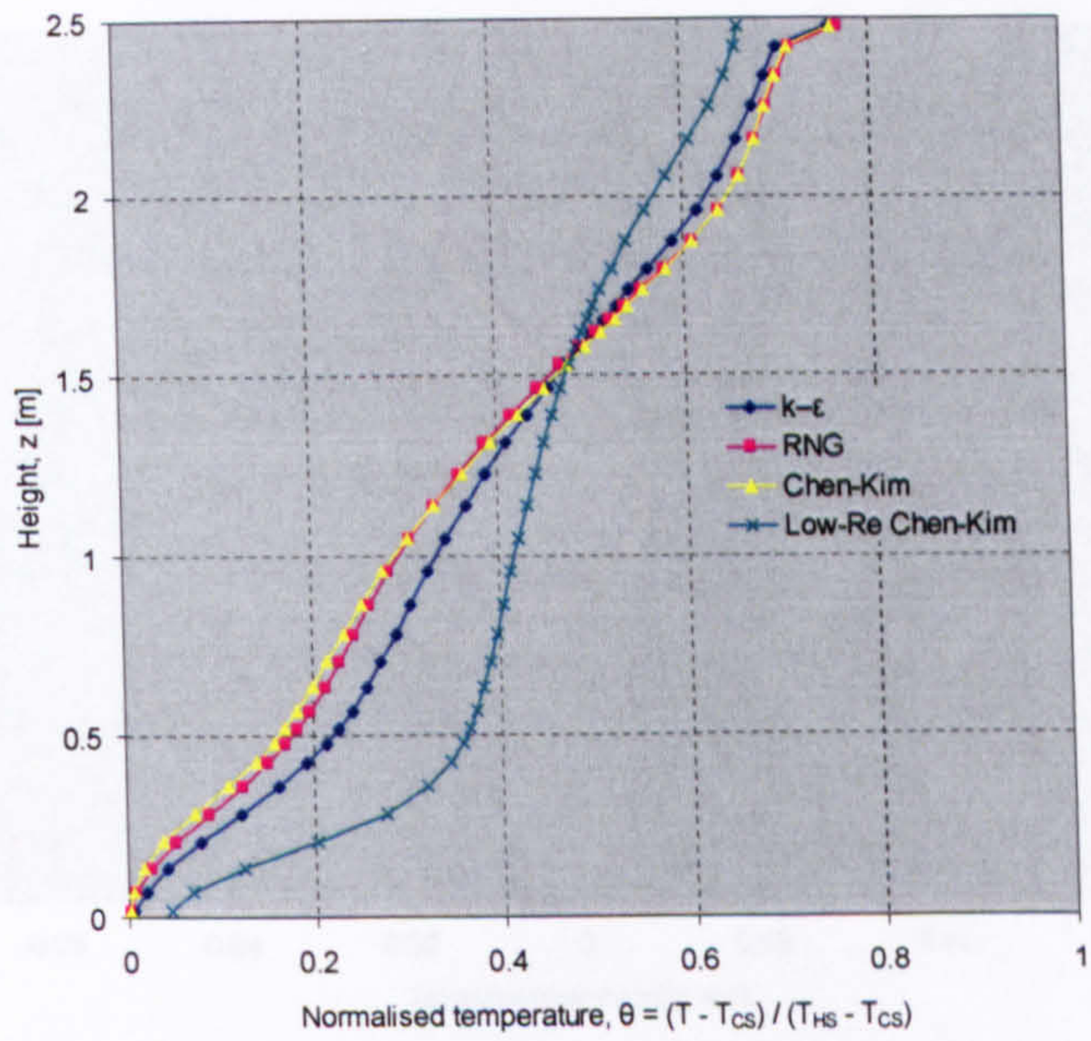

(b) U_{in} **= 0.8 m/s,** $Q_{CS,HS}$ **= 0.2 m³/s;** T_{CS} = 10°C, T_{HS} = 30°C; h_E = 1.6 m.

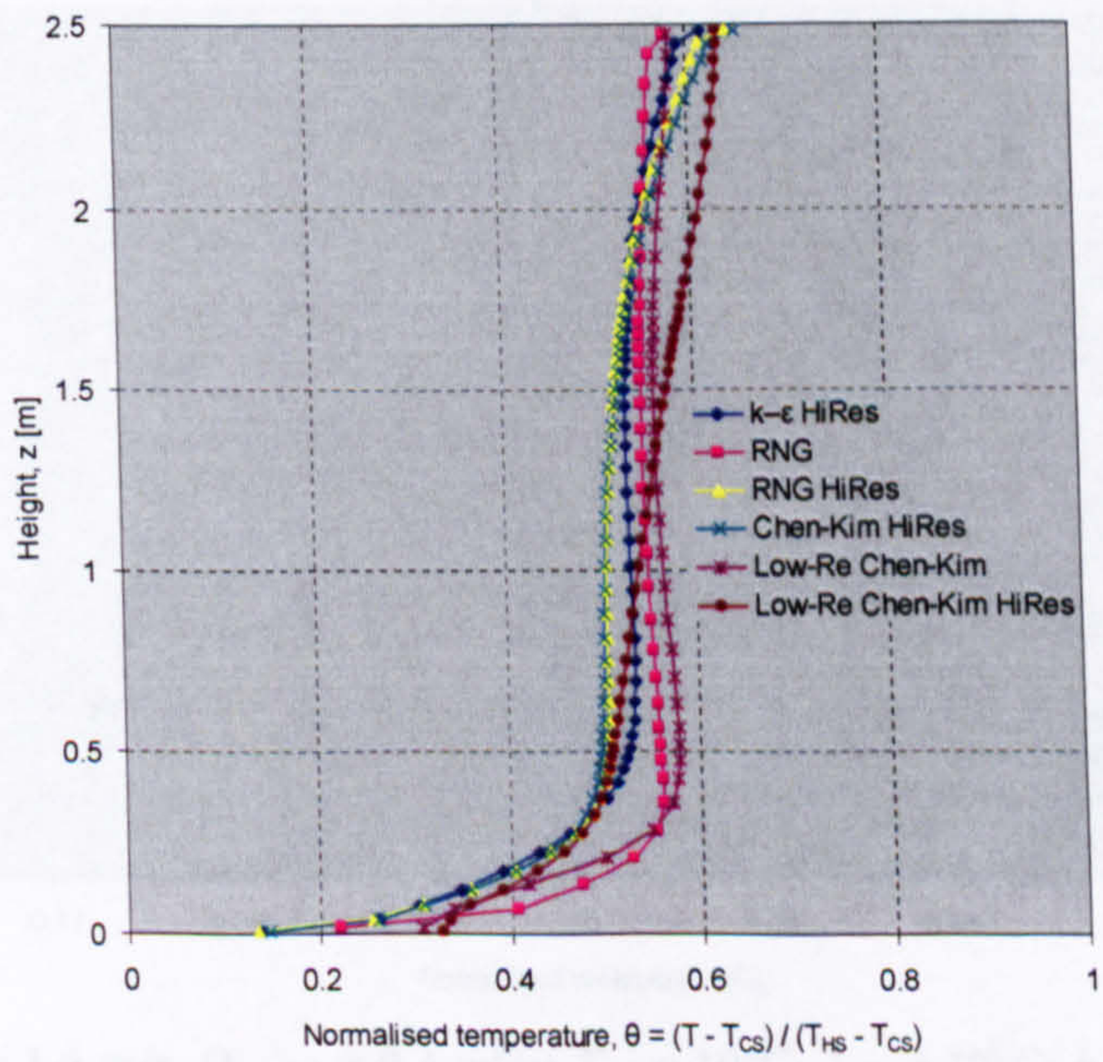

(c) U_{in} **= 1.6 m/s,** $Q_{CS,HS}$ **= 0.4 m³/s;** T_{CS} = 10°C, T_{HS} = 30°C; h_E = 1.6 m.

Figure 5.2: Normalised vertical temperature variation in the middle of the room model versus height.

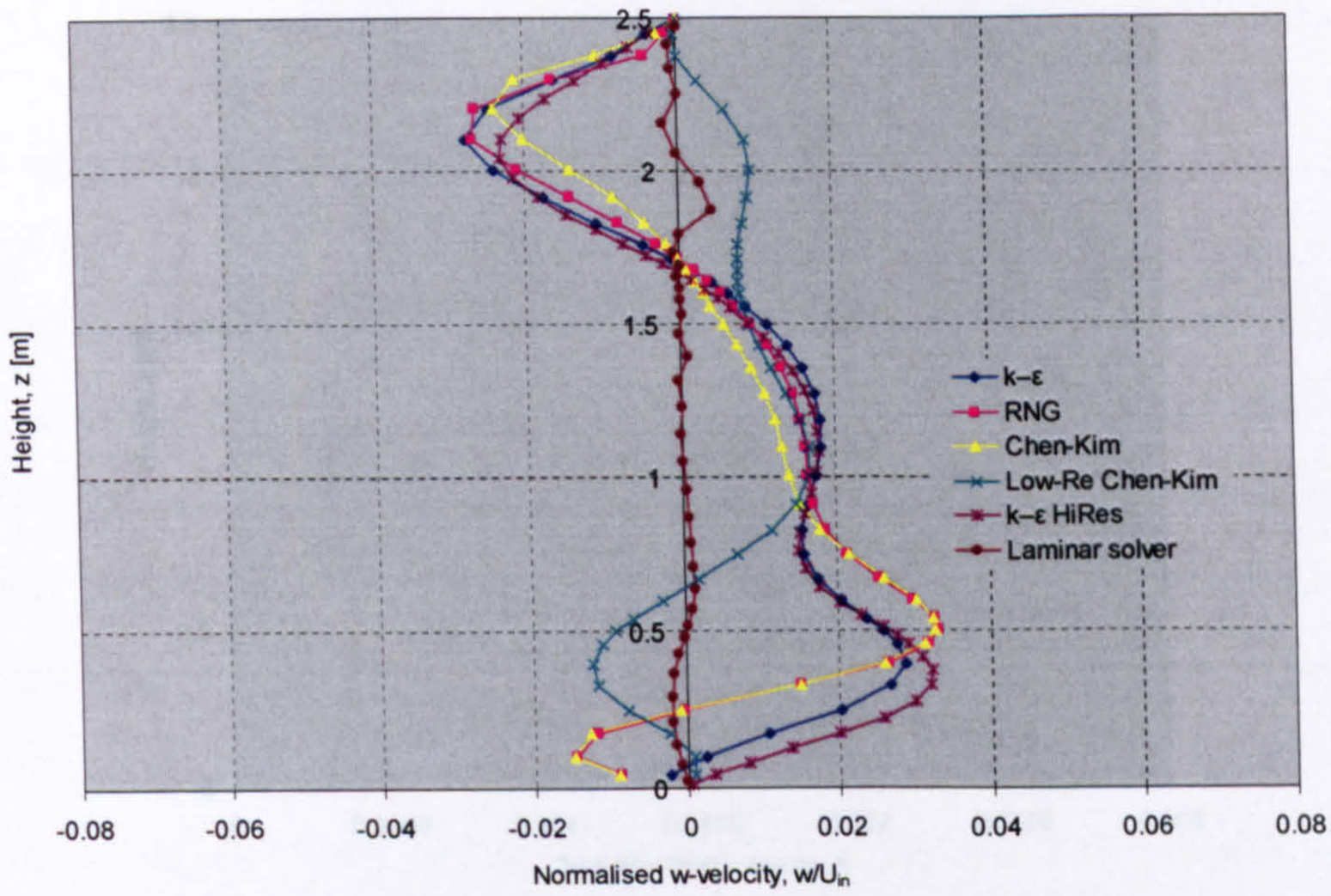

(a) U_{in} = **0.2 m/s,** $Q_{CS,HS}$ **= 0.05 m³/s;** T_{CS} = 10°C, T_{HS} = 30°C; h_E = 1.6 m.

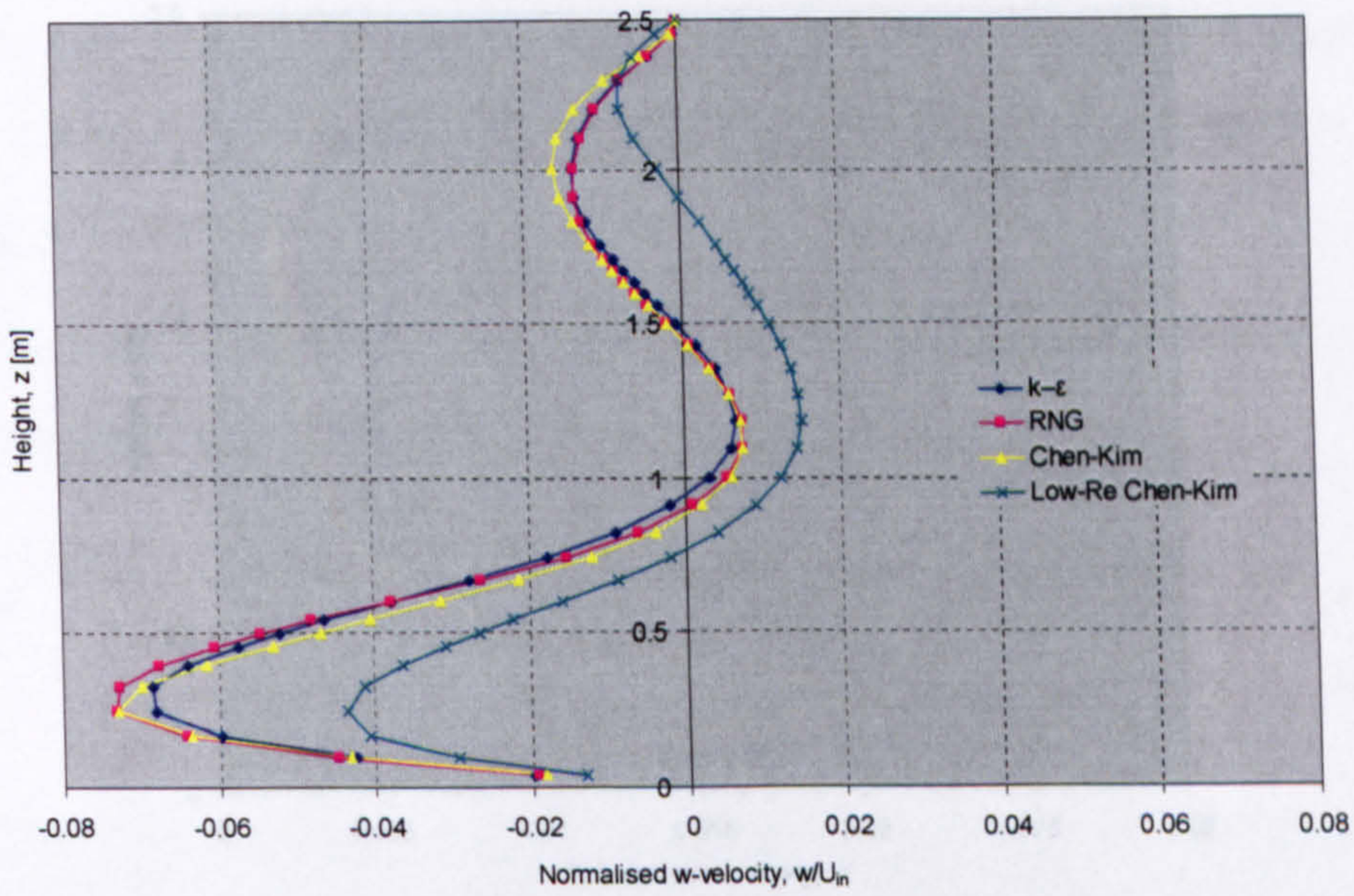

(b) U_{in} = **0.8 m/s,** $Q_{CS,HS}$ **= 0.2 m³/s;** T_{CS} = 10°C, T_{HS} = 30°C; h_E = 1.6 m.

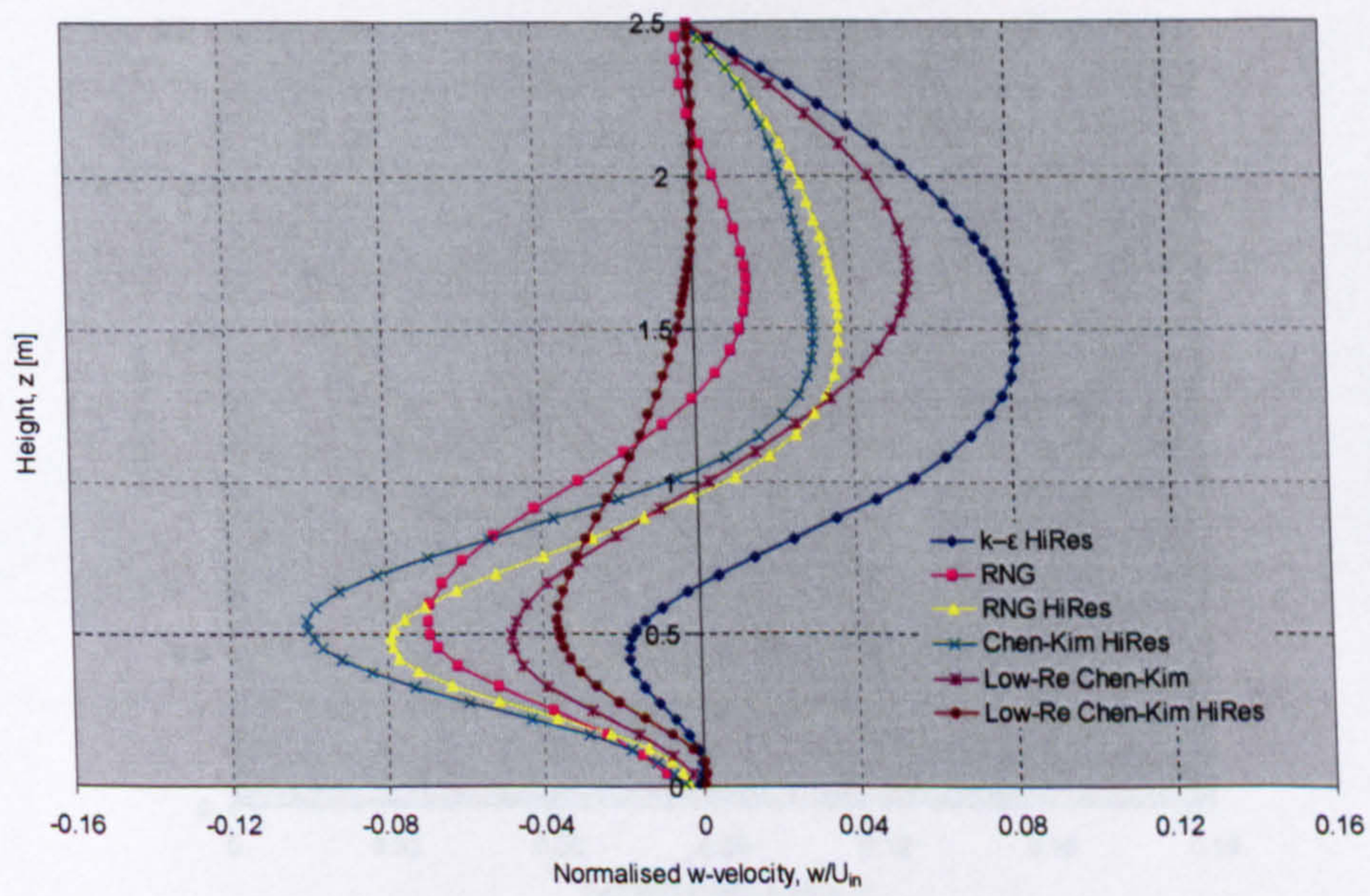

(c) U_{in} = **1.6 m/s,** $Q_{CS,HS}$ **= 0.4 m³/s;** T_{CS} = 10°C, T_{HS} = 30°C; h_E = 1.6 m.

Figure 5.3 Non-dimensional *w*-velocity variation in the middle of the room model versus height.

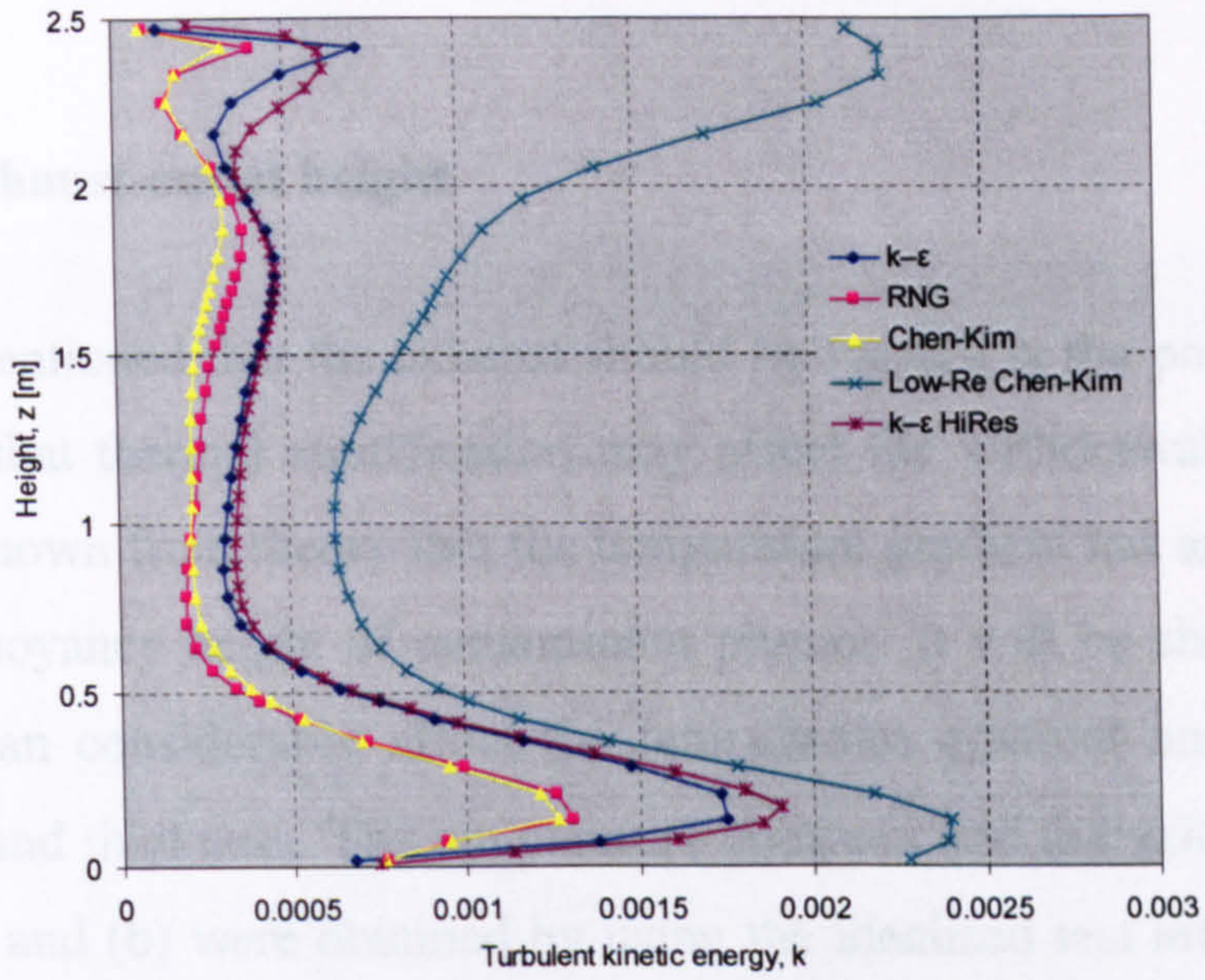

(d) U_{in} **= 0.2 m/s,** $Q_{CS,HS}$ **= 0.05 m³/s;** T_{CS} = 10°C, T_{HS} = 30°C; h_E = 1.6 m.

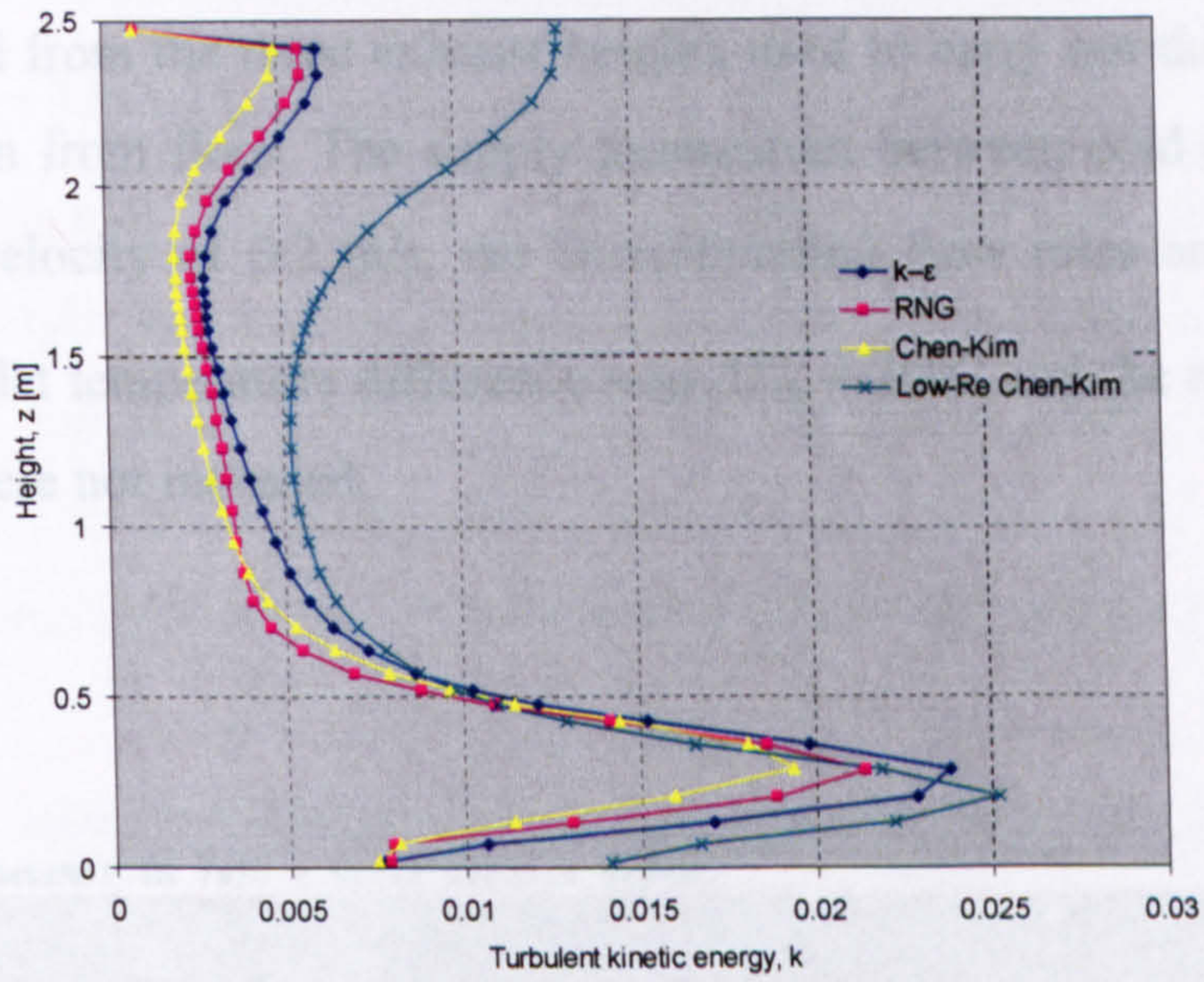

(e) U_{in} **= 0.8 m/s,** $Q_{CS,HS}$ **= 0.2 m³/s;** T_{CS} = 10°C, T_{HS} = 30°C; h_E = 1.6 m.

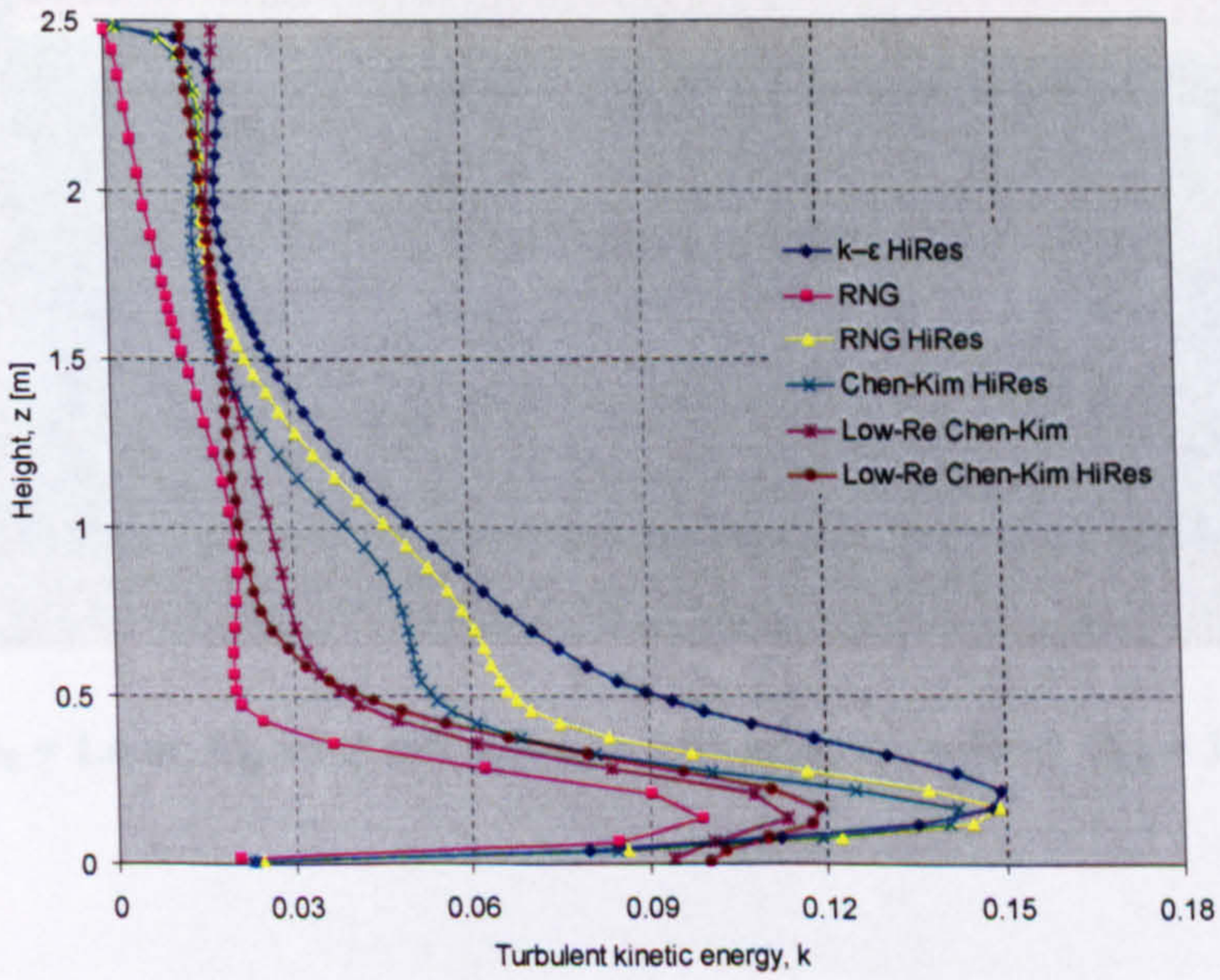

(f) U_{in} **= 1.6 m/s,** $Q_{CS,HS}$ **= 0.4 m³/s;** T_{CS} = 10°C, T_{HS} = 30°C; h_E = 1.6 m.

Figure 5.4: Turbulent kinetic energy variation in the middle of the room model versus height.

5.3.2 Effect of exhaust-outlet height

Skistad (1998) mentioned that the exhaust should be located at the pollutants' height of equilibrium and that thermal stratification may affect the withdrawal thickness of the pollutants. It is known from theory that the temperature gradient has an important effect on the neutral buoyancy height of contaminant plumes. It will be shown here that the exhaust height can considerably affect the temperature gradient and specifically the interface height and thickness. The temperature contours and the velocity vector fields in Figure 5.5 (a) and (b) were obtained by using the idealised test model and show the effect of exhaust height on the temperature-stratified interface. The temperature gradients obtained from the three exhaust heights used to carry out this study were h = 0.8, 1.6 and 2.2 m from floor. The supply momentum between cold and hot air is the same bearing a velocity of 0.2 m/s, the corresponding flow rates are $Q_{CS,HS}$ = 0.05 m^3/s, while the inlet temperature difference was ΔT_{in} = 20°C and the radiation model or any heat losses were not included.

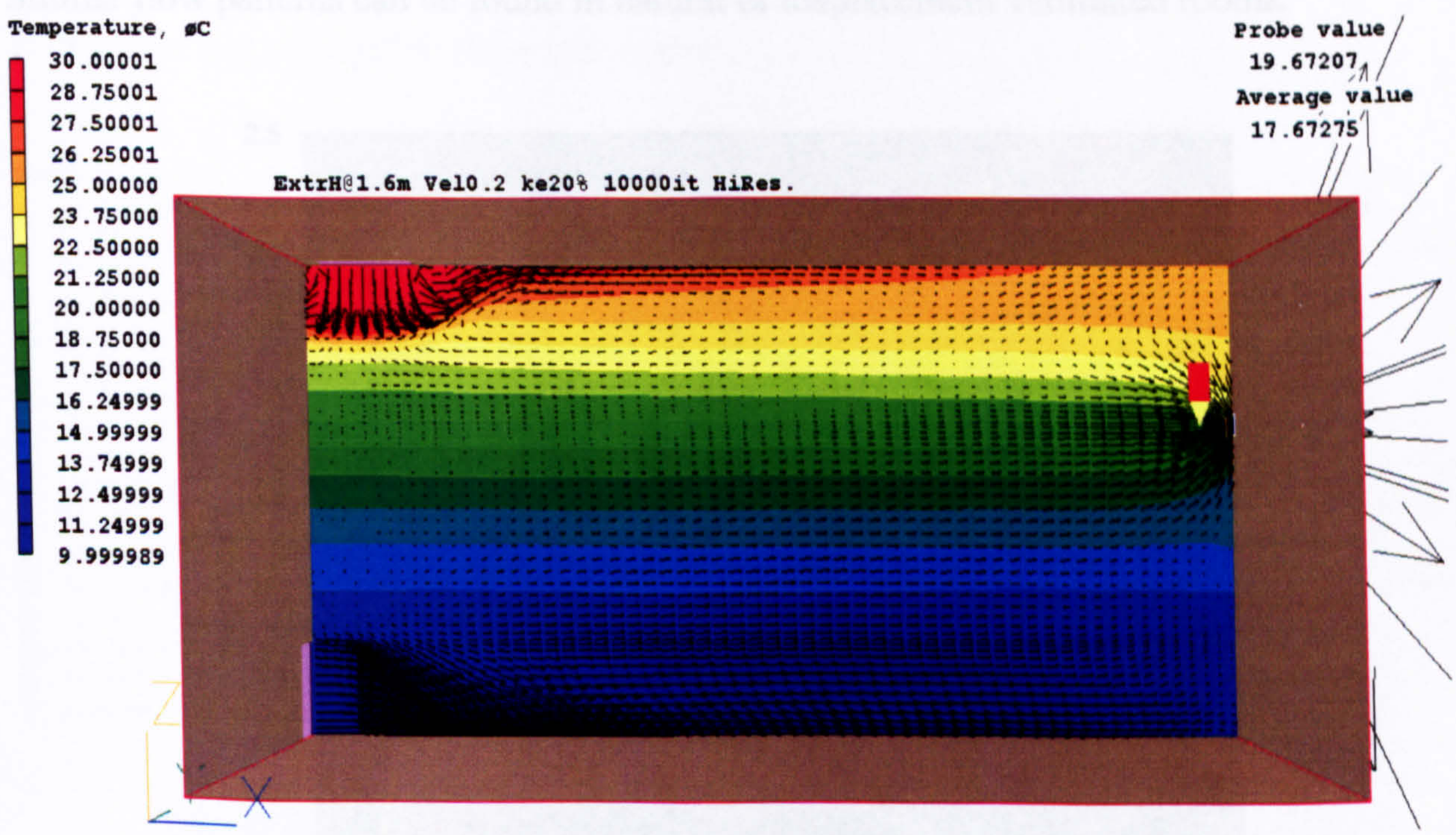

(a) $\boldsymbol{h_E}$ **= 1.6 m**; U_{in} = 0.2 m/s, $Q_{CS,HS}$ = 0.05 m^3/s; T_{CS} = 10°C, T_{HS} = 30°C.

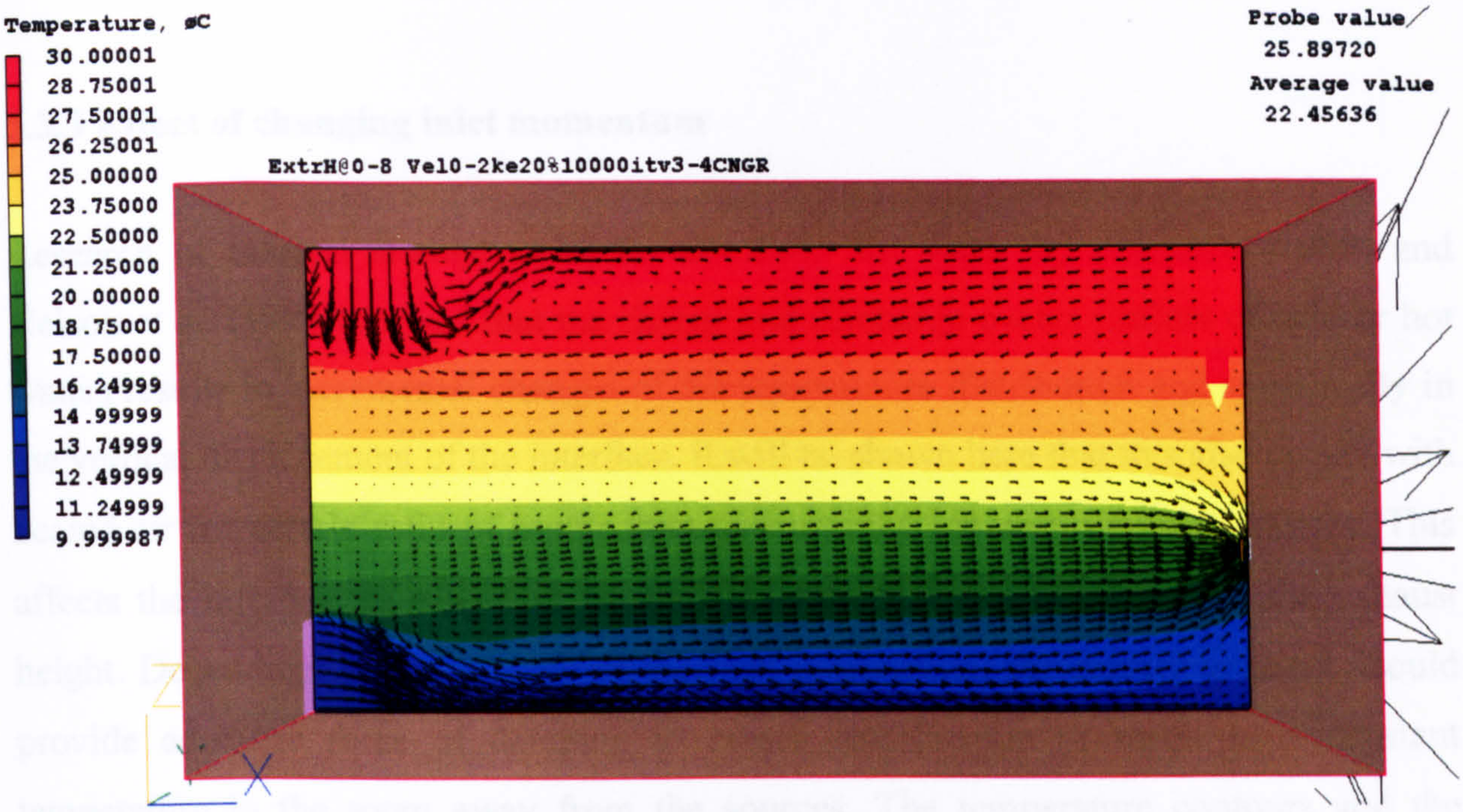

(b) $\boldsymbol{h_E = 0.8}$ **m**; U_{in} = 0.2 m/s, $Q_{CS,HS}$ = 0.05 m^3/s; T_{CS} = 10°C, T_{HS} = 30°C.

Figure 5.5: The effect of changing the exhaust height is shown above in (a) and (b). In (a), the exhaust height is 1.6 m. In (b), the exhaust height is at 0.8 m. Both cases have inlet velocities as low as 0.2 m/s, flow rates are 0.05 m^3/s, which yield a Richardson number, Ri_{in} = 40 well in the stable region as it can also be observed from the pictures. Similar flow patterns can be found in natural or displacement ventilated rooms.

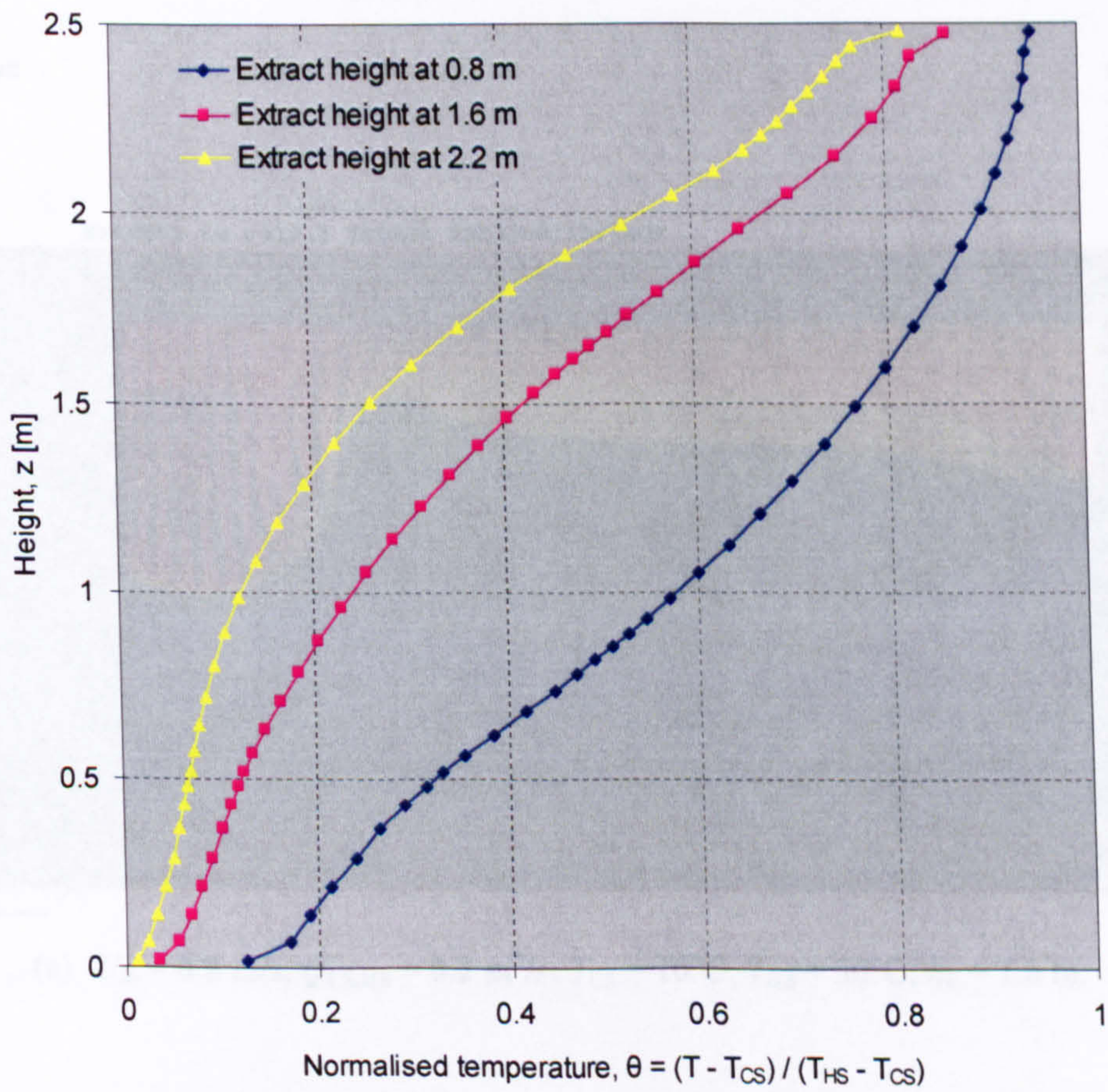

Figure 5.6: Temperature gradient for the three exhaust heights h_E = 0.8, 1.6 and 2.2 m.

5.3.3 Effect of changing inlet momentum

Research of thermal storage tanks for domestic hot water by Alizadeh (1999) and Nelson *et al.* (1999) showed that the charge and discharge cycles (inflow of cold or hot water) results in incremental changes of the temperature distribution and specifically in the vertical displacement of the interface. It will be shown here that this also occurs with heated air for certain ratio of momentum to buoyancy between the inlet sources. This affects the interface causing it to occur at heights that are different than the exhaust height. Depending on the strength of the inlet momentum, the density gradient should provide adequate force of damping to create stratification or result to a constant temperature in the room away from the sources. The temperature contours and the velocity vector fields in Figure 5.7 (a) and (b) were obtained by using the idealised test model and show the effect of momentum from the supply air jets on the stratified flow by increasing the inlet velocities from 0.2 m/s to 1.6 m/s. This is shown here only for 0.8 m/s and 1.6 m/s, the corresponding flow rates were $Q_{CS,HS}$ = 0.2 and 0.4 m^3/s, while the inlet temperature difference was ΔT_{in} = 20°C. The radiation model or any heat losses were not included in these test cases.

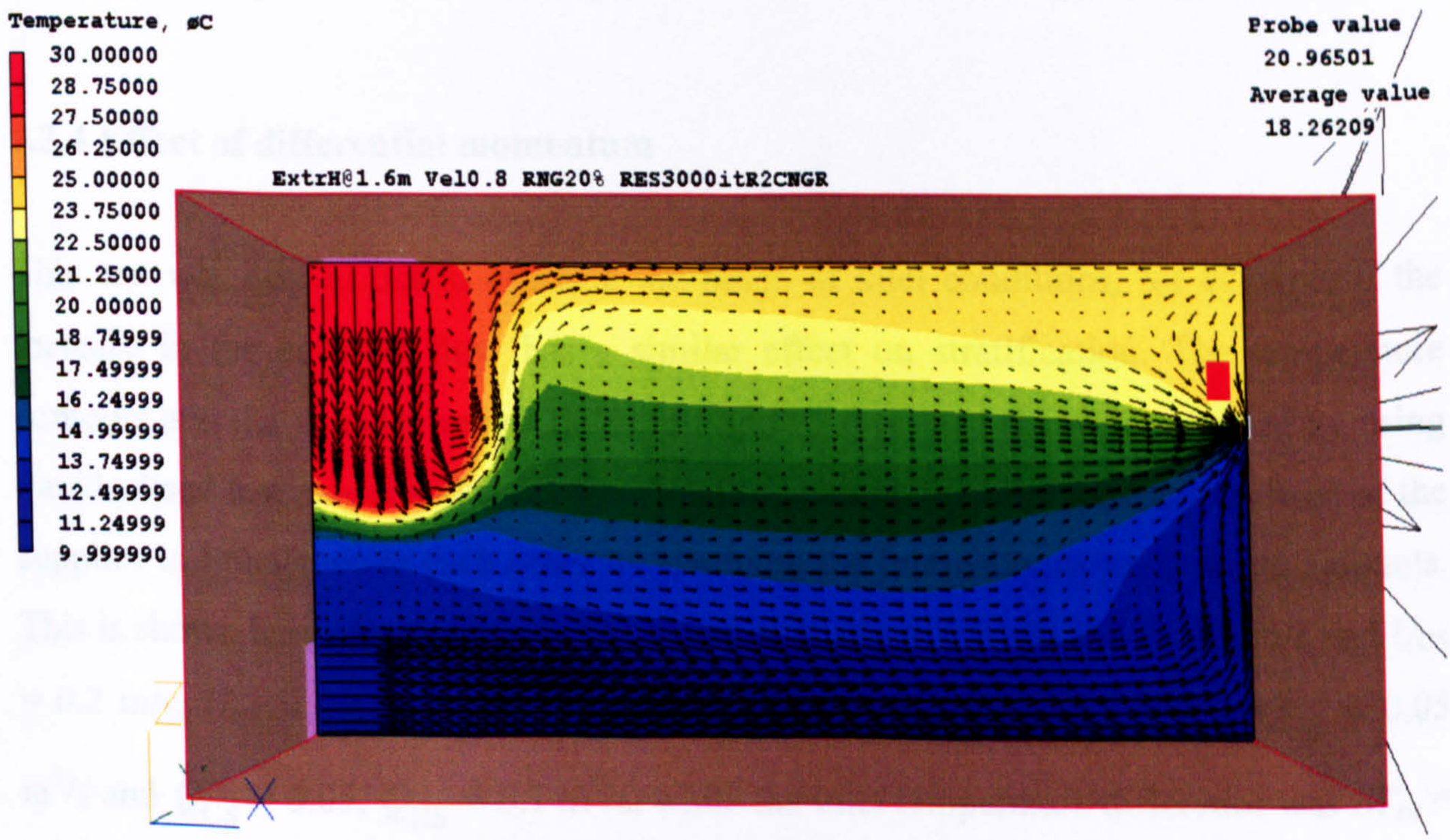

(a) U_{in} = **0.8 m/s,** $Q_{CS,HS}$ **= 0.2 m^3/s;** T_{CS} = 10°C, T_{HS} = 30°C; h_E = 1.6 m.

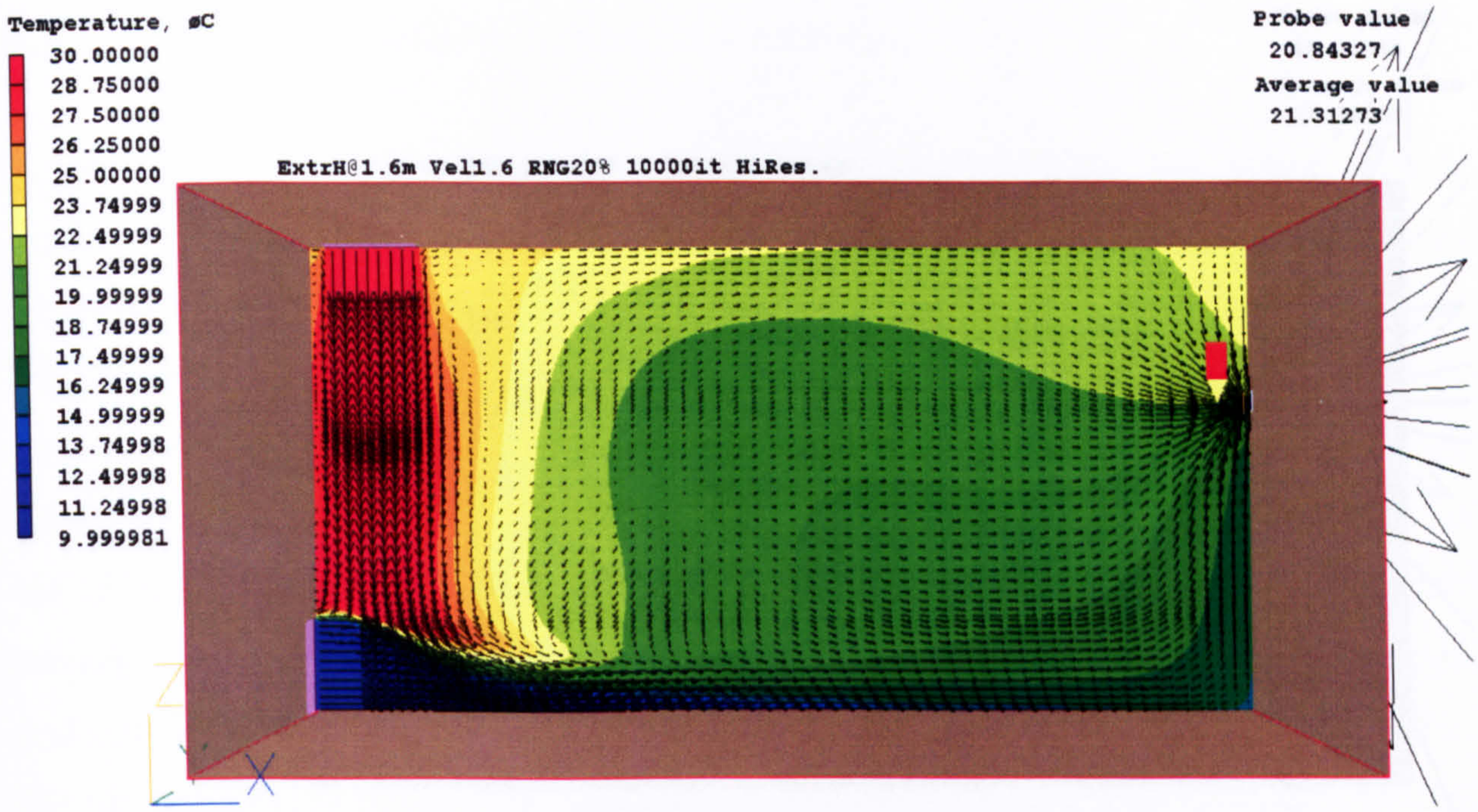

(b) U_{in} **= 1.6 m/s,** $Q_{CS,HS}$ **= 0.4 m³/s;** T_{CS} = 10°C, T_{HS} = 30°C; h_E = 1.6 m.

Figure 5.7: The effect of changing the inlet velocities is shown above in (a) and (b). In (a), the inlet velocities are 0.8 m/s, $Q_{CS,HS}$ = 0.2 m³/s, yielding a corresponding Ri_{in} = 2.6, which suggests that the momentum force from the hot air supply impinging on the stratified layer is getting close to critical values. In (b), the inlet velocities are 1.6 m/s, $Q_{CS,HS}$ = 0.4 m³/s, yielding a corresponding Ri_{in} = 0.6; mixing is occurring and stratification very weak locally or non-existent. In both cases the inlet temperature difference is kept at 20°C. The flow patterns are similar in mixing ventilated rooms.

5.3.4 Effect of differential momentum

This test was carried out to estimate the range of inlet conditions, for example if the increase in the cold air flow has a similar effect on stratification. The temperature contours and the velocity vector fields in Figure 5.8 (a) and (b) were obtained by using the idealised test model and show the effect of keeping the inlet momentum from of the supplies in imbalance to each other by changing the inlet velocity at different amounts. This is shown here only for the set of velocities of U_{CS} = 0.8 m/s, U_{HS} = 0.2 m/s and U_{CS} = 0.2 m/s, U_{HS} = 0.4 m/s, the corresponding flow rates were Q_{CS} = 0.2, Q_{HS} = 0.05 m³/s and Q_{CS} = 0.05, Q_{HS} = 0.1 m³/s, while the inlet temperature difference was ΔT_{in} = 20°C. The radiation model or any heat losses were not included in these test cases.

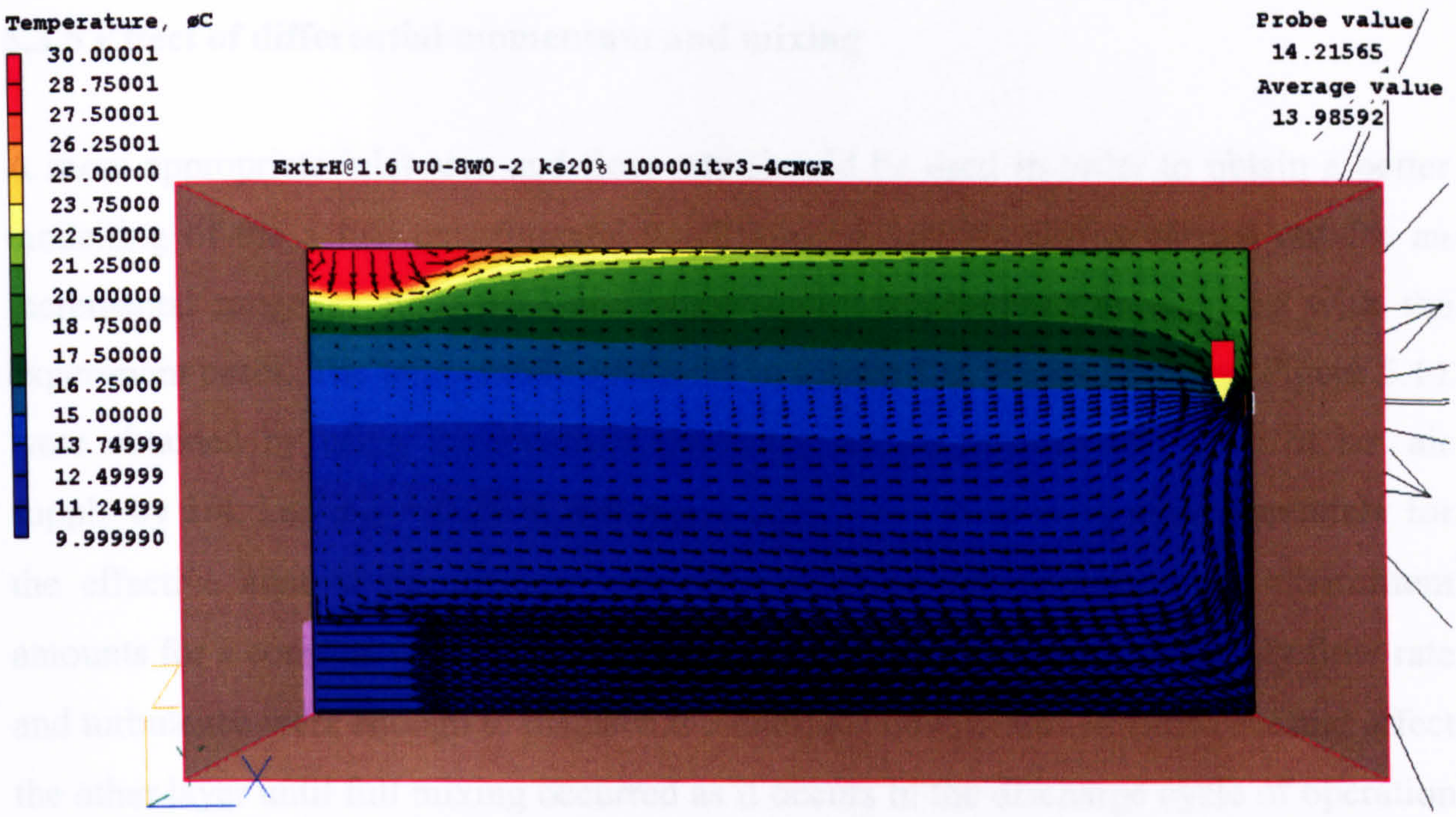

(a) U_{CS} = **0.8 m/s,** U_{HS} = **0.2 m/s and** Q_{CS} = **0.2 m³/s,** Q_{HS} = **0.4 m³/s;** T_{CS} = 10°C, T_{HS} = 30°C, h_E = 1.6 m.

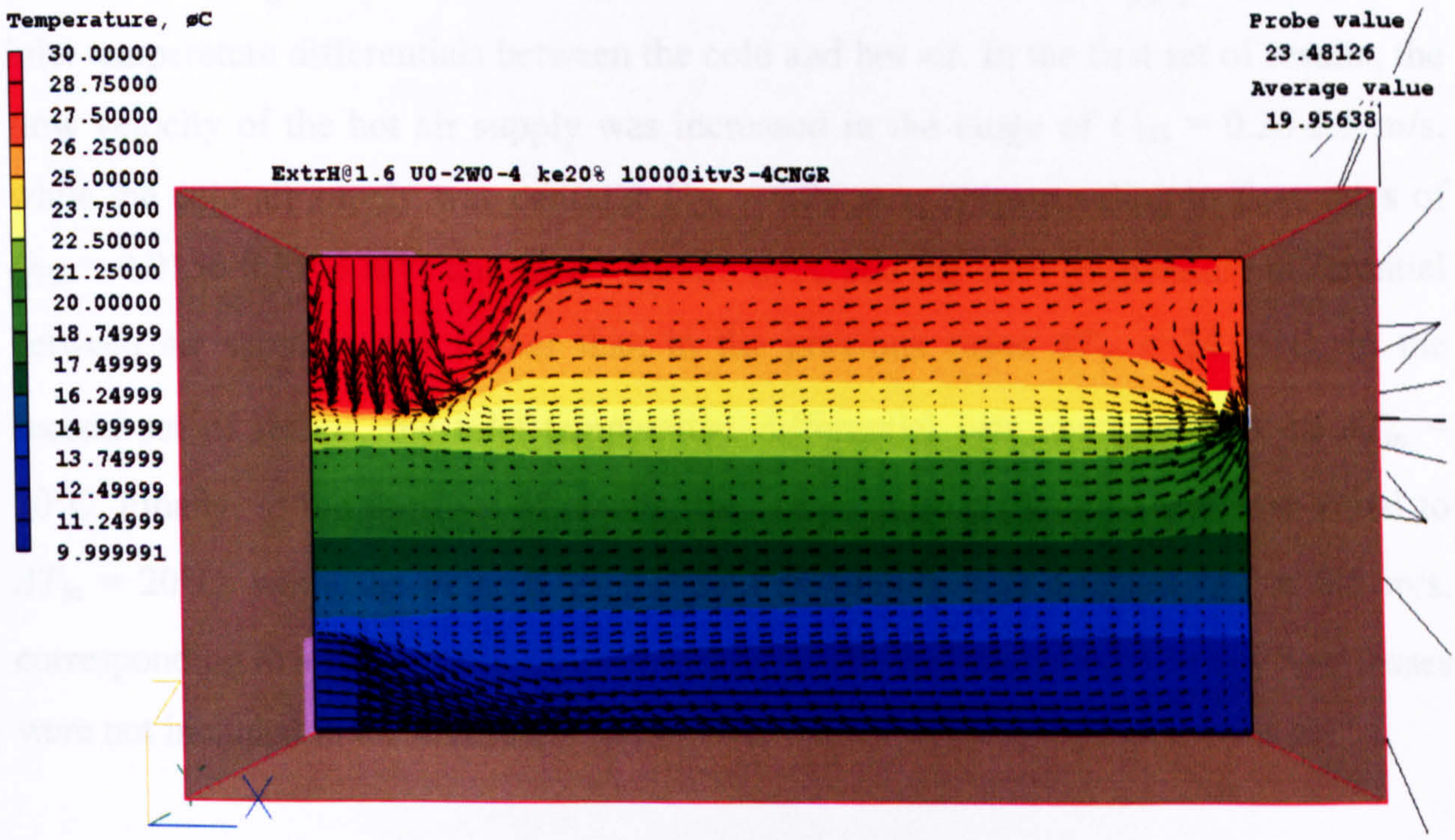

(b) U_{CS} = **0.2 m/s,** U_{HS} = **0.4 m/s and** Q_{CS} = **0.05 m³/s,** Q_{HS} = **0.2 m³/s;** T_{CS} = 10°C, T_{HS} = 30°C; h_E = 1.6 m.

Figure 5.8: The effect of changing the inlet velocity by disproportional amounts can be seen above in (a) and (b). In (a), the velocity from the cold air supply is higher than the hot air supply velocity covering a large part of the lower space of the room. In (b), this relation is in contrast to (a), by comparing the temperature contours covering a smaller part in the upper space of the room. In this way the height of the interface can be modified. Similar flow patterns can be found in rooms ventilated by displacement or mixing methods.

5.3.5 Effect of differential momentum and mixing

A more appropriate inlet area and flow rate should be used in order to obtain a better modelling of the actual experimental conditions. A test should be carried out for an incremental range of flow rates and temperatures appropriate to compare with the experiment cases. The temperature gradients in Figure 5.9, Figure 5.10 and Figure 5.11 were obtained by using the idealised geometry with a reduced inlet area of hot air supply by 1/4, i.e., a_{HS} = 0.25 m and A_{HS} = 0.0625 m², to account more accurately for the effective area of the diffuser. The inlet velocity was increased by intermittent amounts for a constant cold air supply flow rate. The amount of hot air supply flow rate and turbulence were enough to displace the interface downwards in each case and affect the other layer until full mixing occurred as it occurs in the discharge cycle of operation of thermal storage tanks. This is tested for two different cold air supply velocities and inlet temperature differentials between the cold and hot air. In the first set of results, the flow velocity of the hot air supply was increased in the range of U_{HS} = 0.25-2.5 m/s, while the cold air supply was constant U_{CS} = 0.25 m/s, corresponding to flow rates of Q_{HS} = 0.0156-0.1563 m³/s and Q_{CS} = 0.0625 m³/s, and the inlet temperature differential between air supplies was higher than in the previous cases ΔT_{in} = 24.25°C. In the second set of results, the inlet temperature differential was changed back to ΔT_{in} = 20°C. Finally, in the third set of results, the temperature differential was also equal to ΔT_{in} = 20°C, while the velocity of the cold air supply was doubled U_{CS} = 0.5 m/s, corresponding to a flow rate of Q_{HS} = 0.125 m³/s. The radiation model or any heat losses were not included in these cases.

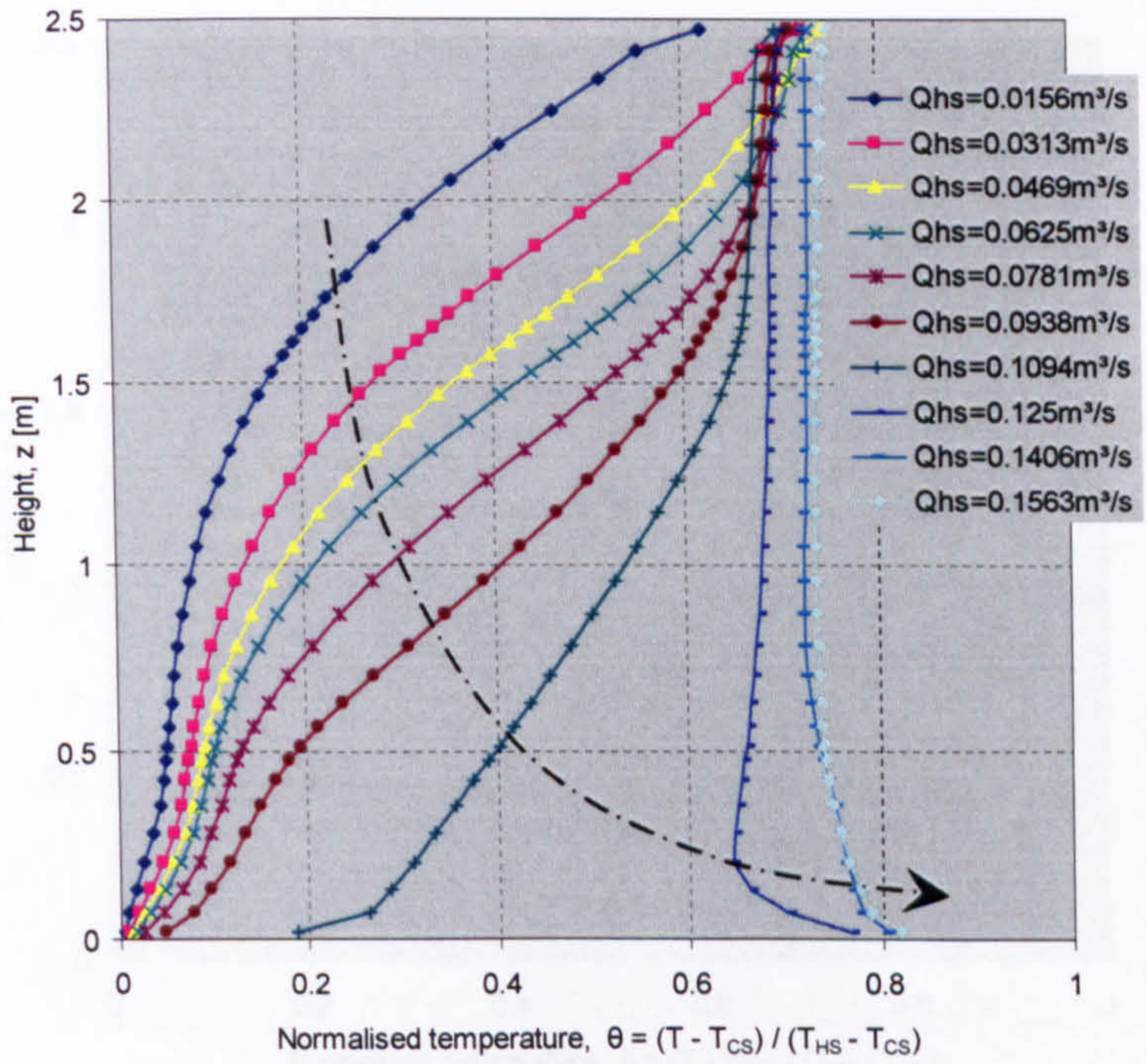

Figure 5.9: The effect of hot air supply flow rate on the temperature gradient and the interface in the middle of the room at constant incremental changes, constant inlet temperatures and a constant cold air supply flow rate using the idealised model with a reduced area of hot air supply and for a higher temperature range; $\boldsymbol{a_{HS}}$ **= 0.25 m,** a_{CS} = 0.5 m and $\boldsymbol{A_{HS}}$ **= 0.0625 m²,** A_{CS} = 0.25 m²; U_{HS} = 0.25-2.5 m/s, U_{CS} = 0.25 m/s and Q_{HS} = 0.0156-0.1563 m³/s, Q_{CS} = 0.0625 m³/s; $\boldsymbol{T_{CS}}$ **= 8.25°C,** $\boldsymbol{T_{HS}}$ **= 32.5°C;** h_E = 1.6 m.

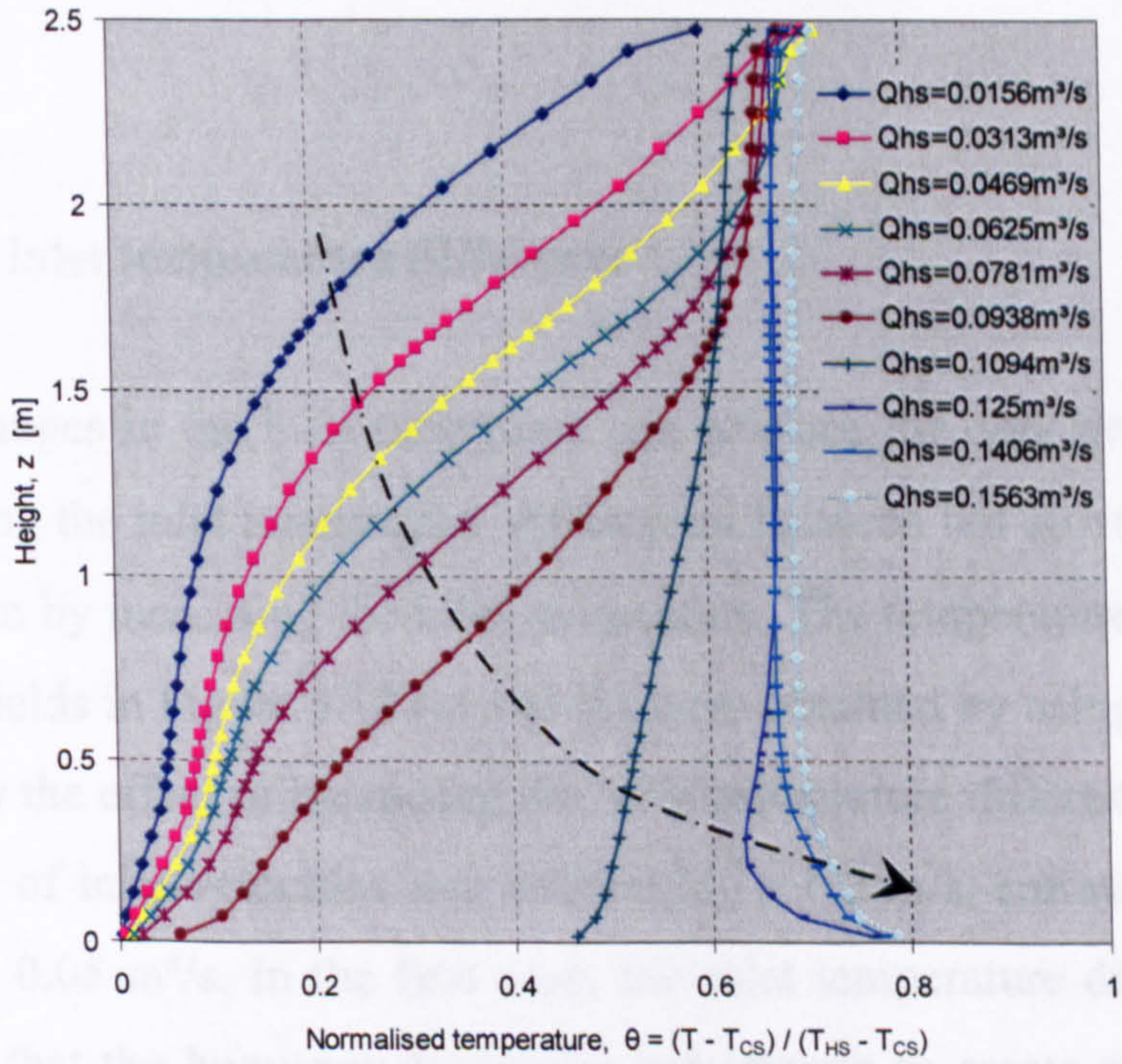

Figure 5.10: The effect of hot air supply flow rate on the temperature gradient and the interface in the middle of the room at constant incremental changes, constant inlet temperatures and a constant cold air supply flow rate using the idealised model with a reduced area of hot air supply; $\boldsymbol{a_{HS}}$ **= 0.25 m,** a_{CS} = 0.5 m and $\boldsymbol{A_{HS}}$ **= 0.0625 m²,** A_{CS} = 0.25 m²; U_{HS} = 0.25-2.5 m/s, U_{CS} = 0.25 m/s and Q_{HS} = 0.0156-0.1563 m³/s, Q_{CS} = 0.0625 m³/s; T_{CS} = 10°C, T_{HS} = 30°C; h_E = 1.6 m.

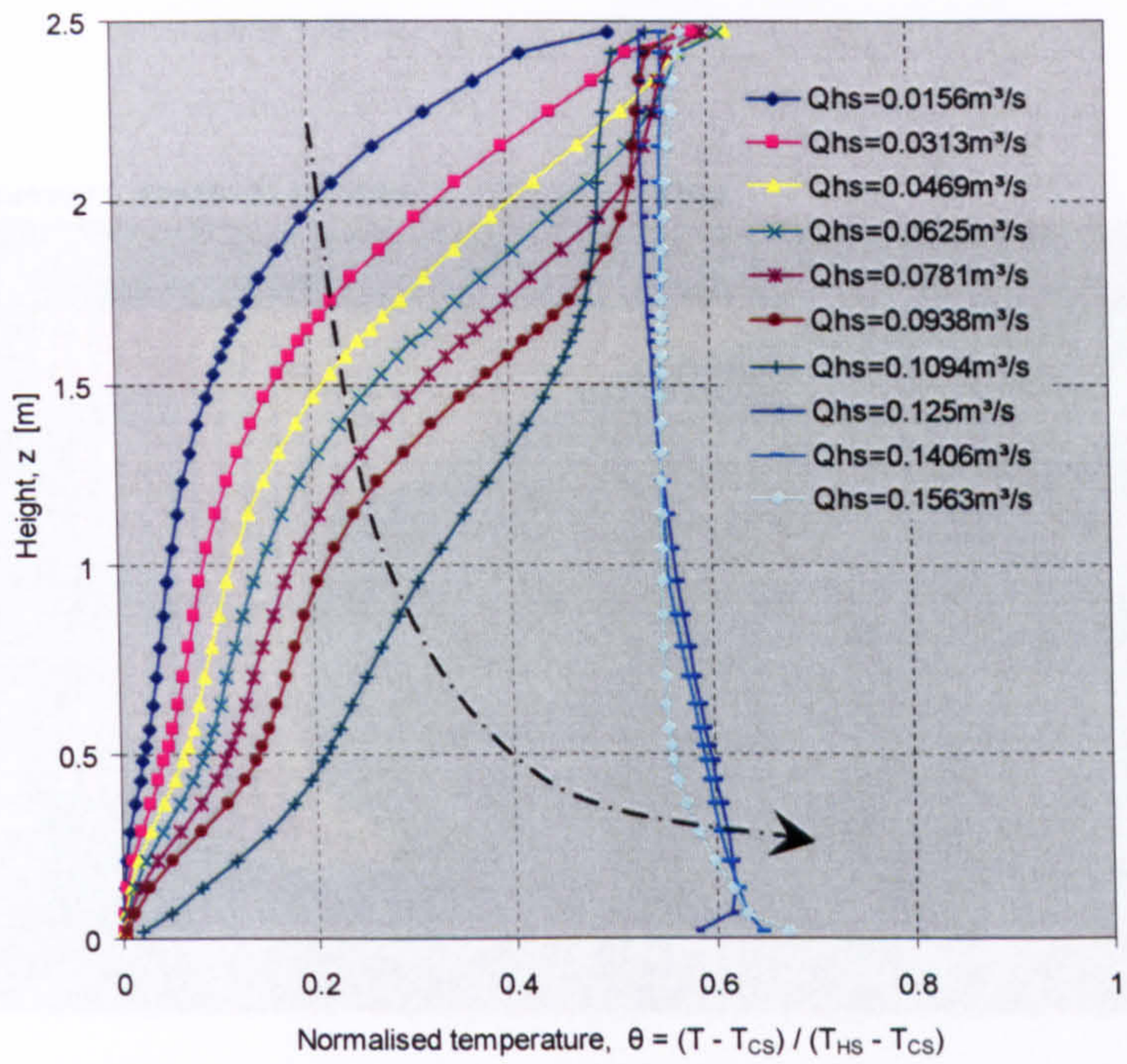

Figure 5.11: The effect of hot air supply flow rate on the temperature gradient and the interface in the middle of the room at constant incremental changes, constant inlet temperatures and a constant cold air supply flow rate using the idealised model with a reduced area of hot air supply and for a higher cold air supply flow rate; $\boldsymbol{a_{HS}}$ **= 0.25 m,** a_{CS} = 0.5 m and $\boldsymbol{A_{HS}}$ **= 0.0625 m²,** A_{CS} = 0.25 m²; U_{HS} = 0.25-2.5 m/s, $\boldsymbol{U_{CS}}$ **= 0.5 m/s** and Q_{HS} = 0.0156-0.1563 m³/s, $\boldsymbol{Q_{CS}}$ **= 0.125 m³/s (**$\boldsymbol{U_{CS}}$**×2);** T_{CS} = 10°C, T_{HS} = 30°C; h_E = 1.6 m.

5.3.6 Increasing inlet temperature difference

To test if the changes in the buoyancy force can produce the opposite effect, it can be done by increasing the inlet temperature differential between hot air supply and cold air supply rather than by increasing the inlet momentum. The temperature contours and the velocity vector fields in Figure 5.12 (a) and (b) were obtained by using the idealised test model, and show the effect of increasing the inlet temperature differential. In both cases the lowest value of inlet velocities was utilised U_{in} = 0.2 m/s, corresponding to a flow rate of $Q_{CS,HS}$ = 0.05 m³/s. In the first case, the inlet temperature difference is ΔT_{in} = 0.2°C, showing that the buoyancy forces are not enough to create stratification in the room. In (b), inlet temperature difference is ΔT_{in} = 2.4°C, showing that stratification starts to occur. The difference in the inlet temperature difference in (b) is 12 times higher than (a), showing similarities with previous cases of the same ratio of momentum to buoyancy. The radiation model or any heat losses were not included.

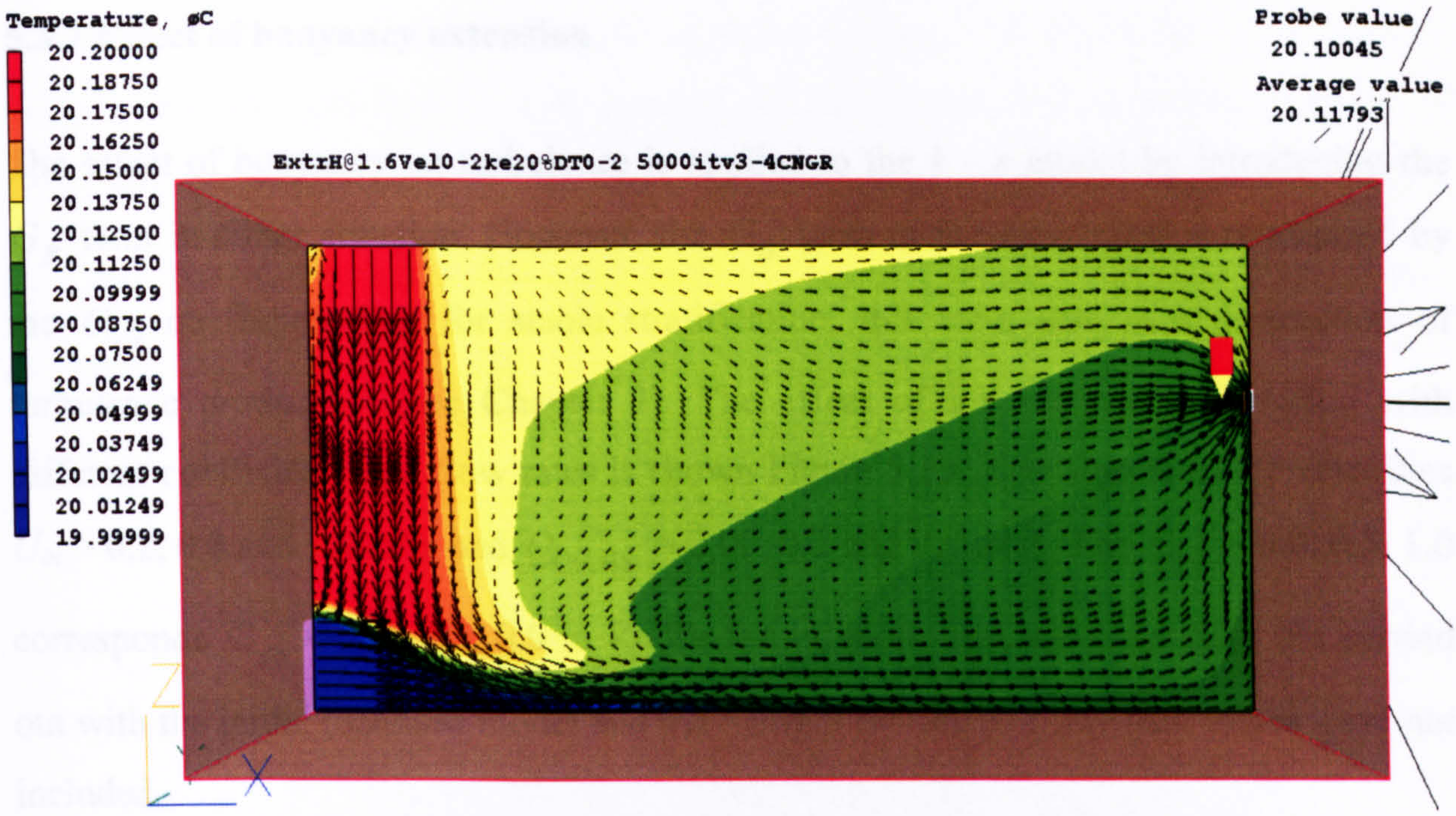

(a) T_{CS} = **20°C**, T_{HS} = **20.2°C**; U_{in} = 0.2 m/s and $Q_{CS,HS}$ = 0.05 m^3/s; h_E = 1.6 m.

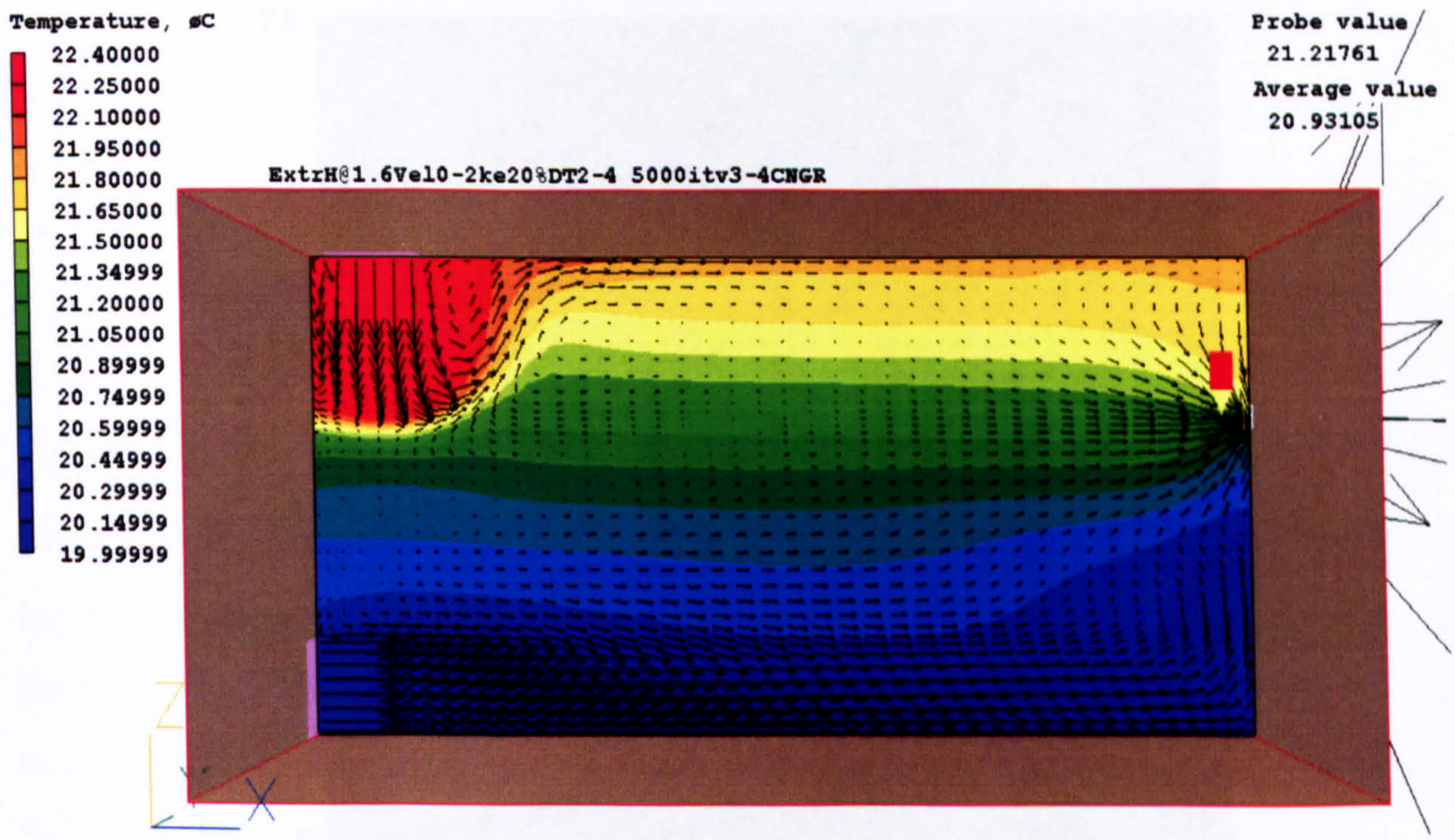

(b) T_{CS} = **20°C**, T_{HS} = **22.4°C**; U_{in} = 0.2 m/s and $Q_{CS,HS}$ = 0.05 m^3/s; h_E = 1.6 m.

Figure 5.12: The effect of changing the inlet temperature difference is shown above in (a) and (b). In both (a) and (b) above, the flow rates are kept low, in order to keep a low Ri_{in}, due to the effect of velocity in the current case. In (a), inlet temperature difference is ΔT_{in} = 0.2°C, showing that the buoyancy forces are not enough to create stratification in the room. In (b), inlet temperature difference is ΔT_{in} = 2.4°C, showing that stratification starts occurring.

5.3.7 Effect of buoyancy extension

The effect of buoyancy on turbulence is applied to the $k-\varepsilon$ model by introducing the G_B term in either equation. However, the G_B term in the ε-equation is multiplied by the $C_{\varepsilon 3}$ coefficient that for stable stratification, this term acts as a destruction of turbulence production (see Chapter 3). The effect of the buoyancy extension with different coefficients and flow rates is shown Figure 5.13. The flow rates for velocities U_{in} = 0.2, 0.8 and 1.6 m³/s and $Q_{\mathrm{CS,HS}}$ = 0.05, 0.2 and 0.4 m³/s. The $C_{\varepsilon 3}$ = 0.0, 0.5, 1.0 corresponds $C_{\varepsilon 3}$ = 1.0, 0.5, 0.0 in Rodi's formulation. The test cases here are carried out with the initial idealised model and the thermal radiation or any heat losses were not included.

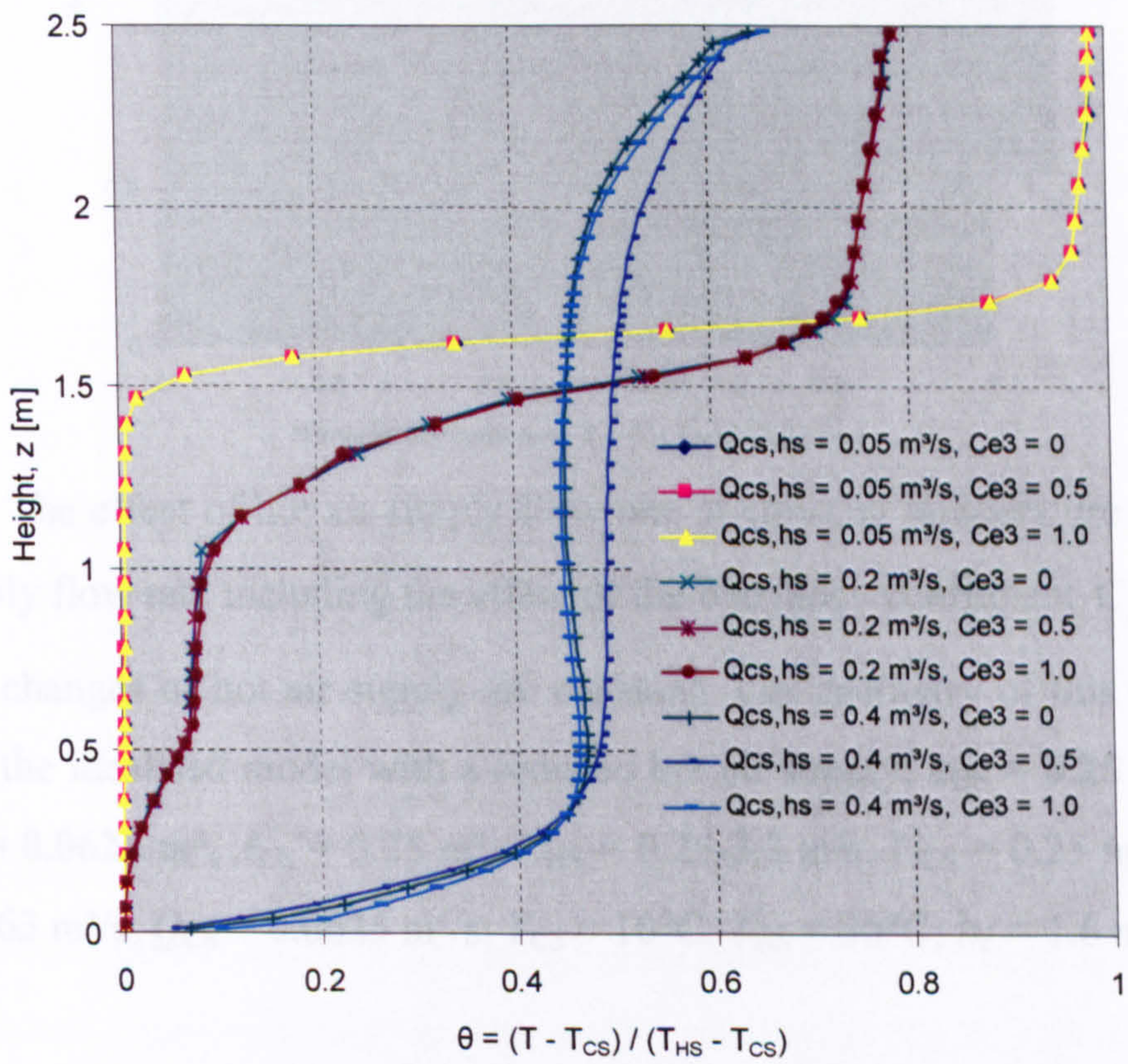

Figure 5.13: The effect of equal momentum change at constant temperature with different values buoyancy coefficient $C_{\varepsilon 3}$. The geometry of this test model is the same as the idealised model with equal inlet sizes; $a_{\mathrm{CS,HS}}$ = 0.5 m and $A_{\mathrm{CS,HS}}$ = 0.25 m²; $U_{\mathrm{CS,HS}}$ = 0.2-1.6 m/s and Q_{CS} = 0.05-0.4 m³/s; ΔT = 10-30°C; h_{E} = 1.6 m.

Further the effect of constant incremental changes at hot air supply flow rate was tested at constant temperature and constant cold air supply flow rate including the effect of the buoyancy coefficient $C_{\varepsilon 3}$ = 0.5. The geometry of this test model is the same as the

idealised model with a reduced hot air supply by 1/4, a_{HS} = 0.25 m. The hot air supply velocity was changed from 0.25 to 2.5 m/s at 0.25 m/s increments, bearing a range of flow rates $Q_{HS} = 0.015625 - 0.15625\,m^3/s$, while cold air supply flow rate velocity was 0.25 m/s, the corresponding flow rates is $Q_{CS} = 0.0625\,m^3/s$, and the inlet temperature difference was ΔT_{in} = 20°C. This is shown in Figure 5.14,

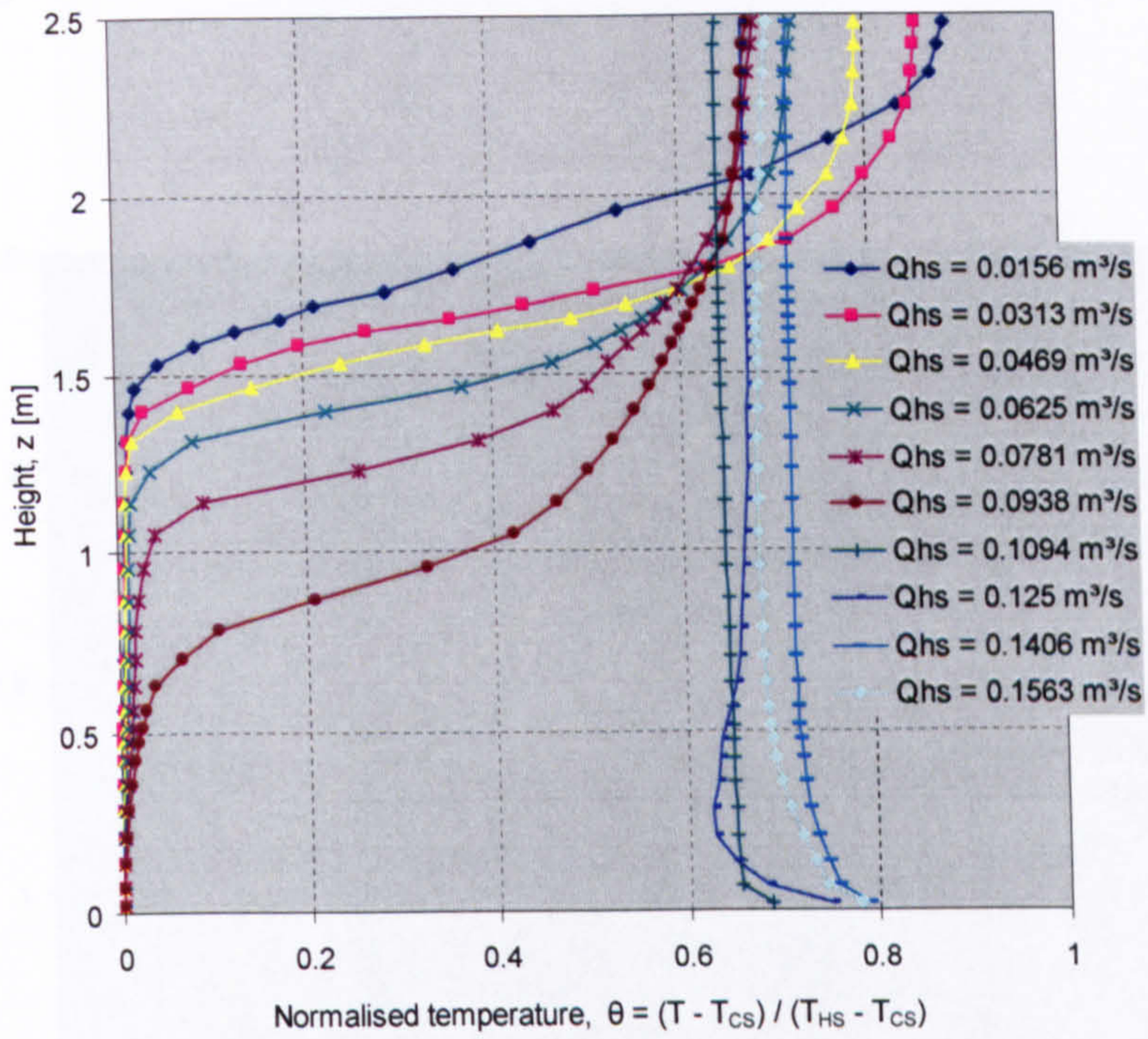

Figure 5.14: The effect of hot air supply flow rate at constant temperature and constant cold air supply flow rate including the effect of the buoyancy coefficient $C_{\varepsilon 3}$ = 0.5. The incremental changes of hot air supply are constant. The geometry of this test model is the same as the idealised model with a reduced hot air supply; $\boldsymbol{a_{HS}}$ **= 0.25 m,** a_{CS} = 0.5 m and $\boldsymbol{A_{HS}}$ **= 0.0625 m²,** A_{CS} = 0.25 m²; U_{HS} = 0.25-2.5 m/s, U_{CS} = 0.25 m/s and Q_{HS} = 0.0156-0.1563 m³/s, Q_{CS} = 0.0625 m³/s; T_{CS} = 10°C, T_{HS} = 30°C; h_E = 1.6 m.

5.3.8 Effects of emissivity – surface radiation and flow rate

Thermal radiation effects primarily arise due to the colour and surface finish of walls that are located at some distance form each other. The grey concrete floor and the textured surface finish of the supported ceiling are subject to significant radiative heat transfer exchange. These effects are stronger here between the floor and the ceiling because they were maintained at different temperatures and they were facing opposite to each other. The effect of thermal radiation on the mean temperature gradient was observed by CFD-modelling performing parametric studies with the effects of thermal

radiation. The temperature gradients in Figure 5.15 were obtained in the middle of the room using the idealised test model with the reduced hot air supply inlet, a_{HS} = 0.25 m and A_{HS} = 0.0625 m, and show the effect of mixing in thermally stratified flow. The effect of mixing in the near and far locations of the middle space of the room is shown in Figure 5.16 (a) and (b) respectively. The supply momentum of cold and hot air were changed by intermittent amounts from 0.25 to 2.5 m/s, corresponding to flow rates in the range of $Q_{HS} = 0.015625 - 0.15625\,\mathrm{m^3/s}$, while the inlet temperature difference was ΔT_{in} = 20°C.

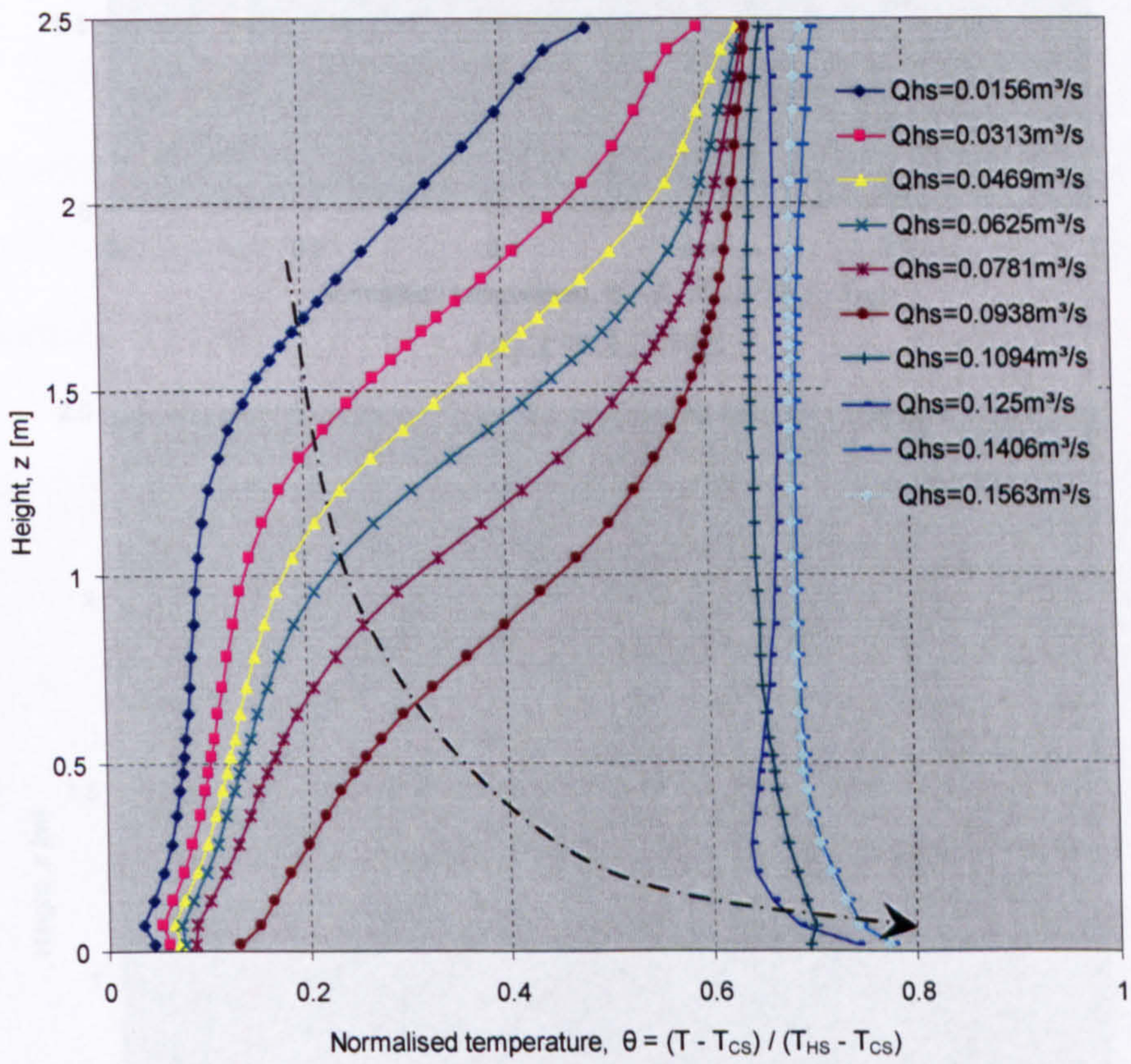

Figure 5.15: The effect of hot air supply flow rate on the temperature gradient and the interface in the middle of the room at constant incremental changes, constant inlet temperatures and a constant cold air supply flow rate using the idealised model with a reduced area of hot air supply and the radiation due to opposite surfaces at different temperatures, i.e., the inside room surfaces of the ceiling and the floor. The incremental changes of hot air supply are constant. The area of the hot air supply is 1/4 of the initial idealised model; $\boldsymbol{a_{HS}}$ **= 0.25 m,** a_{CS} = 0.5 m and $\boldsymbol{A_{HS}}$ **= 0.0625 m²,** A_{CS} = 0.25 m²; U_{HS} = 0.25-2.5 m/s, U_{CS} = 0.25 m/s and Q_{HS} = 0.0156-0.1563 m³/s, Q_{CS} = 0.0625 m³/s; T_{CS} = 10°C, T_{HS} = 30°C; h_E = 1.6 m.

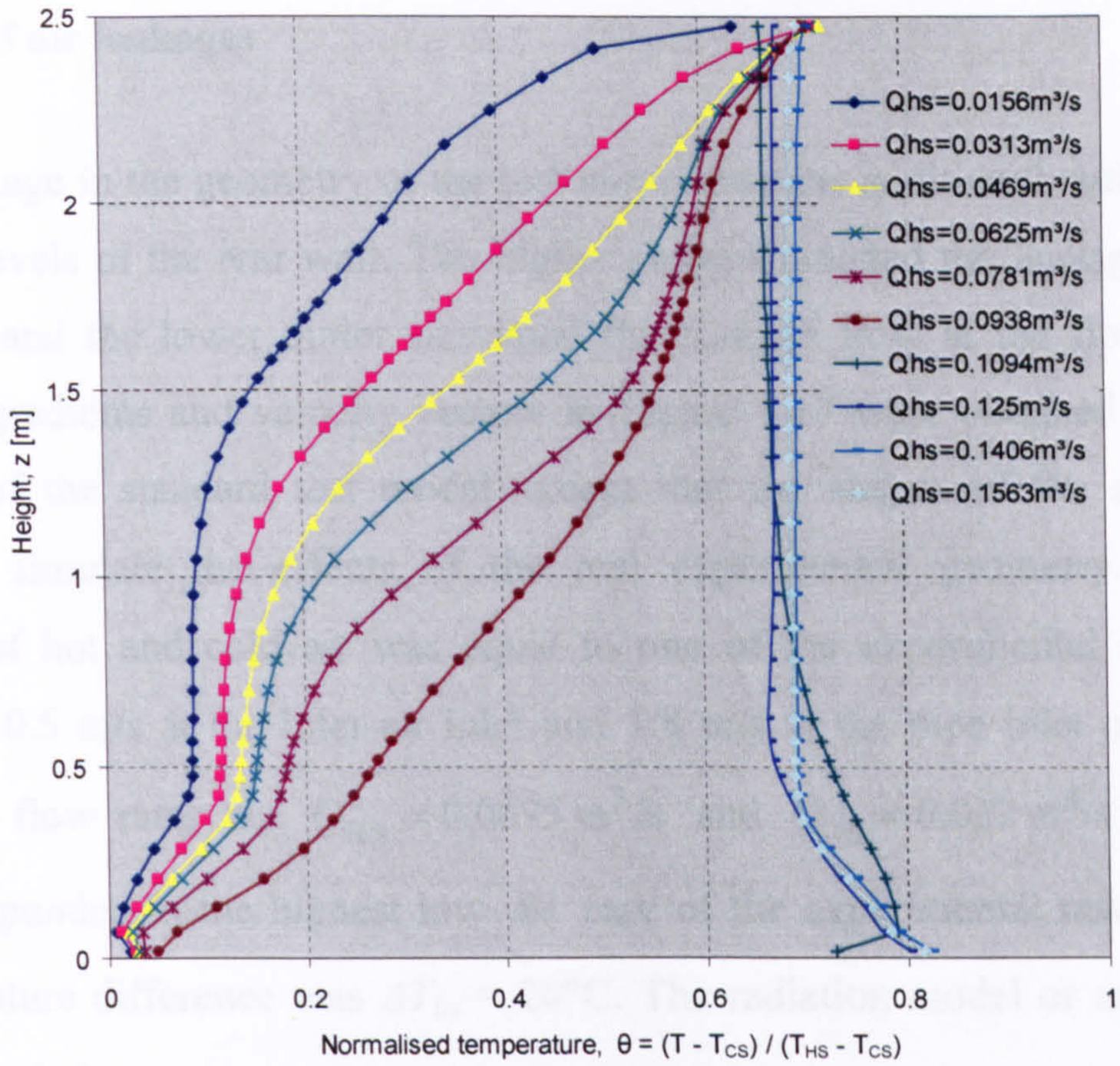

(a) $x = 1.25$ m.

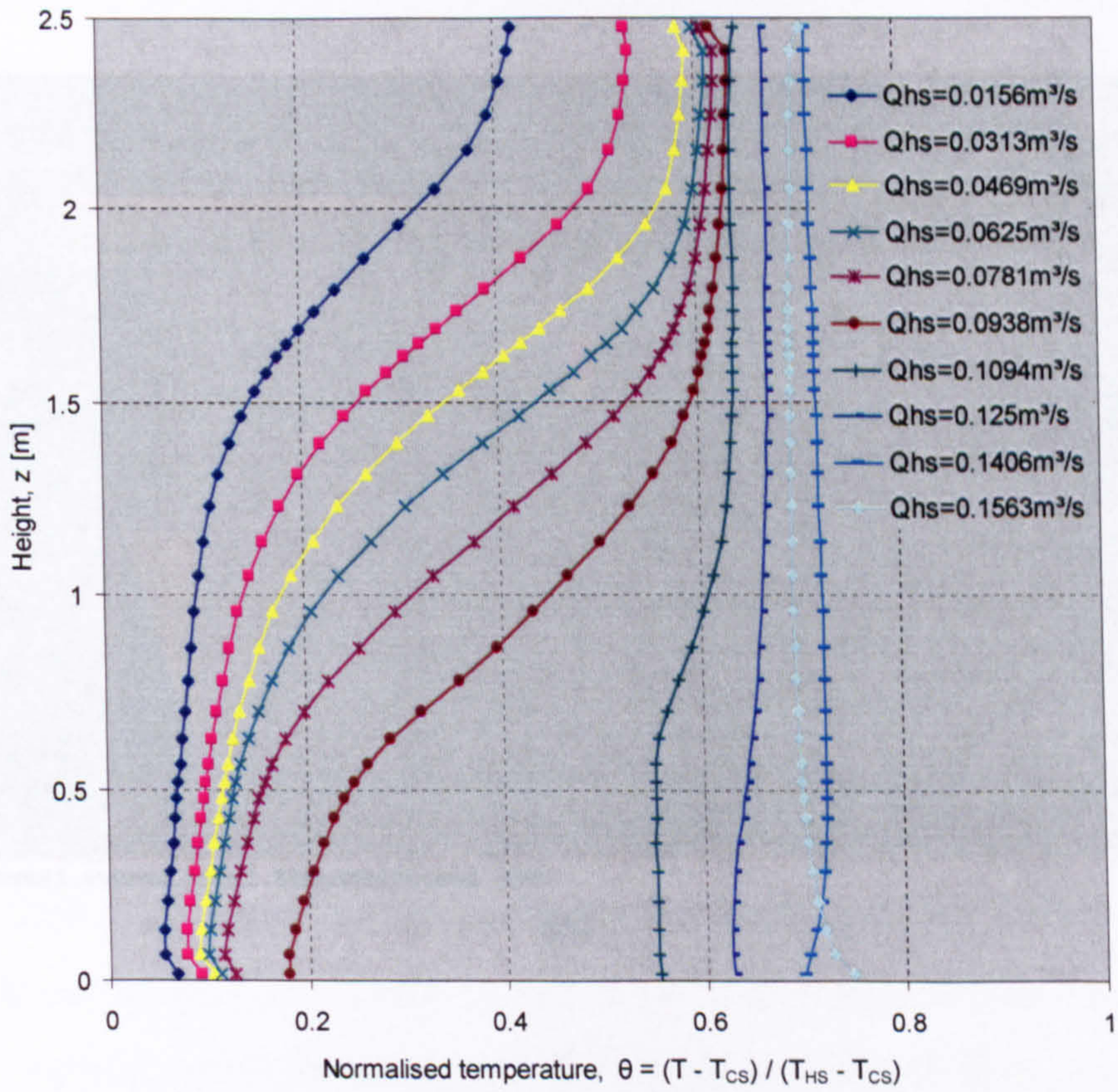

(b) $x = 3.75$ m.

Figure 5.16: Temperature gradients corresponding to the results shown in Figure 5.15, but at $x = 1.25$ m and $x = 3.75$ m in (a) and (b) respectively, indicating a slight tilt in the isotherms or a small Wedderburn number and hence slightly more stratification.

5.3.9 Effect of air leakages

The main change in the geometry of the test model was the additional outlets at the top and bottom levels of the rear wall. The higher outlet simulated the leakage flow at the ceiling level and the lower outlet simulated the leakage flow at the floor level. The temperature gradients and velocity vectors in Figure 5.17 were obtained by using the dimensions of the standard test model except that the shapes of the supplies were modified to simulate the effects of the real experimental geometry. The supply momentum of hot and cold air was equal to one of the experimental cases bearing velocities of 0.5 m/s at the inlet air inlet and 1.8 m/s at the pipe inlet of the cold air diffuser, the flow rates are $Q_{HS} = 0.0675\,\mathrm{m}^3/\mathrm{s}$ and $Q_{CS} = 0.032\,\mathrm{m}^3/\mathrm{s}$ respectively, which corresponded to the highest low Re case of the experimental results, while the inlet temperature difference was ΔT_{in} = 20°C. The radiation model or any heat losses were not included.

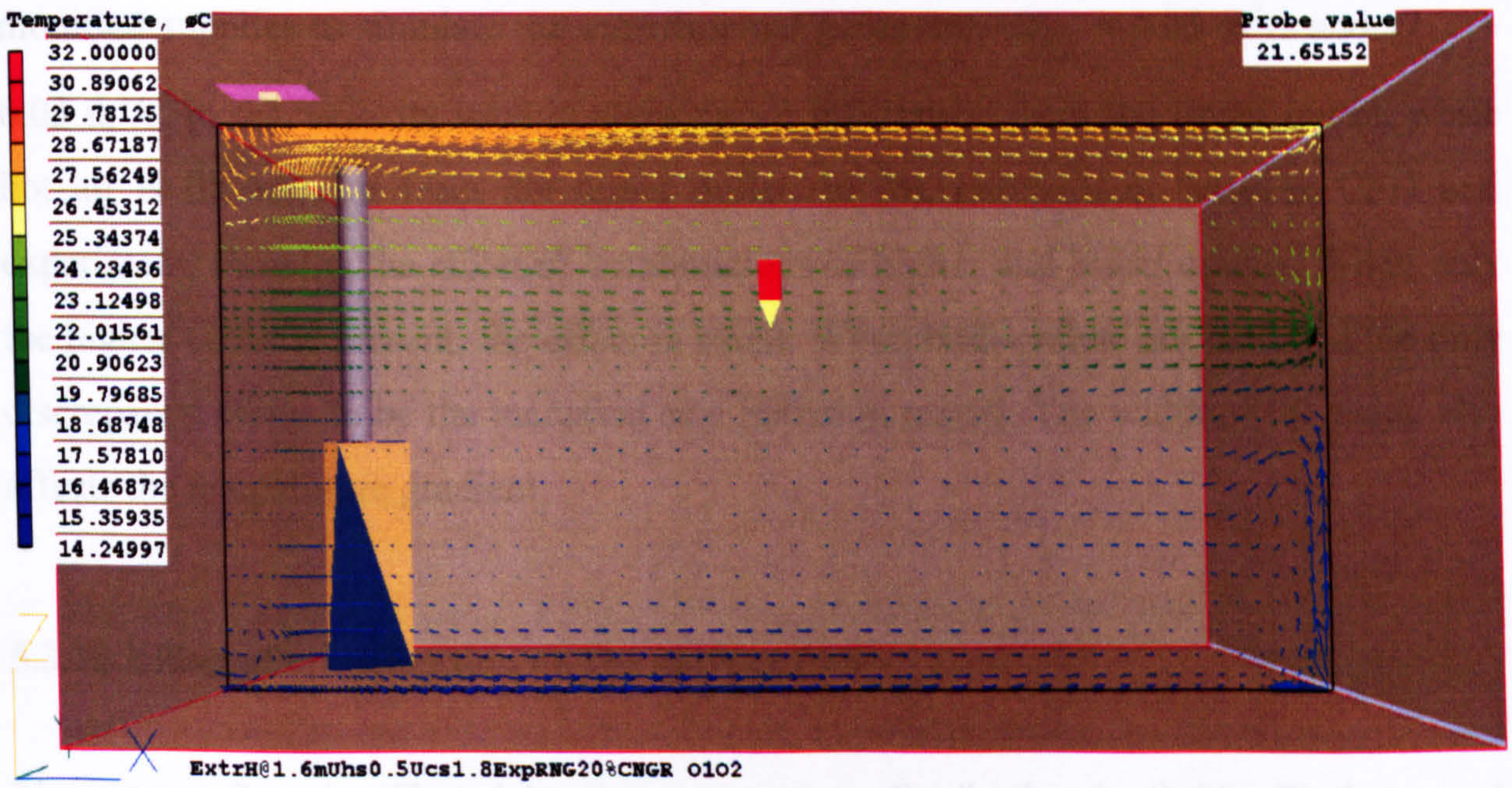

(a)

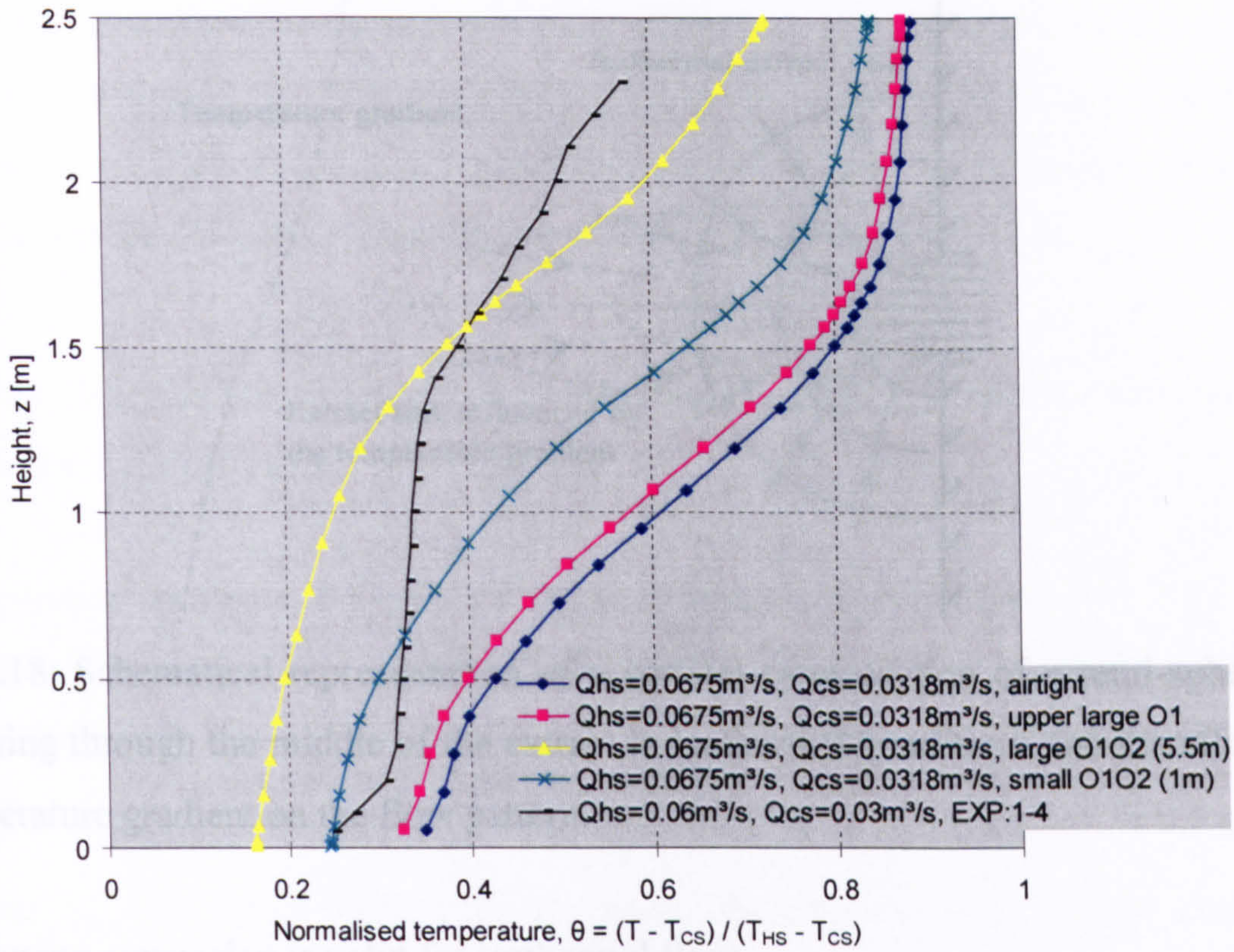

(b)

Figure 5.17: Effect of leakage due to additional outlets in the test model with the modified supplies to simulate the experimental geometry, Q_{HS} = 0.05 m^3/s and Q_{CS} = 0.03 m^3/s. In (a), velocity vectors showing air infiltration from the lower outlet, while hot air is flushed out from the upper outlet. In (b), comparison between CFD and experiment, showing the effect of combinations of higher and lower outlets. When only the higher outlet is present, the effect is small. When both outlets are included the only discrepancy seems to be the inclusion of a radiation model. The width of the crack also affects the temperature gradient.

5.3.10 Effect of stratification on the extract flow

The extract flow is affected by the temperature distribution in fluids, Fischer *et al.* (1979) and hence it may be useful to carry out some calculations here in order to evaluate the current result obtained by CFD. For isothermal flow, the extract sink normally forms a semi-spherical iso-surface around the opening. It was reported by Heiselberg *et al.* (1998) and to some further extent by Goodfellow and Tähti (2001) that Skistad (1994) illustrated that the vertical air movement is more restricted than the horizontal air movement because the flow must act over the buoyancy forces in the case of a temperature gradient. This is illustrated diagrammatically in Figure 5.18,

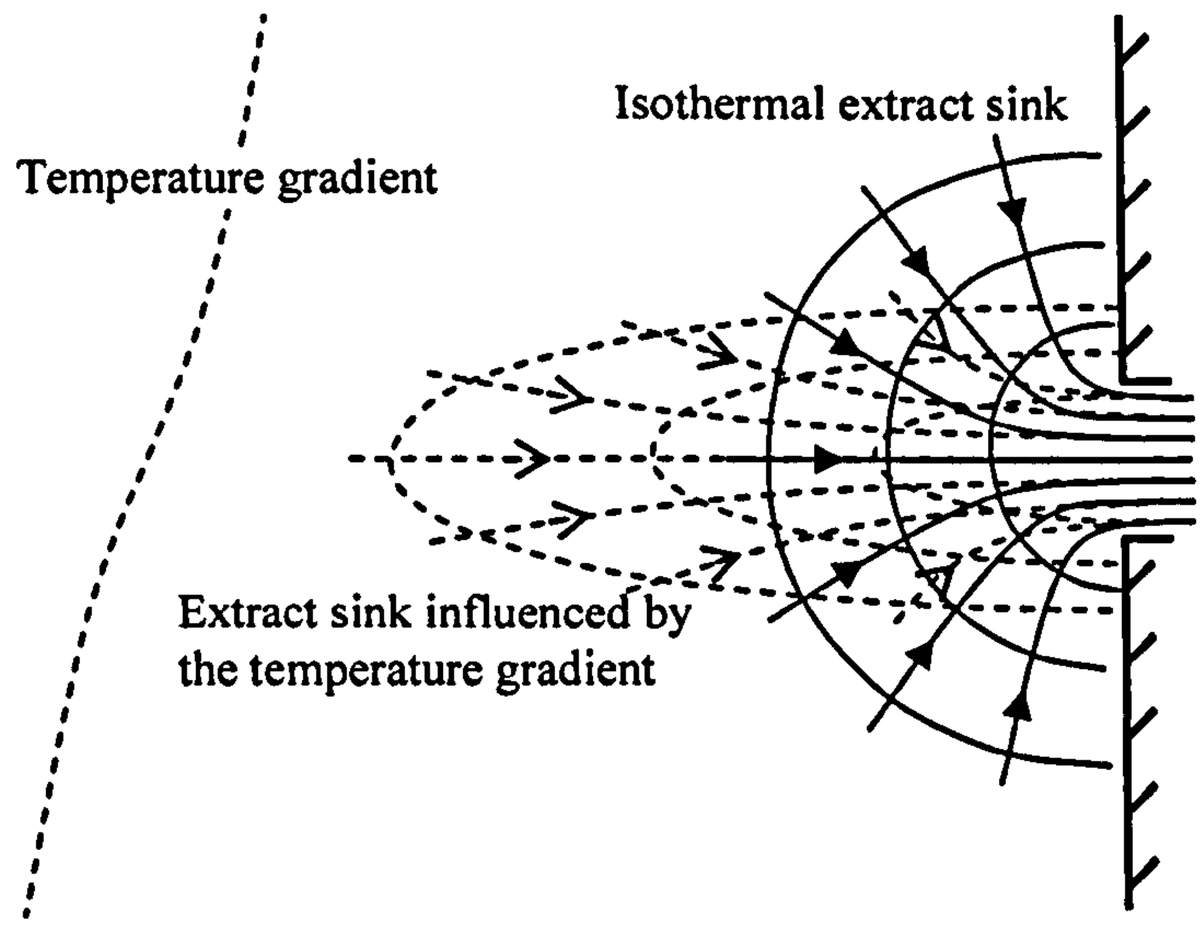

Figure 5.18: Schematical representation of a vertical cross-section of a semi-spherical sink passing through the middle of the extract in isothermal conditions and the effect of the temperature gradient on the flow pattern.

The following expression is valid for isothermal flow,

$$u_x = \frac{Q_E}{A_E + 2\pi x^2} \tag{5.1}$$

and rearranging equation (5.1) for x, the distance is,

$$x = \sqrt{\frac{Q_E - A_E u_x}{2\pi u_x}} \tag{5.2}$$

For isothermal flow, the distance for the extract speed setting in the experimental conditions where the streamlines start to curve towards the extract can be evaluated as x = 0.7 m. However, due to ΔT affecting the extract flow, the horizontal radius where the flow shrinks is estimated as $x \approx 1.2$ m, which is obtained from the current CFD simulations by applying the leakage openings to the virtual CFD model in Figure 5.17 (a). This occurs in the vertical plane shown in the same Figure 5.17 (a) at a reduced distance by approximately a factor of 2 where u_x = 0.02 m/s, while it expands by a factor of 2 in the horizontal direction perpendicular to the plane. The effect of the extract flow on the interface is shown in Figure 5.17 (b) by the curves when applied both openings for the entire width of the room, i.e., 5.5 m, and a smaller width of 1 m. The vertical sink of the extract flow becomes squashed by approximately a half, while

the horizontal sink increases by approximately a half to compromise the reduction from the vertical direction of the flow. The extract sink seems to be detached from the rest of the air medium in the room at u_x as specified above. Any flow of openings or cracks to the outside was also detached from the rest of the air medium in the room.

5.3.11 Modelling the hot air supply momentum effect and direction for different cold air supply rates

The temperature contours, velocity vectors and temperature gradients in Figure 5.19 were obtained by using the dimensions of the standard test model, except that the shape of the hot air supply diffuser was modified to simulate the effects of the real geometry. The neck area was used for the hot air diffuser which is $A_{HS} = 0.045\,\mathrm{m}^2$ and the side length was $a_{HS} = 0.225\,\mathrm{m}$ without the blades and the centre core as a plane inlet. For the cold air diffuser, the effective area was used that resulted from the measuring distance of the anemometer, which is $A_{CS} = 0.25\,\mathrm{m}^2$ and side is $a_{CS} = 0.5\,\mathrm{m}$. However in this case, the actual difference was the flow direction from the hot air supply diffuser in contrast to the previous normal direction to simulate the directional effects that occurred in the experiments. Although the actual diffuser blades were at a smaller angle to the horizontal, coalition of the slot jets can occur below the diffuser face that can slightly increase the downward angle to the flow direction in relation to the speed of the individual jets, and hence this was changed here to 45° to represent a more general case. A more detail investigation follows in the next section where the shape of the hot air diffuser is represented in more detail to simulate more appropriately the outflow direction. The supply momentum of hot and cold air was closely matching one of the experimental cases, where initially $Q_{HS} = 0.1\,\mathrm{m}^3/\mathrm{s}$ and $Q_{CS} = 0.05\,\mathrm{m}^3/\mathrm{s}$, while Q_{CS} was later changed to 0.1 and $0.144\,\mathrm{m}^3/\mathrm{s}$ representing a high Re case and the inlet temperature difference was $\Delta T_{in} = 20°\mathrm{C}$. A set of cases with $A_{HS} = 0.135\,\mathrm{m}^2$, $a_{HS} = 0.375\,\mathrm{m}$ and $A_{CS} = 0.25\,\mathrm{m}^2$, $a_{CS} = 0.5\,\mathrm{m}$ represented a low Re case with the larger diffuser. The flow rates in this set of cases are $Q_{HS} = 0.0382\,\mathrm{m}^3/\mathrm{s}$, $Q_{CS} = 0.05\,\mathrm{m}^3/\mathrm{s}$ and $Q_{HS} = 0.0382\,\mathrm{m}^3/\mathrm{s}$, $Q_{CS} = 0.05\,\mathrm{m}^3/\mathrm{s}$. The radiation model or any heat losses were not included in these cases.

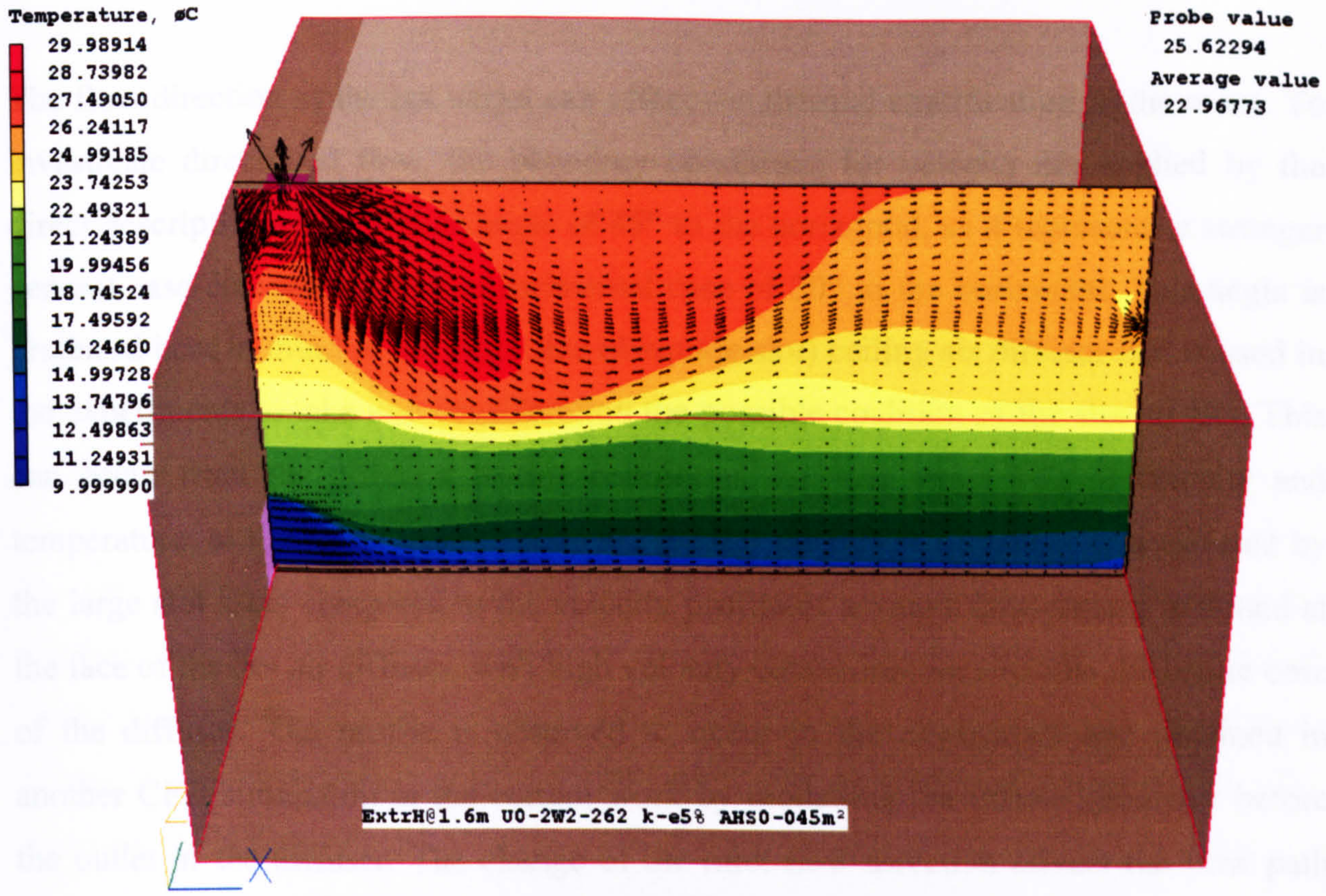

(a)

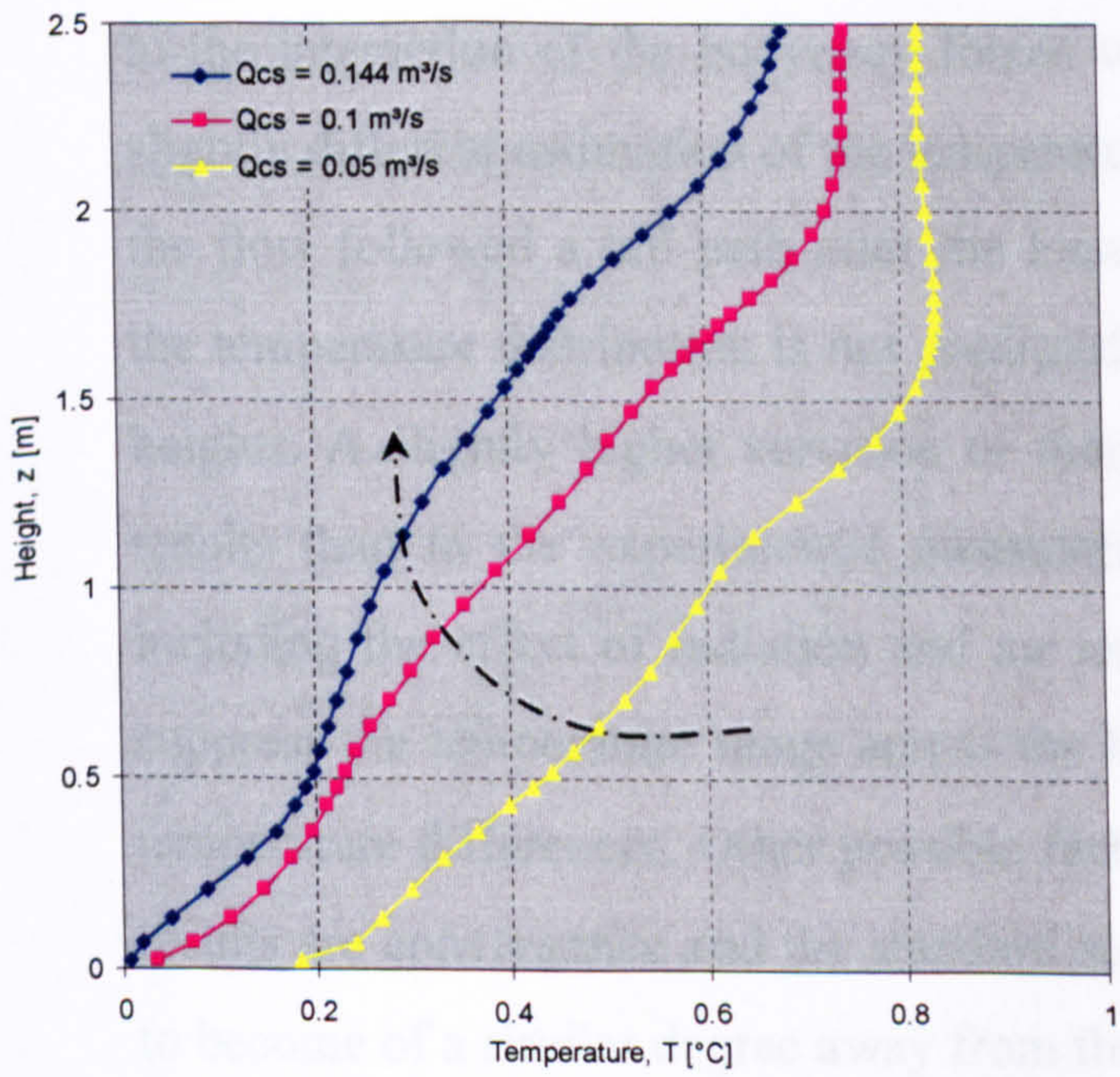

(b)

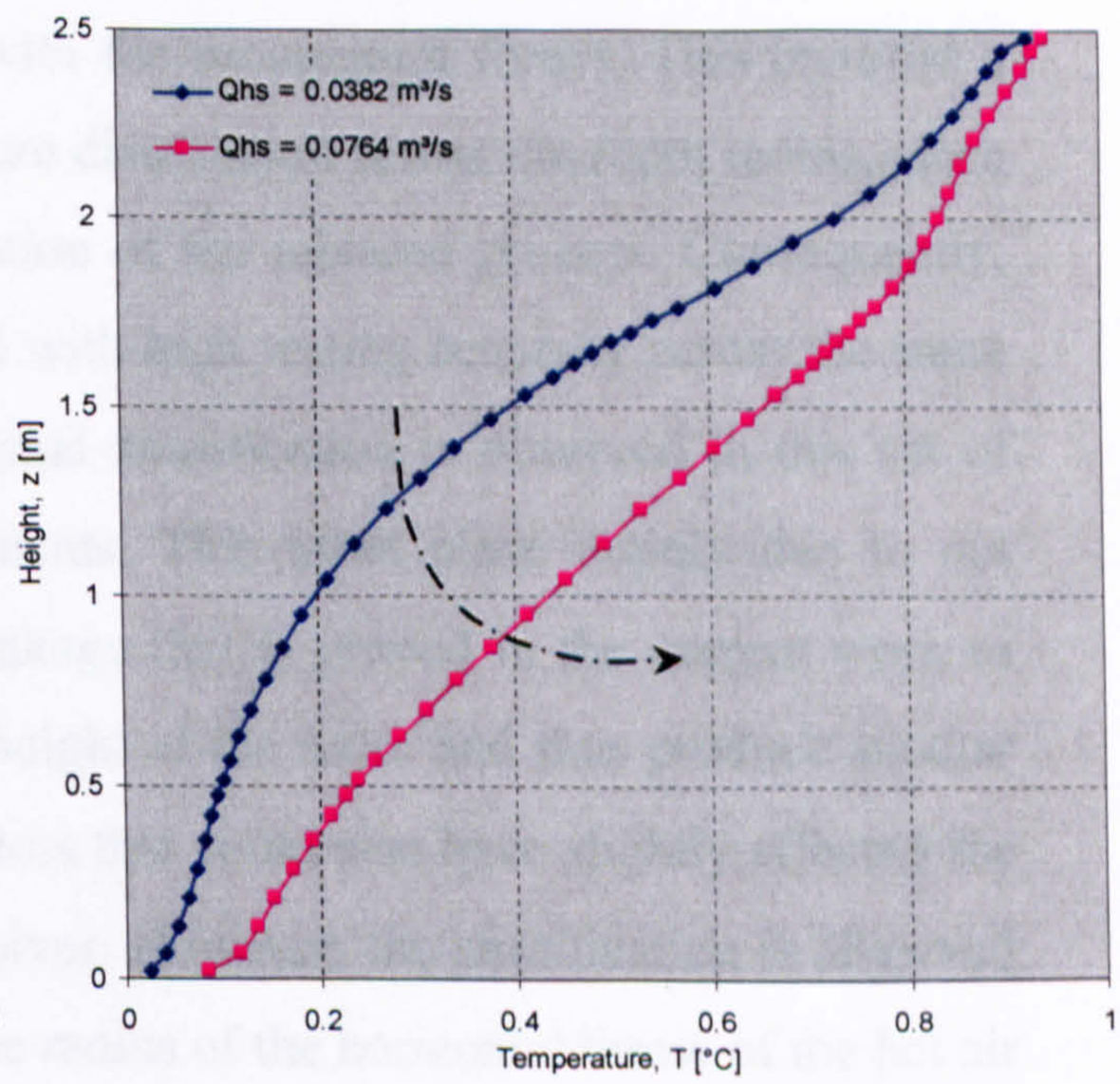

(c)

Figure 5.19: Effect of direction of flow from hot air supply diffuser and supply area, while the cold air diffuser area is constant, A_{CS} = 0.25 m² (0.5×0.5m). In (a), temperature contours and velocity vectors around the diffuser to study stratification due to inlet momentum direction. In (b), comparison of temperature gradients between three different cold supply air flow rates, keeping the hot air supply constant, Q_{HS} = 0.1 m³/s and area of hot air supply, A_{HS} = 0.045 m² (0.225×0.225m). In (c), the effect of increasing hot air supply flow rate, while the cold air supply is constant Q_{CS} = 0.05 m³/s and area of hot air supply, A_{HS} = 0.135 m² (0.375×0.375m).

The flow direction of the hot air jet can affect the thermal stratification in the room. To investigate directional flow, the boundary conditions for velocity are applied by the direct description method at an angle of 45° to the horizontal, as it represents a stronger general case compared to the experimental case of 30° to the horizontal. This angle is preferred here in mind of the large size (4-square slot) ceiling air diffuser that is used in the experiments to take into consideration the possible coalition of the slot air jets. This can occur from the different testing conditions, i.e., the magnitude of velocity and temperature, as the direct method does not predict the inflow direction. It is affected by the large slot sizes compared to the velocity profile of a round flow pattern obtained at the face of the hot air diffuser, with high velocity concentrations towards the centre core of the diffuser. The profile is observed to occur in the experiment and obtained in another CFD simulation in the current work by modelling the inflow geometry before the outlet of the diffuser. The change of the inlet flow direction affects the flow path close to the middle of the room where the rebound process of the hot air takes place due to the interaction of the buoyancy forces with the momentum forces. This incurred a slightly different estimation of the temperature distribution across the room radius, since the flow followed a hill path after the location of the rebound process. Consequently, the temperature distribution is not predicted with high testing accuracy across the same heights. A slightly higher variation of thermal stratification is observed in this set of results than in the experimental measurements. This takes place mainly due to not including the effect of radiation and air leakage that is proved in the current work to suppress the temperature range across the height of the room and thus produce smaller temperature differences. Other possible factors that could also have slightly affected the results are convergence and the standard solver. However, the stratification is observed to become of a similar degree away from the radius of the horizontal throw of the hot air jet, although it is slightly more linear. The temperature gradient close to the exhaust is slightly more stratified owing to the immediate interaction of the sink flow pattern and the relatively higher flow rate creating a higher sink as opposed to a downward oriented jet that mixes the stratified flow as soon as it reaches the floor. The simulations with the vertically downward flow show less variation. Thus, the temperature gradient can vary with location by a small range of values depending on the influence of hot or cold air jets on the stratified flow (the location of measurements has also been mentioned in Chapter 4). Therefore, the best choice for the location of measurements in using a directional jet would be the place where the temperature gradient becomes desensitised

by the influence of the jet flow. This is also affected by the room size and hence the ratio of the throw distance with room size would become important to describe the testing of stratification correctly. However, the important point here is to show the influence of the flow direction on the average temperature distribution that can be obtained in the middle area of the room and could have slightly affected the corresponding performance of the experimental measurements.

5.3.12 The 3-dimensional ceiling air diffuser – Coanda effects and outlet profile

The temperature contours in Figure 5.20 were obtained by using the dimensions of the standard test model up to the face of the cold air supply terminal with primary consideration given to the shape of the hot air supply. This was modified to simulate the effects of the geometry of the 4-square-slot diffuser used in the experiment. The direction of the vanes in the hot air supply diffuser was at 30° to the horizontal same as in the experiment. The supply momentum of hot and cold air were of equal flow rates, i.e., $Q_{\mathrm{HS,CS}} = 0.06\,\mathrm{m^3/s}$, at the supply inlets as an initial combination, representing a high Re case, while the inlet temperature difference was $\Delta T_{in} = 20°\mathrm{C}$ and the radiation model was not included.

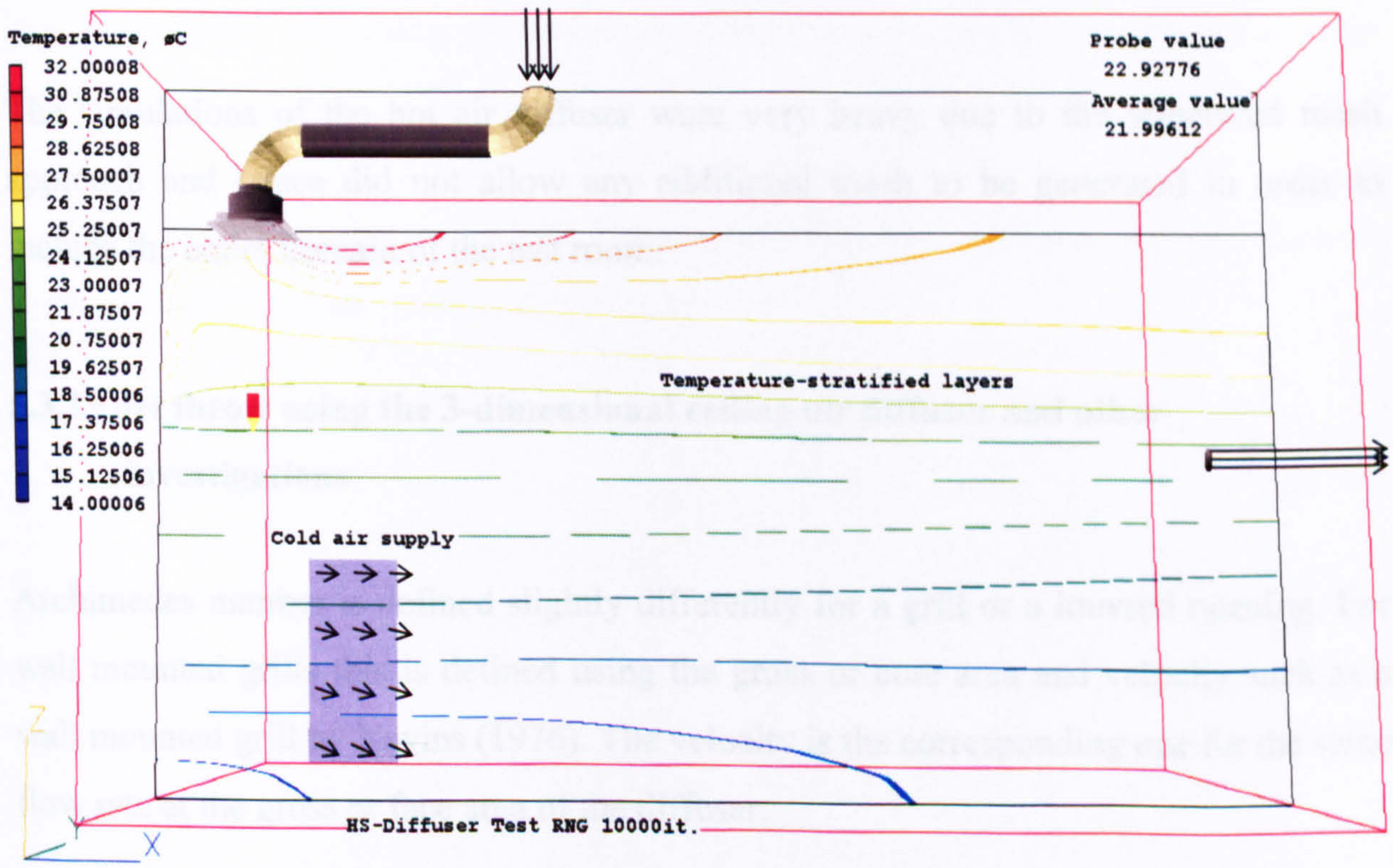

(a)

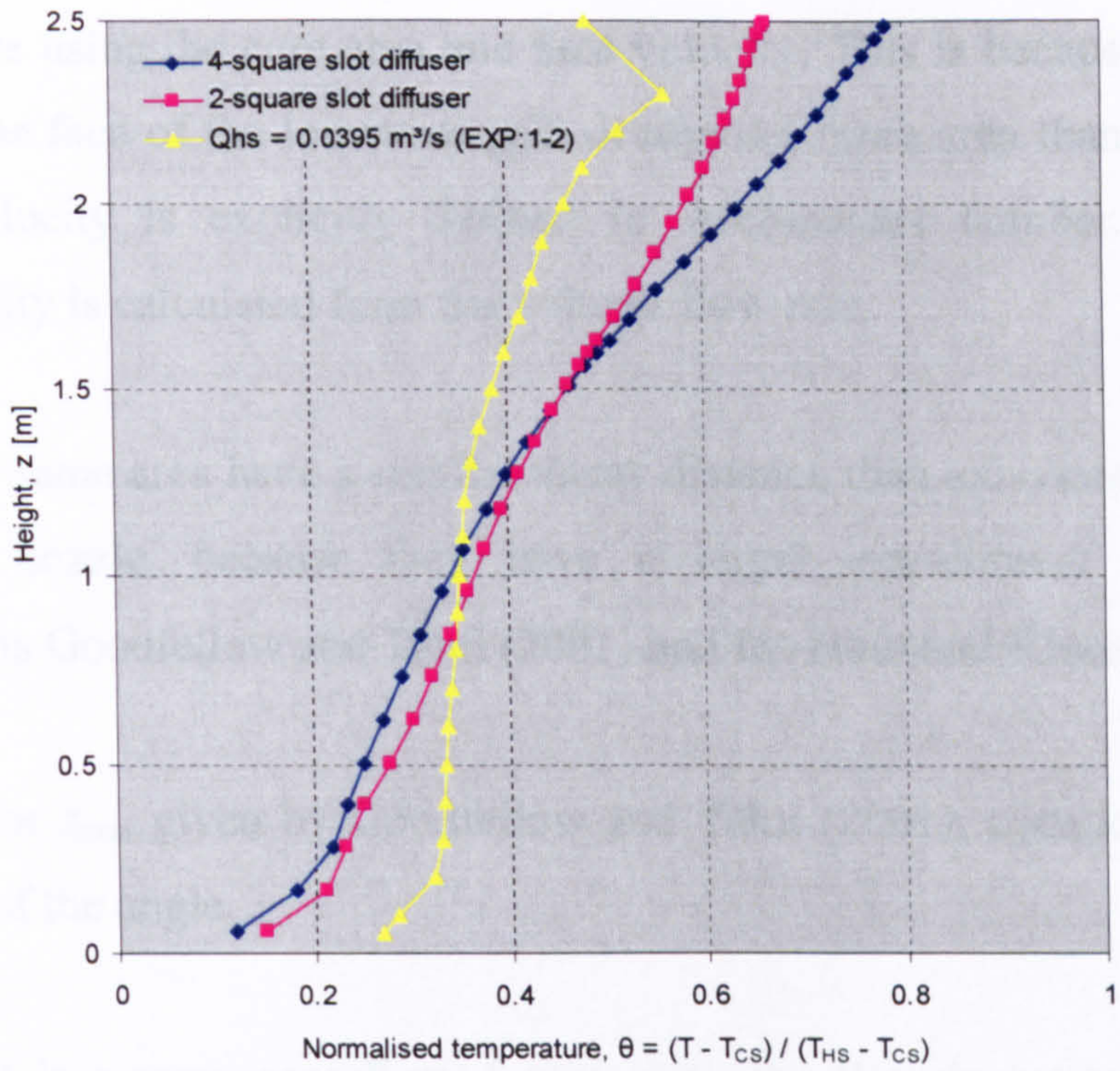

(b)

Figure 5.20: The effect of modelling the hot air supply diffuser geometry. In (a), temperature contour plot showing temperature distribution around the 3-dimensional diffuser such as, coanda effects around the front wall and stratified layers obtained. In (b), a comparison of temperature gradients between the experiment, a corresponding CFD case for the 4-square slot diffuser and a CFD of the 2-square slot diffuser, where the radiation model or any heat losses were not applied.

The simulations of the hot air diffuser were very heavy due to the structured mesh approach and hence did not allow any additional mesh to be generated in order to include the entire domain of the test room.

5.3.13 Jet throw using the 3-dimensional ceiling air diffuser and other investigations

Archimedes number is defined slightly differently for a grill or a louvred opening. For wall mounted grills this is defined using the gross or core area and velocity such as a wall mounted grill by Nevins (1976). The velocity is the corresponding one for the same flow rate at the gross or face area of the diffuser.

Most supply air openings in the literature are ideally for discharge of circular openings, i.e., they do not include vanes or cones. To make a comparison between a grill or a louvre opening the equivalent Archimedes number was obtained here for the equivalent

size of the louvre using the core area and face velocity. This is because of the velocity distribution at the face of the louvre or grill occupying more area than in the case of a nozzle. The velocity is explicitly defined in Archimedes number. Therefore, the equivalent velocity is calculated from the volume flow rate.

Linear jet of the same area have a smaller throw distance than axisymmetric jets issuing from a round nozzle, because they have a larger entrainment coefficient than axisymmetric jets Goodfellow and Tähti (2001) and Int-Hout and Kloostra (1999).

The equations for z_{max} given by Goodfellow and Tähti (2001), equations (7.92-95), do have the effect of the angle.

The ribbed duct is a more complicated case since the flow is not supplied vertically downward as prescribed originally due to the bend above the ceiling. The characteristic scale of turbulence in this case may also be related to the duct diameter. From preliminary studies using this duct, the jet travels at a larger distance than the interface height for velocities of 1.5-3.5m/s. Therefore, it can be difficult to correlate the throw from this pipe with Archimedes number with respect to the other outlets. Measurement at a higher accuracy could be required to obtain a good correlation at lower flow rates. In any other case, the mixing resulted from an impinging jet mixed the flow in the entire room.

A comparison of the throw from the 3-dimensional 2-square-slot diffuser with the data from literature has been made in Figure 5.21.

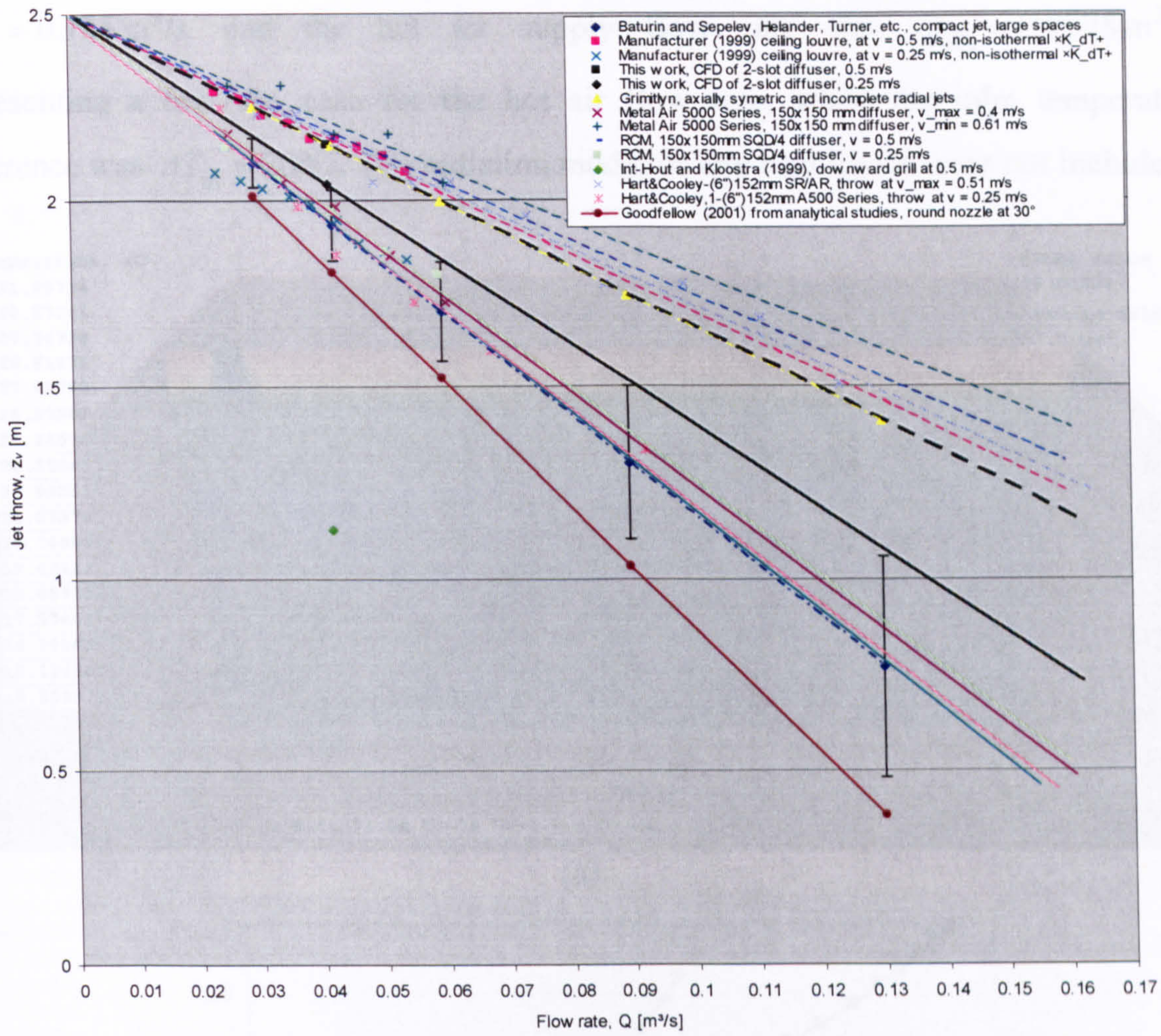

Figure 5.21: Downward throw from analytical studies and CFD of 2-square-slot diffuser.

5.3.14 Virtual CFD modelling of the cold air supply diffuser

Similar to the hot air diffuser, the difference in modelling the actual cold air diffuser was in the direction of the supply flow rate to match the outlet profile observed in the experiment. This was changed to 45° to the horizontal flow through a pipe from the ceiling with a 90° bend to provide with cold air through the cold diffuser. This was positioned a practically similar position to match the original location as shown in Figure 5.20. to simulate the directional effects that occurred in the experiments at the larger area of the cold air diffuser. This is in contrast to the idealised test model with a normal direction applied to a plane inlet and the larger area where the mean velocity is smaller than the reduced effective area. The temperature contours, velocity vectors and temperature gradients in Figure 5.22 were obtained by using the dimensions of the standard test model, except that the shape of the cold air supply diffuser was modified to simulate the effects of the experimental geometry. The cold air supply flow rate was

$Q_{CS} = 0.135\,\mathrm{m^3/s}$ and the hot air supply flow rate was $Q_{HS} = 0.0378\,\mathrm{m^3/s}$, representing a low Re case for the hot air flow rate, while the inlet temperature difference was $\Delta T_{in} = 20°\mathrm{C}$. The radiation model or any heat losses were not included.

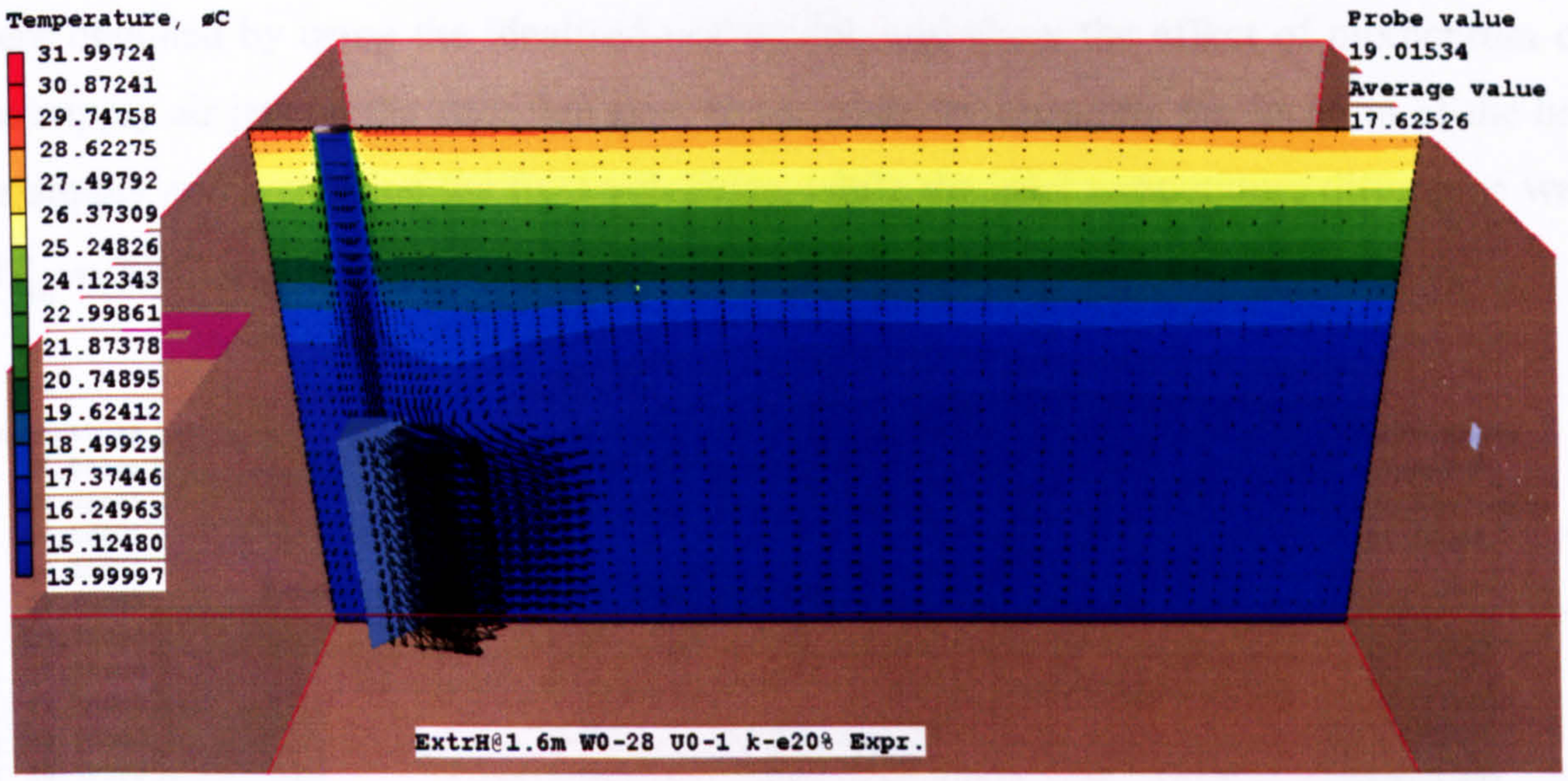

(a)

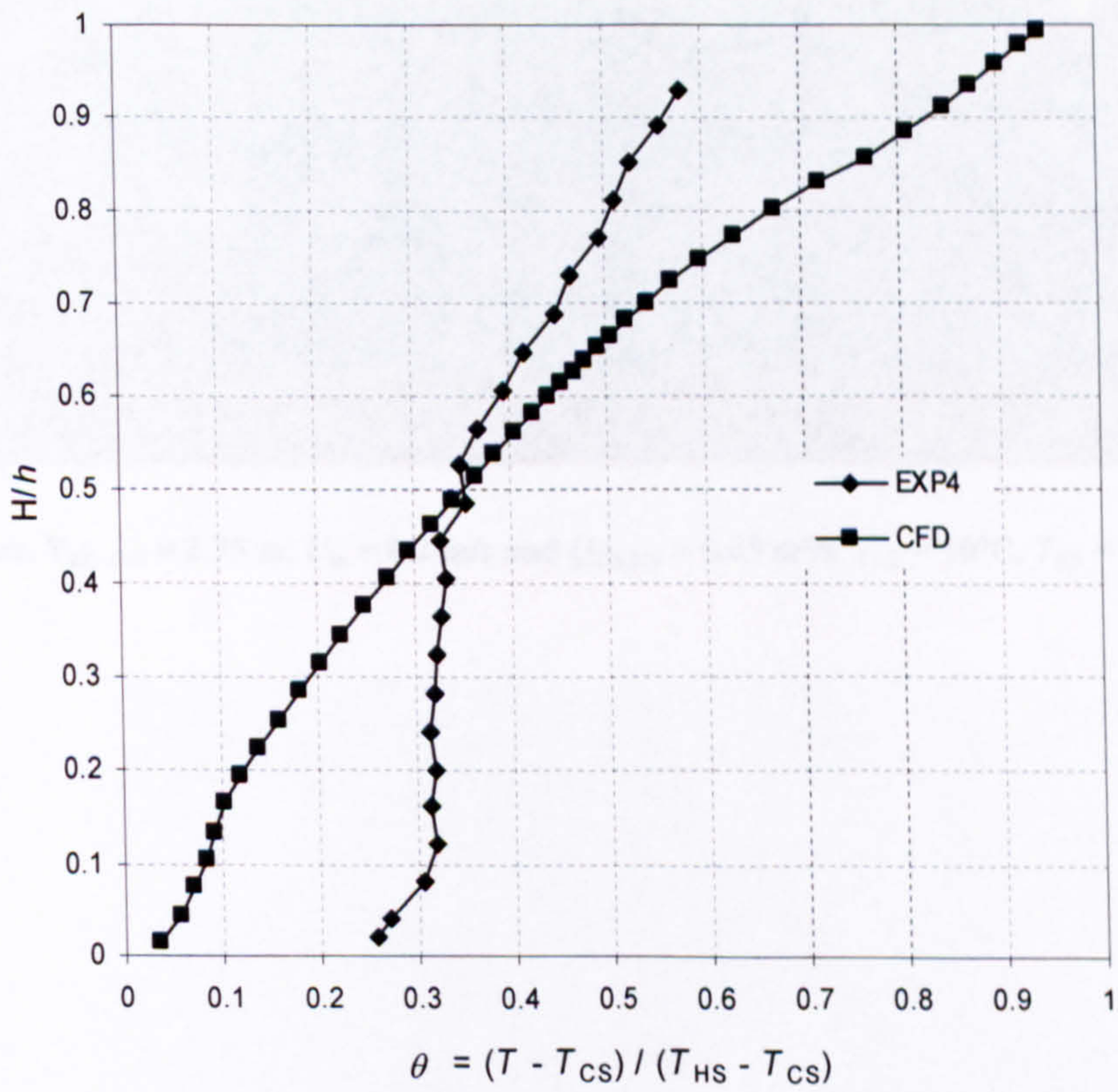

(b)

Figure 5.22: The effect of modelling the cold air supply diffuser geometry. In (a), temperature contour plot from model of cold air supply diffuser exactly modelled showing cold draughts from supply pipe, entrainment from the cold air supply diffuser, outlet profile and temperature-stratification obtained. In (b), comparison of temperature gradients between CFD and experiment, showing inconsistencies due to radiation and heat losses.

5.3.15 Position of the hot air supply

The temperature contours and the velocity vector fields in Figure 5.23 and Figure 5.24 were obtained by using the idealised test model, and show the effect of momentum of the supply air jets on the stratified flow in the room by changing the location of the hot air supply and increasing the inlet velocities, while the inlet temperature difference was $\Delta T_{in} = 20°C$ and the radiation model was not included.

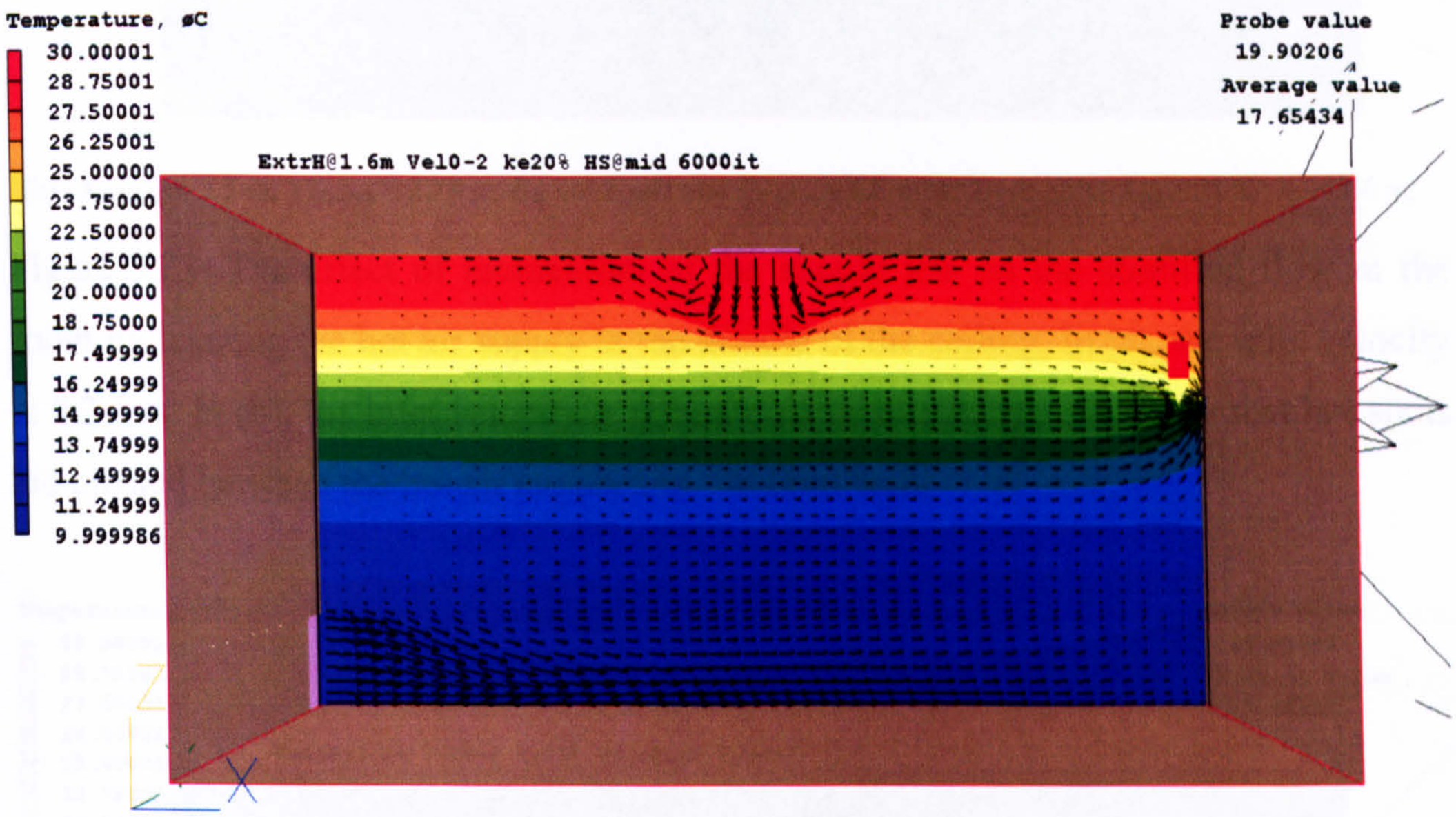

(a) **$X_{HS\text{-}Diff}$ = 2.5 m, $Y_{HS\text{-}Diff}$ = 2.75 m; U_{in} = 0.2 m/s and $Q_{CS,HS}$ = 0.05 m³/s**; T_{CS} = 10°C, T_{HS} = 30°C; h_E = 1.6 m.

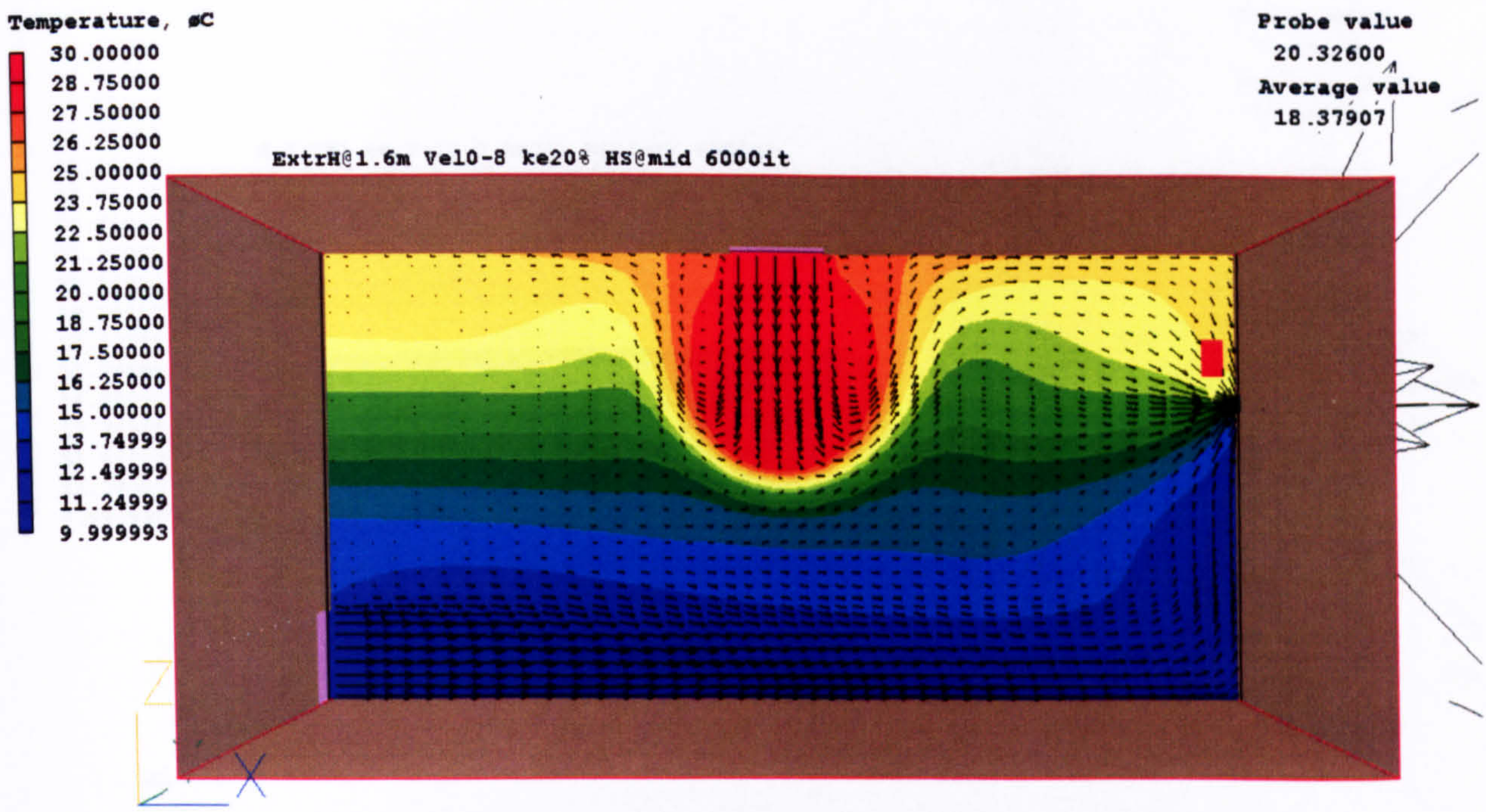

(b) $X_{HS\text{-}Diff}$ = 2.5 m, $Y_{HS\text{-}Diff}$ = 2.75 m; U_{in} = 0.8 m/s and $Q_{CS,HS}$ = 0.2 m³/s; T_{CS} = 10°C, T_{HS} = 30°C; h_E = 1.6 m.

Figure 5.23: The effect of momentum of the supply jets on the stratified flow in the room by locating the hot air supply in the middle of the ceiling. In (a), the inlet velocity is 0.2 m/s. In (b), the inlet velocity is 0.8 m/s. At this velocity, it is likely that hot spots are created between the hot air supply and the front wall.

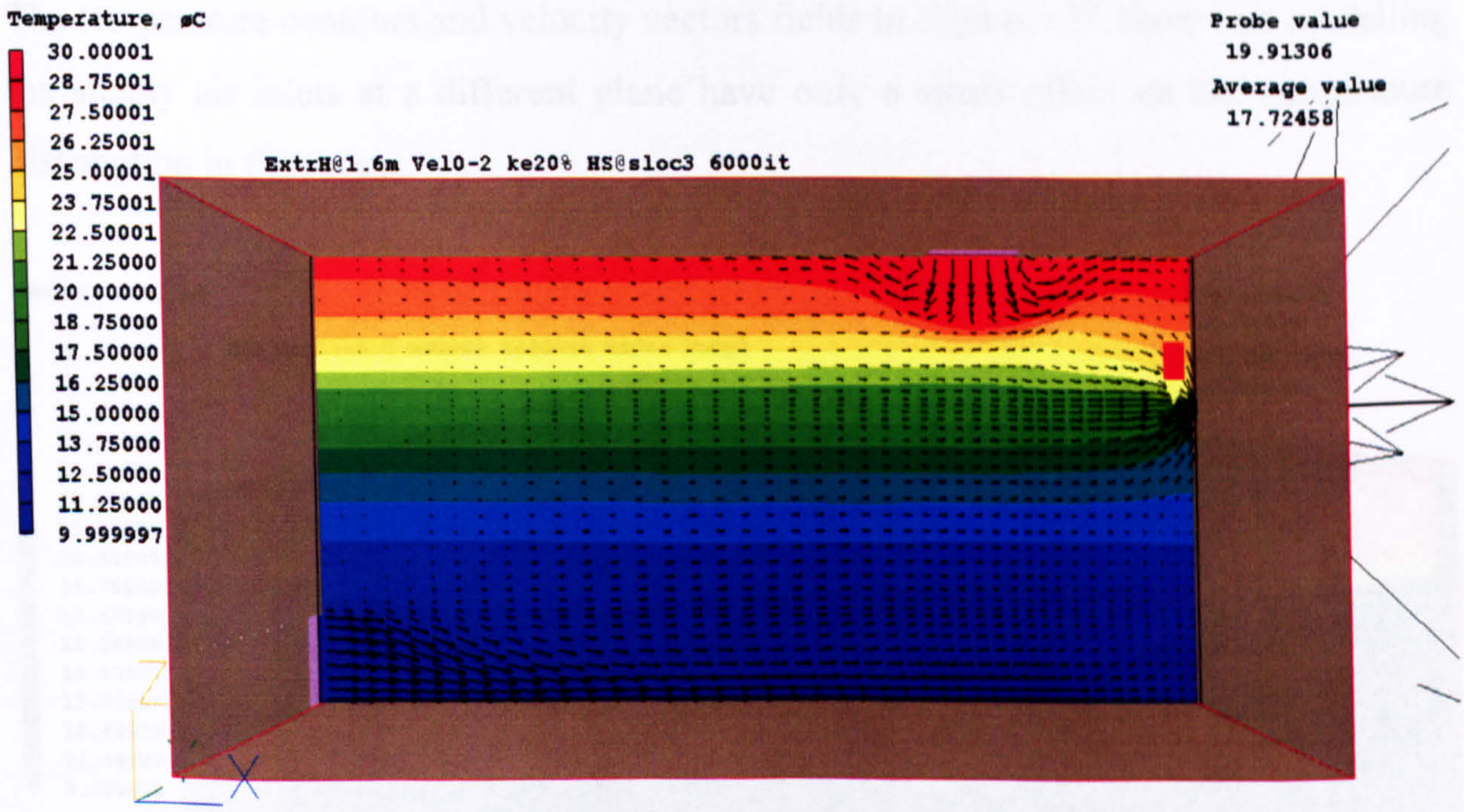

(a) $X_{HS\text{-}Diff}$ = 3.75 m, $Y_{HS\text{-}Diff}$ = 2.75 m; U_{in} = 0.2 m/s and $Q_{CS,HS}$ = 0.05 m³/s; T_{CS} = 10°C, T_{HS} = 30°C; h_E = 1.6 m.

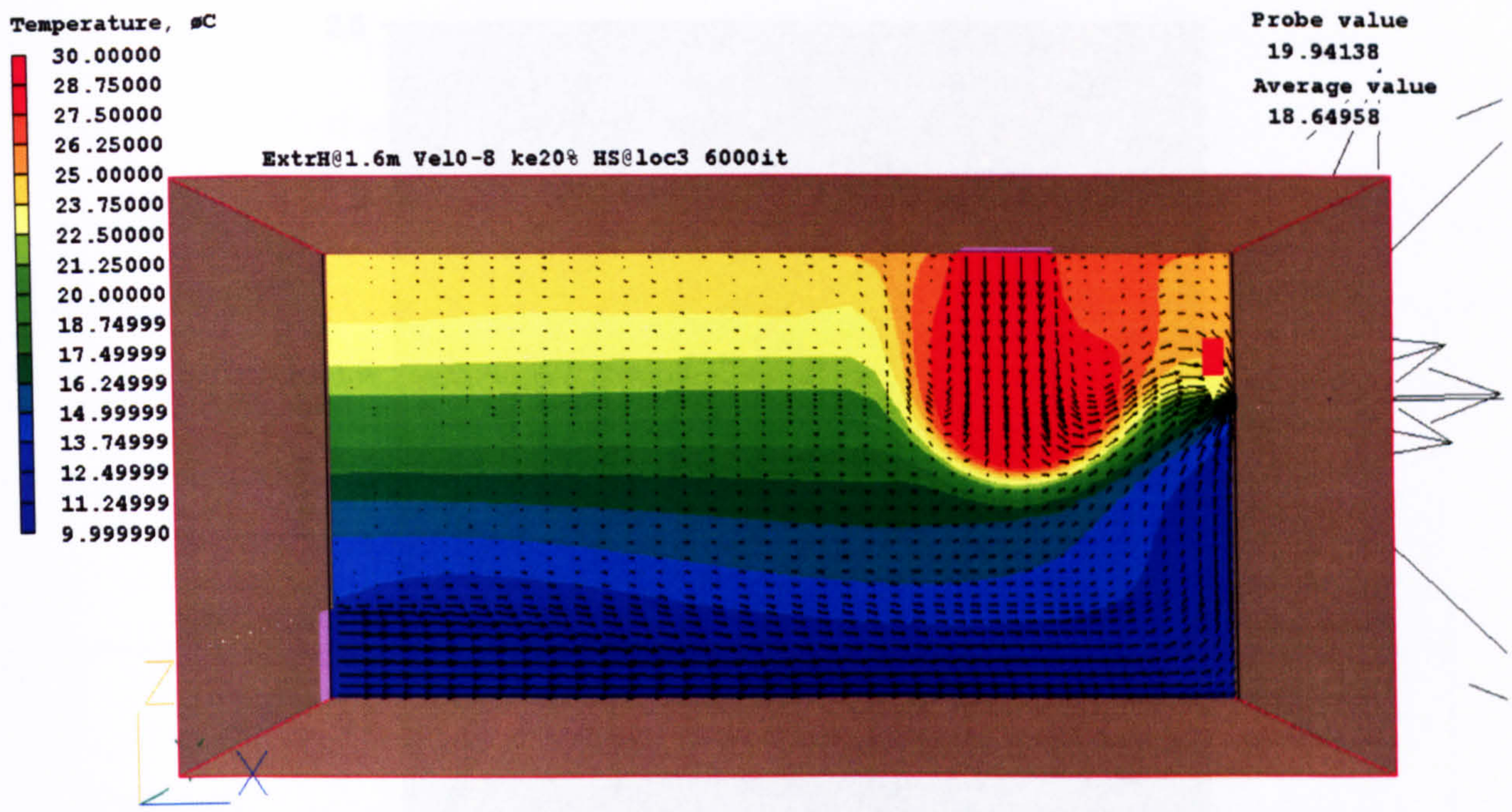

(b) $\mathbf{X_{HS\text{-}Diff} = 3.75}$ **m**, $\mathbf{Y_{HS\text{-}Diff} = 2.75}$ **m**; $\boldsymbol{U_{in}}$ **= 0.8 m/s**; T_{CS} = 10°C and T_{HS} = 30°C, h_E = 1.6 m.

Figure 5.24: The effect of momentum of the supply jets on the stratified flow in the room, by locating the hot air supply in the rear part of the ceiling. In (a), the inlet velocity is 0.2 m/s. In (b), the inlet velocity is 0.8 m/s. At this velocity it is likely that draught-like flow between the hot air supply and the exhaust is pronounced.

The temperature contours and velocity vectors fields in Figure 5.25 show that modelling the supply air inlets at a different plane have only a small effect on the temperature distribution in the room.

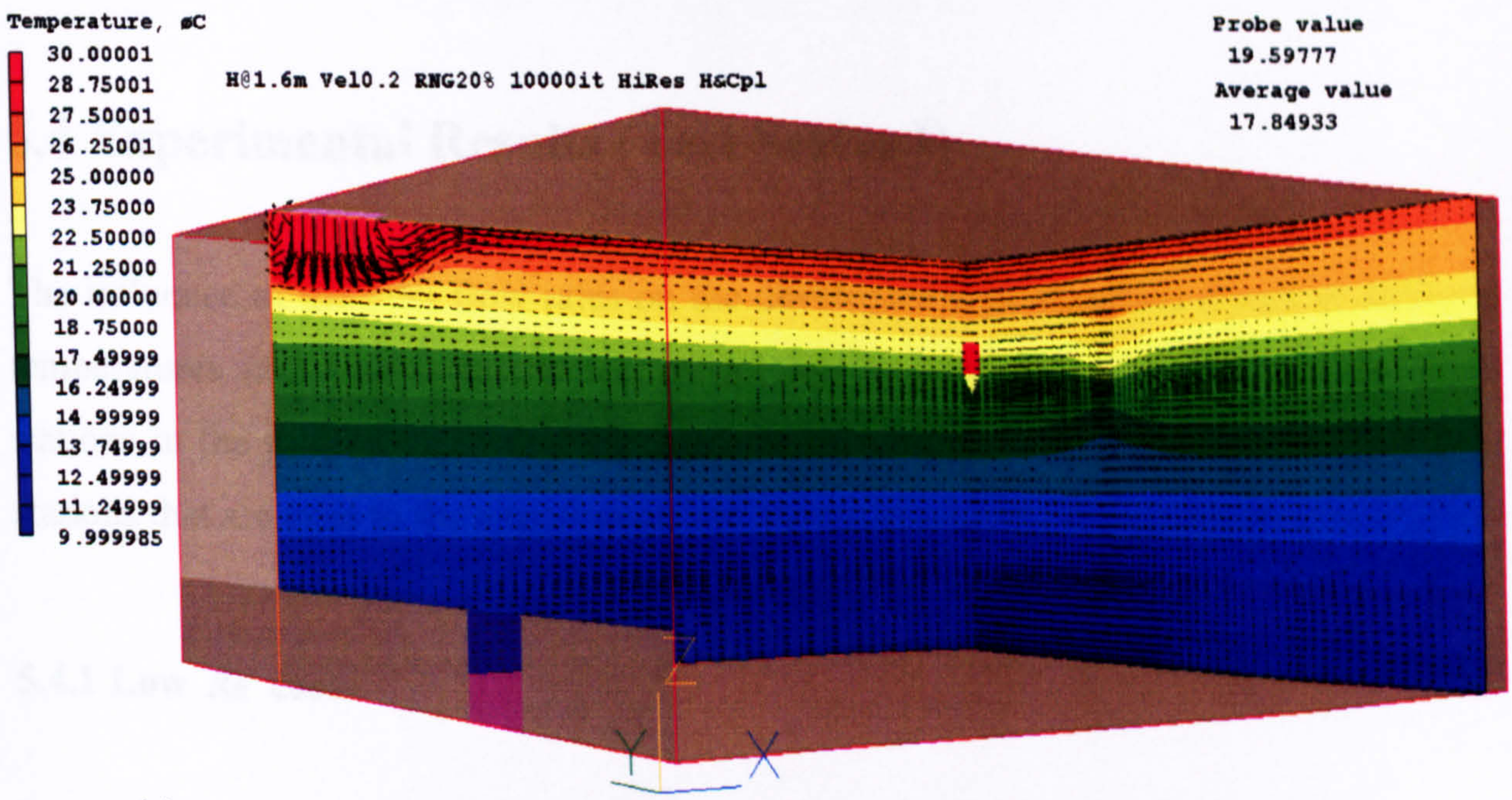

(a) $\mathbf{Y_{CS\text{-}Diff} = 1.75}$ **m and** $\mathbf{Y_{HS\text{-}Diff} = 3.75}$ **m**; $\boldsymbol{U_{in}}$ **= 0.2 m/s**; T_{CS} = 10°C and T_{HS} = 30°C, h_E = 1.6 m.

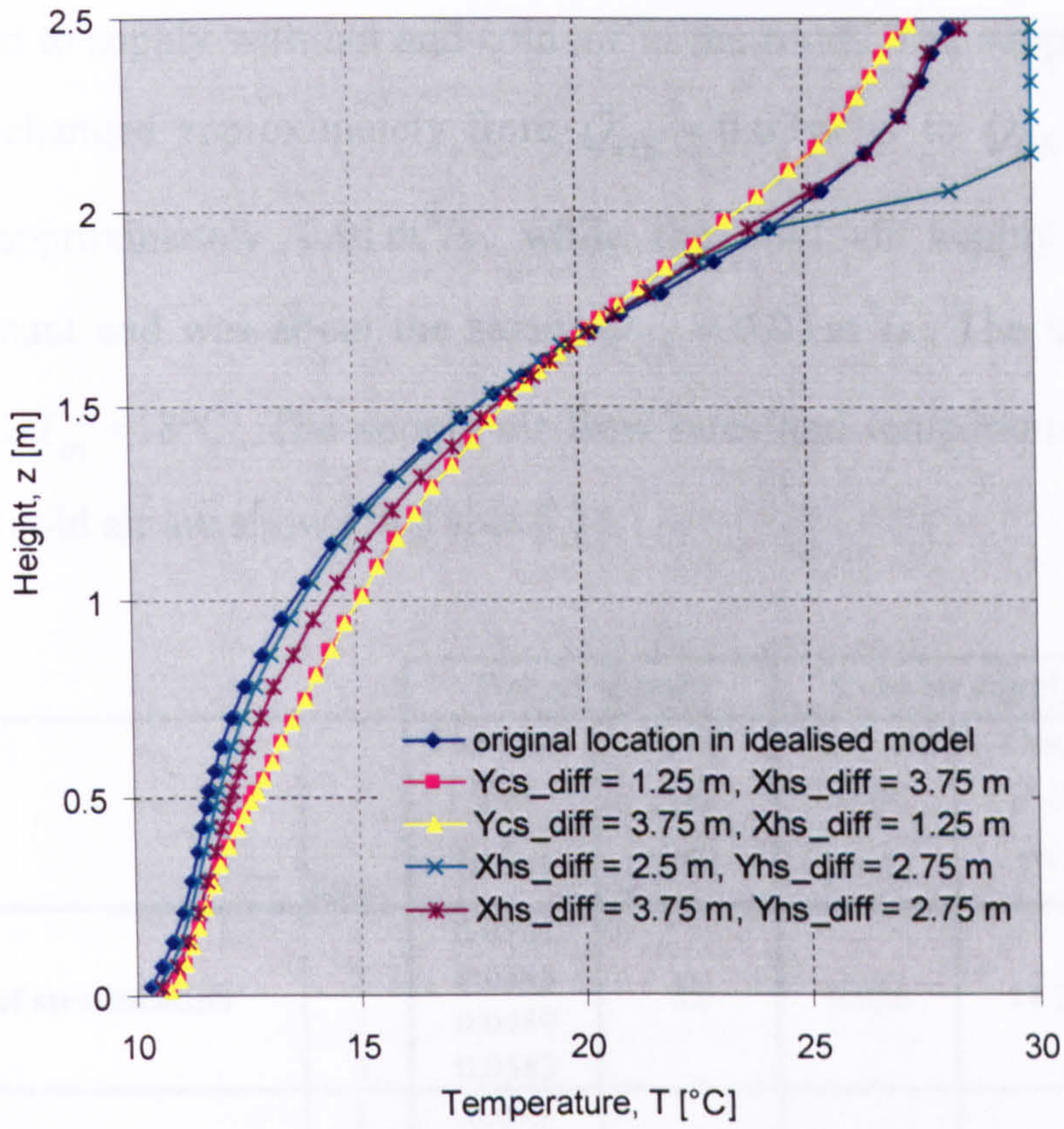

(b)

Figure 5.25: CFD results with inlets at different planes show that the Wedderburn effect is negligible. In (a), a combined plot of a streamwise and a vertical plane to the flow. This simulation was run with the location of inlet opposite to the experiment. However, comparison with simulation of the opposite location was not significant. This result is shown here because it easier to show the cross-sectional planes of temperature contours. In (b), results at different location and iteration number.

5.4 Experimental Results (Test Series I)

The influence of the inlet flow rates on the development of stratified layers at different temperatures and heights in the test model can be seen in Figure 5.1 and the data-stations in the middle space that are used for the comparison of the results. The data-stations that are used in the experiments are shown in Chapter 4 Figure 4.4.

5.4.1 Low *Re* cases

The temperature gradients in Figure 5.26 were obtained experimentally by using the dimensions of the standard test model. A ceiling air diffuser and a floor air terminal were used to reduce the effect of turbulence length scale from the flexible surface of

inflow ducts used to supply with hot and cold air in the room. The supply air flow rates of hot air were changed approximately from $Q_{HS} = 0.03\,m^3/s$ to $Q_{HS} = 0.06\,m^3/s$ by increments of approximately $0.01\,m^3/s$, while the cold air supply flow rate was maintained constant and was about the same, $Q_{CS} = 0.03\,m^3/s$. The inlet temperature difference was $\Delta T_{in} = 18°C$. The supply air flow rates and temperatures used in each case for hot and cold air are shown in Table 5.1.

		Hot air supply		Cold air supply		Extract
Experiment:	case:	Flow rate Q_{HS} [m³/s]	Temp. T_{HS} [°C]	Flow rate Q_{HS} [m³/s]	Temp. T_{CS} [°C]	Height h_E [m]
1. Formation of stratification	1 2 3 4	0.0301 0.0395 0.0489 0.0583	32	0.026	14.25	1.6
2. Full range of stratification	1 2 3 4	0.039 0.0649 0.0996 0.1385	32.25	0.064	8.25	1.6
3. Full ragne of stratification	1 2 3 4 5	0.0346 0.0693 0.1039 0.1385 0.1731	32.5	0.026	14.5	1.6
4. Effect of extract height.	1 2 3	0.0583	32	0.026	14.25	0.8 1.6 2.2

Table 5.1: Input parameters in the experimental work carried out in this thesis[2].

[2] The values shown here do not include the design data of the diffusers. For more information, the reader is referred to Appendix B.

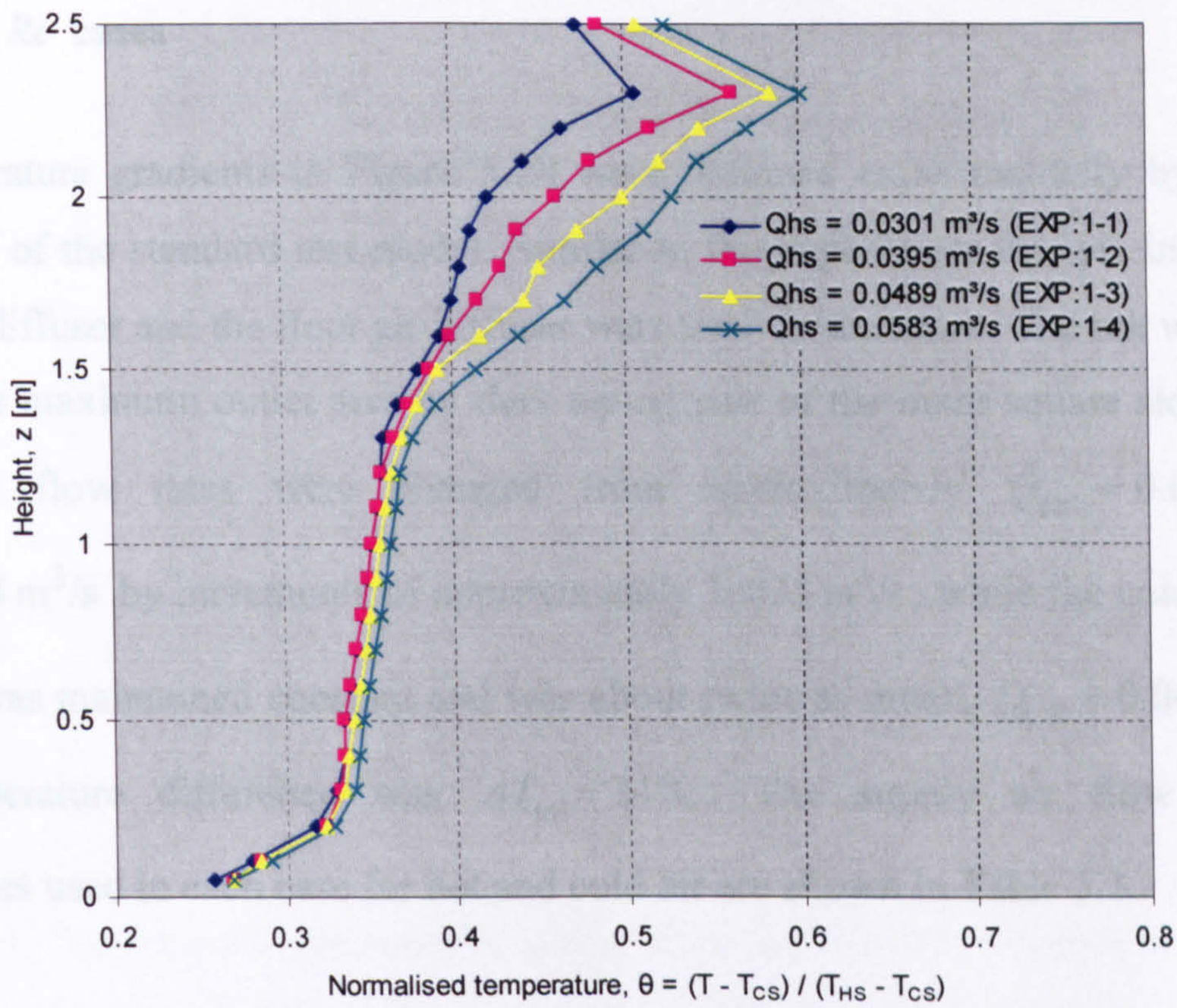

Figure 5.26: Effect of the temperature change across the height of the room, by slightly increasing the volumetric flow rate of the hot air supply in small equal amounts.

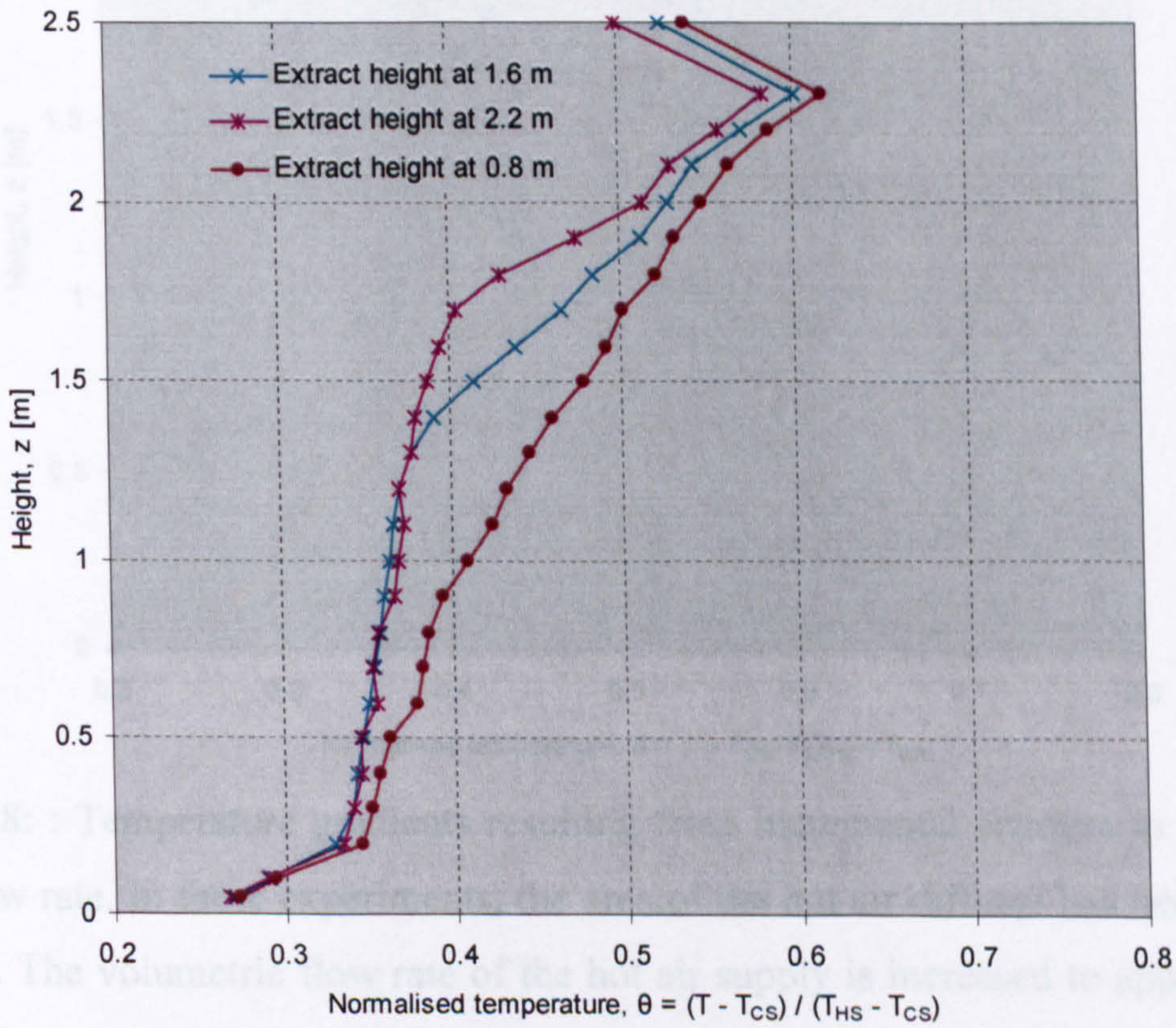

Figure 5.27: Effect of the extract height on the temperature gradient.

5.4.2 High *Re* cases

The temperature gradients in Figure 5.28 were obtained experimentally by using the dimensions of the standard test model. Similar to the experiment for low inlet Re, the ceiling air diffuser and the floor air diffuser were used in the room. The hot was reduced to 1/3 of its maximum outlet area by duct taping pair of the outer square slots. The hot air supply flow rates were changed from approximately $Q_{HS} = 0.04\,\mathrm{m^3/s}$ to $Q_{HS} = 0.14\,\mathrm{m^3/s}$ by increments of approximately $0.035\,\mathrm{m^3/s}$, while the cold air supply flow rate was maintained constant and was about twice as much, $Q_{CS} = 0.04\,\mathrm{m^3/s}$. The inlet temperature difference was $\Delta T_{in} = 24°\mathrm{C}$. The supply air flow rates and temperatures used in each case for hot and cold air are shown in Table 5.1.

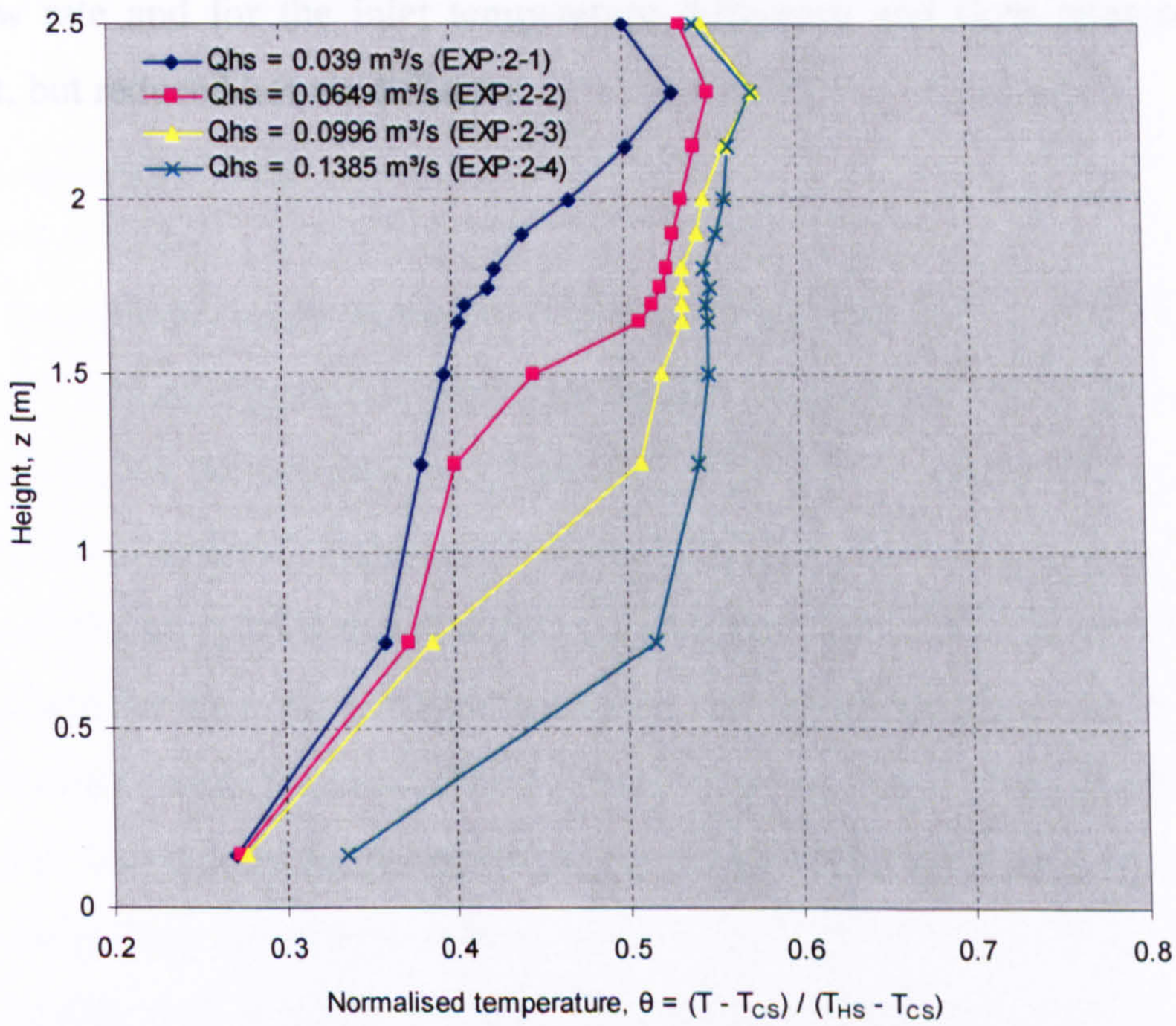

Figure 5.28: : Temperature gradients resulting from incremental changes in the hot air supply flow rate. In these experiments, the area of the hot air diffuser has been reduced by a third. The volumetric flow rate of the hot air supply is increased to approximately the second setting of the previous experiment and the cold air supply is increased to approximately the second setting of the current experiment as well as the inlet temperature range.

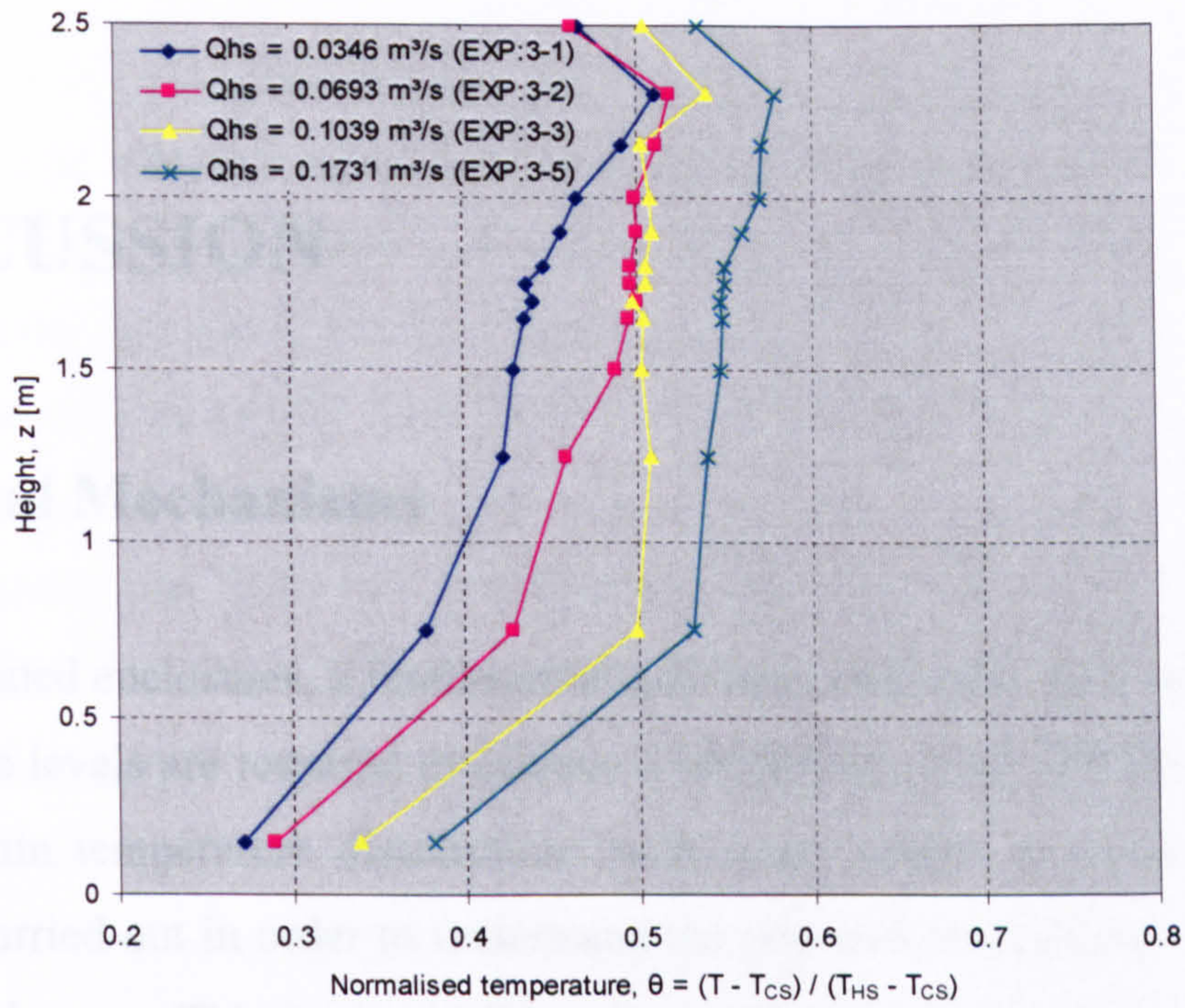

Figure 5.29: Temperature gradients resulting from incremental changes in the hot air supply flow rate and for the inlet temperature difference and flow rates of the first experiment, but reduced hot air diffuser.

6. DISCUSSION

6.1 Physical Mechanisms

In most ventilated enclosures, a fundamental question could arise as to what momentum or temperature levels are required to achieve a satisfactory level of mixing. This would result to certain temperature distributions with room height. A series of parametric studies was carried out in order to understand the physical mechanisms taking place in ventilated enclosures. This is shown from the parametric studies done by experiments and CFD.

6.1.1 Experimental results

The main fundamental cases involved in the experimental work are shown in Figure 5.26, Figure 5.28 and Figure 5.29 and a qualitative assessment of the effect of hot air supply flow rate on the temperature gradient is depicted schematically in Figure 6.1. The schematic shows a summary of the different shapes of the temperature gradients in the middle of the room by increasing the hot air supply flow rate, while maintaining a constant volumetric flow rate of cold air supply and constant supply air temperatures. This produces the temperature gradients shown from (1) to (6). Opposite effects occur by increasing the cold air supply flow rate, while maintaining the hot air supply flow rate constant ending up with temperature gradients viewed from (6) to (1). This is usually followed with a minor decrease in the temperature of the hot air layer that usually occurs due to mixing originating from the air flow increments of the opposite air supply, similar to the water experiments by Nelson *et al.* (1999). One set of experimental cases in this work was carried out for low inlet volumetric flow rates. The initial flow rates were nominally $0.03\,m^3/s$ and the hot air supply increments nominally $0.01\,m^3/s$ (see Table 5.1). The gross value of the exposed area of the hot air diffuser at the measuring distance of the anemometer used to obtain the temperature gradients in Figure 5.26 is 0.375 m and has a centre core side of 0.075 m making up an outlet area of

$0.135\,m^2$. This is the same as the neck area of the diffuser tabulated by the manufacturer. The effective side length at the measuring distance of the anemometer can then be defined by multiplying this area with a C_d coefficient. Four curves were produced with the full-size diffuser for low increments of hot air supply flow rate 0.01 m^3/s, while the cold air supply flow rate was maintained constant. The second set of experimental cases was carried out for higher inlet volumetric flow rates. The gross value of the square side of the hot air diffuser used to obtain the temperature gradients in Figure 5.28 is reduced to 0.225 m by duct taping a pair of the outer square slots making up an outlet area of $0.045\,m^2$. This is also the same as the tabulated neck area of the 2-square slot diffuser of the manufacturer. Four curves were produced with the reduced diffuser increasing the hot air supply flow rate by 0.035 m^3/s, which is of the order of the initial flow rate, while maintaining the cold air supply flow rate constant and about twice as much as the hot air supply flow rate. Additionally, the temperature of the cold air supply was reduced to expand the range of the initial air temperature differential. This determined more clearly the formation of an interface and the change in the temperature gradient of the hot air layer. There was only a small increase in the temperature magnitude of the cold air layer. It was found that by using this configuration produced more discrete stratification. The experiment was carried out again for the higher supply air flow rate of hot air, as shown in Figure 5.29, but for the temperature range and cold air supply flow rate of the first experiment to explore the stability of stratification beyond the range of values used in the previous experiments. This made the temperature across the room height become almost uniform and increase in magnitude at the final setting. The results were comparable to the second experiment but with a reduced range of temperatures that were also slightly smaller than in the first experiment. The range of incremental changes of the hot air supply in the second and third experiments produced a set of temperature gradients that were of certain engineering significance overwhelming the results of the first experiment. It was further understood that the larger area of the hot air diffuser in the first experiment reduced the outlet velocity significantly that caused the temperature gradient in the hot air layer to become more gradual and exhibit a larger temperature range, without considerably affecting the cold air layer or showing any strong stratification.

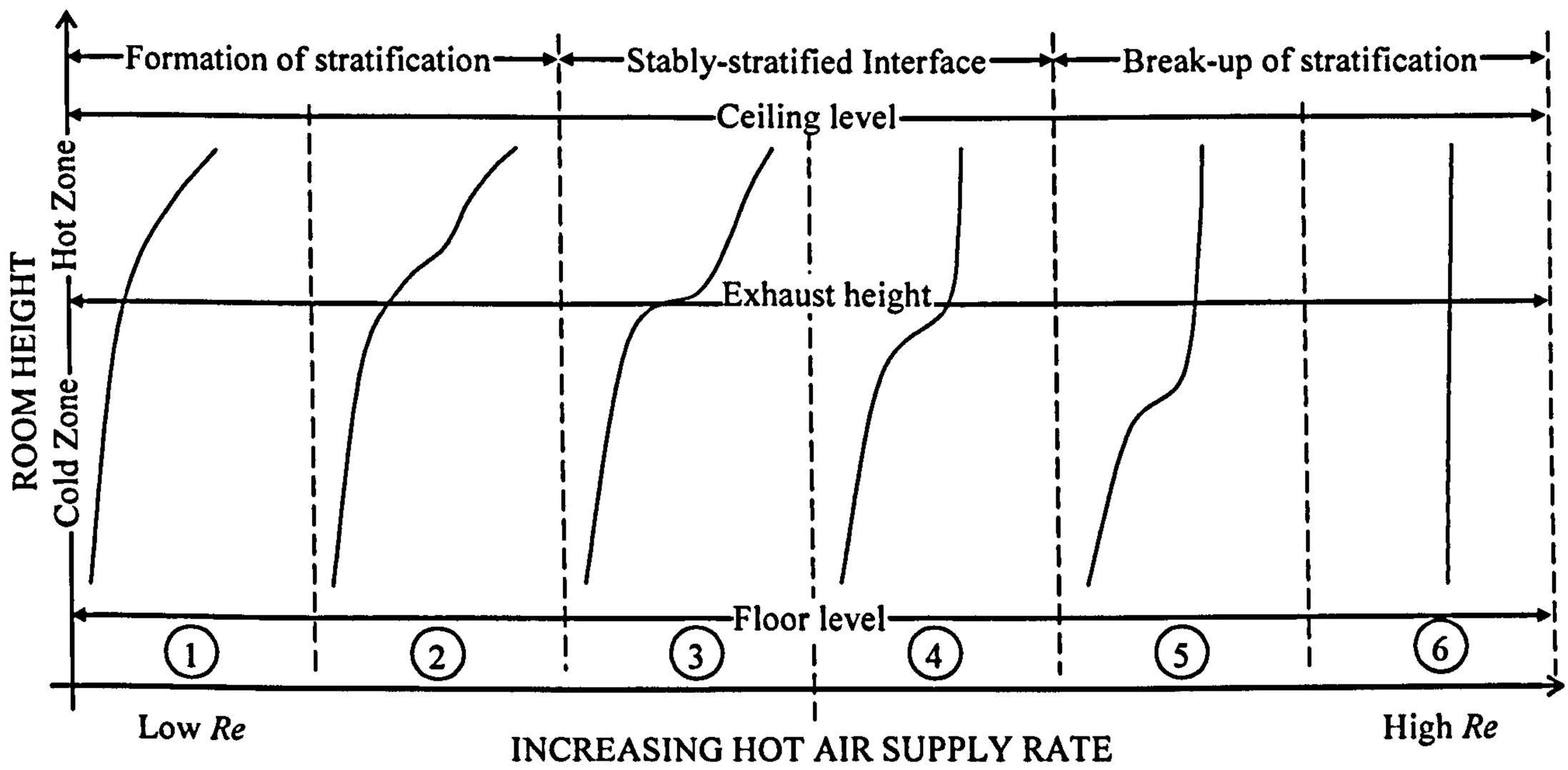

Figure 6.1: Schematical summary of the fundamental experimental cases depicting the main stages of stratification formation and break-up on the shape of the temperature distribution.

In region (1) of Figure 6.1, stratification formation is shown at very low air supply flow rates. The flow rates are insufficient to produce a well-defined temperature interface. A combination of the extract height and the rebound process of the hot air jet can affect the local slope of the temperature gradient. This can influence the formation of the interface. The temperature gradient in the hot air zone shows stable stratification that builds up over a gradual change of temperatures that occurs almost across the entire height of the room. This looks like an exponential error decay curve with the upper limit at a small distance below the ceiling and the lower limit down to temperatures of the cold air zone at some distance above the floor. The temperature gradient in the cold air zone is very small.

In region (2) of Figure 6.1, increasing the hot air flow rate has a proportional effect on the hot air layer and the local gradient of the interface. The gradient of the interface is fairly straight and it becomes a continuation of the hot air layer. In the lower layer, the interface diffuses into the cold air zone following an exponential distribution curve similar to the hot air zone of the previous case. The difference in the temperatures between the hot and cold air zones suggests that the interface is not yet that strong. The

quantitative difference of the gradient in the cold air layer with the previous case is very small, while there is almost not very large qualitative difference.

In region (3) of Figure 6.1, increasing the supply rate, the formation of the interface is more pronounced and the gradient diffuses into the cold air zone similar to the previous case. The gradient in the hot air zone has become steeper compared to the previous case depending on the strength of the convective currents in the development of the upper mixed layer. Additionally in this case, the change in the gradient of the cold air zone is small compared to the previous case but slightly larger than the change between the gradient in (1) and (2). Once again, there is a certain degree of similarity between the temperature gradients of the cold air zone. In this case there is a clearer similarity in the temperature gradient with the one obtained from the penetrative cooling in lakes and estuaries at nightfall that results from the rise and fall of convective currents due to the cooling of the surface layers.

In region (4) of Figure 6.1, the effects described in the previous case become realised more effectively as the hot air supply speed reaches a value at which the hot air zone becomes fully mixed. The mixing from the upper mixed layer above the interface reduces the thickness of the interface and causes the appearance of an intermediate diffusion layer below. This stretches into the cold air zone which is clearer than in the previous case. The result is a uniform temperature in the hot air zone, while the temperature gradient in the cold air zone is slightly greater than before due to the turbulent eddies penetrating the lower zone from above. The lower layer appears as a continuation of an end-point error distribution from the lower limit of the interface and the intermediate layer that becomes slightly smaller. As a result of the intermediate layer formation affected by shear flow and the larger temperature differences, there is a sharper interface definition compared to the previous cases (2) and (3). The associated turbulence leads to a slight increase in the temperatures of the bottom layer. Although some similarity may have been achieved with case (3), there is very little overall similarity with the preceding cases of developing stratification. There is a clearer similarity in this case with convective diffusion that can be parallelised with a gravity front of an oil discharge entraining heavier fluid from the bottom of the ocean in its horizontal path.

In region (5) of Figure 6.1, the hot air supply flow rate is further increased to the point that it increases the vertical thickness of the hot air zone regardless of the extract height. The changes in the temperatures of the cold air layer due to the associated turbulence with the large-scale fluctuating motion become a little higher compared to the previous case. This is attributed to the fact that the height of the cold air layer has become relatively smaller than the height of the hot air layer. The down-gradient heat flux (DGHF) acting in the opposite vertical direction becomes higher than in the previous case due to the proportional increase in the vertical height of the hot air zone in combination with the higher flow rate. In this case, the turbulent eddies occurring in the convective process across the height of the room act as the "filling-box" mechanism in the room that have a redistributive action. This is realised as the hot air zone increases its vertical thickness by mixing and the amount of warmer air in the room succeeds over the amount of cooler air.

In region (6) of Figure 6.1, the flow rate increases to a limit causing sufficient mixing across the entire room. This results in an almost uniform temperature across the height of the room. The experiments carried out with the ceiling diffuser show that there is still a small region close to the floor where the cold air has not fully mixed. However, this was not evident when the diffusers were not used.

The formation and break-up of stratification in a ventilated enclosure leads to the development of two main zones that act independently from each other. The reason for this is the formation of the temperature-stratified interface, which acts as an insulating buffer between the hot and the cold air layers. The interface is influenced by the ratio of the buoyancy forces over the inertial forces by turbulent diffusion and shear causing redistribution and mixing on the upper and lower horizontal bounds. The results of these mechanisms are present in all the experimental cases exhibiting strong stratification. The zonal system of this kind can be found in stratified cooling used to reduce the cooling load of the building, Allen (1979). Although there is an increase of temperatures in the cold air zone, this is insignificantly small for the incremental range of the low air supply flow rates. However, there is only a small increase of the temperatures of the cold air zone with high air supply flow rates and that is due to the higher down-gradient heat flux (DGHF). This occurs based on the stratified flow theory due to the turbulent eddies passing through the interface. This has influenced the interface and caused an

intermediate layer to appear that depend on the hot air supply flow rate and on the vertical length of the hot and the cold air zones. A constant temperature could be achieved by mixing in the hot air zone, while a constant temperature can be maintained by the displacement flow in the cold air zone. The interface moves with regard to the flow rate of the controlled air supply while the speed causes mixing. Penetrative convection occurs that moves the interface further away from the original height, while the associated effects of the "filling-box" mechanism take place causing redistribution. This idea can be used for dividing a large space into two separate zones, while mixing any pollutants in the upper zone and maintaining them at certain temperatures. At the same time, the cold air zone where the occupants are located could be maintained at good levels of comfort.

6.1.2 CFD results

Heat is transported in the main direction of the flow by convection, while turbulence diffusion occurs in the direction perpendicular to the flow, mainly in the z-direction. Heat transport in the other cross-stream directions is insignificantly small. In the simulation of the lower Re without a transport equation for turbulence (denoted thereon as the laminar simulation), the transport of heat is small in the cross-stream direction compared to the direction of the main flow that is a stronger case than one might want because it overestimates the effects of stratification and underestimates the effects of mixing and redistribution. There are neither any mixing effects prescribed at the inlets of the computational domain nor any turbulence model to solve for turbulence mixing in the cross-stream direction of the flow. As a result, the gradient in the hot and cold air zones is unaffected maintaining the constant inlet temperature and there is a very sharp interface between the two main zones, as shown in Figure 5.2 (a). The thickness of the interface is very sharp because there is almost no internal mixing except the one resolved by the grid size. However, using this approach to predict the temperature gradient as suggested by Børresen (2001) (personal communication) in industrial and tunnel ventilation, may have been confused with fire ventilation problems and is in disagreement with the following observations.

Using a Low-Re $k-\varepsilon$ turbulence model will render the temperature gradient to a diffused mode, as it can be seen from Figure 5.2 (a) and Figure 5.3 (b). The temperature gradients of the medium Re cases in Figure 5.2 (b) computed by the high Re turbulence models show more stratification.

Using a high Re $k-\varepsilon$ turbulence model will produce sufficient mixing, which affects the temperature gradient in Figure 5.2 and this can be seen making qualitative comparisons with the gradients obtained experimentally. The temperature gradient in this case shows the right levels of diffusion of heat in the vertical sense as shown in Figure 5.3.

An imbalance of inlet momenta will change the height of the interface as shown in Figure 5.8 (a) and (b).

When approaching the interface in steady state, the cold and hot air flow is vertically towards above and below the interface (CFD) that is coherent with Dyer (2000).

6.1.3 Low Re cases – formation of thermal stratification

In the first experiment, the inlet velocities were kept as low as possible. The results of this experiment are presented graphically in Figure 5.26 and show the effect of small intermittent increments of the volumetric flow rate of the hot air supply and discussed in section 6.1.1 (for flow rates see Table 5.1). At such low volumetric flow rates, the hot air jet does not present a strong downward momentum case for overturning and mixing the entire air medium in the room. This presents the initial stages of building up stratification such as in a typical air-conditioning case. The effect of increasing the temperature gradient in the hot air zone, while keeping the extract height constant can be observed as the extract is kept at the same height. These flow rate settings and the current extract height maintain the hot air layer at a predefined height. The velocity below the ceiling is small and the transport of heat is mainly in the flow direction. In an attempt to overcome the pressure drop in the chamber, the extract flow rate setting compared to the total supply flow rate can also affect the interface. This results in the development of the interface at the extract height. The volumetric flow rate of the

extract is approximately 0.05 m^3/s that corresponds to 0.025 m^3/s per supply (not considering the leakage openings). The thermal stratification changes the shape of the extract sink and increases the effective radius that can cause this effect to appear more readily on the temperature gradient. However, this is destroyed after the volumetric flow rate of the hot air supply becomes the same as the extract flow rate, third curve. The extract interface shows up at the extract height on the temperature gradient in a large shipyard that is ventilated by displacement, measured by Skistad (1998) using a laser for a certain time step when opening the lead of a container to release a tracer gas. Similar effects on the temperature gradient can be observed by the opening a window in the heated conduit of Seifert *et al.* (2000). Hence, there can be a layer development by extract flow. In the first two or three cases, the initial interface started at a height of $z/\mathrm{H} \approx 0.5$ from the floor and extends up to $z/\mathrm{H} \approx 0.7$ making a vertical thickness of an initial interface of $\delta/\mathrm{H} \approx 0.2$, which is very much diffused in the *z*-direction along with the hot air zone. The first curve and the second curve show that the convective heat transfer is in the *x*-direction and diffusion occurs in the streamwise direction of the main flow down to the height of the extract by an exponential error distribution curve. The increase in the hot air supply becomes more effective in the case of the third curve and the fourth curve. At this stage, the hot air zone starts getting into a step-like shape and a large interface is established as a result of the development of the hot air zone. More hot air seems to be accumulated below the ceiling, which started forming the stratified layers across the height of the hot air zone up to $z/\mathrm{H} \approx 0.1$ below the extract height. The gradient of the interface increases in proportion to the hot air supply rate. There is a negligible increase in the magnitude of the temperatures in the cold air zone of the order of $\theta = 0.05$. Close to the floor, all the temperature curves change significantly at $x/\mathrm{H} = 0.1$, which is similar to an exponential error distribution curve. At the lowest measurement point of $x/\mathrm{H} = 0.02$, the difference in the dimensionless temperature is $\theta = 0.1$. The values at the edges of the cold and hot air zones are away from the values at the supply air outlets by around $5 \pm 1°\mathrm{C}$ higher or lower at the measurement points close to the floor level, where $x/\mathrm{H} = 0.02$, and ceiling level respectively, where $x/\mathrm{H} = 0.96$. This may be attributed primarily to surface radiation and convective heat transfer, and secondarily to heat leakages due to the poor airtightness of the rear wall and conduction losses.

At the low intermittent increases of hot air supply, the temperature gradient in the hot air zone is directly proportional to the inlet volumetric flow rate and the stability of stratification becomes stronger across the height of the hot air zone. The temperature gradient in the cold air zone remains undisturbed. The small temperature differential in the cold air zone presents a good case for comfort level. There is only a small increase in temperature of the order of the error value, i.e., 0.1°C. The cold air zone can be treated separately, since it is unaffected by the temperature increases of the hot air zone. This idea can be applied to ventilating a large space selectively. In the same way as selective withdrawal of fluids occurs in reservoirs and estuaries, Imberger *et al.* (1976), fluid could be removed from the thermocline, while the other zones are still maintained intact. In a similar way, a large space could be separated without additional physical partitions.

6.1.4 High *Re* cases – break-up of thermal stratification

The influence of high input volumetric flow rates of hot air supply was investigated in this section to study the break-up of stratification. The initial set of the results of this study (second set) are shown in Figure 5.28. The starting flow rates were at an average about twice as much as in the low *Re* cases, while the area of the hot air supply was reduced by a third. The flow rate increments of the hot air supply were also twice as much as in the low *Re* cases (see Table 5.1). The large interface at the extract height does not show up, most likely due to the larger inlet flow rates and jet flow. In this way, the interface was also kept at the required height, while the increase in the aspect ratio of the jet increased flapping motion and subsequent turbulence production resulted in higher mixing across the height of hot air zone. It was evident in Figure 5.28 that mixing was high in the hot air zone, yielding a range of fairly sharp temperature gradients across the interface. When the flow rate of the hot air supply was increased, the height of the hot air zone was also increased. With the hot air supply flow rate increased to the final setting, which is approximately 0.14 m^3/s, the temperature stratification disappeared and an almost constant temperature prevailed in the room. The result of the increased mixing in the hot air zone had a reduction effect on the interface thickness. Although in these cases the interface is much thinner than in the case of the low volumetric flow rates, the insulating effects of the interface are still quite effective.

The reposition of the interface and persistent mixing in the hot air zone was a result of a higher hot air supply flow rate lowering down the interface towards the floor, while the temperatures in the cold air zone were not affected significantly. The results are similar to the third set of experimental cases in Figure 5.29.

This case considers what happens when heating up a room by using a hot air jet at the ceiling. Alternatively, this is also similar to a case where the room is cooled and the heat sources increase the heat load in the room.

6.1.5 Validation with other experimental work

The similarity relationship is studied for the two cases of flow rates of cold air supply used in the experimental work (see Table 5.1) where the corresponding velocities are approximately 0.1 m/s and 0.2 m/s. A case for zero cold air velocity used in the stability equation is also plotted for comparison purposes. The flow rate of hot air was increased intermittently from approximately 0.01 m^3/s to 0.13 m^3/s. These flow rates are plotted against overall Richardson number in Figure 6.2,

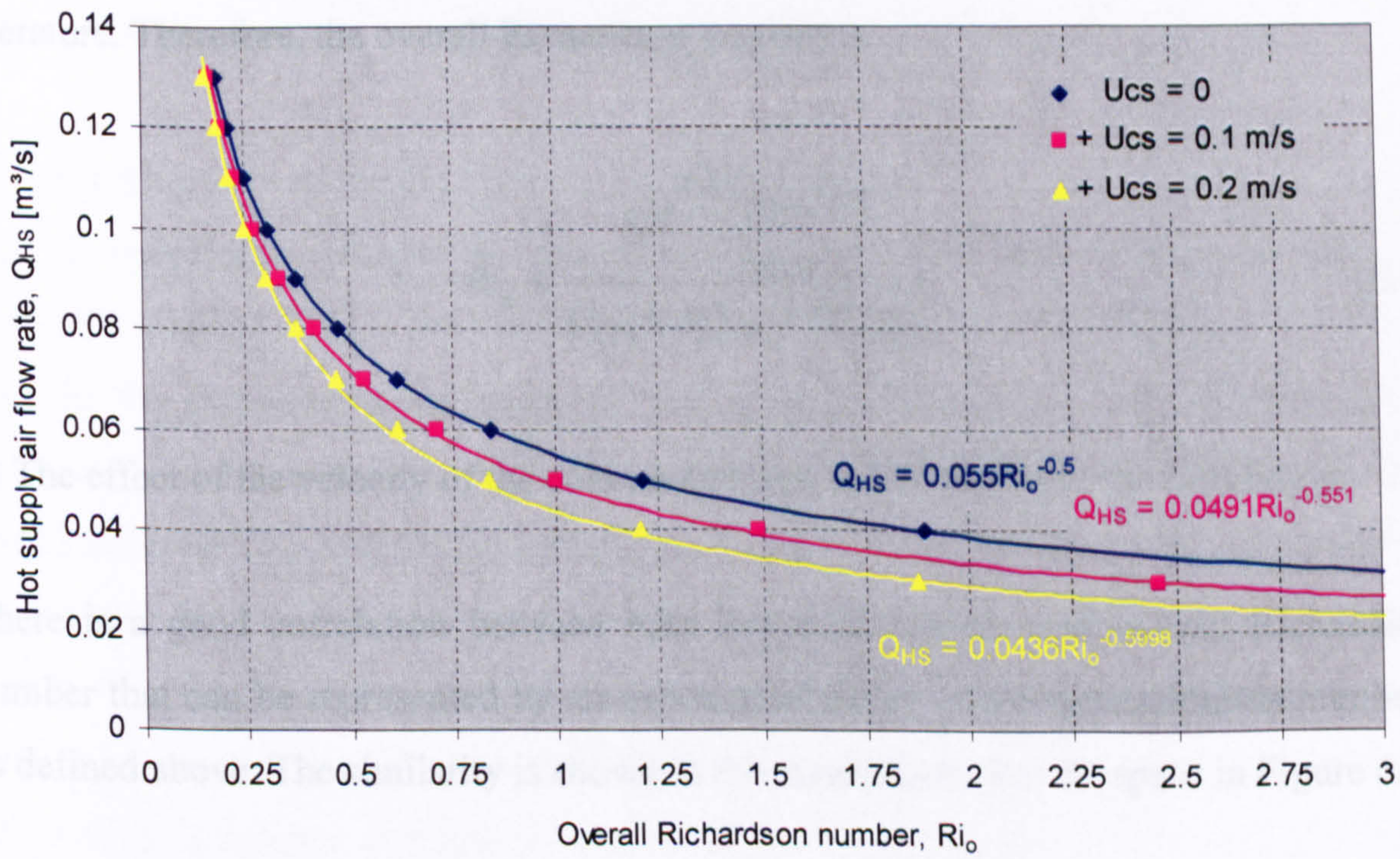

Figure 6.2: Total flow rates for two cases of cold air supply by increasing hot air supply against overall Richardson number.

By looking at the correlations in Figure 6.2, it is obvious that it is possible to derive a non-dimensional similarity relationship between inflow parameters and overall Richardson number although there are some minor differences due to the speed of the cold supply air flow. There is 89% similarity between the line coefficients and 91% similarity in the curvature exponents. This similarity can be developed according to the following assumptions,

1) It has been suggested in the literature that it is the horizontal velocity in a moving layer that affects the stability of that layer. However, in the current work, it is the entire velocity that characterises the outlet opening affecting the layer. Therefore, the entire velocity is used instead (not the velocity components), since the layer is supposed to be affected by the total velocity.

2) The overall Richardson numbers are calculated for the total velocities that apply to the gross areas of the diffusers, since it is the effect of the entire face area of the diffuser that affects the stability. This makes sense because otherwise the stability threshold is reached much earlier, but in this way the values are consistent with the threshold reached in the experiments at mixing and the maximum downward throw data from the literature. Therefore, the overall Richardson number is,

$$Ri_{\mathrm{o}} = \frac{gH\dfrac{(\Delta T_{\mathrm{room}})_{\mathrm{HS}}}{T_{\mathrm{room}}}}{Q_{\mathrm{HS}}/(A_{\mathrm{c}})_{\mathrm{HS}} + (U_{\mathrm{o}})^2_{\mathrm{CS}}} \tag{6.1}$$

3) The effect of the velocity of the cold air terminal is introduced in the correlation.

There is a good correlation between inlet Reynolds number and overall Richardson number that can be represented by an exponential decay of the dimensionless numbers as defined above. The similarity is shown in the logarithmic Re - Ri space in Figure 6.3,

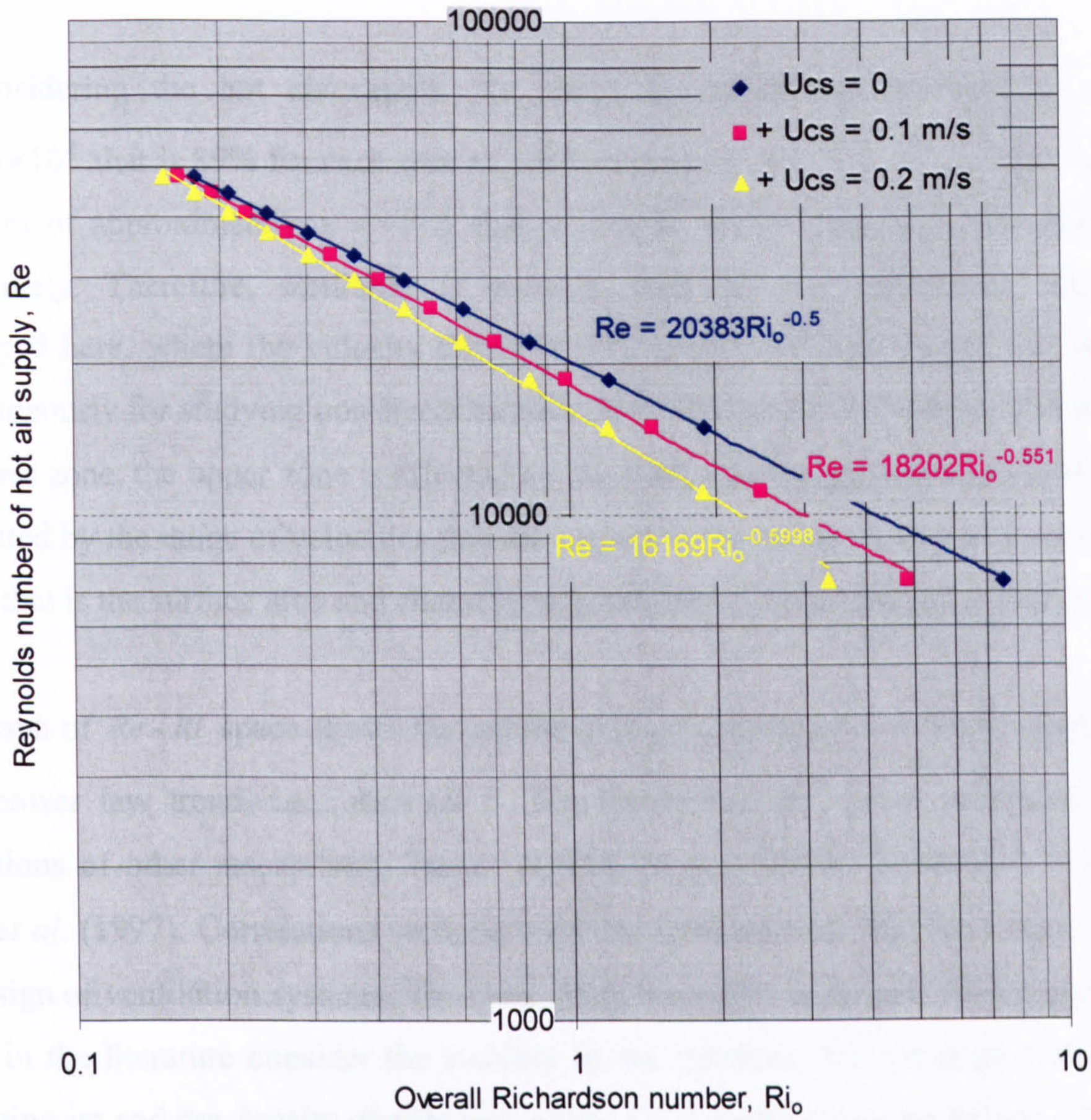

Figure 6.3: Similarity of overall Richardson number for different inlet conditions.

There is not a very strong similarity for the total Reynolds numbers by looking at Figure 6.3. However, this can give an idea of how the similarity will be affected with the Reynolds number. This is for a coefficient in the range starting from 1.6×10^4 to 2.0×10^4 and for the exponent in the range of -1/2 to slightly less than -2/3. The similarity between the line coefficients of $U_{CS} = 0$ and $U_{CS} = 0.1$ m/s is 82% and between the line coefficients of $U_{CS} = 0.1$ m/s and $U_{CS} = 0.2$ m/s is 80%, while the corresponding similarities for the curvature exponents is 85% and 84%. The curves that are higher denote that the Richardson stability has been affected as the total Reynolds number is getting higher. For the current experiments, $T_{HS} = 32°C$ and $T_{room} = 18°C$, the threshold $Ri_o = 0.25$ is reached at a hot air flow rate between 0.1 and 0.11 m³/s. If $T_{HS} = 32°C$ and $T_{room} = 20°C$, the Ri_o threshold is reached at a hot air flow rate of 0.09 m³/s. As the inlet temperatures are getting smaller, $T_{HS} = 25°C$ and $T_{room} = 20°C$, the Ri_o threshold is reached at a hot air flow rate of 0.055 m³/s.

By considering the hot air supply Re only, the coefficient obtained is around $c = 2.6 \times 10^4$ that is 89% for each case of cold air velocity, i.e., 0.1 and 0.2 m/s, and the exponent of approximately $n = -1/2$ that is similar by 91% and 92% for each case respectively. Therefore, similarity is possible with the test model that has been developed here, where the velocity fields of both upper and lower zones are affected simultaneously for studying non-linear stratification. In the case of a plume rise through the lower zone, the upper zone is affected by the plume discharge, while the lower zone is affected by the range of velocities that are related to the entrainment coefficient of the plume that is the surface area and characteristic velocity in the centreline of the plume.

The graph of Re - Ri space shows that all the gradients in Figure 6.4 can be represented by a power law trend, i.e., $Re = cRi^{-n}$. Similarities can be found compared to the predictions of other researchers, Turner (1968), Linden (1973), Fernando (1991) and Cotel *et al.* (1997). Correlations were derived for stratified flow that have been used in the design of ventilation systems. The flow fields have also been used. The experiments found in the literature consider the stability in the interface that develops between an impinging jet and the density distribution of the fluid medium in a container. The fluid medium is maintained at constant temperature or concentration. In this work, the cold air zone is maintained at constant temperature, while the hot air jet forms stratified layers mainly in the upper part of the room. Stability was considered in the interface that developed between the hot and cold air zones in the middle of the room.

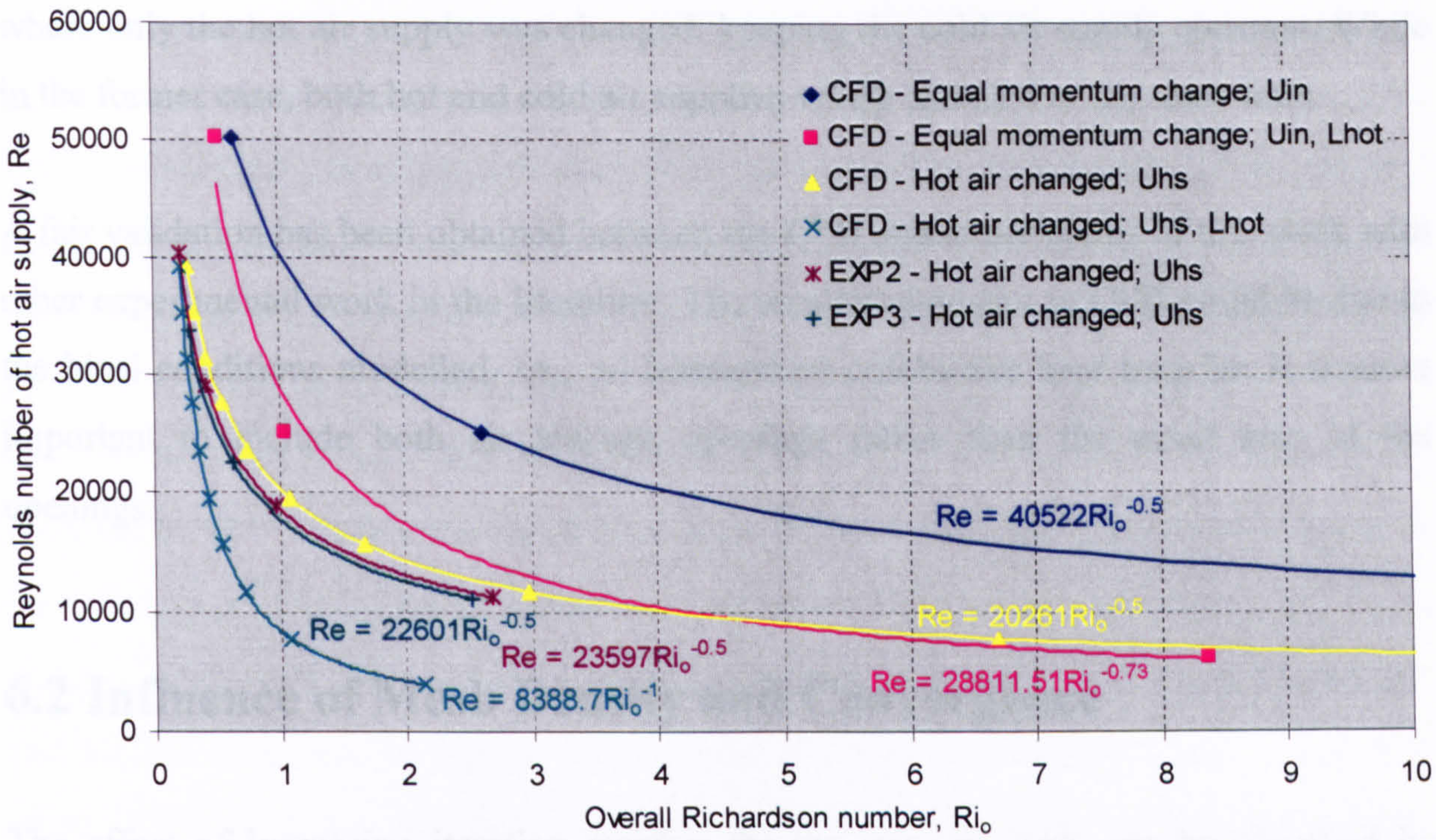

Figure 6.4: *Re - Ri* space showing a comparison between current CFD and current experimental work for certain combinations of input parameters.

The evaluation of the exponent and the comparison of the value of the exponent with other researchers is a common approach found in similar research work. In the experimental work carried out here, the value of the exponent obtained is -1/2. In Turner's work (1968), where the density step is made due to salinity, the exponent takes the value of -1. However, when the change in density is produced by a temperature difference, the value of the exponent is -3/2. Nevertheless, Fernando (1991) pointed out that the value of the exponent can vary over a wide range, typically from -1/2 to -3/2 or -2, which validates the experiments of the current work as the values found here fall within that range. The coefficient *c* is different here and that can be attributed to air being used in this experiment, while saline water was used in most of the experiments described in the literature. The differences between the CFD results varying the hot air supply and the experimental results in the current work may be attributed to the fact that in CFD, heat and mass losses were not considered, while in a real case occurring with the configuration of the current experiments such effects occurred naturally. In most experiments involving liquids reported in literature, leakage does not occur, except for some conduction, Nelson *et al.* (1999). The difference between the CFD results when changing both supplies and when changing only the hot air supply is obvious. The difference can be attributed to the area of the hot air supply being smaller in the case

where only the hot air supply was changed, keeping the cold air supply constant. While in the former case, both hot and cold air supplies where changed at the same time.

A fair validation has been obtained between the CFD and experiments of this work with other experimental work in the literature. The smaller exponent in CFD could be due to the ideal conditions modelled, i.e., no leakages or conductive heat transfer. It is more important to include both air leakage openings rather than the exact area of the openings.

6.2 Influence of Mesh Density and Convergence

The effect of increasing iteration number for the low *Re* case can be observed by looking at the temperature gradients shown in Figure 4.22. The relaxation factors had to be decreased from the default values for all velocity components prior to the simulation by an order of magnitude, i.e., 10^{-1}. To achieve good convergence while optimising for the yield time of convergence, the residual errors were brought down in the region of 10^{-2} or less for all variables. For those residuals, the error in the mass balance for the simulation was in the region of 10^{-2} in the whole field. Energy was balanced after all other variables were converged. The energy balance was also in the region of 10^{-2} in that case in the whole field that was a good value. The results were fully converged at 5,000 iterations for the low and medium *Re* cases, while good convergence values were observed from 2,000 iterations.

Comparing the different temperature gradients of the low *Re* case in Figure 4.22, the difference between the gradients at consecutive iterations along the height of the room is higher at 500 iterations, while the difference vanishes when approaching 10,000 iterations. Comparing the temperature gradients of the high *Re* case in Figure 4.23, the heat diffusion terms are still oscillating when the CGR solver was not used. However when the CGR solver was used, the diffusion terms became smaller while the momentum terms took over.

However in the high *Re* case, convergence was more difficult, much slower and a significantly low error in the mass balance was required until energy was balanced. The

results of the high *Re* case are shown in Figure 4.23. Special numerical algorithms to enhance convergence, such as the conjugate gradient (CGR) solver, were necessary. Before using the CGR solver, a further decrease in the relaxation factors for the velocity components, i.e., 10^{-2}, was needed for achieving convergence, which only slightly speeded up the solution. Also necessary was an increase in the internal iteration limit for pressure to speed up its convergence, which was previously not converging, affecting in that way all other linked variables. In those cases, the error in the mass balance had to go down to 10^{-7} while the error in the energy balance was only reaching the region of 10^{-2}. A value of more than 10,000 iterations was needed to achieve converged results without using the CGR solver. As it could also be observed from the graphs at 5,000 and 10,000 iterations, in Figure 4.23, it was obvious that the convergence was slow when CGR solver was not used. There were sharp changes in the temperature gradient at 5,000 iterations and the results were neither fully converged even at 10,000 iterations. However, in some later attempts with the CGR solver, the simulations converged from the very early stages. Around 5,000 iterations only were needed to achieve fully converged results with the CGR solver to 10^{-2}.

However, the effect of using CGR solver is evident even in the low *Re* cases with low mesh density of Figure 4.24. As mesh density increases, numerical instabilities may be triggered. When using a dense grid, more non-linearities are added into the system, although they are more likely to be of smaller scale and thus the inclusion of the CGR solver can become necessary. That would influence the yield time of convergence, since more time will be taken for the simulation to achieve steady state. In the high *Re* cases, the temperature gradients in Figure 4.28 show the effect of mesh density and numerical solver. The first two curves were obtained without the CGR solver and it was observed that however small, there were still fluctuations present for a few final consecutive iterations. The other two curves show the effect of simulations using different mesh, in combination with the CGR solver. Both simulations were fully converged. Increasing mesh resolution to 200,000 cells may not be that necessary when low inlet velocities are used. On the other hand, the simulation that utilises a mesh density of 200,000 cells, when higher inlet velocity is used, it was obviously better than the one using a mesh density of 100,000 cells.

Comparing the temperature gradients of the low *Re* case in Figure 4.27, the differences between the gradients when using a mesh density of 50,000 and 100,000 cells along the height of the room are higher in the later case. Comparing the temperature gradients of the high *Re* case in Figure 4.28, the heat diffusion terms are still oscillating when the CGR solver was not used and there was not much difference in the gradients. However, when the CGR solver was used, the difference became smaller.

In the low *Re* cases considered here, it can be concluded that a mesh density of the region of 85,000 cells using the CGR solver will give adequate results. In the medium *Re* cases a mesh density of 130,000 cells was required in order that the solution became independent of the mesh density. Finally, in the high *Re* cases of this work, a mesh density of 200,000 cells was required. The simulations performed for testing mesh independence are all summarised in Table 6.1,

	Mesh density case		
	(1)	(2)	(3)
Low *Re*	50,000	85,000	100,000
Medium *Re*	100,000	130,000	150,000
High *Re*	100,000	200,000	400,000

Table 6.1: Mesh resolution tests.

6.3 Choosing the Correct Turbulence Model

6.3.1 Performance Evaluation of K – ε Models Applied To Stratified Ventilation

The effect of not solving for a turbulence model transport equation can be seen from the temperature gradients in Figure 5.2 (a). This shows a comparison of the same problem solved as a laminar case and as a turbulent case by using different turbulence models. It is apparent that turbulent mixing was not being properly represented in the laminar simulation of the same problem. Less mixing imposed on the interface from the two zones reduces the thickness of the interface which according to the literature. Additionally, the extreme temperatures at ceiling and floor are very close to the values of the supply outlets, indicating that mixing has been misrepresented which made the effects appear sharper than they are in reality.

From the comparison of the temperature gradients in Figure 5.2 (a), it is obvious that the laminar simulation does not consider the effect of turbulence mixing in the smaller scale. Hence, the diffusion of heat in the cross-stream direction is not because of the turbulence viscosity. It is more likely that the mesh resolution in this case is more important since the turbulence fluctuations are due to the refinement of the grid. Looking at the temperature gradient of the laminar simulation, the interface is a temperature step between the hot and cold air zones. The zones are of an almost constant temperature similar to a mixed situation. But in this case, it is because the heat is transported in the main direction of the flow, while transport of heat by turbulence diffusion in the cross-stream direction is determined by the grid size. The velocity contours are drawn into the interface, coherent with Dyer (2000) although they follow an S-shaped curve at the location where the flow reaches the rear wall.

In contrast to the laminar case in Figure 5.2 (a), the effect of using the Chen-Kim model with the Low-Re modification was shown to present a more diffused case when comparing the temperature gradient in Figure 5.2 (a). The temperature gradient of the Low-Re Chen-Kim model is closer to the other models for the medium Re of this work, i.e., Re = 25,000, as it can be seen in Figure 5.2 (b). The temperature gradients of all the models for the high Re of this work, i.e., Re = 50,000, present an even better match, as it can be seen in Figure 5.2 (c). However, the higher mixing which could be observed from the temperature gradients of the Low-Re Chen-Kim model also shows up in Figure 5.3 (c) as the vertical components of velocity have different signs which suggest that mixing was higher than in any other case.

Looking back at the temperature gradients in Figure 5.2 (a), in the low Re case of this work, i.e., Re = 4,000, the RNG model predicts a slightly sharper interface and it is also a little closer to the laminar case of this work than the other models. In Figure 5.3 (a), the RNG model shows a stronger jet flow compared to temperature stratification or as opposed to zero stratification, which could be because it is derived for high Re numbers, due to non-linearities associated with this model. The model still shows lower mixing characteristics in the high Re case of Figure 5.3 (c).

Comparing the Chen-Kim model at low Re numbers with the other models by looking at the temperature gradients in Figure 5.2 (a), it can be seen that the Chen-Kim model was closer to the standard $k-\varepsilon$ model. However, in Figure 5.3 (c), the model shows a little higher mixing than the RNG model in the upper zone of the enclosure.

The similarities between all high Re models in Figure 5.2 (a), (b) and (c) are owing to the fact that the high mesh density used must have an influence on the diffusion of heat in the cross-stream direction, i.e., the counter-gradient heat-flux (CGHF) becomes important. The results of the standard $k-\varepsilon$ model match the Chen-Kim model for the low Re and medium Re cases of this work, shown in Figure 5.2 (a) and (b), and Figure 5.3 (a) and (b), where there is stratification. In the high Re cases of this work, mixing and CGHF become stronger and the standard model predicts higher level of vertical disturbances, as shown in Figure 5.3 (c). Overdiffusive effects are even higher in the Low-Re Chen-Kim model. The differences obtained between the high Re models of this work and the Low-Re Chen-Kim model may be attributed to the calculation of the length scale in the Chen-Kim modification. The modified length-scale in this case involves higher values of turbulence viscosity that suggest higher levels of diffusion of heat in the cross-stream direction, i.e., higher CGHF.

Both RNG and Chen-Kim models modify the standard $k-\varepsilon$ model in a similar way by the inclusion of a source term in the ε-equation. In the case of RNG, the modification is present only when the mean strain is strong, when the mean strain is weak the original $k-\varepsilon$ model is restored. The modification acts locally depending on the local strain. The main effects are due to the ratio of the strain rate over the shear stress. The strain rate is proportional to the shear stress which becomes small in low Re flows. As a consequence, the RNG yields a more diffused velocity gradient at low Re numbers as expected. On the other hand, in the Chen-Kim model the modification is mainly due to the turbulent production over the turbulent kinetic energy. This takes into account a range of turbulence spectra that the standard $k-\varepsilon$ is incapable of resolving. In the low Re case of this work, the gradient of vertical disturbance of the Chen-Kim model is closer to the standard $k-\varepsilon$ model. In the high Re case, where the standard $k-\varepsilon$ case is rather more diffusive and closer to the Low-Re Chen-Kim model shows larger differences when compared to the RNG model and Chen-Kim model.

It is stated in the literature that the RNG model yields results that are closer to experiment than any other model. The similarity in the filtering approach between RNG and LES, which is used to separate the large from the small eddies, could be one of the reasons that the RNG results are generally in good agreement with the experimental results. The turbulence anisotropy is expected to be ruled out with increasing number of cells. The time-averaged turbulence model can then be used to include the average effects of turbulence in the ensemble. Hence, the formulation of the RNG model could be better than any other model referred to in literature. The only problem is the non-linearities which arise from the RNG procedure that increases the distortion ratio between production and dissipation. This is taken over by the Chen-Kim model.

For the current test model, a high mesh density in combination with one of the modifications of the standard $k-\varepsilon$ model can produce good results. Increasing mesh resolution, the results obtained by the standard model are better based on the grid rather than the turbulence model. The RNG model uses the turbulence model extension depending on the local strain rate. The shear stresses become large at high Re numbers, thus the extension is more likely to be used when local Re is high. In the low Re case of this work, the more diffusive nature of the standard $k-\varepsilon$ model utilised by the RNG model is expected to be more realistic, since turbulence is almost isotropic due to strain being more symmetrical than in the high Re case. On the other hand, the Chen-Kim model utilises the extension in a larger range of turbulence spectrum. Although the Chen-Kim model is more favourable than the other models, because it takes into account a larger range of turbulence scales, the RNG approach yields a slightly sharper interface for the low Re case of this work. However, the differences between the two models were very small and at convergence, the results obtained were almost identical.

6.3.2 Effect of interface height using CFD

At the exhaust height of 1.6 m, i.e., $z/\mathrm{H}=0.64$, shown in Figure 5.5 (a), a larger amount of hot air is effectively removed compared to cool air. However, when the exhaust is lowered down to 0.8 m, i.e., $z/\mathrm{H}=0.32$, shown in Figure 5.5 (b), the amount of cool air is much smaller and the amount of hot air is increased occupying

more space in the upper part of the room. Another difference can be observed by the larger termination zone, which encounters the buoyancy forces at a lower height as a direct effect due to the lowering of the exhaust.

Changing the exhaust height has a direct effect on the interface height for particular inlet supply rates. This is shown by comparing the temperature fields in Figure 5.5 (a) and Figure 5.5 (b). The interface height changes in proportion to the exhaust height, while the thickness of the interface stays approximately constant.

The height of the interface can be changed by changing the height of the exhaust when using low air supply rates. The height of the interface is very important, because it is acting as an insulating buffer and can prevent pollutants from being buoyed further up in height due to the different temperature zones that are created. The gradients in Figure 5.6 show that the interface is almost lost in the case of the 0.8 m height because there is a larger space for the momentum of the downward jet to diffuse. The interface becomes more effective as the exhaust height is raised at 1.6 m and 2.2 m. This is associated with a higher mixing due to large-scale motion in the hot air zone and to a lesser extent due to turbulence. In most ventilation cases, the supply velocity at the terminals affects the levels of comfort. Therefore, it is very likely that in the case of natural and displacement ventilation, the position of the exhaust will influence the air quality inside the room. Better air quality may be achieved, by positioning the exhaust at a relatively high level. However, if the exhaust is set at a very high level, it may have a very little effect in the occupied space. This is especially problematic to large spaces that need to be selectively ventilated where the occupied zone is small compared to the size of the enclosure.

6.3.3 Comparison with experiments

Changing the height of the extract in the experiments had a proportional effect on the height of the temperature interface under stable stratification, as shown in Figure 5.27. The flow rates of this experiment were the same as in the final experimental case of the first experimental series (see Table 5.1). The interface height was initially at an average breathing height as a default position, i.e., $1.6\,\mathrm{m}$ or $z/\mathrm{H} = 0.64$, and then that height was changed to $2.2\,\mathrm{m}$ or $z/\mathrm{H} = 0.88$ and $0.8\,\mathrm{m}$ or $z/\mathrm{H} = 0.32$. In the standard case,

the stratification was as previously investigated in the first experiment as already mentioned. However, in the $z/H = 0.88$ case, stratification diffused vertically downwards as a logarithmic decay function from $2\,m$ or $z/H = 0.8$ down to $1.4\,m$ or $z/H = 0.56$ and similarities can be noticed in the previous experiments. One of the differences with the previous experiments was the smaller height utilised in the hot air zone in which the amount of hot air was piled up and diffused vertically in the downward direction. In the case where the interface was forced to lower down to $0.8\,m$ or $z/H = 0.32$ by repositioning the extract resulted in a diffused interface that occupied almost the entire height of the room. This is because the insulating effects of the interface were no longer effective, because the heat had already been diffused across the height of the hot air zone.

There is a good agreement between the CFD results of the current work obtained by changing the height of the exhaust-outlet in Figure 5.6 and the current experimental results in Figure 5.27 for the low volumetric flow rates of supply air flow. The small discrepancies are owing to radiation and heat losses not being modelled in the current set of CFD results. A more detail study follows where the effects of radiation and heat losses demonstrate the importance of modelling these physical mechanisms that result in the decrease of the temperature range between ceiling and floor as well as a significant decrease in the mean temperature of the hot air zone due to the comparatively small outside temperature.

A comparison between experimental results and CFD results is shown in Figure 6.5,

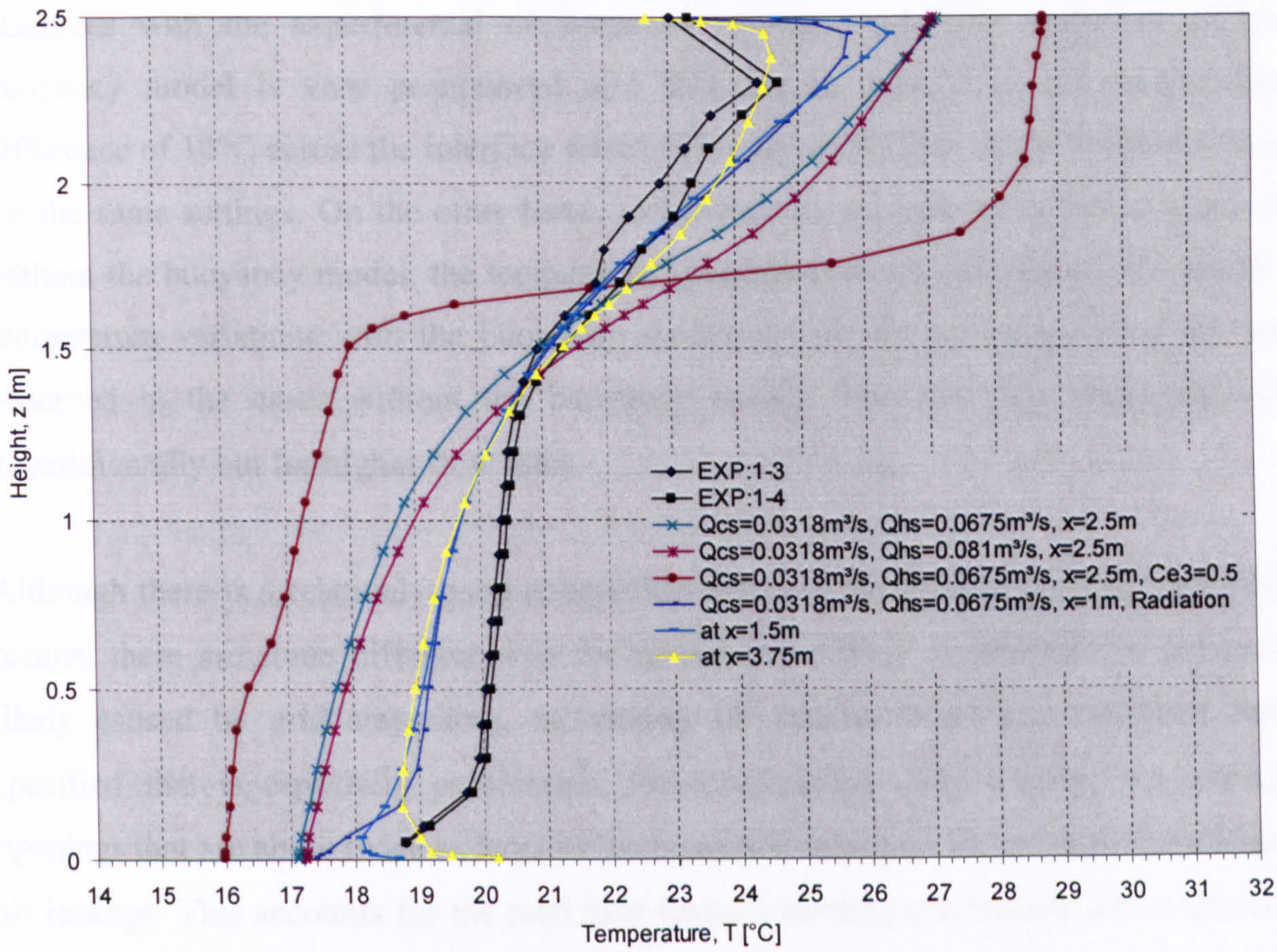

Figure 6.5: Direct comparison between CFD and experimental results.

It can be seen from Figure 6.5 that when including the higher and the lower outlets representing the cracks in the experiment, there is a large change in the temperature gradient. Increasing the volumetric flow rate of hot air has a proportional effect in the temperature gradient similar to the experiments. The temperature gradient is influenced by the inclusion of the buoyancy model and the radiation model, as well as the size of the upper and the lower outlets.

The radiation model reduces the temperature difference across the height of the room. This effect can be observed as the thickness of the interface is also increased that is in contrast to the buoyancy extended model where the top and lower layers appear to have much larger and constant temperatures than in the real case. The constant temperatures occur due to the flow not being mixed appropriately as the turbulent kinetic energy is reduced and turbulence is damped that is not is not rather what happens in the real case as turbulence coexists with stratification (Chapter 2). As a consequence, the interface is similar to a laminar case, although there is not very much difference in the vertical thickness. Additionally the hot layer seems to have been displaced higher up that

disagrees with the experimental observations of this work. The influence of the buoyancy model is very pronounced and this can be seen from the temperature difference of 10°C across the interface which is highly unlikely to occur in the real case for the same settings. On the other hand, looking at the temperature gradient obtained without the buoyancy model, the temperature gradient is much smoother. The step-like temperature variations with the buoyancy model at low hot air supply rates are not observed in the cases without the buoyancy model. This has also been observed experimentally but for higher flow rates.

Although there is a relatively good comparison between the experimental and the CFD results, there are some differences in the nominal boundary conditions that are most likely caused by grid staggering, accounting for smaller boundary conditions than specified that is especially problematic for round inlets. Additionally, the leakage openings that are about twice as large as the measured ones provide in a way for a larger air leakage. This accounts for the total heat losses including conduction losses this can be realised as the mean temperature in the modelled room is almost equal to the experimental one in Figure 5.17. From measurements and calculations across the polyurethane wall there is approximately 20%. There is another about 20% due to air leakage. However, there is a fair agreement with the experimental data.

Therefore, the $k - \varepsilon$ turbulence model in this work gives a relatively good match compared with current experimental data without the buoyancy extension. However, very accurate measurements at very low inlet flow rates are required in order to obtain an exact match with the real heat transfer rates that occur in the experiment.

6.3.4 Effect of changing momentum on the thickness of the interface

The effect of inlet momentum on the stratified flow in the room for the low Re case in this work, $Re = 4{,}000$, can be seen from temperature contours of the previous case in Figure 5.5 (a) which shows a uniformly distributed stratification across the height of the room. Increasing momentum to a medium Re case, $Re = 25{,}000$, can be seen in Figure 5.7 (a), which shows that the effect is a more diffused stratification bearing a smaller extreme of temperatures between ceiling and floor and a higher thickness of the

interface. Finally, a high *Re* case, *Re* = 50,000, can be seen in Figure 5.7 (b), shows the effect of high momentum leading to a mixed flow of a nearly uniform temperature throughout the height of the room.

The results obtained by all other turbulence models were similar except in the case of the Low-*Re* Chen-Kim model in which the temperature gradient was more diffused across the height of the room than the other models tested in this work. The flow pattern of the cold air supply is that of a wall jet. The velocity decreases linearly with distance cooling the entire lower space of the room up to the opposite wall where a low velocity circulation is formed. Circulating flow is inherent due to the entrainment of the cold air jet and the presence of the wall. On the other hand, the hot air jet is confined close to the wall where a circulation is formed. The wake of the hot air jet terminates at some distance below, at the top of the interface, where the momentum forces of the hot air encounter the buoyancy forces in the opposite direction. This results in the rebounding process of the jet that becomes evident as the jet is buoyed up. When the inlet *Re* of the hot air supply is high enough, in this work at medium *Re*, the momentum of the jet is higher than the buoyancy force encountered at the height where the interface develops and an impingement dome forms on the interface shown in Figure 5.1. This can be observed as a temperature interaction on the isosurface at the interface height. Consequently, there is a circulation of hot air in the unconfined side of the hot air jet. At that instance, some of the buoyed air is re-circulated back to the hot air jet by the entrainment process, whereas buoyed air accumulates under the ceiling and heads with very low velocity towards the exhaust. An interface of elevated temperatures is formed at the exhaust height providing that the pressure differential is zero at that height. It is close to the area affected by the exhaust, however, where the velocity vectors point in the main direction. The area close to the exhaust is affected by the convergence of the streamlines of the exhaust which increases the horizontal component of velocity. In that location, stratification height in the interface is decreased. This results to a decrease in the vertical thickness of the exhaust sink and a proportional increase in the horizontal thickness of the exhaust sink also observed by Skistad (1994) reported by Heiselberg *et al.* (1998) and to some further extent by Goodfellow and Tähti (2001).

Changing the momentum has a direct effect on the interface thickness for particular inlet supply rates. The decrease in the interface thickness when increasing the supply

momentum was seen by comparing Figure 5.5 (a) and Figure 5.7 (a) from which in the latter case it was followed by a decrease in the temperature extremes between ceiling and floor.

Increasing the inlet momentum by equal amounts can decrease the thickness of the interface while decreasing the extreme temperature between ceiling and floor, results in weakening stratification. This is particularly useful in the application of clean rooms and rooms that use the idea of mixing ventilation. In those cases the momentum of the supply jet that is usually located at the upper part of the room, must exceed the buoyancy force and dilute the pollutants in the room. Therefore, the critical ratio of momentum to buoyancy needs to be exceeded.

6.3.5 Effect of differential momentum on the height of the interface

The effect of using a lower volumetric flow rate of hot air supply than cold air supply, i.e., $Q_{HS} < Q_{CS}$, can be seen in Figure 5.8 (a), which shows that the interface has moved towards the ceiling. While this relation is in contrast, i.e., $Q_{HS} > Q_{CS}$, Figure 5.8 (b) as seen from the temperature contours which show the opposite effects occurring in this case.

The height of the interface can be changed by imbalancing the supply rates. The imbalance of the mass flow rates changes the pressure gradient. The neutral level is where the pressure differential is zero, which was initially imposed by the level of the exhaust height. The modification of the neutral pressure level is the main reason for displacing the layers at different height in the room. If the imbalance in the momentum supersedes the effect of the exhaust, it can modify the height of the interface. Subsequently, high inlet pressure gradient resulting from high inlet momentum can modify the height of the interface. It should further be mentioned that the pressure level is also a function of the pressure gradient in the outside of the building. That is used for safety measures in fire modelling with respect to the airtightness of the building.

Similar flow patterns can be found in rooms which are ventilated by displacement or mixing methods. There are several applications where a displacement method may

suffer. In industrial buildings during the summer period, the amount of hot air that is accumulated below the roof during the solar radiation process from the outside has to be counteracted in order to achieve a comfortable working environment. While in the case of mixing ventilation, the momentum of the supply needs to be high enough to mix the flow in the entire region without the appearance of hot spots and regions that are poorly ventilated.

6.3.6 Effect of differential momentum and mixing – mixing efficiency

Figure 5.9 shows a turbulent case in which the flow rate of the upper jet is not as strong as the one shown in the previous case, Figure 5.8 (b) and similar to the high *Re* experimental cases to move the interface towards the floor. However, it should also be taken into account that there were some directional effects from the diffuser, which transported hotter fluid in the upper part of the interface. In the current case, the purpose of the hot air supply is to render the adjacent region into a mixing mode. The mixed upstream region of the hot air supply affects the entire hot air zone. The inlet velocity of the hot air supply was changed intermittently. At low air velocities, the effect of the diffusion of hot air into the vertical temperature gradient was a logarithmic decay in the part of the hot air zone. This was similar to the first curve of the first set of experiments. When the hot air supply velocity was increased to twice that of the cold air supply, the volumetric flow rates were equal and the interface was sharper than in the other cases. However, it should not be ignored that the CFD model is an ideal case, using walls that are adiabatic and 100% airtight. This is similar to the second curve of the second set of experiments. Additionally, the inlet geometry in the CFD cases imposes less turbulence in the system than the experimental cases. In the experiments, the temperature gradient in the hot air zone was constant also in the first curve. In the cases where the resultant momentum from the volumetric flow rate of the hot air supply is as high as four times the initial value and the flow mixes in the whole domain. This is similar to the third curve of the experiment. It is very difficult to apply the correct boundary conditions in the CFD model. However, similar results can be generated with great accuracy for the precise boundary conditions if they become available.

The results in these cases have illustrated the effect that mixing has from the hot air supply, as seen in Figure 5.9. Comparing the results with Figure 5.8, it was shown that in the case where the momentum of the hot air supply jet is high relative to the momentum of the cold air supply jet, the hot air supply does not exert enough pressure and turbulence on the medium to push the stratified layers towards the floor.

The interface height depends on the rate at which heat flows from one zone to the other which is modified by the amount of the volumetric flow rates between the different sources in the room as well as mixing. Therefore, an imbalance between the input sources can either position the interface at a different level or mix the flow in the room. If the neutral pressure level is different from the exhaust level, then exhaust and interface lie at different levels. Mixing ventilation systems acting from the ceiling can be affected by this effect and as a result, the occupied zone would not benefit from the dilution effect of the jet. Additionally, such effects are referred to in the literature in tunnels that are ventilated at the end-points, which can suffer ventilation problems at high rush hours. The heat emission from the cars can increase the hot air zone making ventilation by displacement difficult to occur.

6.3.7 Increasing inlet temperature difference – ratio of buoyancy force to momentum force

At very low supply temperatures, the momentum forces are high compared to the buoyancy forces for the given inlet temperature differences across the height and thus there is very little or no stratification as it can be seen from the temperature contours in Figure 5.12 (a). Increasing the inlet temperature difference by a few degrees has a substantial effect on velocity vectors and temperature contours in the room, shown in Figure 5.12 (b).

The temperature contours of Figure 5.7 (a) and Figure 5.12 (b) show similar extreme temperatures between the ceiling and floor and in the interface.

Similar stratification patterns can be obtained by maintaining a constant ratio of momentum to buoyancy. In most ventilation cases the initial conditions may change and

can result to a different inlet temperature difference that can alter the ratio of ventilation rate to input rates. This may not be affected by the aspect ratio of the room and the location of the supplies providing that the mixing characteristics are also similar between similar geometric directions.

6.4 Buoyancy Extension

The buoyancy extension to the $k-\varepsilon$ turbulence model is present in both the k- and ε-equations: it is the term involving G_B in each case. However, the $C_{\varepsilon 3}$ value modifies the G_B term only in the ε-equation. When the extension is not activated, there is no G_B source term in either equation. For stably-stratified flow, the value of G_B is negative and hence, with buoyancy activated, the turbulent kinetic energy levels are reduced and turbulence is dumped (see equations in Chapter 3). The choice of the $C_{\varepsilon 3}$ coefficient depends on the set-up of the inlet sources in the CFD model that produce the stratification. A value close to zero is usually recommended in the literature for an experimental configuration of stably-stratified flow that would be suitable for all the test cases here, while a value close to one is recommended for a configuration of unstably-stratified flow. Therefore, a buoyancy dominated case should exhibit stronger stratification with the extension activated and without the G_B term in the ε-equation, i.e., when the $C_{\varepsilon 3}$ coefficient is zero.

The main buoyancy effect is on the k-equation. The G_B source term in the k-equation is comparable in size to the other source terms that are not multiplied by any coefficients. The nett source terms that are printed in the PHOENICS results file are small for k and ε due to the low speed nature of the problem. The nett turbulence levels are very small, typically in the order of 10^{-3} or less. The dissipation levels are approximately one order of magnitude smaller than the turbulence kinetic energy levels.

The effect of buoyancy extension with equal momentum change is shown in Figure 5.13. The effect due to $C_{\varepsilon 3}$ coefficient on the temperature gradient is found to be negligible as it only affects the G_B term in the ε-equation. The difference between the

temperature gradients with flow rates was also negligible for the case of building up stratification (low inlet flow rates) and for the strongly stratified case (medium inlet flow rates), while there was a larger but yet relatively small difference for the case of breaking up stratification (high inlet flow rates) due to time-dependent terms in the flow become significant at high flow rates as the "asymptotic" state reduces progressively as discussed by Gerz *et al.* (1989) (Chapter 2). Therefore, the effect of $C_{\varepsilon 3}$ coefficient does not seem to have a significant effect in stably-stratified flow of the current investigation that agrees with the conclusions of Markatos *et al.* (1982) (Chapter 3). However, it is observed that the flow stratified more when using the extension as the effect of mixing on the temperature gradient became significantly less than in the cases without the extension. There is a significant increase in stratification when using the extension similar to a laminar case, i.e., without using a turbulence model. This is because of the reducing effect of turbulent kinetic energy due to the G_B term present in the k-equation (see equations in Chapter 3) that has also been observed by Markatos *et al.* (1982). The extension predicts more stratification than observed in the current experimental work. Although this may entirely agree with thermal stratification in liquids, it does not quite agree with the experimental observations in the current work. This is because the thermal stratification is a combination of several physical mechanisms: thermal radiation, air leakages, conduction through the walls and the resulting directional mixing effect from the air supply jets. Every building is different and hence the effect of some of the boundary conditions can have particular effects on the CFD model. The simulations of this work without using the extension and the set of thermal radiation also without the extension proved to be more realistic. Therefore, any simulation case for building stratification should be built up according to the sources that influence thermal stratification and boundary conditions, and not artificially configured to show more stratification by adding the extension to the turbulence model.

A set of steady states at different hot air supply flow rates was also studied for buoyancy extended turbulence with reduced inlet size ($A_{HS} = 0.0625\,\mathrm{m}^2$) when only the hot air supply was changed while the cold air supply and inlet temperatures were constant and $C_{\varepsilon 3}$ = 0.5. As it is shown in Figure 5.14, there are differences as well as similarities with the set of cases without the buoyancy extension. There is slightly more stratification than one might want buoyancy extended turbulence model similar to the

simulation results discussed in the previous paragraph. There is a convergence difficulty at the low hot air supply flow rates, most likely due to the presence of oscillating velocities and temperatures that can be resembled to internal seiching (due to large scale oscillations over certain number of iterations - not turbulence). An average is obtained from the 7,000 iteration to 10,000 iteration from the 500 iteration dumps. This effect appears to take longer to reach its steady-state amplitude similar to liquid observations by Imboden (2004) that leads here to slower convergence. The cold air layer is negligibly affected by the mixing effect from the upper jet that represents rather a strong buoyancy case. The oscillatory behaviour vanishes after the third case (0.75 m/s or 0.0469 m^3/s). There is a higher remaining temperature in the hot air zone at low flow rates that is not observed in the experiments or in the set of cases without the extension and in the set of cases with the radiation effect. This temperature reduces after each intermittent change in the hot air supply and becomes closely similar to the other cases. However, there is an extremely sharp definition of the interface and there is also less mixing in the cold air layer from the upper jet that does not quite agree with the experimental work.

A combination of the Low-*Re* Chen-Kim model and the buoyancy extension has not been exploited here. However, the nature of the Low-*Re* Chen-Kim model is to reduce the range of temperatures and show lesser stratification as opposed to the buoyancy extension of the turbulence model. A combination of these two modifications may show a more accurate modelling of thermal stratification. However, there are drawbacks in terms of mesh resolution close to boundaries when using the Low-*Re* modification. The increase in thermal stratification due to the extension may still be significant, although there is a significant reduction in the increase due to the Low-*Re* modification. A remedy would be by using a multiplying coefficient C_{k3} for the G_B term in the *k*-equation similar to the $C_{\varepsilon 3}$ coefficient in the ε-equation. The extra coefficient C_{k3} would, however, require further testing. When not using the extension, the thermal stratification is also observed in a non-linear three layer system. This does not quite agree with the complete disappearing of stratified layers by Markatos *et al.* (1982) but with the statement of a more homogeneous flow, since the layers are closer to a more linear or "diffusive" state. The approximately constant temperature could have been obtained by Markatos *et al.* (1982) due to the 2-dimensional equations that are by

definition over diffusive as there are physical issues with the energy cascade in 2-dimensional simulations where the strain rate can not be represented as accurately as in a 3-dimensional simulation, Davidson (2004) (for further discussion see Chapter 3). The overdiffusive nature of the $k-\varepsilon$ model will also fall back to account with high accuracy the effect of complex strain fields and body forces, Gibson (2005). However, simulations by many researchers in the literature with the buoyancy extension reported with different $C_{\varepsilon 3}$ values, only to simulate the effect of buoyancy in the flow and achieve a fairly good match with experimental work. Other simulations make use of the C_{μ} and σ_t modifications to account for mixing more accurately. However, all these parameters provide enough artificial tuning to overcome the numerical diffusion in the results when using 2-dimensional/2-equation modelling approach. Theoretically, the buoyancy exists in all scales. The simulations obtained with the unmodified models for buoyancy in the current work do not include the buoyancy effect on scales below the mesh size. It was also supported in the literature in Chapter 3 that extensive modification on the small scales of turbulence may be a step too much regarding the accuracy. Hence the physical processes can be slightly misinterpreted in the attempt to increase the accuracy cancelling out the effort for a further increase of accuracy. For example, in the case of non-isotropic turbulence described in Chapter 3 for the RNG model, the non-isotropic model can give results that may not be as good as RNG depending on the tuning of several modelling constants, since the turbulence anisotropy is not that strong in turbulent flows that are experienced in normal conditions. The extra source term in either equation is expected to have a larger effect in flows with high enough speed of a stably-stratified case such as the flow coming out of a hot nozzle, where the streamline curvature and turbulence have a much higher effect on the mean flow. There may be too many assumptions regarding buoyancy extension used with Low-Re modifications and additional tuning may be required to obtain little extra accuracy that is beyond the scope of the current work.

Besides a high speed flow, in an unstable-stratification case the buoyancy force acts as an additional source of turbulence that is likely to increase the turbulence kinetic energy levels significantly. Consequently, the dissipation levels will also be increased. Therefore, the value of $C_{\varepsilon 3}$ coefficient is likely to play a more important role in the dissipation levels of an unstable case that will affect the temperature gradient further

away from the sources more significantly than in the stably-stratified case considered here. However, the fire and smoke cases by Markatos *et al.* (1982) and Chow and Leung (1989), which are inherently set up for unstable stratification, did not show any considerable differences when changing the $C_{\varepsilon 3}$ coefficient. There are still issues involved with the buoyancy effects to the turbulence model, the 3-dimensionality of the flow and the associated numerical diffusion, since there is a fourth layer in the velocity field at the interface height that is not predicted by the CFD modelling.

If a boundary condition of a contaminant release was to be used at the floor level at the different steady states as in the idealised model of the current work, the buoyancy extension and the resulting step-like stratification would have a limiting effect on the maximum height of the contaminant plume, Chen and Rodi (1980) and Hart (1961) (Chapter 2). Therefore, a more realistic simulation of the temperature distribution and associated flow patterns inside the room is required to predict correctly the maximum height of contaminants. This should take into account also other effects that are very likely to affect the distribution such as radiation and air leakages.

6.5 Influence of Modelling Radiation and Conduction

The difference between simulation and experiment in the case of fire and smoke by Chow and Leung (1989) was 150 K, which caused the temperature curve to lie above the experimental one, and was attributed for not including the effect of radiation. Temperature differences close to the ceiling and the floor were observed in the simulation of fire and smoke by Markatos *et al.* (1982) of the order of 100 K that was slightly larger than 30% of the temperature range and is believed that also occurred due to excluding radiation effects from the simulation.

The thermal radiation effect exists at all temperature ranges and can be of relative significance when considering convection and heat losses at normal climatic conditions. The inclusion of a proper representation of radiation is difficult because it is resource intensive. It is also difficult to consider radiation very accurately as well as conduction and convection at walls by using only a set of simplified set of equations, since the radiation effect on the interfaces of the hot and cold layer with the walls is considered

here at an average of around 2°C depending on the strength of stratification. This is large enough to be required in the calculations, yet small enough to consider very accurately. The influence of the effect of radiation by modelling the effect of temperatures involved in the heat contribution due to the most important radiation components is relatively easy to do using the IMMERSOL model in PHOENICS. An adverse effect on stratification is imposed in the low *Re* cases of this work when applying radiation. Four tests were presented in Figure 5.15. The first set of two was the case of the low *Re* number of this work where the convective heat transfer was relatively lower than the other *Re* cases, i.e., volumetric flow rates were up to $0.0313\,\mathrm{m^3/s}$ ($U_{\mathrm{HS}} = 0.5\,\mathrm{m/s}$, $A_{\mathrm{HS}} = 0.0625\,\mathrm{m^2}$). When a higher convective heat transfer rate was used in the next two cases, i.e., when the volumetric flow rates up to $0.0625\,\mathrm{m^3/s}$ ($U_{\mathrm{HS}} = 1\,\mathrm{m/s}, A_{\mathrm{HS}} = 0.0625\,\mathrm{m^2}$), the effect of convective heat transfer was more pronounced than radiative heat transfer. Describing the tests in more detail, the effect of radiation becomes more obvious. The effect is a diffused temperature distribution compared to the cases without modelling radiation, which is shown in Figure 5.15 comparing the first curve with the second curve, and the third curve with the fourth curve. The relative contribution from radiation and convective heat transfer affects the net heat transfer. If the magnitude of the convective heat transfer is higher than radiative heat transfer, then radiative heat transfer may be ignored. This is shown in Figure 5.15 comparing only curves of different velocities, i.e., the second curve and the fourth curve.

An additional layer effect appears at low flow rates at a distance of 1.25 m from the front wall shown in Figure 5.16 (a) is more pronounced than further away from the sources and is similar to the experimental cases of low flow rates, owes to two influencing parameters. The first is the extract flow which affects the interface height more effectively when using relatively small flow rates. The second and most important is that the measuring locations in the experiments were too close to the hot and cold sources, these were in fact a shorter distance than in the CFD cases, that capture more clearly the rebounding effect of the jet on the interface. Further away from the middle at 3.75 m from the front wall, the temperature gradients inside that cold and hot layers are almost constant and slightly more stratified that signifies a higher mixing effect inside layers. The effect at different locations such as closer to the extract as seen in the

experiments is better predicted when taking the temperature gradient a closer distance than 1.25 m from the extract and the circulation flow that is not of important in this work.

The thermal radiation between opposite surfaces containing the fluid medium leads to a more discrete interior stratification. The surface temperature at steady state is a result of energy balance of the conduction through the wall, surface radiation, convective heat transfer and sources present within the fluid. The result is that the temperature gradient in the hot and cold layers becomes closer to uniform reducing the temperature range across the height of the room. This achieves a better qualitative comparison with the experimental results.

A cross-sectional plane of WDIS in the thermal radiation CFD model that was used for the study of the steady states at different hot air supply flow rate is shown in Figure 6.5,

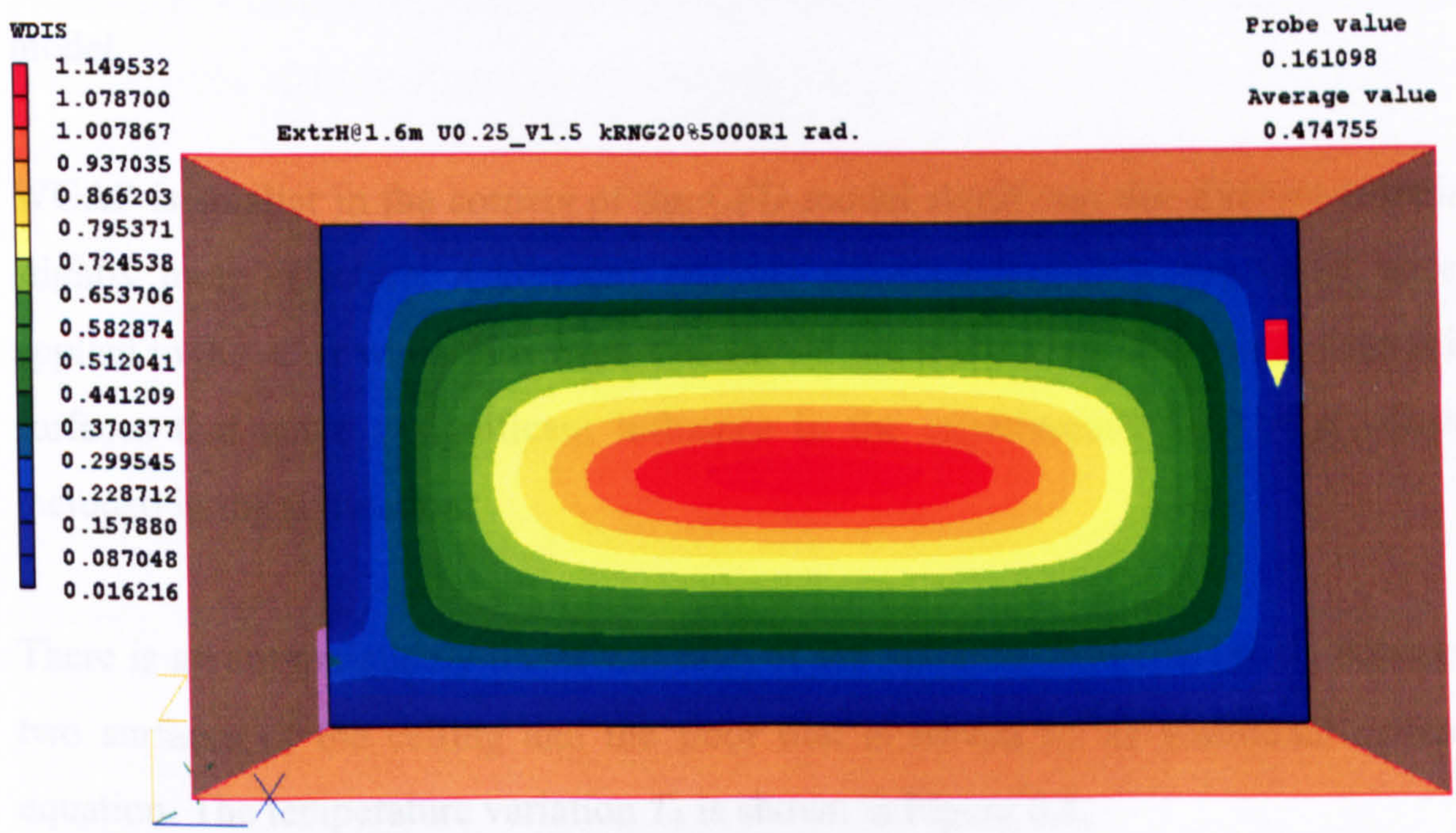

Figure 6.6: Cross-sectional distribution of the WDIS in the thermal radiation CFD model.

WDIS is similar to the LTLS distance as it becomes higher near the centre of the model.

WGAP distances are important in the accurate calculation of thermal radiation heat transfer between wall surfaces. A cross-sectional plane of WGAP in the thermal

radiation CFD model that was used for the study of the steady states at different hot air supply flow rate is shown Figure 6.6,

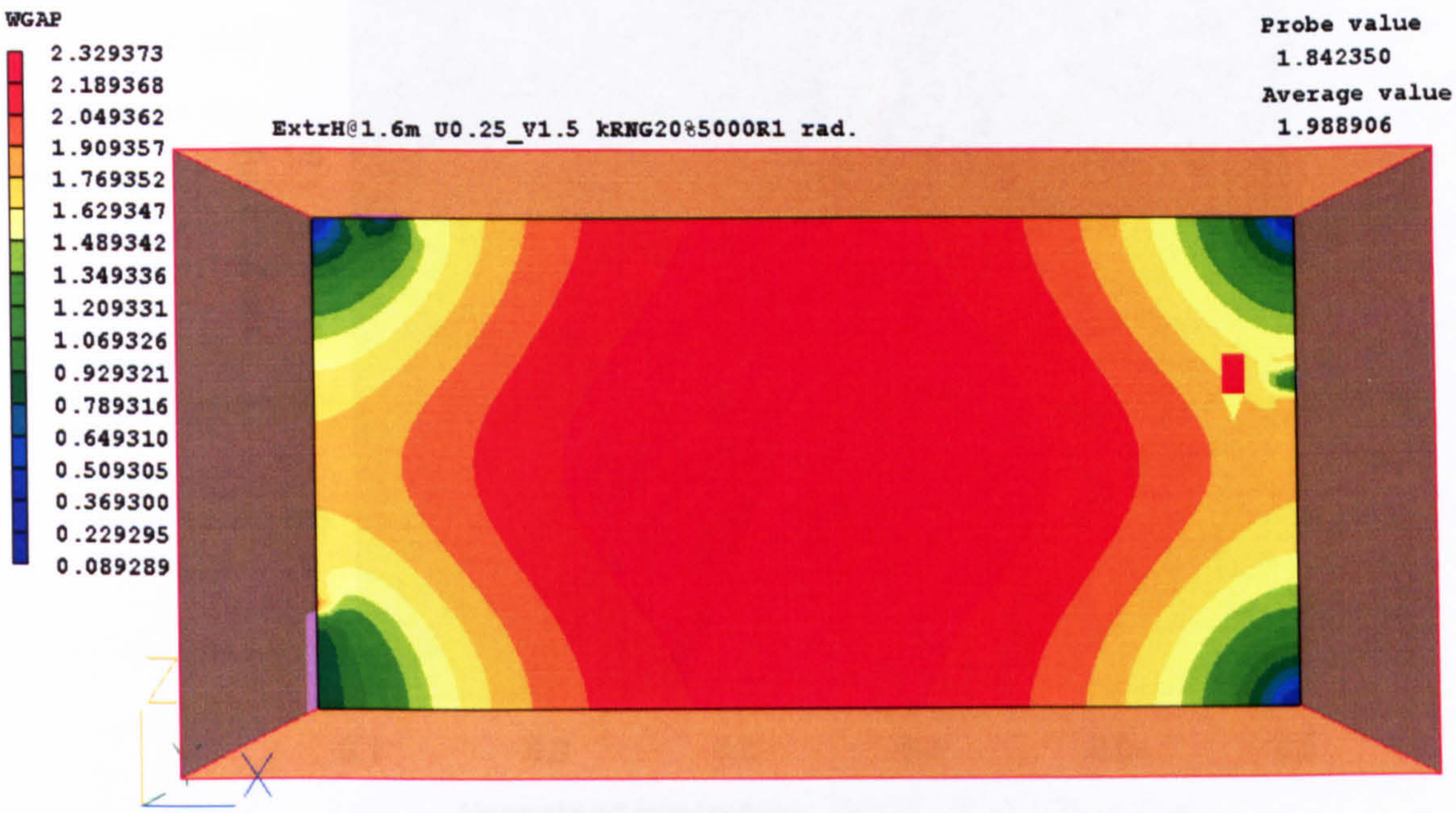

Figure 6.7: Cross-sectional distribution of the WGAP in the thermal radiation CFD model.

WGAP is smaller in the corners of the CFD model signifying that thermal radiation is slightly more effective. Additional, thermal radiation boundary conditions were not applied to the other walls. However, this should not make a big difference, since it is the surfaces that make a significant influence in the experimental work that should be included in the simulation.

There is an approximately linear variation of the radiative temperatures T_3 between the two surfaces of the ceiling and the floor that is solved by an additional differential equation. The temperature variation T_3 is shown in Figure 6.8,

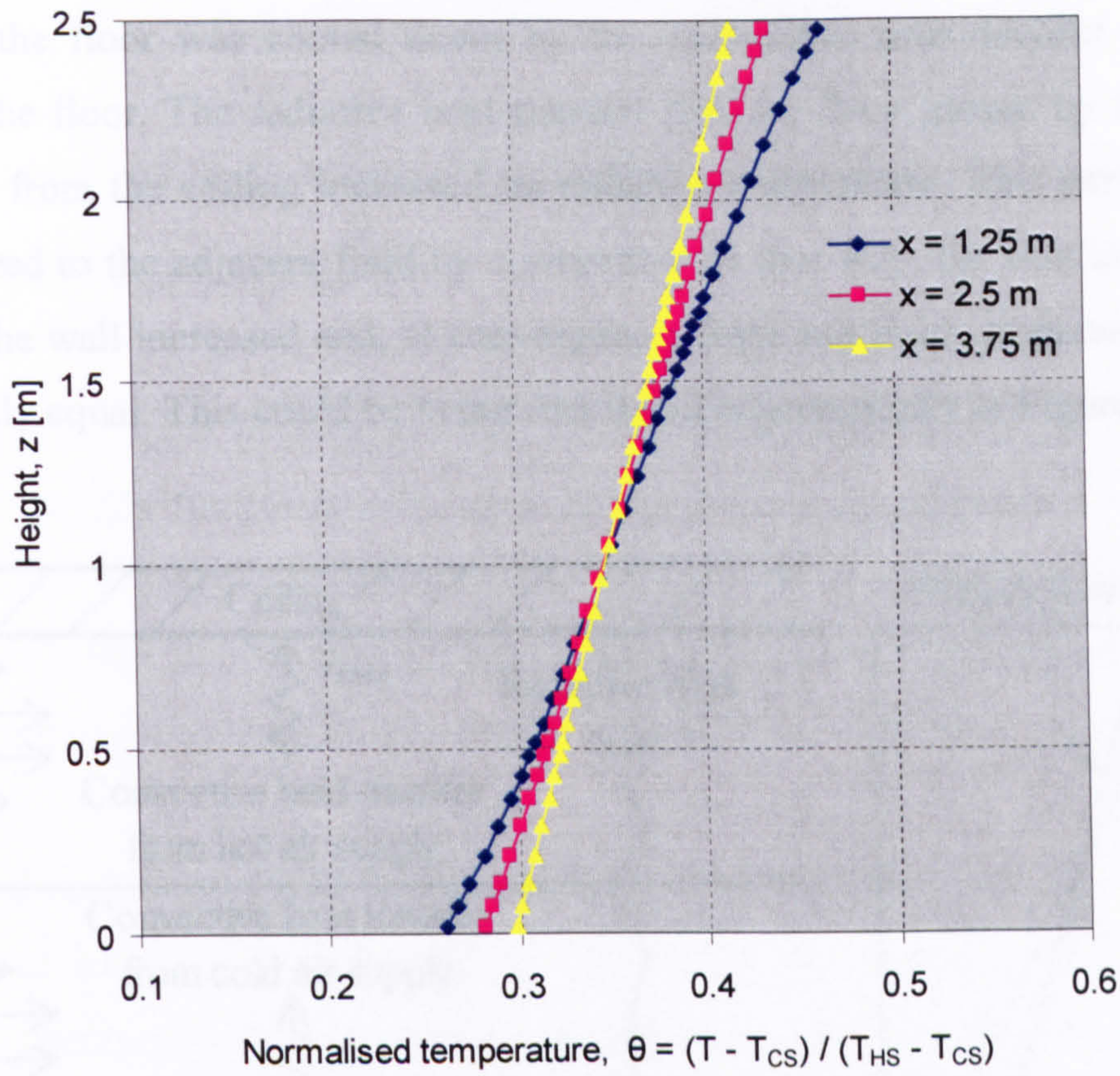

Figure 6.8: Calculation results of thermal radiation temperature gradient between the solid surfaces of the ceiling and the floor at the three data-stations (mid-way) in the *x*-direction.

The mean T_3 increases with incremental changes in the hot air supply as parallel radiative temperature gradients that become constant when full mixing occurs. When increasing the hot air supply further than the mixing threshold, the slope changes as the hot air jet reaches the floor causing the floor to become warmer and radiate to the ceiling.

The main effects rise due to the surfaces of ceiling and floor that are maintained at different radiative temperatures which are calculated from the convective flow of the supplies adjacent to ceiling and floor. The ceiling gained heat from the convective heat transfer from the flow below it. The heat gained from the adjacent fluid was radiated towards the floor. After carrying out tests with radiation effects on the vertical walls, the amount of heat by radiation was found to be negligible, because opposite walls are subjected to same the temperature gradient due to stratified flow. The temperature of the ceiling decreased asymptotically down to the level at which, at full convergence, the temperature of the adjacent fluid became equal to the temperature of the ceiling. On the

other hand, the floor was cooled down by the convective heat transfer of the flow adjacent to the floor. The radiative heat transfer that the floor gained by the radiative heat transfer from the ceiling increased its radiative temperature. This part of the heat was transferred to the adjacent fluid by convection. In that way, the heat in the cold air adjacent to the wall increased and, at convergence, floor and fluid temperatures became asymptotically equal. This could be better illustrated schematically in Figure 6.9,

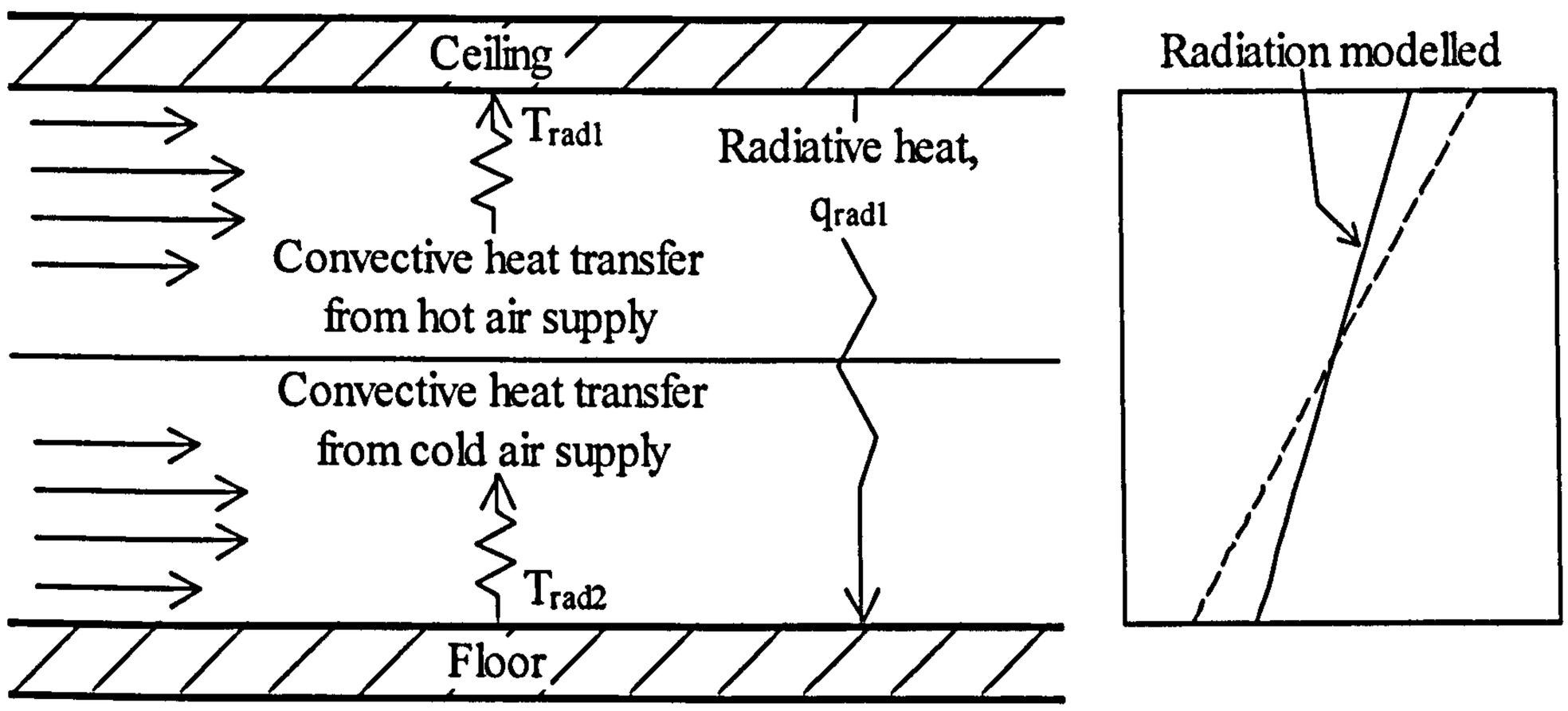

Note: The arrows show the direction of heat flow from hot to cold.

Figure 6.9: The effect of radiation model at steady-sate.

Generally, in cases of low ventilation rates, where low convective heat transfer rates are used, the effect of radiation is more pronounced compared to the high convective heat transfer cases for the same supply temperatures. Displacement ventilation methods utilise low input velocities to satisfactory levels of comfort. Radiation in this case will affect the temperature gradient across the height of the room. Buildings utilising the natural ventilation method would also be affected by radiation that would influence the temperature gradient across the height of the room. In the general case of displacement ventilation where low supply velocities are used, the increase in the temperature gradient of the occupied zone cannot be neglected. Hence, due to the increase in the temperature gradient in the occupied zone, if it is required to decrease the temperatures, it may be necessary to decrease the supply temperature or increase the ventilation air. Large buildings utilising the displacement ventilation method with comparatively low heat transfer rates would also be affected by radiation. Taking into account radiation effects is, therefore, important for natural and displacement ventilation methods.

6.6 Influence of Leakage Modelling and other losses on the Temperature Gradient

When setting up a CFD model, the solid boundaries are assumed to be adiabatic and subsequently airtight too. When trying to replicate such conditions, it is difficult to achieve and thus, the results obtained from a real case will always deviate from an ideal case. To achieve this, the boundary conditions in CFD can be appropriately modified so that the external conditions will influence the internal flow medium.

It is expected that heat sources in the medium, more particularly in the cold air zone, will smear the interface from below, which will affect the vertical thickness of the interface. A decrease in the thickness of the interface will result in an increase in the vertical heat transfer rates.

In order to achieve some comparison between the experiments of this work and CFD, two outlets were added to investigate the effect of the cracks and openings of the actual experiment on the mass and heat leakage. One outlet was added at a time while adjusting the flow rates did not affect much the temperature gradient in the room. The RNG showed previously a sharper definition of the interface and therefore it was adopted here for further studying the effect of mass and heat leakage. Including only the top outlet has an effect on removing some of the heat from the upper part of the hot air zone, although not very significant. However, when both outlets were included, the temperature gradient was similar to the one observed in the experiments of the current work. This is shown by the temperature gradients in Figure 5.17. The picture of the room model shows 2.5-cm thick outlets added on the rear wall of virtual CFD model. The effect is present when the lower outlet is added. There is mass leakage out of the room from the top outlet. On the other hand, from the lower outlet, the flow is predominantly going into the room because the temperature of the outlet is slightly higher than the adjacent cold air zone. The superimposed velocity vectors on the room model show the inflow occurring. The fluid is buoyed at the height of the interface, where it increases the turbulence levels from below and reduces its thickness. Eventually, this causes the two temperature gradients to become identical. At these low

convective heat transfer rates, the radiation effects should also be added, because they increase the heat transfer rates in the vertical direction. This is better shown in Figure 5.8,

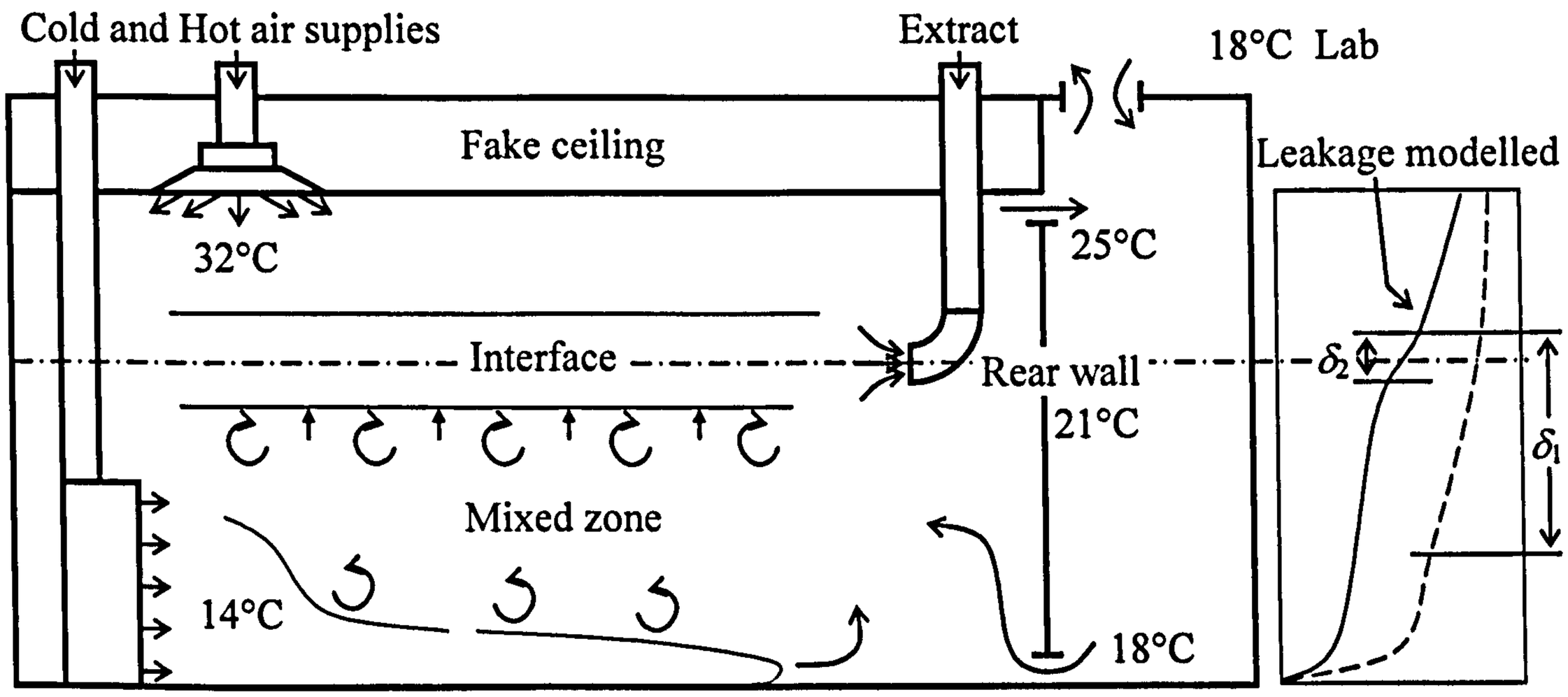

Figure 6.10: The effect of leakages in the test chamber at low inlet flow rates as predicted by CFD. The interface thickness δ_1 is before leakage was modelled and δ_2 after leakage was modelled. However, at higher inlet flow rates, there is leakage from both zones to the outside in which case can be considered insignificant.

At the point were the curves show a reasonable match in Figure 5.17, the heat losses are only due to air leakage. The air leakage was not the only parameter that influenced the experiments. Heat losses by conduction occurs at the ceiling and the floor as well as the walls, but in this current case such losses were assumed to be small compared to heat losses due to air leakages. However to some extent, the heat losses due to conduction can be represented by mass leakages. Heat exchange will also occur between the layers by radiation depending on the scattering coefficient of the layers and the relative humidity of the medium under investigation that is not considered here. The radiative heat exchange between the layers can be estimated in the order of 10% which will give an almost spot on match with the experimental data, as shown in Figure 6.5. Finally, the overall effect is that the temperature gradient presents more closely a case of low *Re* case instead of a high *Re* case as shown in Figure 5.17 and Figure 6.10.

There is a larger gradual change in the cold air layer when not including the leakage openings. There is internal mixing in the interface and this appears as an internal mixing layer that causes entrainment from the cold air zone and hence reduction in temperatures in the hot air zone. Experimental data obtained with higher accuracies may be required than reported by traditional standards as discussed by Chen and Rodi (1980) (Chapter 3), to further extend the accuracy of turbulence models.

The effect of different size (width) of leakage openings to the mean temperature in the room can be seen in Figure 6.11,

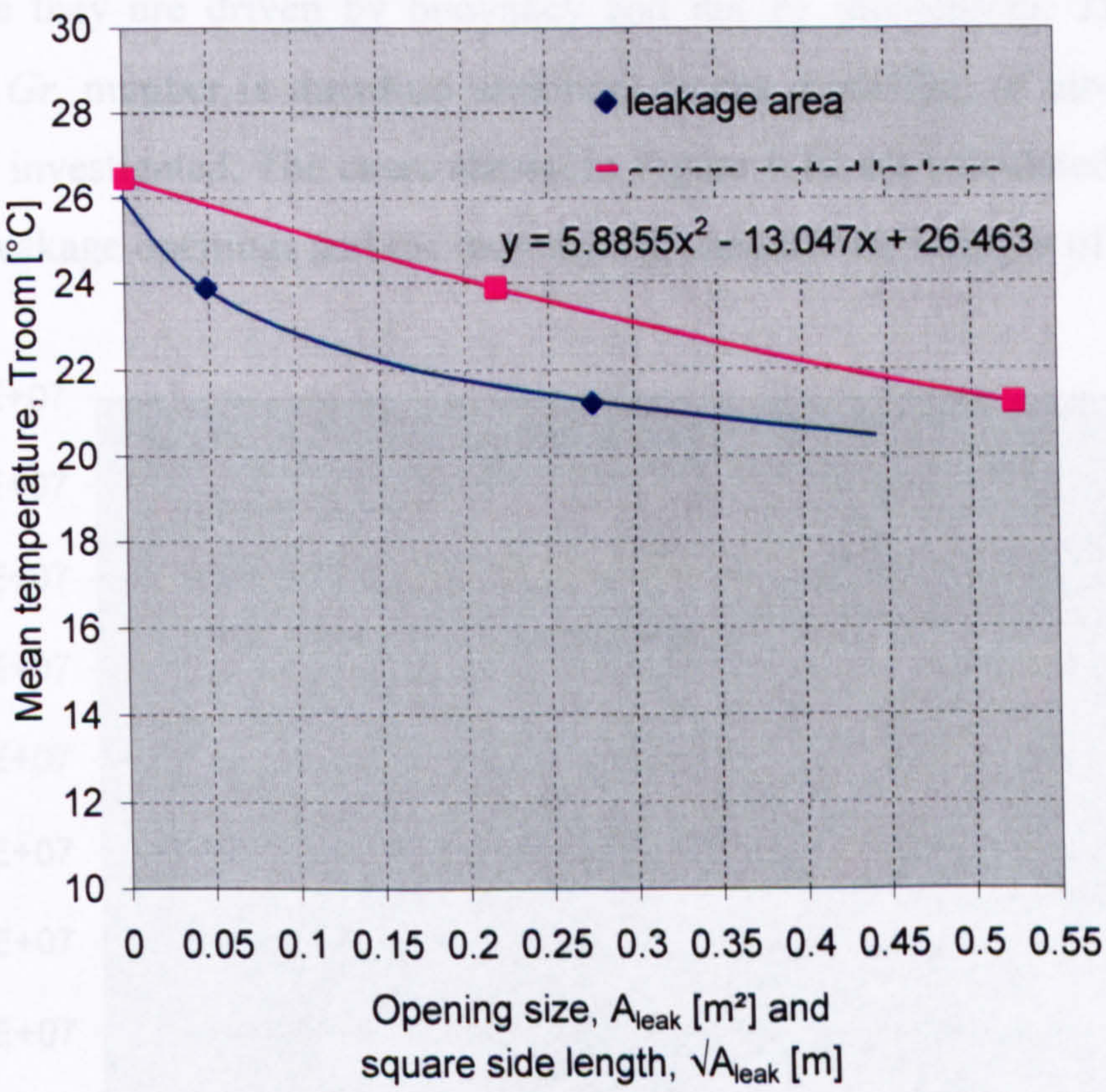

Figure 6.11: Effect of the leakage opening side on the mean temperature inside the room.

There is a weak decay law for the leakage area, A_{leak}, that is approximately linear for square side length, $\sqrt{A_{leak}}$.

The actual air-leakage area of the openings has been estimated in Chapter 2 section 4.1.5. The velocity for the air leakage area of the experimental model can be evaluated by interpolating between observed velocities at the openings of the air-leakage CFD

models shown in Figure 5.17. For the 5.5-m width of openings, the velocity is 0.215 m/s and for the 1-m width of openings, the velocity is 0.445 m/s. The width of the openings of the experimental model for the chosen arbitrary thickness of 0.025 m is 2 m. This yields a velocity of approximately 0.4 m/s or an average infiltration flow rate of 0.02 m^3/s that corresponds to a medium air leakage according to CIBSE (2000b) TM 23 and Brundrett (1997).

The effect of turbulence can have a significant effect on the mesh density and can further increase the significance of time dependent terms due to the interaction with the interior flow. The Gr number can be used to characterise the flow of the air-leakage openings since they are driven by buoyancy and not by momentum. The maximum magnitude of Gr number is therefore important in the modelling of air-leakage flow and should be investigated. The cases shown in Figure 6.12 are calculated for different widths of air-leakage openings and the incremental temperature changes of EXP:3,

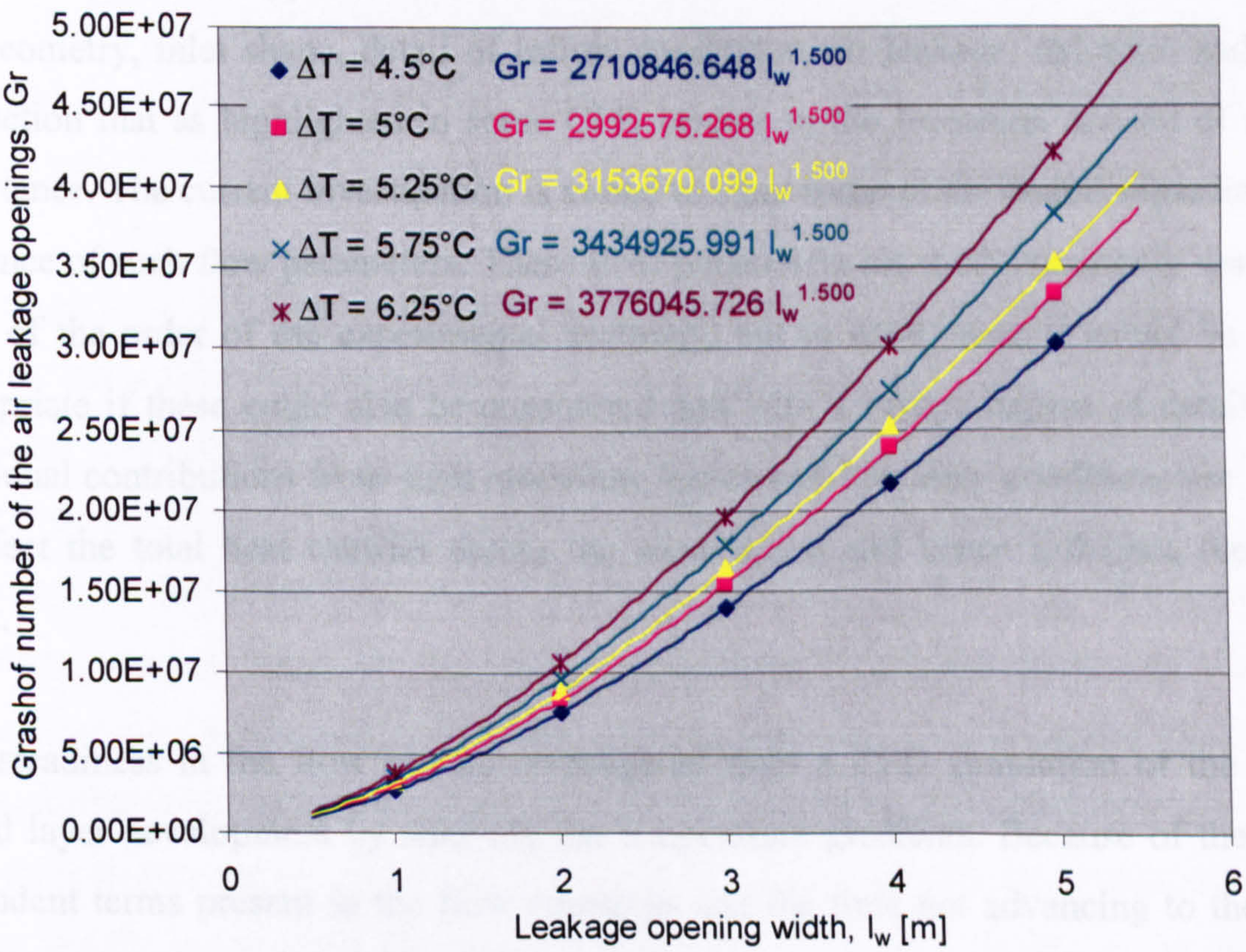

Figure 6.12: Effect of Gr number for the cases where and $\Delta T_{in} \approx 18°C$ and $\Delta T_{room} > 4°C$, EXP:3. Appendix B (EXP-08-12-00).

In the cases shown in Figure 6.12, the range of Grashof numbers is $10^6 < Gr < 10^9$ that indicates closer to a laminar regime of transitional flow for all cases. When using the

height of the openings, which is the characteristic length scale of turbulence for the linear opening, the range of Grashof number is $10^4 < Gr < 1.5\times10^4$ and this corresponds to laminar flow. The magnitudes seem to stay quite low for the room temperatures and area or the height of the openings.

The airtightness of a residential dwelling may seem to be a small amount. However, when this is multiplied by the size of the building it has a significant effect on the energy costs.

6.7 Further issues attempted by using the Virtual CFD Model – a quantitative comparison with transient simulations

There are a certain number of modelling issues, for example: the requirement of using a turbulence model as opposed to a laminar solver when the CFD model is closer to the real geometry, inlet shape, detail of inflow conditions, air leakage, radiation and heat conduction that as highlighted in some CFD studies in the literature, are not of much importance. The current investigation is aimed to clear some of the doubts regarding the influence of such flow parameters. These flow parameters are most commonly assumed to be of the order of the experimental accuracy, but in most cases it would be more appropriate if these could also be considered and with a certain degree of detail. The individual contributions from such modelling issues and boundary conditions are likely to affect the total heat transfer across the room space and hence influence the final result.

A unsteadiness in the flow can be investigated from a CFD simulation of the upper mixed layer development by studying the temperature gradients. Because of the time-dependent terms present in the flow equations and the time not advancing to the final step in one go for each time step as in steady-state simulations, 500 iterations seem to suffice. The temperature gradients present a case of mixed layer development of the upper layer that can be seen in Figure 6.13,

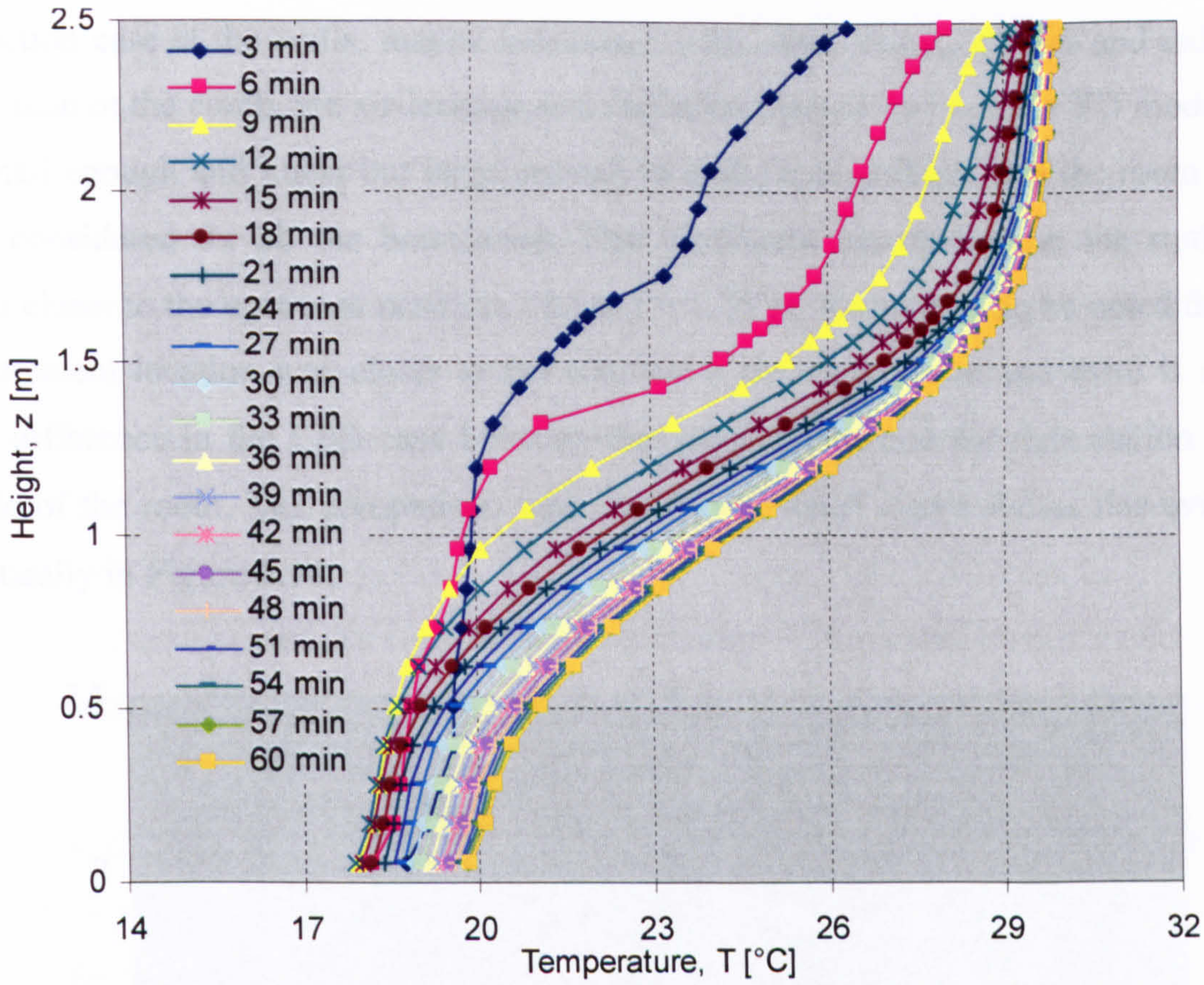

Figure 6.13: Upper mixed layer development obtained by temperature gradients in the middle of the room from transient simulations using the RNG turbulence model for the airtight case of the virtual CFD model at 500 iterations per time step.

The temperature gradients in the case of the upper mixed layer development in Figure 6.13 reaches a final time step that is the same as that shown in Figure 5.17 when the additional openings are not added yet. This occurs as the gradients seem to follow an asymptotic behaviour. The same temperature distribution is obtained as the temperature gradient is similar at different data-stations in the room, in all of the time steps. The directional mixing effect on the temperature gradient becomes more important for higher flow rates as the near field of the upper jet occupies a larger part of the domain, as the surface area bounded by the effective region of the jet is proportionally larger compared to the rest of the room. Additionally, the closer the measurements to the inflow jets the more likely the temperature gradient is to be affected by the jets. The upper layer can appear to be subdivided into a uniform layer below and a larger interface below that layer, as it has also been observed in some CFD simulations and the experiments. However, the effect of the exhaust on the total temperature gradient is an indirect effect of buoyancy in the room. The effect of exhaust velocity is negligible or non-existent compared to the velocity of the upstream flow. This is similar to a stronger

conduction case at the walls, maybe associated with small downdraughts and radiation fluxes than in the combined air-leakage and radiation case of the virtual CFD model that are small enough and linear but large enough to make a contribution in the room space when considered for all the boundaries. This similarity occurs here at the station of results closer to the upstream position, i.e., at $x = 1.25$ m. It should also be noted that the measurement location was closer to the sources in the experiment and there is a very small difference in the CFD case between that data station and the data station in the middle of the room. The comparison with the experimental curve shows this evidence realistically in Figure 6.14,

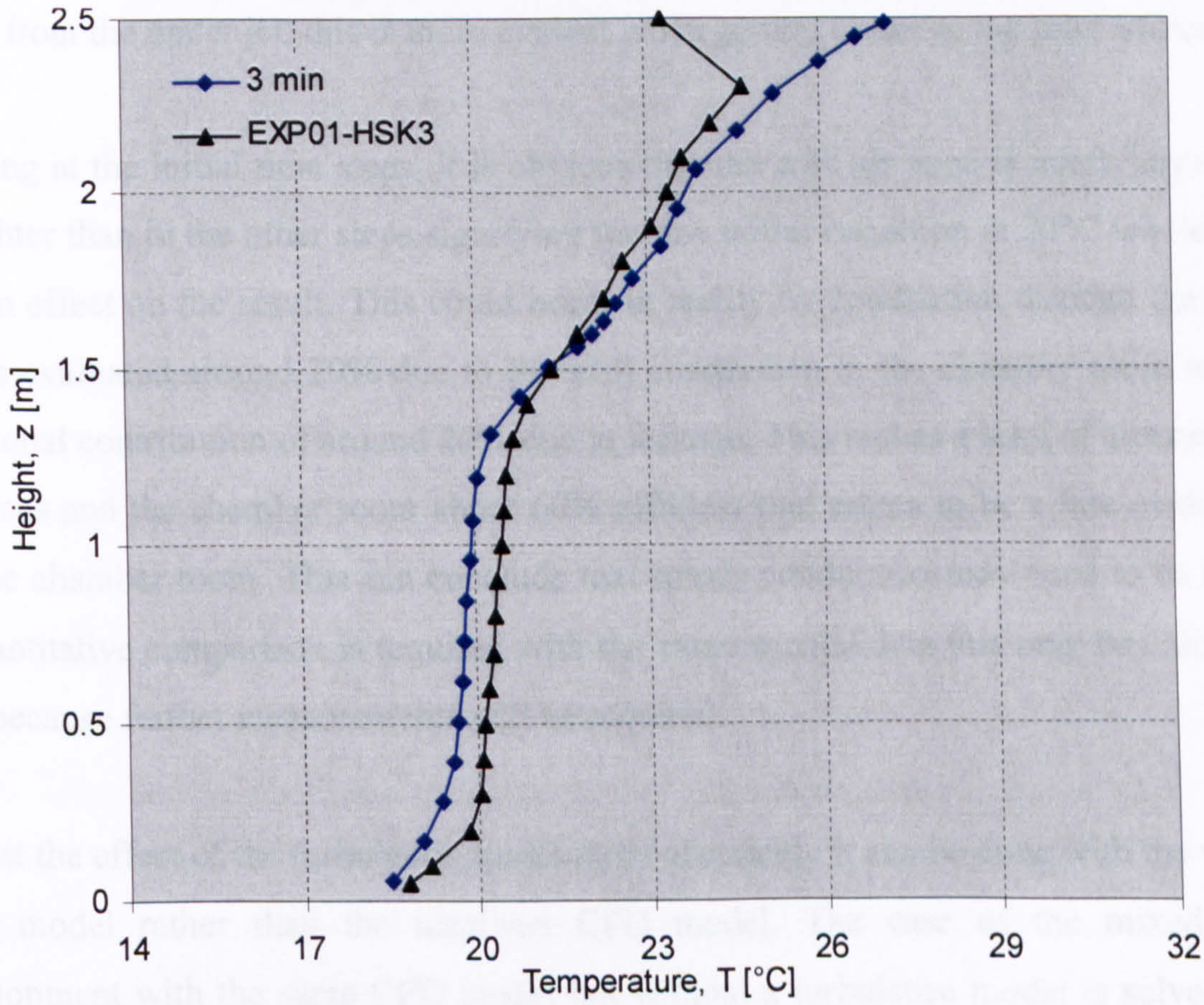

Figure 6.14: A temperature gradient obtained from the initial time step at 500 iterations for the airtight case of the virtual CFD model with the RNG turbulence model, superimposed on the corresponding experimental curve that indicates similar heat transfer characteristics at data station $x = 1.25$ m.

It is obvious Figure 6.14 that the jet finds it even more difficult to surpass the horizontal plane bounded from the upper level of the cold air zone at the initial time step where the initial conditions balance the inlet sources.

The temperature distribution is different close to the inlet sources than in the rest of the room, although there is stratification as implied by comparing Figure 6.14 with Figure 6.13. The flow in the room is observed as being separated from the upstream flow, although it has been affected by the upstream flow conditions. When comparing with the corresponding temperature gradient in Figure 6.13, it proves that the temperature distribution is almost the same in the middle space of the room (defined in Chapter 4), as it was also the case when compared with other data-stations in the room. Therefore, stratification exists in the room even at the initial time steps. However, the temperature gradients at the initial time step have some minor differences in the range of temperatures across the height of the room. In taking into consideration the directional effect from the upper jet, this is more evident when getting closer to the inlet sources.

Looking at the initial time steps, it is obvious that the cold air zone is much larger and straighter than in the other steps signifying that the initial condition at 20°C whole field had an effect on the result. This could occur in reality by conduction through the walls that is evaluated around 20% due to the wall conduction in the chamber room and an additional contribution of around 20% due to leakage. This makes a total of around 40% in losses and the chamber room about 60% efficient that seems to be a fare evaluation for the chamber room. This can conclude that steady conduction may need to be added if quantitative comparison is required with the experimental data that may be a difficult task because further measurements will be required.

To test the effect of the turbulence model more accurately it can be done with the virtual CFD model rather than the idealised CFD model. The case of the mixed layer development with the same CFD model but without a turbulence model is solved by a laminar solver and the temperature gradients in the middle of the room are shown in Figure 6.15,

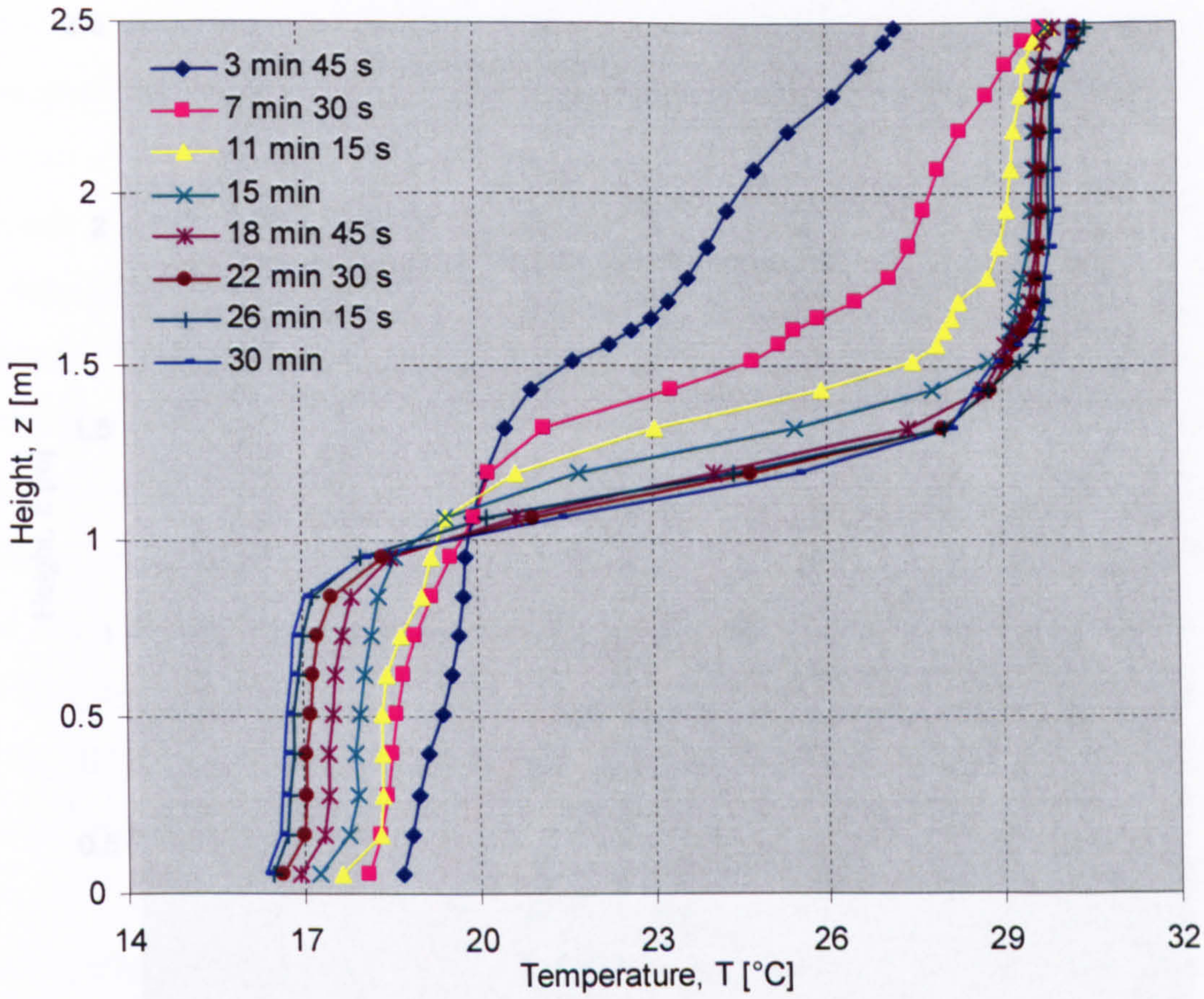

Figure 6.15: Upper mixed layer development obtained by temperature gradients in the middle of the room from transient simulations using the laminar flow solver for the airtight case of the virtual CFD model at 100 iterations per time step.

The stratification in the case shown in Figure 6.15 is the same in the other two stations in each case. The temperature gradient in this case is more stratified that leads to a further reduction in the time-dependent terms of the flow. A comparison between the turbulent simulations and the corresponding laminar cases in the mixed layer development are compared with different iterations per time step and a steady state at full convergence in Figure 6.16,

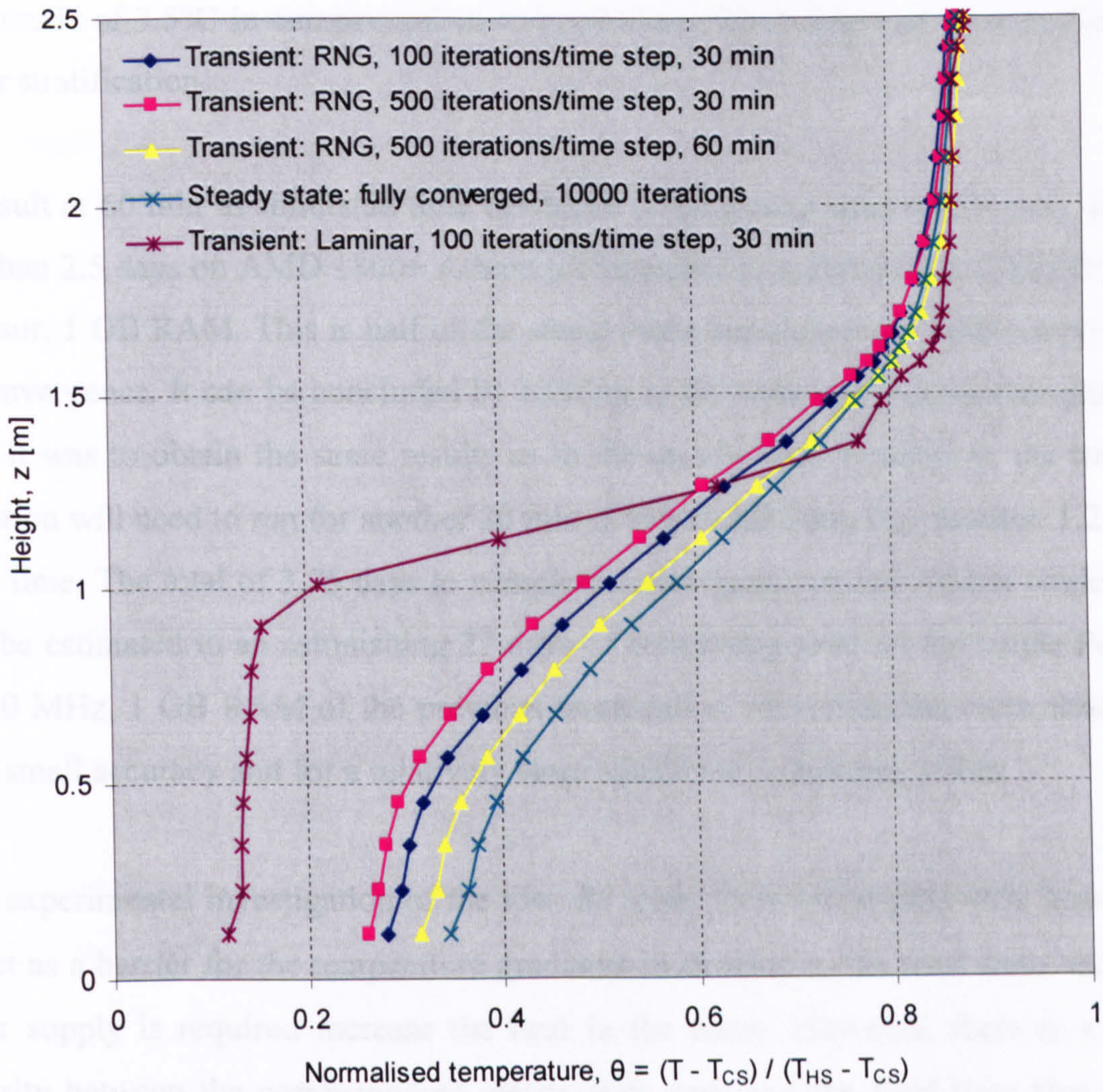

Figure 6.16: Comparison of time-dependent and steady-state simulations at different number of iterations per step.

There are differences in the range of the temperature gradients with lower iterations per time step, although they are relatively small, they still need to be considered more accurately. The difference between the turbulent simulations is relatively small. This difference is approximately 2°C that is significant in ventilation modelling. The difference between the time-dependent simulation at 500 iterations per time step and the steady state simulation at 10000 iterations is 0.5°C that the transient simulation will take many more time steps to achieve the steady-state case as the flow follows an asymptotic behaviour, but it is not of any particular interest in this work. When the time-dependent terms are solved, the equations are discretized in space as well as in time and at specified time steps, the number of iterations is smaller compared to final steady state, but it still takes the same corresponding computing load to achieve the same result. Although the effect of mixing is also accounted for by eddies larger than the grid size that is the case in the laminar simulation, there is a significant temperature difference of

a magnitude of 3.5°C in comparison to corresponding RNG case and an unrealistically sharper stratification.

The result at 60 min in simulated time has taken a computing time that is only slightly more than 2.5 days on AMD 1800+ Athlon (comparable to a Pentium 4, 1.8 GHz), twin processor, 1 GB RAM. This is half of the steady-state simulation at 10,000 iterations at full convergence. It can be concluded by looking at the transient temperature gradients that if it was to obtain the same results as in the steady-state simulation, the transient simulation will need to run for another 30 min in simulated time, i.e., another 1.25 days in real time. The total of 3.75 days to complete convergence on the Athlon workstation could be estimated to an astonishing 27 days of computing time on the single Pentium III, 550 MHz, 1 GB RAM of the previous workstation. However, the extra time steps give a small accuracy and for a relatively large additional computing effort.

In the experimental investigation of the low *Re* case, there are around 40% heat losses that act as a barrier for the temperature gradients to develop to the final steps and more hot air supply is required increase the heat in the room. However, there is a strong similarity between the corresponding steady-state case and the final time step of this transient case signifying that the transient terms do not play a dominant role when there is stratification. This is because stratification suppresses the time-dependent modes in the flow. In general, there is a small difference in the quantitative results when the leakage openings are added and the qualitative data such as the upper mixed layer development seem to be very realistic. Nevertheless, any additional effects such as due to conduction seem to be small enough and can be accounted for posterior to the CFD simulations to account for the final temperature gradients.

The air medium inside the room space in reality resists to the heat transfer from the inlet sources in the way that it is similar to the initial steps of the development of the upper mixed layer. This most probably occurs due to conduction that is partially modelled with the air leakages and the heat losses from the ceiling and the floor.

The temperature gradient at x = 1.25 m and the one with leakage signify that since the stratification further away is not affected by the jets, it can probably be accounted for by a single equation and add the effects of radiation, conduction, etc. afterwards, as it has

been done in the past by integral methods. However, this is a step further to the "CFD as a prediction tool" and that is not primarily aimed only to achieve a better much with the experimental data.

The upstream mixing can be reduced by introducing diffusers that can bring down the *Re* number of the inlet ducts by increasing the effective outlet area. Similar ideas have been explored in the study of the performance of the thermal storage tanks by Wildin and Truman (1989).

6.8 Quantitative comparison of mean room temperature

The changes in the room temperature in the middle space were studied between experiments, EXP:2 and EXP:3, and the corresponding CFD model, where thermal radiation and heat conduction losses were applied at the ceiling and the floor. This is shown in Figure 6.17,

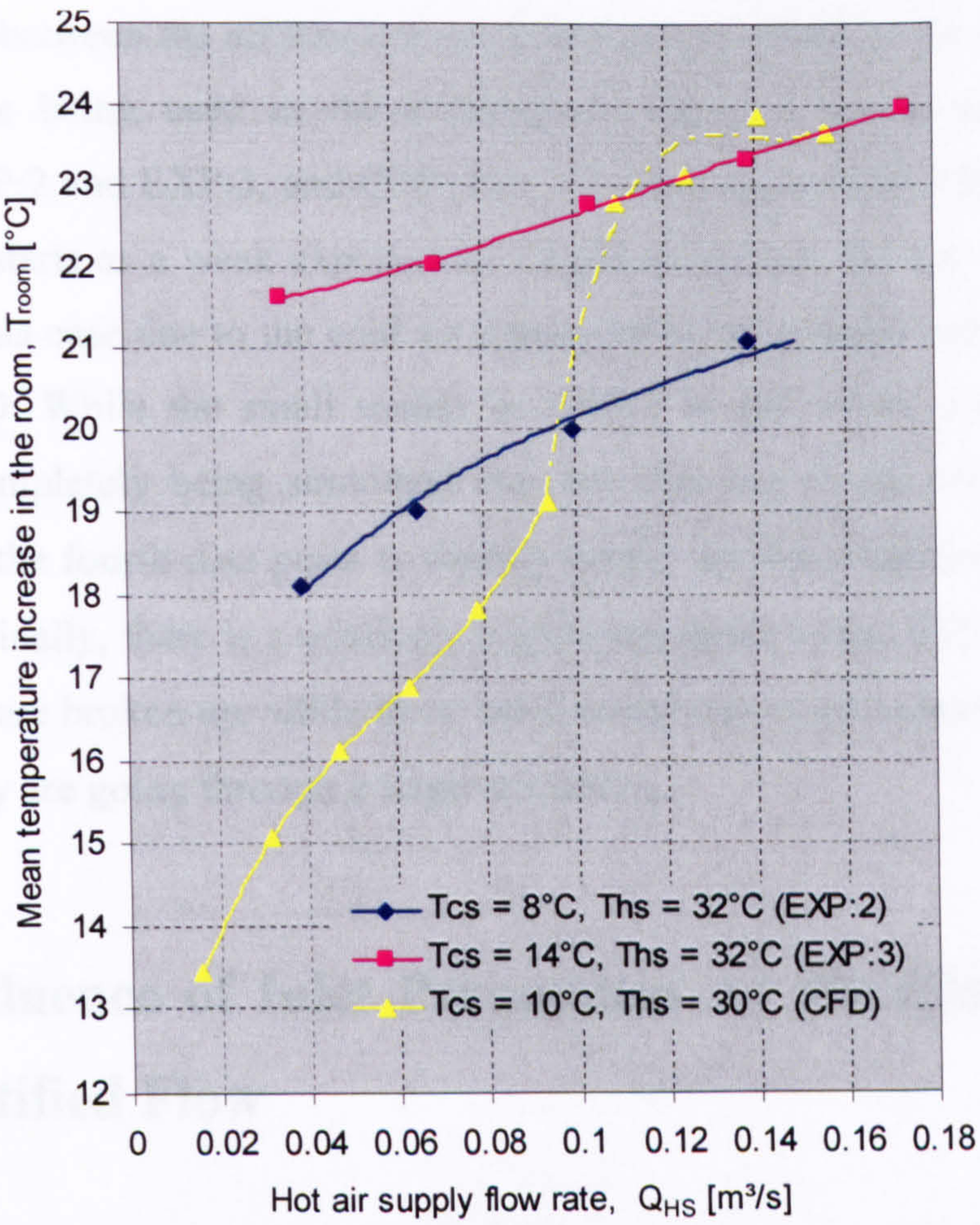

Figure 6.17: Variation of average air temperature in the middle space of the room, experimentally and by the thermal radiation CFD model.

Although there is not too much difference between the supply air temperature ranges in the experiments and the CFD model in Figure 6.17, the mean temperature in the middle of the room is larger in the experimental work rather than by CFD. This is because the air leakage and heat losses are at an outside temperature that is close to the average temperature of the hot and cold supply air flow. This occurs due to air leakage and conduction. Conduction mainly occurs due to convection and radiation at the inside and outside surfaces of the walls of the experimental room reducing the temperature range of across the room height and at the same time keeping a higher mean room temperature. The experiments never fully break for the supply air flow rates being used, due to the higher mean room temperature and limited supply air flow rates, but also due to the directional flow from the ceiling air diffuser. While CFD breaks almost completely at around 0.11 m³/s as specified by equation (6.1) because of the specified vertically downward oriented flow that increases mixing with the cold air flow.

The relationship between the air temperature in the middle space of the room and hot air supply flow rate being used in the experiments obeys a power law increase for experiments EXP:2 and EXP:3, and CFD. For the experiment EXP:3 the average room air temperature starts as a weak exponential variation because the hot air supply is not as effective in this case due to the cold air supply being at a higher temperature than in EXP:2 and CFD. While the small scatter in EXP:2 is due to the cyclic temperature variation not completely being smoothed out, but also due to the breaking up of the stratification as the fourth data point is slightly higher up that expected that is not very clear here yet. Finally, there is a relatively high temperature in the CFD model after the stratified layers are broken up, while there are fluctuations in the experimental results at this stage as they are going through a larger transition.

6.9 The Influence of Inlet Parameters on the Characteristics of Stratified Flow

Although the thickness and slope of stratification appears to be dependent on the situation, i.e., mass and heat flow, inlet turbulence, etc., a correlation between inlet parameters and characteristics of stratified flow is sought in this work.

In analysing the stability of stratification according to Ri number, the value of the entrainment exponent can be obtained for the interface. The overall Richardson number, Ri_o, was investigated by using the temperature differences at the two boundaries of the interface in the vertical direction and the average velocity calculated for the cross-section in the middle of the room. In Figure 6.4, it can be seen that the value of the exponent was equal to -1/2.

The correlation between the Reynolds number, Re, of the hot air supply, overall Richardson number, Ri_o, and stratification slope, S, of the current experimental model is illustrated in Figure 6.18. Power law and exponential interpolation were used appropriately. For air, the thermal diffusivity of heat depends on the sum of thermal conductivities for turbulent and laminar flow. However, increasing the volumetric flow rates of hot air by small amounts, affects the stratification of the interface by increasing

locally the temperature range. This correlation is true for low Re numbers. Data outside this range of flow rates will produce the opposite effect. Instead, overturning and mixing will occur. The correlation between Ri_o and Re can be observed in Figure 6.18,

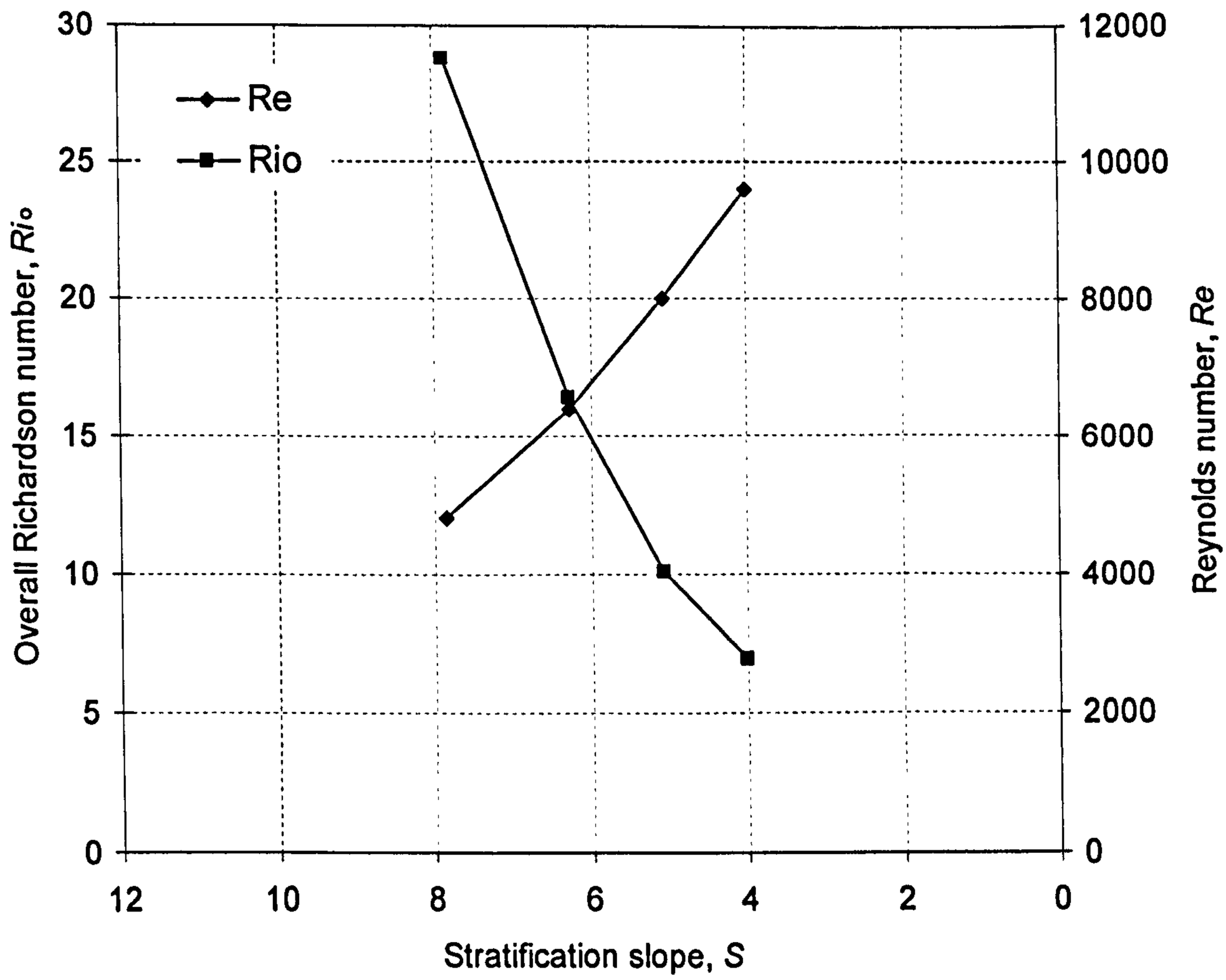

Figure 6.18: A correlation between overall Richardson number Ri_o and inlet Reynolds number, Re with stratification slope, S, for the low Re case.

6.10 Layers in Ventilation

It has been demonstrated that the atmosphere of a building is affected by thermal stratification that influences the ventilation system of the building. The isothermal layers that exist across the height of the building characterised by $dT/dz = 0$. These layers are packed into zones that for stable stratification, $(\Delta T/\Delta z)_{zone} \geq 0$. This is shown in Figure 6.19 (a) below. The pressure is reduced as a linear function of density by the integral,

$$p = p_o - g\int_0^z \rho dz \tag{6.2}$$

where p_o is the reference pressure and ρ is density. The pressure and density variation are shown in Figure 6.19 (b),

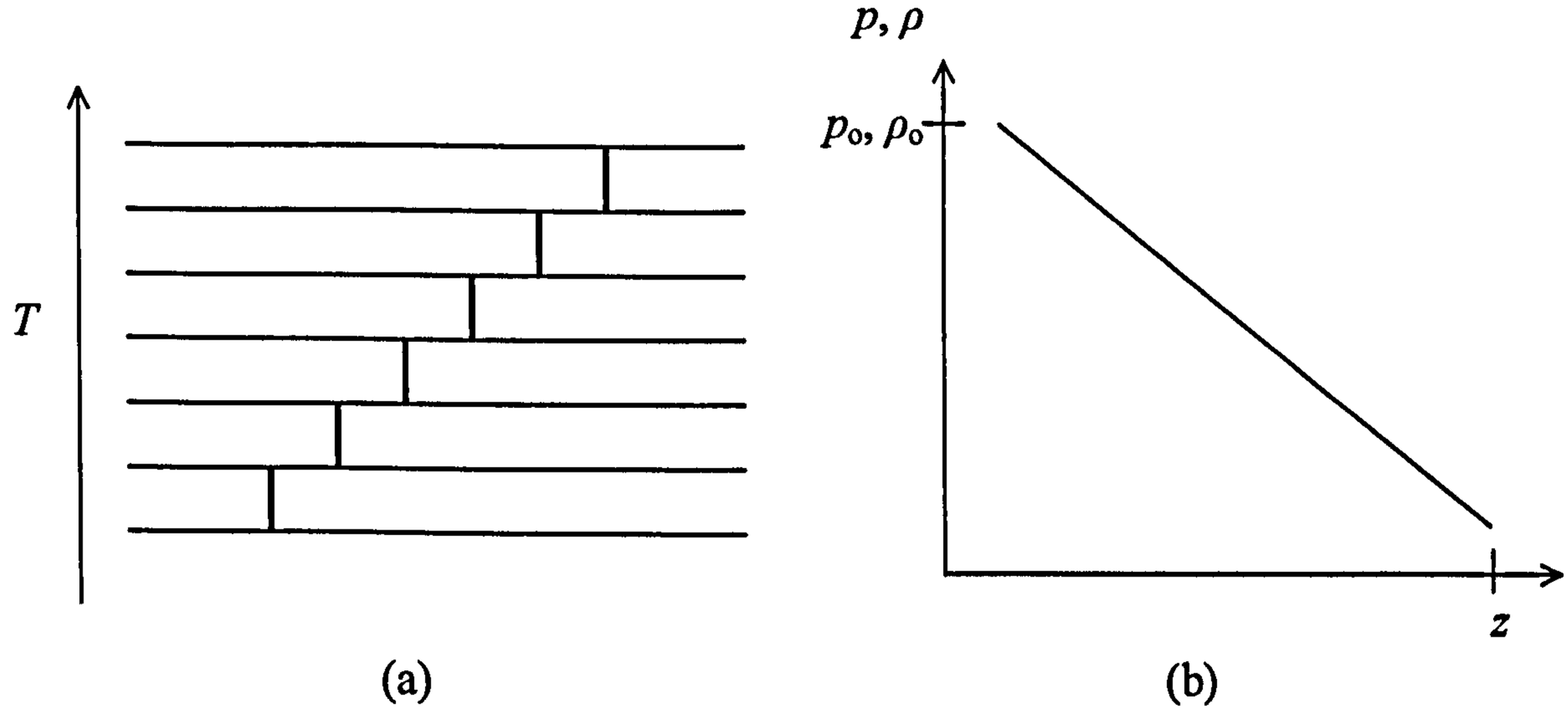

Figure 6.19: In (a), temperature layers with height. In (b), pressure and density variation with height.

There is no clear definition of such layers or zones involving temperature differences in the literature. The present study has shown that two main zones, separated by an interface, exist in ventilated buildings, involving air at different temperatures. This is shown in some detail by the schematic in Figure 6.20,

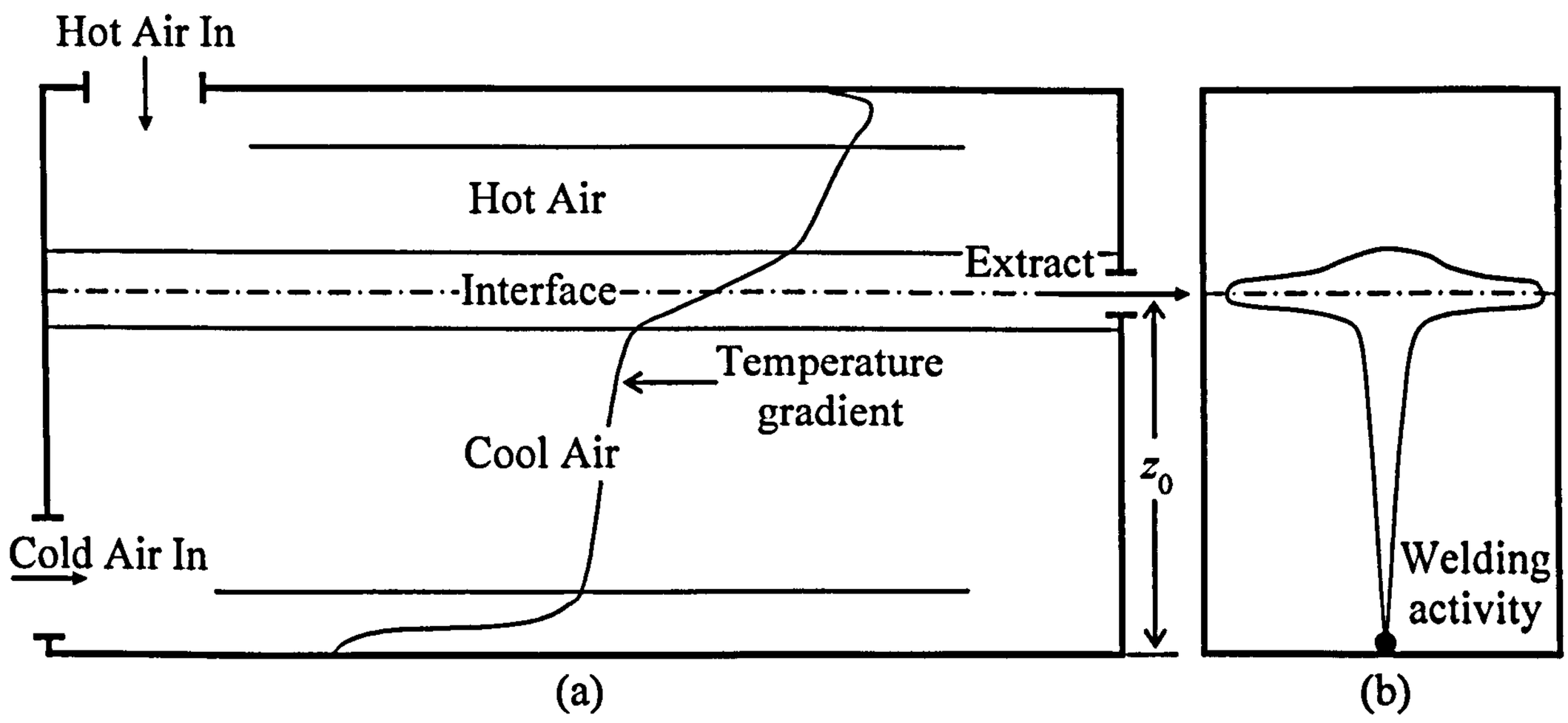

Figure 6.20: Thermal layers inside buildings from (a) a test case and (b) a displacement case of a buoyant plume in an industrial hall.

Fluid of higher density flows near the floor, while fluid of lower density flows near the ceiling creating stratification in the building. Depending on the inlet parameters, like ratio of momentum to buoyancy and turbulence, there will be two main zones in the medium. In-between the zones, there is an interfacial layer at a height z_0 where warmer air defuses into cooler air (denoted as hot and cold air). The difficulty in defining the interface is due to the difficulty in separating out the two main zones.

6.10.1 Cool air zone

The lower zonal layer can be defined as the "cool air zone" which starts from the floor and terminates at some point P above the floor. In the literature, the interface is considered as part of the cool air zone. This is most frequently referred to as the "cool air zone" or "occupied zone" in the ventilation of office buildings, and the "working zone" or "the shift zone" in the displacement ventilation of tall industrial buildings.

From the floor to some height of the order of inlet size, the temperatures are affected by the convective heat transfer from the cold air supply terminal. Boundary layer flow develops at some distance above the floor. Unlike velocity boundary layer flow, where the magnitude of the velocity gradient becomes zero approaching the floor, at z_0, $u = 0$ and $du/dz = 0$, the temperature gradient above the floor has to follow the gradient

inside the concrete floor, implying that the values of dT/dz as $z \to 0+$ and $z \to 0-$ are equal. The two boundary layers follow the square root relation of Prandtl number, i.e., $\delta_v / \delta_t = (Pr)^{-1/2}$ where $Pr \approx 1.0$. The temperature will be approximately constant at some differential distance above the floor. This is illustrated schematically in Figure 6.21 below,

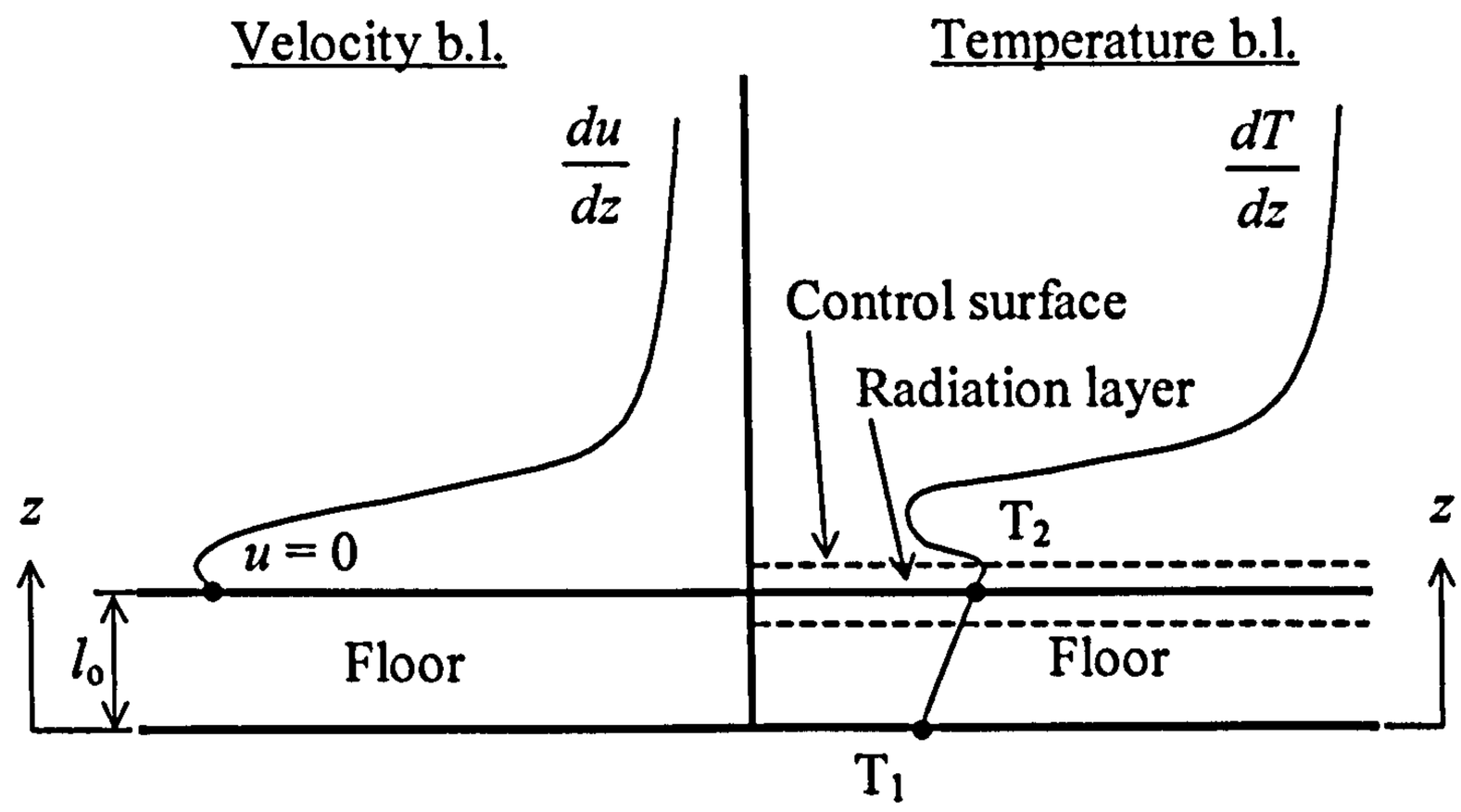

Figure 6.21: Velocity and temperature boundary layers at the floor.

Additionally, depending on the magnitude of the convective heat transfer above the floor, the effect of conduction as well as radiation could be considered in a thinner layer adjacent to the floor. The effect of radiation heat transfer compared to the convective heat transfer and the heat losses is relatively small. A logarithmic law could be a good approximation to represent the temperature boundary layer at some small distance above the floor. With increasing height, at some further distance above the floor of the order of inlet size, the temperature differences become very small, or there is a mild change in the temperature gradient. A nearly constant temperature can even be obtained as a result of the mixing. At the upper limit of the cool air zone, there is a level at which the temperature starts varying with small changes in height at a higher rate than that at the lower levels. The curvature of the temperature distribution with upward distance changes very rapidly at some height above the floor that signifies the upper limit of the cool air zone at point P_1.

6.10.2 Hot air zone

The upper zonal layer can be defined as the "hot air zone" which starts from the ceiling and terminates at some point P above the floor. This is sometimes referred to as the "hot air zone" in the modelling of fire scenarios and zonal models are used to model two zones that are important in the distribution of smoke. In the displacement ventilation of tall industrial buildings, when buoyant contaminant stratification is involved and the pollutants stratify at approximately the same level as the hot air, the zone is referred to as the "stale air zone".

At certain distance below the ceiling, the temperatures may not vary too much. A constant temperature distribution may be observed across the rest of the zone down to the interface. The curvature of the distribution with downward distance changes very rapidly and this signifies the lower limit of the hot air zone at point P_2.

The zone is very similar to an error function distribution for the case of weak stratification.

6.10.3 Interface zone

Having defined the limits of the hot and cool air zones, the interfacial limit between the zones can also be defined. In the literature, not much has been mentioned about the properties of the interface in the ventilation of buildings. In the stratification of reservoirs and estuaries, the interface has been defined as a thermocline of finite vertical thickness. The temperature stratification affects the thickness of the interface that could influence the thickness of the withdrawal layer affecting the ventilation rates of the buildings. The strength of the interface acts as an artificial barrier separating the two main zones.

Providing that there are no disturbances below the hot air zone and the interface, and any disturbances due to turbulence fluctuations are settled down, a smooth pattern of thermal stratification can be obtained across the height of the interface. Additionally, a smooth temperature distribution is established at steady state and any potential energy

stored at lower levels due to unstable stratification is released by the turbulence fluctuations, rendering the medium into a stably-stratified temperature mode. The interface thickness can be derived by investigating the monotony of the function denoted by the experimental points on the graph of the temperature distribution with room height, i.e., find the magnitude of the 1st and the 2nd derivatives of temperature with room height, i.e., $T' = dT/dz$ and $T'' = dT^2/d^2z$. The slope changes very sharply at the limits of the interface, thus the limits with the two main zones can be found, i.e., curvature points P_1 and P_2. The curve is concave at the lower limit and convex at the upper limit. The sharply varying temperatures in the interface can be thought as if they lie on the curves extending at the zonal limits of the hot air zone and the cool air zone. The point P_{int} is the point of inflection which occurs at the interfacial contact between the two main zones where the two curves interface. At this point, T' is a maximum and T'' is zero. Depending on the intensity of the measurement points with room height, a maximum could be observed at z_0 in the middle of the interface of distance a either side from the cool and hot air zones. The thickness of the interface zone is thus $\delta = 2a$ and the height of the interface occurs at height z_0. This is all interpreted in Figure 6.22,

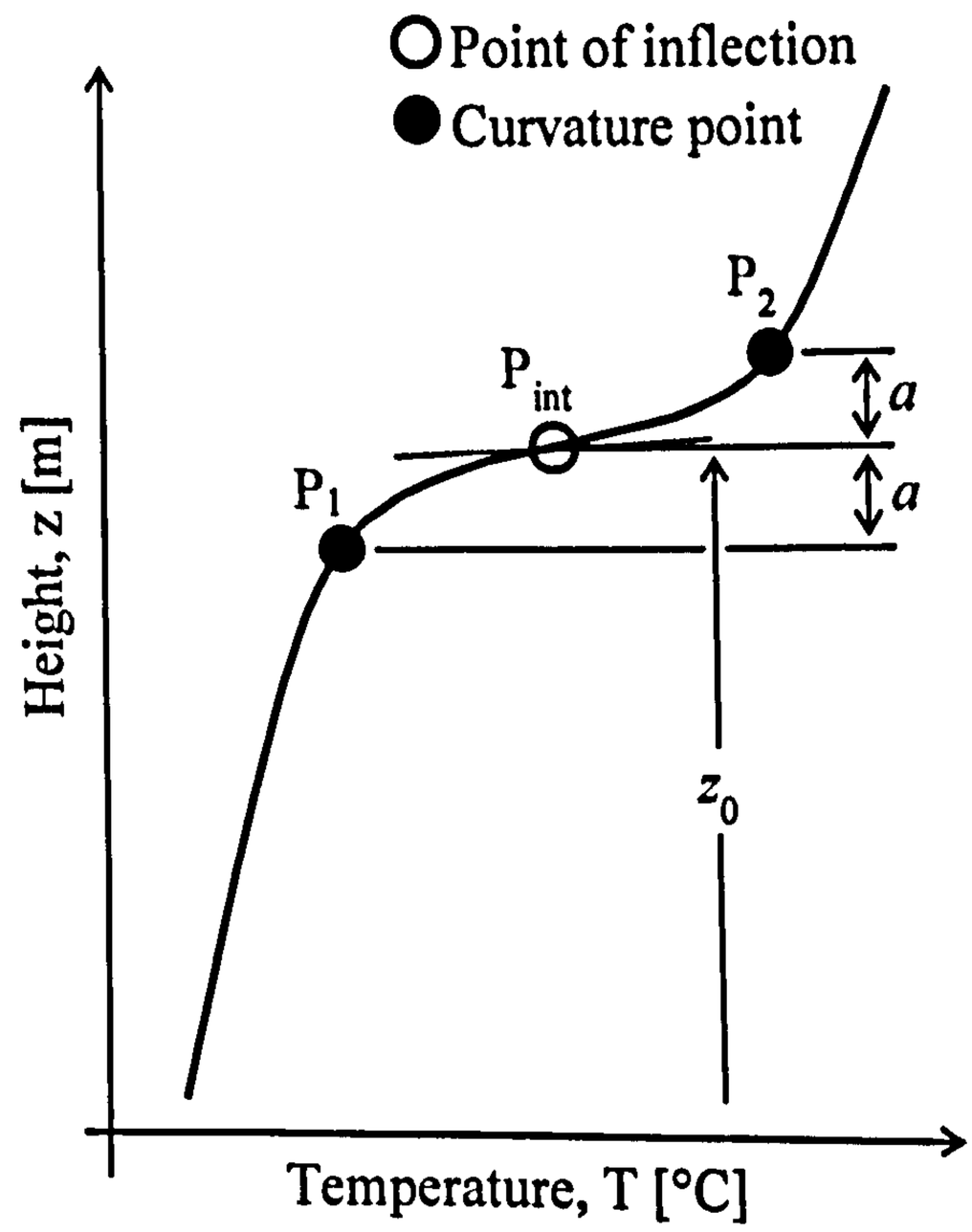

Figure 6.22: Curvature points and point of inflection on the stratified temperature distribution with room height.

It is important to point out that either side of the interface point the value of T' changes sign. However in the case of low stratification, the value of T' does not change sign because the temperature distribution follows a curve of an error function.

If the temperature gradient is not particularly uniform, then it is difficult to obtain the curvature points by evaluating the derivatives. An averaging process must be applied so that the temperature inconsistencies are averaged out. Then point P_1 could be found by evaluating the difference in the arithmetic mean value of the change in the slope obtained from a few points on the temperature gradient and compared to the adjacent value. Each mean value should be subtracted separately by the adjacent middle value. The operation must be carried out throughout the whole range of values. The relative changes in the curvature can be evaluated by a search procedure using the following integral,

$$\frac{1}{(k-1)-l}\sum_{i=l}^{k-1}(T_i^*)'' < (T_k^*)''$$

and

$$(T_k^*)'' > \frac{1}{m-(k-1)}\sum_{k+1}^{m}(T_i^*)'' \qquad (6.3)$$

in order for equation (6.3) to be valid, the conditions: $1 < l < m < n$ must apply, where T_i^* is the value of normalised temperature at height z_i, l is the height of the starting point at which a relatively constant slope is observed and similarly m is the starting point from the upper limit (that are preset to specified values). If $(T_k^*)'' = 0$, $\lim_{z \to P_{\text{int}}^+}(T^*)'' + \lim_{z \to P_{\text{int}}^-}(T^*)'' \approx 0$ and $(T^*)'$ is a maximum point. Otherwise the same procedure can be carried out using equation (6.3) and substituting for $(T^*)'$. For the test cases of weak and medium stratification, changes in the slope inside the zones where observed in the region of 1.5 ± 0.2°C/m for the case of weak stratification, any higher than that can be considered as a curve point.

6.10.4 Test cases

It should be made clear beforehand whether the gradient signifies weak, medium or strong stratification. This can be done by looking at the dimensionless temperature distribution. For cases of weak stratification, the interface may be difficult to define. For medium stratification, enough points are needed in order to find the right pick that signifies an inflection point. This could also be a local minimum of T' depending on the strength of stratification and the accuracy of the measurements.

To achieve a qualitative comparison between the different sets of experimental cases carried out in this work, the values obtained were non-dimensionalised. The temperature values across the height of the chamber obtained from the thermocouples were non-dimensionalised by multiplying the dimensionless ratio, $\theta = (T_i - T_{CS})/(T_{HS} - T_{CS})$, where T_i is the average temperature obtained at the specified room heights. The values of stratification slope can be plotted against the dimensionless ratio of momentum to buoyancy $r_S = F_S / M_{HS}$. The momentum of the supply jets based on the inlet size can be calculated by $M_{HS} = \rho U_{HS}^2 A_{HS}$, where A_{HS} is the area of the hot air supply in m^2 and U_{HS} is the velocity of the jet in m/s. The buoyancy force can be calculated by $F_S = \rho A^{1.5} g(\Delta T_S / T_o)$, where ΔT_S is the temperature difference at the supplies in °C and T_o is the reference temperature in K. The distance in the vertical direction was divided by the height of the chamber which was $H = 2.5\,m$. The dimensionless local stratification slope, s, is given by $s = (\Delta T / \Delta z)_{zone} \times h_{zone}$ and S is the total stratification slope. The stratification values obtained that controlled the stratification slope, r_S, are tabulated below,

	Ratio of momentum to buoyancy, r_S						
	Experimental cases on formation of stratification (set-1)				Experimental cases on break down of stratification (set-2)		
Local stratification slope, *s*	0.01	0.02	0.04	0.06	0.3	0.6	1.2
Cool air zone	0.07	0.08	0.08	0.08	0.16	0.16	0.03
Interface	0.3	0.36	0.52	0.62	0.99	0.8	0.01
Hot air zone	0.17	0.38	0.5	0.53	0.03	0.03	0.01
Total slope, *S*	0.12	0.19	0.24	0.26	0.231	0.208	0.023

Table 6.2: Dimensionless stratification slopes, S for certain ratios of momentum to buoyancy.

The values from Table 6.2 can give an idea for the slope of stratification in the room for different flow rates in the different zones. However, although the values of temperature are not very consistent for the experiment at higher volumetric flow rates, a good idea of the slope of stratification could be obtained.

Increasing the ratio of momentum to buoyancy in the low Re case of the CFD simulations and varying the inlet temperature ΔT_S at only 2.4°C (without buoyancy and radiation) yielded a temperature range of 2°C. The thermal stratification with room height becomes very stable and looks very similar to the CFD simulations for the high Re case when $\Delta T_S = 20°C$ (without modified buoyancy and radiation) yielded a temperature range of 16°C. In a laminar case, the temperature distribution is more pronounced $\Delta T_S = 20°C$ and there is a very fine interface.

The ratio of momentum to buoyancy for two test cases obtained by CFD, one changing U_{HS} while keeping ΔT_S the same and another test case keeping U_{HS} the same while changing ΔT_S, yielded the same temperature patterns. The ratio of momentum to buoyancy for the two cases was in the range of $r_S[0.014,0.018]$. In the experimental work of formation of stratification, denoted as: set-1, ΔT_S was $\Delta T_S = 15°C$ and the set

of case studies of break down of stratification, denoted as: set-2, $\Delta T_S = 25°C$. The temperature difference between the ceiling and floor was 5°C and 7°C. The ratio of momentum to buoyancy, r_S, is also different. In the experimental cases of set-1, the changes in the ratio of r_S are much smaller than in set-2 due to the forming stratification in the former while breaking stratification in the latter. Mapping the temperature gradients of set-2 onto set-1, or the opposite, is very difficult. However, in experimental set-1, the speed of the supply air was much lower than set-2, it is expected that the values would not deviate much if the same was carried out by set-2, due to the low speed nature of the problem. Hence, using the ratio r_S as a guide, dimensionless stratification slopes for both sets could be plotted on the same graph. The changes in the slope of stratification at the different zones for different r_S are shown in Figure 6.25. The changes in the slope of the interface with increasing r_S are shown in Figure 6.26.

Determination of zonal layers for the low Re cases of this work

The interface is a little difficult to define in the cases of low and medium thermal stratification in this work.

The average height in the layer adjacent to the floor is $z/H = 0.12 - 0.16$. The average height of the cool air zone is $z/H = 0.9 - 1.0$.

If the measurement points are not enough to draw an accurate curve and there are unfiltered fluctuations in the temperatures, then a single maximum may appear as an array of minima could be observed in the middle of local maxima. The choice of the maximum point of interest can then be found by looking at the temperature gradient. The thermocouples at $z/H = 0.52$ and $z/H = 0.68$ are the limits of the interface. Between $z/H = 0.52$ and $z/H = 0.56$ the temperature gradient changes.

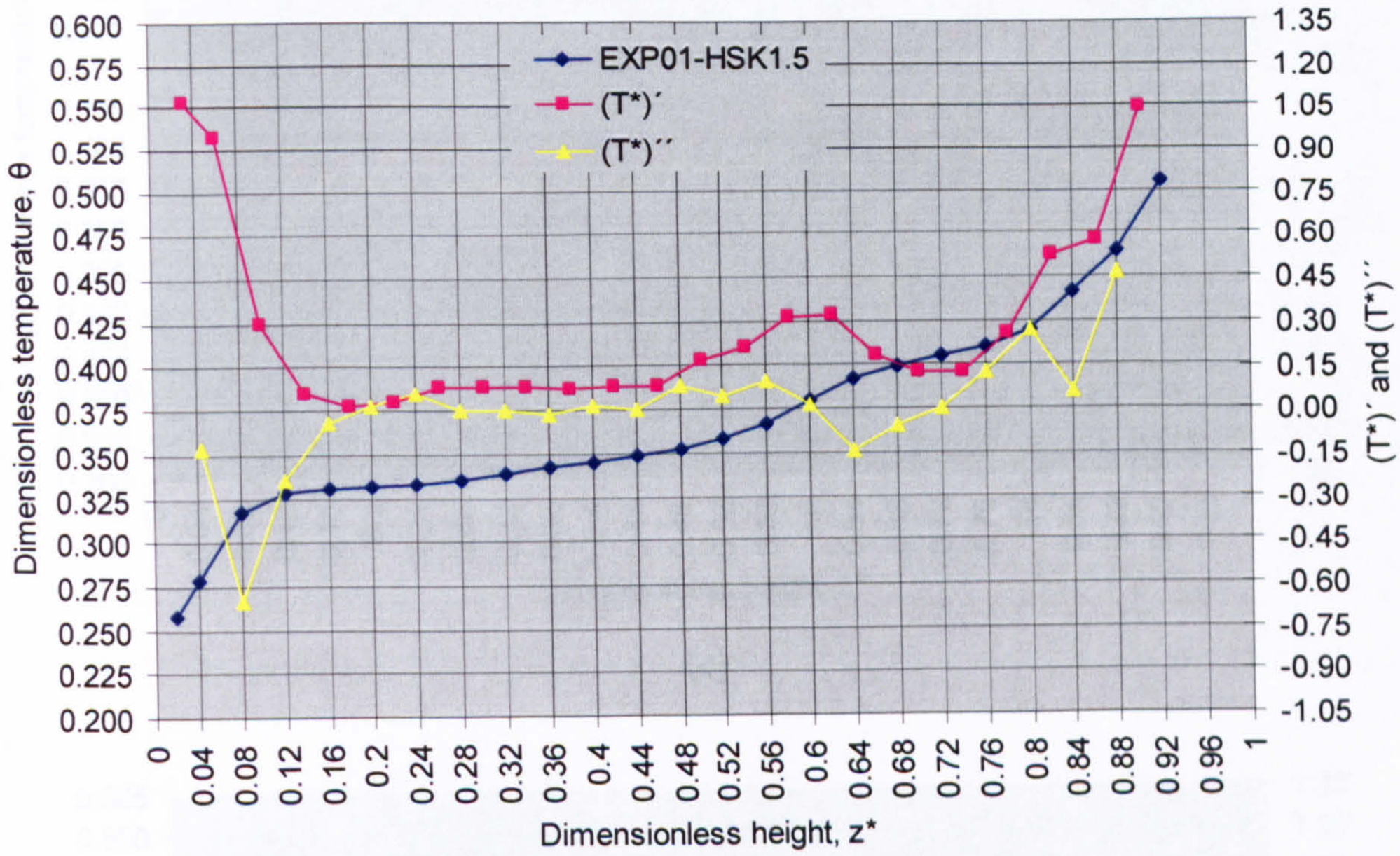
EXP01-HSK1.5
(T*)´
(T*)´´
Dimensionless temperature, θ
(T*)´ and (T*)´´
Dimensionless height, z*

(a)

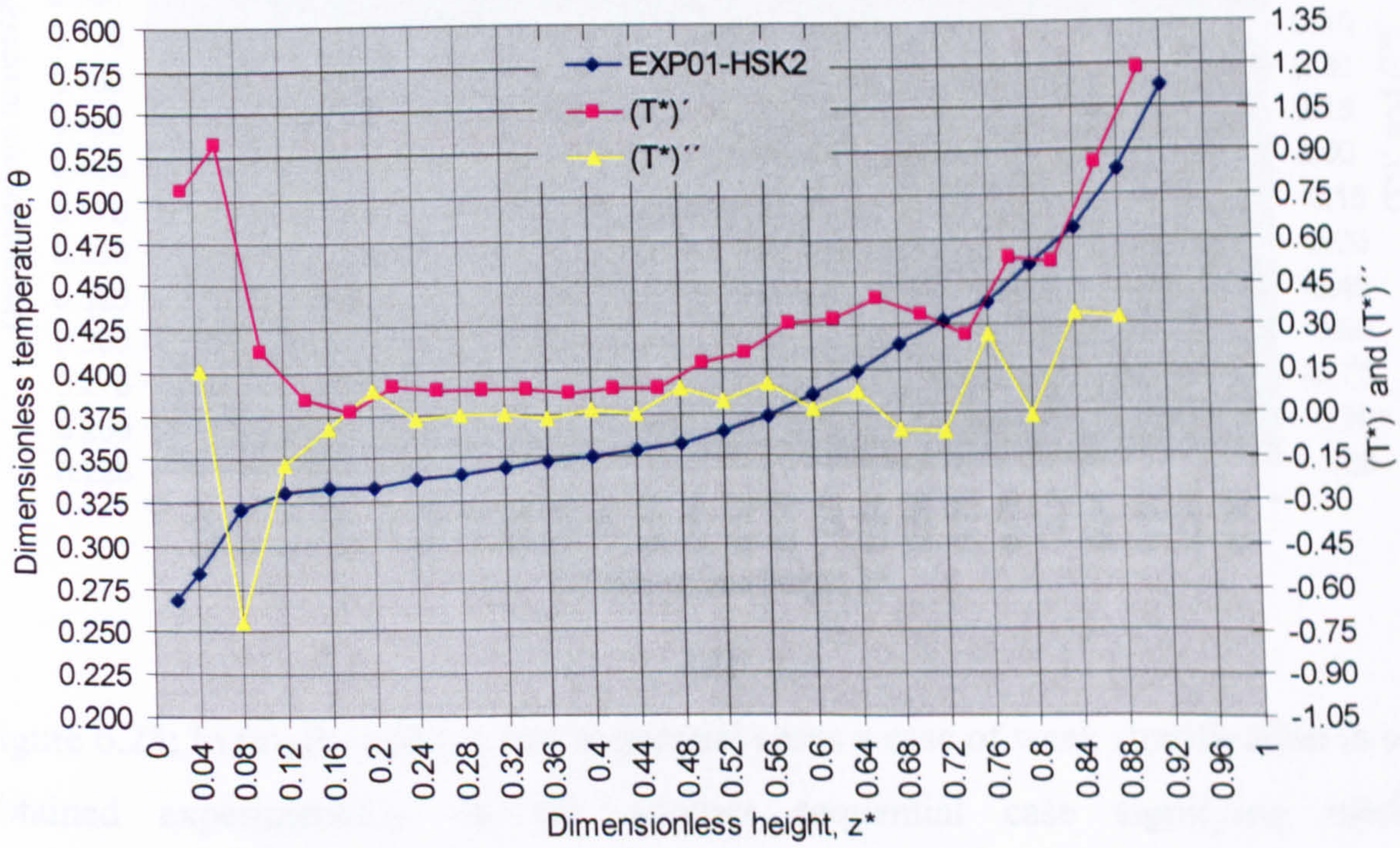
EXP01-HSK2
(T*)´
(T*)´´
Dimensionless temperature, θ
(T*)´ and (T*)´´
Dimensionless height, z*

(b)

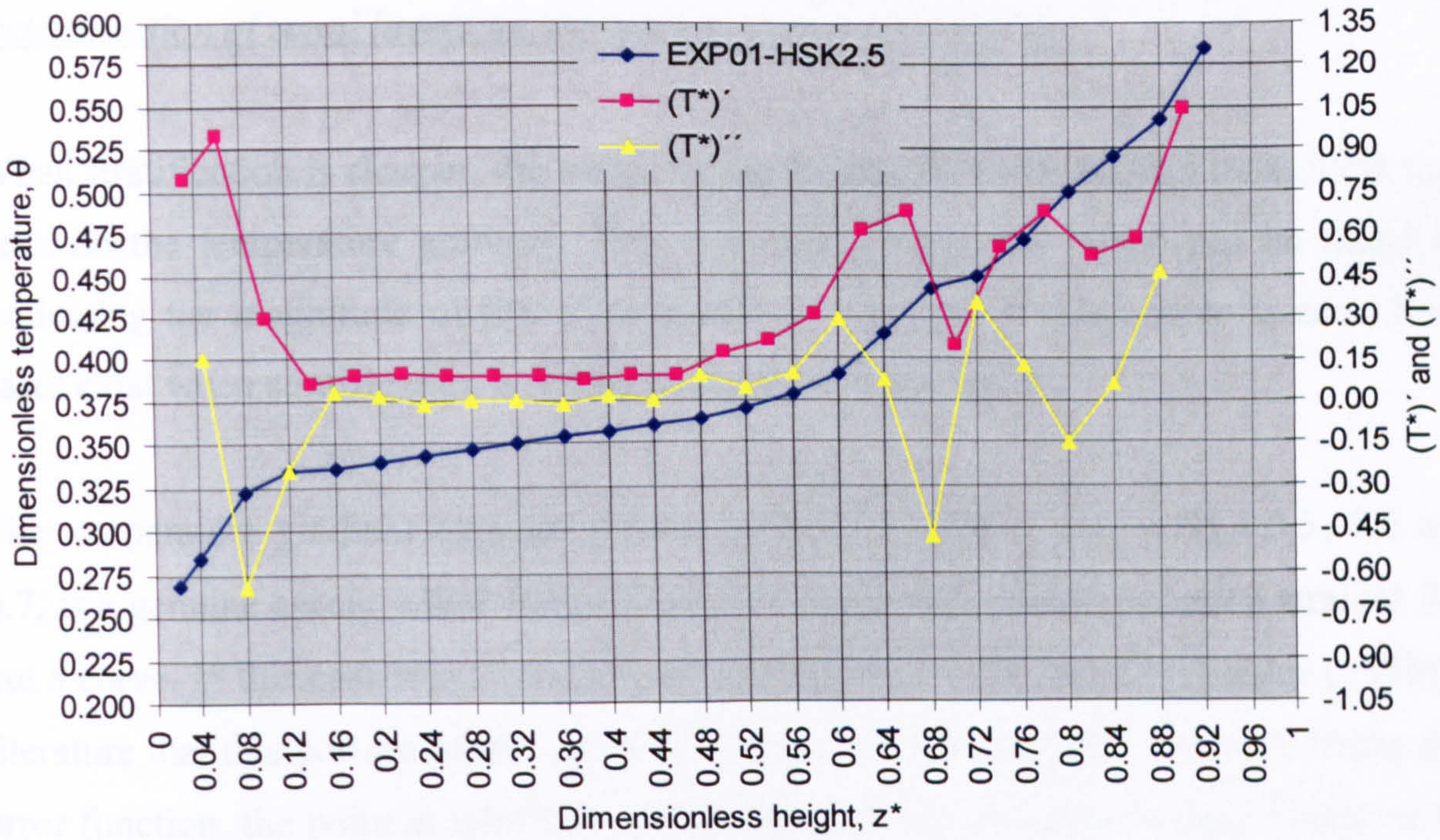

(c)

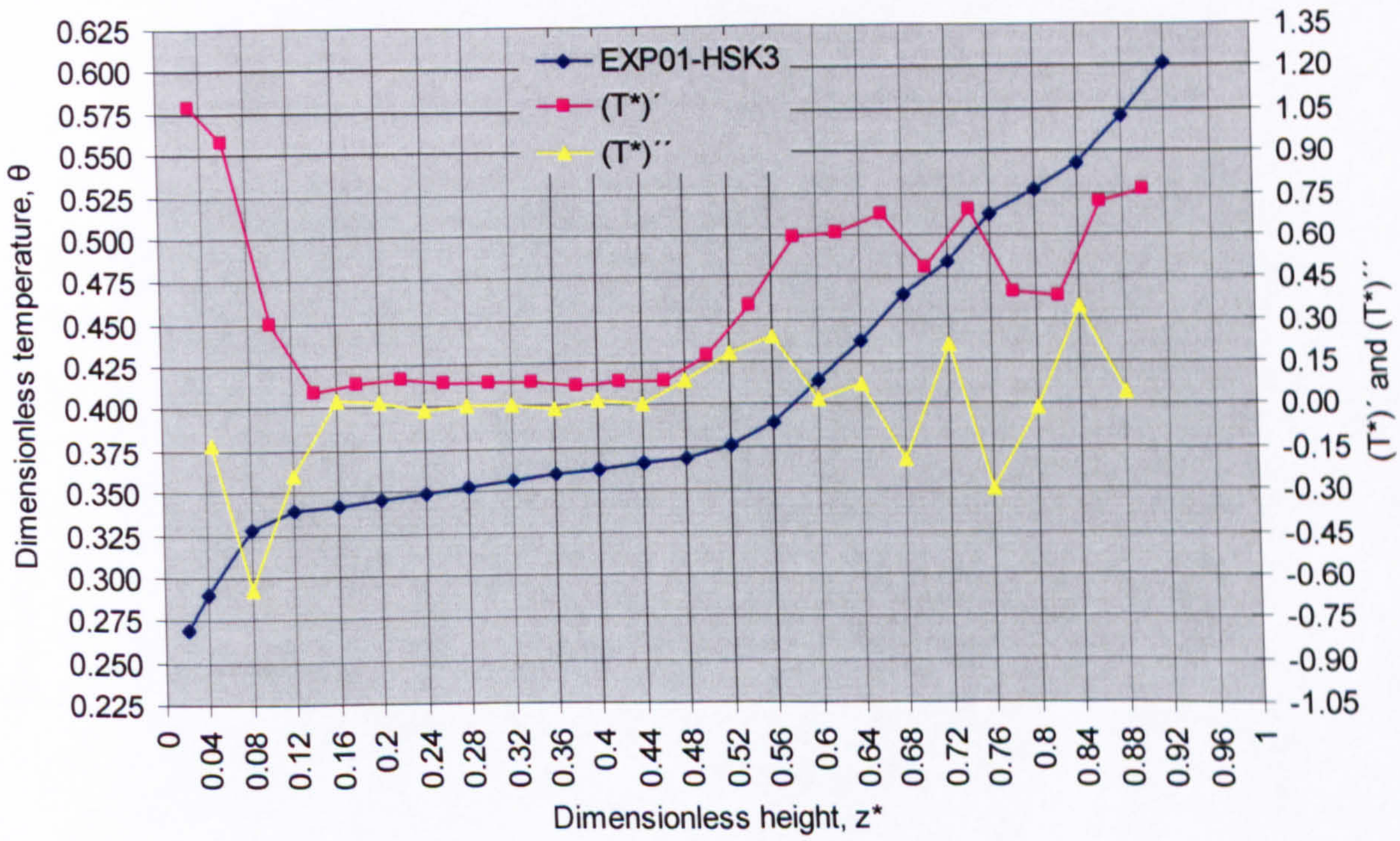

(d)

Figure 6.23: In (a), (b) and (c), two sequential cases a case of weak stratification in set-2 obtained experimentally. In (d), another sequential case signifying medium stratification.

Determination of zonal layers for the high Re cases of this work

When stratification is sharper, the height of the interface can be defined by a single high peak on the temperature gradient. This is a maximum point which can be found by evaluating the magnitude of the 1st derivative, where the 2nd derivative is zero. Such cases exist when stratification is strong as shown in Figure 6.24.

The temperature gradient between three consecutive heights, i.e., $z/H = 0.5$, 0.6 and 0.7, is a genuine ascent which means that the temperature gradient is not a straight line but a curve. In this case it is a concave curve. It has been suggested by Linden (1980) in literature that this portion of the curve follows an error distribution function. Using this error function, the point at which the slope changes that signifies the upper limit of the cool air zone is at $z/H = 0.565$. This yields a vertical thickness of 0.25 m or $z/H = 0.1$.

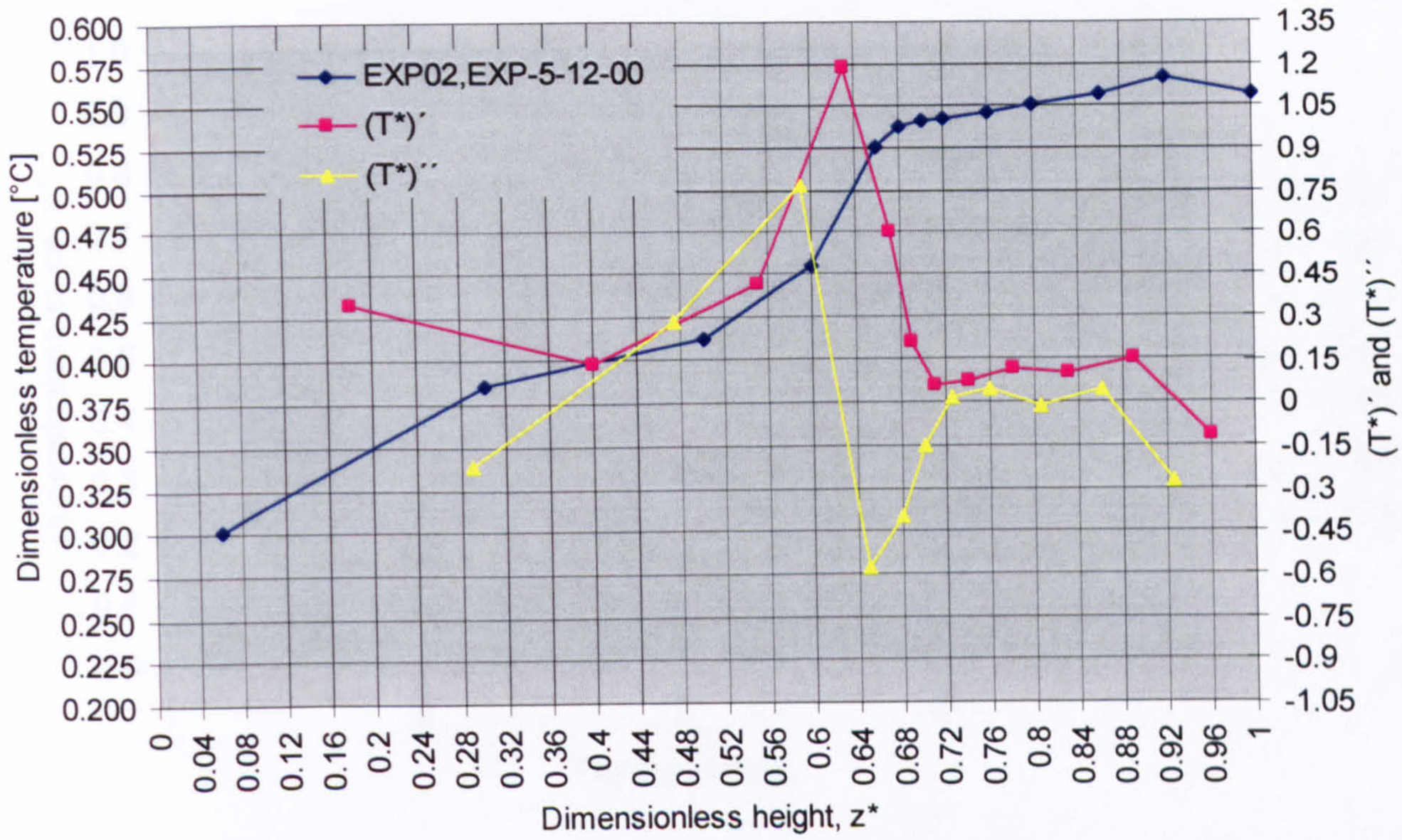

(a)

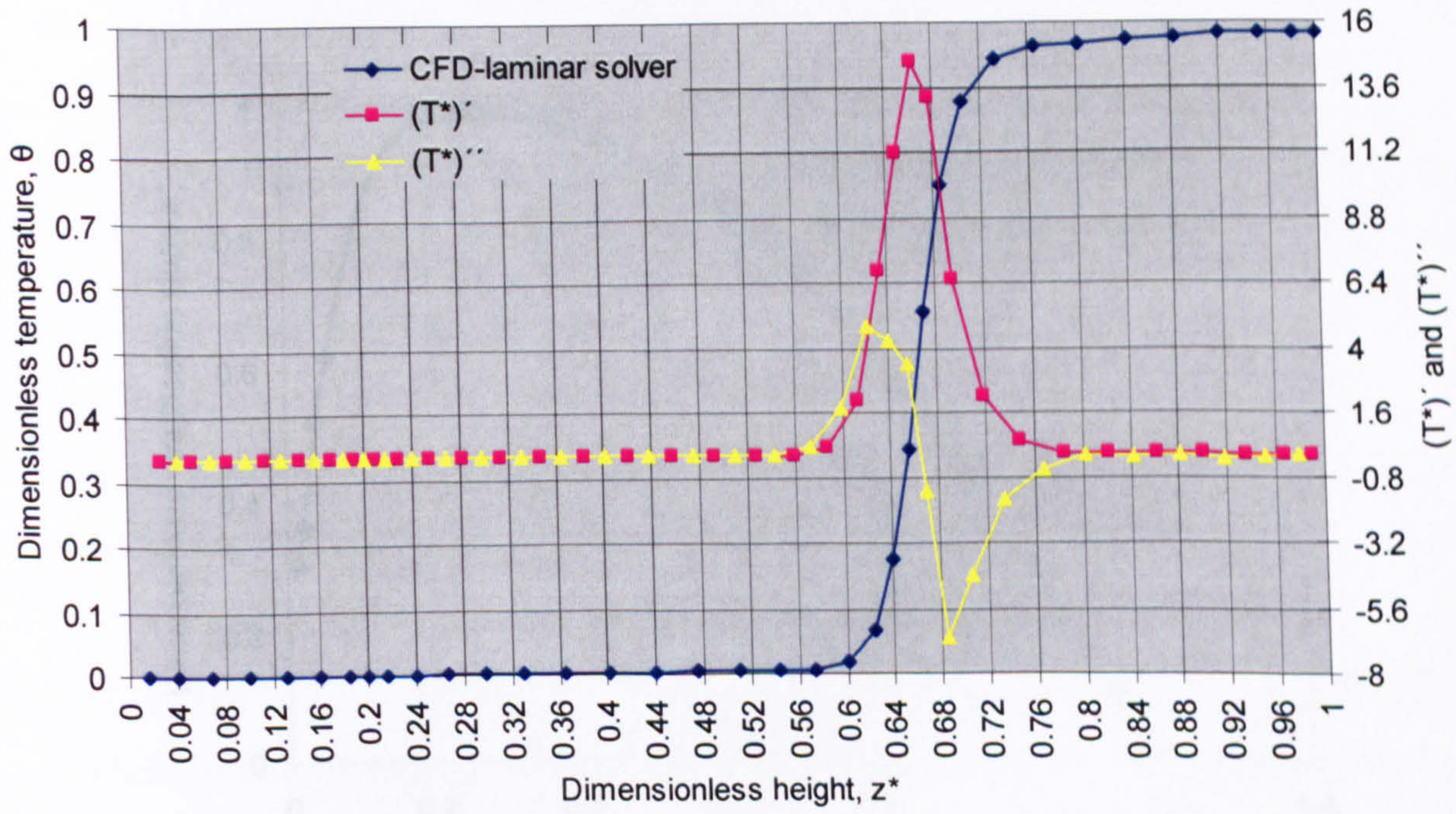

(b)

Figure 6.24: In (a), a case of strong stratification obtained experimentally. In (b), a test case of strong stratification with the laminar solver, by CFD. This case does not include radiation heat looses and turbulence effects.

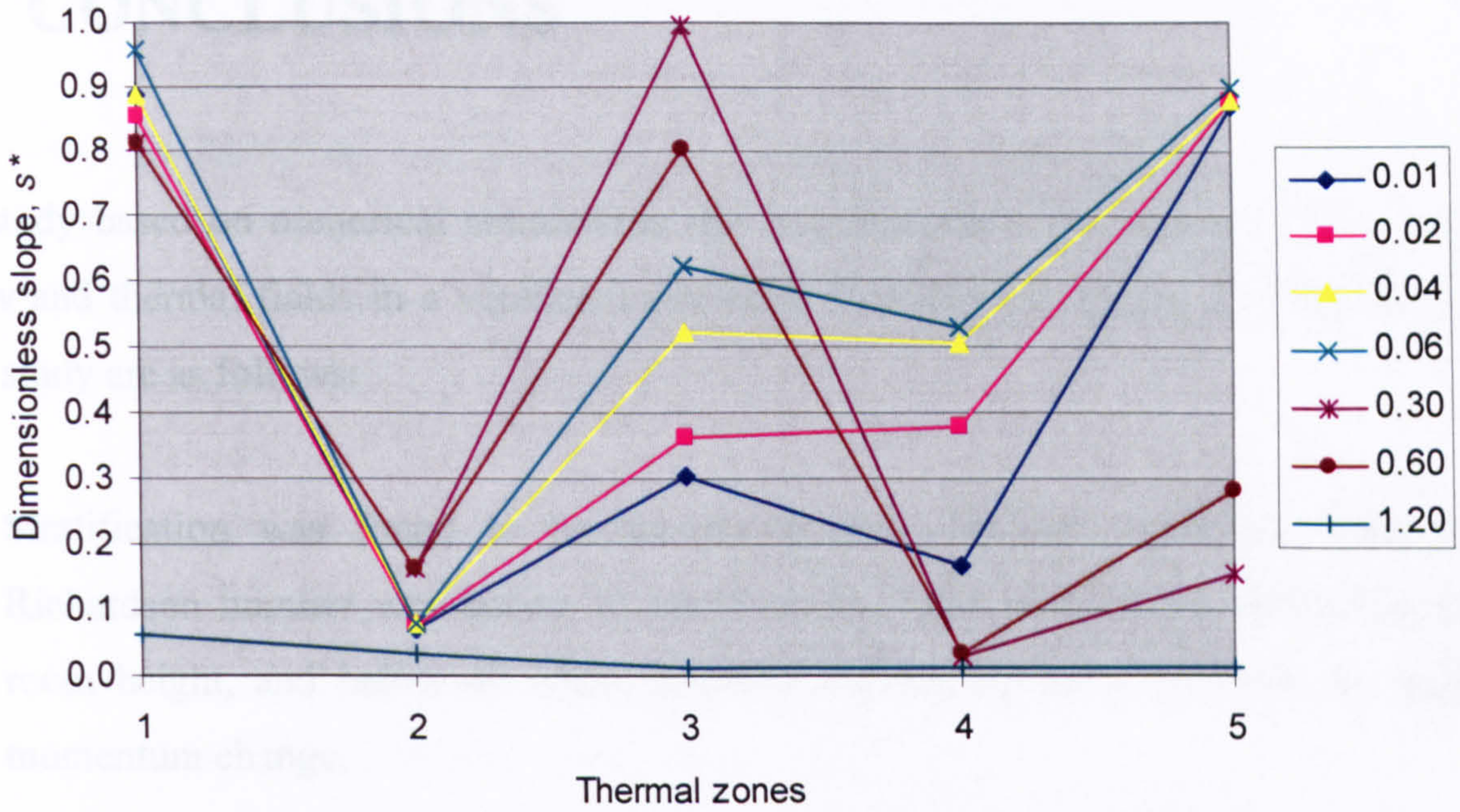

Figure 6.25: Dimensionless slope in the main air zones and local zones of convective currents with increasing momentum to buoyancy ratio, r_S.

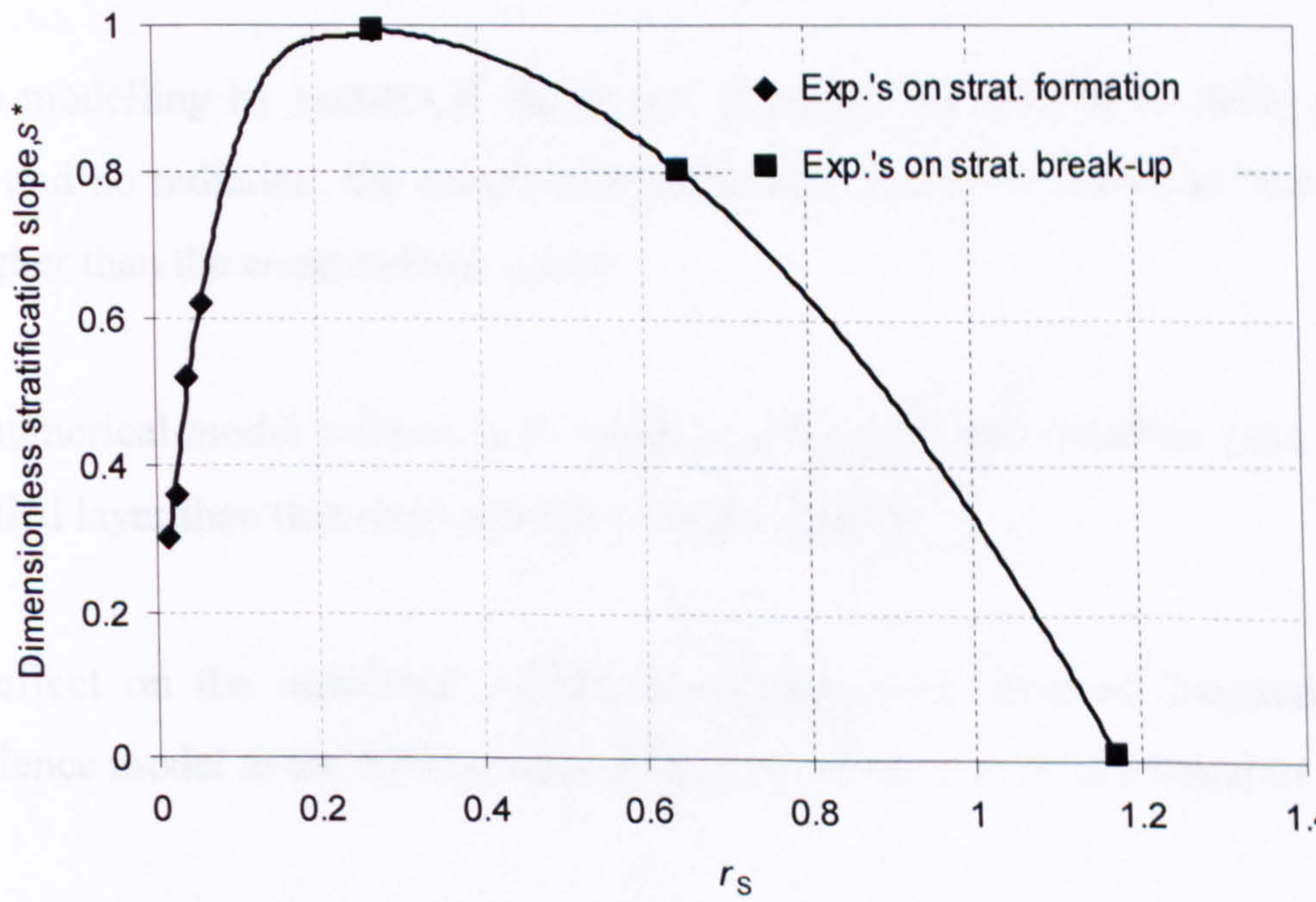

Figure 6.26: Dimensionless stratification slope in the interface.

7. CONCLUSIONS

A study based on numerical simulations and experimental measurements of the fluid flow and thermal fields in a ventilated enclosure has been conducted. The findings of the study are as follows:

- Stratification was found to be present in the ventilated enclosure when the Richardson number was below 10 based on the inlet temperature difference and room height, and below 40 when based on the hot air layer thickness for equal momentum change.

- When modelling by numerical means the experimental conditions using adiabatic walls and no radiation, the location of the stratified layer was found to be lower than the experimental values.

- When modelling by numerical means the experimental conditions using adiabatic walls and no radiation, the maximum temperature in the hot air zone was found to be higher than the experimental values.

- The numerical model without heat transfer on the wall and radiation gave a thinner stratified layer than that observed from measurements.

- The effect on the numerical results of changing the standard 2-equation $k - \varepsilon$ turbulence model to the RNG model or the Chen-Kim model was found to be small.

- The effect on the numerical results when including the buoyancy effect on the turbulence model was found to overestimate stratification.

- The effect of altering the exhaust height was to move the interface height. The change in the interface height was in proportion to the exhaust height.

- The effect of inlet velocity for constant flow rate was to increase large scale mixing in the hot air zone. This gives a more diffused interface and greater mixing within the enclosure.

- When the numerical results include air leakage and heat transfer modelling, the numerical results give an interface height in agreement with experimental results. However, the maximum and minimum temperatures from the numerical study are not in agreement with experimental values.

- When the numerical results include both air leakage modelling and radiation modelling, the numerical results are in agreement with experimental values both in terms of interface height and maximum and minimum temperatures across the room height within experimental accuracy.

- Best practice for numerical modelling of ventilated enclosures should consequently include both radiation and air leakage modelling.

- Estimates of air leakage area are given in Liddament (1996a) and BSRIA (1998). In addition to air leakage, the heat transfer coefficients can be obtained according to CIBSE (1988) Guide A and ASHRAE (1993), (2001) or any latest versions of standards, as well as by direct measurements for known cracks.

8. Recommendations for Further Work

The field of ventilation with interaction of thermal stratification offers a potential area of investigation. This study has mainly dealt with steady-state flow conditions, while in reality the room environment is affected by unsteady flows, also associated with solar light and weather. However, both laboratory and CFD studies were in good correlation.

However, more work can be undertaken to quantify more accurately the heat conduction rates in real buildings that can be retrofitted in CFD modelling. More control is required over the environmental conditions to make more accurate validations for smaller values of heat losses as the *U*-values become smaller. More accurate equipment is also required to describe certain ranges of temperatures and velocities pertinent to a wider variety of interior climatic conditions with minimum calibration.

Although excluding the buoyancy effects from the turbulence model may not have a significant effect on the calculated steady-state flow, the effect is present. Further investigation may shed more light to the range of Re numbers that buoyancy effects need to be taken more correctly into consideration such as introducing C_{k3} in the k-equation. A combination of a Low-Re modification and a buoyancy extension may also be a step closer to achieving a better match with experimental results.

The effect of additional boundary conditions for humidity and contaminant concentrations can increase the understanding of the room environment. Thermal stratification is influenced by the resulting density differences from the thermal radiation and conduction of contaminant particles.

Air diffusers may disturb the air flow patterns that can raise additional complications with thermal stratification. Adding more details in a CFD simulation requires a higher mesh resolution that can be done more accurately using a more powerful computer.

It is hoped that some of the ideas expressed throughout this thesis will stimulate an interest in exploring further this phenomenon.

References

Abramovich, G.N. (1963). The theory of turbulent jets. MIT press USA, pp.671.

Agonafer, D., Gan-Li, L., Spalding, D.B. (1996). The LVEL turbulence model for conjugate heat transfer at low Reynolds numbers. *In* PHOENICS Encyclopaedia, published in Proc. of the 1996 ASME Int. Mechanical Engineering Congress and Exposition, **18**:23-26.

Airflow (2001). "LCA 6000 Anemometer – Velocity range, Personal communication.

Albertson, M.L., Dai, U.B., A., J.R., Rouse, H. (1948). Diffusion of Submerged Jets. paper No. 2409, ASCE Proceedings **74**(10): 639-697.

Alizadeh, S. (1999). "An experimental and numerical study of thermal stratification in a horizontal cylindrical solar storage tank." Solar Energy **66**(6): 409-421.

Allen, C.J. (1979). "Stratification by design." ASHRAE J. **21**(4): 32-34.

Anderson, J.D. (1995). Computational fluid dynamics : the basics with applications. Mechanical Engineering Series. McGraw-Hill International Editions, pp.672.

ASHRAE (1993). Ashrae handbook : fundamentals. American Society of Heating Ventilating and Air-Conditioning Engineers, Inc., SI, Atlanta Georgia USA.

ASHRAE (1996). Ashrae handbook : systems and equipment. American Society of Heating Ventilating and Air-Conditioning Engineers, Inc., SI, Atlanta Georgia USA.

ASHRAE (2001). Ashrae handbook : fundamentals. American Society of Heating Ventilating and Air-Conditioning Engineers, Inc., SI, Atlanta Georgia USA.

ASMT (1993). Manual on the use of thermocouples in temperature measurement. ASTM manual series, MNL 12. Philadelphia, PA, pp.290.

Awbi, H.B. (1995). Ventilation of Buildings. E & FN Spon, An Imprint of Routledge, pp.313.

Awbi, H.B. (1998). "Calculation of convective heat transfer coefficients of room surfaces for natural convection." Energy and Buildings **28**(2): 219-227.

Bagheri, H.M. and Gorton, R.L. (1987). "Verification of stratified air-conditioning design." ASHRAE Trans. **93**(2): 211-227.

Baines, W.D. (1983). "A technique for direct measurement of volume flux of a plume." J. Fluid Mech. **132**: 247-256.

Batchelor, G.K. (1953). The theory of homogeneous turbulence. Cambridge University Press, New York, pp.197.

Baturin, V.V. (1972). Fundamentals of industrial ventilation. International Series of Monographs in Heating, Ventilation and Refrigeration. Pergamon Press, 3rd, pp.486.

Beltaos, S. (1976). "Oblique impingement of circular turbulent jets." Journal of Hydraulic Research **14**(1): 17-36.

Biggs, M.C.B. (2000). Iterative solutions of system of linear equations. Lecture notes. Dept. Math. Phys. Hatfield, Univ. of Hertfordshire, UK, pp.31.

Børresen, B.A. (2001). "Turbulence model used in industrial ventilation and tunnel ventilation, Personal communication, Technoconsult.

Bradshaw, P. (1969). "The analogy between streamline curvature and buoyancy in turbulent shear flows." J. Fluid Mech. **36**(1): 177-191.

BRE (1996). Indoor air quality in homes: Part 1 - The Building Research Establishment Indoor Environment Study. Report CI/SfB 81 (H6) (L2), Berry, R.W., Brown V.M. *et al.* (Eds.), Garston, Watford, pp.118.

Brundrett, G. (1997). "Building pressure." Building Services Journal. September Issue: 24-25.

Bruun, H.H. (1995). Hot-Wire Anemometry—Principles and Signal Analysis. Oxford University Press, pp.507.

BS EN ISO 5167-1 (1997). Measurement of fluid flow by means of pressure differential devices – Part 1: Orifice plates, nozzles and Venturi tubes inserted in circular cross-section conduits running full, British Standards Institution, London.

BS EN ISO 7730 (1995). Moderate thermal environments – Determination of PPD indices and specification of the conditions for thermal comfort, British Standards Institution, London.

BSRIA (1998). Air tightness specifications. Report 10/98, The Building Services Research and Information Association, Brackel, Berkshire, pp.8.

Cardoso, S.S.S. and Woods, A.W. (1993). "Mixing by a turbulent plume in a confined stratified region." J. Fluid Mech. **250**: 277-305.

Cehlin, M. and Moshfegh, B. (2002). Numerical and experimental investigations of air flow and temperature patterns of a low velocity diffuser. Proceedings of the 9th International Conference on the Air Quality and Climate, Indoor Air 2002, Monterey, USA **3**: 765-770.

Celik, B.I., Umbel, M.R., Wilson, W.M. (1999). Computations of turbulent mixing at the interface of a density stratified, shear layer. Proc. of the 3rd ASME/JSME Joint Fluids Engineering Conference, San Francisco, California.

Chandrasekhar, S. (1961). Hydrodynamic and hydromagnetic stability. International Series of Monographs on Physics. Clarendon Press, Oxford, England, pp.654.

Chen, C.J. and Rodi, W. (1980). Vertical Buoyant Jets - A review of experimental data.

Chen, Q. (1995). "Comparison of different k - e models for indoor air flow computations." Numerical Heat Transfer Part B **28**: 353-369.

Chen, Q. (1996). "Prediction of room air motion by Reynolds-stress models." Building and Environment **31**(3): 233-244.

Chen, Q.Y. and Chao, N.-T. (1997). "Comparing turbulence models for buoyant plume and displacement ventilation simulation." Indoor Built Environment **6**(3): 140-149.

Chen, Y.S. and Kim, S.W. (1987). Computation of turbulent flows using an extended k - e turbulence closure model, NASA.

Cheng, M., Liu, G.R., Lam, K.Y., Cai, W.J., Lee, E.L. (1999). "Approaches for improving airflow uniformity in unidirectional flow cleanrooms." Building and Environment **34**(3): 275-284.

Chow, W.K. and Leung, W.M. (1989). "Fire induced convective flow inside an enclosure before flashover: Numerical experiments." Building Serv. Eng. Res. Technol. **10**(2): 51-59.

CIBS (1976). Guide C3: Heat transfer, The Chartered Institute of Building Services, London, pp.24.

CIBSE (1988). Guide A: Design data. The Chartered Institute of Building Services, 5th edition, London.

CIBSE (2000a). AM 13: Mixed mode ventilation, The Chartered Institute of Building Services Engineers, London, pp.77.

CIBSE (2000b). TM 23: Testing buildings for air leakage, The Chartered Institute of Building Services Engineers, London, pp.15.

CIBSE (2001). Guide B2: Ventilation and air conditioning. The Chartered Institute of Building Services, London, pp.160.

Ciofalo, M. (1994). Large-Eddy Simulation: A critical survey of models and applications. *In* Advances in Heat Transfer (Chapter 4). (Eds.) Hartnett, J.P. and Jr. Irvine, T.F., Academic Press, **25**, p.321-419.

Comte-Bellot, G. and Corrsin, S. (1966). "The use of a contraction to improve the isotropy of grid-generated turbulence." J. Fluid Mech. **25**(4): 657-682.

Cook, M.J. and Lomas, K.J. (1998). Buoyancy-driven displacement ventilation flows: evaluation of two eddy viscosity turbulence models for prediction. Proc. CIBSE A: Building Serv. Eng. Res. Technol. **19(1)**: 15-21.

Cooper, P. and Linden, P.F. (1996). "Natural ventilation of an enclosure containing two buoyancy sources." J. Fluid Mech. **311**: 153-176.

Cotel, A.J., Gjestvang, J.A., Ramkhelawan, N.N., Breidenthal, R.E. (1997). "Laboratory experiments of a jet impinging on a stratified interface." Experiments in Fluids **23**: 155-160.

Crawford, T.V. and Leonard, A.S. (1962). "Observations of buoyant plumes in calm stably stratified air." J. Appl. Meteorol. **1**(2): 251-256.

Dagestad, S. (1991). Numerical simulation of stratified flows with different k - e turbulence models. PhD thesis. Dept. of Farming, Ventilation and Sanitation. Trondheim Norway, University of Trondheim, pp.196.

Dagestad, S. and Holdø, A.E. (1991). "Natural ventilation in offshore modules of rectangular shape." Trans. IMarE **103**.

Dai, Z., Tseng, L.K., Faeth, G.M. (1995). "Velocity statistics of round, fully developed, buoyant turbulent plumes." J. Heat Transfer **117**: 138-145.

Daly, B.J. and Harlow, F.H. (1970). "Transport equations of turbulence." Physics of Fluids **13**: 2634-2649.

Davidson, L. (2004). Turbulence : An introduction for scientists and engineers. Oxford University Press, New York, pp.657.

De Silva, I.P.D., Brandt, A., Montenegro, L.J. (1999). "Gradient Richardson number measurements in a stratified shear layer." Dyn. Atmos. Oceans **30**(1): 47-63.

De With, G. (2001). Dynamic grid adaptation applied to large eddy simulation turbulence modelling. PhD thesis. ACME Dept., Univ. of Hertfordshire, pp.123.

Djunaedy, E. and Cheong, K.W.D. (2002). "Development of a simplified technique of modelling four-way ceiling air diffuser." Building and Environment **37**(4): 393-403.

Dyer, K.R. (2000). Estuaries : a physical introduction. John Wiley, 2nd edition, Chichester, pp.195.

Ellison, T.H. (1957). "Turbulent transport of heat and momentum from infinite rough plane." J. Fluid Mech. **2**(5): 456-466.

Ellison, T.H. and Turner, J.S. (1959). "Turbulent entrainment in stratified flows." J. Fluid Mech. **6**(3): 423-448.

Fanger, P.O., Melikov, A.K., Hanzawa, H., Ring, J. (1988). "Air turbulence and sensation of draft." Energy and Buildings **12**: 21-39.

Fanger, P.O., Melikov, A.K., Hanzawa, H., Ring, J. (1989). "Turbulence and draft : The turbulence of airflow has a significant impact on the sensation of draft." ASHRAE J. **31**(4): 18-25.

Fernando, H.J.S. (1991). "Turbulent mixing in stratified fluid." Annu. Rev. Fluid Mech. **23**: 455-493.

Fernando, H.J.S. and Hunt, J.C.R. (1996). "Some aspects of turbulence and mixing in stably stratified layers." Dyn. Atmos. Oceans **23**(1-4): 35-62.

Fischer, H.B., List, E.J., Koh, R.C.Y., Imberger, J., Brooks, N.H. (1979). Mixing in inland and coastal waters. Academic Press, Inc. (London) Ltd., pp.483.

Folkard, A.M., Davies, P.A., Fernando, H.J.S. (1997). "Measurements in a turbulent patch in a rotating, linearly-stratified fluid." Dyn. Atmos. Oceans **26**(1): 27-51.

Fontaine, J.R., Biolley, F., Rapp, R., Sérieys, J.C., Cunin, J.C. (1994). "Analysis of three-dimensional ventilation flow: Experimental validation on a water scale model of numerical simulations." Numerical Heat Transfer, Part A **26**: 431-451.

Fontaine, J.R., Rapp, R., Koskela, H., Niemelä, R. (2001). Evaluation of air diffuser flow modelling methods - Experiments and CFD, Institut National de Recherche et de Sécurité, Vandoeuvre-les-Nancy, France.

Fornoff, M. (1978). Expementelle und theoretische Untersuchung von Drallstrahlen. Diplomarbeit. University of Karlsruhe.

Gan, G. (1995). "Evaluation of room air distribution systems using computational fluid dynamics." Energy and Buildings **23**(2): 83-93.

Gan, G. and Awbi, H.B. (1994). "Numerical simulation of indoor environment." Building and Environment **29**(4): 449-459.

Gerz, T., Schumann, U., Elghobashi, S.E. (1989). "Direct numerical simulation of stratified homogeneous turbulent shear flows." J. Fluid Mech. **200**: 563-594.

Gibson, C.H. (1981). Fossil turbulence and internal waves. AIP Conf. Proc., American Institute of Physics, New York **76**: 159-179.

Gibson, C.H. (1987). "Fossil turbulence and intermittency in sampling oceanic mixing processes." J. Geophys. Res. **92**(C5): 5383-5404.

Gibson, M.M. (2005). "Turbulence modelling, http://iehmtu.edata-center.com/toc/chapt_t/ch20s192.html. Available [Accessed: 27-6-2006].

Gibson, M.M. and Younis, B.A. (1986). "Calculation of swirling jets by a Reynolds stress closure." Physics of Fluids **29**: 38-48.

Gilberts (1999). "Series DG louvred face ceiling diffusers, http://www.gilbertsblackpool.com/UserFiles/File/diffusers/SERIESDG.pdf. Available [Access: 22-4-2001].

Goodfellow, H. and Tähti, E., (Ed.) (2001). Industrial ventilation design guidebook. Academic Press, San Diego, pp.1519.

Goussebaile, J. and Viollet, P.L. (1982). On the modelling of turbulent flows under strong buoyancy effects in cavities with curved boundaries. Proceeding of the international symposium on refined modelling of flows, Presses Pont et Chaussees, Paris: 165-174.

Grimitlyn, M.I. (1993). "Fundamentals in optimising air distribution in ventilated spaces." ASHRAE Tans. **99**(1): 1128-1138.

Halton (1998). "Quarter-circular low velocity displacement diffuser, http://www.halton.fi/catalog/pdf/en/low_velocity_devices/afq_en.pdf. Available [Access: 23-4-2001].

Hart, W.E. (1961). Jet discharge into a fluid with density gradient. Proc. ASCE Hydr. Div. **87**(HY6): 191-200.

Heiselberg, P. (Ed.) (2002). Principles of Hybrid Ventilation. IEA-ECBS Annex 35 Final Report, Hybrid Ventilation Centre, Aalborg University, Denmark, pp.73.

Heiselberg, P., Murakami, S., Roulet, C.-A. (Eds.). (1998). Ventilation of large spaces in buildings: analysis and prediction techniques. Subtask-2 summary report, IEA Annex 26, Aalborg University, Denmark, Indoor Environmental Engineering, pp.324.

Heiselberg, P., Svidt, K., Nielsen, P.V. (2001). "Characteristics of airflow from open windows." Building and Environment **36**(7): 859-869.

Hinkley, P.L. (1988). "Comparison of an established method of calculation of smoke filling of large scale spaces with recent experiments." Fire Science & Technology **8**(1): 1-8.

Hinze, J.O. (1975). Turbulence. McGraw-Hill, 2nd edition, New York, pp.790.

HMSO (2000). The Building Regulations: Conservation of Fuel and Power – Part L, Department of the Environment and The Welsh Office.

Hopfinger, E.J. (1987). "Turbulence in stratified fluids: A review." J. Geophys. Res. **92**(C5): 5287-5303.

Hossain, M.S. (1980). Mathematische Modellierung von turbulenten Auftriebsströmungen. PhD thesis. University of Karlsruhe.

Hunt, G.R. and Linden, P.F. (1999). "The fluid mechanics of natural ventilation—displacement ventilation by buoyancy-driven flows assisted by wind." Building and Environment **34**: 707-720.

Imberger, J., Thomson, R., Fandry, C. (1976). "Selective withdrawal from a finite rectangular tank." J. Fluid Mech. **78**(3): 487-512.

Imboden, D.M. (2004). Mixing of lake waters. *In* The lakes handbook: Limnology and limnetic ecology. (Eds.) O'Sullivan, P.E. and Reynolds, C.S., Oxford, Blackwell Science, **1**(2), p.115-196.

Int-Hout, D. and Kloostra, L. (1999). "Practical Guide to Museums and Historic Renovation - Air Distribution for Large Spaces." ASHRAE J. **41**(4): 57-64.

Jaakkola, J.J.K., Reinikainen, L.M., Heinonen, O.P., Majanen, A., Seppänen, O. (1991). "Indoor air quality requirements for healthy office buildings: recommendations based on an epidemiologic study." Environmental International **17**: 371-378.

Jackman, P.J. (1991). Displacement ventilation. CIBSE National Conference, University of Kent, Canterbury.

Jensen, L. (1986). "Determination of leakages in the building envelope using pressurization test measurements." AIR 7(4): 6-8.

Jones, B.E. and Whittle, G.E. (1992). "Computational fluid dynamics for building air flow prediction – Current status and capabilities." Building and Environment **27**(3): 321-338.

Koestel, A., Hermann, P., Tuve, G.L. (1950). "Report No.1404: Comparative study of ventilating jets from various types of outlets." ASHVE Transactions **56**: 459.

Kolmogorov, A.N. (1962). "A refinement of previous hypotheses concerning the local structure of turbulence in a viscous incompressible fluid at high Reynolds number." J. Fluid Mech. **13**(1): 82-85.

Komori, S., Ueda, H., Ogino, F., Mizushina, T. (1983). "Turbulence structure in stably stratified open-channel flow." J. Fluid Mech. **130**: 13-26.

Labfacility Ltd. (1996). Labfacility temperature handbook : A practical guide to temperature measurement and calibration using thermocouples and resistance thermometers. Labfacility Ltd., Middlesex UK, pp.126.

Lam, C.K.G. and Bremhorst, K. (1981). "A modified form of the k - e model for predicting wall turbulence." Issue of Journal of Fluids Engineering, Trans. ASME **103**: 456.

Lam, C.-Y. (1994). Applied numerical methods for partial differential equations : An introduction with spreadsheet programs. Prentice Hall South East Asia, Singapore, pp.262.

Larson, M. and Jönsson, L. (1996). "Efficiency of mixing by a turbulent jet in a stably stratified fluid." Dyn. Atmos. Oceans **24**(1-4): 63-74.

Lauder, B.E. (1975). "On the effects of a gravitational field on the turbulent transport of heat and momentum." J. Fluid Mech. **67**(3): 569-581.

Launder, B.E. (1976). Heat and mass transport. *In* Turbulence. (Ed.) Bradshaw, P., Springer, **12**, p.232-287.

Launder, B.E., Reece, G.J., Rodi, W. (1975). "Progress in the development of a Reynolds-stress turbulence closure." J. Fluid Mech. **68**(1): 537-566.

Launder, B.E. and Spalding, D.B. (1974). "The numerical computation of turbulent flows." Comp. Meth. in Appl. Mech. & Eng. **3**: 269-289.

Lecompte, J.G.N. (1990). Influence of natural convection in an insulated cavity on the thermal performance of a wall. Insulation Materials, testing, and Applications, ASTM STP 1030, American Society for Testing Materials, Philadelphia: 397-420.

Lee, H. and Awbi, H.B. (2004). "Effect of internal partitioning on indoor air quality of rooms with mixing ventilation – basic study." Building and Environment **39**(2): 127-141.

Lemaire, A.D. (Ed.) (1993). Air flow patterns within buildings, Evaluation of computational methods. Subtask-1 summary report, IEA Annex 20, TNO Building and Construction Research, Delft, Netherlands, pp.82.

Leonard, B.P. (1979). "A stable and accurate convective modelling procedure based on quadratic upstream interpolation." Comp. Methods Appl. Mech. Eng. **48**: 1-24.

Li, Y., Fuchs, L., Sandberg, M. (1993a). "Numerical prediction of airflow and heat-radiation interaction in a room with displacement ventilation." Energy and Buildings **20**: 27-43.

Li, Y., Sandberg, M., Laszlo, F. (1993b). "Effects of thermal radiation on airflow with displacement ventilation: an experimental investigation." Energy and Buildings **19**(4): 263-374.

Liddament, M.W. (Ed.) (1996a). A guide to energy efficient ventilation, Air Infiltration and Ventilation Centre, Coventry, pp.254.

Liddament, M.W. (1996b). "Two air flow studies completed." AIR **17**(4): 10-14.

Liddament, M.W. (Ed.) (1998). TSR 04: Energy-efficient ventilation of large enclosures. Technical synthesis report, IEA Annex 26, Coventry, UK, pp.35.

Linden, P.F. (1973). "The interaction of a vortex ring with a sharp density interface: a model for turbulent entrainment." J. Fluid Mech. **60**(3): 467-480.

Linden, P.F. (1979). "Mixing in stratified fluids." Geophys. & Astrophys. Fluid Dyn. **13**(3).

Linden, P.F. (1980). "Mixing across a density interface produced by grid turbulence." J. Fluid Mech. **100**(4): 691-703.

Linden, P.F. and Cooper, P. (1996). "Multiple sources of buoyancy in a naturally ventilated enclosure." J. Fluid Mech. **311**: 177-192.

Linden, P.F., Lane-Serff, G.F., Smeed, D.A. (1990). "Emptying filling boxes: the fluid mechanics of natural ventilation." J. Fluid Mech. **212**: 309-335.

Linke, W. (1962). "Ventilation from above or below?" Kältetechnik **14**(5): 142-149.

Malin, M.R. and Younis, B.A. (1990). "Calculation of turbulent buoyant plumes with a Reynolds stress and heat flux transport closure." Int. J. Heat Mass Transfer **33**(10): 2247-2264.

Malmström, T.G., Kirkpatrick, A.T., Christensen, B., Knappmiller, K.D. (1997). "Centreline velocity decay measurements in low-velocity axisymmetric jets." J. Fluid Mech. **246**: 363-377.

Markatos, N.C., Malin, M.R., Cox, G. (1982). "Mathematical modelling of buoyancy induced smoke flow in enclosures." International Journal of Mass Transfer **25**: 63-75.

Mellor, G.L. and Strub, P.T. (1980). "Similarity solutions for the stratified turbulent Rayleigh problem." J. Phys. Oceanogr. **10**(3): 455-460.

Mohammadi, B. and Pironneau, O. (1994). Analysis of the k-epsilon turbulence model. Research in Applied Mathematics. John Wiley and Sons, Paris, pp.194.

Monin, A.S. and Yaglom, A.M. (1975). Statistical Hydrodynamics. Vol. 2. MIT Press, Cambridge, Massachusetts.

Morton, B.R. (1959). "Forced plumes." J. Fluid Mech. **5**(1): 151-163.

Moum, J.N. and Smyth, W.D. (2000). Upper ocean mixing. *In* Encyclopedia of Ocean Sciences, Academic Press.

Mundt, E. (1995a). "Displacement ventilation systems—convection flows and temperature gradients." Building and Environment **30**(1): 129-133.

Mundt, E. (1995b). The performance of displacement ventilation systems—experimental and theoretical studies. PhD thesis. Dept. of Building Services. Stockholm Sweden, University of Stockholm, pp.155.

Murakami, S. and Kato, S. (1989). "Numerical and Experimental Study on Room Airflow -- 3-D Predictions using the k - e Turbulence Model." Building and Environment **24**(1): 85-97.

Murakami, S., Kato, S., Suyama, Y. (1997). Three-dimensional numerical simulation of turbulent airflow in a ventilated room by means of a two-equation model. ASHRAE Trans. **97**: 621-642.

Nelson, J.E.B., Balakrishnan, A.R., Murthy, S.S. (1999). "Experiments on stratified chilled-water tanks." Int. J. Refrigeration **22**(3): 216-234.

Nevins, R.G. (1976). Air diffusion dynamics – Theory, Design and Application. Business News Publishing, Birmingham, MI.

Nielsen, P.V. (1974). Flow in air conditioned rooms. PhD thesis. Copenhagen, Technical University of Denmark.

Nielsen, P.V. (1992). "Description of supply openings in numerical models for room air distribution." ASHRAE Tans. **98**(1): 963-971.

Nielsen, P.V. (1994). Stratified flow in a room with displacement ventilation and wall-mounted air terminal devices. ASHRAE Trans.: Symposia **NO-94-16-2**: 1163-1169.

Nielsen, P.V., Restivo, A., Whitelaw, J.H. (1978). "The velocity characteristics of ventilated rooms." J. Fluid Eng. - Trans. ASME **100**(1): 291298.

Ohira, N., Kato, S., Murakami, S. (2000). CFD analysis of thermal plume and indoor airflow using k - e models with buoyancy effect. 3rd Symposium on Turbulence Heat and Mass Transfer, Nagoya Japan.

Ozmidov, R.V. (1965). "On the turbulent exchange in a stably stratified ocean." Atmos. Ocean Phys. **8**: 853-860.

Palonen, J., Majanen, A., Seppänen, O. (1991). "Performance of displacement ventilation air distribution in an office room." Environmental International **17**(4): 303-309.

Papakonstantinou, K.A., Kiranoudis, C.T., Markatos, N.C. (2000). "Numerical simulation of air flow field in single-sided ventilated buildings." Energy and Buildings **33**(1): 41-48.

Patankar, S.V. (1980). Numerical heat transfer and fluid flow. McGraw Hill, New York, pp.193.

Patankar, S.V. and Spalding, D.B. (1972). "A calculation procedure for heat, mass and momentum transfer in three-dimensional parabolic flows." Int. J. Heat Mass Transfer **15**(10): 1787-1806.

Redondo, J.M., Sanchez, M.A., Cantalapiedra, I.R. (1996). "Turbulent mechanisms in stratified fluids." Dyn. Atmos. Oceans **24**: 107-115.

Rhie, C.M. and Chow, W.L. *(1983)*. "Numerical study of the turbulent flow past an airfoil with trailing edge separation." AIAA J. **21**(11): 1527-1532.

Rodi, W. (1972). The prediction of free turbulent boundary layers by use of a two-equation model of turbulence. PhD thesis, University of London.

Rodi, W. (1975). "Note on the empirical constant in the Kolmogorov-Prandtl eddy-viscosity expression." J. Fluid Eng.-Trans. ASME **97**(3): 386-389.

Rodi, W. (1979). Influence of buoyancy and rotation on equations for the turbulent length scale. Proc. 2nd Symp. Turbulent Shear Flows, Imperial College, London: 10.37 - 10.42.

Rodi, W. (Ed.) (1980). Turbulence models and their application in hydraulics : a state-of-the-art review. Monograph Series, International Association for Hydraulic Research, Delft, The Netherlands, pp.104.

Rodi, W. (1987). "Examples of calculation methods for flow and mixing in stratified fluids." J. Geophys. Res. **92**(C5): 5305-5328.

Säämanen, A., Andersson, I.-M., Niemelä, R., Rosén, G. (1995). "Assessment of horizontal displacement flow with tracer gas pulse technique reinforced plastic plants." Building and Environment **30**(1): 135-141.

Sandberg, M. and Blomqvist, C. (1989). "Displacement ventilation in office rooms." ASHRAE Tans. **95**(2): 1041-1049.

Schumann, U. (1977). "Realizability of Reynolds-Stress turbulence models." The Physics of Fluids **20**(5): 721-725.

Seifert, J., Gritzki, R., Rösler, M., Grundmann, R. (2000). Contribution of flows through large openings. Presented at the 4th IEA-ECBCS-Annex 35 Expert Meeting, Hybrid Ventilation in New and Retrofitted Office Buildings, Athens, Greece.

Seppänen, O.A., Fisk, W.J., Mendell, M.J. (1999). "Association of ventilation rates and CO_2 concentrations with health and other responses in commercial and institutional buildings." Indoor Air **9**: 226-252.

Shabbir, A. and George, W.K. (1994). "Experiments on a round turbulent buoyant plume." J. Fluid Mech. **275**: 1-32.

Shaw, C.Y. and Brown, W.C. (1982). Effect on of a gas furnace chimney on the air leakage characteristic of a two-story detached house. 12.1 Proceedings of the 3rd IEA Conference of the Air Infiltration Centre, London.

Shih, L.H., Koseff, J.R., Ferziger, J.H., Rehmann, C.R. (2000). "Scaling and parameterization of stratified homogeneous turbulent shear flow." J. Fluid Mech. **412**: 1-20.

Shilkrot, E.O. (1993). "Determination of design loads on room heating and ventilation systems using the method of zone-by-zone balances." ASHRAE Tans. **99**(1): 987-991.

Shin, M.-S., Kim, H.-S., Jang, D.-S., Lee, S.-N., Lee, Y.-S., Yoon, H.-G. (2004). "Numerical and experimental study on the design of a stratified thermal storage system." Applied Thermal Engineering **24**(1): 17-27.

Simpson, B.A.F. and Holdø, A.E. (1998). "The Influence of Inlet Boundary Conditions on the Near Field of a Plane Turbulent Jet." J. Theoretical and Applied Fluid Mechanics.

Sivashinsky, G. and Yakhot, V. (1985). "Negative viscosity effect in large-scale flows." J. Fluids Eng. **28**(4): 1040-1042.

Skistad, H. (1994). Displacement ventilation. Control of the built environment. John Wiley & Sons Inc., pp.168.

Skistad, H. (1998). Utilizing selective withdrawal in the ventilation of large rooms: Select-vent. *Room Vent Conference*, Techno Consult, Stockholm.

Skistad, H. (2000). "Ventilation of a shipyard, Personal communication.

Spalding, D.B. (1980). A mathematical modeling of fluid dynamics, heat transfer and mass transfer processes. Report HTS/8011, Imperial College, London.

Spalding, D.B. (1981). "A general purpose computer program for multi-dimensional one and two-phase flow." Math. Comp. Simul. **23**(3): 267-276.

Spalding, D.B. (1996). IMMERSOL: Radiation Models in PHOENICS. *In* PHOENICS Encyclopaedia.

Staquet, C. (2000). "Mixing in a stably stratified shear layer: two- and three-dimensional experiments." Fluid Dynamics Research **27**(6): 367-404.

Stillinger, D.C., Helland, K.N., Van Atta, C.W. (1983). "Experiments on the transition of homogenous turbulence to internal waves in a stratified fluid." J. Fluid Mech. **131**(1): 91-122.

Svensson, U. (1978). A mathematical model of the seasonal thermocline. Rep. No. 1002. Dept. of Water Resour. Eng., Univ. of Lund, Lund, Sweden, pp.187.

Taylor, G.I. (1935). Statistical theory of turbulence. Proc. R. Soc. London A **151**(873): 421-478.

TC Ltd. (1999). Guide to thermocouple and resistance thermometry: A wealth of information on thermocouple and resistance thermometry. Issue 6.0. TC Ltd., Uxbridge UK, pp.73.

Thorpe, S.A. (1973). "Turbulence in stably stratified fluids: A review of laboratory experiments." Boundary-Layer Meteorology **5**: 95-119.

Thorpe, S.A. (1977). "Turbulence and mixing in Scottish Loch." Philos. Trans. R. Soc. London A **286**(1334): 125-181.

Turner, J.S. (1968). "The influence of molecular diffusivity on turbulent entrainment across a density interface." J. Fluid Mech. **33**: 639-656.

Turner, J.S. (1973). Buoyancy Effects in Fluids. Cambridge at the University Press, pp.367.

Van Doormal, J.P. and Raithby, G.D. (1984). "Enhancements of the SIMPLE method for predicting incompressible fluid flows." Numerical Heat Transfer **7**: 147-163.

Viollet, P.L. (1985). The modelling of turbulent recirculating flows for the purpose of reactor thermal-hydraulic analysis, Elec. de France, Chatou, France.

Viollet, P.L. (1986). On the numerical modelling of stratified flows. Symp. Physical Processes In Estuaries, Delft, the Netherlands.

Webster, C.A.G. (1964). "An experimental study of turbulence in a density-stratified shear flow." J. Fluid Mech. **19**(2): 221-245.

Werle, H. (1968). Flows with Large Velocity Fluctuations, motion picture film no. 575, ONERA, Chatillon, France.

Wildin, M. and Truman, C. (1989). "Performance of stratified vertical cylindrical thermal storage tanks, part I: Scale model tank." ASHRAE Transactions **95**(1B): 1086-1095.

Xue, H., Hihara, E., Saito, T. (1994). "Temperature stratification of heated air flow in a fire tunnel." JSME Int. J. Series B **37**(1): 187-194.

Xue, H. and Shu, C. (1999). "Mixing characteristics in a ventilated room with non-isothermal ceiling air supply." Building and Environment **34**(3): 245-251.

Yakhot, V. and Orszag, S.A. (1986). "Renormalization-Group Analysis of Turbulence." Journal of Scientific Computing **1**(1): 3-51.

Yakhot, V., Orszag, S.A., Tangam, S., Gatski, T.B., Speziale, C.G. (1992). "Development of turbulence models for shear flows by a double expansion technique." American Institute of Physics **4**(7): 1510-1521.

Yakhot, V. and Smith, L.M. (1992). "The Renormalization Group, the ε-expansion and derivation of turbulence models." Journal of Scientific Computing **7**(1): 35-61.

Yoo, J., Wildin, M.W., Truman, C.R. (1986). "Initial formation of a thermocline in stratified thermal storage tanks." ASHRAE Tans. **92**: 280-292.

Zhang, J.S., Wu, G.J., Christianson, L.L. (1993). "A new similitude modeling technique for studies of non-isothermal room ventilation flows." ASHRAE Trans. **99**(1): 129-138.

Zou, Y. (2000). Velocity decay in air jets for HVAC applications. submitted to ASHRAE winter meeting.